



HAL
open science

Dynamics of seafloor spreading from hydroacoustic analyses of seismic swarms along the three Indian Ocean ridges

Vaibhav Vijay Ingale

► **To cite this version:**

Vaibhav Vijay Ingale. Dynamics of seafloor spreading from hydroacoustic analyses of seismic swarms along the three Indian Ocean ridges. Geophysics [physics.geo-ph]. Université de Bretagne occidentale - Brest, 2023. English. NNT : 2023BRES0057 . tel-04428278

HAL Id: tel-04428278

<https://theses.hal.science/tel-04428278>

Submitted on 31 Jan 2024

HAL is a multi-disciplinary open access archive for the deposit and dissemination of scientific research documents, whether they are published or not. The documents may come from teaching and research institutions in France or abroad, or from public or private research centers.

L'archive ouverte pluridisciplinaire **HAL**, est destinée au dépôt et à la diffusion de documents scientifiques de niveau recherche, publiés ou non, émanant des établissements d'enseignement et de recherche français ou étrangers, des laboratoires publics ou privés.

THESE DE DOCTORAT DE

L'UNIVERSITE DE BRETAGNE OCCIDENTALE

ECOLE DOCTORALE N° 598

Sciences de la Mer et du Littoral

Spécialité : *Géosciences Marines*

Par

Vaibhav Vijay INGALE

Dynamique de l'accrétion océanique à partir de l'analyse de données hydroacoustiques sur des essais sismiques le long des trois dorsales de l'océan Indien

Dynamics of seafloor spreading from hydroacoustic analyses of seismic swarms along the three Indian Ocean Ridges

Thèse présentée et soutenue à Plouzané, le 20 Octobre 2023

Unité de recherche : 6538 Geo-Ocean

Comité de thèse avant la soutenance :

Chastity AIKEN

Chercheur, IFREMER

Christine DEPLUS

Chargée de recherche, CNRS-IPGP

Composition du Jury :

Président :

Marcia MAIA

Directrice de recherche, CNRS Geo-Ocean

Rapporteurs :

Wayne CRAWFORD

Directeur de recherche, CNRS-IPGP

Ross PARNELL-TURNER

Assistant Professor, SIO-UCSD

Examineurs :

Marcia MAIA

Directrice de recherche, CNRS Geo-Ocean

Karin SIGLOCH

Directrice de recherche, CNRS Geoazur

Dir. de thèse :

Jean-Yves ROYER

Directeur de recherche, CNRS Geo-Ocean

Co-dir. de thèse : Sara BAZIN

Physicienne Adjointe, UBO Geo-Ocean

Dedicated to
All my Gurus

Abstract

Mid-ocean ridges represent divergent plate boundaries characterized by the interaction of volcanic and tectonic processes, resulting in the creation of a new ocean floor. These complex interactions lead to the occurrence of numerous low-magnitude earthquakes ($M \leq 4$), which often go unnoticed by terrestrial seismic networks due to the rapid attenuation of seismic waves within the Earth's crust. But, these earthquakes generate T-waves with frequencies of up to 60 Hz in the water column from the conversion of seismic waves into low-frequency hydroacoustic waves at the seafloor which propagate over large distances (several thousands of km) with little attenuation through an acoustic waveguide known as the sound fixing and ranging (SOFAR) channel. The OHASISBIO and IMS-CTBTO networks of hydrophones, designed to record these T-waves in the Indian Ocean, encompass three mid-ocean ridges with contrasted spreading rates: the ultraslow spreading Southwest Indian Ridge (SWIR; 14 mm/yr), the slow spreading Central Indian Ridge (CIR; 40 mm/yr), and the intermediate spreading Southeast Indian Ridge (SEIR; 60 mm/yr) which converge at Rodrigues Triple Junction (RTJ). In this study, we have investigated seismic swarms along these three ridges through the analysis of continuous hydroacoustic records from 2012 to 2020. A comprehensive catalog of 38,910 hydroacoustic events, associated with 15 discrete seismic swarms distributed along the SWIR (3), CIR (5), and SEIR (7) has been constructed. They are observed near two transform faults along the SWIR, on ridge segments along the three ridges, and in the vicinity of hydrothermal fields along the CIR and SEIR. Five swarms include many short-duration (~ 10 -15 seconds) and high-energy impulsive events up to 60 Hz, which we attribute to interactions between hot lava and seawater. Through a closer examination of the spatio-temporal distribution of events within each seismic swarm, we have discerned three distinct origins: magmatic, tectonic, or a complex interplay of both processes. These processes are independent of the spreading rates but depend on the tectonic environments.

Résumé

Les dorsales médio-océaniques sont des limites de plaques caractérisées par l'interaction de processus volcaniques et tectoniques, entraînant la création de nouveaux fonds océaniques. Ces interactions complexes génèrent de nombreux séismes de faible magnitude ($M \leq 4$), passent souvent inaperçus auprès des réseaux sismiques terrestres en raison de l'atténuation rapide des ondes sismiques dans la croûte terrestre. Mais, ces séismes génèrent des ondes T (avec des fréquences allant jusqu'à 60 Hz) dans la colonne d'eau à partir de la conversion de l'énergie sismique en ondes hydroacoustiques basse-fréquence au niveau du plancher océanique; celles-ci se propagent sur de grandes distances (plusieurs milliers de km) avec une faible atténuation à travers le guide d'onde acoustique appelé canal SOFAR (*sound fixing and ranging*). Les réseaux d'hydrophones OHASISBIO et IMS-CTBTO, conçus pour enregistrer ces ondes T dans l'océan Indien, englobent trois dorsales médio-océaniques aux vitesses d'expansion contrastées : la dorsale sud-ouest Indienne ultra-lente (SWIR ; 14 mm/an), la dorsale centrale Indienne lente (CIR ; 40 mm/an) et la dorsale sud-est Indienne à taux intermédiaire (SEIR ; 60 mm/an) qui convergent à la jonction triple de Rodrigues. Dans cette étude, nous avons examiné des essaims sismiques le long de ces trois dorsales à partir d'un ensemble de données hydroacoustiques continues de 2012 à 2020. Un catalogue exhaustif de 38 910 événements hydroacoustiques, couvrant 15 essaims sismiques distincts répartis le long des dorsales SWIR (3), CIR (5), et SEIR (7), a été établi. Ils sont observés à proximité de deux failles transformantes de la SWIR, le long de segments de dorsales des trois rides, et à proximité de champs hydrothermaux de la CIR et de la SEIR. Cinq essaims comprennent de nombreux événements impulsionnels de courte durée (10-15 secondes) et de haute énergie, jusqu'à 60 Hz, que nous attribuons à des interactions entre laves éruptives et eau de mer. En examinant la distribution spatio-temporelle des événements de chaque essaim, nous discernons trois origines distinctes: magmatique, tectonique, ou une interaction complexe des deux processus. Ces processus semblent être indépendants des taux d'expansion, mais varier avec le contexte tectonique.

Acknowledgements

In the depths of the ocean and the tremors of the Earth, I embark on a journey of discovery guided by two extraordinary mentors, whose expertise spans the vast expanse of marine sciences. This scientific voyage would not have been possible without their combined wisdom, enthusiasm, passion, and unwavering belief in my potential. To **Jean-Yves ROYER**, your boundless knowledge, and your love for the deep blue have been an endless source of inspiration. Your ability to decode the language of the ocean and interpret its secrets has fueled my fascination for marine mysteries. To **Sara BAZIN**, your expertise in deciphering the Earth's inner workings has ignited a shift in my understanding of various phenomena. Your mentorship has been the bedrock upon which I built my academic journey. Together, both of you formed a dynamic duo of knowledge and exploration, pushing the boundaries of advanced and creative research. Your encouragement, guidance, freedom of work, and intellectual camaraderie have shaped me into a better scientist and a more curious explorer. Your guidance has been the compass that steered me through the ever-changing currents of research. I must admit that, over the last three years, you both not only helped in my research journey but also in my overall development, the top most will be calmness. I owe a big thanks for improving my writing skills which initially were very unorganized and full of grammatical mistakes. I am grateful for your continuous support in improving my scientific thinking, content writing, and presentation skills.

I am grateful to **Julie PERROT**, **Anne BRIAIS**, and **Jean-Arthur OLIVE** for their invaluable contributions. Your expertise and spirit of collaboration have elevated this project, making it an unforgettable journey. Thank you for being part of this enriching experience.

I am immensely grateful to all the lab members of Lab Geo-Ocean. Your camaraderie, collaborative spirit, and dedication to scientific pursuit have turned the lab into a second home. The discussions, the shared excitement of discoveries, the occasional celebratory high-fives, and BBQ parties, have made this journey all the more memorable. A very special thank you to the admin department, **Margot**, **Charlotte**, and **Véronique**, for your patience with our inability to organize the administrative side of things. To **Christophe Martin**, computer scientist and magician by profession, a petabyte of thanks for services rendered.

My heartfelt appreciation goes to my fellow researchers, **Aude** and **Pierre-Yves** whose cama-

raderie and support have made this scientific voyage a joyous one. Time to time discussions have opened so many interesting questions and I enjoyed traversing through them. To my all lab-mates, **Paul, Lucas, Noémie, Zoé, Edgar, Léa, Théo, Pedro**, the shared laughter, the collaborative brainstorming, and the occasional "eureka" moments have made this academic pursuit an adventure.

The crew on R/V *Marion Dufresne*, you were just amazing. Spending time, carrying out experiments, and exploring the middle-of-nowhere part of the world, fun discussions with **Solena, Llyod, Nadege, Guillaume, Valentin, Syl** was one of the memorable periods during my thesis.

I would also like to thank the University of Brest and the Regional Council of Brittany for the financial support during my thesis, through the ISblue project, Interdisciplinary Graduate School for the blue planet (ANR-17-EURE-0015 under the French government's program "Investissements d'Avenir" for France 2030).

To my best friend, **Dadu**, your unwavering belief in my potential has kept me grounded and inspired, thank you for being the colorful brushstrokes that painted this chapter of my life with joy and laughter. Your presence through thick and thin was always the cherry on the cake.

The last three years in Brest would not have been special without the support of my friends here. Exploring good restaurants in Brest with **Ajay**, was always fun. **Abhi** and **Chinmayi** were my strong supporters during the good and bad times here. Both academic and general discussions with them were always motivating to me. I have always looked up to them in all the walks over the last three years. **Steffi**, the bumper pack full of energy, has given me strong support during the last stages of thesis work. I would also like to thank **Valerie** and **Wayne** for helping me to shift smoothly from Paris to *8 Place de la Liberte, Brest*. Thank you **Antonin** for accommodating me and being a nice housemate.

To the members of **PSLV-AK6** gang, Pankaj, Shekhar, Lokesh, Ameya, and Kshitij, you have been the lighthouse that guided me through the stormy seas of academia. Your love, encouragement, and belief in my abilities have been the buoy that kept me afloat during the challenging times. I am always thankful to the **Sahajach** gang, Rijyuta, Shriya, and Hitesh, for their consistent encouragement. To Sanyukta, Poornima, Sama, Samiksha, and Purva, your presence in my life has been a constant reminder of the strong bonds that tie us together.

I owe a very big thanks to **Ketaki**, without her immense and continuous support, I wouldn't have stood stronger during this thesis work. She has been the fearless co-explorer, the unwavering cheerleader, and the guardian angel of sanity. Her quirky humor, late-night brainstorming sessions, and endless supply of energy have been the secret ingredients that made this thesis journey truly unforgettable. From conquering challenging chapters to celebrating small victories, we've weathered it all together, laughing our way through my academic storms.

In the vast ocean of academia, my family, **Aai, Pappa, Di, Jiju, Aaru**, you have been the lighthouse that has guided me through stormy seas and calm waters alike. Your love, unwavering sup-

port, and encouragement have been the steady winds that propelled me forward. With heartfelt sincerity, I extend my gratitude to each of you for anchoring me and illuminating my path like a guiding star. This thesis stands as a tribute to the resilience of our connection, and I am forever indebted for the luminance you've brought into my life.

I acknowledge all those who contributed to this thesis in their own unique ways. Each one of you has left an indelible mark on this scientific expedition, and I am grateful beyond words. As I set sail into the uncharted waters of the future, I carry with me the invaluable lessons learned and the bonds forged during this doctoral odyssey. To everyone who has been a part of this journey, I extend my heartfelt gratitude and look forward to the adventures that lie ahead.

Contents

Abstract	5
Résumé	7
Acknowledgements	9
List of Figures	17
List of Tables	21
List of Publications and Proceedings	23
Introduction (In English)	25
Introduction (En français)	29
1 Mid-oceanic Ridges	33
1.1 Introduction to mid-ocean ridges	33
1.1.1 Driving forces behind mid-ocean ridges	35
1.1.2 Spreading rates	36
1.1.3 Faults on Mid-ocean ridges	36
1.2 Spreading rates and ridge geometry	38
1.2.1 Fast spreading ridges	39
1.2.2 Intermediate spreading ridges	39
1.2.3 Slow spreading ridges	40
1.2.4 Ultraslow spreading ridges	41
1.3 Mid-ocean ridges in the Indian Ocean	41
1.3.1 The Southwest Indian Ridge	42
1.3.2 The Central Indian Ridge	43
1.3.3 The Southeast Indian Ridge	44
1.4 Seismicity along mid-ocean ridges	44

<i>CONTENTS</i>	13
1.4.1 Earthquake swarms	46
1.4.2 Diking and magmatism	47
1.4.3 Hydrothermal Systems	48
1.4.4 Transform Fault and Ridge Segment	49
1.4.5 Tidal Triggering	51
1.5 Monitoring seafloor spreading seismicity	51
1.5.1 Seismicity along fast spreading ridges	52
1.5.2 Seismicity along intermediate spreading ridges	52
1.5.3 Seismicity along slow-spreading ridges	55
1.5.4 Seismicity along ultraslow spreading ridges	57
1.5.5 Importance of studying the seismicity in the Indian Ocean	60
1.5.6 Importance de l'étude de la sismicité dans l'Océan Indien (En français)	61
2 Seismicity in the Ocean: Contribution of Hydroacoustic Monitoring	63
2.1 Nature and propagation of hydroacoustic sounds	63
2.1.1 Acoustic waves in a fluid medium	63
2.1.2 Sound velocity in the ocean	64
2.1.3 Sound Level measurement	66
2.2 Ambient noises	66
2.3 T-waves	69
2.3.1 Definition	69
2.3.2 Generation and propagation of T-waves	70
2.3.3 Propagation loss of T-waves	74
2.4 Seismic sources and T-waves	75
2.5 Hydrophone arrays	78
2.5.1 The OHASISBIO network	79
2.5.2 The IMS-CTBTO network	84
2.6 Seismic clusters	85
2.6.1 Extracting seismic clusters from land-based catalogs	85
2.6.2 Detection of T-waves	88
2.7 Elaboration and analysis of hydroacoustic catalogs	92
2.7.1 Selection of time-window	93
2.7.2 Source Level Estimation	94
2.7.3 Detection Threshold	94
2.7.4 Temporal distribution of seismicity	96
2.7.5 Modified Omori law	97

2.7.6	Faulting and stress-induced modeling	98
2.7.7	Tidal Oscillations	99
2.8	Elaboration et analyse des catalogues hydroacoustiques (En français)	100
2.8.1	Sélection de la fenêtre temporelle	100
2.8.2	Estimation du niveau de la source	101
2.8.3	Seuil de détection	101
2.8.4	Distribution temporelle de la sismicité	101
2.8.5	Loi d’Omori modifiée	102
2.8.6	Modélisation des failles et des contraintes	103
2.8.7	Oscillations des marées	103
3	Southwest Indian Ridge Swarms	105
3.1	Swarms in 2018: MDPI-Geosciences Article	106
3.2	Swarms in 2016: BSSA Article	128
3.3	Summary of the observations of the SWIR swarms	157
3.4	Résumé des observations sur les essaims SWIR (En français)	158
4	Central Indian Ridge Swarms	159
4.1	Introduction	161
4.2	Data and Methods	163
4.3	Results	166
4.3.1	Seismicity in February-May 2013	166
4.3.2	Seismicity in November-December 2013	168
4.3.3	Seismicity in April 2019	169
4.3.4	Seismicity in April 2020	170
4.3.5	Seismicity in April-September 2020	171
4.4	Discussion	173
4.4.1	Geographical extent of the swarms	173
4.4.1.1	Events in February-May 2013	173
4.4.1.2	Events in November-December 2013	175
4.4.1.3	Events in April 2019 and April 2020	176
4.4.1.4	Events in April-September 2020	177
4.4.2	Tidal effect on the seismicity	181
4.4.3	Magmatic and tectonic processes in the vicinity of Hydrothermal Fields	184
4.5	Summary of the observations	185
4.6	Résumé des observations (En français)	186

<i>CONTENTS</i>	15
5 Southeast Indian Ridge Swarms	189
5.1 Introduction	190
5.2 Data and Methods	193
5.3 Results	197
5.3.1 On SEIR Segment at 29°S	197
5.3.2 On SEIR Segment at 28°S	199
5.3.3 On SEIR Segment at 40°S	200
5.4 Discussion	203
5.4.1 Tidal effect on seismicity distribution	203
5.4.2 Nature of seismicity and accretion process	205
5.4.3 Repetitive nature of swarms	208
5.5 Summary of observations of the SEIR swarms	210
5.6 Résumé des observations sur les essais SEIR (En français)	210
6 Discussion	213
6.1 Contribution of hydroacoustics	213
6.1.1 Magnitude of completeness	214
6.1.2 Spatial variation in b-values	216
6.1.3 Mainshock-aftershock sequences (modified Omori's laws)	220
6.1.4 Presence of impulsive events	221
6.2 Effects of the network geometry on localization errors	234
6.3 Origin of the seismic swarms along the three Indian ridges	237
6.4 Origine des essais sismiques le long des trois dorsales indiennes	245
Conclusions	253
Conclusions (En français)	257
Prospects	261
Perspectives (En français)	265
A Seas Manual	269
A.1 Seas: Picking and Analysis	269
A.2 Format of Input files	273
A.3 Format of Output file	276
B Hydrophone sensitivities	278

C	Supplementary material for MDPI-Geoscience Paper	279
D	Supplementary material for BSSA Paper	285
E	Magnitude of Completeness	297
F	Swarms near Saint-Paul-Amsterdam Plateau	299
	References	303

List of Figures

1.1	Movement of plate boundaries	34
1.2	Global map of mid-ocean ridges	35
1.3	Ridge push and slab pull	36
1.4	Fault plane geometry	37
1.5	Oceanic vs continental transform faults	38
1.6	Schematic of the axial region of mid-ocean ridges	39
1.7	Axial morphology and spreading rates	40
1.8	Seafloor spreading and magma supply	41
1.9	Southwest Indian Ridge profile	42
1.10	Central Indian Ridge profile	43
1.11	Methods to detect seismicity along mid-ocean ridges	45
1.12	Sesmic swarm vs. mainshock-aftershock sequence	46
1.13	Cartoon showing dike propagation	47
1.14	Seismicity near hydrothermal field on the East Pacific Rise	49
1.15	Focal mechanisms along the ridge axis	50
1.16	Frequency-size distribution of earthquakes along the Mid-Atlantic Ridge	50
1.17	Tidal triggering of microseismicity	51
1.18	Hydroacoustic detections along the East Pacific Rise	53
1.19	Hydroacoustic detections along the Endeavor Segment	54
1.20	ISC catalog events along the SEIR between 1980 and 2020	55
1.21	Hydroacoustic detections along the Mid-Atlantic Ridge	56
1.22	ISC catalog events along the CIR between 1980 and 2020	58
1.23	Seismicity along the Gakkel Ridge	58
1.24	ISC catalog events along the SWIR between 1980 and 2020	59
2.1	Sound velocity, temperature, and salinity profiles in the Indian Ocean	65
2.2	A bend in sound velocity profile	65
2.3	Spectra of oceanic ambient noise	67

2.4	Shape of T-wave	70
2.5	First detection of T-wave	71
2.6	Potential T-wave generation mechanisms	72
2.7	T-waves of the Aleutian earthquake on 29 July 1965	73
2.8	Cartoon of the generation and propagation of T-waves	75
2.9	Example of a relation between SL and mb	76
2.10	Example of the relation between SL and M_w	77
2.11	OHASISBIO and IMS-CTBTO network in the Indian Ocean	79
2.12	Hydrophone mooring	81
2.13	Method of triangulation to locate hydrophone	82
2.14	Acoustic release	83
2.15	Hydrophone recovery	83
2.16	Global IMS-CTBTO network	84
2.17	IMS-CTBTO hydrophone triplet near the Crozet Island	85
2.18	Seismic clusters from 2010 to 2020 along the three Indian MORs	86
2.19	Selection of seismic clusters for this study	87
2.20	30-minute T-wave spectrogram (<i>Seas</i> window)	90
2.21	Example of event detection	92
2.22	10 minute T-wave spectrogram (<i>Seas</i> window)	93
2.23	Flow chart of the work	93
2.24	Frequency-size distribution of hydroacoustic events (SL)	95
2.25	Type of earthquake sequences	97
4.1	Study region along the CIR	161
4.2	Histogram of localization errors along the CIR	164
4.3	Magnitude of completeness for the events detected along the CIR	165
4.4	Relation between SL and different magnitude scales for the events along the CIR	167
4.5	Events near the Pelagia and Kairei HFs in 2013	167
4.6	Events near the Kairei HF in Nov-Dec 2013	169
4.7	Events along the CIR segments in April 2019	170
4.8	Events along the CIR segments in April 2020	171
4.9	Events near the Edmond HF in April-September 2020	172
4.10	Temporal distribution of events near the Edmond HF	173
4.11	Stress modeling for M_w 5.0 event near the Pelagia HF	174
4.12	Stress modeling for M_w 5.0 event near the Kairei HF	174
4.13	GCMT events near the Kairei HF in Nov-Dec 2013	175

4.14	Aftershock sequence near the Kairei HF starting on 25 November 2013	176
4.15	Stress modeling for M_w 5.1 event near the Kairei HF	176
4.16	Aftershock sequence along segments 8-9 starting on 11 April 2019	177
4.17	GCMT events near the Edmond HF between April and September 2020	178
4.18	Aftershock sequence near the Edmond HF starting on 17 April 2020	179
4.19	Stress modeling for M_w 5.8 event near the Edmond HF	179
4.20	Aftershock sequence near the Edmond HF starting on 29 April 2020	180
4.21	Stress modeling for M_w 4.9 event near the Kairei HF	181
4.22	Impulsive events near the Edmond HF	181
4.23	Aftershock sequence near the Edmond HF starting on 07 June 2020	182
4.24	Comparison of tidal heights and seismicity near the Pelagia HF	183
4.25	Comparison of tidal heights and seismicity along the segments 8-9	184
5.1	Study region along the SEIR	191
5.2	Bathymetry of Saint-Paul-Amsterdam Region	193
5.3	Histogram of localization errors along the 28°S-29°S SEIR segments	194
5.4	Magnitude of completeness for the events detected along the 28°S-29°S SEIR segments	195
5.5	Relation between SL and different magnitude scales for the events along the 28°S-29°S SEIR segments	196
5.6	Relation between SL and different magnitude scales for the events along the J3 segment	196
5.7	Events along the 29°S segment in 2012	198
5.8	Events along the 29°S segment in 2018	199
5.9	Events along the 28°S segment in 2015	200
5.10	Events along the 28°S segment in 2019	200
5.11	Events along the J3 segment in 2020	201
5.12	Histogram of localization errors along the J3 segment	202
5.13	Comparison of tidal heights and seismicity along the SEIR segments	203
5.14	Dynamics of a magma chamber and tidal influence	204
5.15	Comparison of tidal heights and seismicity along 29°S segment in 2018	205
5.16	Aftershock sequence along the J3 segment starting on 4 December 2020	207
5.17	Stress modeling for M_w 5.0 event along the J3 segment	208
6.1	Magnitude of completeness for all the swarm events	216
6.2	Spatial variation of b -values along the transform faults	219
6.3	Spatial variation of b -values along the ridge segments	219
6.4	Spatial variation of b -values near the hydrothermal fields	220

6.5	Similarity of Impulsive signal (Tiktak volcano and Melville TF)	222
6.6	Pre- and post-seismic bathymetry grids near the Edmond HF	223
6.7	Pre- and post-seismic bathymetry contours near the Edmond HF	223
6.8	Backscatter imagery near the Edmond HF	224
6.9	Network geometry and localization errors	234
6.10	Histogram of errors for the different number of hydrophones	236
6.11	Location and origin time uncertainties of events near the Melville TF	237
A.1	Example of the loc file for <i>Seas</i> software	273
A.2	Example of the Input file for <i>Seas</i> software	274
A.3	Example of wfdisc file for <i>Seas</i> software	275
A.4	Example of event detection	276
E.1	Relation between SL and magnitude scales of completeness near the Melville TF	297
E.2	Relation between SL and magnitude scales of completeness near the Novara TF	297
E.3	Relation between SL and magnitude scales of completeness along the segment 4	297
E.1	Event along the SPA plateau in 2012	300
E.2	Histogram of localization errors of the events near the SPA plateau	300
E.3	Temporal distribution of events near the SPA plateau (Mar-Apr 2012)	301
E.4	Temporal distribution of events near the SPA plateau (Oct-Nov 2012)	301

List of Tables

1.1	Spreading rates of mid-ocean ridges	36
2.1	Hydrophones of OHASISBIO network	80
2.2	List of seismic clusters along the three Indian Ocean Ridges	88
4.1	OHASISBIO hydrophones for CIR swarms	163
4.2	Summary of results along the CIR	182
5.1	OHASISBIO and IMS-CTBTO hydrophones for SEIR swarms	194
5.2	Summary of results along the SEIR	209
6.1	Summary of the detection thresholds in terms of the magnitude of completeness	215
6.2	Summary of b -values along the three Indian MORs I	217
6.3	Summary of b -values along the three Indian MORs II	218
6.4	Summary of impulsive events along the three Indian MORs	225
6.5	Summary of error distribution seismic swarms studied in this thesis	235
6.6	Summary of seismic swarms studied in this thesis	238
6.7	Interpretation of seismic swarms studied in this thesis	239

List of Publications and Proceedings

Scientific Publications

1. **Ingale, V. V.**, Bazin, S., Olive, J.-A., Briais, A., and Royer, J.-Y. (2023). Hydroacoustic study of a seismic swarm in 2016-2017 near the Melville Transform Fault on the Southwest Indian Ridge. *Bulletin of Seismological Society of America*, 113 (4), 1523-1541 ([Link](#))
2. **Ingale, V. V.**, Bazin, S., and Royer, J.-Y. (2021). Hydroacoustic observations of two contrasted seismic swarms along the Southwest Indian Ridge in 2018. *Geosciences*, 11, 225, ([Link](#))

Conference Papers

1. **Ingale, V. V.**, Bazin, S., and Royer, J.-Y. (2023). Energetic and short water-born signals from mid-oceanic ridges, *Underwater Acoustics Conference and Exhibition Series (UACE)*, June 2023, Kalamata, Greece.

Conference Proceedings

1. **Ingale, V. V.**, Raumer, P.-Y., Bazin, S., and Royer, J.-Y. (June 2023). Detection of T-waves associated with mid-ocean ridge seismicity recorded by hydroacoustic networks: manual versus automatic approaches, *Science and Technology Conference (SnT)*, Vienna, Austria.
2. **Ingale, V. V.**, Bazin, S., and Royer, J.-Y. (September 2022). Hydroacoustic detections of seismic clusters along the mid-ocean ridges in the Indian Ocean using hydrophones of CTBTO and OHASISBIO network, *International Hydroacoustic Workshop*, Vienna, Austria. ([Link](#)).
3. **Ingale, V. V.**, Bazin, S., and Royer, J.-Y. (June 2022). Hydroacoustic observations of a seismic cluster at Melville Fracture Zone along the Southwest Indian Ridge in 2016-17. *SERENADE Workshop*, Brest, France, ([Link](#)).
4. **Ingale, V. V.**, Bazin, S., and Royer, J.-Y. (May 2022). Hydroacoustic observations of a seismic cluster at Melville Fracture Zone along the Southwest Indian Ridge in 2016-17. *EGU General Assembly 2022*, Vienna, Austria, EGU22-462 ([Link](#)).

5. **Ingale, V. V.**, Bazin, S., and Royer, J.-Y. (**March 2022**). Hydroacoustic observations of seismic swarms along the Southwest Indian Ridge of the Indian Ocean. *International Indian Ocean Science Conference*, online, Goa, India, ([Link](#)).
6. **Ingale, V. V.**, Bazin, S., and Royer J.-Y. (**October 2021**). Hydroacoustic detections of seismic swarms along mid-ocean ridges in the Indian Ocean. *EMSO Time Series Conference on Observing Ocean Sound*, PLOCAN, Gran Canaria, ([Link](#)).
7. **Ingale, V. V.**, Bazin, S., and Royer, J.-Y. (**April 2021**). Hydroacoustic observations of two contrasted seismic swarms along the Southwest Indian Ridge in 2018. *EGU General Assembly 2021*, online, EGU21-5131, ([Link](#)).

In collaboration

1. Raumer, P.-Y., Bazin, S., Cazau, D., **Ingale, V. V.**, Lavayssière, A., and Royer, J.-Y. (**May 2023**). Application of machine learning to hydro-acoustic seismic and magmatic events detections, *EGU General Assembly 2023*, Austria, EGU23-7028 ([Link](#)).
2. Raumer, P.-Y., Bazin, S., Cazau, D., **Ingale, V. V.**, Lavayssière, A., and Royer, J.-Y. (**May 2023**). Application of machine learning to hydro-acoustic volcanic event detections, *HPC Workshop for Nuclear Explosion Monitoring*, Vienna, Austria.

Complementary activities

1. Participation in **OBS-AUSTRAL** ocean campaign from 1 February to 5 March 2022 on R/V *Marion Dufresne* (MD236) to recover and re-deploy OHASISBIO hydrophones

Introduction

**BROTHER: IF I MAKE A PEANUT BUTTER AND
JELLY SANDWICH AM I THE MID OCEAN RIDGE**

ME: NO WHY



Rising up to 2000 meters below the sea surface with graceful prominence from the oceanic depths, mid-ocean ridges (MORs) represent the divergent boundaries of tectonic plates and play a foundational role in shaping the composition and dynamics of the oceanic lithosphere. Stretching across an impressive expanse of approximately 70,000 kilometers, this unbroken chain of volcanic mountain range crisscrosses the world's oceans, standing as one of the most commanding and consequential geological features etched upon Earth's surface. The elucidation of the oceanic magnetic anomalies, due to alternating bands of positive and negative magnetized crust, symmetrically paralleling the axis of the ridges, brought forth pivotal evidence that bolstered the concept of seafloor spreading in the theory of plate tectonics.

As plates diverge and move apart, the underlying asthenospheric mantle experiences an ascent, leading to the partial melting of mantle rocks and the birth of nascent oceanic crust. This freshly minted crust, subject to considerable forces and stresses, undergoes the development of fractures and faults, facilitating the circulation of hydrothermal fluids and catalyzing transformative chemical processes. Within this dynamic interplay, which encompasses tectonic actions through active faulting, volcanic phenomena including dike intrusions and seafloor eruptions, and the intricate choreography of hydrothermal fluid movement, earthquakes emerge as a natural outcome. Importantly, volcanic activities often engender seismic swarms typified by the prevalence of low-magnitude seismic events. The magnitudes and frequencies of these events within these swarms exhibit intricate temporal variations, reflecting the complexity of subsurface processes. In the realm of tectonics, robust mainshocks followed by aftershocks adhere to an exponential decay law, with a decay parameter known as p -value, closely linked to the thermal characteristics of the oceanic lithosphere.

In the era preceding the 1990s, investigations of the seismicity occurring along mid-ocean ridges (MORs) were primarily reliant on data from terrestrial seismological networks, despite their limitations in capturing the full spectrum of low-magnitude seismic events. The advent of sonobuoys and ocean-bottom seismometers marked a notable advancement, elevating the sensitivity of event detection and localization. However, these methods were constrained by their applicability to specific ridge segments and temporal windows. The post-Cold War period witnessed a paradigm shift in naval operations with the establishment of hydrophone networks, ushering in a transformative phase in seismic detection capabilities. This revolutionary approach not only facilitated the identification of low-magnitude events but also extended the spatial coverage, transcending the limitations of previous methodologies.

At the crux of this hydroacoustic revolution lies the recording of T waves, a distinctive acoustic phase generated by seismic waves at the epicentral regions. Notably, these T-waves propagate over vast distances with minimal attenuation through an acoustic waveguide termed the sound fixing and ranging channel. The strategic utilization of T-wave detection has since emerged as a

cornerstone in the hydroacoustic framework, exhibiting unparalleled efficacy in enabling the observation of low-magnitude seismicity across the expanse of the world's oceans like the Pacific and Atlantic (e.g. [Fox et al., 1995](#); [Smith et al., 2003](#); [Dziak et al., 2004](#); [Bohnenstiehl et al., 2004](#)). This methodology has notably augmented our capacity to glean insights from ocean ridges, thereby expanding our comprehension of the underlying geophysical processes that govern seismic phenomena within these submerged geological terrains.

In the southern Indian Ocean, the convergence of three spreading ridges with varying rates of spreading takes place at the Rodrigues Triple Junction. The Southwest Indian Ridge (SWIR) separates the Antarctic and Nubian plates at an ultra-slow spreading rate of 14 mm/yr. The Central Indian Ridge (CIR) separates the Indo-Australian and Nubian plates at a slow spreading rate of 40 mm/yr. The Southeast Indian Ridge (SEIR) is the fastest of the three, with an intermediate spreading rate of 60 mm/yr, separating the Indo-Australian and Antarctic plates. This unique configuration of ridges offers an exceptional opportunity to investigate the relationship between seismic swarms and spreading rates. Systematic analyses of hydroacoustic records of seismic swarms along these three ridges should provide a more complete collection of events per swarms, representative of the different seafloor spreading contexts. Based on such information, this thesis attempts to address the following questions:

- What are the different types of seismic activity along mid-oceanic ridges?
- What does seismicity tell about underlying lithosphere?
- How does the seismicity reflect different spreading environments?
- What does the distribution of seismic swarms tell us about accretionary processes?
- In terms of tectonic mainshock-aftershocks sequences, what is the behavior of the decay rate, known as p -value, in varying spreading environments?

In pursuit of these objectives, I did a comprehensive analysis of hydroacoustic data spanning from 2012 to the end of 2020 and collected along the SWIR, the CIR, and the SEIR by the OHA-SISBIO and IMS-CTBTO networks of hydrophones. This study provides novel insights into the dynamic geological processes taking place beneath the oceanic crust. This research seeks to unravel the complexities of tectonic and magmatic interactions by quantifying seismic parameters such as event locations, uncertainties in location and origin time, source levels, and frequency content.

Hence, this thesis is divided into six different chapters covering the state-of-the-art and key results from my analyses:

1. The first chapter introduces MORs and their segment scale structures, and discusses their morphology in different spreading regimes and the associated seismicity. It also includes a literature review of the three Indian Ocean ridges: the SWIR, the CIR, and the SEIR.
2. The second chapter is devoted to the hydroacoustic approach and its contribution to the study of seismic swarms along spreading ridges. It presents a few general points on acoustic sound waves and T waves in particular, and how they were recorded. The state-of-the-art defines the extraction of clusters of earthquakes from the terrestrial catalogs to select the hydroacoustic records associated with them. The chapter then describes the following steps, which are to produce a hydroacoustic catalog from these data and to analyze these catalogs.
3. The third chapter describes my analyses of three seismic swarms observed along the SWIR. These swarms, near Novara transform fault (TF) in 2018, near Melville TF in 2016-17, and along a ridge segment at 67°45'E in 2018 were among the strongest swarms, in terms of the number of events reported in land-based catalogs along the SWIR. Here I discuss their detailed characteristics and nature based on the spatio-temporal distribution of events and associated geodynamic context. The results from this chapter have been published in 2021 and 2023 in two journals.
4. The fourth chapter focuses on a seismicity study of the southern end of CIR. Along this ridge, near the Indian Ocean Triple Junction, five distinctive seismic swarms were reported. Three of them are located in the vicinity of hydrothermal fields (HF) including two near the Kairei HF in 2013, one near the Edmond HF in 2020, and two on a CIR segment, north of Edmond HF in 2019 and 2020. Chapter four documents their characteristics and nature based on the spatio-temporal distribution of the events.
5. The fifth chapter moves on the SEIR, where some seismic swarms occurred repetitively on ridge segments at 29°S, in July, and December 2012, and 2018, and at 28°S, in 2015 and 2019. Apart from them, a major one occurred on the J3 segment in 2020, at the southern edge of the Saint-Paul Amsterdam plateau. The chapter will highlight the key findings of these repetitive swarms based on improvised catalogs.
6. The sixth chapter summarizes and discusses the key observations and differences associated with all the seismic sequences studied along the three Indian ridges. It also addresses the questions posed at the start of the thesis.
7. The main conclusions and some perspectives will be developed in the final section of this dissertation.

Introduction (En français)

Gracieuses proéminences s'élevant des profondeurs océaniques jusqu'à 2 000 mètres sous la surface de la mer, les dorsales médio-océaniques (MOR) représentent les limites divergentes des plaques tectoniques et jouent un rôle fondamental dans la construction et la dynamique de la lithosphère océanique. S'étirant sur une distance impressionnante d'environ 70 000 kilomètres, cette chaîne ininterrompue de montagnes volcaniques traverse les océans du monde entier et constitue l'une des structures géologiques les plus imposantes et les plus importantes de la surface de la Terre. L'élucidation des anomalies magnétiques océaniques, dues à l'alternance de bandes crustales magnétisées positivement et négativement, et disposées symétriquement et parallèlement à l'axe des dorsales, a apporté les preuves décisives qui ont étayé le concept d'expansion des fonds océaniques dans la théorie de la tectonique des plaques. Expression visible des courants convectifs sous-jacents de la Terre, les dorsales sont chorégraphiées par le mouvement des plaques tectoniques.

Lorsque les plaques divergent et s'écartent, le manteau asthénosphérique sous-jacent subit une ascension adiabatique, qui entraîne la fusion partielle des roches du manteau et la naissance d'une nouvelle croûte océanique. Cette croûte fraîchement créée, soumise à des forces et à des contraintes considérables, se fracture; les failles facilitent la circulation de fluides hydrothermaux qui catalysent des processus chimiques d'altération. Dans une interaction dynamique, les mouvements tectoniques le long des failles actives, les phénomènes volcaniques, notamment les intrusions de dikes et les éruptions sur les fonds marins, et les circulations hydrothermales, génèrent de nombreux tremblements de terre. Notamment, l'activité volcanique engendre souvent des essaims sismiques caractérisés par la prédominance d'événements de faible magnitude. L'ampleur et la fréquence de ces événements au sein de ces essaims présentent des variations temporelles reflétant la complexité des processus souterrains. Dans le domaine de la tectonique, les séquences avec un fort séisme suivi de répliques obéissent à une loi de décroissance exponentielle, caractérisée par le paramètre appelé p étroitement lié aux caractéristiques thermiques de la lithosphère océanique.

Avant les années 1990, l'étude de la sismicité le long des dorsales médio-océaniques (MOR) se fondait principalement sur les données des réseaux sismologiques terrestres, malgré leurs limites à capturer l'ensemble du spectre des événements sismiques de faible magnitude. L'avènement des bouées acoustiques et des sismomètres de fond de mer a marqué un progrès notable, en augmentant le seuil de détection et en améliorant la localisation des événements. Toutefois, la mise en oeuvre de ces méthodes est limitée à des petites sections de dorsale et par leur autonomie. L'après-guerre froide a vu un changement de paradigme avec la mise en place de réseaux d'hydrophones élargissant les capacités de détection sismique. Cette approche révolutionnaire a non seulement facilité la détection et la localisation d'événements de faible magnitude, mais a également étendu la couverture spatiale, transcendant les limites des méthodologies précédentes.

Au cœur de cette révolution hydroacoustique se trouve l'enregistrement des ondes T, une phase acoustique distincte générée par les ondes sismiques dans les régions épacentrales. Ces ondes T possèdent la propriété unique de se propager sur de grandes distances avec une faible atténuation, principalement en raison de leur capture par le guide d'ondes acoustiques appelé canal SOFAR (*SOund Fixing And Ranging channel*). La détection des ondes T s'est depuis lors imposée comme un outil privilégié pour l'observation de la sismicité de faible magnitude à travers l'étendue des océans du monde. Cette approche a notamment augmenté notre capacité à glaner des informations sur les dorsales océaniques, élargissant ainsi notre compréhension des processus géophysiques sous-jacents qui régissent les phénomènes sismiques sous-marins.

Dans le sud de l'océan Indien, trois dorsales d'expansion à taux d'expansion contrastés se rejoignent au point triple de Rodrigues. La dorsale sud-ouest Indienne (SWIR) sépare les plaques antarctique et africaine à une vitesse d'expansion ultra-lente de 14 mm/an. La dorsale centrale Indienne (CIR) sépare les plaques indo-australienne et africaine à une vitesse d'ouverture lente de 40 mm/an. La dorsale sud-est Indienne (SEIR) est la plus rapide des trois, avec une vitesse d'ouverture intermédiaire de 60 mm/an, séparant les plaques indo-australienne et antarctique. Cette configuration de dorsales dans le sud de l'océan Indien offre une occasion exceptionnelle d'étudier la relation entre essaims sismiques et les taux d'expansion. Une analyse systématique d'enregistrements hydroacoustiques d'essaims sismiques le long de ces trois dorsales devraient fournir une collection plus complète d'événements par dorsale, représentatifs des différents contextes d'expansion des fonds océaniques. Sur la base de ces informations, cette thèse tente de répondre aux questions suivantes:

- Quels sont les différents types d'activité sismique le long des dorsales médio-océaniques?
- Comment la sismicité reflète-t-elle les différents environnements d'expansion?
- Quelle est la récurrence des essaims magmatiques à différentes vitesses d'ouverture?

- Concernant les séquences tectoniques de type choc principal-répliques, le taux de décroissance, ou paramètre p , varie-t-il selon le contexte d'expansion?

Pour atteindre ces objectifs, j'ai procédé à une analyse complète des données hydroacoustiques recueillies de 2012 à fin 2020 le long des trois dorsales SWIR, CIR et SEIR par les réseaux d'hydrophones OHASISBIO et IMS-CTBTO. Cette étude apporte un éclairage nouveau sur les processus géologiques dynamiques qui se déroulent sous la croûte océanique. Cette recherche vise non seulement à démêler les complexités des interactions tectoniques et magmatiques, mais aussi à quantifier les paramètres sismiques tels que la localisation des événements, les niveaux source et leur contenu en fréquence, afin de mettre en lumière les mécanismes sous-jacents qui régissent l'activité sismique dans cet environnement marin unique.

Cette thèse sera ainsi divisée en six chapitres couvrant l'état de l'art et les principaux résultats de mes analyses:

1. Le premier chapitre présente les dorsales médio-océaniques et leurs structures à l'échelle du segment, et discute de leur morphologie dans différents régimes d'expansion et de la sismicité associée. Il comprend également une revue de la littérature sur les trois dorsales de l'océan Indien : SWIR, CIR et SEIR.
2. Le deuxième chapitre est consacré à l'approche hydroacoustique et à sa contribution à l'étude des essais sismiques le long des dorsales. Il présente quelques points généraux sur les ondes acoustiques et les ondes T en particulier, ainsi que sur la manière dont elles ont été enregistrées. L'état de l'art explique l'extraction d'essais de séismes à partir des catalogues terrestres pour sélectionner les enregistrements hydroacoustiques associés. Le chapitre décrit les étapes suivantes, la construction d'un catalogue hydroacoustique à partir de ces données et les outils d'analyse de ces catalogues.
3. Le troisième chapitre décrit mes analyses de trois essais sismiques observés le long de la dorsale sud-ouest Indienne: à proximité de la faille transformante de Novara (TF) en 2018, à proximité de la TF de Melville en 2016-17, et le long d'un segment de dorsale à 67°45'E en 2018. Ces essais sont les plus importants, en termes de nombre d'événements détectés par les réseaux terrestres le long de cette dorsale. Je discute ici de leurs caractéristiques détaillées et de leur nature sur la base de la distribution spatio-temporelle des événements et du contexte géodynamique associé. Les résultats de ce chapitre ont été publiés en 2021 et 2023 dans deux revues à comité de lecture.
4. Le quatrième chapitre est consacré à une étude de la sismicité de l'extrémité sud de la dorsale centrale Indienne. Le long de cette dorsale, à proximité du point triple de l'océan In-

dien, cinq essais sismiques distincts sont observés. Trois d'entre eux sont situés à proximité de champs hydrothermaux (HF), dont deux près du HF de Kairei en 2013, un près du HF d'Edmond en 2020, et deux sur un segment du CIR, au nord du HF d'Edmond en 2019 et 2020. Le chapitre documente leurs caractéristiques et leur nature sur la base de la distribution spatio-temporelle des événements.

5. Le cinquième chapitre porte sur la dorsale sud-est Indienne, où certains essais sismiques se sont produits de manière répétitive sur des segments de dorsale à 29°S, en juillet et décembre 2012, et 2018, et à 28°S, en 2015 et 2019. En outre, un essaim important s'est produit sur le segment J3 en 2020, à la limite sud du plateau de Saint-Paul Amsterdam. Le chapitre décrit les principales caractéristiques de ces essais.
6. Le sixième chapitre résume et discute les principales observations et différences associées à toutes les séquences sismiques étudiées le long des trois dorsales indiennes. Il aborde également les questions posées au début de la thèse.
7. Les principales conclusions et quelques perspectives seront développées dans la dernière partie de ce mémoire.

Chapter 1

Mid-oceanic Ridges

1.1 Introduction to mid-ocean ridges

The contemporary acknowledgment of Earth's landmasses as dynamic entities has become widespread, but this perception was not universally established in the past. It was during the early 20th century that Alfred Wegener, a German scientist, advanced the hypothesis of "Continental Drift," positing the motion of Earth's continents. Wegener's proposition originated from his astute observation of the remarkable similarity between the coastlines of western Africa and eastern South America, exhibiting a puzzle-like congruence. This observation prompted him to speculate on the potential past connection and subsequent separation of these land masses. Wegener's theory faced criticism but sparked inquiries despite a lack of evidence. Oceanic exploration in the 1950s reignited interest, leading to the formulation of the "theory of plate tectonics" in the late 1960s. It encompasses the geological framework wherein the Earth's lithosphere, characterized by its brittle surface layer, is divided into multiple rigid plates. These plates undergo continuous motion, over the underlying ductile asthenosphere and are described in terms of the motions of rigid plates on a sphere ([McKenzie and Parker, 1967](#)). It also emerged as the pioneering phenomenon that provided a comprehensive explanation for a wide range of observations, such as the geographical distribution of fossils, earthquake occurrences, the distinct metamorphic facies, and the formation of mountain ranges ([McKenzie, 1967](#); [Sykes and Sbar, 1973](#)).

The core of plate tectonics is the movement of adjacent plates, either continental or oceanic, with most deformation occurring at their interacting boundaries. These boundaries are broadly classified into three types (Figure 1.1):

1. **Divergent** or constructive boundaries: where two tectonic plates spread apart and molten

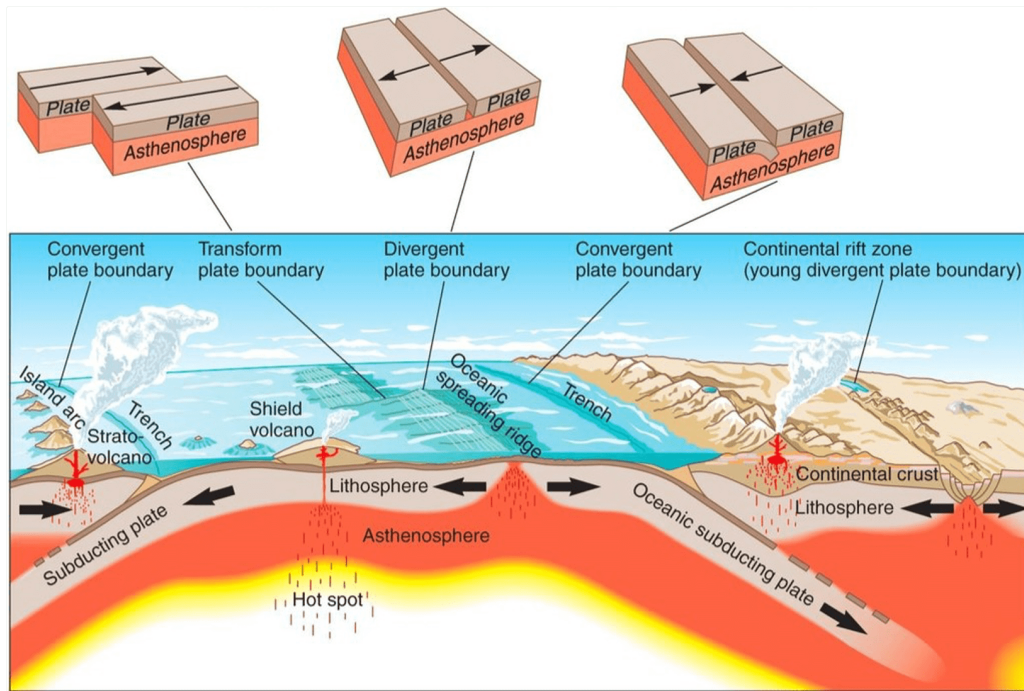


Figure 1.1: Schematic cross-section illustrating plate boundaries (by José F. Vigil from *This Dynamic Planet*)

rock from the mantle upwelling forms a new solid crust (e.g. oceanic spreading centers).

2. **Convergent** or destructive boundaries: where two plates move toward each other. At subduction, denser oceanic plate sinks beneath the continental plate, forming deep ocean trenches (e.g. Sunda trench). The rocks either pulled down under the continental melt or can rise to the surface, creating a line of volcanoes and islands.
3. **Transform** or conservative boundaries: where two plates slide past each other (e.g. San Andreas fault).

The oceanic spreading centers, also called ridges, occur along divergent plate boundaries (Le Pichon, 1968). These spreading centers are characterized by the upwelling of magma from the mantle, which fills the gap created as tectonic plates move apart. The magma solidifies as lava, resulting in the creation of a new oceanic crust. This process, known as seafloor spreading, contributes to the continuous expansion of the ocean basins and the growth of ridges.

The existence of such spreading centers, hidden deep beneath the ocean, was unknown until the 1950s (Heezen et al., 1959). The development of echo-sounding techniques in the early 20th century was a game changer in revealing the seafloor morphology by a single beam following the path of a ship. Through ocean floor surveys conducted, such as by the *Vema* research vessel from Columbia University, data revealed a massive mountain chain running through the Atlantic, named the Mid-Atlantic Ridge. Initially believed to be unique to the Atlantic, further surveys discovered ridge segments in all oceans. Although only in the Atlantic is the ridge centered in the

ocean, nonetheless, they are universally referred to as "mid-ocean" ridges. Globally, it forms the longest chain of underwater volcanoes, which is approximately 70,000 km in length (Figure 1.2). It hosts several volcanic, tectonic, and hydrothermal activities. The ridges rise 1000–3000 m above the sea floor and have average depths of about 2000 m.

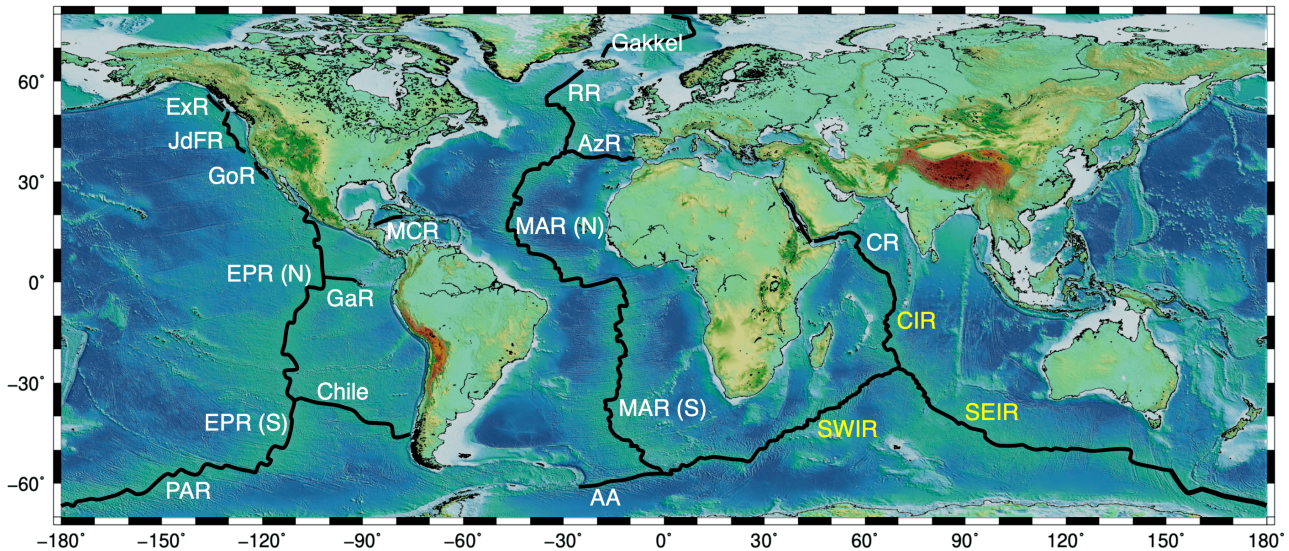


Figure 1.2: Global mid-ocean ridges: AA, America-Antarctic ridge; AzR, Azores ridge; CR, Carlsberg ridge, Chile ridge; CIR, Central Indian ridge; EPR, East Pacific Rise (north and south); ExR, Explorer ridge, Gakkel ridge; GaR, Galapagos ridge; GoR, Gorda ridge; JdFR, Juan de Fuca ridge; MAR, Mid-Atlantic ridge (north and south); MCR, Mid-Cayman ridge; PAR, Pacific-Antarctic ridge; RR, Reykjanes Ridge; SEIR, Southeast Indian ridge; SWIR, Southwest Indian ridge. The ridges studied in this work are marked in yellow.

1.1.1 Driving forces behind mid-ocean ridges

There could be two main driving forces behind the plate motion and the formation of spreading ridges (Forsyth and Uyeda, 1975):

1. **Ridge push:** The ridges formed as a consequence motion of two plates away from each other, at divergent plate boundaries. As a result, hot mantle material (magma) enters the cracks (fault) left along the plate boundaries and cools down to create a solidified oceanic plate that has higher potential energy. To attend a ground energy level (under gravity), this denser material slides downhill and "push" the two plates away from each other (Figure 1.3).
2. **Slab pull:** where denser oceanic plate subduct into the mantle beneath lighter continental plates, at convergent plate boundaries, under their own weight, they "pull" the rest of the plate along behind it.

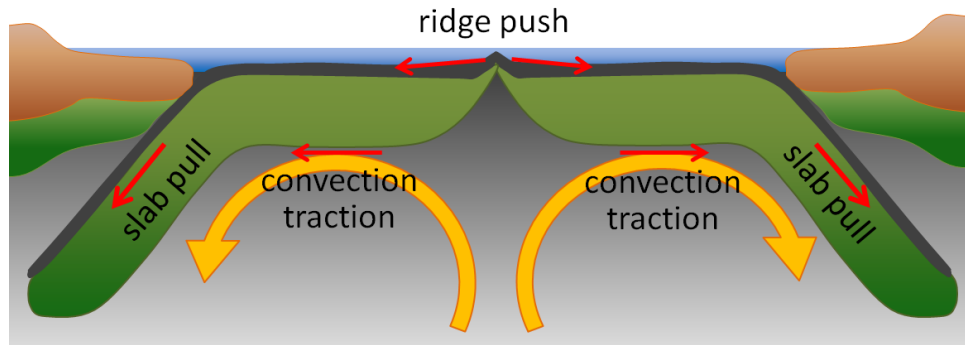


Figure 1.3: Schematics of ridge push and slab pull associated with plate motion along the spreading ridges, inspired from Kearey *et al.* (2009).

1.1.2 Spreading rates

As the mid-ocean ridges spread apart, it is possible to estimate the rate at which they spread apart. The oceanic crust is rich in basalt, a fairly magnetic substance. Using magnetometer sensors above the seafloor, in the early 1950s, researchers observed clear "stripes" of seafloor magnetized in opposite polarities following the periodic reversal of the Earth's magnetic field (summarised in review by Glen, 1982). This led to determining the age at which the seafloor is generated. By identifying the age of magnetic reversal and determining the distance between that particular reversal and the spreading center, the half-spreading rate along the ridges could be determined. The full spreading rate is twice the half-spreading rate assuming symmetric spreading on either side of the spreading center. It ranges from 13 to 150 mm/yr and governs the seafloor morphology, magma supply, and tectonic styles of mid-ocean ridges, which classify them into 5 types (Table 1.1, Figure 1.2).

Type	Spreading rate [mm/yr]	Examples
Ultra-fast	> 130	East Pacific (S)
Fast	90-130	East Pacific (N)
Intermediate	50-90	Gorda, Juan de Fuca, Southeast Indian
Slow	20-50	Carlsberg, Central Indian, Mid-Atlantic
Ultra-slow	< 20	Gakkel, Southwest Indian

Table 1.1: Type of mid-oceanic ridges (MOR) based on spreading rates and associated examples

1.1.3 Faults on Mid-ocean ridges

The process of seafloor spreading along mid-ocean ridges is mostly an effect of the extension and faulting of the existing crust. A fault is a fracture or collection of fractures between rock blocks that enable relative movement, where sudden movements result in earthquakes. The horizontal extent of faults goes up to thousands of km. Most faults undergo repeated displacements over

geological times, with one side slipping abruptly during an earthquake. The relative position of two blocks along the fault plane can either be called **hanging wall** (block above the fault plane) or **foot wall** (block below the fault plane). As a simplification, the geometry of both the hanging and footwall is described by three parameters: **strike** which defines the orientation of the fault plane that intersects with the horizontal plane, **dip** which defines the dipping of the fault plane that is perpendicular to its strike, and **slip** marks a vector indicating the direction in which the hanging wall moves with respect to the footwall. The faults are classified either as **dip-slip** fault, when the fault motion is vertical (direction of dip plane) or as **strike-slip** fault when the fault motion is horizontal (Figure 1.4):

- **Normal fault:** A dip-slip fault in which the hanging wall moves downward relative to the footwall. It mostly occurs in response to extension (e.g. mid-ocean ridges)
- **Reverse fault:** also called thrust fault, in which the hanging wall moves upward relative to the footwall. It occurs in the areas of compression (e.g. subduction zones)
- **Strike-Slip fault:** A fault along which two blocks slide past each other in translation (e.g. transform faults).

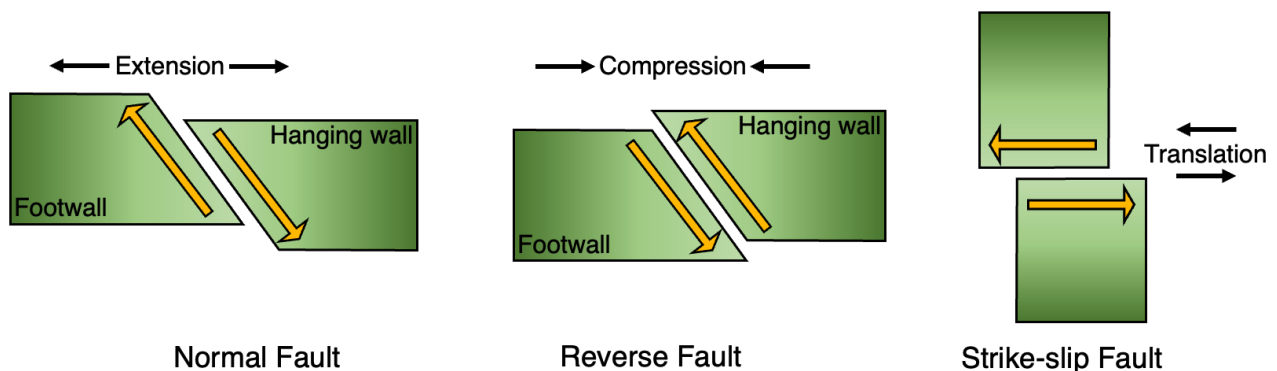


Figure 1.4: *Schematic representation of normal, reverse, and strike-slip faults*

Early ocean maps had identified lateral discontinuities along mid-ocean ridges, implying an active offset between ridge segments. This active zone is subject to shearing (translation) stresses and is called transform fault. Fracture zones are the outer parts of these faults and are inactive, but can sometimes generate earthquakes if reactivated by changes in the regional stress field or by horizontal thermal contraction. These fracture zones are prominent on the sea floor, leaving traceable scars across ocean basins. Unlike continental transforms like the North Anatolian fault in Turkey or the San Andreas fault in the United States, most oceanic transforms exhibit a remarkable "slip deficit," with 85 % of motion occurring without earthquakes (Boettcher and Jordan, 2004). The aseismic phenomena are assumed to be a form of gradual displacement caused by both the

thermal regime underneath and the materials altered by hydrothermal circulation (McGuire et al., 2012). These aseismic events are believed to serve as precursors of stronger earthquakes. In contrast, continental transforms mainly experience seismic plate motion during fault slippage events that generate earthquakes (Figure 1.5).

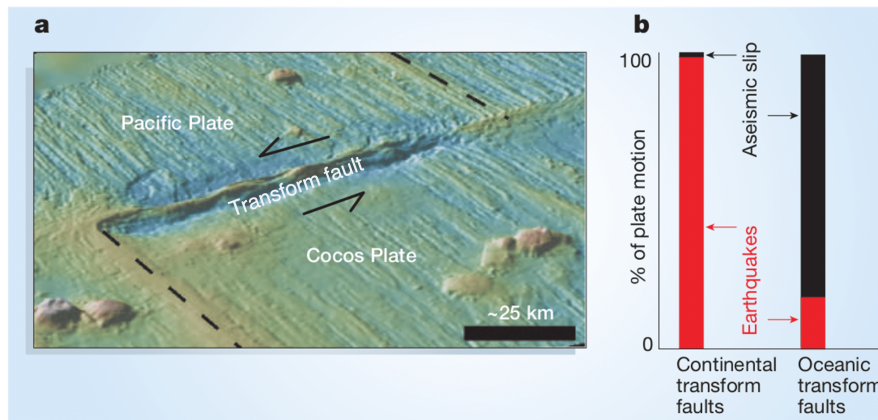


Figure 1.5: **a)** Geometry of an oceanic transform fault accommodating horizontal displacements between two spreading ridge segments (here along the East Pacific Rise), **b)** Amount of plate motion accommodated by seismic and aseismic processes along the continental and oceanic transform faults, (after Bohnenstiehl, 2005)

1.2 Spreading rates and ridge geometry

A cross-section of a MOR is composed of three regions: the axial zone, the crest or extrusive zone, and the flanking zone (Figure 1.6). Ridge flanks show gradual flattening away from the ridge axis, whereas crest zones show rough topography due to the presence of sub-vertical faults and fissures. Their azimuth is generally parallel to the strike of the ridge axis. Fissures are caused by tensional failure of the crust due to dike intrusions instead of cracking due to thermal contraction. Magmato-tectonic activities are concentrated within a 10-20 km wide axial zone, specifically, active magmatism is confined in a narrow (1-2 km wide) extrusive or neo-volcanic zone (Rundquist and Sobolev, 2002). The nature of neo-volcanic zone and fissure geometry varies from one spreading rate to another. These fissures are fed by an underlying magma chamber (a subsurface reservoir within the Earth's crust where melt accumulates over time).

Along slow-spreading ridges, the axial zone or valley is 20-40 wide. Magma chambers are generally absent and discrete basaltic magmatism as well as fractures and sub-vertical normal faults are observed (Solomon and Toomey, 1992). Here, discrete basaltic magmatism as well as fractures and sub-vertical normal faults are generally observed.

As mentioned earlier, the varying spreading rates govern the seafloor morphology, crust and lithosphere, magma supply, and tectonic features along the MOR spreading axes (Figure 1.7).

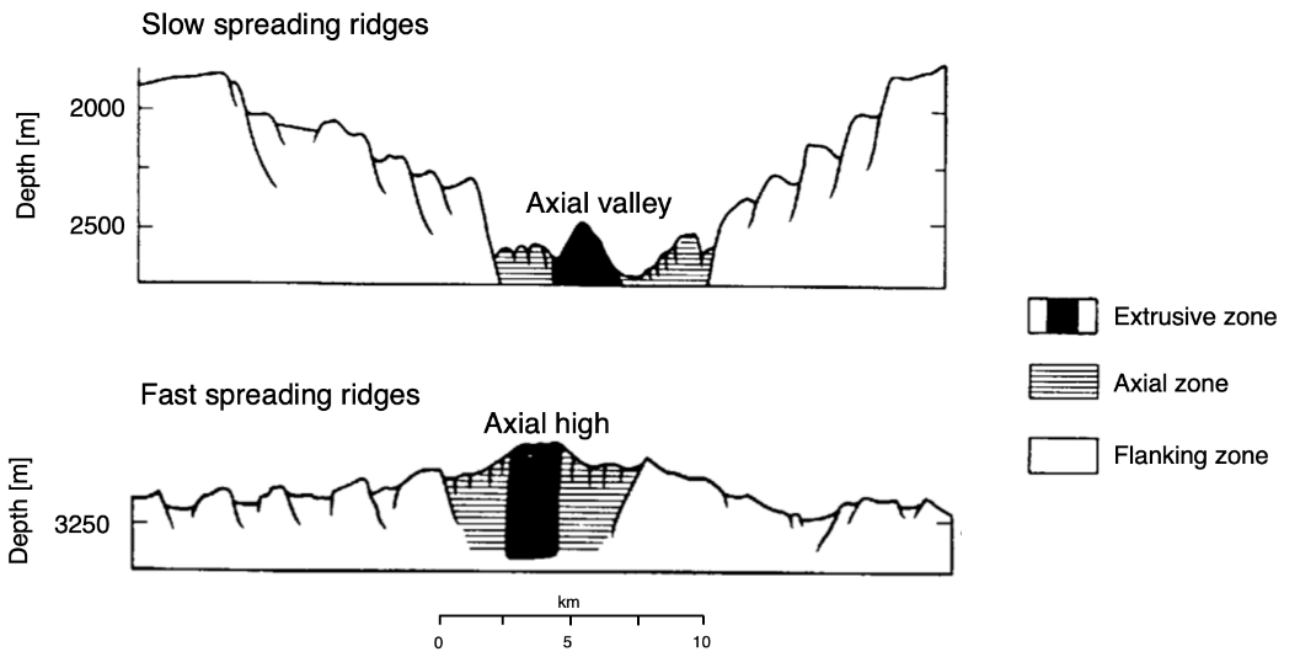


Figure 1.6: Cross section of a slow spreading (top) and a fast-spreading (bottom) ridges showing the extrusive or crest (black), axial (striped) and flanking (white) zones, (after [Rundquist and Sobolev, 2002](#)).

1.2.1 Fast spreading ridges

Fast-spreading ridges mostly exhibit ~ 10 km wide and several meters elevated triangular-shaped axial highs. Numerous axis-facing faults with narrow offsets of ~ 10 m dissect the axial high flanks (Figure 1.7a). These faults are generally pronounced at the edge of the axial high ([Escartín et al., 2007](#)) and cut through the brittle portion of the thinner (< 2 km) axial lithosphere. They tilt the seafloor which is rich with basaltic lava flows ([Macdonald et al., 1996](#)) and shape the tall abyssal hills (100s of m in height), spaced by ~ 1 -3 km. Cumulative fault offsets suggest that they contribute to a small fraction ($< 5\%$) of total plate divergence, which is mostly ($> 95\%$) accommodated by magmatic emplacement (Figure 1.8). Here the oceanic crust is ~ 6 km thick with lava flows and dikes down to ~ 1.5 km, depth of axial melt lens (AML), in the upper crust, and gabbros accreting through multiple lenses and crystal mush zone in the lower crust ([Kelemen et al., 1997](#)). The axial highs may host several high-temperature (> 350 °C) hydrothermal vents, that lie above fluid upwelling zones along the ridge-axis convection cells within a thin lithosphere ([Tolstoy et al., 2008](#)).

1.2.2 Intermediate spreading ridges

Intermediate-spreading ridges show similar characteristics to that of fast-spreading, except that they are straddled either by the axial high or axial valley (Figure 1.7c). Axial valleys are mostly ~ 1 km deep and ~ 10 km wide and bounded by axis-facing faults on either side. Here similar to fast-spreading ridges, tectonic plates spread symmetrically with magma intrusion creating the new

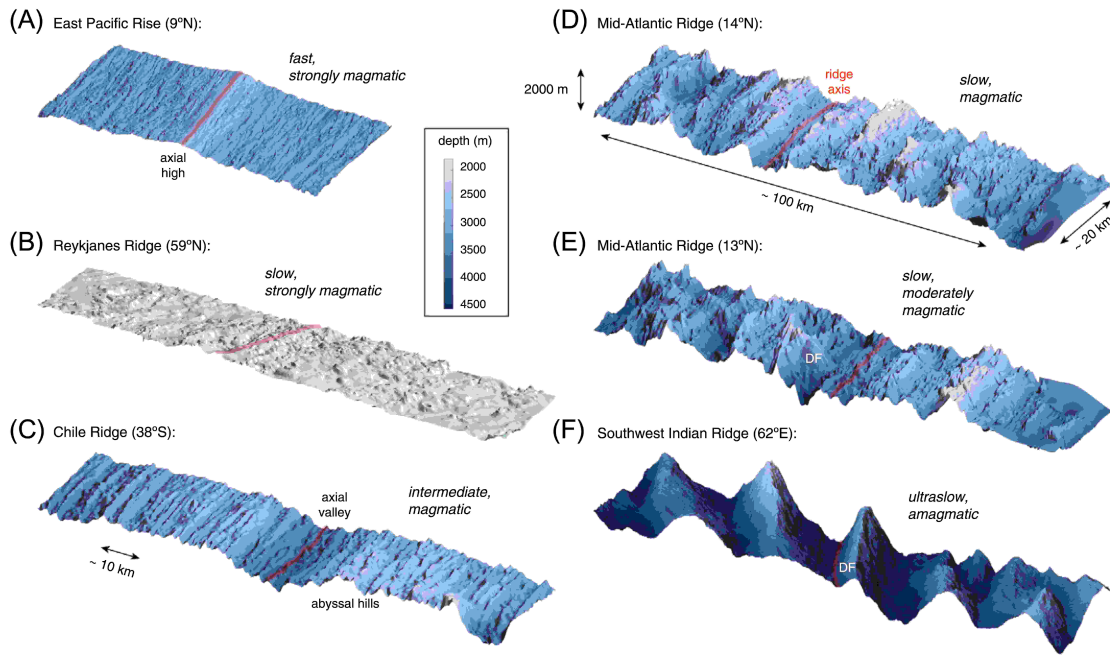


Figure 1.7: Schematic of ridge morphology for different spreading rates as a function of magma supply. On the vertical axis, M indicates a fraction of magma supply underlining the plate divergence. The orange arrow represents the magma flux to the shallowest reservoir, (after Olive, 2023).

crust, but steep and transient faults break the existing crust. Such faults have greater offsets, cumulatively, and hence accommodate $\sim 5\text{-}30\%$ of the total plate divergence (Figure 1.8). They shape abyssal hills higher than 100 m, with wider spacing of $\sim 3\text{-}5$ km. These ridges are characterized by thicker axial lithosphere, $\sim 2\text{-}3$ km deep AMLs, and several high-temperature hydrothermal fields (Tivey and Johnson, 2002).

1.2.3 Slow spreading ridges

Along such ridges, the axial valley is well-defined and is generally > 1 km deep and > 10 km wide. The abyssal hills are $\sim 2\text{-}8$ km spread apart with depths going down to 1 km and are bounded by steep axis-facing normal faults (Figure 1.7d,e), accommodating $\sim 15\text{-}40\%$ of total plate divergence (Figure 1.8). Here, magma emplacement accounts for the remaining $\sim 60\text{-}85\%$ of the divergence rate. Such ridges are populated by asymmetric segments (one side of the ridge shows a steeper and more rugged slope compared to the other side), hosting AMLs at depths of 3-4 km with active volcanic flows on one side, and detachment faults (a long-lived fault that is rooted at the ridge axis and dipping towards the axis) cutting the oceanic crust on the other side. Over time, the detachment fault can bring deep-seated crust and mantle rocks to the surface, forming an oceanic core complex. The prolonged activity (over a million years) along such faults creates tilted, domed fault surfaces having corrugated texture. The ridge segments show thinner lithosphere at centers

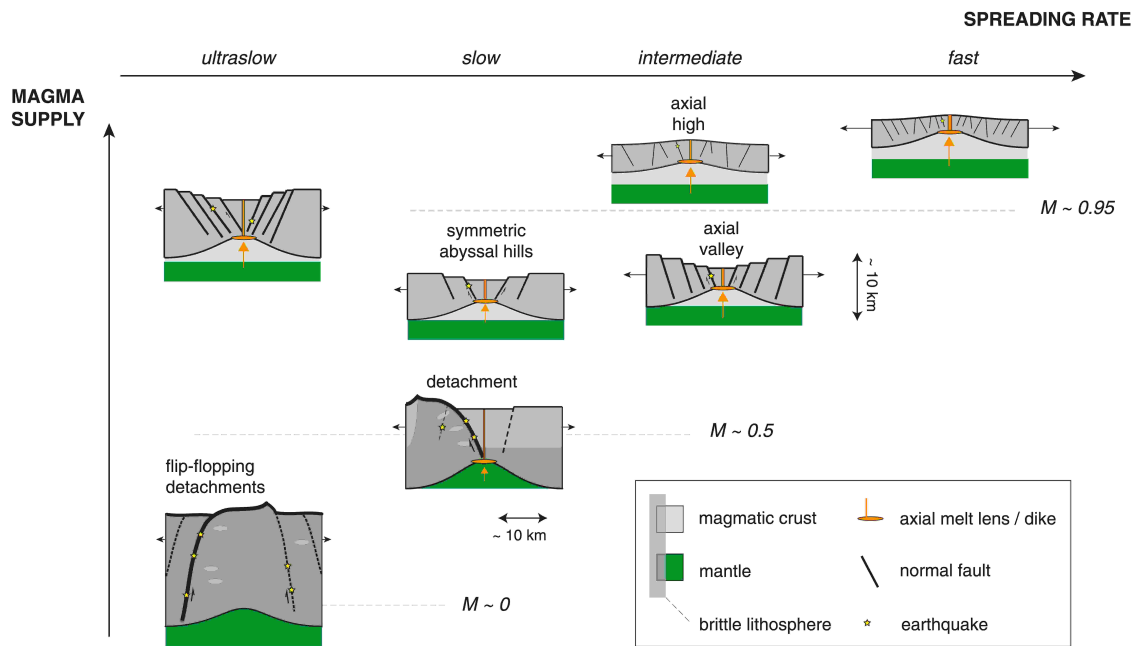


Figure 1.8: Schematic of ridge morphology for different spreading rates as a function of magma supply. M points out a fraction of magma supply underlining the plate divergence. The orange arrow represents the magma flux to the shallowest reservoir, (after Olive, 2023).

and thicker at ends based on the thermal structure of the ridge since melt focuses at the segment centers.

1.2.4 Ultraslow spreading ridges

These ridges display amagmatic segments or magma-poor sections (Sauter et al., 2013), and areas of smooth seafloor topography (Chapman and Marrett, 2006) due to flip-flopping detachment faults bringing serpentinized peridotites (mantle rocks altered by seawater) to the surface. As shown in Figure 1.7f, seafloor spreading proceeds by prolonged slip on large-offset faults which results in spectacular axial relief (≥ 4 km). Some of the faults can root down to ~ 16 km depth suggesting a thicker lithosphere (Chen et al., 2023). Uneven crustal thickness suggests that local magma supply can vary along the ridge axis. But most of the plate divergence is due to amagmatic processes (Figure 1.8). It is based on the absence of evidence of hummocky lava flows as well as corrugated detachment faults.

1.3 Mid-ocean ridges in the Indian Ocean

The mid-ocean ridges in the Indian Ocean comprise the Carlsberg Ridge (CR), the Central Indian Ridge (CIR), the Southwest Indian Ridge (SWIR), and the Southeast Indian Ridge (SEIR). In this

thesis, I did not study the CR due to its remoteness from the hydroacoustic networks in the Indian Ocean. The CIR, SWIR, and SEIR meet at a ridge-ridge-ridge intersection called the Rodrigues Triple Junction (RTJ) forming an inverted Y-shaped ridge system (Figure 1.2).

1.3.1 The Southwest Indian Ridge

The Southwest Indian Ridge is the boundary between the Nubian and Antarctic plates and is an ultra-slow spreading ridge with a spreading rate of 14 mm/a (Chu and Gordon, 1999). It extends from the Bouvet Triple Junction in the southern Atlantic Ocean to the Rodrigues Triple Junction (RTJ) in the Indian Ocean. The western end of SWIR is older than its eastern end due to the lengthening and eastward propagation of the ridge axis toward the RTJ (Patriat et al., 1997). Along this extensive section, bathymetric data and irregular gravity anomalies (Figure 1.9) indicate the presence of infrequent yet substantial volcanic structures, separated by seemingly amagmatic segments (Cannat et al., 1999). The cyclic nature of volcanic construction and tectonic dismember-

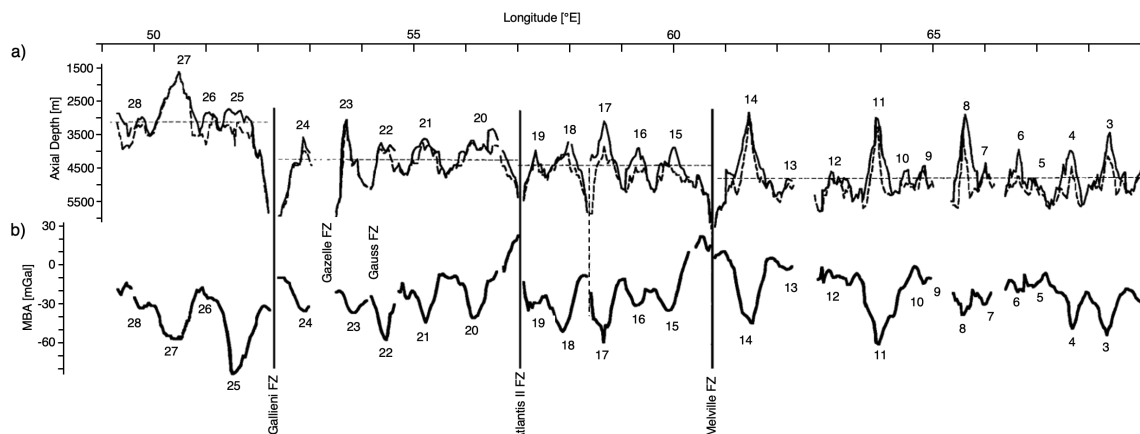


Figure 1.9: **a)** Bathymetry and **b)** Mantle Bouguer gravity anomaly profiles along the SWIR axis. The axial depth and maximum depth of the axial domain are shown in solid and dashed lines. Horizontal lines show average axial depth in the specified region, (after Cannat et al., 1999).

ment across the SWIR is responsible for the ridge crest and rugged morphology (Mendel et al., 2003). It is mostly characterized by the obliquity of the ridge axis with respect to the main fracture zone's orientation (Cannat et al., 1999). The section between Gallieni and Melville FZ shows an obliquity of 40° and contains several long-lived transform and non-transform discontinuities. The obliquity changes to 25° between Melville FZ and RTJ. The Melville fracture zone is a significant feature that demarcates the ridge both morphologically and thermally (Patriat et al., 1997). East of this fracture zone, the median valley is deep and nearly continuous, with no transform faults segmenting the axis for nearly 1000 km up to the RTJ (Mendel et al., 1997).

1.3.2 The Central Indian Ridge

The Central Indian Ridge (CIR), separating the Nubian and Indo-Australian plates in the Central Indian Ocean, is a slow-spreading ridge with a spreading rate between 23 and 50 mm/yr (DeMets et al., 1990). While the spreading rate increases from north to south, CIR's overall morphology remains relatively homogeneous and characteristic of slow-spreading ridges (Briais, 1995). The CIR has NNW trending and a 5 to 8 km wide rift valley (Parson et al., 1993; Briais, 1995) with increasing depth from 500 to 1800 m towards the southern end. In the southern part of the CIR (Figure 1.10), the ridge axis is segmented by several transform faults and non-transform offsets (Briais, 1995).

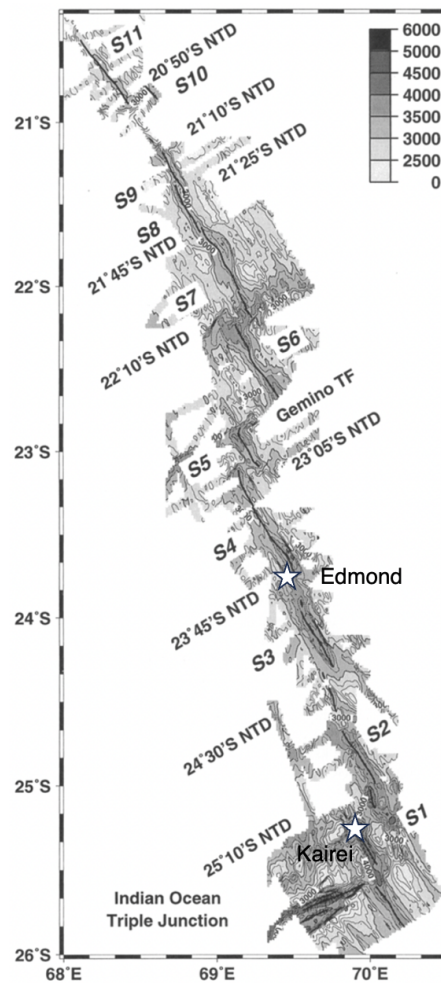


Figure 1.10: Bathymetry of Central Indian Ridge highlighting non-transform discontinuities and transform fault, (after Briais, 1995). Stars show the locations of two hydrothermal fields.

A single discontinuity offsets the CIR axis by 40 km (Gemino, 22°40'S). Between 20°S and 25°S, two hydrothermal vent fields have been discovered (Okino et al., 2015). From South to North, they are named as Kairei (25°19'S) and Edmond (23°52'S). The Kairei field, near the RTJ, was the first observed hydrothermal field in the Indian Ocean and is a black-smoker-type high-temperature field with an unusually high concentration of H₂ (Van Dover et al., 2001). The Edmond located 160

km north of the Kairei, is another high-temperature hydrothermal field, but its H_2 concentration is typical of basalt-hosted hydrothermal fluids (Kumagai et al., 2008).

1.3.3 The Southeast Indian Ridge

The Southeast Indian Ridge (SEIR), separating the Indo-Australian and Antarctic plates, has an intermediate spreading rate, ranging from 59 mm/yr at the RTJ to up to 75 mm/yr south of Australia. This ridge has maintained a consistent separation rate for at least 10 million years (Royer and Schlich, 1988). Certain segments of the ridge display distinct axial valleys accompanied by parallel and smooth relief features (Sauter et al., 1991). The ridge axis is divided into multiple segments by transform faults, resulting in lateral displacements of 20 km to 100 km between neighboring segments. To the south (38°S), the presence of a hotspot in the Saint-Paul and Amsterdam (SPA) plateau region beneath the ridge disrupts this morphological pattern (Conder et al., 2000). This hotspot activity influences volcanic processes along the ridge (Nicolaysen et al., 2007). Near this plateau, the Boomerang seamount, approximately 50 km south of the ridge axis, is presently active (Johnson et al., 2000b).

1.4 Seismicity along mid-ocean ridges

Axial magma lenses are abundant in regions where mid-ocean ridges experience fast spreading rates. Conversely, along slow-spreading ridges, the occurrence of crustal-level melt beneath the ridge axis is scarce, with melt bodies often being temporary or concentrated beneath specific axial volcanoes. On intermediate spreading ridges, the distribution of melt displays a range of possibilities, lying somewhere between the two extreme scenarios mentioned earlier. The build-up of molten material within the crustal chamber results in an increase in pressure compared to the surrounding host rock, leading to the occurrence of numerous earthquakes in the vicinity of the chamber. The investigation of oceanic accretion processes heavily relies on the analysis of seismic activity, which plays a crucial role in understanding the various mechanisms. Different methods exist for recording seismicity, each with its own strengths and capabilities. Some methods involve the detection of ground movements and seismic waves, including terrestrial seismic stations and ocean bottom seismometers (OBSs), while others capture hydroacoustic waves with instruments like sonobuoys or hydrophones (Figure 1.11).

Terrestrial networks, due to their global distribution, provide a comprehensive view of seismicity worldwide without temporal limitations. However, their limited coverage in oceanic environments able to detect earthquakes with magnitudes greater than 4 and suffer some accuracy

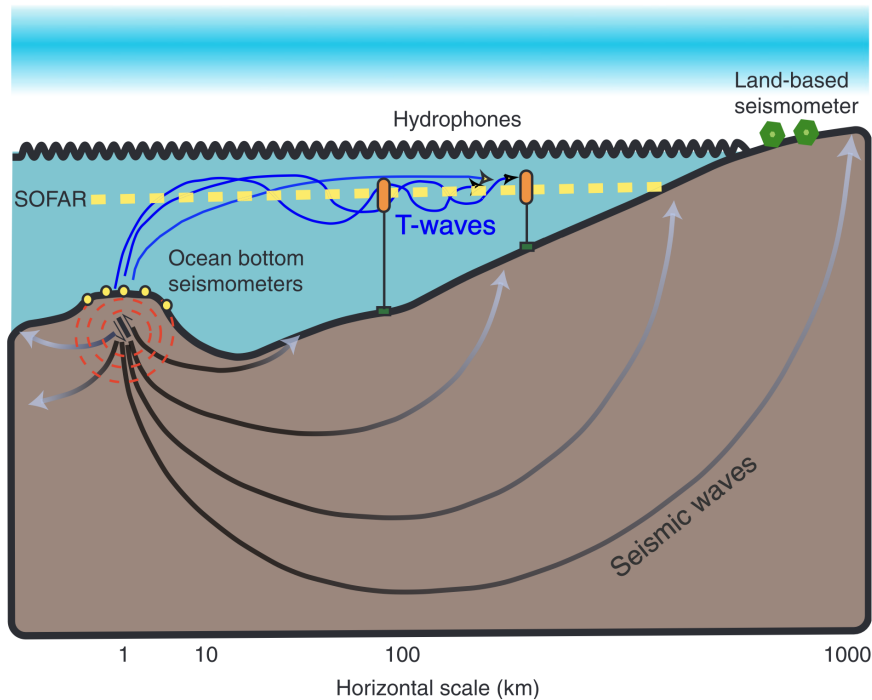


Figure 1.11: *Methods for monitoring the seismic activity of spreading ridges: terrestrial networks, ocean bottom seismometers, and hydrophones, (after Bohnenstiehl and Dziak, 2009)*

issues at long range, with localization errors on the order of 10-20 km in epicenter determination. In contrast, OBSs allow for the detection of lower-magnitude events, typically below 4, which are often associated with ridge processes, and offer good accuracy but within the limited spatial and temporal autonomy of OBS networks. Hydrophone networks in the oceans overcome these two limitations as they are sensitive to lower magnitude events, typically around 2.5-3, can cover wide areas (250 000 to 1 000 000 km²) with few instruments, and locate acoustic sources within 2-3 km by triangulation. They are very adapted to monitor the low-level seismicity associated with seafloor spreading processes over significant extents of mid-oceanic ridges (e.g. Fox et al., 1995, 2001; Bohnenstiehl et al., 2004; Dziak et al., 2004). Since they detect acoustic waves converted from seismic waves near the epicenters, they cannot provide actual seismic magnitudes nor focal mechanisms.

In a general sense, events occurring at oceanic ridges can be classified into two categories. Firstly, events triggered by dike emplacements or volcanic eruptions, which occur in large numbers within a relatively short time period without a prominent strong event and with fluctuating magnitudes; they are often referred to as "swarms" (Mogi, 1967). Secondly, events associated with ruptures of the oceanic crust resulting from tectonic extension (Bergman and Solomon, 1990), and sometimes occurring in one main shock followed by aftershocks with decaying magnitude (Figure 1.12). The detailed examination of seismic patterns can tell which mechanism prevails along mid-ocean ridges. This differentiation is akin to the categorization of earthquakes at Kilauea

volcano as "rift" events, accompanying magmatic episodes, and "flank" events, representing the stress-readjustment induced by the intrusion (Klein, 1982).

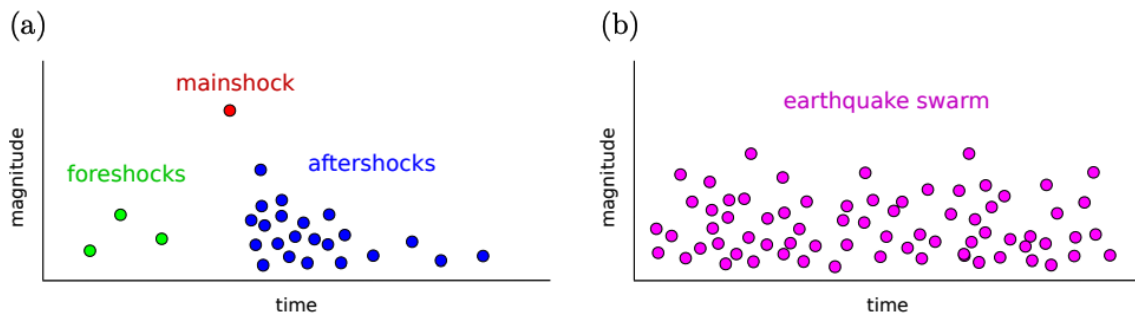


Figure 1.12: Schematic magnitude-time distribution of events in the case of **a**) foreshocks-mainshock-aftershocks sequence **b**) earthquake swarm

1.4.1 Earthquake swarms

Volcanic activity and earthquake swarms often have an association, although they are not always linked. Sykes (1970) observed frequent occurrences of teleseismic earthquake swarms along MOR segments and documented a close connection between such seismicity and magmatic processes involved during plate divergence. Micro-earthquake swarms detected by ocean bottom seismometers (Francis et al., 1978; Tolstoy et al., 2008; Yu et al., 2018) or floating sonobuoys (Reichle and Reid, 1977) and teleseismic studies of the most significant swarm events (Schlindwein, 2012) contributed to understanding the relationship between volcanism and swarm activity. However, opportunities for both types of studies are limited, and swarms of events with magnitudes between micro-earthquakes and the largest ridge-axis earthquakes have received little attention. As a result, our understanding of the significance of mid-ocean ridge earthquake swarms has seen limited improvement over the past four decades, and the possibility that swarms indicate active volcanism on the accretionary axis remains a common suggestion (Lilwall, 1982; Cesca et al., 2023).

In principle, earthquakes on mid-ocean ridges can be classified into two categories based on their origin: (1) the creation of new oceanic crust involves the intrusion of crustal dike systems from shallow axial magma chambers and extrusion of magmatic rocks onto the seafloor (Dziak et al., 1995), and (2) extensional tectonism occurring on the newly formed crust, leading to faulting and uplift (Rundquist and Sobolev, 2002). This differentiation is akin to the categorization of earthquakes at Kilauea volcano as "rift" events, accompanying magmatic episodes, and "flank" events, representing the stress-readjustment induced by the intrusion (Klein, 1982). However, an exception to this classification may be the large earthquake swarm in the Galapagos Islands in June 1968, which Francis (1974) attributed to the collapse of the Fernandina caldera following the withdrawal of magma from shallow crustal levels.

Sykes (1970) has speculated three mechanisms underlying the generation of swarms: 1) magmatic activity creating a concentrated source of stress; 2) inhomogeneous stress distribution at the loci of volcanoes; 3) presence of concentrated sources of high fluid pressure along the MORs (Julian and Sipkin, 1985). It could be also possible that some swarms jointly reflect magmatic activity that reaches the seafloor and non-magmatic activity resulting from stress readjustments. Several models have been proposed to link the occurrence of swarms with magmatism. Hill (1977) attributed seismic swarms to shear failure between the tips of *en echelon* magma-filled dikes. Subsequently, Shaw and Hargraves (1980) included in the model dike tips acting as magma conduits between dike segments. Rubin and Pollard (1988) later suggested that earthquake swarms track the moving front of magma intrusions.

1.4.2 Diking and magmatism

Magma can escape from the chamber by surpassing the minimum confining stresses and tensile strength of the surrounding rock. The dike's alignment follows the direction of the least compressive stress, which is the spreading axis. Seismicity concentrates in a narrow extension zone above the dike and a broader zone beyond its endpoints, inciting seismic activity during dike propagation and lithospheric compression adjacent to the dike (Figure 1.13) (Rubin et al., 1998). The higher magnitude events are the result of the reactivation of pre-existing faults in a zone located above the dike and do not necessarily correspond to tectonic sequence (Schlindwein, 2012). While minor earthquakes are observed near the dike tip, significant seismic events are thought to transpire on existing fault surfaces (Bohnenstiehl and Dziak, 2009).

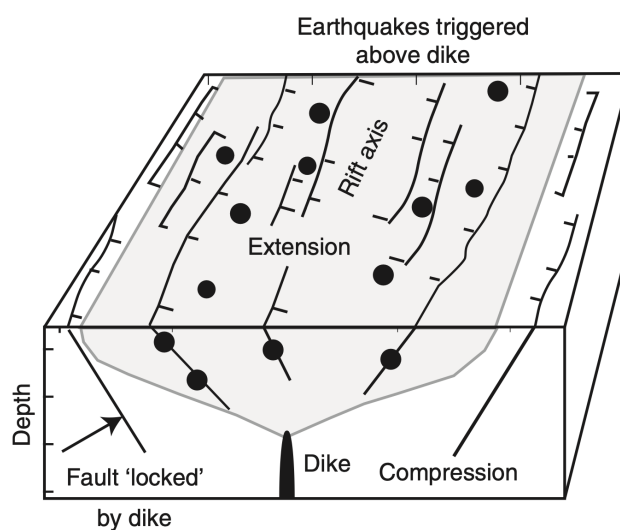


Figure 1.13: Cartoon representation of compression (white) and extension (gray) associated with vertical dike propagation. Normal faults are marked by black lines and earthquakes (black dots) are projected within the extensional region, (after Bohnenstiehl and Dziak, 2009).

The first documented instance of dike intrusion and of its lateral propagation was observed at the Juan de Fuca ridge (Fox et al., 1995). Similar events have later been reported in the same region, with varying rates of migration, thanks to a hydroacoustic array (Dziak and Fox, 1999). These magmatic swarms generate several hundred hydroacoustic events which are rarely discernable in teleseismic data (Dziak et al., 2007). A magmatic episode involving lateral injection of a dike has also been identified at the Southeast Indian Ridge (Tsang-Hin-Sun et al., 2016). The absence of horizontal migration of low-magnitude activity along the Juan de Fuca ridge suggests that it could occur due to the filling of a magma reservoir (Dziak et al., 2004). Other possible mechanisms include magmatic pocket filling (Wilcock et al., 2009), vertical intrusion of dikes within the Earth's crust (Tolstoy et al., 2006), and the effusion of lava onto the seafloor (Tan et al., 2016). A few magmatic episodes have been documented at ultra-slow ridges. At the Gakkel Ridge, a swarm (252 teleseismic events, $3.2 < mb < 5.8$, including 21 focal mechanisms) evidences a lateral dike migration (Müller et al., 2000) was detected. Some years later, a potential volcanic eruption at this ridge generated a strong magmatic episode (Schlindwein et al., 2005). In the Indian Ocean, teleseismic swarms of more than 100 events over a few days have been observed (Schlindwein, 2012).

Tolstoy et al. (2001) suggested the existence of a negative power law relationship between the parameters of size, frequency of magmatic swarms, and spreading rate. The power law is influenced by the properties of the surrounding rocks, as highlighted by Grandin et al. (2011). Fast spreading ridges typically exhibit lower magnitude events, as the thickness of the brittle layer is generally insufficient to generate earthquakes of strong magnitudes to those observed in slow or ultraslow spreading ridges (Läderach et al., 2012). Slow or ultraslow spreading ridges exhibit less frequent swarm episodes that involve a larger number of events. These ridges have a colder, more brittle, and thicker lithosphere, which requires higher stresses for magmatic intrusions to occur within the oceanic crust (Schlindwein, 2012).

1.4.3 Hydrothermal Systems

At mid-ocean ridges, newly formed lithosphere's faults channel seawater. Heated by magma, it creates active fluids that rise, fueling hydrothermal convection at mid-ocean ridges. This process crucially exchanges heat and chemicals between Earth's crust and the ocean. In such hydrothermal environments (fields), seismic events can be initiated through two mechanisms: 1) hydrothermal cooling by the extraction of heat may cause thermal contraction with a subsequent formation of cracks; 2) the heating of confined fluid pockets can lead to hydrofracturing. Both processes generally generate small-magnitude earthquakes, which can only be recorded by local surveys (OBSs or ocean-bottom hydrophones). Different studies near hydrothermal fields suggest a complex relationship between seismic activity and vent hydrology. For instance, a vent-scale OBS investiga-

tion conducted in 1995 at 9°50'N on the East Pacific Rise for 105 days recorded a swarm of 162 microearthquakes spanning approximately 3 hours (Figure 1.14). Notably, during this period, a rapid increase in fluid temperature was observed for 7 days (Sohn et al., 1999). A comparative analysis with vent temperatures monitored continuously over more than 3 years showed that this post-seismic fluctuation represented the most significant deviation ever recorded.

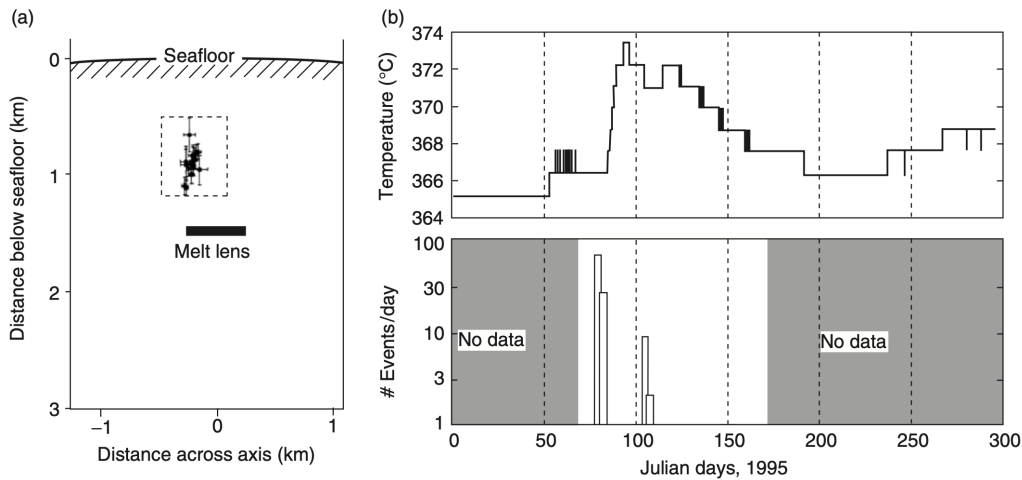


Figure 1.14: **a)** Cross-section of East Pacific Rise beneath 9°50'N hydrothermal vent site. **b)** Fluid release temperature along at the vent site and histogram of microearthquakes per day, (after Sohn et al., 1999).

1.4.4 Transform Fault and Ridge Segment

During the late 1960s, the study of focal mechanisms along oceanic transform earthquakes played a crucial role in supporting the plate tectonic theory. This theory required opposite strike-slip motions on left-lateral and right-lateral transform offsets. Sykes (1967) demonstrated that the direction of P-wave motion during transform earthquakes was parallel to the transform and in opposite directions according to the transform offset. Today, earthquake focal mechanisms are routinely determined for global events ($M_w > 4.5$; Ekström et al., 2012).

The occurrence of transform seismicity is primarily limited to the area between two active spreading centers. As schematized in Figure 1.15, transform boundaries mostly display strike-slip fault mechanisms whereas ridge segments show normal fault mechanisms. As slip propagates, its extent is limited by the transform offset. The largest transform earthquakes are associated with slow-spreading ridges (<40mm/yr) and may reach magnitudes up to M_w 7.5. At fast-spreading ridges (>100mm/yr), the maximum observed magnitude is limited to M_w 6.5. This phenomenon can be attributed to the thermal characteristics of the oceanic lithosphere, where higher spreading rates lead to shallower seismogenic rupture depths (Sykes, 1970). Reverse faulting events could occur at the inner corners of transform boundaries as well as within axial valleys (Figure 1.15). They could be triggered by the inflation of a magma chamber (Kong et al., 1992) or downward fluid

movements along the extended faults (Waldhauser and Tolstoy, 2011). Generally, swarms occur along ridge crests and a few of them near the transform faults. In the frequency-size distribution (cumulative number of events vs. magnitude) plot, the former shows a higher ratio of the low magnitude of events to that of the high magnitude events (high value of slope), and the latter shows a lower ratio, i.e. a low value of slope (Figure 1.16; Francis, 1968).

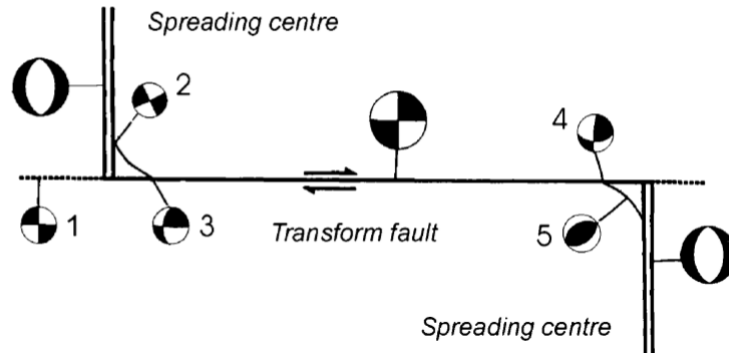


Figure 1.15: Focal mechanisms of earthquakes along a mid-oceanic ridge: normal faulting is expected on ridge segments, strike-slip mechanism along transform faults, mixed mechanisms, including pure thrust faulting, at the inner corners between ridge segments and transforms, (after Engeln et al., 1986).

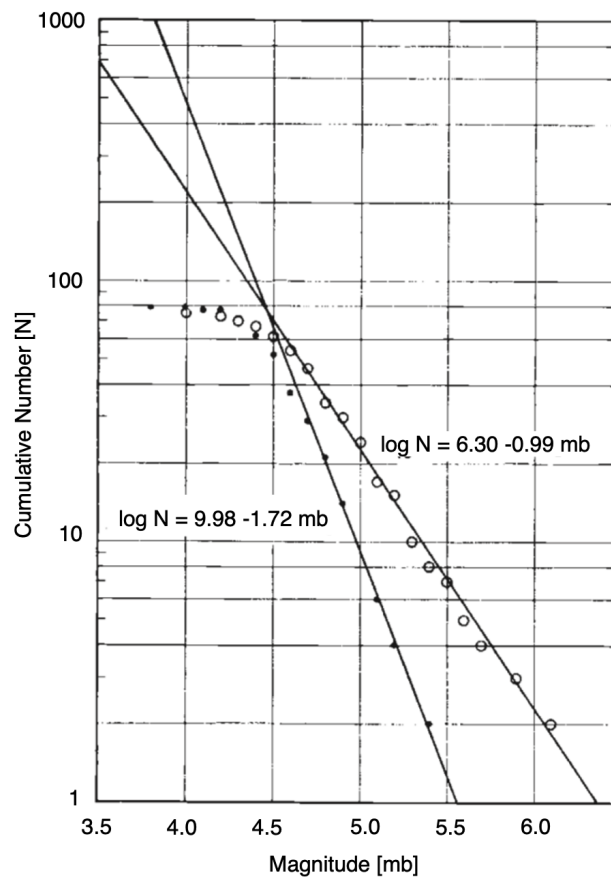


Figure 1.16: Cumulative plot of 79 rift zone earthquakes (black circles) and 75 fracture zone earthquakes (white circles) of the Mid-Atlantic ridge, (after Francis, 1968).

1.4.5 Tidal Triggering

Short-term stress fluctuations in the Earth's surface are induced by solar and lunar tidal forces. These stress variations impact earthquake occurrence in coastal areas and beneath the oceans, notably due to the loading effects of ocean tides. These stress changes, typically ranging from 10^{-3} to 10^{-4} Pa, are considerably smaller than the average stress drop during an earthquake or the strength of crustal rocks. By analyzing a comprehensive global dataset comprising 442,412 events, [Métivier et al. \(2009\)](#) contended for a noteworthy signal of tidal triggering, particularly enhanced for smaller and shallower earthquakes. Tidal triggering of seismic activity has been extensively observed across MORs (e.g. [Wilcock, 2001](#); [Tolstoy et al., 2002](#); [Scholz et al., 2019](#)). The microseismicity ($M \leq 2$) within axial hydrothermal systems often has a significant correlation, as earthquakes tend to transpire during periods of heightened extensional stress. In some instances, such as micro-earthquake swarms along the Juan de Fuca Ridge (JdFR), where the ocean tides reach substantial amplitudes, these periods of maximum extension align with low tide, when the seafloor experiences unloading due to the minimal height of the water column above it, ([Figure 1.17](#); [Wilcock, 2001](#)).

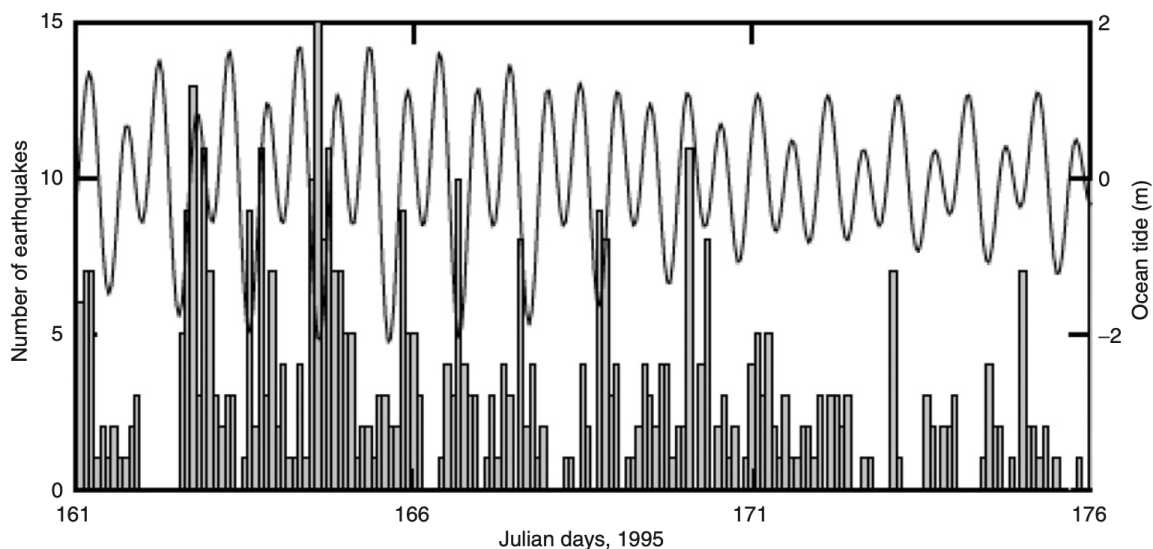


Figure 1.17: Fifteen-day long time histogram of the earthquake count in 2-h bins with the ocean tide time series superimposed. Earthquakes are triggered on the Endeavour segment of Juan de Fuca ridge at periods of a low ocean tide when the seafloor is unloading and crustal stress is most extensional, (after [Wilcock, 2001](#)).

1.5 Monitoring seafloor spreading seismicity

Deploying hydrophone networks in oceans allows the recording of small earthquakes near the ridge axis with relatively low localization errors. This section gives a comprehensive overview of

seismic swarms comprising low-magnitude earthquakes detected primarily by hydrophone networks along the world MOR system in different spreading contexts.

1.5.1 Seismicity along fast spreading ridges

The fast-spreading East Pacific Rise (EPR), spreading at 90-170 mm/yr, has attracted extensive scientific investigations with hydrophone (Fox et al., 2001) and seabed seismometer networks (Tolstoy et al., 2006) to detect tectonic and magmatic events. Since the 1990s, local networks of hydrophones and seafloor seismometers have been deployed in the region, but the long-term data is still limited. As a result, several aspects of the ridge's behavior remain enigmatic, with the periodicity of magmatic episodes being one of the key unanswered questions.

The seismic activity is irregular, mainly concentrated at transform faults, while ridge segments are mostly aseismic, except for intermittent swarms of several dozen events (Figure 1.18). Although the lithosphere extends by 4 to 8 % on both sides of the ridge, the seismic activity observed represents only 1 % of the total deformation (Bohnenstiehl and Dziak, 2009). This suggests that a substantial part of the deformation is either aseismic or generates seismic events of such low magnitude that they remain undetected, even by hydrophones. Magmatic events are rare along the EPR, despite the presence of magma reservoirs. Over 8 years of hydroacoustic monitoring, only a few volcano-tectonic swarms were detected in specific ridge segments (Bohnenstiehl and Dziak, 2009), but the periodicity of eruptive episodes remains poorly understood. The first recorded eruption at 9°50'N in 2006 provided insights into tectonic processes before an eruption. Preceding the eruption, seismic activity surged from ten to several hundred events per day over two years (Tolstoy and Bohnenstiehl, 2006), indicating an increased stress field induced by magma reservoir replenishments.

1.5.2 Seismicity along intermediate spreading ridges

Intermediate spreading ridges have spreading rates in the range of 50-90 mm/yr. Notable examples of such ridges include the Gorda, Juan de Fuca (JdFR), and Explorer ridges in the North-East Pacific, the Galapagos Ridge in the East Pacific, and the Southeast Indian Ridge in the Indian Ocean.

In the Pacific Ocean

The Explorer, JdFR, and Gorda ridges have been extensively studied since the 1990s by continuous hydroacoustic monitoring of events (magnitudes $m_b > 2.5$). Despite similar expansion rates (~ 60 mm/yr), each ridge displays distinct morphologies and seismicity patterns (Dziak et al., 2011).

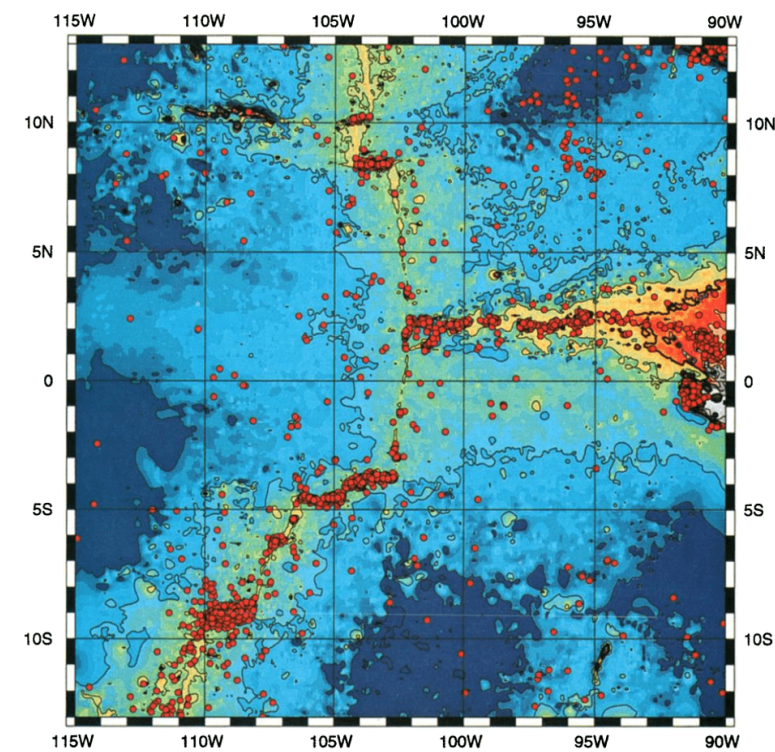


Figure 1.18: *Seismicity detection on the East Pacific Rise and Galapagos Ridge between May 1996 and May 1999 using autonomous underwater hydrophone array. The seismicity is concentrated on the fracture zones with fewer events along the spreading axis, (after Fox et al., 2001)*

The Explorer and Gorda Ridges have shown abundant seismic activity over the past two decades, characterized by alternating phases of continuous activity, seismically quiet periods, and brief intense swarm phases. In contrast, the Juan de Fuca Ridge has been mostly aseismic during the observation period, except for magmatic swarms near the Axial volcano and the CoAxial segment (Fox et al., 1995; Dziak et al., 2007). On the other hand, the Endeavour segment of the Juan de Fuca Ridge at $48^{\circ}10'N$ displays more sustained seismic activity around a seamount, indicating the presence of a significant magma reservoir in that area (Figure 1.19).

Hydroacoustic recordings of magmatic episodes mainly come from the above-mentioned ridges in the Pacific Ocean. Over twenty years, seven magmatic episodes were identified as earthquake swarms. These swarms share several common characteristics, as outlined by (Bohnenstiehl and Dziak, 2009): absence of a strong triggering earthquake; a large number of events over a longer duration (several weeks to months). In segments with high and smooth bathymetry, like the southern segments of the JdFR, seismicity is infrequent and resembles that observed in fast ridges. On the other hand, the Gorda Ridge, characterized by an axial valley and steeper relief, exhibits more abundant seismic activity, concentrated both within the valley and on its flanks (Bohnenstiehl and Dziak, 2009). These findings demonstrate that seismicity in intermediate ridges can exhibit characteristics similar to both slow and fast-spreading ridges.

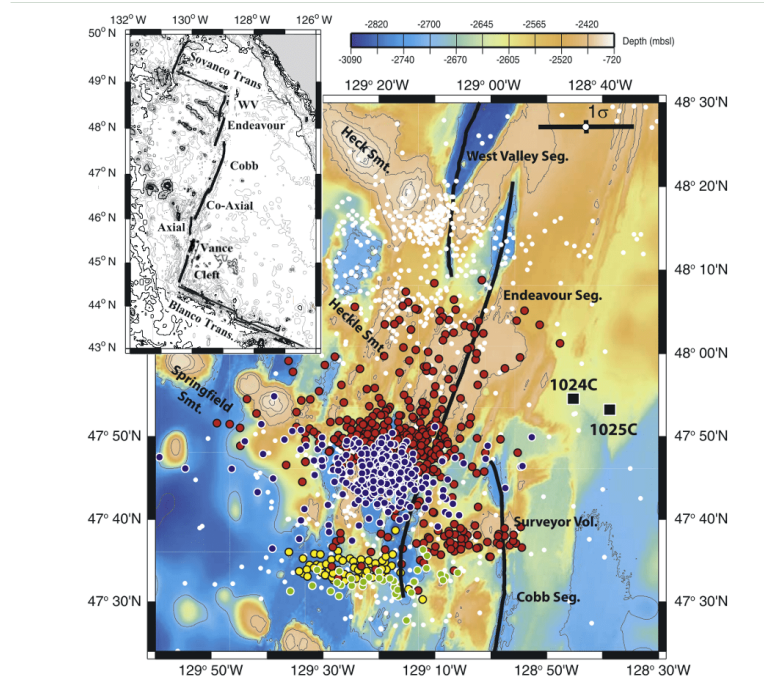


Figure 1.19: Hydroacoustic detection of earthquakes between January 1998 and August 2001 along the Endeavour segment with several distinct swarms: in March, June, July 1999 and January 2000 shown in yellow, red, green, and blue, respectively, (after [Bohnenstiehl et al., 2004](#))

Along SEIR in Indian Ocean

The seismicity of the Indian Ocean ridges has been primarily studied in the 1960s and 1970s, during the early stages of global monitoring networks ([Sykes, 1970](#)). Magmatic swarms comprising few events are rarely detected by terrestrial seismological networks along the SEIR. The few swarms that have been detected are often represented by only small clusters of events, insufficient to fully characterize their nature.

Significant progress in understanding microseismicity in the Indian Ocean came from the implementation of long-term hydroacoustic networks ([Hanson and Bowman, 2005](#); [Royer et al., 2015](#); [Tsang-Hin-Sun et al., 2016](#)). Generally, the distribution of earthquakes has a strong correlation with ridge morphology. Along the SEIR, the transform faults are the most seismically active, while the ridge segments exhibit little to no seismicity, as observed along fast-spreading ridges. Among them, three segments stand out as exceptions, situated between 27°S to 29°S, ~400 to 750 km from the RTJ, where seismicity occurred at the center of these ridge segments ([Sauter et al., 1991](#); [Tsang-Hin-Sun et al., 2016](#)), as shown in Figure 1.20. Along the other segments, there is little or no seismic activity, suggesting that the separation of the plates along SEIR is accommodated by magmatic episodes or by earthquakes of magnitude $mb < 4$.

The seismic activity over the Saint-Paul and Amsterdam Plateau along the SEIR seems to be primarily influenced by transforming discontinuities rather than magmatic episodes ([Royer et al.,](#)

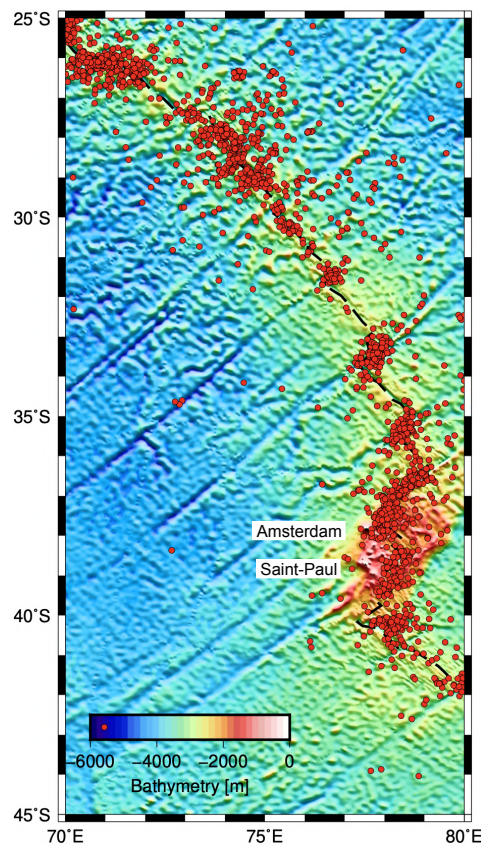


Figure 1.20: Locations of seismic events between 1980 and 2020 obtained from the ISC catalog along the SEIR. Between 27°S-30°S, events are focused on the center of the ridge segment. Another active area is near the Saint-Paul Amsterdam plateau.

2015). Due to the limitations of terrestrial seismological networks, our knowledge of the seismicity along the SEIR remains limited. Nevertheless, the distribution of earthquakes generally aligns with the ridge morphology and conforms to the traditional model of deformation distribution, with tectonic processes prevailing along transform faults and magmatic processes occurring along segments.

1.5.3 Seismicity along slow-spreading ridges

The slow-spreading Mid-Atlantic Ridge (MAR), and the CIR, including the Carlsberg, and Sheba ridges have spreading rates in the range of 20 mm/yr to 50 mm/yr. The seismic activity of the MAR from 12°N to 54°N has been extensively studied, benefiting from successive deployments of autonomous hydrophone networks by PMEL-NOAA (Pacific Marine Environmental Laboratory of National Oceanic and Atmospheric Administration) and LGO (Lab Geo-Ocean, UMR6538) since the 1990s (e.g. Smith et al., 2003; Simão et al., 2010; Goslin et al., 2012), as shown in Figure 1.21.

Seismic events are mainly concentrated within 40 km from the ridge axis and primarily occur within the axial valley (Smith et al., 2003). The rate of seismicity varies along the ridge axis

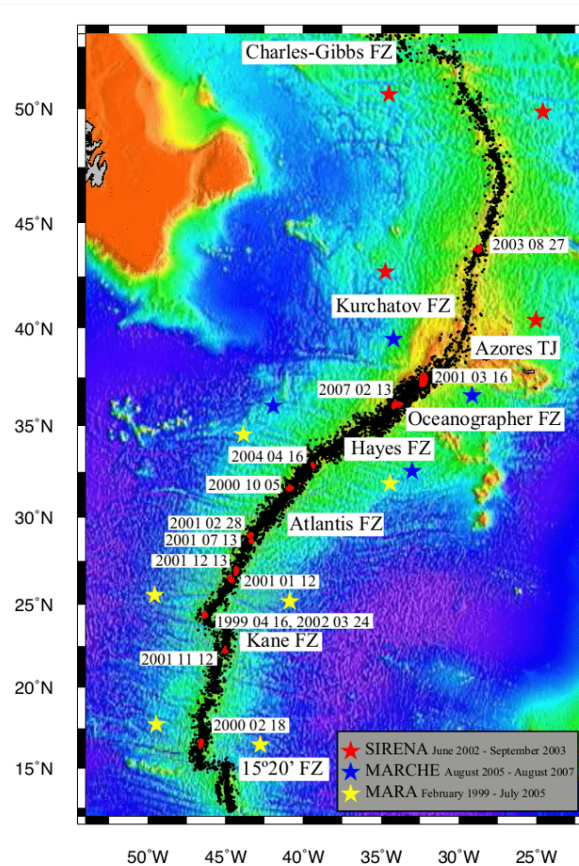


Figure 1.21: *Seismicity along the Mid-Atlantic Ridge using AuH networks, SIRENA (red stars), MARCHE (blue stars) and MARA (yellow stars) with distinguished sequences shown by red dots, (after ?).*

differently compared to fast and intermediate spreading ridges: typically, magmatic swarms are found at the center of segments, while tectonic sequences are observed at the ends of segments and along discontinuities (Goslin et al., 2012). Segments with hotter, thicker volcanic crust, a thinner underlying lithosphere, higher bathymetry, and significant variations in the Bouguer gravity anomaly tend to produce fewer earthquakes. Conversely, segments with deep valleys, less pronounced mantle Bouguer anomaly variations, colder extremities, and thicker lithosphere exhibit increased seismicity, concentrating tectonic processes (Smith, 2002), resulting from crustal cooling after volcanic events or tectonic extension. Numerous seismic swarms are often situated at the ends of segments, coinciding with detachment faults that bring deep material to the surface in the absence of sufficient magma supply to bridge the plate separation (Escartín et al., 2008; Simão et al., 2010). These seismic sequences exhibit characteristics of mainshock-aftershocks sequences and often show high p -value, and decay factor in the modified Omori's law (Utsu et al., 1995), indicating greater decay rates along these faults. The presence of serpentine likely lubricates these faults (Simão et al., 2010), leading to a reduced seismicity rate along them, suggesting that part of the slip may be aseismic or generate seismic events of lower magnitude than the detection threshold of hydrophones.

Despite the oceanic extension being primarily driven by magmatic processes along the slow-spreading MAR, only a few instances of magmatic accretion have been recorded, such as near the Lucky Strike volcano situated at 37°N on the MAR, which was also detected by terrestrial seismological stations. Along the Reykjanes ridge in the North Atlantic, [Goslin et al. \(2005\)](#) reported large magmatic swarms with characteristics indicating a hydrothermal origin. Typically, these magmatic swarms are found at the center of segments, while tectonic sequences are observed at the ends of segments and along discontinuities, well-matched with variations in the thickness of the oceanic crust and associated Bouguer gravity anomalies ([Goslin et al., 2012](#)).

Despite the oceanic extension being primarily driven by magmatic processes along the slow-spreading MAR, only a few instances of magmatic accretion have been recorded, such as near the Lucky Strike volcano situated at 37°N on the MAR, which was also detected by terrestrial seismological stations. Along the Reykjanes ridge in the North Atlantic, [Goslin et al. \(2005\)](#) reported large magmatic swarms with characteristics indicating a hydrothermal origin.

Along CIR in the Indian Ocean

The teleseismicity of the Central Indian Ridge (CIR) displays irregular patterns along its axis, where earthquakes are primarily clustered along both transforming and non-transforming discontinuities, while many segments exhibit minimal seismic activity, remaining nearly aseismic at the threshold of completeness in the ISC catalog. Between the triple junction and 21°S, most rupture mechanisms appear to be extensive, except for the Gemino fracture zone, which produces only a few earthquakes ranging between *mb* 4-4.5. Hydrothermal sites such as Kairei and Edmond are the most active regions (Figure 1.22) but till now the seismicity surrounding them has not been extensively studied. North of 22°S, the majority of earthquakes align along transform faults, majorly displaying strike-slip mechanisms. Overall, the seismicity rate along the CIR is low comparable to that of the SEIR. Hydroacoustic studies of the region show seismicity patterns similar to those recorded by global seismological networks ([Hanson and Bowman, 2005](#); [Royer et al., 2015](#)). Also, earthquake swarms are more concentrated at the ridge axis, within the central valley.

1.5.4 Seismicity along ultraslow spreading ridges

Along ultra-slow ridges, like the Gakkel in the Arctic and SWIR in the Indian Ocean, where plate separation is mainly accommodated by tectonic processes, one would anticipate even greater seismic activity than on slow-spreading ridges. However, these ridges have been relatively understudied due to their remote locations and challenging access conditions. In the Arctic region, the presence of ice hinders the deployment of autonomous hydrophones or seismometers. The Gakkel Ridge, being relatively close to the coast, benefits from better coverage by land-based seismolog-

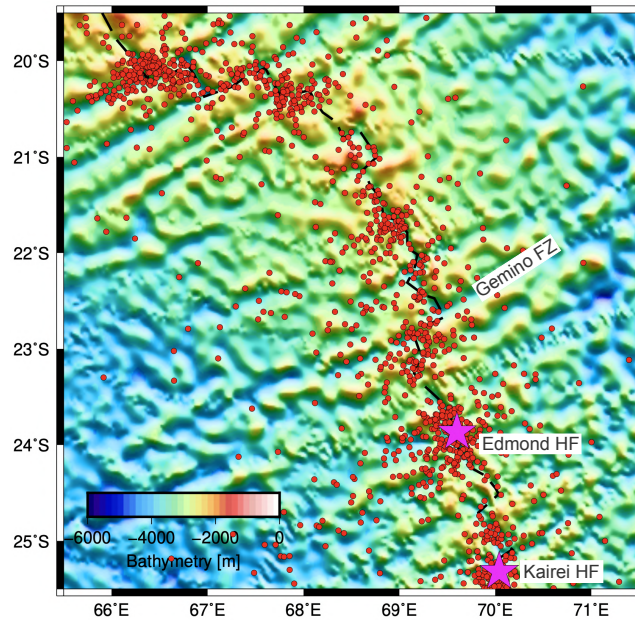


Figure 1.22: Locations of seismic events between 1980 and 2020 obtained from the ISC catalog along the CIR. A majority of events cluster in the vicinity of two hydrothermal fields, Edmond and Kairei (pink stars).

ical stations in Scandinavia, up to a magnitude threshold of $m_b = 3.5$. Additionally, seismometers have been installed on the ice pack as part of the AMORE project since 2001 (Schlindwein et al., 2007). Here, regions with scarce magmatic material and abundant peridotites experience few earthquakes and lack earthquake swarms (Figure 1.23). Conversely, in magmatic zones, seismicity is more frequent and of higher magnitude, often accompanied by significant seismic swarms (Schlindwein et al., 2015).

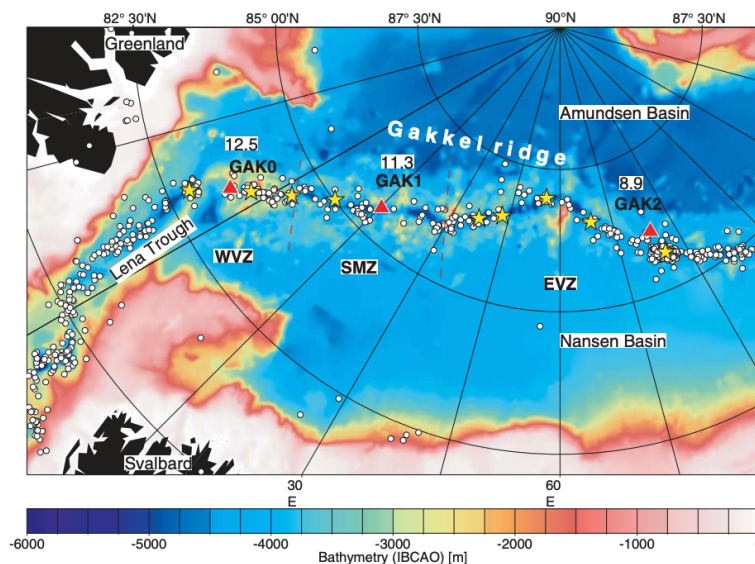


Figure 1.23: Locations of earthquakes obtained from the ISC catalog along the Gakkel ridge. Yellow stars mark inferred hydrothermal vent fields, (after Schlindwein et al., 2007).

On both the Gakkel and the SWIR, seismic swarms are dense and long-lasting (Schlindwein,

2012) compared to those along slow to fast-spreading ridges and are mostly concentrated along magmatic segments. In 1999, a swarm of 250 earthquakes, magmato-tectonic in nature, was recorded by seismological stations along the Gakkel Ridge (Müller et al., 2000). Similarly, between 1997 and 2002, several swarms of over 10 events each suggested magmatic activity on the SWIR, occurring in the vicinity of a volcanic edifice (Schlindwein, 2012). Despite these observations, the specific processes involved in magma emplacement are not yet well understood. However, large magnitude events along such ultra-slow spreading ridges are mostly associated with rupture mechanisms of normal faults, primarily reactivated by variations in stress after dike emplacement.

Along SWIR in Indian Ocean

The seismic activity of the SWIR has received limited attention in research. Nevertheless, the seafloor displays substantial deformation, and investigations into the rupture mechanisms reveal intricate processes of deformation (Tsang-Hin-Sun et al., 2016). Among the noteworthy seismic events recorded since the initiation of seismological recordings are two swarms comprising over 10 events each, occurring between 1997 and 2002. (Schlindwein, 2012) interpreted these particular episodes as of magmatic origin. Along the ridge, earthquakes are found to be distributed relatively uniformly and persistently over time (Figure 1.24). Unlike the CIR and SEIR, the fracture zones are not the most seismically active regions, and the segments exhibit seismic activity of comparable intensity. Several OBS surveys have revealed the magmatic nature of seismicity along SWIR segments, e.g. at 13°E (Schmid and Schlindwein, 2016; Grevemeyer et al., 2019), at 49°36'S (Yu et al., 2018), at 66°30'S (Schmid et al., 2017).

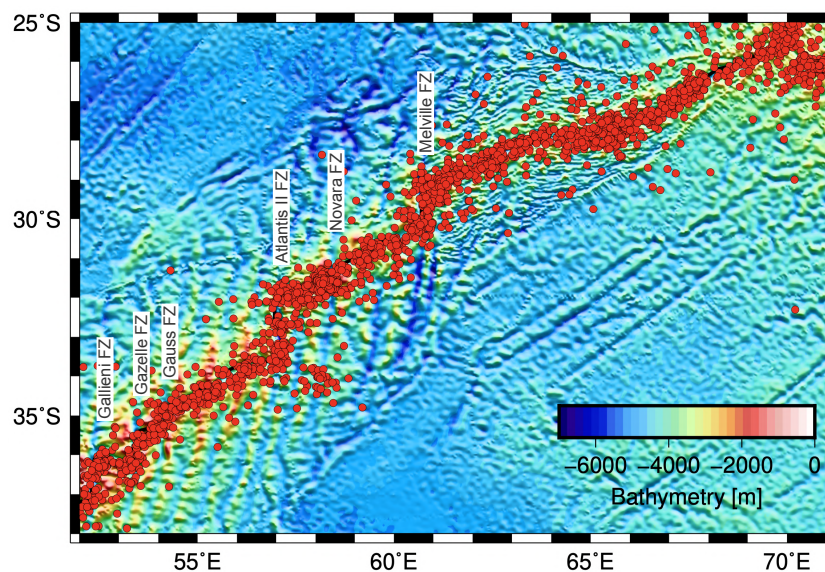


Figure 1.24: Locations of seismic events between 1980 and 2020 obtained from the ISC catalog along the SWIR. Here events are primarily distributed along the ridge axis.

1.5.5 Importance of studying the seismicity in the Indian Ocean

A notable disparity emerges between the seismicity rates as well as the nature of seismic swarms at fast and slow spreading ridges. Fast-spreading ridges, characterized by high relief, exhibit a scarcity of swarm activity (Fox et al., 2001), while slow ridges display an abundant presence of notable low-magnitude seismic swarms nested in the axial valleys (Smith et al., 2003). In between, ridges with intermediate spreading rates present a strong correlation between spreading rate, morphology, and frequency of swarms (Bohnenstiehl et al., 2004). There exists a strong correlation between seismicity rate with fast or slow-spreading ridges. However, an in-depth investigation into ultraslow and intermediate ridges reveals a more intricate relationship. Additional factors, such as the thickness and composition of the oceanic crust, the temperature of the mantle, and the influx of magma, potentially exert control over the seismicity of oceanic ridges.

To gain further insights into the underlying tectonic processes at ridges, hydrophone networks play an important role by detecting low-magnitude seismic events which are primary contributors to swarm activity. This avenue of investigation facilitates a deeper comprehension of ridge dynamics and their intricate interplay with the spreading rate. Nonetheless, it is essential to acknowledge the paucity of comparative studies, hindered by the reliance on in-homogeneous data sets due to the networks' varying sensitivities. A pressing need arises for a homogeneous data set that can facilitate a robust comparison of the seismicity among ridges with contrasting spreading rates. This imperative quest for uniformity in data will pave the way for a more comprehensive understanding of the seismic phenomena underlying ridge formations.

Hydrophone and OBS networks have ushered in a new era of understanding seismic swarms in the vast expanses of the Pacific and Atlantic oceans. These advanced technologies, particularly adept at recording microseismicity, have bestowed us with invaluable insights into the intricate movements of oceanic transform faults and the placement of magma both at depth and along ridge segments. One must tread cautiously, as the diverse observations stem from networks endowed with distinct characteristics - differing in size, geometry, detection threshold, and observation time. Such disparities can inadvertently introduce observation bias, rendering the task of comparison a formidable challenge. Yet, a beacon of hope shines in the Indian Ocean, where three ocean ridges converge at the RTJ. Within this unique convergence, lies an opportune setting for a comparative study, untangling the enigmatic relationship between swarm activity and spreading rates. Presently, the seismicity of Indian Ocean ridges remains veiled in mystery, as only a handful of studies have ventured into this realm (Royer et al., 2015; Tsang-Hin-Sun et al., 2015), extended over the ridge axes with short-term monitoring of hydroacoustic data.

The DEFLO hydroacoustic experiment in 2007-2008 has unveiled a hidden world of seismic activity in the southern Indian Ocean. With a network of three autonomous hydrophones, numer-

ous low-magnitude earthquakes were detected, eluding the grasp of terrestrial catalogs. Inspired by these groundbreaking results, the OHASISBIO network expanded its reach, deploying five more observation sites since 2010, delving into the heart of the three ocean ridges. The focus of this thesis rests on data collected from 2010 to 2020. This rich dataset spanning over 10 years serves as the focal point of this work, with the ambition to unravel the spatial and temporal distribution of seismic swarms along the three ridges. My aim is to uncover the relationships between the nature of these swarms and spreading rates, peering into the essence of geodynamic forces.

Before dwelling on the seismicity of three MORs in the Indian Ocean, I will give a comprehensive overview of the generation and propagation of hydroacoustic waves, hydroacoustic experiments, and methods to analyze the seismic swarms in the next chapter.

1.5.6 Importance de l'étude de la sismicité dans l'Océan Indien (En français)

L'examen des taux de sismicité et de la nature des essais sismiques révèle une disparité notable entre dorsales rapides et lentes. Les dorsales à ouverture rapide, caractérisées par un relief élevé, présentent peu d'essaims (Fox et al., 2001), tandis que les dorsales lentes présentent une abondance d'essaims sismiques dans leurs vallées axiales (Smith et al., 2003). Entre les deux, les dorsales à taux d'expansion intermédiaires présentent une forte corrélation entre le taux d'expansion, la morphologie et la fréquence des essaims (Bohnenstiehl et al., 2004). Les dorsales ultra-lentes révèlent une relation plus complexe entre taux de sismicité et taux d'expansion. Il apparaît que des facteurs supplémentaires tels que l'épaisseur et la composition de la croûte océanique, la température du manteau et l'afflux de magma pourraient potentiellement exercer un contrôle sur la sismicité de ces dorsales.

Pour obtenir de plus amples informations sur les processus tectoniques aux dorsales, les réseaux d'hydrophones apportent une information nouvelle en détectant les événements sismiques de faible magnitude. Leur observation complète notre compréhension de la dynamique des dorsales et des effets des taux d'ouverture. Cependant, il est essentiel de reconnaître le manque d'études comparatives, faute de données adéquates en raison de la disparité des réseaux et de leur sensibilité. Il manque ainsi de données homogènes permettant une comparaison robuste de la sismicité entre dorsales à taux de propagation contrastés, qui ouvrira la voie à une compréhension plus complète des phénomènes sismiques associés à l'activité des dorsales.

Les réseaux d'hydrophones et d'OBS ont inauguré une nouvelle ère dans la compréhension des essaims sismiques dans les océans Pacifique et Atlantique. Ces technologies avancées, particulièrement aptes à enregistrer la microsismicité, ont apporté des connaissances inestimables sur l'activité des segments de dorsales et des failles transformantes océaniques, mais aussi sur la mise en place du magma en profondeur. Il est cependant nécessaire de progresser avec prudence, car

les observations diverses proviennent de réseaux dotés de caractéristiques distinctes : différences de couverture géographique, de géométrie, de seuil de détection et de durée d'observation. De telles disparités peuvent introduire involontairement un biais d'observation, faisant de toute tentative de comparaison un défi redoutable. Pourtant, une lumière d'espoir brille dans l'océan Indien, où trois dorsales convergent en un point triple (RTJ). Cette configuration unique en fait un cadre propice à une étude comparative, démêlant la relation énigmatique entre l'activité sismique et les taux d'ouverture. Actuellement, la sismicité des dorsales de l'océan Indien reste voilée de mystère, car les études à grande échelle sur ce domaine restent limitées (Royer et al., 2015; Tsang-Hin-Sun et al., 2016).

L'expérience hydroacoustique DEFLO en 2007-2008 a révélé un monde caché d'activité sismique dans le sud de l'océan Indien. Avec un réseau de trois hydrophones autonomes, de nombreux tremblements de terre de faible magnitude ont été détectés, échappant aux catalogues terrestres. Motivé par ces résultats, le réseau OHASISBIO a étendu ce réseau en déployant cinq sites d'observation supplémentaires en 2010, couvrant les trois dorsales océaniques. L'objectif de cette thèse repose sur les données collectées par ce réseau de 2010 à 2020. Cet ensemble de données continues sur plus de 10 ans est au coeur de ce travail, avec l'ambition de dévoiler la distribution spatiale et temporelle des essais sismiques le long des trois dorsales. Mon objectif est de découvrir les relations entre la nature de ces essais et les taux d'ouverture, scrutant l'essence des forces géodynamiques.

Chapter 2

Seismicity in the Ocean: Contribution of Hydroacoustic Monitoring

2.1 Nature and propagation of hydroacoustic sounds

The marine environment hosts a multitude of sounds, rendering it a dynamic and rich soundscape. These sounds originate from a variety of sources and interact with one another, resulting in a complex acoustic environment. To acquire a comprehension of the numerous sound sources present in the ocean, along with their inherent variability and the possibility of interference, it is imperative to cultivate a profound understanding of their intrinsic characteristics.

2.1.1 Acoustic waves in a fluid medium

From a physics perspective, sound can be conceptualized as an acoustic wave, which represents a vibratory phenomenon propagating through space. This wave instigates mechanical disturbances that modify the spatial attributes of particles within the medium. Analogous to other propagating phenomena, acoustic waves can be characterized by a physical parameter known as the speed of sound, which depends on the mechanical properties of the medium. In the context of a liquid medium, the speed of sound can be expressed as follows:

$$c = \frac{1}{\sqrt{\mu\rho}} \quad (2.1)$$

where c is the speed (m/s), μ is the coefficient of adiabatic compressibility (m^2/N), and ρ is the density (kg/m^3), both of which are parameters dependent on the type of material.

Seawater has a density of approximately $1030 \text{ (kg}/\text{m}^3)$ and an average sound velocity of 1475 m/s . By comparison, sediments have compressional velocities ranging from 1500 to 2500 m/s

and densities spanning 1300 to 2000 kg/m³. In the air, where the density is approximately 1300 (kg/m³), the speed of sound is 340 m/s.

2.1.2 Sound velocity in the ocean

In the ocean, the speed at which acoustic waves propagate is influenced by thermodynamic factors and the composition of seawater. Seawater primarily consists of H₂O molecules and dissolved salts such as Cl⁻, Na⁺, SO₄²⁻, and Mg²⁺. The proportion of these salts determines the salinity of the water, which varies across different locations but averages around 35 ‰ in the Atlantic, Pacific, and Indian oceans. Salinity generally remains relatively constant with depth, except in specific cases (e.g. ice melting). On the other hand, temperature decreases from the ocean's surface to the seafloor, with significant variations occurring only in the surface layer due to factors like ocean currents, water mixing, solar radiation, and interactions with the continents and the atmosphere (Figure 2.1). Below this thermocline (the transition layer between the warmer mixed water at the surface and the cooler deep water below), the primary factor influencing sound speed is pressure. The speed of sound in seawater can be determined using empirical equations of state, such as the International Equation of State of Seawater (IES80). There are many other simplified relationships available. One widely used formula in the field of underwater acoustics is proposed by [Medwin \(1975\)](#):

$$c = 1449.2 + 4.6T - 0.055T^2 + 0.00029T^3 + (1.34 - 0.01T)(S - 35) + 0.016z \quad (2.2)$$

where c is the sound velocity in m/s, T is the temperature in °C, z is the depth in m, and S is the salinity in ‰.

As shown in Figure 2.1, due to the combined effects of decreasing temperatures and increasing pressures (and moderate changes in salinity) with depth, the sound speed first decreases then reaches a minimum near ~1000 m and then increases with depth. This low sound-velocity zone defines the SOund Fixing And Ranging or SOFAR channel and plays a major role in the propagation of acoustic waves in the water column. Acoustic rays entering this low sound-velocity zone with a low incidence will be refracted within this layer and will propagate over long distances with minimal attenuation. Consequently, the SOFAR channel serves as an efficient waveguide for acoustic waves (Figure 2.2). The existence of this channel was initially identified by [Swainson \(1936\)](#). However, it was not until World War II that its full potential for long-range acoustic communication was realized ([Ewing et al., 1946](#)). Although the specific characteristics of the SOFAR channel, such as its depth and the location of the velocity minimum, can vary from one geographical area to another (mainly with the latitude), it is present in all oceans, except in the high latitudes where the temperature is nearly constant (particularly in winter). The depth at which the sound velocity

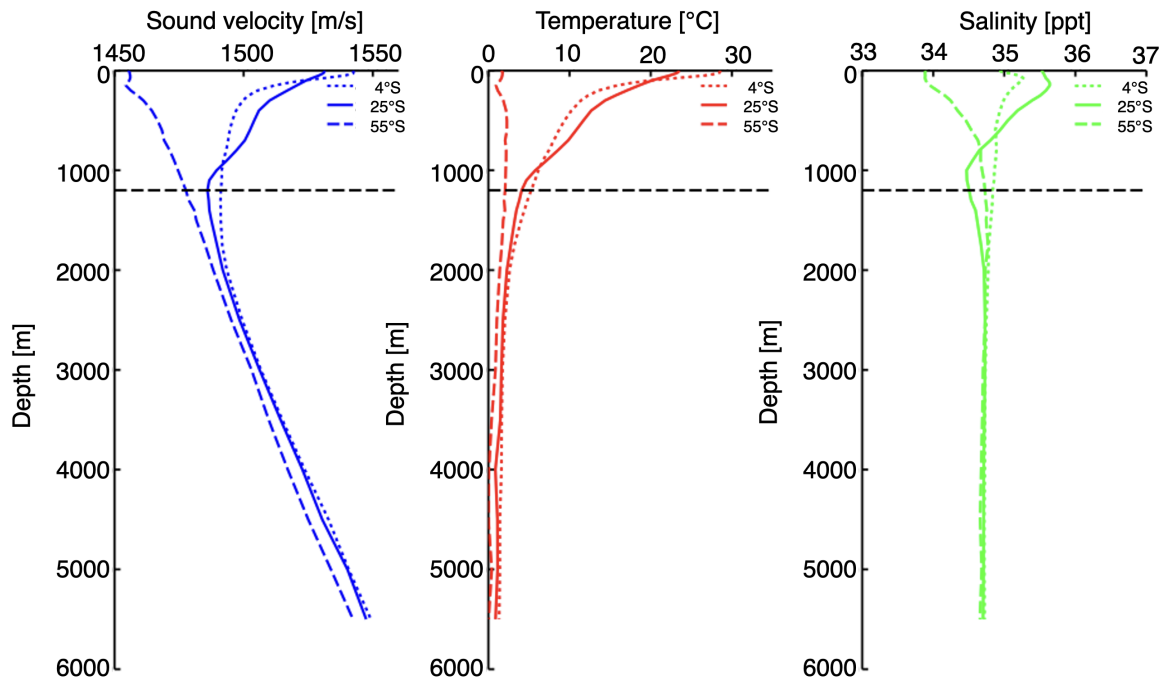


Figure 2.1: Relationship between sound speed, temperature, and salinity as a function of depth in the Indian Ocean at three different latitudes. The minimum sound velocity at 25°S (solid blue line), which corresponds to the axis of the SOFAR channel, is represented by a dashed black line.

reaches its surface value is called the critical depth; the SOFAR channel will be comprised between the sea surface and this critical depth, it thus may encompass the whole water column.

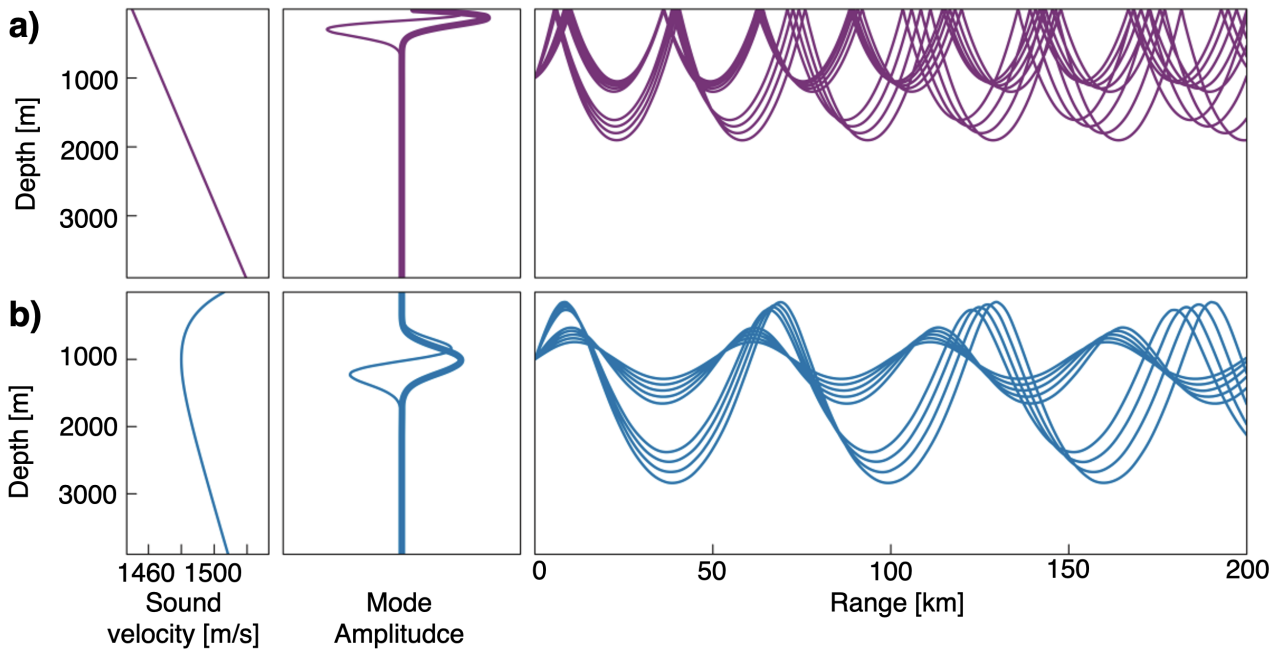


Figure 2.2: A graph illustrating the impact of a minimum-induced bend in the sound velocity profile on the propagation of acoustic waves in the water column, (after Wilcock et al., 2014).

The SOFAR channel plays a crucial role in facilitating the long-distance transmission of vari-

ous signals. This channel serves as a natural conduit for acoustic waves generated by underwater earthquakes and volcanic activity. The detection and recording of such signals have significantly contributed to our understanding of oceanic tectonics (Dziak et al., 1995; Fox et al., 1995; Smith, 2002). Other sounds also propagate through the SOFAR channel, such as iceberg cracking (Talandier et al., 2006), marine mammal calls (Leroy et al., 2016), anthropogenic noise originating from shipping, seismic exploration, and industrial activities.

2.1.3 Sound Level measurement

The oceanic sound pressure level (*SPL*) is measured in decibels (dB), which represents the ratio of the decimal logarithm of two power values (P_1 and P_2) multiplied by ten:

$$SPL = 10 \log \frac{P_1}{P_2} \quad (2.3)$$

As the power (P_i) is proportional to the square of the sound pressure (pi^2), the *SPL* is expressed as:

$$SPL = 20 \log \frac{p_1}{p_2} \quad (2.4)$$

The absolute sound level, measured in sound pressure units, can be written as:

$$SPL = 20 \log \frac{p}{p_{ref}} \quad (2.5)$$

With $p_{ref} = 1 \mu Pa$ in the water. If the measurements are conducted in air, then the *SPL* is expressed in dB re $20 \mu Pa^2$, whereas in water, it is expressed in dB re $1 \mu Pa^2$. This means that all else being equal, the *SPL* in water will be 20 dB less than the *SPL* for the same sound in air. For this study, all measurements are conducted in water, so the sound level is expressed in dB re $1 \mu Pa^2$, and for practical purposes may simply expressed in dB (with re $1 \mu Pa^2$ omitted).

2.2 Ambient noises

Contrary to popular belief, the ocean is far from a silent world as it harbors numerous natural and anthropogenic sources of sound that collectively contribute to the ocean's ambient noise. These sources encompass a wide range of phenomena, including earthquakes, icequakes, whale vocalizations, and ship engines. Each of these sources emits sounds within specific frequency ranges, as illustrated in Figure 2.3. The term "ambient ocean noise" refers to the cumulative effect of all these sounds propagating through the water column, as defined by Kibblewhite and Jones (1976).

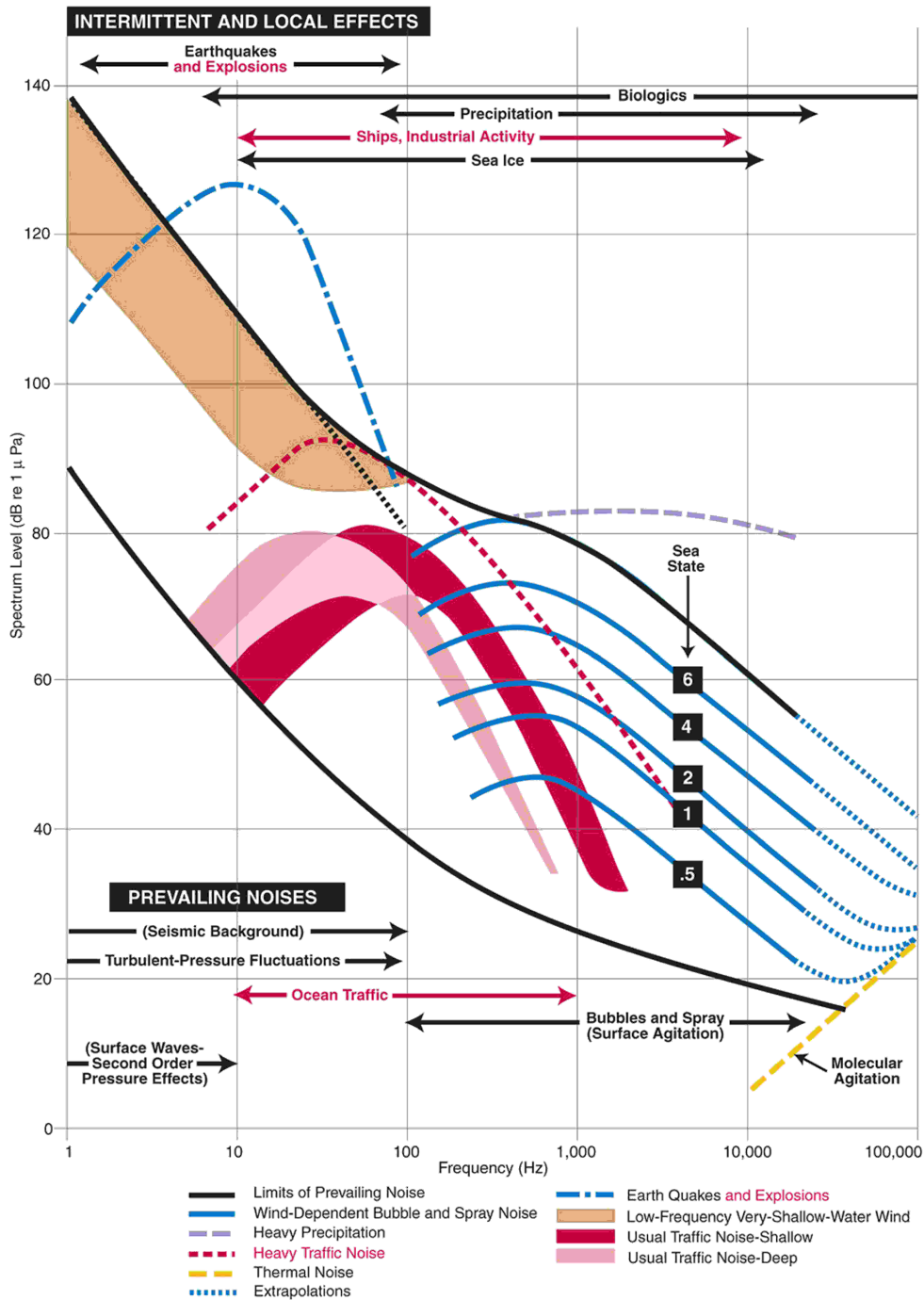


Figure 2.3: Frequency spectra of oceanic ambient noise, or Wenz curves, (after Miksis-Olds et al., 2013) and (adapted from Wenz, 1962)).

Natural sound sources

Natural sound sources in the ocean can be classified into biological and non-biological sources, with their intensity and frequency varying by location and season. In open seas, biological sources primarily involve marine mammals, such as whales, utilizing vocalizations and calls for communication and navigation. Non-biological sources include:

- **Submarine Earthquakes:** generates acoustic waves, which can travel long distances in the water column and help in understanding the geodynamical processes associated with ocean floor generation.
- **Cryoseisms (Icequakes):** similar to earthquakes, are caused by the movement of ice. The breakup of the Antarctic ice pack during the southern summer leads to the formation of icebergs. Collisions between icebergs can generate sounds with high amplitude, long duration, and a wide frequency range of up to 400 Hz due to temperature and pressure changes as well as shockwaves ([Dziak et al., 2013](#)).
- **Wind, storms, and rain:** These weather conditions generate high-level noise, particularly at frequencies above 100 Hz.

Anthropogenic sound sources

Anthropogenic sound sources in the ocean arise from human activities and can significantly impact ambient noise levels:

- **Resource Exploration and Extraction:** Activities such as seismic blasting, platform operations, drilling, and explosions related to mining and petroleum extraction contribute to noise pollution. These activities are prevalent in regions such as the Gulf of Mexico, California, and Brazil coastlines, and the North Sea. The source levels of airgun arrays used for seismic exploration are estimated to be 200–260 dB.
- **Shipping:** Cargo ships, supertankers, and liners contribute to ambient noise levels with sounds generated by their engines, propellers, or generators. These sounds range from 20 Hz to 300 Hz and can reach high levels, with a large cargo ship emitting sounds of 192 dB when sailing at a speed of 16 knots ([Hildebrand, 2009](#)).
- **Naval Sonar:** Naval sonar systems emit powerful, high-frequency waves above 10 kHz over long distances, often spanning thousands of kilometers.
- **Controlled source explosions:** Underwater explosions can also emit high energy ([Nielsen et al., 2021](#)).

The assessment of noise levels associated with human activities in the ocean has become a topic of significant concern across various scientific fields. The concept of noise pollution, already familiar in urban environments, is now gaining attention in discussions about the ocean. Extensive research has been conducted in the Atlantic and Pacific oceans to measure ambient noise levels and identify the sources of noise ([Andrew et al., 2002](#); [Hildebrand, 2009](#)). These studies have

revealed a strong correlation between the increase in anthropogenic noise and the rise in marine traffic over the past four decades, particularly in the North Atlantic and North Pacific regions (Hildebrand, 2009). The Indian Ocean has also witnessed a significant surge in marine traffic in the past decade (Tournadre, 2014).

The relationships among various sound sources in the ocean are intricate and not yet clearly understood, and even the sources themselves are not well comprehended. The primary sound source at low frequencies (< 60 Hz) is seismic activity caused at oceanic plate boundaries (ridges), which is the main subject of this study. The following sections highlight the generation and propagation of seismoacoustic waves and methods to characterize them.

2.3 T-waves

2.3.1 Definition

T-waves are low-frequency sound waves in the ocean, typically ranging from 5 to 60 Hz. They are generated by the conversion of seismic waves that originate from an earthquake in the oceanic lithosphere. This conversion occurs when seismic waves encounter a solid/fluid interface, such as the seafloor (Tolstoy and Ewing, 1950). Once generated, some T-waves will be entrapped within the SOFAR channel and propagate with minimal attenuation, meaning a very little loss of energy due to absorption or reflection at interfaces within the channel. This low attenuation allows T-waves to travel significant distances through the ocean, making the SOFAR channel an important pathway for the long-range propagation of underwater sound.

The term "T waves" (short for Tertiary waves) is derived from their late arrival on a seismogram, where they appear after P waves (primary) and S waves (secondary). When they reach the shoreline, they may convert back to seismic waves and arrive as the third set of waves after the P and S seismic waves on seismological stations near the coast (Jamet et al., 2013). This arrival delay is attributed to the propagation of T waves at the oceanic sound speed, around 1500 m/s, compared to seismic waves traveling through the solid Earth between the earthquake source and ground stations; P wave velocities (V_p) typically range from 4.5 to 8 km/s (4500-8000 m/s) and that of S wave (V_s) are generally 0.57 times of V_p . Recent modeling by Lecoulant et al. (2019) suggests that T waves travel at a velocity of approximately 1230 m/s near the seismoacoustic conversion zone due to discontinuities in the acoustic front, up to 1500 m/s beyond a horizontal distance of 50 to 100 km from the epicenter.

T waves exhibit a distinctive waveform, which resembles a lens or a cigar, where the wave amplitude increases to a maximum and then slowly decays to ambient noise levels, as shown in Figure 2.4. This unique cigar shape distinguishes T waves from seismic waves. Models of T-phases

generally consider two regions: a relatively short excitation region where the T-phase characteristics are established and a propagation region where the T-phase energy is totally trapped in the ocean sound channel. The maximum amplitude of the T-phase lens is considered to correspond to the location on the seafloor where the conversion of seismic energy to acoustic energy reaches its maximum within the T-phase excitation region (Slack et al., 1999).

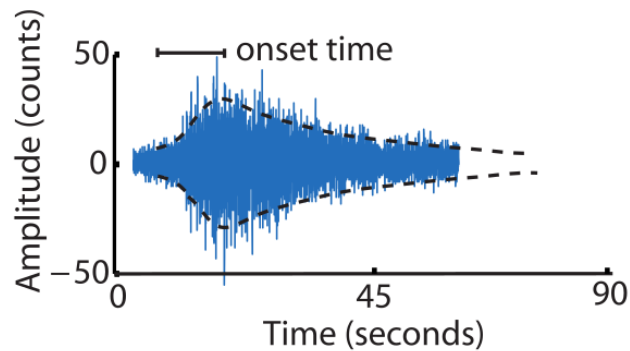


Figure 2.4: Example of a T-phase time signal. The T-phase is composed of a lens or envelope of energy lasting a minute or more. After a short onset time, it gradually decays back after its maximum amplitude, (after Williams et al., 2006)

T waves are seismic waves that undergo partial interaction with the oceanic water column, and their propagation is facilitated by the presence of the SOFAR channel. In certain cases (steep seafloor slope), when a T wave encounters a fluid/solid boundary such as a continental shelf or an island, it can convert back into a seismic wave. As a result, T waves can be detected by land-based monitoring stations, providing valuable seismic information from oceanic regions (Talandier and Okal, 1998).

The discovery of T waves can indeed be traced back to approximately 100 years ago in 1927. Jaggard (1930) observed high-frequency oscillations on a seismic station record from the Hawaii Volcano Observatory (HVO) following the main seismic wave arrivals from the Alaska earthquake on October 24 (Figure 2.5). These oscillations were initially interpreted as the resonance of the volcano. Collins (1936) interpreted the third wave train observed on a seismogram of an earthquake originating in the Caribbean on September 15, 1935, as an independent phase, providing a closer interpretation of the T-wave principle. However, Linehan (1940), who extensively studied this earthquake, is credited with first using the term "T-wave" in 1940. It was not until the end of World War II, in 1945, that the phenomenon of T waves was more clearly defined by Tolstoy and Ewing (1950). Since then, different models of T-wave generation have been established and further research has contributed to our understanding of T-wave propagation and behavior.

2.3.2 Generation and propagation of T-waves

Williams et al. (2006) summarized several potential mechanisms (Figure 2.6), that could explain

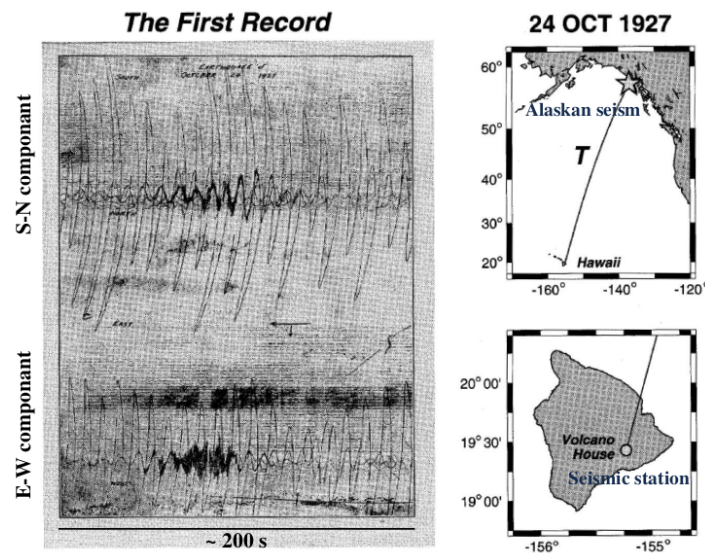


Figure 2.5: First historic recording of a T-wave at Hawaii Volcano Observatory in 1927, (after Jaggard, 1930).

the confinement of T-waves within the SOFAR channel. Their study indicates that acoustic wave produced at the boundary between the Earth's crust and the ocean has a low angle of incidence, primarily attributed to the disparity in velocity between the ocean floor and the water column.

If an earthquake generates acoustic waves in the ocean within a sloped region, the seismoacoustic conversion zone occurs. In this zone, multiple reflections of waves between the ocean floor and the water surface can take place, resulting in a gradual increase in the horizontal propagation path of the wave (Figure 2.6a). This process continues until the wave becomes trapped in the SOFAR channel, which occurs when it reaches a critical grazing angle of approximately 12° (Okal, 2008). This particular model, referred to as the downslope conversion phenomenon, is based on geometric acoustics and was initially proposed by Johnson et al. (1963). This model has its limitations in explaining the "abyssal T-wave" observed in abyssal areas with no significant landforms. To account for this phenomenon, alternative hypotheses beyond geometric acoustics are required.

In situations where the seismoacoustic conversion zone encompasses areas with significant relief or seamounts, the detection of T-waves in the abyss may not occur. Instead, these T-waves can directly emerge into the SOFAR channel, as illustrated in Figure 2.6d. These landforms can function as radiators, leading to the efficient generation of T-waves within the SOFAR channel compared to a flat seabed near the seismic source (Chapman and Marrett, 2006). This can introduce errors in the determination of an earthquake epicenter as the acoustic source since T-waves originated from a seamount nearby.

Other studies, such as those conducted by de Groot-Hedlin and Orcutt (1999); Park et al. (2001); Yang and Forsyth (2003), have also put forth the idea of a diffusion mechanism resulting from the roughness of the seafloor (Figure 2.6b). de Groot-Hedlin and Orcutt (1999) propose a model

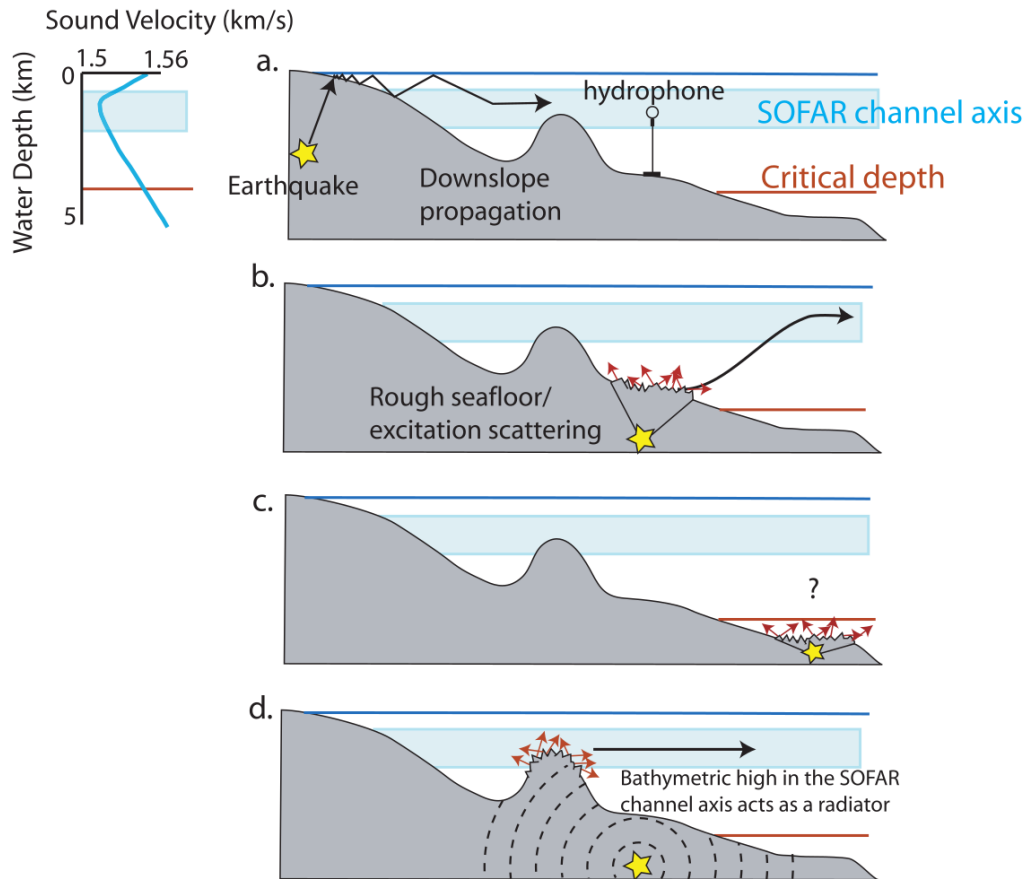


Figure 2.6: Possible T-wave generation mechanisms described by (Williams *et al.*, 2006): **a**) Downslope Conversion: A ray traveling downslope undergoes repeated reflections, gradually approaching a horizontal path with an angle corresponding to twice the slope of the seafloor. **b**) Scattering by Rough Seafloor: T-waves can result from scattering caused by an uneven seafloor. **c**) Critical Depth: Waves below a certain depth are unable to reach the axis of the SOFAR (Sound Fixing and Ranging) channel. **d**) Direct Acoustic Emission: Acoustic energy is emitted directly within the SOFAR channel, possibly originating from a seamount functioning as an acoustic radiator.

that characterizes an acoustic standing wave in terms of its modes, which are solutions derived from the propagation equation. They argue that the generation of T-wave modes is significantly influenced by the roughness of the seafloor interface or seafloor scattering, as well as the depth of the seafloor. At shallow depths, the lowest order modes are excited, enabling efficient propagation within the SOFAR channel. At greater depths, higher-order modes are excited but face limitations in propagation due to their low angle of incidence, vertical propagation, and energy loss caused by reflections. Horizontal propagation becomes feasible through energy transfers occurring between modes, facilitated by the roughness of the seafloor interface.

In the seismic records of the July 29, 1965 earthquake, off the Aleutian Islands, Johnson and Norris (1968a) observed two distinct phases of T-waves (Figure 2.7). One phase was associated with the conversion of waves from a sloped region (referred to as downslope T-phases), while the other phase corresponded to the abyssal region. To address the challenge of lacking a bathymet-

ric radiator for T-wave generation in the abyssal areas, [Johnson and Norris \(1968a\)](#) proposed a phenomenon called diffusion, which arises from the roughness of the water surface. When acoustic waves are generated at the seafloor, they possess a nearly vertical incidence angle. Through multiple reflections at the water surface, a diffusion phenomenon occurs, enabling the generation of waves with favorable incident angles for trapping within the SOFAR channel in the absence of slopes. The initial idea of scattering by a rough sea surface ([Johnson and Norris, 1968b](#)) is now revived ([Bottero et al., 2023](#)).

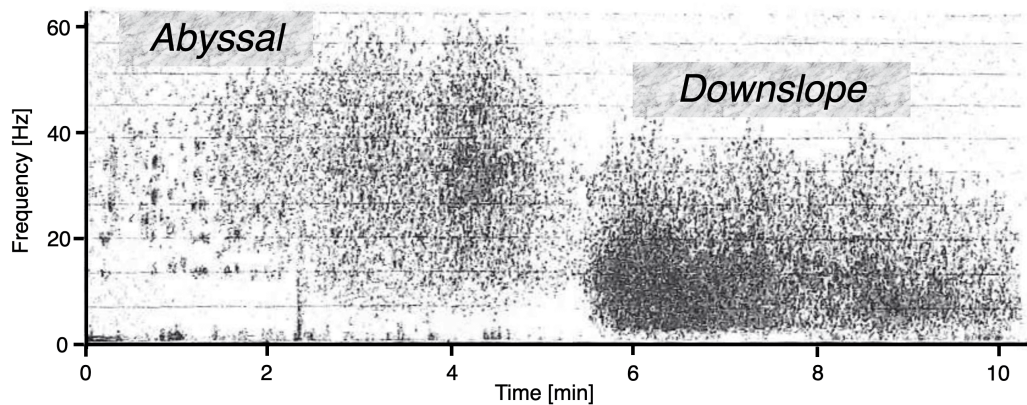


Figure 2.7: According to [Johnson and Norris \(1968b\)](#) and [Okal \(2008\)](#), the T-waves generated by the Aleutian earthquake of 29 July 1965 can be divided into two phases. The first phase, known as the abyssal phase, is created by the scattering of an uneven sea surface. On the other hand, the second phase, known as the downslope converted phase, is formed by the slopes of the islands, resulting in a delay in its arrival time compared to the first phase. The first phase is produced near the epicenter, while the second phase is generated further away due to the presence of the islands.

Despite the various proposed mechanisms for T-wave generation and their confinement within the SOFAR channel, none of these approaches provide a comprehensive explanation for all the characteristics observed in recorded T-waves. Furthermore, they fail to account for certain cases, when the seafloor lies below the critical depth of the SOFAR channel (as shown in Figure 2.6c). As a response to these gaps, researchers at the Lab Geo-Ocean (LGO) at the University of Brest have focused investigations on modeling T-waves, their conversion, and their propagation within the SOFAR channel. This research, documented in three theses ([Balanche et al., 2009](#); [Jamet et al., 2013](#); [Lecoulant et al., 2019](#)) contributes to a deeper understanding of T-wave behavior and aims to provide more comprehensive explanations for their generation and propagation characteristics. [Jamet et al. \(2013\)](#) conducted simulations of T-waves using the spectral element code-SPECFEM2D, achieving strong agreement with observed T-waves in the Atlantic Ocean. Their simulations comprehensively considered key aspects of T-wave propagation, including the radiation pattern of the source, seismic wave propagation, seismoacoustic conversion at a rough seafloor, and the propagation of acoustic waves in the water column. Analytical model by [Lecoulant et al. \(2019\)](#), describing T-wave propagation as Rayleigh modes in a 2D configuration with a flat bottom and a uniform

ocean, demonstrated excellent agreement between theoretical and simulated T-wave modes. This numerical model is confidently applied to configurations where deriving an analytical model is challenging, such as a crust/ocean interface with a seamount, with or without a SOFAR channel in the ocean, and a flat seabed with short-wavelength roughness. The simulations shed light on the conditions required for generating energetic T-waves, confirming the predominant role of Rayleigh modes in their propagation. The model's outputs, particularly with a rough sea bottom, align well with hydroacoustic records from a significant earthquake beneath an abyssal plain.

2.3.3 Propagation loss of T-waves

Acoustic waves undergo attenuation during propagation mainly by three means:

1. **A transmission loss** due to the geometrical spreading of a wavefront occurs as the sound radiates away from its source, covering larger and larger surfaces. In a homogeneous three-dimensional (3D) medium, when a point source emits sound in all directions, the wavefront takes the shape of a sphere. As the wave propagates, the surface area of the sphere increases, resulting in a decrease in the intensity of the sound signal proportional to the inverse square of the distance (R_1) between the source and a given point. This decrease in intensity, known as spherical divergence, can be quantified by the transmission loss (TL) expressed as $TL = 20 \log R_1$, where R_1 is the distance from the source and a reference distance (R_0) of 1 meter is used. The TL is measured in decibels (dB re 1 m). However, the lower and upper limits of the SOFAR channel vary, which means that wavefront conservation cannot be maintained over propagation distances that exceed the thickness of the SOFAR channel or the water layer. Consequently, the wavefront assumes a cylindrical shape, and the intensity of the sound signal decreases proportionally to the propagation distance R_2 (Figure 2.8). This decrease in intensity due to cylindrical divergence can be expressed as $TL = 10 \log R_2$ (dB re 1 m). Therefore, the total TL is the sum of these two types of divergences, spherical and cylindrical (Jensen et al., 1994).

$$TL = 20 \log_{10} \frac{R_1}{R_0} + 10 \log_{10} \frac{R_2}{R_0} \quad (2.6)$$

2. **Absorption** refers to the phenomenon where energy is dissipated within the ocean water medium itself. This dissipation occurs mostly due to the composition of the ocean water. At high frequencies, typically around 1 MHz, it is influenced by the viscosity of the water medium. Additionally, at frequencies below 100 kHz, chemical relaxations within the water also contribute to absorption effects. It is important to note that this type of attenuation is not considered significant for frequencies below 100 Hz.

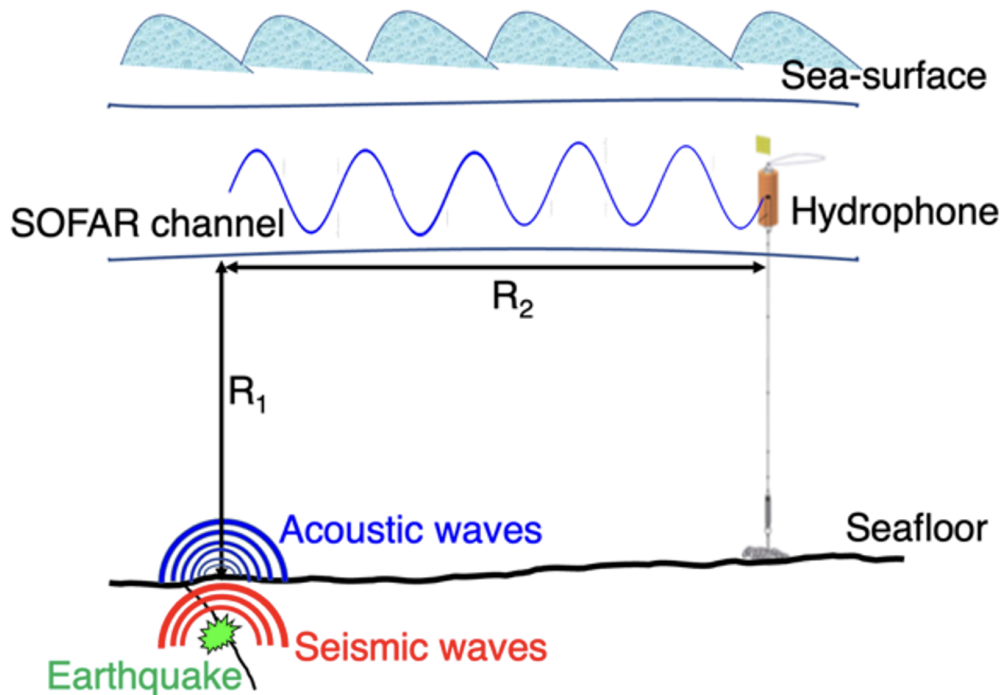


Figure 2.8: Cartoon of T-wave generation and its propagation. R_1 is the distance between the source and point of contact at the SOFAR channel, R_2 is the distance traveled in the SOFAR channel.

3. **Interaction** refers to the attenuation of T-waves due to their interaction with obstacles present in the medium, such as interfaces (e.g. seafloor) or point objects (e.g. fish or other marine creatures). Unlike the previously discussed losses (absorption and spreading), quantifying the exact interaction loss is challenging.

2.4 Seismic sources and T-waves

Currently, there exists a limited understanding of the process by which seismic energy is converted into acoustic energy. Consequently, establishing a direct relationship between the characteristics of a T-wave (such as its waveform, source level, and amplitude) and the seismic event that generated it is not possible. Unlike seismic wave recordings obtained from ground stations, T-wave recordings do not provide information about the source's depth, its focal mechanism, or its magnitude. Moreover, determining the epicenter of an earthquake in the oceanic crust poses challenges. Uncertainty arises from the ambiguity surrounding the location of the acoustic source of the T-wave. Factors such as the extent of the conversion zone (which can span tens of kilometers of the seabed) and the effects of bathymetry on T-wave conversion contribute to this uncertainty (Jamet et al., 2013; Lecoulant et al., 2019).

The relationship between the Source Level (SL) of a T-wave and the magnitude of the earthquake it originates from does not have a direct physical connection. Instead, empirical models

based on linear regression are employed to establish a link between these two parameters (e.g. Fox et al., 2001; Bohnenstiehl and Tolstoy, 2003; Dziak et al., 2004; Pan and Dziewonski, 2005; Royer et al., 2015). However, these models have limitations since they can only compare SL and magnitudes of earthquakes with $mb \geq 4$ or 4.5 (the limit of land-based catalogs in remote oceanic areas). Consequently, the empirical relationship between SL and magnitudes is primarily based on high-magnitude events recorded by land stations. In addition, the early generation of hydrophones had limitations, including saturation during strong earthquakes, resulting in a smaller number of usable events for analysis. While there are extensive catalogs of hydroacoustic earthquakes, only a few events can be matched to an equivalent number of seismic magnitudes from terrestrial seismic catalogs. Studies have demonstrated a strong correlation between the SL and seismic magnitude (mb) for events in the Pacific with magnitudes ranging from 4 to 5 (Figure 2.9; Fox et al., 2001). Other authors have compared SLs with moment magnitude M_w (e.g. Dziak, 2001; Olive and Escartín, 2016; Parnell-Turner et al., 2022). Similar correlations between SL and different types of magnitudes (e.g. volume mb , surface M_s , and moment M_w) have been established for events in the Indian Ocean (Tsang-Hin-Sun et al., 2016). The best correlation coefficients were obtained for moment magnitude (correlation coefficient $R^2 = 0.8$ for M_w , $R^2 = 0.7$ for M_s and $R^2 = 0.53$ for mb). It is important to note that the relationship between SL and earthquake magnitude also depends on the specific terrestrial catalogs considered. Also, different acoustic magnitudes can be associated with the same Source Level, and vice versa (Royer et al., 2015).

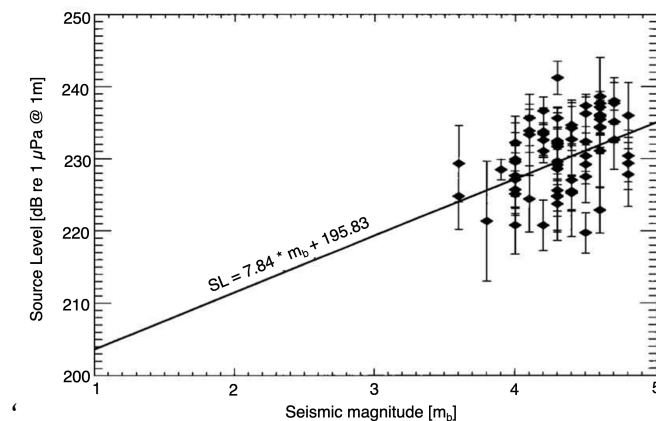


Figure 2.9: Relationship between acoustic source level derived from the hydrophone array of the Pacific ocean with corresponding seismic magnitude, (after Fox et al., 2001)

The complexities involved in the conversion process and the variations in propagation conditions make it challenging to establish a direct and universal relationship between acoustic level and seismic magnitude. Additional factors such as the characteristics of the source, the surrounding medium, the bathymetry in the epicenter region, and the propagation path also influence the observed acoustic level. Therefore, a comprehensive understanding of T-wave generation and propagation mechanisms is necessary to fully characterize the energy of the seismic source.

Different types of earthquakes can be classified based on their rupture mechanism, with normal rupture and shear rupture being the most common mechanisms observed in oceanic ridges (Sykes, 1970). Dziak (2001) conducted a study to examine the relationship between moment magnitude and acoustic magnitude for earthquakes with different rupture mechanisms which resulted in an empirical relationship indicating that shear rupture mechanisms generate higher acoustic energies compared to normal rupture mechanisms (Figure 2.10). Similarly, Tsang-Hin-Sun et al. (2016) applied a similar approach to earthquakes in the Indian Ocean and found that earthquakes caused by shear faults are associated with higher magnitudes ($M_w > 6$) compared to those caused by normal/reverse faults ($M_w < 5.5$). Park et al. (2001) and Balanche et al. (2009) have developed models to study seismoacoustic conversion processes and have observed that S-waves produce more energetic T-waves compared to compressional P-waves. Therefore, the type of earthquake rupture mechanism and the type of seismic wave generated can influence the magnitude of the T-wave recorded by hydrophones.

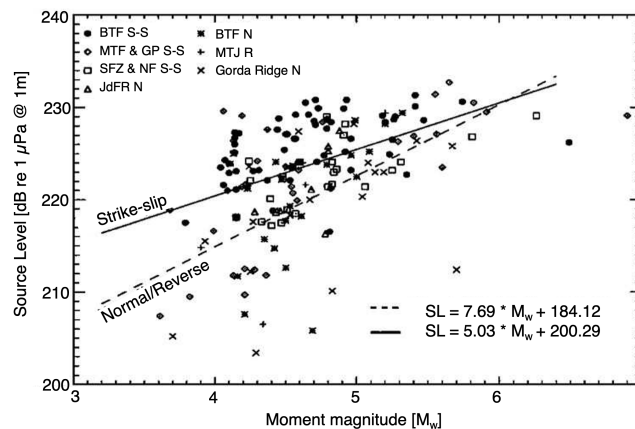


Figure 2.10: Relationship of earthquake T-wave acoustic source level and earthquake moment magnitude depending on fault mechanisms, (after Dziak, 2001)

Previous studies have shown that while the general shape of the T-wave can be identified, there is significant variability in its details. For example, Williams et al. (2006) have categorized different T-wave signals based on their rise time, which is the duration between the onset of the wave and the arrival of its maximum amplitude. They observed that long rise times correspond to deep events, while short rise times correspond to shallow events (<2 km). These findings contradict those of de Groot-Hedlin and Orcutt (1999) and Yang and Forsyth (2003), who observed the opposite. This suggests that the variability in the details of T-waves is influenced by various factors. Importantly, this study emphasizes that the differences between T-waves and seismic waves at their source primarily arise from the seismoacoustic conversion at the seafloor and their propagation in the SOFAR channel.

2.5 Hydrophone arrays

The establishment of the initial global network of seismological stations on land during the early 1960s was a remarkable accomplishment, providing extensive coverage for detecting seismicity worldwide. However, these terrestrial networks have limitations when it comes to capturing seismic events in remote regions such as mid-ocean ridges. It is worth noting that earthquakes resulting from magmatic processes often have magnitudes below the detection threshold of terrestrial networks, which means they often go unnoticed (Bergman and Solomon, 1990). As a result, the global terrestrial networks are not as effective in capturing seismic activity along mid-ocean ridges when it comes to earthquakes of moderate magnitudes. To overcome this limitation, ocean bottom seismometers (OBS) were deployed in the 1980s to study regional seismicity and microseismicity. OBS devices, function similarly to land-based seismometers and provide accurate seismic measurements at great depths on the ocean floor. However, OBS deployment is expensive, and the geographical coverage is limited due to the rapid attenuation of seismic waves over relatively short distances (typically 50-150 km), compared to the vast expanse of a ridge that can span ~15,000 km.

During the past two decades, passive marine acoustics has emerged as a leading approach to address the challenges associated with the remote locations and low magnitudes typically found in ridge seismicity. This method involves the deployment of hydrophone arrays in the SOFAR channel, far from coastal areas. The hydrophones, deployed on moorings, continuously capture low-frequency background ocean noise throughout their deployment duration, providing a wealth of valuable information. In some cases, the recorded data can be retrieved directly from the equipment, or it can be partially transmitted using radio or satellite networks for further analysis and interpretation. This capability of acquiring data from remote locations contributes significantly to our understanding of ridge seismic activity.

Hydrophone arrays offer a significantly enhanced detection capability compared to land-based stations, enabling the identification of up to 20 to 50 times more seismic events. This increased sensitivity lowers the seismic event detection threshold of the global array from 4.6 mb to below 3 mb (Fox et al., 1995, 2001; Dziak et al., 2004). The hydrophone networks exhibit superior precision in locating earthquake epicenters along ridges with location uncertainties of ~2-3 km compared to land stations where uncertainties are ~10-20 km (Fox et al., 2001). While hydroacoustic data are valuable for pinpointing earthquake locations, they are unable to provide information about seismic source attributes such as magnitude, focal mechanisms, or depth. Therefore, complementary approaches are necessary to gain a comprehensive understanding of the seismic characteristics of ridge events.

The declassification of the US Navy's SOund SURveillance System (SOSUS) program at the end

of the Cold War opened up various possibilities for utilizing hydroacoustic data. In 1991, the Pacific Marine Environmental Laboratory (PMEL) at NOAA initiated the monitoring of seismic activity along ridges using data obtained from the Pacific Ocean (Fox et al., 1995; Fox and Dziak, 1998). This initial effort was followed by the deployment of the first autonomous hydrophone array (AUH) by PMEL-NOAA in 1996, to monitor seismic and volcanic activity on oceanic ridges (e.g. Fox et al., 2001; Bohnenstiehl et al., 2002). Subsequently, since 2002, the PMEL-NOAA and the Lab Geo-Ocean have collaborated extensively in monitoring oceanic ridges with hydrophone arrays. These endeavors have contributed significantly to advancing our understanding of ridge processes and seismic events in the marine environment.

2.5.1 The OHASISBIO network

The OHASISBIO (*Observatoire HydroAcoustique de la Sismicité et de la Biodiversité*) network provides extensive coverage of a significant portion of the Indian Ocean Basin. With strategically placed hydrophones at 7 to 12 stations (Figure 2.11), this network serves two main purposes: monitoring large baleen whales and investigating seismic activity related to the three Indian Ocean ridges (Royer, 2009).

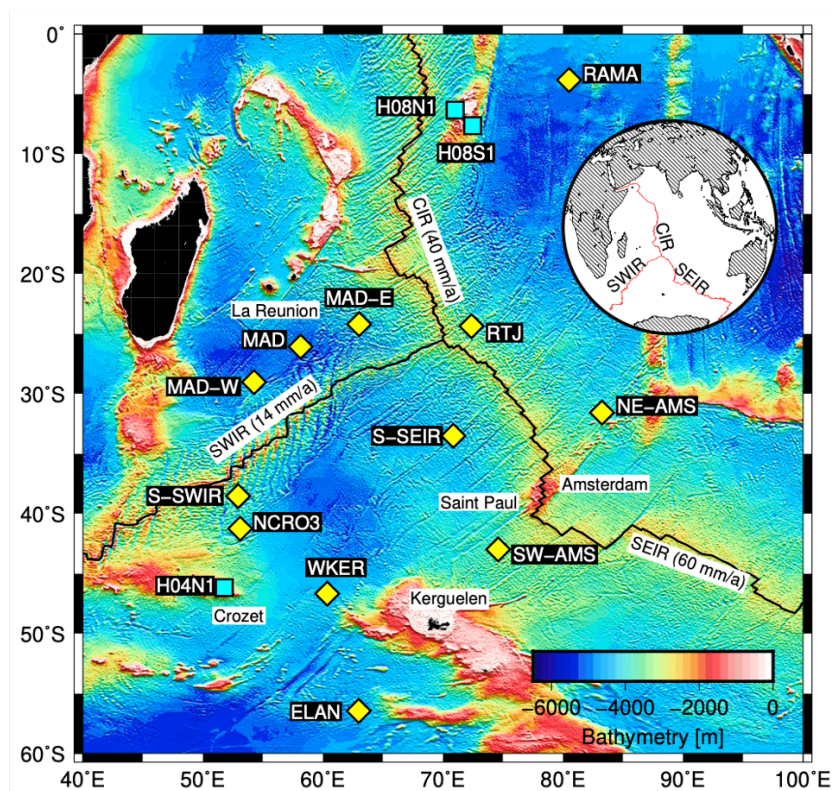


Figure 2.11: Temporary stations of the OHASISBIO network (yellow diamonds). The permanent stations of the IMS-CTBTO (cyan squares) complemented its geographical coverage.

In this network, triads of hydrophones were deployed to the west of the Kerguelen Islands

(WKER) and north of the Crozet Archipelago (NCRO), in addition to the previous locations of the hydrophone DEFLO experiment: MAD, NE-AMS, and SW-AMS (Figure 2.11, Royer, 2008). The primary objective of these hydrophones placed 30 km apart at the apex of a triangle, was to capture and accurately analyze whale vocalizations, as well as to track passing whales. However, the NCRO triad of hydrophones turned out to be located at a very noisy site due to strong local ocean currents, resulting in only one usable sensor. Taking advantage of the ship's opportunities to expand the network up to equatorial latitudes, the RAMA station at 4°S was incorporated into the network in 2012-2013. Subsequently, in 2014 and 2018, two new stations were established south of the Southeast Indian Ridge (S-SEIR) and of the Southwest Indian Ridge (S-SWIR), respectively (Table 2.1). These stations complemented the monitoring of these two ridges (the latter also replaced the NCRO station). Furthermore, since 2017, two additional stations (MAD-W and MAD-E) have been set up in the Madagascar Basin instead of the initial MAD station. In 2018, an additional hydrophone was installed north of the Rodrigues triple junction (RTJ).

The OHASISBIO network is a prime example of its dynamic and adaptable nature, catering to the evolving demands of scientific research. Operating as a multidisciplinary observatory, it was efficiently maintained at a low cost, largely due to the regular expeditions of the research vessel *Marion Dufresne* in the southern Indian Ocean. By strategically utilizing existing resources, continuous monitoring, and data collection are made possible, facilitating comprehensive studies across various scientific disciplines.

Year	2012	2013	2014	2015	2016	2017	2018	2019	2020
MAD-W	-	-	-	-	✓	✓	✓	✓	✓
MAD	✓	✓	✓	✓	✓	-	-	-	-
MAD-E	-	-	-	-	✓	✓	-	✓	-
RTJ	-	-	-	-	-	-	✓	-	✓
RAMA	✓	✓	-	-	-	-	-	-	-
NE-AMS	✓	✓	-	-	-	✓	✓	✓	✓
S-SEIR	-	-	✓	✓	✓	✓	✓	✓	✓
SW-AMS	✓	✓	✓	✓	✓	✓	✓	✓	✓
ELAN	-	-	-	-	-	-	✓	✓	✓
WKER	✓	✓	✓	✓	✓	✓	-	✓	✓
NCRO3	✓	✓	✓	-	-	-	-	-	-
S-SWIR	-	-	-	-	-	✓	✓	✓	-

Table 2.1: OHASISBIO hydrophones, with their active acquisition duration (ticks)

Instrumentation

The OHASISBIO hydrophones were developed at the Lab Geo-Ocean (LGO) and have the same general design as those of the PMEL (Figure 2.12a).

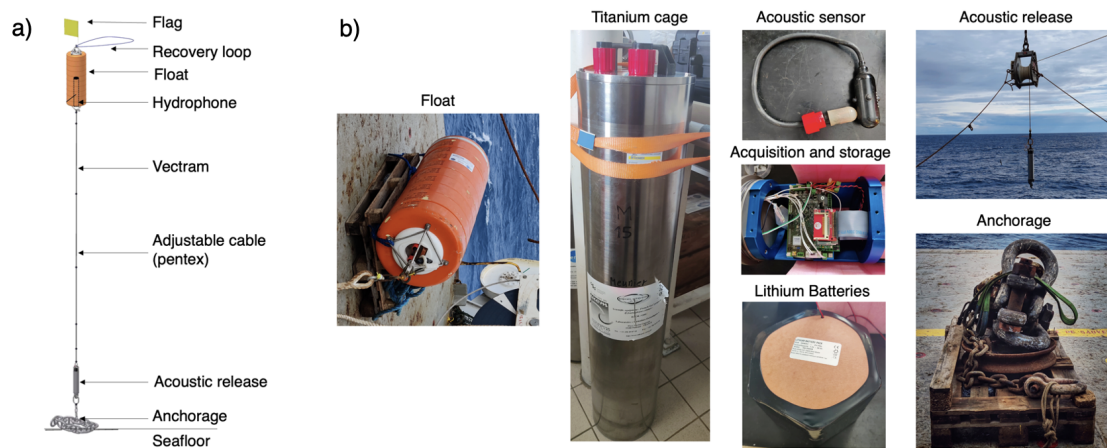


Figure 2.12: **a)** *Hydrophone mooring developed at Lab Geo-Ocean.* **b)** *Mooring components: float, titanium cage, acoustic sensor, acquisition-storage device, lithium battery, acoustic release, and Anchorage.*

A mooring line is normally made up of the following components:

- A disposable anchor (300-400 kg) on the seafloor;
- An acoustic release;
- A mooring line composed of pieces of several cables that can be adjusted in length so that the hydrophone in the float is in the SOFAR channel axis;
- A float that keeps the line taut and protects the instrument itself (recorder in a titanium cylinder) during acquisition, and brings the line to the surface when it is released from the anchor.

The hydrophone itself has two main components: an acoustic sensor and a titanium cylinder that serves as the housing for the acquisition system, storage device, and a set of lithium batteries (usually two to three packs, but the instrument can hold up to 5 of them), as shown in Figure 2.12b. The batteries run approximately for 24 months, providing long-term operational capability. The instrument is equipped with a high-precision quartz clock and records samples at a frequency of 240 Hz. Before deployment, the quartz clock is synchronized with the GPS time to ensure accurate timing. Upon recovery of the instrument, the calibration of the clock is crucial for assessing its drift. This is performed by re-synchronizing the clock with the GPS time; the discrepancy between the two clocks yields drift over time. To minimize drift, before deployment, the frequency of the quartz clock is adjusted such that the deviation remains within acceptable limits, typically 0.01 ppm, yielding a long-term drift in the order of 1 to 5 seconds over one year. The acoustic sensor is a piezometer calibrated by its manufacturer (High Tech Inc.). The calibration process involves determining the response curve, which characterizes the sensor's sensitivity to different frequencies. For the sensors we used (mostly HTI-90U), the response curve is flat in the frequency range from 2

Hz to 1 kHz. This calibration information ensures accurate interpretation of the recorded acoustic data within the specified frequency range.

Deployment

In the deployment phase, the float is initially released into the ocean, then the mooring cable as the ship sails towards the selected mooring site, at its end the the acoustic release is mounted, and finally the weight chain is dropped. To account for the pendulum effect caused by the line around the float as the weight descends, the release point for the weight is strategically positioned about 1/7th to 1/10th the length of the line after passing above the targeted site. This arrangement helps to mitigate the swinging motion of the line. Once the weight has reached the sea bottom (descent at ~ 2 m/s), the exact location of the mooring on the ocean floor is determined by a triangulation method (trilateration). It requires at least three points, $\sim 120^\circ$ from one another around the estimated location of the mooring line, where an acoustic modem queries the acoustic release. By measuring the travel times between the ship, whose GPS position is known, and the acoustic release, the position of the mooring is calculated by trilateration (Figure 2.13), so that the exact coordinates of the mooring are determined. This information is needed both for its recovery and the data interpretation (assuming the line remains always vertical).

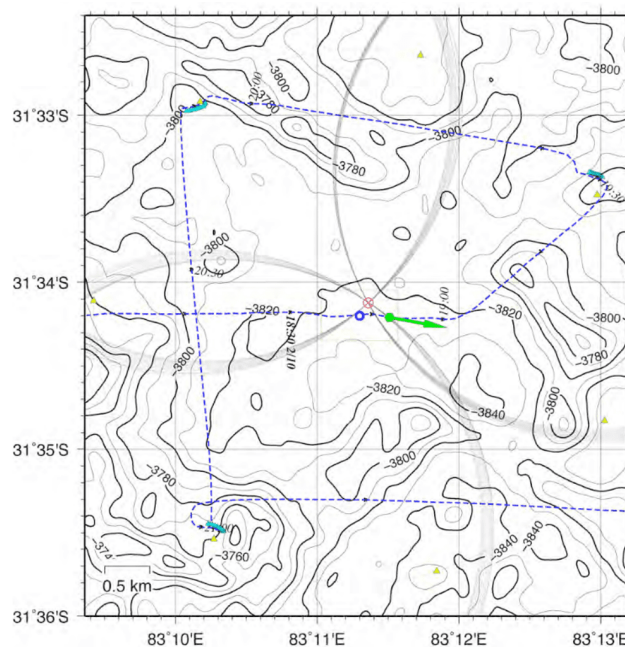


Figure 2.13: Location of the mooring line anchor at the NEAMS station in 2014 after trilateration (red symbol) based on the intersection point of ranging circles (gray). Ship tracks and locations of ranging stations used for triangulation are shown by dashed blue lines and blue triangles. The anchor release point and vessel heading are shown by a green circle and arrow. The anchor landed very close to the targeted site (blue symbol).

Recovery

The recovery process of the mooring line requires an acoustic modem to order the acoustic release to open. Upon arrival at the mooring site, the modem sends a signal to interrogate the acoustic release, prompting its release once located (Figure 2.14). If the acoustic release does not respond, the mooring cable can be severed with grapples, to cut the line from the anchor. These actions allow the float to ascend to the surface. Once the float surface and is successfully located, the ship is maneuvered towards it to facilitate its retrieval (grapples are thrown from the ship to seize it; Figure 2.15). On board the ship, the mooring cable is carefully wound onto wheels, and thoroughly inspected to identify any potential defects. Finally, the acoustic release is collected on board, completing the recovery process. The duration of the entire process, from locating the instrument to its arrival on board, typically takes approximately 3 hours. This time frame may vary depending on specific circumstances and conditions encountered during the retrieval operation.

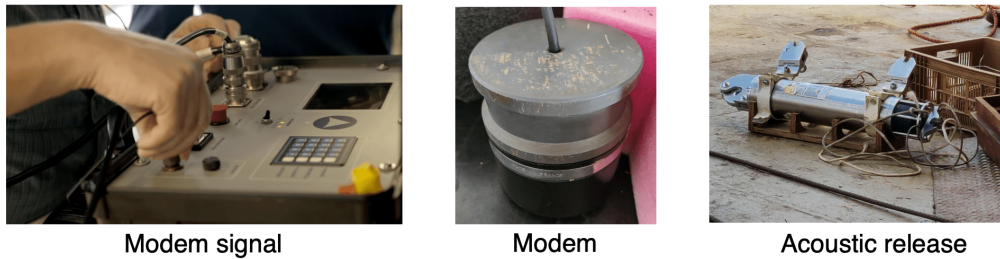


Figure 2.14: *Sending a signal from ship via modem to acoustic release*



Figure 2.15: *Recovery of hydrophone instrument on ship*

2.5.2 The IMS-CTBTO network

The implementation of the Comprehensive Nuclear-Test-Ban Treaty (CTBT) by the United Nations necessitates the surveillance and monitoring of acoustic disruptions occurring within the Earth's oceans. This measure is crucial to prevent the concealment of a potential nuclear test, either within the water column or on a remote island. By monitoring these acoustic disturbances, the treaty aims to ensure compliance with the ban on nuclear testing and maintain the integrity of the treaty's enforcement mechanisms (Okal, 2001).

The verification regime for the CTBTO includes networks of sensors from four distinct technologies (Figure 2.16): 50 primary and 120 auxiliary **seismic** stations to measure shockwaves traveling through the Earth's crust; 60 **infrasound** stations to listen to ultra-low frequency sound waves in the atmosphere; 11 **hydroacoustic** stations to detect sound waves in the oceans from a potential underwater explosion; 80 **land** stations to detect radioactive particles or gases from potential atmospheric explosions, or vented by underground or underwater nuclear explosions. All these networks form the International Monitoring System (IMS) of CTBTO.



Figure 2.16: Distribution of the IMS-CTBTO worldwide sensor network. The hydro-acoustic stations are comprised of five T-phase stations (black triangles) equipped with three-component seismometers typically deployed on small oceanic islands or close to the coast, and six hydrophone stations (black circles) each composed of triplets of underwater hydrophones, (after Nielsen et al., 2021).

IMS-CTBTO network in the Indian Ocean

In the Indian Ocean, IMS-CTBTO hydrophones are located 180 km northwest (H08N) and ~25 km south (H08S) off Diego Garcia Island, ~100 km southwest off Cape Leeuwin, Australia (H01W),

and since 2017, ~30 km north (H04N) and ~40 km south (H04S) off Crozet Island. All these stations comprise a triad of hydrophones moored in the SOFAR channel and deployed in a triangular configuration with 2 km spacing between instruments. These triads have a 20-year design life and are based on a linear non-modular design which offers the advantages of high reliability and efficient deployment in one continuous operation. This linear non-modular system is deployed from a ship in one contiguous operation, with the seafloor trunk cables bearing the deployment stresses (Figure 2.17). Each hydrophone from the triad is set to record acoustic waves continuously at a rate of 250 Hz with a 24-bit analog-to-digital resolution (similar to the OHASISBIO hydrophones that sample at 240 Hz).

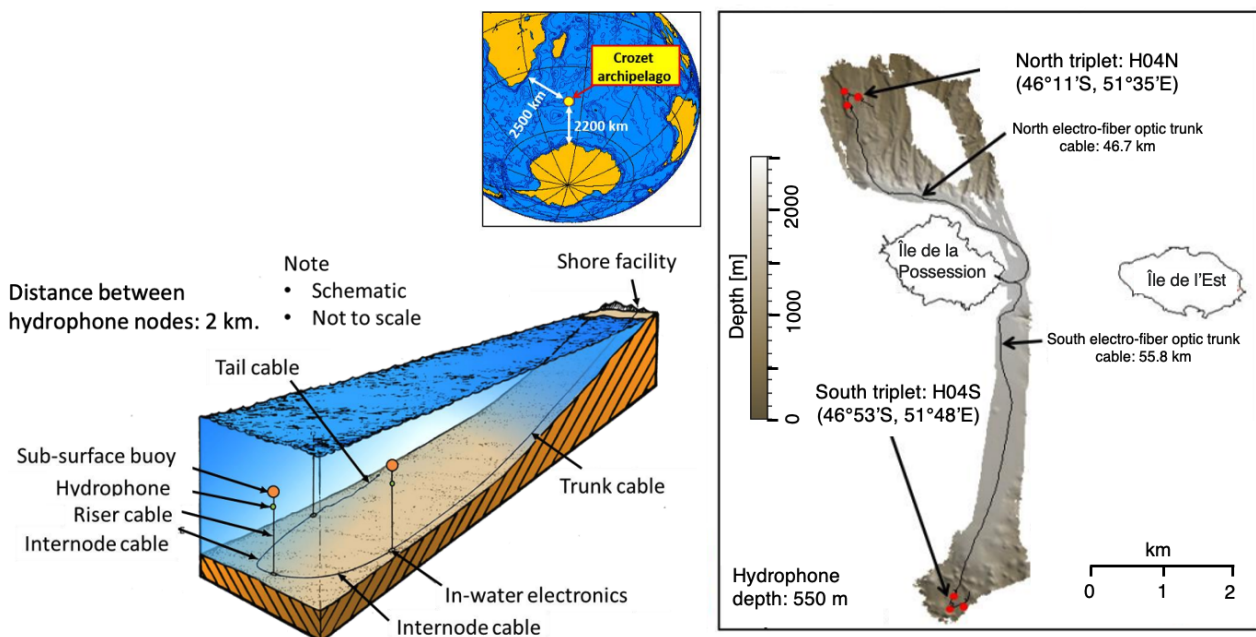


Figure 2.17: Schematics of hydrophone mooring of IMS-CTBTO. Configuration of the north and south triplet of hydrophone mooring near Crozet islands, (after Zampolli et al., 2021).

2.6 Seismic clusters

2.6.1 Extracting seismic clusters from land-based catalogs

In this thesis, my main objective is to understand the relationship between the spreading rates of MORs and the nature and distribution of earthquake swarms. To achieve this goal, I have extensively scanned the earthquake catalogs from the International Seismological Centre (ISC) ([Link](#)) along the SWIR, CIR, and SEIR in the Indian Ocean. ISC is one of the most detailed seismicity catalogs for global earthquake activity. It not only compiles many available catalogs but also provides its determinations. In this catalog, hypocenter solutions and magnitudes are based on the

"ak135" velocity model. The average accuracy of the epicenter location is estimated as $\sim 10\text{--}20$ km. The situation with teleseismic depth determination is much less accurate. Reliable figures for large events are very rare, but for shallow sources, the depth is generally set at 10 km below the seabed.

Seismic swarms can be either short-lasting (a few days) or long-lasting (up to a year). Based on the ISC catalog, I have extracted seismic clusters along the three Indian Ocean ridges between 2010 and 2020 using the following criteria:

- Occurrence of 5 or more earthquake events in a grid of 3×3 degrees in latitude and longitude within a 15-day period. We chose such a large geographical area because events in the ISC catalog are not well localized in remote regions of the MORs, i.e. have larger uncertainties (10-20 km) in locations. A similar method to extract swarm (cluster of at least 5 events) was applied by [Sykes \(1970\)](#), along the East Pacific Rise and Mid-Atlantic Ridge based on the earthquake epicenters compiled by the US Coast and Geodetic Survey.
- Define the duration of the cluster based on the origin time of the first and last event.

This criterion has obtained a total of 94 clusters. Out of them 15, 34, and 45 were located on the SWIR, CIR, and SEIR between 01 January 2010 and 31 December 2020, respectively (Figure 2.18). I have used the term "seismic cluster" for a group of events extracted from the ISC catalog before interpreting its origin. I also extracted the moment tensor solutions for available events from the Global Centroid Moment Tensor (GCMT) solutions ([Ekström et al., 2012](#)).

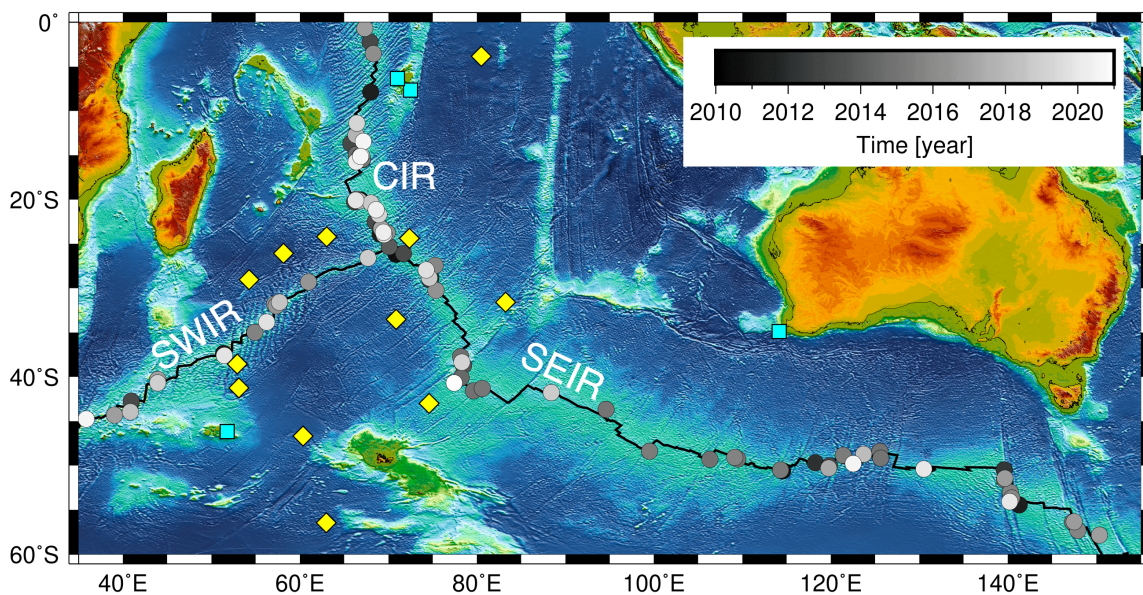


Figure 2.18: Median location of seismic clusters along the three Indian Ocean ridges: SWIR, CIR, and SEIR from 2010 to 2020, in gray-scale. Yellow diamonds and blue squares mark the location of the OHASISBIO and IMS-CTBTO stations, respectively.

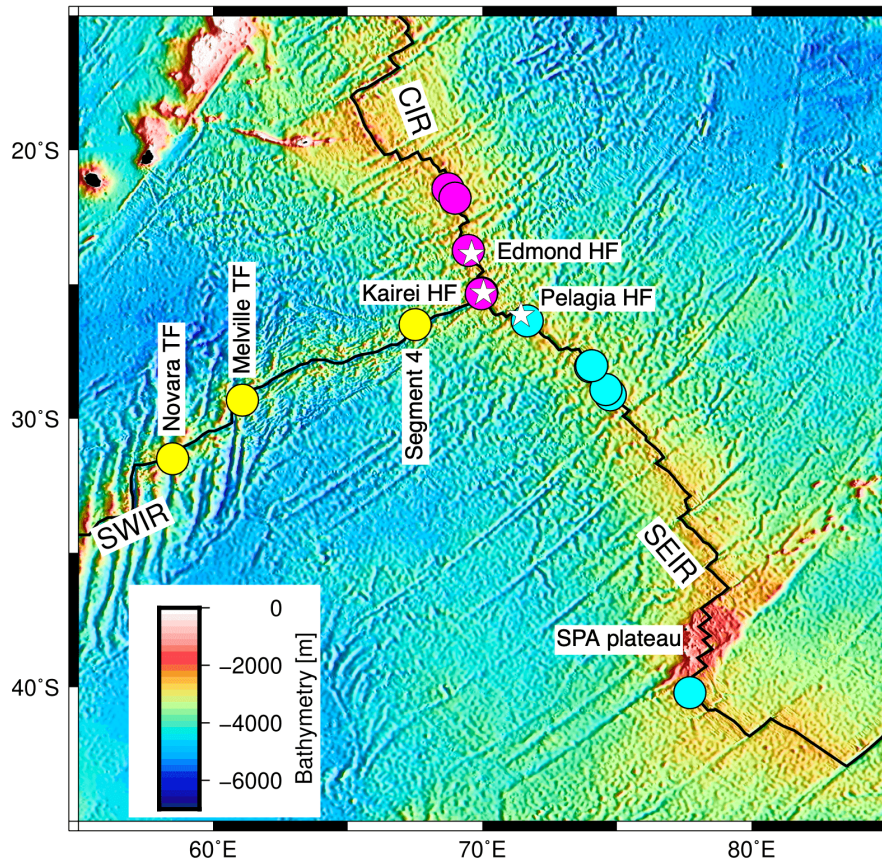


Figure 2.19: Selection of seismic clusters between 2012 and 2020 analyzed in this study: 3 along the SWIR (yellow), 5 along the CIR (pink), and 8 along the SEIR (cyan). White stars mark known hydrothermal fields along the CIR and SEIR.

Out of them, I have selected 15 clusters which are the largest in terms of a number of events per swarm and long-lasting in terms of their duration. They are located well inside the hydrophone network and in different tectonic contexts as shown in (Figure 2.19) and summarized in Table 2.2:

- On the SWIR: Three clusters, 1) near Novara TF, 2) near the Melville TF, and 3) near segment 4 at 67°45'S (segment numbers from Cannat et al., 1999), stand out clearly, as they comprised a large density of events (258, 231, and 92, resp). Cluster 1, which occurred in 2016-17, was the strongest cluster that will be studied in this thesis. Clusters 2 and 3 occurred in 2018 and were separated by just 5 months along the two extreme ends of the SWIR axis.
- The CIR did not comprise large seismic clusters like on the SWIR. Three clusters (4, 5, and 8) were situated in the proximity of the Kairei and Edmond hydrothermal fields, close to the triple junction (Figure 2.19). Two recurrent clusters (6 and 7), occurred slightly north of the Edmond HF, on segments 8-9 of the CIR (segments numbers from Briais, 1995). These 5 clusters were strongest among all the 34 clusters along the CIR.
- Along the SEIR, seismicity is primarily focused near the FZs except at two ridge segments at

Ridge	Sr No	Year	Dates (dd/mm)	Nbr of days	Median location	Region	Nbr of ISC	Nbr of GCMT
SWIR	2	2016-2017	09/06/16-25/03/17	290	29°11'S, 61°02'E	Melville TF	258	17
SWIR	1	2018	10/07-15/07	6	31°41'S, 58°18'E	Novara TF	231	7
SWIR	3	2018	27/09-27/10	31	26°35'S, 67°43'E	Segment 4	92	6
CIR	4	2013	16/02-07/05	83	25°24'S, 70°01'E	Kairei HF	7	3
CIR	5	2013	24/11-12/12	19	25°49'S, 69°58'E	Kairei HF	36	9
CIR	6	2019	10/04-27/04	18	21°41'S, 68°53'E	Segments 8-9	13	2
CIR	7	2020	10/04-15/04	6	21°46'S, 68°40'E	Segments 8-9	19	0
CIR	8	2020	17/04-04/09	141	23°42'S, 69°29'E	Edmond HF	68	7
SEIR	9	2012	04/07-12/07	9	29°02'S, 74°49'E	29°S segment	19	2
SEIR	10	2012	12/12	1	28°56'S, 74°38'E	29°S segment	13	0
SEIR	11	2013	16/02-07/05	83	26°18'S, 71°37'E	Pelagia HF	28	2
SEIR	12	2015	21/10-22/10	2	27°58'S, 73°59'E	28°S segment	10	0
SEIR	13	2018	26/08-15/09	21	28°47'S, 74°32'E	29°S segment	21	3
SEIR	14	2019	12/09-12/09	1	27°54'S, 74°02'E	28°S segment	5	0
SEIR	15	2020	04/12-15/12	12	40°13'S, 77°57'E	J3 segment	14	9

Table 2.2: Summary of seismic clusters between 2012 and 2020 along the SWIR, CIR, and SEIR extracted from the ISC catalog. These clusters are an integral part of this thesis work

28°S and 29°S (Tsang-Hin-Sun et al., 2016). In the period from 2010 to 2020, there were recurrent clusters along those two segments. Two clusters (11 and 13) occurred on a segment at 28°S and three (9, 10, and 12) occurred on a segment at 29°S. Also, the intersection of the SPA plateau with the SEIR axis near 40°S at J3 segment, (segment name from Scheirer et al., 2000) showed a cluster of 14 events, out of which nine events with normal faulting mechanisms in December 2020 (cluster14), the strongest cluster in this region between 2010-2020.

Cluster 4 which occurred in February 2013 near the Kairei HF simultaneously occurred at the Pelagia HF on SEIR (Cluster 11). The simultaneous analysis of the events may help to understand the similarities or differences between them. Having said that, I have analyzed 3 clusters along the SWIR, 5 along the CIR, and 7 along the SEIR to widely understand the relationship between the nature of seismicity, its origin with that of different tectonic settings like transform boundaries, ridge segments, and hydrothermal fields along the different ridges (Table 2.2).

2.6.2 Detection of T-waves

Currently, T waves are predominantly detected through networks of autonomous hydrophones that are deployed at sea. These networks undergo periodic maintenance after one or two years and accumulate vast amounts of data, reaching several hundred gigabytes. The processing of these data is primarily carried out manually (i.e. visually), although advancements have been made in

automated event detection. However, there are several challenges associated with the automated processing of T wave data:

1. Diversity of acoustic signals and sources: T waves can originate from various sources such as earthquakes and volcanic eruptions.
2. Variations in waveform: The waveform of T waves can vary depending on the azimuth or distance of the source, adding complexity to their analysis.
3. Large propagation distances: The hydrophone stations are often widely dispersed, resulting in significant propagation distances between them.

To address these challenges, the Pacific Marine Environment Laboratory (PMEL) has developed the "Seas" software, which facilitates the visualization and processing of data from their hydrophone fleet. This software, based on IDL libraries and X-window graphics, offers various tools for spectral analysis, filtering, audio conversion, as well as event identification, and localization. Operators can simultaneously visualize traces and spectrograms from multiple hydrophones within the same network (Figure 2.20). By recognizing the spectral characteristics of a particular event, the operator can interactively pick the arrival times of the corresponding signals on different traces. Determining the first arrival of an emergent T wave can be challenging, so typically, the arrival time of maximum energy is chosen. The software then derives a preliminary location based on these inputs, which can be checked for plausibility. If determined from 3 arrival times, then the software can predict the arrival times on the other sensors. In a new iteration, additional times will be repicked, a new location and origin time computed and checked, and so forth until a satisfactory level of certainty is achieved (best fit between the picked and predicted arrival times). This work is solely based on a visual examination and manual picking of arrival times in the hydrophone continuous records.

With the Seas software, investigating seismic clusters provides a substantial advantage relative to constructing a hydroacoustic catalog for a large region and long time span. Once an event in a cluster has been identified in the hydroacoustic data, for instance, a large magnitude event in the ISC catalog, then all the subsequent and earlier events from this cluster will be more or less aligned in a display like Figure 2.20. Because they all originate from the same location (or its immediate vicinity), the offset in travel times among the available hydrophones will remain more or less constant. This property greatly eases the association of T waves from clustered events, even when they are closely spaced in time in the hydrophone records. Conversely, if a hydrophone records an event that does not show in the other "aligned" hydrophone records, then the event is not related to the cluster and originates from another region of the ocean.

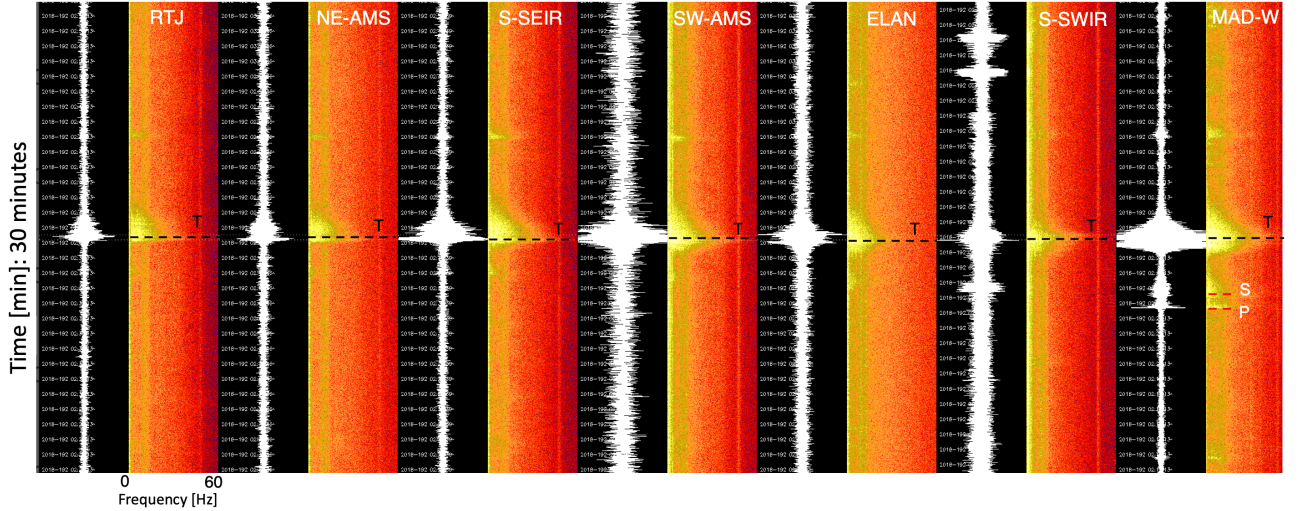


Figure 2.20: *T*-wave waveforms and spectrograms (5-60 Hz) originating from the same event on different hydrophones. The maximum *T*-wave energy peaks in the spectrograms are connected by a black dashed line. The MAD-W (rightmost) records display *P* and *S*-wave arrivals, converted at the foot of mooring (dashed red line) about 4 minutes before the *T*-wave arrivals (white horizontal marks in the time signal correspond to a 1-minute interval).

The non-linear least squares method for estimating the source location and origin time minimizes the arrival times as follows:

$$\min \sum_{i=1}^N w_i (a_i - b_i)^2 \quad (2.7)$$

where w_i is the weight (=1 for unweighted solution) and equal to the inverse of the travel time, a_i is the recorded arrival time on hydrophone i , b_i is recorded arrival time on hydrophone i and N is a total number of hydrophones recording the event. Hydrophones near the source, with presumably better-recorded arrivals and better arrival time determination, are given a higher weight.

The predicted arrival time is calculated based on an assumed location and origin time as:

$$b_i = t + d_i/c_i \quad (2.8)$$

where t is origin time, d_i/c_i is travel time in seconds, d_i is distance between hydrophone location i and assumed origin, and c_i is sound speed along the path i from hydrophone to assumed origin. The distances (d_i) are calculated by using a geodesic algorithm with a spheroidal Earth assumption. The sound speed estimates (c_i) a hydrophone to the event assumed origin. The distances (d_i) are geodesic distances assuming a spheroidal Earth. The sound speed estimates (c_i) along each path are derived from the Generalized Digital Environmental Model (GDEM) developed by the Naval Oceanographic Office (Teague et al., 1990). GDEM provides seasonal sound speed profiles from the sea surface to the seafloor on a 30 arc-minute grid. A harmonic average of the sound speed is computed from that at the SOFAR depth for each grid node along the path, for the given season (or month).

The least-square solution is derived iteratively by measuring arrival times and hydrophone locations and calculating travel times based on an initial estimate of the source location and origin time. The selection of an initial estimate can be critical to the convergence and stability of the solution. If an initial estimate does not fall within the general region of the actual event, it is possible that the solution can converge to a local minimum on the solution surface and derive a grossly incorrect source location. The incorrect location can be easily recognized by the relatively high residual errors (if more than three hydrophones were used). To improve the chances of deriving the global minimum solution, three origins are tested for each determination as follows:

1. A location in the center of the array (assuming the event inside the array)
2. A location outside the array in the direction of the hydrophone that recorded the first arrival (assuming the event is outside)
3. A location of the minimum residual error of a coarse grid over the entire region

After a solution is derived for all three cases, the case producing the lowest root-mean-square (RMS) residual error is selected as the source location. The iterative least squares calculation is performed by using a gradient expansion algorithm derived from the Marquardt method, which combines the best features of the gradient search method with the method of linearizing the fitting function (Bevington et al., 1993). When four or more receivers are available, the standard error for latitude, longitude, and origin time is derived from the variance-covariance matrix as modified by the mean squares residual.

In this work, T-waves associated with an event were manually picked in a two-iteration process (Appendix A). In the first iteration, 30-minute-long time windows were used for picking the maximum T-wave energy in the spectrograms (Figure 2.20). Figure 2.21 shows a typical output from an event detection. It contains (row-wise) the number and location of hydrophones used to detect the event; sound velocity between hydrophones and source; arrival time and received level on each hydrophone (based on the last arrival time); normalized weights given for the location of the event in the least-square minimization and the summary of event detection in the last row. It defines the event ID in the form of date and time; the number and names of hydrophones used to locate the event; its latitude, longitude, and SL; the 1σ uncertainties in latitude and longitude (in degrees), origin time (in seconds), and SL (in dB). Note that SL being in a logarithmic scale (dB), the given uncertainty should be read as $SL \pm \sigma$.

In this work, we manually picked T-waves associated with an event in a two-iteration process (Appendix A). In the first iteration, we used a 30-minute-long time window for picking the maximum T-wave energy in the spectrograms (Figure 2.20). Figure Figure 2.21 shows a typical output from an event detection. Row wise, such output file contains the number and location of

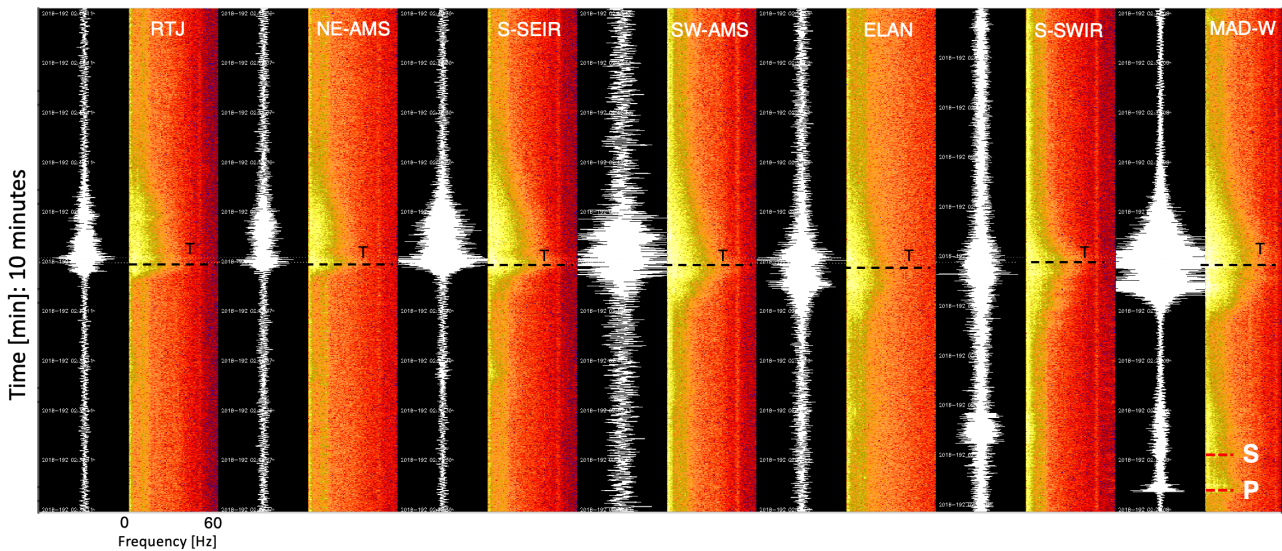


Figure 2.22: 10 minutes zoomed window of Figure 2.20

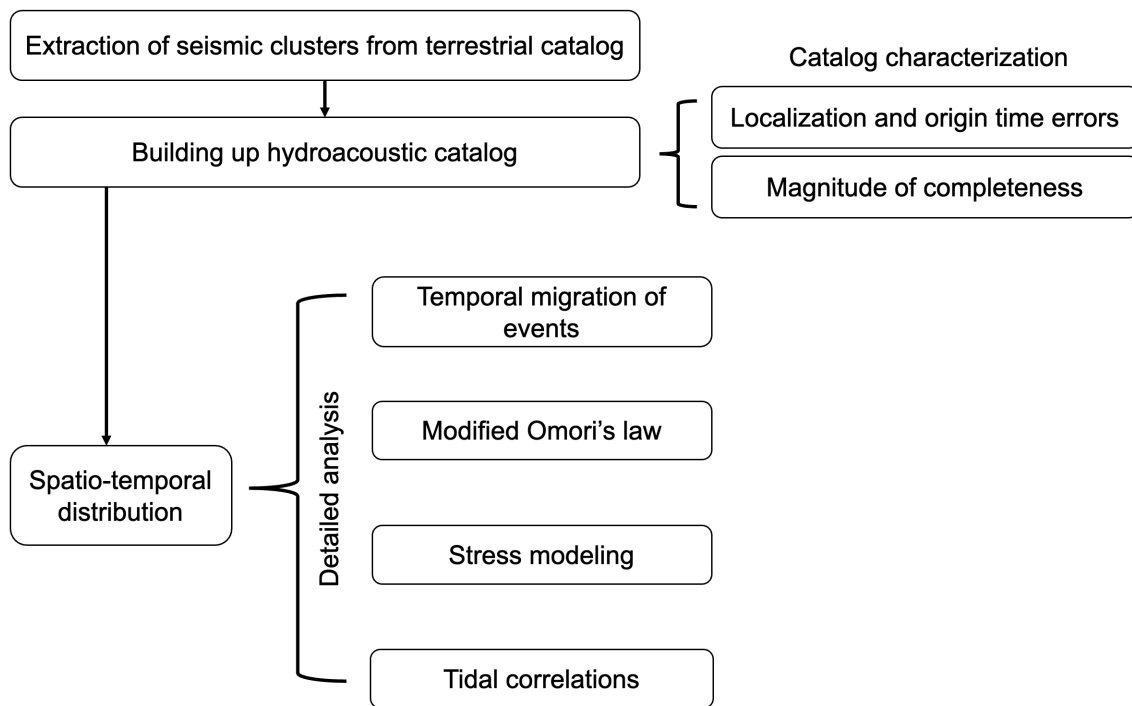


Figure 2.23: Flow chart describing a tentative way to analyze seismic clusters

2.7.1 Selection of time-window

We thoroughly investigated the seismic clusters identified in the ISC catalog through hydroacoustic analyses to gain insight into their characteristics. The first step is the establishment of a temporal framework for extracting the relevant hydroacoustic catalog. Specifically, if the initial event within the ISC cluster was recorded on a given day denoted as D_0 , provided a starting date to display the hydroacoustic data. Subsequently, to ascertain the presence of any earlier events, we examined the data from five days before D_0 (i.e., D_0-5). This process of extending the temporal

window (in reverse) occurred in sequential intervals of five days until no further events were encountered. Conversely, if the last occurrence within the ISC cluster transpired on the day D_N , we progressively extended the hydroacoustic window to detect any later additional events. However, if we did not observe events over a continuous span of five days after the final detection, we terminated the analysis.

2.7.2 Source Level Estimation

The Source Level (SL), measures the acoustic level of the T-wave at its source and establishes the size of a seismoacoustic event. Its unit of measurement is in dB re $1 \mu Pa$ @ $1m$. The Seas software calculates the SL based on i) the event location, ii) the sound levels recorded at the receivers (Receiver Level, RL) dB re $1 \mu Pa$, iii) the sensitivity of the hydrophone or instrumental response (IR) in dB re $1 \mu Pa$ provided by the sensor manufacturers (Appendix B), and iv) the transmission loss (TL) along the T-wave path in dB re $1 m$ (as given by equation 2.6). The relationship can be expressed as:

$$SL = RL + TL \quad (2.9)$$

with

$$RL = 20 \log_{10} \left(\frac{P}{P_0} \right) + IR \quad (2.10)$$

Here, P represents the pressure level recorded by the hydrophone, P_0 is the acoustic reference pressure level ($1 \mu Pa$).

2.7.3 Detection Threshold

The law defined by [Gutenberg and Richter \(1954\)](#) in seismology describes the relationship between the total number of earthquakes and their magnitude. It is given by:

$$\log N = a - bM \quad (2.11)$$

Here, N stands for the total number of seismic events having magnitudes (M) that are either equal to or larger than the magnitude of completeness (M_C), the lowest magnitude value necessary for a catalog to be deemed complete. Parameters a and b are empirical constants that depend on the site and seismic activity. The constant a , which measures the seismicity rate, is dependent on the overall number of events. The constant b denotes the ratio of small to large-magnitude occurrences, a smaller value of b shows fewer low-magnitude events. In most cases, the value of b is close to 1 ([Frohlich and Davis, 1993](#)).

Here, N stands for the total number of seismic events having magnitudes (M). Parameters a and b are empirical constants that depend on the site and seismic activity. The constant a , which measures the seismicity rate, is dependent on the overall number of events. The constant b denotes the ratio of small to large-magnitude occurrences, a smaller value of b shows fewer low-magnitude events. In most cases, the value of b is close to 1 (Frohlich and Davis, 1993). The magnitude of completeness (M_C), the lowest magnitude value necessary for a catalog to be deemed complete, is the magnitude at which the cumulative distribution of events deviates from slope b of equation 2.11.

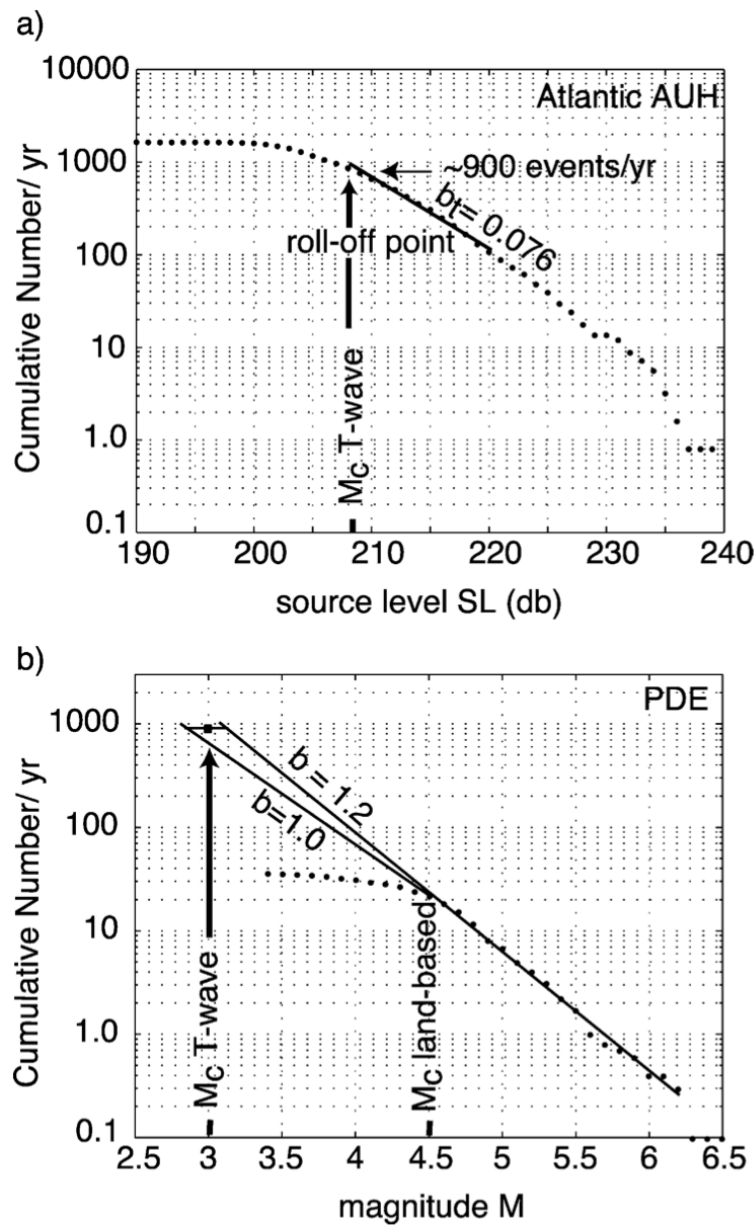


Figure 2.24: **a)** Frequency-SL distribution of events with $SL_C = 209$ dB with a roll-off point at 900 events per year. **b)** Gutenberg-Richter law fitting the corresponding land-based catalog and extrapolated to obtain M_C of hydroacoustic catalog, (after Bohnenstiehl et al., 2002).

Ridge earthquakes follow the Gutenberg-Richter law just like continental earthquakes (Francis, 1968). Bohnenstiehl et al. (2002) established an empirical association between size and frequency while taking the SL of the events into account (Figure 2.24), similar to equation 2.11:

$$\log N = a - bSL \quad (2.12)$$

N is the total number of events having SL greater than or equal to the completeness Source Level (SL_C). Temporal as well as spatial variations in SL_C may reflect mechanism-dependent differences in the efficiency of T-wave generation, ambient noise levels, instrument failure, or local topographic blockage (Dziak, 2001; Park et al., 2001). The size-frequency distribution is correlated with the empirical constants a and b . Its value is believed to be impacted by the SL of the cataloged events and to represent the network's threshold for detection. It is vital to note that the interpretation of b becomes more complicated because the SL of the T-waves does not solely express the energy of an earthquake.

2.7.4 Temporal distribution of seismicity

There are two main causes of the seismic activity seen on mid-ocean ridges: tectonic processes and magmatic processes. It should be highlighted that both these processes may be involved in a single cluster. According to Mogi (1967), there are three different kinds of seismic events (Figure 2.25): 1) A mainshock followed by aftershocks; 2) Foreshocks followed by a mainshock and then by aftershocks; 3) A lack of a strong mainshock and any related aftershocks, called as a seismic swarm.

The temporal distribution of events within a sequence, as a function of their SLs, provides preliminary insights into the triggering mechanisms in the absence of complete knowledge about the deformation mechanisms at the source. For instance, sequences with a mainshock with a high SL followed by events with SL decline are signs of tectonic events related to a fault plane rupture. Swarms, on the other hand, are sequences that don't have a mainshock and have rather consistent SLs, typical of magmatic activity-related phenomena including dike intrusion and/or volcanic eruptions (e.g. Fox et al., 2001; Goslin et al., 2012; Dziak et al., 2004; Dziak and Fox, 1999).

Classifying sequences in this manner can be challenging, and additional analyses are often required to gain insight into the underlying phenomena driving these seismic swarms. Several researchers have presented evidence supporting the idea that the migration of epicenters within the same seismic sequence indicates the lateral intrusion of magmatic dikes (e.g. Einarsson et al., 1980; Dziak et al., 2004; Tsang-Hin-Sun et al., 2016).

Furthermore, tectonic sequences that involve a main shock followed by stress readjustments in the crust exhibit a decay pattern akin to tectonic crises observed on land. This similarity implies that comparable physical processes may be at work in both terrestrial and mid-ocean ridge

environments. By studying the temporal characteristics and decay behavior of these tectonic sequences, researchers can gain valuable insights into the mechanisms underlying their occurrence.

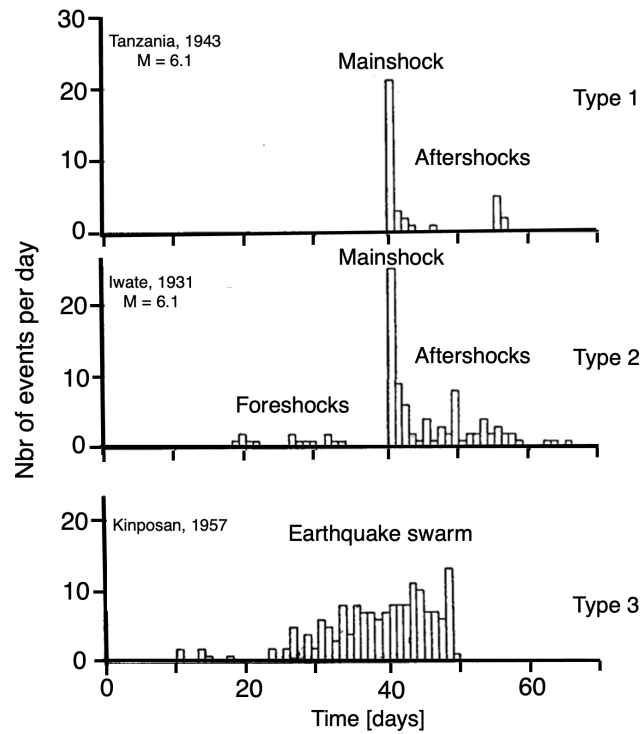


Figure 2.25: Three examples of earthquake sequences (Mogi, 1967): Type 1 shows a typical mainshock-aftershocks sequence, type 2 displays a sequence of foreshocks-mainshock-aftershocks and type 3 describes a sequence of unrelated earthquakes in a swarm. Types 1 and 2 are commonly found in tectonic contexts whereas type 3 is often found in magmatic contexts.

2.7.5 Modified Omori law

The Modified Omori Law (MOL) offers a useful tool for identifying seismic processes with a main shock followed by aftershocks, occurring within a tectonic framework. It was initially proposed by Omori (1894) and was later modified by Utsu et al. (1995). Omori compared the accumulation of clustered earthquakes over time after a main shock and found that the number of aftershocks decays exponentially. The MOL is defined by the following exponential function:

$$N(t) = K(c + t)^{-p} \quad (2.13)$$

where N is the cumulative number of aftershocks at time t , K defines the size of the main shock, c represents the event activity rate at the beginning of the sequence, and p reflects the decay rate of events over time. The original Omori law is derived when $c = 0$ and $p = 1$. The exponential decay factor, p -values range from 0.6 to 2.5 with a median of 1.1 based on a compilation of more than 200 mainshock-aftershocks sequences (Utsu et al., 1995). In tectonic contexts, p -values are

generally found in the 0.8-1.2 range (Utsu, 1999; Schmid and Grasso, 2012; Hainzl et al., 2016) and in the range of 0.9–1.2 for various aftershock sequences observed along the oceanic transform faults (Davis and Frohlich, 1991; Bohnenstiehl et al., 2002).

Among the MOL parameters, p has received significant attention as it would reflect the characteristics of the fault system and the underneath lithosphere (e.g. Mogi, 1967; Kisslinger, 1996). Notably, there appears to be no statistical correlation between p and the magnitude of the mainshock (Utsu et al., 1995). Several authors have explored the potential relationship between p -values and heat flow, which serves as a proxy for hypocentral temperature (e.g. Kisslinger, 1996; Creamer, 1993). Mogi (1967) proposed that in regions with higher temperatures, the ability of rocks to "flow" leads to a rapid decline in residual stress following the mainshock, resulting in higher p -values. Subsequent modeling work by Dieterich (1994), utilizing rate- and state-dependent fault strength indicated that $p > 1$ could arise when the applied stress on the fault surface decreases with time after the mainshock. Simão et al. (2010) observed high p values (2.7 and 2.3) in two seismic sequences along the detachment faults on the Mid-Atlantic Ridge. Detachment faults are characteristic of asymmetric accretion, where the presence of low-strength minerals leads to rapid stress release along the fault plane.

Estimation of the MOL parameters

The MOL parameters, K , c and p , are estimated using the maximum likelihood method (Ogata, 1983). Consider a series of aftershock occurrence times $\{t_1, t_2, \dots, t_N\}$ within a time interval $[0, T]$, where $t = 0$ is the time of mainshock. With an assumption of aftershocks having non-stationary Poisson distribution:

$$\lambda(t) = n(t) = K(c + t)^{-p} \quad (2.14)$$

parameters K , c , and p are estimated by finding those values maximizing the logarithm of the likelihood function

$$L = \left\{ \prod_i^N \lambda(t_i) \right\} \exp \left\{ - \int_0^T \lambda(t) dt \right\} \quad (2.15)$$

This maximization is based on the Fletcher-Powell optimization procedure (Ogata, 1983)

2.7.6 Faulting and stress-induced modeling

The application of elastic dislocation theory is extensively employed to compute the displacements, strains, and stresses linked with faulting, spanning from seismic rupture during earthquakes (e.g. Burgmann et al., 2002). Fault surfaces can be simplified as rectangular planes with a constant slip. Meade (2007) has developed a solution for the static elastic response to slip on an arbitrary set of triangular dislocation elements (TDEs). These algorithms enable precise modeling

of fault zones with intricate geometries. They have potential applications in computing Coulomb failure stress, simulating quasi-dynamic ruptures, modeling geodetic measurements, and evaluating the geometric consistency of active faults.

To calculate the displacements \mathbf{u} at a point \mathbf{r} , due to slip b_i , on a dislocation element with a surface S , integrate the product of the displacement discontinuity and stress produced at a point \mathbf{r}' , over the surface,

$$\mathbf{u}(\mathbf{r}) = \int_S b_i C_{ijkl} n_j \partial \mathbf{u}_k(\mathbf{r}' - \mathbf{r}) dS \quad (2.16)$$

where n_j is a unit vector in the j direction, b_i is the slip vector in the i direction, and \mathbf{u}_k is a tensor Green's function for the elastic displacement (Meade, 2007). For the homogeneous elastic body with Lamé parameters μ and λ , the elastic moduli tensor can be written as $C_{ijkl} = \mu(\delta_{ik}\delta_{jl} + \delta_{il}\delta_{jk}) + \lambda\delta_{ij}\delta_{kl}$ (δ is Kronecker's delta).

The strain associated with TDEs can be obtained from the computed displacement using the following equation

$$\boldsymbol{\varepsilon} = \frac{1}{2}(\nabla \mathbf{u} + (\nabla \mathbf{u})^T) \quad (2.17)$$

where $\nabla \mathbf{u}$ is the deformation gradient tensor obtained from the displacement vector. The associated stress hence can be calculated using Hooke's law for a linear elastic solid given by

$$\boldsymbol{\sigma} = \lambda \text{tr}(\boldsymbol{\varepsilon}) \mathbf{I} + 2\mu \boldsymbol{\varepsilon} \quad (2.18)$$

Here, $\text{tr}(\boldsymbol{\varepsilon})$ is the trace of the strain tensor, and \mathbf{I} is the identity matrix. The analytical model to compute the stress induced by an earthquake was developed in MATLAB. The scalar value of slip (b) from a fault rupture is obtained from the seismic moment and given as

$$b = \frac{M_0}{G \times \text{area} \times 10^6} \quad (2.19)$$

where G is the shear modulus, the seismic moment is given by Olive and Escartín (2016)

$$\log_{10}(M_0) = \frac{3}{2}(M_w + 6.033) \quad (2.20)$$

for the known magnitude (M_w) of an earthquake and the rupture area is given by Hanks and Bakun (2002) scaling law:

$$\text{area} = 10^{(M_w - 3.98)} \quad (2.21)$$

2.7.7 Tidal Oscillations

There have been instances of the tidal triggering of seismicity along the mid-oceanic ridges (e.g. Tolstoy et al., 2002; Wilcock et al., 2009). Inspired by this, we also have compared the seismicity

pattern (for a particular cluster) with that of either ocean or solid-Earth tides. Both tides occur as a response to gravitational forces exerted by the Sun and Moon. In our study, we have computed the vertical displacement components of the tides using the Global Oceanic Tidal Correction (GOTIC2) program, developed by [Matsumoto et al. \(2001\)](#). This program is written in FORTRAN. It computes both ocean and gravitational solid-Earth tidal loads based on [Farrell \(1972\)](#) convolution method which requires an ocean tide model, land-sea database, and a mass loading Green's function as input. In this code, the ocean tide model is developed by assimilating tidal solutions of altimeter data into the hydrodynamical model. The land-sea database which includes a digital elevation map is obtained from [Wessel and Smith \(1996\)](#). We observed that both ocean and solid-Earth tides have similar temporal variations (diurnal: ~ 24 h periodicity or semi-diurnal: ~ 12 h periodicity). Their amplitude behavior is slightly different, the former one varies in the range of ± 200 cm, and the latter one in the range of ± 40 cm.

2.8 Elaboration et analyse des catalogues hydroacoustiques (En français)

Ce chapitre développe la manière dont les catalogues d'événements hydroacoustiques ont été construits (sélection de la fenêtre temporelle pour chaque essaim) et la méthode d'analyse utilisée. Parmi les propriétés pouvant être étudiées, on trouve les incertitudes sur la localisation et le temps d'origine, le seuil de détection ou la magnitude de complétude, la distribution temporelle des événements définie ou non par une loi d'Omori modifiée, la distribution spatiale des événements, leur migration géographique éventuelle et l'occurrence d'une corrélation avec les marées. Toutes ces étapes sont résumées dans la Figure [2.23](#).

2.8.1 Sélection de la fenêtre temporelle

La première étape consiste à établir un cadre temporel pour extraire le catalogue hydroacoustique pertinent. Nous avons donc commencé par extraire les essaims sismiques identifiés dans le catalogue terrestre ISC pour rechercher les signaux hydroacoustiques correspondants. La date D_0 du premier événement d'un essaim ISC fournit une date de début pour inspecter les données hydroacoustiques. Pour vérifier la présence d'événements antérieurs, nous avons ensuite examiné les données des cinq jours précédants D_0 (c'est-à-dire à D_0-5). La fenêtre temporelle a ensuite été étendue avec un pas de cinq jours jusqu'à ce qu'aucun nouvel événement ne soit rencontré. De la même façon, si le dernier événement de l'essaim ISC s'est produit le jour D_N , nous avons progressivement étendu la fenêtre hydroacoustique pour détecter des événements ultérieurs. Si aucun événement n'était observé sur une période continue de cinq jours après la dernière détection, la

recherche se terminait et la fenêtre d'analyse des données acoustiques était alors complètement définie.

2.8.2 Estimation du niveau de la source

Le niveau source (SL) mesure le niveau acoustique de l'onde T à sa source et définit la magnitude d'un événement hydroacoustique. L'unité de mesure est le dB *re* $1 \mu Pa @ 1m$. Le logiciel Seas calcule SL en fonction de i) la localisation de l'événement, ii) des niveaux sonores enregistrés par les hydrophones (niveau récepteur, RL) en dB *re* $1 \mu Pa$, iii) la sensibilité de l'hydrophone (IR) en dB *re* $1 \mu Pa$ fournie par le fabricant (Annexe B), et iv), la perte de transmission (TL) le long du chemin parcouru par l'onde T en dB *re* $1 m$ (tel que donné par l'équation 2.6). La formule de calcul est donnée par les équations 2.9 et 2.10.

2.8.3 Seuil de détection

La loi définie par [Gutenberg and Richter \(1954\)](#) décrit la relation entre le nombre total de séismes et leur magnitude. Elle est donnée par l'équation 2.11. La constante b représente le rapport entre les nombres d'événements de faible et de grande magnitude ; une valeur de b faible indique moins d'événements de faible magnitude. Dans la plupart des cas, la valeur de b est proche de 1 ([Frohlich and Davis, 1993](#)). La magnitude de complétude (M_C) est la valeur de magnitude la plus basse nécessaire pour qu'un catalogue soit considéré comme complet ; elle correspond à la magnitude à laquelle la distribution cumulative des événements s'écarte de la pente b . Les séismes de dorsale suivent la loi de Gutenberg-Richter tout comme les séismes continentaux ([Francis, 1968](#)). [Bohnenstiehl et al. \(2002\)](#) ont établi une relation empirique entre la taille et la fréquence des événements hydroacoustiques en utilisant leur SL (équation 2.12; Figure 2.24). N est le nombre total d'événements ayant un SL supérieur ou égal au niveau de source de complétude (SL_C). Les variations temporelles et spatiales du SL_C peuvent refléter des différences d'efficacité des mécanisme de génération des ondes T, ou être dus à des niveaux de bruit ambiant variables, à des défaillances des instrument ou de blocages topographiques locaux ([Dziak, 2001](#); [Park et al., 2001](#)). La valeur de SL_C dépend des SL des événements répertoriés et représente le seuil de détection du réseau. Il est important de noter que l'interprétation de b est ici plus complexe car le SL des ondes T n'exprime pas uniquement l'énergie libérée par un séisme.

2.8.4 Distribution temporelle de la sismicité

Les deux principales causes de l'activité sismique sur les dorsales médio-océaniques sont les processus tectoniques et les processus magmatiques. Il convient de souligner que les deux processus

peuvent être présents dans un même essaim. Selon Mogi (1967), il existe trois types différents d'essaims sismiques (Figure 2.25): 1) Un séisme principal suivi de répliques ; 2) Des séismes précurseurs suivis d'un séisme principal puis de répliques ; 3) Une série de séismes sans événement principal ni répliques associées ; en toute rigueur, seul ce dernier cas devrait être appelé essaim sismique.

La distribution temporelle des événements au sein d'une séquence, en fonction de leurs niveaux de source (SL), offre un aperçu préliminaire sur les mécanismes de déclenchement en l'absence d'informations complètes sur les mécanismes à la source. Par exemple, les séquences avec un séisme principal avec un SL élevé suivi d'événements avec des SL décroissants sont un signe d'un événement d'origine tectonique lié à une rupture sur un plan de faille. Les essaims sismiques, en revanche, sont des séquences sans séisme principal et avec des niveaux de source plutôt homogènes, typiques des phénomènes liés à une activité magmatique, notamment l'intrusion de dykes et/ou une éruption volcanique (e.g. Fox et al., 2001; Goslin et al., 2012; Dziak et al., 2004; Dziak and Fox, 1999).

Classer les séquences de cette manière peut être difficile, et des analyses supplémentaires sont souvent nécessaires pour comprendre les phénomènes à l'origine de ces séquences sismiques. Plusieurs chercheurs ont présenté des preuves d'une migration des épicentres au sein d'une même séquence sismique témoin de l'intrusion latérale de dykes magmatiques (e.g. Einarsson et al., 1980; Dziak et al., 2004; Tsang-Hin-Sun et al., 2016).

De plus, les séquences tectoniques qui impliquent un séisme principal suivi d'ajustements de contrainte dans la croûte présentent un motif de décroissance similaire aux crises tectoniques observées à terre. Cette similarité suggère que des processus physiques comparables peuvent être à l'œuvre à la fois dans les environnements terrestres et sur les dorsales médio-océaniques. En étudiant les caractéristiques temporelles de la décroissance du niveau source de ces séquences tectoniques, il est ainsi possible d'obtenir des informations précieuses sur les mécanismes à leur origine.

2.8.5 Loi d'Omori modifiée

La Loi d'Omori Modifiée (MOL) offre un outil utile pour identifier les processus sismiques avec un séisme principal suivi de répliques, se produisant dans un cadre tectonique. Cette loi, initialement proposée par Omori (1894), a été précisée par Utsu et al. (1995). En analysant le nombre cumulé de séismes au cours du temps après un séisme principal, Omori a constaté que le nombre de répliques décroît de manière exponentielle. La MOL est donc une fonction exponentielle (équation 2.13). Le facteur de décroissance exponentielle, appelé p , varie de 0.6 à 2.5 avec une médiane de 1.1, sur la base d'une synthèse de plus de 200 séquences choc-répliques (Utsu

et al., 1995). Dans un contexte tectonique, les valeurs de p se situent généralement entre 0.8 et 1.2 (Utsu, 1999; Schmid and Grasso, 2012; Hainzl et al., 2016), voire même entre 0.9 et 1.2 pour diverses séquences de répliques observées le long de failles transformantes océaniques (Davis and Frohlich, 1991; Bohnenstiehl et al., 2002). Parmi les paramètres de la MOL, p a suscité une attention particulière car il refléterait les caractéristiques du système de failles et de la lithosphère sous-jacente. En revanche, il semble n'y avoir aucune corrélation statistique entre p et la magnitude du séisme principal (Utsu et al., 1995). Plusieurs auteurs ont exploré la relation potentielle entre les valeurs de p et le flux de chaleur, proxy pour la température hypocentrale (e.g. Kisslinger, 1996; Creamer, 1993). Mogi (1967) a proposé que dans les régions avec des températures élevées, la capacité des roches à fluer conduit à un déclin rapide du stress résiduel après le séisme principal, résultant en des valeurs de p plus élevées. Les travaux de modélisation ultérieurs de Dieterich (1994), utilisant la force de rupture dépendante du taux et de l'état thermique, ont indiqué que $p > 1$ pouvait survenir lorsque le stress appliqué à la surface de la faille diminue avec le temps après le choc principal. Simão et al. (2010) ont observé des valeurs de p élevées (2.7 et 2.3) pour deux séquences sismiques le long de failles de détachement sur la dorsale médio-atlantique. Les failles de détachement caractérisent l'accrétion asymétrique, où la présence de roches de faible résistance entraîne une libération rapide du stress le long du plan de faille.

2.8.6 Modélisation des failles et des contraintes

L'application de la théorie de la dislocation élastique est largement utilisée pour calculer les déplacements, les déformations et les contraintes liés à la faille, allant de la rupture sismique pendant les séismes (e.g. Burgmann et al., 2002). La surface de faille peut être simplifiée par un plan rectangulaire avec un glissement constant. Meade (2007) a développé une solution pour la réponse élastique statique au glissement sur un ensemble arbitraire d'éléments de dislocation triangulaires (TDE). Ces algorithmes permettent une modélisation précise des zones de failles avec des géométries complexes. Ils ont des applications potentielles dans le calcul des contraintes de rupture de Coulomb, la simulation de ruptures quasi-dynamiques, la modélisation des mesures géodésiques et l'évaluation de la cohérence géométrique des failles actives.

2.8.7 Oscillations des marées

Il existe des observations de sismicité déclenchée par les marées le long des dorsales médio-océaniques (e.g. Tolstoy et al., 2002; Wilcock et al., 2009). Inspirés par ces travaux, nous avons comparé l'occurrence de la sismicité (pour une séquence particulière) avec l'amplitude des marées océanique et terrestre. En effet, deux cycles de marées surviennent en réponse aux forces gravitationnelles exercées par le Soleil et la Lune. Dans notre étude, nous avons calculé les composantes

de déplacement vertical des marées en utilisant le programme Global Oceanic Tidal Correction (GOTIC2), développé par [Matsumoto et al. \(2001\)](#). Ce programme en FORTRAN calcule à la fois les charges de la marée océanique et la marée terrestre en se basant sur la méthode de convolution de [Farrell \(1972\)](#), qui nécessite un modèle de marée océanique, une base de données terre-mer et une fonction de Green de chargement de masse en entrée. Dans ce code, le modèle de marée océanique est développé en assimilant les solutions de marée des données altimétriques dans le modèle hydrodynamique. La base de données terre-mer, comprenant une carte numérique de l'élévation, est obtenue auprès de [Wessel and Smith \(1996\)](#). Nous avons observé que les marées océaniques et solides de la Terre présentent des variations temporelles similaires (périodicité diurne : ~ 24 h ou semi-diurne : ~ 12 h). Leur comportement en amplitude est légèrement différent, le premier variant dans la plage de ± 200 cm et le second dans la plage de ± 40 cm.

Chapter 3

Southwest Indian Ridge Swarms

Abstract

Along the ultraslow-spreading Southwest Indian Ridge (SWIR) separating the Nubian and Antarctic plates, Melville TF marks the major boundary between two sections, in terms of offset, segmentation, and magma supply. To the west of the TF, the SWIR contains several long-lived transform and non-transform discontinuities; whereas the SWIR is continuous with minor discontinuities to the east of the TF. Between 2010 and 2020, three strong seismic clusters were reported in the ISC catalog (west to east): near the Novara TF in July 2018; near the Melville TF from June 2016 to March 2017, and a segment close to Rodrigues Triple Junction in September-October 2018, comprising 231, 258 and 92 events, respectively. Based on hydroacoustic data analyses using 3 to 9 hydrophones, we have detected 1109, 27624, and 4880 events in the respective seismic clusters. We also have detected several short-duration and highly energetic, impulsive events assumed to be associated with the lava-water interactions. The absence of a mainshock-aftershock sequence fitting Modified Omori's Law, the spatio-temporal distribution of events led to the interpretation of them as magmatic swarms. We presented the results associated with these three swarms in two journal articles.

3.1 Swarms in 2018: MDPI-Geosciences Article

In this first article (Ingale et al., 2021), published in *Geosciences*, we compared two earthquake swarms that occurred in 2018 in two different sections of the SWIR. The first one near the Novara TF with 1109 hydroacoustic events spanned 13 days (06 to 18 July) and the second on the segment close to the triple junction with 4880 events spanned 33 days (25 September to 27 October). The detailed analyses showed that the activity rate (number of events per day) was lower in the first swarm; the Source Level of the events was higher in the second swarm. The main conclusion from this study was the magmatic origin of both the swarms initiated by dike intrusions, followed by the stress re-adjustments in the surrounding crust. The supplementary material associated with this article is provided in Appendix C.

Citation: Ingale, V. V., Bazin, S., and Royer, J.-Y. (2021). Hydroacoustic observations of two contrasted seismic swarms along the Southwest Indian Ridge in 2018. *Geosciences*, 11, 225, <https://doi.org/10.3390/geosciences11060225>.

Extended Abstract

Two seismic swarms along the Southwest Indian Ridge (SWIR) along segment 18 near the Novara fracture zone and segment 4 west of the Rodrigues Triple Junction in July 2018 and September-October 2018, respectively stand out as distinctive and focused swarms, separated by just 5 months in completely contrasting tectonic settings. Lasting for 13 days, the first swarm, comprising 1109 hydroacoustic events shows slightly different characteristics compared to the second swarm, comprising 4880 events, spanning over 33 days. The temporal distribution of events reveals a complex pattern, challenging the conventional mainshock-aftershock sequence model in both swarms.

The spatio-temporal analysis shed light on variations in lithospheric brittleness and stress readjustment mechanisms. With only 1109 events, swarm-1 in Segment 18 showcased lower brittleness, suggesting a less pronounced response to stress perturbations. In contrast, Swarm-2 in Segment 4 displayed higher brittleness, releasing additional stress through strong and numerous 4880 events. Geospatial distribution analysis revealed clusters of seismic events around seamounts, hinting at potential volcanic centers. Interestingly, variations in activity levels among these seamounts were observed, emphasizing the importance of considering the contrasting geological context in these two regions.

Both swarms are also characterized by short-duration, high-energy, and impulsive events, suggesting H-waves or water-borne events, likely associated with lava-seawater interactions. Seismic-

ity analysis unveiled intriguing dynamics within each swarm. Swarm-1, comprised of 1109 events, exhibited fluctuations in activity. Swarm-2, featuring a larger dataset of 4954 events, demonstrated a sharp onset followed by a gradual decline, punctuated by significant events on October 14 and 18. In both the swarms, temporal clusters of impulsive events aligned with changes in the cumulative event count slope, signifying potential magmatic processes.

The magmatic nature of both swarms emerged as a key finding. The swarms were interpreted primarily as magmatic, triggered by dike intrusions by observing temporal migration of events and followed by stress readjustments in their vicinity. Differences in swarm characteristics were attributed to variations in lithospheric strength and stress load related to the distinct tectonic settings of Segment 4 and Segment 18. This interpretation aligns with observations of similar magmatic events along ultra-slow spreading Gakkel Ridge.

Résumé étendu (En français)

Deux essaims sismiques le long de la dorsale sud-ouest de l'océan Indien (SWIR), le premier le long du segment 18 près de la zone de fracture de Novara et le second à l'ouest du carrefour triple de Rodrigues en juillet 2018 et septembre-octobre 2018, se distinguent comme des essaims distinctifs et ciblés, séparés de seulement 5 mois dans des contextes tectoniques complètement contrastés. D'une durée de 13 jours, le premier essaim, composé de 1109 événements hydroacoustiques, présente des caractéristiques légèrement différentes par rapport au deuxième essaim, comprenant 4880 événements, s'étendant sur 33 jours. La distribution temporelle des événements révèle un schéma complexe, remettant en question le modèle conventionnel de séquences choc-répliques dans les deux essaims.

L'analyse spatio-temporelle met en lumière des variations dans la fragilité lithosphérique et les mécanismes de réajustement de contrainte. Avec seulement 1109 événements, l'essaim-1 dans le segment 18 présente une fragilité inférieure, suggérant une réponse moins prononcée aux perturbations de contrainte. En revanche, l'essaim-2 dans le segment 4 présente une fragilité plus élevée, libérant une contrainte supplémentaire à travers des événements nombreux et forts de 4880. L'analyse de la distribution géospatiale révèle des amas d'événements sismiques autour des monts sous-marins, laissant entrevoir des centres volcaniques potentiels. De manière intéressante, des variations dans les niveaux d'activité parmi ces monts sont observées, soulignant l'importance de prendre en compte le contexte géologique contrasté entre ces deux régions.

Les deux essaims se caractérisent également par des événements de courte durée, à haute énergie et impulsionnels, suggérant des ondes H générés dans la colonne d'eau, probablement associés à des interactions lave-eau de mer. L'analyse de la sismicité a révélé des dynamiques intrigantes au sein de chaque essaim. L'essaim-1, composé de 1109 événements, présente des fluctu-

ations d'activité. L'essai-2, avec un ensemble de données plus important de 4954 événements, montre un début brusque suivi d'un déclin progressif, ponctué d'événements significatifs les 14 et 18 octobre. Dans les deux essais, des amas temporels d'événements impulsionnels apparaissent lors des changements dans la pente du nombre cumulé d'événements, indiquant des processus magmatiques potentiels.

La nature magmatique des deux essais est une des conclusions clés. Les essais sont interprétés principalement comme magmatiques, déclenchés par des intrusions de dykes en d'après la migration temporelle des événements, suivis de réajustements de contrainte dans leur voisinage. Les différences dans les caractéristiques des essais sont attribuées à des variations de la résistance de la lithosphérique et de la charge de contrainte liées aux contextes tectoniques distincts des segments 4 et 18. Cette interprétation concorde avec les observations d'événements magmatiques similaires le long de la dorsale ultra-lente de Gakkel.

Article

Hydroacoustic Observations of Two Contrasted Seismic Swarms along the Southwest Indian Ridge in 2018

Vaibhav Vijay Ingale * , Sara Bazin and Jean-Yves Royer Laboratoire Geosciences Ocean, University of Brest & CNRS, 29280 Plouzané, France; sara.bazin@univ-brest.fr (S.B.); jean-yves.royer@univ-brest.fr (J.-Y.R.)**Citation:** Ingale, V.V.; Bazin, S.;

Royer, J.-Y. Hydroacoustic

Observations of Two Contrasted

Seismic Swarms along the Southwest

Indian Ridge in 2018. *Geosciences* **2021**, *11*, 225. <https://doi.org/10.3390/geosciences11060225>

Academic Editors: Jesus

Martinez-Frias, Maria Grazia Ciaccio,

Paola Baccheschi and Diana Latorre

Received: 5 April 2021

Accepted: 18 May 2021

Published: 24 May 2021

* Correspondence: vaibhavvijay.ingale@univ-brest.fr

Abstract: In 2018, two earthquake swarms occurred along spreading ridge segments of the ultra-slow Southwest Indian Ridge (SWIR). The first swarm was located at the spreading-ridge intersection with the Novara Fracture Zone, comprising 231 events (ISC catalogue) and spanning over 6 days (10 July to 15 July). The second swarm was more of a cluster of events focusing near a discontinuity, 220 km west of the Rodrigues Triple Junction, composed of 92 events and spanning over 31 days (27 September to 27 October). We examined these two swarms using hydroacoustic records from the OHASISBIO network with seven to nine autonomous hydrophones moored on either side of the SWIR. We detected 1109 hydroacoustic events spanning over 13 days (6 July to 18 July) in the first swarm and 4880 events spanning over 33 days in the second swarm (25 September to 27 October). The number of events per day was larger, and the hydroacoustic magnitude (source level) was, on average, smaller during the second swarm than the first. The spatio-temporal distribution of events from both swarms indicates a magmatic origin initiated by dike intrusions and followed by a readjustment of stresses in the surrounding crust.

Keywords: seismic swarm; hydroacoustics; mid-ocean ridge; Indian Ocean; impulsive events

Publisher's Note: MDPI stays neutral with regard to jurisdictional claims in published maps and institutional affiliations.



Copyright: © 2021 by the authors. Licensee MDPI, Basel, Switzerland. This article is an open access article distributed under the terms and conditions of the Creative Commons Attribution (CC BY) license (<https://creativecommons.org/licenses/by/4.0/>).

1. Introduction

Seismic swarms are sequences of earthquakes with no major mainshock. They do not have a well-defined temporal order in the magnitude of events and seismicity rate [1,2]. Seismic swarms at mid-ocean ridges have been investigated since the 1970s (e.g., [3–8]). Swarms of volcanic and tectonic events along mid-ocean ridges are inherent to seafloor spreading [9]. Because of the remoteness of most of the mid-ocean ridges and due to the rapid attenuation of seismic waves in the solid Earth, land-based seismic networks lack the low-level seismicity associated with seafloor spreading processes [10,11]. Since the late 1980s, local studies using ocean-bottom seismometers (OBS) (e.g., [12–14]) and regional studies using autonomous underwater hydrophones (AuH) (e.g., [15–17]) have greatly contributed to a detailed understanding of mid-ocean ridge seismicity [18–20]. This is possible because seismic events produce low-frequency hydroacoustic waves, known as T-waves, that are excited in the water column by earthquakes through the conversion of seismic waves into acoustic waves at the solid–liquid interface (i.e., sea-bottom) [10,15,20] and which propagate through the sound fixing and ranging (SOFAR) channel over long distances with little attenuation [21–23].

The Southwest Indian Ridge (SWIR) is a major seafloor spreading ridge separating Africa and Antarctica. It extends from the Bouvet Triple Junction in the southern Atlantic Ocean to the Rodrigues Triple Junction (RTJ) in the Indian Ocean [24–26]. The western end of SWIR is older than its eastern end due to the lengthening and eastward propagation of the ridge axis toward the RTJ [27,28]. The SWIR is among the world's slowest spreading ridges, with a full spreading rate of ~14 mm/a [24,29,30]. It is also characterized by several large-offset transform faults that divide the ridge into spreading segments of various lengths [31,32] with several magmatic and amagmatic ridge segments [33] and a

deep axial valley bounded by ~3 km high ridges [26,28,32]. The cyclic nature of volcanic construction and tectonic dismemberment across the SWIR is responsible for the ridge crests and rugged morphology of this spreading ridge [32]. As shown in Figure 1, the SWIR is mostly characterized by the obliquity of the ridge axis with respect to the main fracture zone's (FZ) orientation [34,35]. The section of the ridge between the Gallieni (52° E) and Melville FZ (60° E) shows an obliquity of 40° and contains several long-lived transform and non-transform discontinuities. The section between Melville FZ and RTJ (70° E) has an obliquity of 25° and is continuous with minor discontinuities.

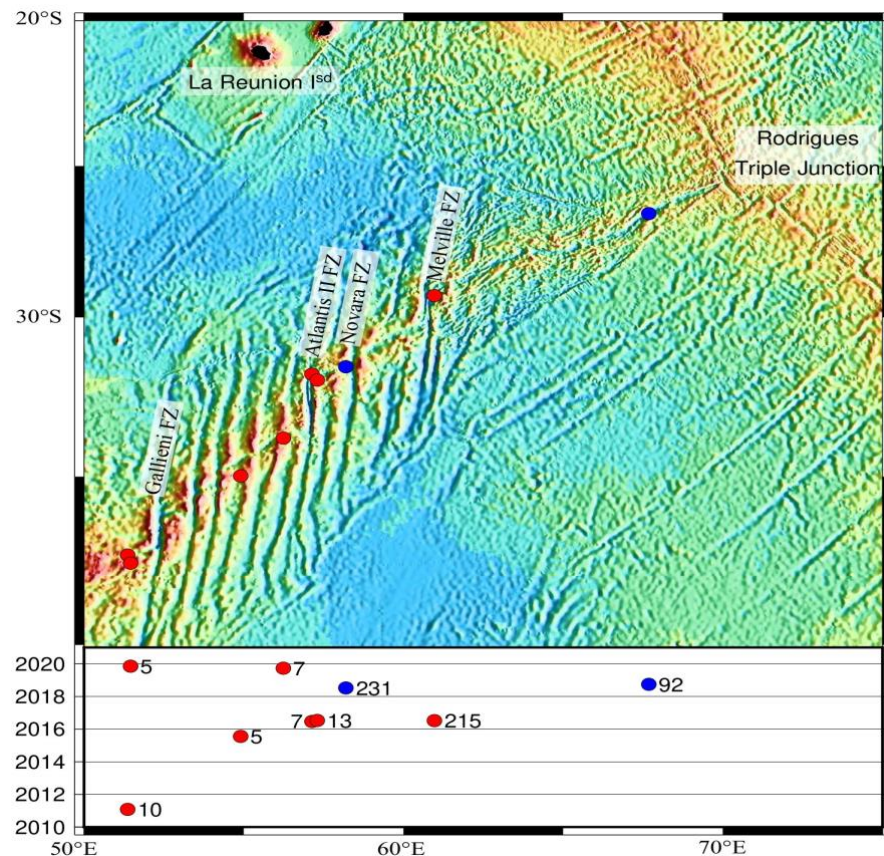


Figure 1. Bathymetric map of the Southwest Indian Ridge, between 50° E and 70° E, showing the geographic and temporal distribution of swarms reported in the ISC catalogue from 2010 to 2020. The numbers next to the symbols refer to the number of teleseismic events in the ISC catalogue for each individual swarm. The blue dots show the location of the two 2018 swarms investigated in this paper.

Only a few seismic swarms have been reported along the SWIR based on teleseismic observations (e.g., [36,37]), hydroacoustic observations (e.g., [38,39]) or local OBS surveys (e.g., [40,41]). In a comprehensive study of teleseismic earthquakes between 1976 and 2010 at ultra-slow spreading ridges, Schlindwein [42] showed that earthquake swarms occur at volcanic centers or segments with magmatic accretion that are separated by stretches of nonvolcanic seafloor. These swarms are mostly associated with diking events. In the western part of the SWIR, based on regional and teleseismic earthquakes, Läderach et al. [43] showed that earthquake swarms are associated with along-axis melt flow mechanisms. Seismic swarms observed in local OBS studies in the eastern part of the SWIR are also interpreted as the result of magma movement related to diking episodes [7,40,44].

From 2010 to 2020, in the International Seismological Centre catalogue [45], we found only nine seismic swarms between 50° E and 70° E. We considered as swarms, the occurrence of at least five consecutive events within 15 days clustered in a grid of 3 × 3 degrees. Figure 1 shows their distribution: eight of them occurred west of Melville FZ and only one east of it. Most of them count about 10 or less (teleseismic) events, except three swarms: one in 2016 with 215 events and two in

2018 with 231 and 92 events. The latter two are remarkable: the one west of Melville FZ included the most $M_w > 5$ events (7) compared to the 2016 swarm (5); the one east of Melville FZ was the only one occurring in the nearly 1000 km long continuous section of the SWIR and also included 6 $M_w > 5$ events. Their occurrence only a few months apart in two distinct tectonic settings made a further investigation worthwhile.

Based on the ISC catalogue, the first swarm (swarm-1) lasted for 6 days, from 10 July to 15 July 2018 and the second swarm (swarm-2) lasted for 31 days from 27 September to 27 October 2018 (Figure 2). Although locational uncertainties of the ISC catalogue are large (~ 20 km) in this remote part of the ocean, the occurrence of dense teleseismic events in a limited time period can be representative of seismic swarms [7]. Swarm-1 was located along SWIR Segment 18 at $58^\circ 10'$ E (as numbered after Cannat et al. [35]) near the spreading-ridge intersection with the Novara FZ and comprised 231 events (Figure 2b). It started with a $M_w = 4.9$ event on 10 July at 03h55. Seven events with a $M_w > 5.0$ occurred after this onset and their focal mechanisms express normal faulting with azimuths parallel to the ridge axis. Swarm-2 occurred near a small axial discontinuity along SWIR Segment 4 at $67^\circ 40'$ E, 220 km away from the RTJ and comprising 92 events (Figure 2c), started with a $M_w = 4.2$ event on 27 September at 13h58. Six events with $M_w > 5.0$ occurred afterward, also with normal faulting focal mechanisms approximately parallel to the ridge axis. The ISC catalogue events are more scattered in swarm-1 than in swarm-2.

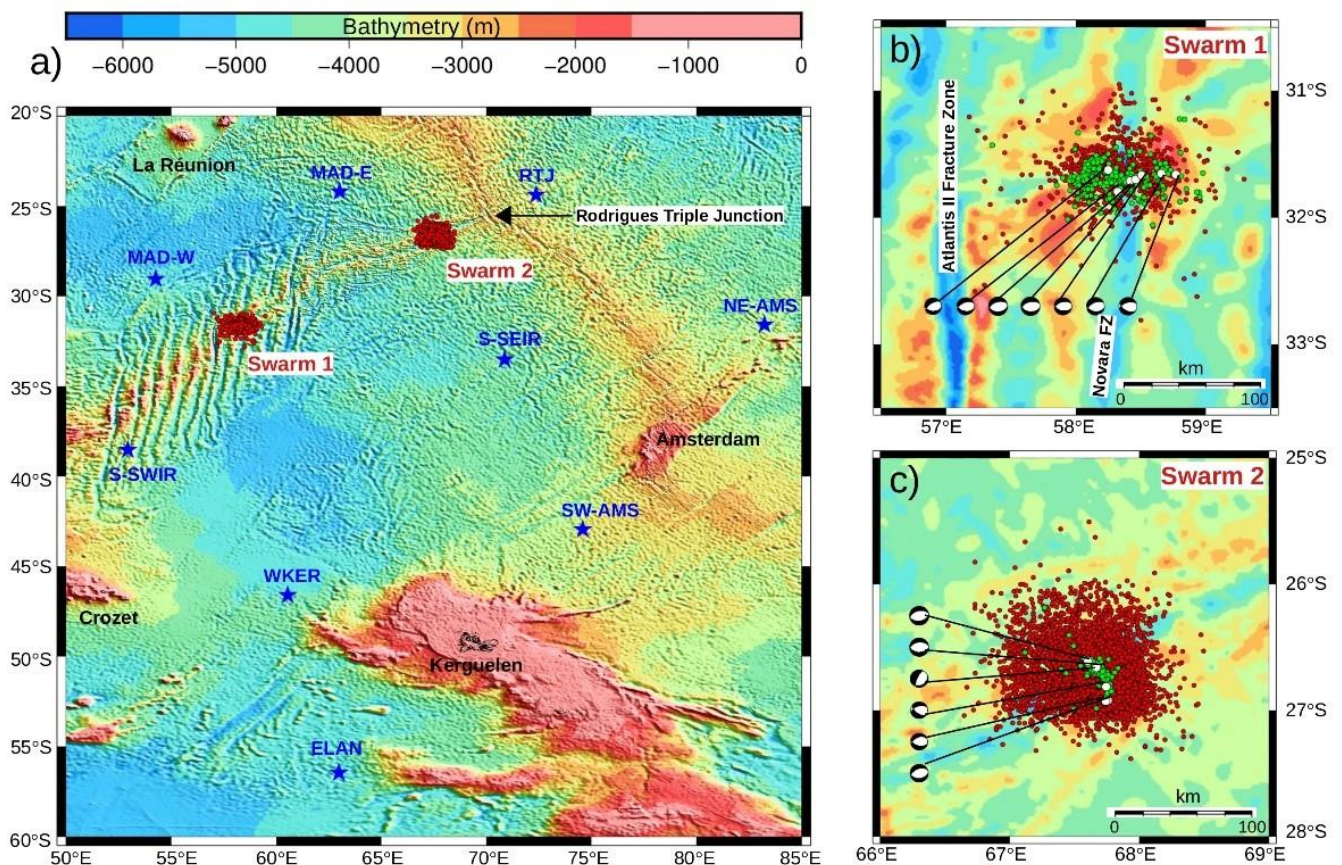


Figure 2. The locations of the two 2018 swarms along the Southwest Indian Ridge: (a) hydroacoustic events (red dots) detected by the OHASISBIO network of hydrophones (blue stars); (b,c) enlarged sections for swarm-1 along ridge Segment 18 and swarm-2 along ridge Segment 4 with the hydroacoustic events (red dots), events from the land-based ISC catalogue (green dots), and events with $M_w > 5.0$ (white dots) along with their focal mechanisms (GCMT catalogue [46]).

To detect low-magnitude earthquakes associated with swarm-1 and swarm-2, lacking from land-based catalogues (due to the fact of their detection threshold) and to better understand whether these two swarms are tectonic or magmatic in origin, we examined hydroacoustic data (marine acoustic waves; T-waves) recorded by autonomous hydrophones (AuHs) moored on either side of the SWIR from the OHASISBIO network [47]. The OHASISBIO (Hydroacoustic Observatory

of the Sismicity and Biodiversity in the Indian Ocean) is a long-term hydroacoustic program for monitoring the seismic activity and the vocal activity of large marine mammals in the southern Indian Ocean (e.g., [38,48]). The network is maintained during the yearly voyages of RV *Marion Dufresne* to the French Southern Islands. Since both swarms are located inside the OHASISBIO network, the observed hydroacoustic events have a more accurate location than the events from ISC catalogue. As the AuHs are also more sensitive to low-magnitude events, we detected 1109 hydroacoustic events for swarm-1 and 4880 events for swarm-2. There were thus five times more hydroacoustic events than the ISC catalogue for swarm-1 and 53 times more events for swarm-2. The analysis of this improved and dense catalogue of hydroacoustic events helps to understand the nature of these two swarms and the spreading processes that govern the SWIR.

2. Data and Methods

Because of the coherent nature of the propagation of sound waves in the ocean and the permanence of a well-defined oceanic sound-speed channel, hydrophone arrays provide a significant improvement in the detection threshold [49,50] and location accuracy [10,51,52] of earthquake events, relative to distant land-based seismic networks (as in the ISC catalogue). In this study, we analyzed data from an array of 9 hydrophones of the OHASISBIO network (Figure 2) that are moored in the SOFAR channel axis at depths ranging from 1000 m to 1300 m (Table 1). The hydrophones are located at the south of La Réunion Island (MAD-W and MAD-E), north-east and south-west of Amsterdam Islands (NE-AMS and SW-AMS), off the Southeast and Southwest Indian Ridges (S-SEIR and S-SWIR), near RTJ, west (WKER), and south-west (ELAN) of Kerguelen Island. They are set to record acoustic waves continuously at a rate of 240 Hz on 3 byte long samples. Their high-precision clocks are synchronized with a GPS clock before deployment and after recovery. The data from these hydrophones are analyzed with software developed at the Pacific Marine Environment Laboratory (PMEL) [10] and processed as described in Royer et al. [17].

Table 1. Locations and parameters of the autonomous hydrophones of the OHASISBIO network.

Sites	RTJ	NE-AMS	S-SEIR	SW-AMS	ELAN	WKER	S-SWIR	MAD-W	MAD-E
Latitude (°S)	24.379	31.576	33.518	42.951	56.460	46.602	38.547	29.047	24.205
Longitude (°E)	72.372	83.242	70.866	74.598	62.976	60.548	52.929	54.258	63.010
Depth (m)	1109	1060	1280	1100	1020	960	1230	1288	1238
Sampling rate (Hz)	240	240	240	240	240	240	240	240	240
Sensitivity (dB)	−163.9	−163.5	−163.7	−163.4	−163.8	−163.3	−164.2	−163.4	−163.5
Start time	11/02/2018	05/02/2018	08/02/2018	31/02/2018	16/01/2018	19/01/2018	09/01/2018	06/01/2018	13/02/2018
End time	10/02/2019	30/02/2019	23/12/2018	30/01/2019	23/01/2019	29/07/2018	14/01/2019	03/11/2018	21/07/2018
Clock drift (ppm)	0.0300	−0.2426	−0.2861	0.0048	−0.0222	−0.0348	0.0346	−0.0010	−0.7870

To locate each earthquake, we picked the highest energy arrivals in the T-wave spectrograms [53,54]. After the identification of T-waves on three or more hydrophones, the source localization and origin time estimation were carried out by a non-linear least squares minimization of the arrival times on each of the hydrophones [10]. The errors in the latitude, longitude, and origin time were estimated from the covariance matrix of this least squares minimization, as modified by the mean square of the residuals. The distances and arrival times on each hydrophone were calculated using sound velocities in the ocean based on the Global Digital Environment Model (GDEM) and averaged along great circles joining the sources to each of the receivers [55]. It must be noted that the location of acoustic events actually corresponds to the location of the seismo-acoustic conversion on the seafloor. For shallow earthquakes, such as in a young oceanic crust, this point generally matches with the epicenter. However, in an area with high reliefs or near a seamount, the acoustic “radiator” may not exactly coincide with the epicenter [56]. In addition, T-waves do not provide any information about the depth of seismic events.

Acoustic events can be characterized by the acoustic magnitude or source level (SL) of the T-waves. The SLs are derived from the received levels at each hydrophone, corrected from the transmission loss between the event and the hydrophone locations. The received level (RL), expressed in decibels with respect to 1 micro-Pascal (dB re μPa at 1 m, hereinafter simply noted dB), corresponds to the maximum peak-to-peak amplitude in a 10 s time window centered on the peak of energy in the acoustic signal, in the 3–110 Hz frequency range, which closely resembles the definition of seismic amplitudes. The transmission loss (TL) comes from: (1) the cylindrical sound-spreading between the event location and the hydrophone; (2) the spherical sound-spreading in the water column between the sea-bottom acoustic radiator and the sound channel axis.

The analysis of the data was iterated twice for each swarm. We constructed a first hydroacoustic catalogue (OHA catalogue) containing event information such as the event ID; its latitude, longitude, and SL; the number and names of hydrophones used to locate the event; the calculated errors in the latitude, longitude, origin time, and SL. In a second iteration, we used this event information to re-pick and re-locate the hydroacoustic events. This step improved the catalogue by reducing the errors in latitude, longitude, and origin time by ~ 10 -fold. The median errors in latitude, longitude, and origin time for all events from swarm-1 and swarm-2 (total 5989 events) were 0.33 km, 0.26 km, and 0.18 s, respectively (Figure 3). In the first iteration, the median errors were 4.33 km in latitude, 3.60 km in longitude, and 1.99 s in origin time; then, in the second iteration, the errors improved (by ~ 10 -fold) to 0.44 km, 0.35 km, and 0.19 s, respectively, for swarm-1 events (Figure S1). Similarly, for swarm-2, the median errors improved (by ~ 11 -fold) from 4.00 km to 0.33 km in latitude, 2.89 km to 0.26 in longitude, and 1.92 s to 0.18 in origin time (Figure S2).

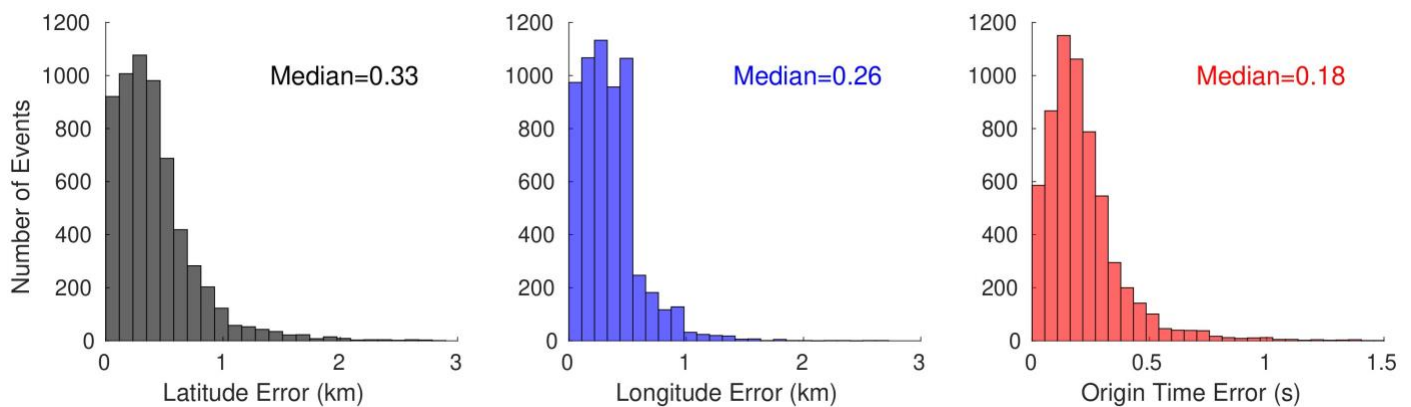


Figure 3. Distribution of errors in the location (i.e., latitude and longitude) and origin time of all hydroacoustic events in swarm-1 and swarm-2 after two iterations of detection and localization.

The detection threshold of an AuH array is defined by the SL of completeness (SL_c) which is derived from the frequency–size distribution of the acoustic events [57]. It can be compared to the magnitude completeness of seismic events from land-based catalogues. Both are calculated by fitting a power–law relationship to the catalogue of events [58]:

$$\log(N) = a - b \text{ SL}$$

where N is the cumulative number of events with a source-level greater or equal to SL , a and b are constants determined with the maximum likelihood method [59]. For swarm-1, the ISC catalogue yielded a b -value of 2.96 (Figure 4a), much greater than the expected value of 1 typical for seismically active regions. The magnitude (m_b) and SL of completeness of the ISC catalogue events were $M_{C(\text{ISC})} = 3.9$ m_b and $SL_{C(\text{ISC})} = 218$ dB, respectively. For the OHA catalogue, the SL_c was 6 dB lower and reached 212 dB, equivalent to $M_{C(\text{OHA})} = 3.4$ m_b . This improvement in the magnitude of completeness led to ~ 5 times more events in the OHA catalogue than in the ISC catalogue (1109 vs. 231).

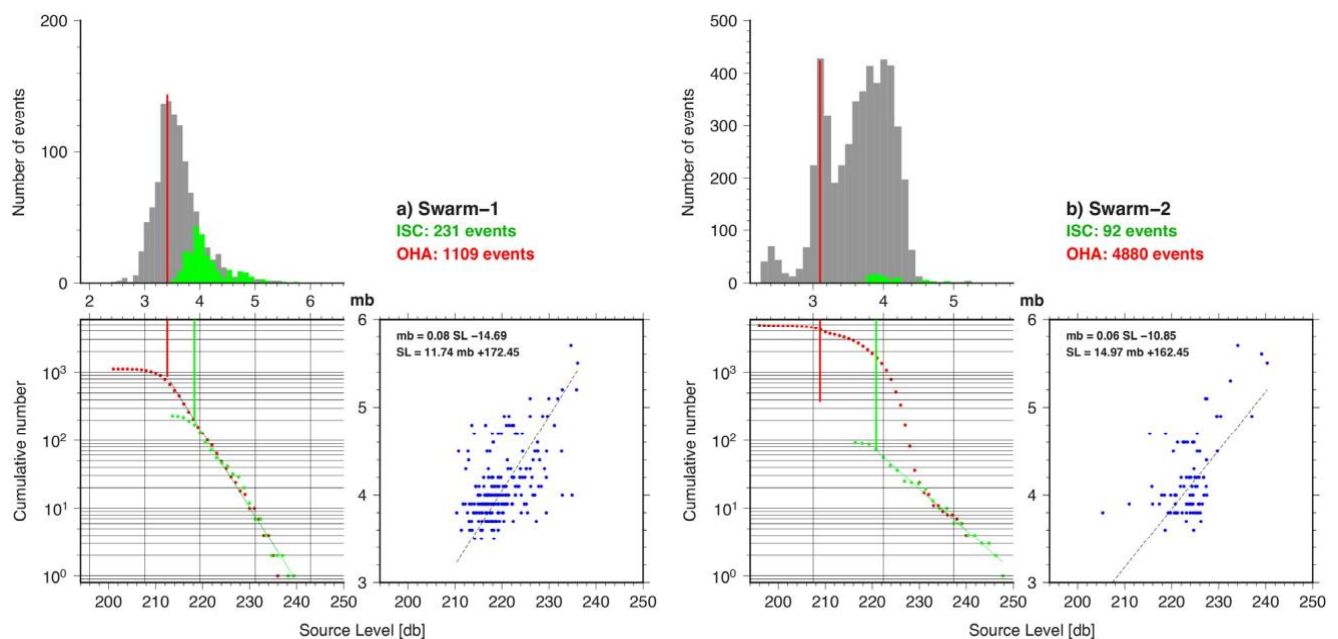


Figure 4. Completeness of the acoustic catalog based on the source levels (SLs) and ISC magnitude (mb) of all events from (a) swarm-1 and (b) swarm-2. The correspondence between the SL and mb scales was based on matching the best-fitting Gutenberg–Richter lines up to the completeness values outlined in green for the ISC catalogue and in red for the OHA catalogue. The upper graph shows the histogram of the hydroacoustic events (gray) and the ISC catalogue events (green). The lower left graph shows the cumulative number of events in the OHA catalogue (red) and ISC catalogue (green). The vertical red and green line denotes the completeness values of the SLs and mb of the OHA and ISC catalogue, respectively. The lower right graph shows the SL-to-mb relationship (and reciprocal) and trend line, obtained from the cumulative number of events.

For swarm-2, the ISC catalogue yielded a b-value of 2.11 (Figure 4b), with a $M_{C(ISC)} = 3.9$ mb and an $SL_{C(ISC)} = 220$ dB, which are quite similar to swarm-1. However, the distribution of the SLs was very different, as they ranged from 207 to 225 dB and was bimodal with a sharp peak at 209 dB and a broad one centered on 220 dB (Figure 4b). Furthermore, swarm-2 had ~53 times more acoustic events than the ISC events (4880 vs. 92), with, among them, an unusually high number of low magnitude events yielding to an $SL_{C(OHA)}$ on the order of 209 dB. As a result, the cumulative log(N) curve was not straight and clearly departed from a characteristic power-law distribution for an $SL < 231$ dB. Comparing the completeness of the AuH records for both swarms was therefore not meaningful. Regardless, the improvement in the magnitude of the completeness of the OHA catalogue over the ISC catalogue demonstrated that hydrophone arrays provide more complete information about the seismicity along distant mid-oceanic ridges over land-based catalogues.

3. Results

3.1. Seismicity of Swarm-1

The iterative analysis of hydroacoustic records from the nine available AuHs starting from 6 July to 18 July 2018, yielded a total of 1137 events. This number was reduced to 1112 after selecting events with origin time-errors less than 10 s. We also excluded three events occurring at less than 40 s from the preceding event. Out of the remaining 1109 events (compared to 231 events in the ISC catalogue), 26 events (2%) were located with four hydrophones, 241 events (22%) with five AuHs, 445 events (40%) with six AuHs, 242 events (22%) with seven AuHs, 125 events (11%) with eight AuHs, and 30 events (3%) with nine AuHs. Only 325 events are discernible in the S-SWIR hydrophone records because of the high seasonal noise, and only 571 events in the ELAN hydrophone due to the fact of its long distance from the swarm (~2000 km).

Between 6 July at 04h54 and the first strong event (10 July at 03h55, $M_w = 4.9$), we found a total of 41 hydroacoustic events (Figure 5), representing very mild seismic activity. Starting 10 July at 03h55, 265 events occurred on 10 July and contributed to a sharp increase in the cumulative number (CN) of the events. Local changes in the seismic activity of the swarm are marked by black arrows in Figure 5a; they correspond to the times when there were local (short-term) changes in the event count (either an increase or a decrease) as seen in Figure 5c. At the swarm onset, the seismicity rose up to ~ 13 events per hour till 10 July at 16h00, after which it continued at a steady rate of ~ 10 events per hour for two days (Figure 5c). Between 10 July and the end of 12 July, the CN slope averaged ~ 250 events per day. Then, after 13 July, the seismic activity began to decline. The CN slope again changed on 14 July and 16 July due to the slight increase in the number of events. After 16 July, the CN curve was nearly flat until the last detected event of the swarm (18 July).

Changes in the CN slope on 12 July, 14 July, and 16 July coincided with the occurrence of a temporal cluster of impulsive events (blue dots/gray ellipses in Figure 5b). Those events were energetic and of short duration (< 10 s) compared to the ~ 100 s duration of strong events (such as the events from the ISC catalogue; Figure 6). The short duration of the impulsive events may indicate that they were H-waves, meaning that the energy was released directly in the water and did not travel in the solid crust. Such impulsive events have previously been observed by Chadwick et al. [60] and Wilcock et al. [61,62] as associated with active and fresh lava flows at different underwater volcanoes. Clustered impulsive events have even been linked to isolated magma lenses [63]. Here, we detected 69 impulsive events. Three distinct temporal clusters of these impulsive events were observed: seven events on 12 July, 10 events on 14 July, and nine events on 16 July. These three temporal clusters coincided with noticeable changes in the CN slope; they resulted in a change in the seismic activity and an increase in the number of events for a short time (Figure 5c).

The SLs of the swarm-1 events ranged between 201.23 dB and 236.08 dB with a median of 212.20 dB. Ten events with an SL > 230 dB, thus highly energetic, were observed after the swarm onset (Figure 5b). These energetic events did not change the rate of seismic activity, and there was no dominating event with a higher SL. Out of these ten events, eight occurred on 10 and 11 July (green circles in Figure 5b) and the remaining two on 12 and 13 July (Table S1 in the Supplementary Materials). The median SL (SL_M) of all 231 events from the ISC catalogue was 218.43 dB and 215.39 dB of all 69 impulsive events. The overall SL of the events before the swarm onset (6 July at 04h54 to 10 July at 03h51) was low with an SL_M of 211.72 dB (thick black line in Figure 5b). The SL increased after the swarm onset, 10 July at 03h55, with the occurrence of abundant strong events, and remained near this level till 10 July at 16h00 with an SL_M of 217.50 dB. After this, the SLs decreased together with the seismicity rate. After 10 July at 16h00, the SL_M decreased to 214.66 dB till occurrence of the first cluster of impulsive events (12 July at 11h14) with SL_M of 214.96 dB. Between 12 July at 11h14 and 13 July at 13h55 (time between the cluster of impulsive events and decreasing seismic activity), SL_M of events reduces to 213.95 dB. From then on to the next cluster of impulsive events on 14 July at 12h55, the SL_M decreased to 213.39 dB and then to 213.09 dB until 16 July at 17h17 (next two clusters of impulsive events), and finally down to 211.93 dB, till 18 July at 12h54 (end of the swarm). Though SLs do not directly represent seismic magnitudes, they follow the same pattern as the magnitude of events from the ISC catalogue, particularly at swarm onset.

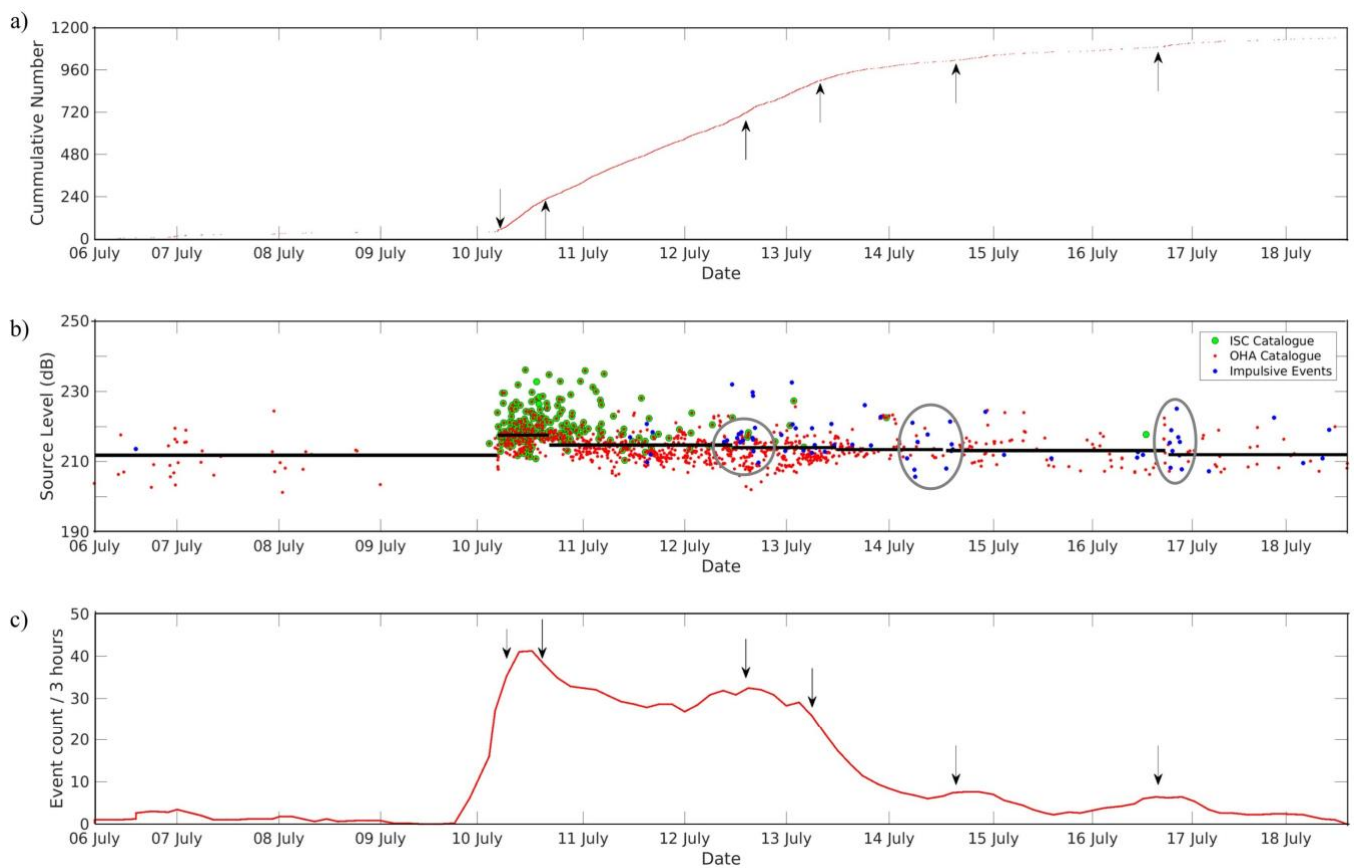


Figure 5. Temporal distribution of Swarm-1 events: (a) Cumulative number (CN) of events vs. time since the origin of the time axis. Black arrows point to changes in the CN slope. (b) Source level distribution of all hydroacoustic events (red dot), impulsive events (blue dot), and events reported in the ISC catalogue (green circles). Thick black lines define the median SL (SL_M) for events occurring between two consecutive black arrows in (a). The gray colored ellipses denote the cluster of impulsive events. (c) Number of events per 3 h in a moving window shifted by intervals of 30 min. The black arrows point to local changes in the event count.

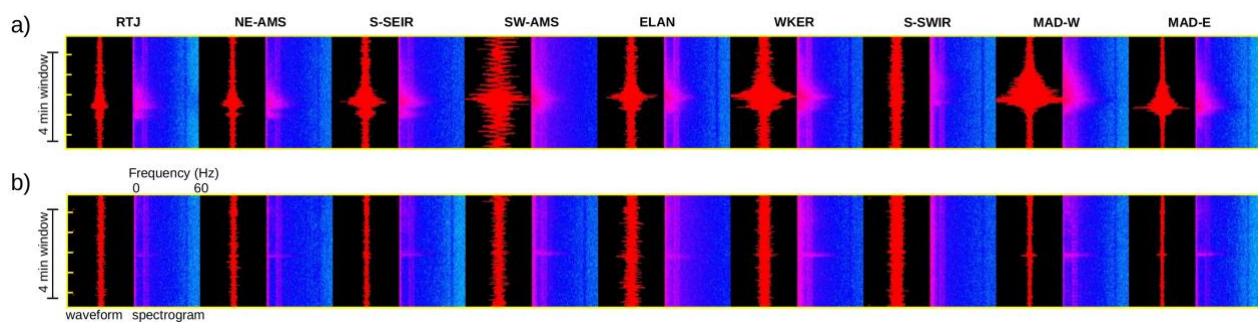


Figure 6. Four-minute-long waveform and corresponding spectrogram of (a) a strong event on 10 July at 03h55 and (b) an impulsive event on 11 July at 16h11 on all nine hydrophones of the OHAISBIO network. The signal for strong event lasts for ~100 s vs. ~10 s for impulsive event. Due to the presence of seasonal noise in the S-SWIR records, the signal was weak for the strong event and absent for the impulsive event.

3.2. Seismicity of Swarm-2

The swarm-2 analysis was based on hydroacoustic records from only seven AuHs (MAD-E and WKER AuHs recorded no data in the period of interest) and from 25 September to 27 October; this analysis led to the location of 5099 events. This number decreased to 5031 after selecting events with origin time-errors less than 10 s. We then removed all events within 40 s of the preceding one, yielding a catalogue of 4954 events (compared with 92 events in the ISC catalogue). After re-picking this first catalogue, 4880 events were relocated of which 782 events (16%) were located

using four hydrophones, 2997 events (61.5%) using five, 1039 events (21%) using six, and 62 events (1.5%) using seven hydrophones. Only 2999 events were discernible in the S-SWIR records because of the high seasonal noise in the data and only 2039 events in ELAN data due to the fact of its remoteness from the swarm (~2500 km).

Only 17 events were detected between 25 September at 21h42 and 27 September at 13h58 (Figure 7), after which the seismicity slightly increased with one impulsive event and several small events, representing mild seismic activity. Similar to Figure 5, black arrows mark the time of changes in the CN slope (either an increase or a decrease in event count per unit of time). Starting from 28 September at 06h21, the swarm abruptly became active with the occurrence of a cluster of ten impulsive events (Figure 7a), leading to a sharp increase in the CN slope. The slope rose up again on 29 September. Seismicity became even more intense with 448 events on 1 October, among which the ISC catalogue lists a short duration temporal cluster. This intense seismic activity continued till 7 October with an average of ~414 events per day. During this period, the number of events increased per day, meaning the seismic activity intensified over time (Figure 7c). The CN slope slightly flattened at the start of 8 October, reflecting an abrupt decrease in seismic activity. The slope rose again on 10 October, with a cluster of ten impulsive events followed by short-time episodes of impulsive events. On 14 October, three strong events ($SL > 230$ dB) marked an increase in the event count (Figure 7c) with a cluster of five impulsive events at the end of 15 October. This activity declined after 18 October ($SL > 230$ dB) and remained even until the last detected event for this swarm (27 October).

In swarm-2, SLs ranged between 196.08 dB and 240.33 dB with a median of 217.70 dB (5.5 dB higher than for swarm-1), with 24 SLs > 230 dB (Figure 7b). Out of these 24 events, only seven are reported in the ISC catalogue (Table S2 in Supplementary Materials). The SL_M of the 92 events in the ISC catalogue is 221.12 dB (2.69 dB higher than for swarm-1) and 221.16 for all 58 impulsive events (5.64 dB higher than that of swarm-1). Before the swarm onset, the SL_M was 220.19 dB (25 September at 21h42 to 27 September at 13h58). It then decreased to 213.75 dB between the swarm onset and abrupt activation of the swarm (27 September at 13h58 to 28 September at 06h21), and at the end of 28 September, the SL_M increased to 216.91 dB. Between 29 September and before the seismicity became intense (1 October at 01h36), the SL_M decreased to 215.44 dB. During the period of intense seismic activity (1 to 7 October), the SL_M increased to 216.94 dB and then to 220.63 dB during 8 to 10 October (before the occurrence of a cluster of impulsive events). It then attained the value of 222.09 dB till 14 October at 12h46 (matching a change in the CN slope) and then 222.69 dB till 15 October at 23h51 (occurrence of another cluster of impulsive events).

Before the occurrence of a strong event on 18 October at 22h53 ($SL = 237.07$ dB), the SL_M decreased to 220.66 dB. In the end, the SL_M decreased to 216.82 dB, as most of the detected events become sparser (constant slope in CN). Here, also, the SL of hydroacoustic events followed the same pattern as the magnitude of events in the ISC catalogue. The results relative to swarm-1 and -2 are summarized in Table 2.

In the case of swarm-1, we observed that the seismic activity (i.e., changes in CN slope) was governed by the occurrence of clusters of impulsive events. Whereas in swarm-2, the seismic activity changed after strong events, with the $SL > 230$ dB (e.g., on 28 September and 14 and 18 October). We interpreted the normal fault event on 28 September at 7 h 6 min ($M_w = 5.6$ or $SL = 239.4$ dB at $26^{\circ}55'0''$ S, $67^{\circ}44'0''$ E) as a mainshock, because it was followed by 30 events over the next ~3.5 h within a distance of ~100 km (Figure S3), of which 22 were closely spaced in the vicinity of the mainshock (<40 km). Although these potential aftershocks had lower SLs, they did not follow a modified Omori law [64]. Similarly, the event on 14 October at 12h32 ($SL = 240.79$ dB; not reported in the ISC catalogue) was followed by 51 events within the next ~4.5 h and in a ~90 km radius (Figure S4). Here, also, subsequent events had lower SLs than the initial event, but did not

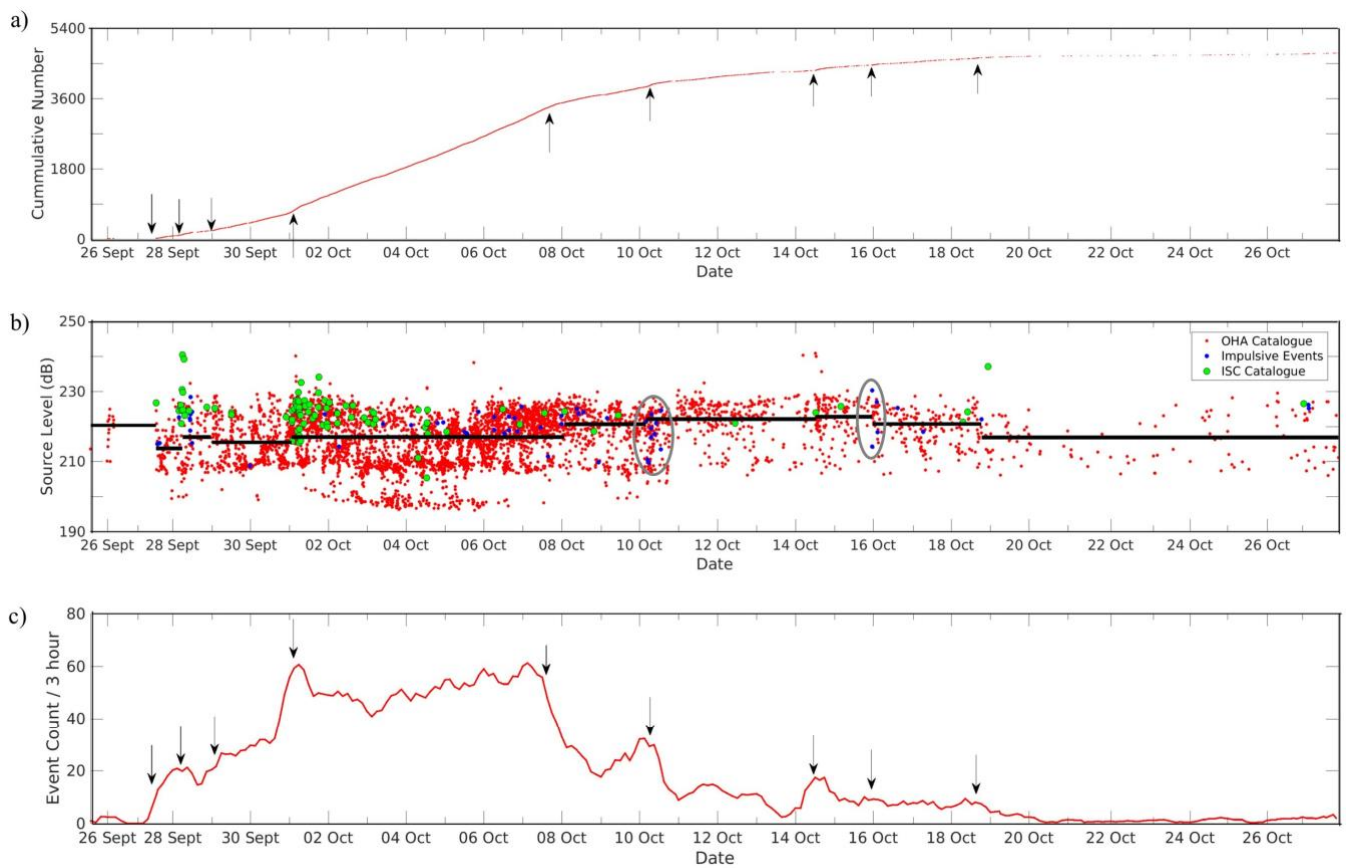


Figure 7. Temporal distribution of Swarm-2 events: (a) cumulative number (CN) of events vs. time since the origin of the time axis. Black arrows point to changes in the CN slope; (b) source level distribution of all hydroacoustic events (red dot), impulsive events (blue dot), and events reported in the ISC catalogue (green circles). Thick black lines define the median SL (SL_M) for events occurring between two consecutive black arrows in (a). The gray colored ellipses denote the cluster of impulsive events; (c) Number of events per 3 h in a moving window shifted by intervals of 30 min. Black arrows point to local changes in the event count.

Table 2. Summary of the analyses of the hydroacoustic data from the OHASISBIO AuH network.

Key Points	Swarm 1	Swarm 2
Date span in 2018	6 July to 18 July	25 September to 27 October
Duration in days	13	33
Number of ISC catalogue events	231	92
Number of hydroacoustic events	1109	4880
Average number of events per hour (over whole duration)	4	8
Number of impulsive events	69	58
Number of AuH stations used	9	7
Most events located with	6 stations (40%)	5 stations (62%)
Median error in latitude (km)	0.44	0.33
Median error in longitude (km)	0.35	0.26
Median error in origin time (s)	0.19	0.18
Range of source level (dB)	201.23–236.08	196.08–240.33
Number of events with SL > 230 dB	10	24
Number of events with SL < 200 dB	0	142
SL of completeness of OHA catalogue	212 dB	209 dB
SL of completeness of ISC catalogue (Figure 4)	218 dB	223 dB
Magnitude completeness of ISC catalogue (mb)	3.9	3.9
Magnitude completeness of OHA catalogue (mb, Figure 4)	3.4	3.1

follow a modified Omori law. Hence, these two sequences were not classical mainshock–aftershock sequences. The strong event on 18 October at 22h53 was also not followed by a pronounced increase in the seismic activity after its occurrence (i.e., the CN slope remains constant after). So, irrespective of the presence of relatively higher magnitude (or SL) events in swarm-2, there was no long exponential decay over several days in the aftershocks as in typical tectonic mainshock–aftershock sequences.

4. Discussion

4.1. Seismic Activity Rate

As expected from the large difference in the number of events and in their duration, the two swarms had very different seismic activity rates. Before the onset of swarm-1 (before 10 July at 03h55), there was only ~1 event per 2.5 h. After the swarm initiation, there were ~11 events per hour (E/H) for the first three days (10 to 12 July), then ~7 E/H between 12 and 14 July. It decreased to ~2 E/H from 14 to 16 July and then to just ~1 E/H till the end of the swarm. For swarm-2, there were ~1 E/H before the swarm onset. Then, ~6 and ~10 E/H from 27 to 28 September and from 29 September to 1 October, respectively. During the period of intense swarm activity (1 to 7 October), the rate increased to ~17 E/H, after which it progressively decreased to ~7 E/H between 8 and 10 October, to ~4 E/H between 10 and 16 October, to ~3 E/H till 18 October and down to ~1 event per 2 h from 18 October until the end of the swarm.

If we assume a uniform temporal distribution of events, the seismic activity rates were ~4 and ~8 E/H for swarm-1 and swarm-2 which span over 13 and 33 days, respectively; this shows that SWIR Segment 4 near the RTJ was seismically far more active than Segment 18 near the Novara FZ. This is indicative of different spreading processes likely due to the different thermal structures between a short ridge segment bounded by a high FZ wall and steep ridge flanks and a long continuous ridge segment. The latter, Segment 4, established ~10 Ma ago, as the result of the continuous eastward propagation of the SWIR, whereas the former, Segment 18, bounded by two large-offset fracture zones (Atlantis II and Novara FZs), is a long-lived spreading segment since ~55 Ma [27,28]. In comparison to the western part of the SWIR, the ridge section between the Melville FZ and the RTJ has no significant fracture zone offsets, transform or major discontinuities, and the axial valley is nearly continuous. Its depth is up to 2 km deeper than expected from Parsons and Sclater's [65] plate cooling model. Seamount abundance is also lower than west of the Melville FZ [31]. Mantle S-wave velocities are higher [66]. These observations indicate that the subaxial crust and mantle temperatures are lower near Segment 4 than they are west of the Melville FZ, i.e., near Segment 18. This results in lower partial melting, less magma supply to the ridge axis, and thinner crust near Segment 4 [35]. This cooler mantle beneath Segment 4 will result in a higher lithospheric strength and thicker brittle layer more prone to accommodating numerous earthquake events. Indeed, large and low magnitude events are both clustered in a small area at Segment 18; in Segment 4, large magnitude events are clustered as well in the axial area, but the low magnitude events are spread over a wider area. The off-axis lithosphere of Segment 18 might therefore be less prone to tectonic seismicity than that of Segment 4 [18].

4.2. Temporal and Geographical Distribution of Events

The swarm-1 events are mostly clustered between three seamounts: T1 at 32° 00' S, 58° 00' E (south seamount), T2 at 31° 20' S, 58° 10' E (north seamount), and T3 at 31° 30' S, 58° 45' E (high FZ crest to the East; Figures 8a and S5a). Just after the onset of swarm-1 on 10 July, events seem to propagate in the east direction (Figures 8a and S6). Before 10 July at 12 h, statistically, most of the events were located in the region between T1 and T2 (flanks of the N–S axial valley at 58° 15' E), and then between 10 July and 11 July at 00h, they occurred next to T3 (ridge-transform intersection). After 11 July at 00h, their distribution became random until the end of the swarm (lacking any spatial pattern; Figure S6). Gridding the number of hydroacoustic events every 1/4th degree in both latitude and longitude (dashed line grid in Figure 8b) shows that 55% of them were

located between T1, T2, and T3 (highlighted in white), and were more numerous in the axial valley than in the transform valley. Also, most of the impulsive events clustered on the southern wall of the T2 seamount (the wall facing the axial valley at $31^{\circ}35'S, 58^{\circ}12'E$). The decreasing number of events across the valley (west to east), the clustering of events between the three bathymetric highs, the initial eastward propagation pattern of events, and the absence of a relatively stronger event initiating the swarm suggest a magmatic origin. The swarm would have initiated with the propagation of several dikes from a same source which connect the seamounts, followed by the readjustment of stresses in the surrounding crust [50,67,68]. The stress readjustment rapidly fades away from the dike locus. The occurrence of three temporal clusters of impulsive events on 12 July, 14 July and 16 July on the southern wall of T2 ($31^{\circ}35'S, 58^{\circ}12'E$), followed by a minor increase in the event count (Figures 5c and 8b) may represent the initiation and propagation of dikes from a source near T2. The T2 bathymetric high was more active compared to T1 and could represent an active volcanic center. The ridge T3, located across the transform, was located on an, at least, 10 Ma old oceanic crust and thus a priori inactive; however, the high and steep wall bounding of this elevated ridge constitutes an ideal radiator for T-waves. The apparent acoustic seismicity surrounding the summit of T3 is thus likely due to the fact of this artefact.

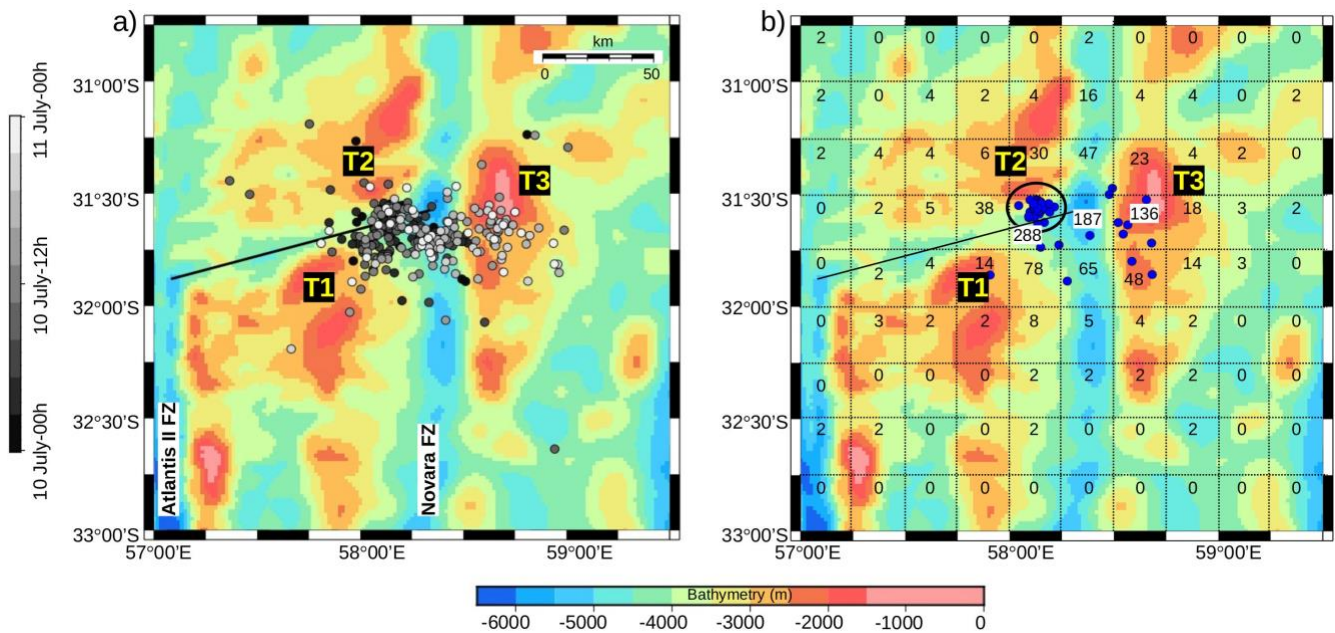


Figure 8. (a) Temporal distribution of location of events between 10 July at 00h and 11 July at 00h. T1, T2, and T3 are local bathymetric highs in the swarm-1 region. The black line shows the axial valley in Segment 18. The gray color scale denotes the origin time of events from 10 July at 00h to 11 July at 00h. (b) Location of all impulsive events (blue dots). Numbers in grid squares are the total event count in each 1/4th grid of latitude and longitude for the entire swarm duration; the highest counts among the seamounts are highlighted in white.

In the case of swarm-2, the events appeared to cluster between two bathymetric highs, T4 and T5, respectively at $26^{\circ}52'S, 67^{\circ}38'E$, and $26^{\circ}29'S, 67^{\circ}21'E$ (T5 is NW of T4; Figures 9a and S5b). The mean location of hydroacoustic events per 12 h from 26 September at 00h00 to 27 October at 12h00 (Figure 9a) was primarily concentrated near T4 before 20 October and then concentrated near T5 till the end of the swarm. It also spreads along the NE–SW bathymetric low separating T4 and T5. The spatio-temporal distribution of these averaged locations suggests an episodic cross-feeding of magma between T4 and T5 by a potential dike propagation [7,37]. It was also observed that the impulsive events were spatially located in the region surrounding T4 and T5 (Figure 9b). They were more clustered near T4 than T5 and, hence, T4 could represent the potential source of magma extrusion or dike initiation (volcanic center). The number of hydroacoustic events per 1/4th degree squares (dashed grid in Figure 9b) shows that 75% of the

events were located near T4 and T5 (highlighted in white), a majority of events (2413 out of 4880) near T4, which again shows that it was more active. The decreasing number of events away from the two bathymetric highs supports the idea of a stress readjustment in the surrounding crust [50]. Moreover, the location of events reported in the ISC catalogue tends to align along a line joining these two seamounts (Figure 2c). This observation together with the focused impulsive events and the event temporal distribution also point for a magmatic origin for swarm-2, initiating with dike propagation from a source near T4.

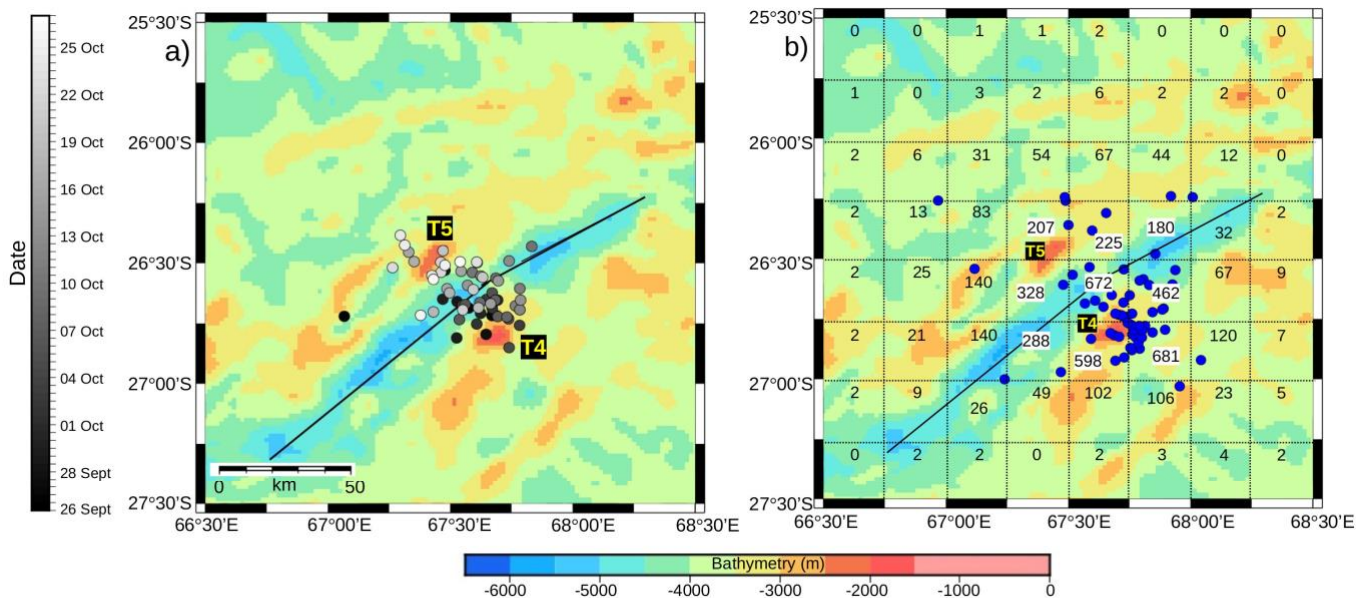


Figure 9. (a) Temporal distribution of mean location (as mean latitude and mean longitude) of swarm-2 events over the bin size of 12 h (gray color scale). T4 and T5 are local bathymetric highs in swarm-2 region. (b) Location of all impulsive events (blue dots). They were mostly clustered towards T4. Numbers in grid squares are the total event count in each 1/4th grid of latitude and longitude for the entire swarm duration; the highest counts around T4 and T5 seamounts are highlighted in white. The black line shows the location of axial valley in Segment 4.

If we compare the number and time distribution of events in swarm-1 and swarm-2, T4 was far more active than T2. Abundant numbers of impulsive events around T2 and T4 also suggest that fresh lava flows were exposed directly on the seafloor at the ridge crest. T2 and T4 seamounts were considered as isolated and shallow volcanic centers. The T2 volcanic center was in an area bounded with long-lived discontinuities (ridge–transform intersection), while T4 was in a region with relatively smoother topography, which would explain the wider spread of events in swarm-2 compared with that in swarm-1. The long distance and 4-month delay between these two swarms is representative of the behavior of a ultra-slow spreading ridge with episodic, distant, and focused magmatic supplies [33,69]. The spatio-temporal distribution of events in both swarms, together with the presence of volcanic centers, suggests a diking episode accompanied with magma movement, similar to that observed in Segment 7 [7,44].

4.3. Source Level of Earthquake Events

Although the geometrical spread of the ISC catalogue events was larger for swarm-1 than for swarm-2, that of the OHA catalogue events was smaller for swarm-1 (Figure 2). This observation might be explained by the fact that Segment 18 (locus of swarm-1) was already intensively fractured and might therefore be less prone to small-scale readjustment to local stress perturbation than Segment 4 (locus of swarm-2). The absence of weak (SL < 200 dB) events in the region of swarm-1 and their abundant number in swarm-2 (142 in total) indicates that Segment 4 is more brittle and, thus, more prone to stress readjustment after a local perturbation caused by strong events. The strong (SL > 230 dB) events are also more abundant (24 in total) in swarm-2

than swarm-1 (10 in total), suggesting that Segment 4 is more prone to tectonic fracturing than segment 18 [43]. After the onset of swarm-1, the progressive decrease of SL_M (Figure 5b) reflects weaker stress readjustments over time until they stopped after 11 July. In swarm-2, the SL_M of events first increased till 16 October after its strong activation on 28 September and then progressively decreased until no event became detectable. This gradual decrease in activity was interspersed with few strong events (Figure 7), which may represent renewed tectonic fracturing or dike intrusions, followed by further stress readjustments. After 16 October, the number of event detections drastically decreased, marking to termination of swarm-2.

4.4. Magmatic Nature of the Swarms

In swarm-1, during its apex from 10 July to 13 July, source levels were fairly homogeneous as the count of event per hour (Figure 5b,c), with no obvious mainshock–aftershock tectonic sequences. In swarm-2, there are three above average events on 28 September at 07h06, 14 October at 12h32, and 18 October at 22h53. However, none of them showed subsequent series of lesser events exceeding few hours; in addition, the source level dropped relative to the initial event was smaller than expected in mainshock–aftershock sequences (e.g., [1,70]). The strong events in swarm-2 do not resemble that found in tectonic swarms on other segments of the SWIR [43] or on other mid-oceanic ridges (e.g., [4,57,71]). The initial propagation of seismicity may indicate a magmatic intrusion, as observed from OBS data in SWIR Segment 7 [44]. Both swarms may therefore be mainly of magmatic nature, which, however, does not preclude the occurrence of normal faulting events [70]. The distribution of events with $M_W > 5$ (white circles in Figure 2b,c), across Segments 4 and 18, could then represent the pathway for magma transport from a volcanic source to the neighboring seamounts [42,72,73]. We observed that the seismicity rate fluctuates over the time for both the swarms and that the normal fault events in the GCMT catalogue occurred later than the swarm onsets. Their later triggering probably reflects the stress-load histories of Segments 4 and 18 [42,74,75]. The observed initiation of magmatic activity and the occurrence of few large magnitude normal faulting events are consistent with the volcanic spreading events along the ultra-slow spreading Gakkel ridge [5,40,42]. The overall analysis of both the swarms suggest that they are both magmatic in origin, possibly triggered by dike intrusions and followed by stress readjustments in their vicinity as observed in Segment 7 [44]. The difference in duration, number, and SL range of events between the two swarms would reflect different lithospheric strength and stress load related to their different tectonic setting and heritage.

5. Conclusions

Due to the remoteness of the Southwest Indian Ridge, most of its seismicity is known from teleseismic records over several decades but limited to magnitudes larger than $m_b = 4.5$. In situ seismicity recordings with ocean bottom seismometers are rare and limited in time (e.g., [7,41]). Long-term seismic monitoring with autonomous hydrophone networks bridges this gap by capturing lower magnitude (down to $m_b = 3.2$) and transient events.

Here, we analyzed the hydroacoustic activity associated with two swarms that occurred in 2018 along the SWIR, using data from the OHASISBIO hydrophone array. These two swarms occurred in contrasting tectonic contexts: swarm-1 on SWIR Segment 18, bounded by two large offset transform faults (Atlantis II and Novara FZ), swarm-2 on SWIR Segment 4, at a ridge discontinuity 200 km from the Rodrigues Triple Junction. The main findings of this study are:

1. Swarm-1 lasted for 13 days and counted 1109 events and occurred at a long-lived ridge segment of the SWIR, whereas swarm-2 lasted for 33 days, counted 4880 events, and occurred at a younger ridge segment that resulted from the eastward propagation of the SWIR.

2. The detection of events over two iterations reduced the uncertainties in location (latitude and longitude) and origin time by ~ 10 -fold in swarm-1 and ~ 11 -fold in swarm-2. For both swarms, they were better than 1 km in latitude and longitude and 0.5 s in origin time.
3. In both swarms, we detected series of short duration (< 10 s) impulsive events. Most of them focused on the slope of a local bathymetric high. We interpreted them as thermal explosions resulting from direct magma supply on the seafloor. The origin of dike intrusions may be located at their apex.
4. Several observations, common to both swarms, pointed to a magmatic origin. The large events, detected on land (ISC; $M_w > 5$), and all hydroacoustic events occurred in an area bounded by or in the vicinity of bathymetric highs. Both showed an initial propagation, followed by spatio-temporal clusters and widespread stress readjustments. Finally, the absence of clear tectonic mainshock–aftershock sequences and a high seismicity rate are common signatures of a magmatic episode, and they lasted nearly two weeks in Segment 18 (swarm-1) and a month in Segment 4 (swarm-2).
5. The abundance of weak ($SL < 200$ dB) and strong ($SL > 230$ dB) events in Segment 4 (locus of swarm-2) suggests that this end of the SWIR is more prone to small-scale readjustments to stress perturbations, here, dike intrusions, and to tectonic fracturing than long-lived, fracture zone bounded sections of the SWIR, such as Segment 18. The difference in the geometrical spread of small events, greater in swarm-2 than in swarm-1, is probably indicative of different lithospheric strengths.

Supplementary Materials: The following are available online at <https://www.mdpi.com/article/10.3390/geosciences11060225/s1>: Tables S1 and S2: Lists of the strongest acoustic events for both swarms ($SL > 230$ dB); Figures S1 and S2: Error distribution improvements in the picking iterations of the two swarms; Figures S3 and S4: Analysis of swarm-2 events after 28 September at 07h06 and 14 October at 12h32, 2018 events (respectively); Figure S5: Detailed bathymetric maps of the swarm areas: (a) For swarm-1; T1, T2 and T3 are three main local seamounts. (b) For swarm-2; T4 and T5 shows two local seamounts on either side of the rift valley; Figure S6: Distribution of swarm-1 events with respect to a reference point at west of it (showing an initial eastward propagation).

Author Contributions: Experiment conception and data acquisition, J.-Y.R.; Initial analysis, S.B. and J.-Y.R.; Formal analysis and original manuscript, V.V.I.; Manuscript review and edition, V.V.I., S.B. and J.-Y.R.; Resources, J.-Y.R. and S.B. All authors have read and agreed to the published version of the manuscript.

Funding: The French Polar Institute (IPEV) and the French Oceanographic Fleet funded the ship-time for the deployment and recovery cruises. INSU-CNRS provided additional support and the Regional Council of Brittany (CPER) funded the hydrophone moorings. V.V.I. was supported by a fellowship from the University of Brest and from the Regional Council of Brittany, through the ISblue project, Interdisciplinary Graduate School for the Blue Planet, co-funded by ANR (ANR-17-EURE-0015) and by the French government under the program “*Investissements d’Avenir*”.

Institutional Review Board Statement: Not applicable.

Informed Consent Statement: Not applicable.

Data Availability Statement: The data presented in this study are available on request from the corresponding author. The data will be publicly available through online repository after the publication.

Acknowledgments: The authors wish to thank the captains and crew of RV *Marion Dufresne* for the successful deployments and recoveries of the hydrophones of the OHASISBIO experiment. Figures were made with the Generic Mapping Tool (GMT; [76]). The authors acknowledge anonymous reviewers for their insightful comments and suggestions to improve the manuscript.

Conflicts of Interest: The authors declare no conflict of interest.

References

1. Utsu, T. Aftershocks and earthquake statistics (2): Further investigation of aftershocks and other earthquake sequences based on a new classification of earthquake sequences. *J. Fac. Sci. Hokkaido Univ. Ser. 7 Geophys.* **1971**, *3*, 197–266.

2. Passarelli, L.; Heryandoko, N.; Cesca, S.; Rivalta, E.; Rohadi, S.; Dahm, T.; Milkereit, C. Magmatic or not magmatic? The 2015–2016 seismic swarm at the long-dormant Jailolo volcano, West Halmahera, Indonesia. *Front. Earth Sci.* **2018**, *6*, 79. [[CrossRef](#)]
3. Sykes, L.R. Earthquake swarms and sea-floor spreading. *J. Geophys. Res.* **1970**, *75*, 6598–6611. [[CrossRef](#)]
4. Bergman, E.A.; Solomon, S.C. Earthquake swarms on the Mid-Atlantic Ridge: Products of magmatism or extensional tectonics? *J. Geophys. Res.* **1990**, *95*, 4943–4965. [[CrossRef](#)]
5. Tolstoy, M.; Bohnenstiehl, D.R.; Edwards, M.H.; Kurras, G.J. Seismic character of volcanic activity at the ultraslow-spreading Gakkel Ridge. *Geology* **2001**, *29*, 1139–1142. [[CrossRef](#)]
6. Schlindwein, V.; Demuth, A.; Korger, E.; Läderach, C.; Schmid, F. Seismicity of the Arctic mid-ocean ridge system. *Polar Sci.* **2015**, *9*, 146–157. [[CrossRef](#)]
7. Schmid, F.; Schlindwein, V.; Koulakov, I.; Plötz, A.; Scholz, J.R. Magma plumbing system and seismicity of an active mid-ocean ridge volcano. *Sci. Rep.* **2017**, *7*, 42949. [[CrossRef](#)]
8. Giusti, M.; Perrot, J.; Dziak, R.P.; Sukhovich, A.; Maia, M. The August 2010 earthquake swarm at North FAMOUS–FAMOUS segments, Mid-Atlantic Ridge: Geophysical evidence of dike intrusion. *Geophys. J. Int.* **2018**, *215*, 181–195. [[CrossRef](#)]
9. Sykes, L.R. Mechanism of earthquakes and nature of faulting on the mid-oceanic ridges. *J. Geophys. Res.* **1967**, *72*, 2131–2153. [[CrossRef](#)]
10. Fox, C.G.; Matsumoto, H.; Lau, T.K.A. Monitoring Pacific Ocean seismicity from an autonomous hydrophone array. *J. Geophys. Res.* **2001**, *106*, 4183–4206. [[CrossRef](#)]
11. Korger, E.I.M.; Schlindwein, V. Performance of localization algorithms for teleseismic mid-ocean ridge earthquakes: The 1999 Gakkel Ridge earthquake swarm and its geological interpretation. *Geophys. J. Int.* **2012**, *188*, 613–625. [[CrossRef](#)]
12. Toomey, D.R.; Solomon, S.C.; Purdy, G.M.; Murray, M.H. Microearthquakes beneath the median valley of the Mid-Atlantic Ridge near 23° N: Hypocenters and focal mechanisms. *J. Geophys. Res.* **1985**, *90*, 5443–5458. [[CrossRef](#)]
13. Wolfe, C.J.; Purdy, G.M.; Toomey, D.R.; Solomon, S.C. Microearthquake characteristics and crustal velocity structure at 29° N on the Mid-Atlantic Ridge: The architecture of a slow spreading segment. *J. Geophys. Res.* **1995**, *100*, 24449–24472. [[CrossRef](#)]
14. Tolstoy, M.; Waldhauser, F.; Bohnenstiehl, D.R.; Weekly, R.T.; Kim, W.-Y. Seismic identification of along-axis hydrothermal flow on the East Pacific Rise. *Nature* **2008**, *451*, 181–184. [[CrossRef](#)]
15. Fox, C.G.; Radford, W.E.; Dziak, R.P.; Lau, T.K.; Matsumoto, H.; Schreiner, A.E. Acoustic detection of a seafloor spreading episode on the Juan de Fuca Ridge using military hydrophone arrays. *Geophys. Res. Lett.* **1995**, *22*, 131–134. [[CrossRef](#)]
16. Smith, D.K.; Escartin, J.; Cannat, M.; Tolstoy, M.; Fox, C.G.; Bohnenstiehl, D.R.; Bazin, S. Spatial and temporal distribution of seismicity along the northern Mid-Atlantic Ridge (15°–35° N). *J. Geophys. Res.* **2003**, *108*, 2167. [[CrossRef](#)]
17. Royer, J.Y.; Chateau, R.; Dziak, R.P.; Bohnenstiehl, D.R. Seafloor seismicity, Antarctic ice-sounds, cetacean vocalizations and long-term ambient sound in the Indian Ocean basin. *Geophys. J. Int.* **2015**, *202*, 748–762. [[CrossRef](#)]
18. Rundquist, D.V.; Sobolev, P.O. Seismicity of mid-oceanic ridges and its geodynamic implications: A review. *Earth Sci. Rev.* **2002**, *58*, 143–161. [[CrossRef](#)]
19. Bohnenstiehl, D.R.; Waldhauser, F.; Tolstoy, M. Frequency-magnitude distribution of microearthquakes beneath the 9° 50' N region of the East Pacific Rise, October 2003 through April 2004. *Geochem. Geophys. Geosyst.* **2008**, *9*, Q10T03. [[CrossRef](#)]
20. Dziak, R.P.; Bohnenstiehl, D.R.; Smith, D.K. Hydroacoustic monitoring of oceanic spreading centers: Past, present, and future. *Oceanography* **2012**, *25*, 116–127. [[CrossRef](#)]
21. Tolstoy, I.; Ewing, M. The T phase of shallow-focus earthquakes. *Bull. Seism. Soc. Am.* **1950**, *40*, 25–51. [[CrossRef](#)]
22. Weston, D.E.; Rowlands, P.B. Guided acoustic waves in the ocean. *Rep. Prog. Phys.* **1979**, *42*, 347. [[CrossRef](#)]
23. Fox, C.; Squire, V.A. On the oblique reflexion and transmission of ocean waves at shore fast sea ice. *Phil. Trans. R. Soc. Lond. A* **1994**, *347*, 185–218. [[CrossRef](#)]
24. Royer, J.Y.; Patriat, P.; Bergh, H.W.; Scotese, C.R. Evolution of the Southwest Indian Ridge from the Late Cretaceous (anomaly 34) to the Middle Eocene (anomaly 20). *Tectonophysics* **1988**, *155*, 235–260. [[CrossRef](#)]
25. Royer, J.Y.; Sclater, J.G.; Sandwell, D.T. A preliminary tectonic fabric chart of the Indian Ocean. *Proc. Indian Acad. Sci. Earth Planet. Sci.* **1989**, *98*, 7–24. [[CrossRef](#)]
26. Sauter, D.; Cannat, M. The ultraslow spreading Southwest Indian ridge. In *Diversity of Hydrothermal Systems on Slow Spreading Ocean Ridges*; Geophysical Monograph Series; The American Geophysical Union: Washington, DC, USA, 2010; Volume 188, pp. 153–173. [[CrossRef](#)]
27. Patriat, P.; Ségoufin, J. Reconstruction of the central Indian Ocean. *Tectonophysics* **1988**, *155*, 211–234. [[CrossRef](#)]
28. Patriat, P.; Sauter, D.; Munsch, M.; Parson, L.M. A survey of the Southwest Indian Ridge axis between Atlantis II Fracture Zone and the Indian Triple Junction: Regional setting and large scale segmentation. *Mar. Geophys. Res.* **1997**, *19*, 457–480. [[CrossRef](#)]
29. Chu, D.; Gordon, G.R. Evidence for motion between Nubia and Somalia along the Southwest Indian Ridge. *Nature* **1999**, *398*, 64–67. [[CrossRef](#)]
30. Cannat, M.; Sauter, D.; Bezos, A.; Meyzen, C.; Humler, E.; Le Rigoleur, M. Spreading rate, spreading obliquity, and melt supply at the ultraslow spreading Southwest Indian Ridge. *Geochem. Geophys. Geosyst.* **2008**, *9*, Q04002. [[CrossRef](#)]
31. Mendel, V.; Sauter, D.; Parson, L.; Vanney, J.R. Segmentation and morphotectonic variations along a super slow-spreading center: The Southwest Indian Ridge (57°–70° E). *Mar. Geophys. Res.* **1997**, *19*, 505–533. [[CrossRef](#)]

32. Mendel, V.; Sauter, D.; Rommevaux-Jestin, C.; Patriat, P.; Lefebvre, F.; Parson, L.M. Magmato-tectonic cyclicity at the ultra-slow spreading Southwest Indian Ridge: Evidence from variations of axial volcanic ridge morphology and abyssal hills pattern. *Geochem. Geophys. Geosyst.* **2003**, *4*, 9102. [CrossRef]
33. Dick, H.J.; Lin, J.; Schouten, H. An ultraslow-spreading class of ocean ridge. *Nature* **2003**, *426*, 405–412. [CrossRef] [PubMed]
34. Sandwell, D.T.; Smith, W.H. Marine gravity anomaly from Geosat and ERS 1 satellite altimetry. *J. Geophys. Res.* **1997**, *102*, 10039–10054. [CrossRef]
35. Cannat, M.; Rommevaux-Jestin, C.; Sauter, D.; Deplus, C.; Mendel, V. Formation of the axial relief at the very slow spreading Southwest Indian Ridge (49° to 69° E). *J. Geophys. Res.* **1999**, *104*, 22825–22843. [CrossRef]
36. Wiens, D.A.; Petroy, D.E. The largest recorded earthquake swarm: Intraplate faulting near the Southwest Indian Ridge. *J. Geophys. Res.* **1990**, *95*, 4735–4750. [CrossRef]
37. Krishna, M.R.; Arora, S.K. Space-time seismicity and earthquake swarms: Certain observations along the slow-spreading mid-Indian Ocean ridges. *Proc. Indian Acad. Sci. Earth Planet. Sci.* **1998**, *107*, 161–173. [CrossRef]
38. Tsang-Hin-Sun, E.; Royer, J.Y.; Perrot, J. Seismicity and active accretion processes at the ultraslow-spreading Southwest and intermediate-spreading Southeast Indian ridges from hydroacoustic data. *Geophys. J. Int.* **2016**, *206*, 1232–1245. [CrossRef]
39. Royer, J.Y.; Beauverger, M.; Torterotot, M.; Lecoulant, J. Seismic Crises along the Southwest Indian Ridge: Insights from Hydroacoustic Observations. 2019. Available online: <https://agu.confex.com/agu/fm19/meetingapp.cgi/Paper/544476> (accessed on 20 May 2021).
40. Schlindwein, V.; Schmid, F. Mid-ocean-ridge seismicity reveals extreme types of ocean lithosphere. *Nature* **2016**, *535*, 276–279. [CrossRef]
41. Yu, Z.; Li, J.; Niu, X.; Rawlinson, N.; Ruan, A.; Wang, W.; Hu, H.; Wei, X.; Zhang, J.; Liang, Y. Lithospheric structure and tectonic processes constrained by microearthquake activity at the central ultraslow-spreading Southwest Indian Ridge (49.2° to 50.8° E). *J. Geophys. Res.* **2018**, *123*, 6247–6262. [CrossRef]
42. Schlindwein, V. Teleseismic earthquake swarms at ultraslow spreading ridges: Indicator for dyke intrusions? *Geophys. J. Int.* **2012**, *190*, 442–456. [CrossRef]
43. Läderach, C.; Korger, E.I.M.; Schlindwein, V.; Müller, C.; Eskstaller, A. Characteristics of tectonomagmatic earthquake swarms at the Southwest Indian Ridge between 16° E and 25° E. *Geophys. J. Int.* **2012**, *190*, 429–441. [CrossRef]
44. Meier, M.; Schlindwein, V. First in situ seismic record of spreading events at the ultraslow spreading Southwest Indian Ridge. *Geophys. Res. Lett.* **2018**, *45*, 10–360. [CrossRef]
45. ISC International Seismological Center. On-Line Bulletin 2021. Available online: <http://www.isc.ac.uk/iscbulletin/search/catalogue/> (accessed on 10 November 2020).
46. Ekström, G.; Nettles, M.; Dziewonski, A.M. The global CMT project 2004–2010: Centroid-moment tensors for 13,017 earthquakes. *Phys. Earth Planet. Inter.* **2012**, *200–201*, 1–9. [CrossRef]
47. Royer, J.Y. OHA-SIS-BIO: Hydroacoustic Observatory of the Seismicity and Biodiversity in the Indian Ocean. 2009. Available online: <https://campagnes.flotteoceanographique.fr> (accessed on 21 May 2021).
48. Samarán, F.; Stafford, K.M.; Branch, T.A.; Gedamke, J.; Royer, J.-Y.; Dziak, R.P.; Guinet, C. Seasonal and geographic variation of southern blue whale subspecies in the Indian Ocean. *PLoS ONE* **2013**, *8*, e71561. [CrossRef]
49. Fox, C.G.; Dziak, R.P.; Matsumoto, H.; Schreiner, A.E. Potential for monitoring low-level seismicity on the Juan-de-Fuca ridge using military hydrophone arrays. *Mar. Technol. Soc. J.* **1993**, *27*, 22–30.
50. Dziak, R.P.; Smith, D.K.; Bohnenstiehl, D.R.; Fox, C.G.; Desbruyeres, D.; Matsumoto, H.; Tolstoy, M.; Fornari, D.J. Evidence of a recent magma dike intrusion at the slow spreading Lucky Strike segment, Mid-Atlantic Ridge. *J. Geophys. Res.* **2004**, *109*, B12102. [CrossRef]
51. Bohnenstiehl, D.R.; Tolstoy, M. Comparison of teleseismically and hydroacoustically derived earthquake locations along the north-central Mid-Atlantic Ridge and Equatorial East Pacific Rise. *Seism. Res. Lett.* **2003**, *74*, 791–802. [CrossRef]
52. Bohnenstiehl, D.R.; Tolstoy, M.; Smith, D.K.; Fox, C.G.; Dziak, R.P. Time-clustering behavior of spreading-center seismicity between 15 and 35 N on the Mid-Atlantic Ridge: Observations from hydroacoustic monitoring. *Phys. Earth Planet. Int.* **2003**, *138*, 147–161. [CrossRef]
53. Schreiner, A.E.; Fox, C.G.; Dziak, R.P. Spectra and magnitudes of T-waves from the 1993 earthquake swarm on the Juan de Fuca Ridge. *Geophys. Res. Lett.* **1995**, *22*, 139–142. [CrossRef]
54. Slack, P.D.; Fox, C.G.; Dziak, R.P. P wave detection thresholds, Pn velocity estimates, and T wave location uncertainty from oceanic hydrophones. *J. Geophys. Res.* **1999**, *104*, 13061–13072. [CrossRef]
55. Teague, W.J.; Carron, M.J.; Hogan, P.J. A comparison between the Generalized Digital Environmental Model and Levitus climatologies. *J. Geophys. Res.* **1990**, *95*, 7167–7183. [CrossRef]
56. Lecoulant, J.; Guennou, C.; Guillon, L.; Royer, J.-Y. 3D-modeling of earthquake generated acoustic waves in the ocean in simplified configurations. *J. Acoust. Soc. Am.* **2019**, *146*, 2110–2120. [CrossRef]
57. Bohnenstiehl, D.R.; Tolstoy, M.; Dziak, R.P.; Fox, C.G.; Smith, G. Aftershock sequences in the mid-ocean ridge environment: An analysis using hydroacoustic data. *Tectonophysics* **2002**, *354*, 49–70. [CrossRef]
58. Gutenberg, B.; Richter, C.F. *Seismicity of the Earth and Associated Phenomena*; Princeton University Press: Princeton, NJ, USA, 1954.
59. Aki, K. Maximum likelihood estimate of b in the formula $\log N = a - bM$ and its confidence limits. *Bull. Earthq. Res. Inst. Tokyo Univ.* **1965**, *43*, 237–239.

60. Chadwick, W.W.; Paduan, J.B.; Clague, D.A.; Dreyer, B.M.; Merle, S.G.; Bobbitt, A.M.; Caress, D.W.; Philip, B.T.; Kelley, D.S.; Nooner, S.L. Voluminous eruption from a zoned magma body after an increase in supply rate at Axial Seamount. *Geophys. Res. Lett.* **2016**, *43*, 12063–12070. [[CrossRef](#)]
61. Wilcock, W.S.; Tolstoy, M.; Garcia, C.; Tan, Y.J.; Waldhauser, F. Live from the Seafloor: Seismic Signals Associated with the 2015 Eruption of Axial Seamount. 2015. Available online: <https://agu.confex.com/agu/fm15/meetingapp.cgi/Paper/73407> (accessed on 20 May 2021).
62. Wilcock, W.S.; Tolstoy, M.; Waldhauser, F.; Garcia, C.; Tan, Y.J.; Bohnenstiehl, D.R.; Caplan-Auerbach, J.; Dziak, R.P.; Arnuif, A.F.; Mann, M.E. Seismic constraints on caldera dynamics from the 2015 Axial Seamount eruption. *Science* **2016**, *354*, 1395–1399. [[CrossRef](#)]
63. Tan, Y.J.; Tolstoy, M.; Waldhauser, F.; Wilcock, W.S. Dynamics of a seafloor-spreading episode at the East Pacific Rise. *Nature* **2016**, *540*, 261–265. [[CrossRef](#)]
64. Utsu, T.; Ogata, Y.; Matsuura, R.S. The centenary of the Omori formula for a decay law of aftershock activity. *J. Phys. Earth* **1995**, *43*, 1–33. [[CrossRef](#)]
65. Parsons, B.; Sclater, J.G. An analysis of the variation of ocean floor bathymetry and heat flow with age. *J. Geophys. Res.* **1977**, *82*, 803–827. [[CrossRef](#)]
66. Debayle, E.; L  v  que, J.-J. Upper mantle heterogeneities in the Indian Ocean from waveform inversion. *Geophys. Res. Lett.* **1997**, *24*, 245–248. [[CrossRef](#)]
67. Sohn, R.A.; Hildebrand, J.A.; Webb, S.C. Postdrifting seismicity and a model for the 1993 diking event on the CoAxial segment, Juan de Fuca Ridge. *J. Geophys. Res.* **1998**, *103*, 9867–9877. [[CrossRef](#)]
68. Rivalta, E.; Taisne, B.; Bungler, A.P.; Katz, R.F. A review of mechanical models of dike propagation: Schools of thought, results and future directions. *Tectonophysics* **2015**, *638*, 1–42. [[CrossRef](#)]
69. Michael, P.J.; Langmuir, C.H.; Dick, H.J.B.; Snow, J.E.; Goldstein, S.L.; Graham, D.W.; Lehnert, K.; Kurras, G.; Jokat, W.; M  he, R.; et al. Magmatic and amagmatic seafloor generation at the ultraslow-spreading Gakkel ridge, Arctic Ocean. *Nature* **2003**, *423*, 956–961. [[CrossRef](#)]
70. McNutt, S.R. Seismic monitoring and eruption forecasting of volcanoes: A review of the state-of-the-art and case histories. In *Monitoring and Mitigation of Volcano Hazards*; Springer: Berlin/Heidelberg, Germany, 1996; pp. 99–146. [[CrossRef](#)]
71. Simao, N.; Escartin, J.; Goslin, J.; Haxel, J.; Cannat, M.; Dziak, R. Regional seismicity of the Mid-Atlantic Ridge: Observations from autonomous hydrophone arrays. *Geophys. J. Int.* **2010**, *183*, 1559–1578. [[CrossRef](#)]
72. Cannat, M.; Rommevaux-Jestin, C.; Fujimoto, H. Melt supply variations to a magma-poor ultra-slow spreading ridge (Southwest Indian Ridge 61   to 69   E). *Geochem. Geophys. Geosyst.* **2003**, *4*, 9104. [[CrossRef](#)]
73. Standish, J.J.; Sims, K.W. Young off-axis volcanism along the ultraslow-spreading Southwest Indian Ridge. *Nat. Geosci.* **2010**, *3*, 286–292. [[CrossRef](#)]
74. Mogi, K. Earthquakes and fractures. *Tectonophysics* **1967**, *5*, 35–55. [[CrossRef](#)]
75. Hainzl, S. Seismicity patterns of earthquake swarms due to fluid intrusion and stress triggering. *Geophys. J. Int.* **2004**, *159*, 1090–1096. [[CrossRef](#)]
76. Wessel, P.; Smith, W.H. New, improved version of Generic Mapping Tools released. *Eos Trans. Am. Geophys. Union* **1998**, *79*, 579. [[CrossRef](#)]

Erratum to the MDPI-Geosciences article

I would like to report a small correction to b -value calculations mentioned in the calculated Gutenberg-Richter law (p. 6 of 18 in the paper, p. 98 in the thesis).

The original text says that:

1. For swarm-1, the ISC catalogue yielded a b -value of **2.96** (Figure 4a), much greater than the expected value of 1 typical for seismically active regions.
2. For swarm-2, the ISC catalogue yielded a b -value of **2.11** (Figure 4b), with a $M_{C(ISC)} = 3.9 mb$ and an $SL_{C(ISC)} = 220$ dB, which are quite similar to swarm-1.

The revised text is as follows:

1. For swarm-1, the ISC catalogue yielded a b -value of **1.29** (Figure 4a), much greater than the expected value of 1 typical for seismically active regions.
2. For swarm-2, the ISC catalogue yielded a b -value of **0.91** (Figure 4b), with a $M_{C(ISC)} = 3.9 mb$ and an $SL_{C(ISC)} = 220$ dB, which are quite similar to swarm-1.

Reason: In the original text, b -values were calculated in a natural \log scale instead of a \log_{10} scale, which is now corrected. The SL vs mb relationships remain unchanged, though (Figures 4a and 4b).

3.2 Swarms in 2016: BSSA Article

In this second article (Ingale et al., 2023), published in the *Bulletin of Seismological Society of America*, we focused on the strongest seismic swarm of this study, which occurred near the Melville TF. Between 01 June 2016 and 25 March 2017 (298 days), we detected 27624 events in this swarm. After scrutinizing the spatio-temporal distribution of events, it was apparent that the conventional patterns of tectonic mainshock-aftershocks sequences, defined by modified Omori's law were not discernible. This swarm showed a magmatic origin comprising several episodes of dike emplacements. The supplementary material associated with this article is provided in Appendix D.

Citation: Ingale, V. V., Bazin, S., Olive, J.-A., Briaies, A., and Royer, J.-Y. (2023). Hydroacoustic study of a seismic swarm in 2016-2017 near the Melville Transform Fault on the Southwest Indian Ridge. *Bulletin of Seismological Society of America*, 113 (4), 1523-1541, <https://doi.org/10.1785/0120220213>

Extended Abstract

The seismic activity along the Southwest Indian Ridge (SWIR) near the Melville Transform Fault (TF) between June 2016 and March 2017 stands out as an unprecedented and prolonged seismic swarm, presenting unique characteristics that deviate from typical tectonic patterns. Lasting for 298 days, this swarm, comprising 27624 hydroacoustic events with an average of approximately 93 events per day, surpasses in duration and total events those reported for other swarms along the SWIR.

The Melville TF, established around 40 million years ago, features a distinct cooler lithosphere inferred from positive shear wave velocity anomalies in the upper mantle. This cooler mantle results in a stronger lithosphere with a thicker brittle layer, accommodating numerous earthquakes. The seismicity in this swarm is diverse, with events categorized into large-magnitude ISC and GCMT catalog events clustered near the axial area and low-magnitude events spread over a wider area parallel to the ridge axis. The off-axis lithosphere near the Melville TF appears more accommodative to magmato-tectonic seismicity.

The swarm is also characterized by short-duration, high-energy, and impulsive events, suggesting H-waves or water-borne events, likely associated with lava-seawater interactions. Similar hydroacoustic impulsive events observed elsewhere have been linked to lava-water interactions during volcanic eruptions. The temporal distribution of events reveals a complex pattern, challenging the conventional mainshock-aftershock sequence model. Instead, the swarm exhibits distinctive

sequences, some triggered by normal faulting GCMT events. Modified Omori's law analysis, which characterizes the decay in seismic activity after a main shock, indicates that several sequences in this swarm do not fit typical tectonic patterns. Seven out of nine sequences triggered by normal faulting events show p-values less than 0.8, suggesting a magmato-tectonic origin.

Tidal effects on seismicity, a factor often considered in mid-ocean ridge seismic studies, appear to be negligible in influencing the observed oscillatory pattern in the swarm. The geographical distribution of events provides insights into potential dike emplacements and normal faulting. The evolution of seismic activity from scattered spatial distribution to focused clusters along the ridge axis or bathymetric highs implies a combination of radial focusing and upward migration of seismic sources. The lack of lateral migration suggests a different mechanism than observed in other parts of the SWIR.

Two distinct events in December 2016 and January 2017 show spatial clustering, abrupt increases in seismic activity, and a gradual decrease. The December event is interpreted as a dike emplacement, while the January event indicates a vertical and elongated dike below the axial valley, likely triggering magma eruption. The absence of clear mainshock aftershock sequences and the occurrence of impulsive events point to a magmatic origin for this prolonged and intense seismic swarm near the Melville TF. Overall, this seismicity provides valuable insights into the complex interplay of tectonic and magmatic processes in a remote oceanic setting, challenging traditional seismic models.

Résumé étendu (En français)

L'activité sismique le long de la dorsale sud-ouest Indienne (SWIR) près de la faille de transformation de Melville (TF) entre juin 2016 et mars 2017 se distingue par un essaim sismique sans précédent par sa durée, présentant des caractéristiques uniques déviant des schémas tectoniques typiques. D'une durée de 298 jours, cet essaim comprend 27 624 événements hydroacoustiques avec une moyenne d'environ 93 événements par jour ; il surpasse en durée et en nombre d'événements tous les autres essaims signalés le long de la SWIR.

La faille transformante (TF) de Melville, établie il y a environ 40 millions d'années, présente une lithosphère distincte, plus froide, d'après les anomalies positives de vitesse des ondes de cisaillement dans le manteau supérieur. Cette lithosphère plus froide est alors plus résistante avec une couche fragile plus épaisse, siège de nombreux séismes. La sismicité dans cet essaim est diverse, avec des événements de forte magnitude dans les catalogues ISC et GCMT, regroupés près de la zone axiale, et des événements de faible magnitude dispersés sur une zone plus large parallèle à l'axe de la ride. La lithosphère hors axe près de la TF de Melville semble être plus accommodante pour une sismicité magmato-tectonique.

L'essai est également caractérisé par des événements de courte durée, à haute énergie et impulsionnels, suggérant des ondes H, c'est-à-dire générées directement dans la colonne d'eau. Ils sont probablement associés à des interactions entre la lave et l'eau de mer d'après événements impulsionnels hydroacoustiques semblables, observés ailleurs, pendant des éruptions volcaniques. La distribution temporelle des événements révèle un schéma complexe, sans séquences choc-répliques classiques. Au lieu de cela, l'essai présente des séquences distinctives, certaines déclenchées par des événements en failles normales (source GCMT). La loi modifiée d'Omori, qui caractérise une décroissance exponentielle (paramètre p) de l'activité sismique après un choc principal, indique que plusieurs séquences dans cet essai ne correspondent pas à des séquences tectoniques typiques. Sept des neuf séquences déclenchées par les événements en failles normales montrent des valeurs de p inférieures à 0,8, suggérant une origine magmato-tectonique.

Les effets des marées sur la sismicité, un facteur souvent pris en compte dans les études sismiques des dorsales médio-océaniques, semblent avoir une influence négligeable sur la variation cyclique de la sismicité observée dans l'essai. La distribution géographique des événements pourrait s'expliquer par d'éventuels emplacements de dykes et de failles normales. L'évolution de l'activité sismique avec des grappes concentrées le long de l'axe de la dorsale ou sur des points culminants bathymétriques suggère une focalisation d'une migration magmatique ascendante sous la dorsale. L'absence de migration latérale suggère un mécanisme différent de celui observé dans d'autres parties de la SWIR.

Deux événements distincts en décembre 2016 et janvier 2017 montrent une augmentation abrupte de l'activité sismique puis une diminution progressive. L'événement de décembre est interprété comme l'emplacement horizontal de dyke, tandis que l'événement de janvier indique un dyke vertical allongé sous la vallée axiale, déclenchant probablement une éruption magmatique. L'absence de séquences claires choc-répliques et la survenue d'événements impulsionnels suggèrent une origine magmatique pour cet essai sismique prolongé et intense près de la TF de Melville. Dans l'ensemble, cette sismicité reflète une interaction complexe entre processus tectoniques et magmatiques.

Hydroacoustic study of a seismic swarm in 2016-2017 near the Melville Transform Fault on the Southwest Indian Ridge

Vaibhav Vijay Ingale¹, Sara Bazin¹, Jean-Arthur Olive², Anne Briais¹, and Jean-Yves Royer¹

¹Lab Geo-Ocean, University of Brest, CNRS, Ifremer, UMR6538, F-29280, Plouzané, France

²Laboratoire de Géologie, CNRS - École Normale Supérieure, PSL University, Paris, France

Corresponding author: vaibhavvijay.ingale@univ-brest.fr

Citation: Ingale V. V., Bazin, S., Olive, J.-A., Briais, A., and Royer, J.-Y. (2023). Hydroacoustic study of a seismic swarm in 2016–2017 near the Melville Transform Fault on the Southwest Indian Ridge. *Bull. Seism. Soc. Am.*, 113(4), 1523-1541, doi: <https://doi.org/10.1785/0120220213>.

Abstract

Hydroacoustic monitoring has become particularly efficient for studying the low-magnitude seismicity occurring at mid-ocean ridges. In 2016-17, a seismic swarm occurred near the Melville Transform Fault of the ultraslow-spreading Southwest Indian Ridge in the Indian Ocean. It comprised 258 events in the land-based International Seismological Centre catalog, extending from June 2016 to March 2017. We examined this seismicity using hydroacoustic records from 3 to 9 hydrophones moored in the Southern Indian Ocean, from the OHASISBIO temporary network and the International Monitoring System of the Comprehensive Nuclear-Test-Ban Treaty Organization. We detected 27624 hydroacoustic events spanning 298 days (June 01, 2016 – March 25, 2017) with lower localization and origin time errors. These include several energetic, short-duration impulsive events, which we interpret as due to lava-water interactions on the seafloor. The spatio-temporal distribution of all the detected events does not show clear tectonic mainshock-aftershock sequences and suggests a magmatic origin of the swarm with bursts of seismicity likely caused by dike emplacements.

Key points:

1. This hydroacoustic study focuses on one of the strongest seismic swarms along the Southwest Indian Ridge
2. Short, energetic impulsive events are attributed to hot lava and seawater interaction on the seafloor
3. The seismicity distribution suggests magmatic origin of the swarm, caused by dike emplacements

Introduction

Along mid-ocean ridges (MORs) or divergent boundaries separating tectonic plates, the oceanic lithosphere is created by a complex interplay of magmatic and tectonic processes, which result in numerous earthquakes that have been investigated since the 1970s (e.g., Sykes, 1970; Bergman and Solomon, 1990; Tolstoy et al., 2001; Rundquist and Sobolev, 2002; Tolstoy and Bohnenstiehl, 2006; Schlindwein et al., 2015; Yu et al., 2018). The associated low-level seismicity is generally lacking in records from land-based seismic networks due to the remoteness of MORs and the rapid attenuation of seismic waves in the solid Earth (Fox et al., 2001; Korger and Schlindwein, 2012). Since the late 1980s, local studies using ocean-bottom seismometers (OBS; e.g., Toomey et al., 1985; Wolfe et al., 1995; Tolstoy et al., 2008; Sahoo et al., 2021) and regional studies using autonomous underwater hydrophones (e.g., Fox et al., 1995; Smith et al., 2003; Bohnenstiehl et al., 2008; Royer et al., 2015) have greatly contributed to a comprehensive understanding of MOR seismicity. This is possible because low-frequency hydroacoustic T-waves from seismic events propagate over long distances with little attenuation within the ocean's low-velocity waveguide, known as the Sound Fixing and Ranging (SOFAR) channel (Tolstoy and Ewing, 1950; Weston and Rowlands, 1979; Fox and Squire, 1994). Earthquakes excite T-waves in the water column through the conversion of seismic waves into acoustic waves at the seafloor (Fox et al., 1995, 2001; Dziak et al., 2012; Jamet et al., 2013). T-wave detection studies provide insights into magmato-tectonic processes and transform fault dynamics over large sections of MORs (Dziak et al., 1997; Bohnenstiehl et al., 2002; Smith et al., 2002; Bohnenstiehl et al., 2003; McGuire et al., 2005; Olive and Escartín, 2016; Giusti et al., 2018; Parnell-Turner et al., 2022). This is the reason why the OHASISBIO (Hydroacoustic Observatory of Seismicity and Biodiversity in the Indian Ocean) network of hydrophones was set up in 2010 to simultaneously monitor the three Indian Ocean ridges with contrasting spreading rates (Royer, 2009). This long-term network has captured 15 swarms since 2010 (e.g., Tsang-Hin-Sun et al., 2016; Ingale et al., 2021),

particularly along the Southwest Indian Ridge (SWIR). This paper focuses on the strongest, longest and most recent swarm on the SWIR.

The ultraslow-spreading SWIR, with a full spreading rate of ~ 14 mm/a (Cannat et al., 1999; Chu and Gordon, 1999), is a major spreading ridge that has separated Africa from Antarctica for over 100 Ma (Patriat et al., 1997). It extends from the Bouvet Triple Junction (BTJ) in the southern Atlantic Ocean to the Rodrigues Triple Junction (RTJ) in the Indian Ocean (Figure 1a; Royer et al., 1988, 1989). Its western end (BTJ) is older than its eastern end (RTJ) due to the lengthening and eastward propagation of the ridge axis at the RTJ (Patriat and Ségoufin, 1988). It is characterized by several large-offset transform faults that divide the ridge into spreading segments of varying lengths (Mendel et al., 1997) with several magmatic and amagmatic ridge segments (Dick et al., 2003) marked by a deep axial valley bounded by ~ 3 km-high ridges (Sauter and Cannat, 2010). The cyclic nature of volcanic construction and tectonic dismemberment across the SWIR has shaped its rugged morphology (Mendel et al., 2003).

The Melville Transform Fault (TF) offsets the SWIR axis to the north by ~ 150 km (Parson et al., 1997) and marks a boundary between two sections of the SWIR in terms of offset, segmentation, bathymetry, seafloor structure, crustal thickness, magma supply, mantle temperature and seismicity distribution (Patriat et al., 1997; Baines et al., 2007). West of the Melville TF ($60^{\circ}45'E$), the SWIR shows an obliquity of 40° and contains several long-lived transform and non-transform discontinuities (Figure 1a). The section east of the Melville TF and up to RTJ ($70^{\circ}E$) has an obliquity of 25° and is continuous with minor discontinuities. Also, segments east of the Melville TF have a less regular pattern of Mantle Bouguer gravity anomalies (MBA), compared with segments west of it (Rommevaux-Jestin et al., 1997). This observation can be explained by a quasi-amagmatic spreading of the SWIR east of the Melville TF, with multiple detachment faults exhuming mantle rocks and scarce volcanic constructions (Sauter et al., 2004). The along-axis depth profile near the Melville TF shows striking variations with bathymetric highs shallower than 3000 m adjacent to axial depth maxima (valley) deeper than 6000 m. Next to this transform fault valley, the obliquity of the ridge axis reaches 40° at $61^{\circ}25'E$. It also shows a spectacular bathymetric high near $61^{\circ}25'E$ with peak-to-trough relief reaching 3700 m and a depth gradient of up to 130 m/km (Patriat et al., 1997). East of this bathymetric high, the rift valley is oblique and continuous up to $63^{\circ}30'E$, with depths ranging between 4500 and 5500 m (segment 14 in Cannat et al., 1999). This segment has a large-amplitude MBA low and its gravity signature is broader than the topography, which can be interpreted as thick crust and/or reduced-density crust or mantle (Cannat et al., 1999).

Several seismic studies have been conducted along the SWIR, both east and west of the Melville TF, based on teleseismic observations (e.g., Wiens and Petroy, 1990), hydroacoustic observations (e.g., Tsang-Hin-Sun et al., 2016), or local OBS surveys (e.g., Yu et al., 2018; Schmid et al., 2017). West of the Melville TF, a teleseismic analysis recorded seismicity associated with an along-axis melt flow mechanism (Läderach et al., 2012). East of the Melville TF, several short-term OBS surveys interpreted the observed seismicity as magma movement related to dikeing episodes (Schlindwein and Schmid, 2016; Meier and Schlindwein, 2018). In the vicinity of the TF (Figure 1b), between June 2016 and March 2017, there was a series of 258 earthquakes reported by the International Seismological Centre (ISC, 2022; triangles in Figure 1b) among which 17 events are reported in the Global Centroid Moment Tensor catalog (GCMT; Ekström et al., 2012; diamonds in Figure 1b). All of the latter show double-couple normal faulting mechanisms, 16 parallel to the SWIR axis and one parallel to the Melville TF.

To investigate this seismic series from the low-level seismicity lacking in the land-based catalogs due to their detection threshold, we examined hydroacoustic data (T-waves) recorded by autonomous hydrophones moored on either side of the SWIR from the OHASISBIO network (Royer, 2009). The OHASISBIO is a long-term hydroacoustic program for monitoring the seismic activity (e.g., Tsang-Hin-Sun et al., 2016) and the vocal activity of large marine mammals in the southern Indian Ocean (e.g., Samaran et al., 2013; Leroy et al., 2017; Torterotot et al., 2020). The network is maintained during the yearly voyages of R/V *Marion Dufresne* to the French Sub-Antarctic Islands. Along with the OHASISBIO network, we also examined hydroacoustic data from the International Monitoring System (IMS) of the Comprehensive Nuclear-Test-Ban Treaty Organization (CTBTO). This global network is designed to detect sounds generated by underwater explosions (Okal, 2001; Gibbons, 2022). Because the seismicity near the Melville TF is located within the OHASISBIO and CTBTO network, observed hydroacoustic events are likely to have more accurate locations than the events from the ISC catalog. Because the hydrophones are more sensitive to low-magnitude events, we detected 27624 events (circles in Figure 1b), i.e., ~107 times more than in the ISC catalog (258 events). The detailed analysis of this improved and dense catalog of hydroacoustic events helps to understand the nature of seismicity near the Melville TF.

Data and Methods

In comparison with seismic wave propagation in the solid Earth, sound waves propagate in the ocean through a more homogeneous sound-velocity channel. For this reason, hydroacoustic data provide a remarkable improvement in the detection threshold (Fox et al., 1994) as well as location accuracy (Fox et al., 2001; Bohnenstiehl and Tolstoy, 2003) of seismic events, compared to distant land-based seismic networks. In this study, we analyzed data from the OHASISBIO hydrophones (Figure 1a) that are moored in the SOFAR channel axis at depths ranging from 1000 m to 1300 m (Table 1). The hydrophones are located south of La Réunion Island (MAD-W, MAD and MAD-E), north-east and south-west of Amsterdam Island (NE-AMS and SW-AMS), south of the Southeast and Southwest Indian ridges (S-SEIR and S-SWIR), and west of Kerguelen Island (WKER2). All sites had a single hydrophone except the SW-AMS, which had a triad of 3 hydrophones. These hydrophones were all set to record acoustic waves continuously at a rate of 240 Hz on 3-byte-long samples. Both before deployment and after recovery, their high-precision clocks are synchronized with a Global Positioning System clock to account for the instrument clock-drift (in the range of 0.002 to 0.100 ppm; Table 1). Among these sites, the hydrophone at MAD was operational from June 2016 to December 2016. In the SW-AMS triad of hydrophones, only SW-AMS3 was operational between June 2016 and November 2016. In January 2017, the SW-AMS triad was replaced by a single hydrophone and the MAD site was no longer operational. However, other sites like MAD-W, MAD-E, NE-AMS and S-SWIR started operating at this time. In the entire duration (June 2016 to March 2017) WKER2 and S-SEIR sites recorded data without any significant intermission.

In the Indian ocean, IMS-CTBTO hydrophones are located ~180 km northwest (H08N) and ~25 km south (H08S) of Diego Garcia Island, ~100 km southwest off Cape Leeuwin, Australia (H01W), and ~30 km north (H04N) of Crozet Island (Figure 1a inset). All these sites comprise a triad of hydrophones also moored in the SOFAR channel and deployed in a triangular configuration with ~2 km spacing between instruments. They are similarly set to record acoustic waves continuously at a rate of 250 Hz with 24-bit analog-to-digital resolution. For this study, we only used one hydrophone from the H08S (H08S1) and H01W triads (H01W1). We could neither use the H04N triad since it started recording

after May 2017 nor the H08N one because it is situated north of the Chagos Bank, which blocked T-waves generated near the Melville TF.

The data from these hydrophones were simultaneously analyzed with the “Seas” software developed at the Pacific Marine Environment Laboratory (PMEL) of the National Oceanic and Atmospheric Administration (Fox et al., 2001) and processed as described by Royer et al. (2015). Each earthquake was located after manually picking the highest T-wave energy in spectrograms (Figure S1; Schreiner et al., 1995; Slack et al., 1999). If two events originate from the same location at different times (> 40 s), or if two events occur at the same time at different locations, the energy arrivals will be distinct (and “pickable”) on all hydrophones due to the spread of the network. Once T-waves were identified on three or more hydrophones, the source location and origin time in UTC were estimated by trial and error using a non-linear least square minimization of the arrival times (Fox et al., 2001). Sound velocities in the ocean were based on the three-dimensional and seasonal Global Digital Environment Model at a resolution of 30 arc-minutes in latitude and longitude (Teague et al., 1990); then the distances and arrival times on each hydrophone were calculated and averaged along great circles joining the sources to each of the receivers. The errors in latitude, longitude and origin time were estimated from the covariance matrix of this least square minimization, weighted by the mean square of the residuals.

Hydroacoustic events are characterized by the acoustic magnitude or Source Level (SL) of the T-waves. The SLs are derived from the Received Levels (RL) at each hydrophone and corrected for the transmission loss (TL) between the event and the hydrophone locations. The TL accounts for the cylindrical sound-spreading loss between the event location and the hydrophone, as well as the spherical sound-spreading loss in the water column between the seafloor acoustic radiator and the sound channel axis (e.g., Jensen et al., 1994). The RL, expressed in decibels with respect to 1 micro-Pascal at 1 meter (dB re μPa at 1 m, hereinafter dB), is based on the average power spectral density in a 10s time-window centered on the peak of energy in the acoustic signal. The RLs are calculated in the 5-60 Hz frequency range, which is optimal for T-wave spectra. This simple RL calculation is performed as the arrival times are picked, and is thus convenient when processing large amounts of data. Furthermore, it is also consistent with previous studies by the PMEL or our group. Methods taking into account scattering effects due to bathymetry or based on T- phase envelopes are perhaps more physically realistic, but require more post-processing and thus are limited to the analysis of small datasets (Yang and Forsyth, 2003).

All the OHASISBIO hydrophones are equipped with HTI-90U sensors with similar sensitivities near -163.5 dB, provided by the manufacturer, except at site SW-AMS3, equipped with an HTI-04ULF sensor with a sensitivity of -168.6 dB (Table 1). Due to this difference in sensitivity, the RL on SW-AMS3 hydrophone differed greatly from that at all other sites. As an example, for some representative events, the median RL was 98.5 ± 2.8 dB on MAD, 102.4 ± 2.6 dB on S-SEIR, 108.3 ± 2.9 dB on WKER2, whereas it was 131.2 ± 3.9 dB on SW-AMS3 (Figure S2a). After correcting these RLs for the transmission loss, SLs for these events detected using all 4 stations was 230.9 ± 3.9 dB, whereas it was 211.1 ± 1.9 dB for the same events picked without SW-AMS3, resulting in a difference of 19.8 dB (Figure S2b). So, instead of recomputing all the SLs to account for this sensitivity discrepancy, we simply reduced them by 19.8 dB when the events were picked using SW-AMS3 until November 28, 2016 (when it failed). Since the same sensor was redeployed at SW-AMS in January 2017, the SLs were also corrected by the same amount (19.8 dB) when SW-AMS was used in the triangulation.

The hydroacoustic catalog (hereinafter OHA) was built in a two-iteration process. In the first iteration, we manually picked T-wave arrivals in a window size of 30 minutes and constructed a catalog

with the following information: the event ID; the number and names of hydrophones used to locate the event; its latitude, longitude and SL; the 1σ uncertainties in latitude, longitude, origin time and SL. In the second iteration, this information was used to zoom-in on the events in a 10-minute time-window to manually re-pick the arrival times and relocate the hydroacoustic events with a higher precision. This step improved the locations and times of the OHA events by reducing the errors in latitude, longitude and origin time by ~ 8 -fold. In the first iteration, the median errors were 2.88 km in latitude, 2.90 km in longitude and 0.90 s in origin time (Figure S3a); in the second iteration, the error improved to 0.38 km, 0.38 km and 0.11 s, respectively (Figure S3b). These errors are calculated only for events recorded by at least four hydrophones. Out of a total of 27624 detected events, only 2095 events (7.6 %) were located using three hydrophones (between November 28, 2016 and January 06, 2017) and the remaining 25529 events were located using four or more hydrophones.

The detection threshold of the hydrophone network is defined by the SL of completeness (SL_c) which is derived from the frequency-size distribution of the acoustic events (Bohnenstiehl et al., 2002). It can be compared to the magnitude of completeness of seismic events from land-based catalogs. This is based on the assumption that acoustic events follow Gutenberg-Richter's law (Gutenberg and Richter, 1954), where SLs would be proportional to the logarithm of the cumulative number of events:

$$\log N = a - b \text{ SL} \quad (1)$$

where N is the cumulative number of events with a source-level greater or equal to SL and constants a and b are the intercept and the slope of the line fitting the distribution of events. For the OHA catalog, the SL_c is 206.6 dB, coinciding with the peak of the normal distribution of SL. The roll-off point of this Gutenberg-Richter's fitting (equation 1) was 14013 for the OHA catalog (Figure 2a-b). The number of ISC events (258) related to this swarm would be too small for a meaningful comparison, furthermore biased towards high magnitudes. We thus considered all ISC events located along the SWIR (i.e., in a similar tectonic context of an ultra-slow spreading ridge) for years 2010 to 2020. The geographical distribution of these events is shown in Figure S4. Still, this collection only amounts to 1933 ISC events vs. 27624 OHA events. The magnitude (mb) of completeness of the 1933 ISC catalog events is $mb_{C(\text{ISC})} = 4.1 \text{ mb}$ and the event distribution still remains biased towards high magnitudes. The equivalent magnitude of completeness for the OHA catalog $mb_{C(\text{OHA})} = 3.3 \text{ mb}$ was estimated by extrapolating the frequency-size distribution with a b -value = 1.29 from the ISC events up to the number of events defining SL_c (Figure 2c). This magnitude of completeness is 0.8 mb better than $mb_{C(\text{ISC})}$ and demonstrates that hydrophone arrays provide more complete information about the seismicity along remote mid-oceanic ridges than land-based catalogs. The total number of events detected by the OHASIBIO and CTBTO networks over 10 months at a single location (June 2016 – March 2017) is ~ 14 times bigger than that detected by land-based networks over 10 years along the whole SWIR (2010-2020). Similar approaches for comparing mb_c and SL_c have been used for hydroacoustic events detected along MORs (Bohnenstiehl et al., 2002; Olive and Escartín, 2016; Tsang-Hin-Sun et al., 2016). The b -value = 1.29 for the ISC catalog means that there is likely a deficit of large events ($mb_{C(\text{ISC})} > 4.1$) relative to small ones. This deficit suggests that a $b = 0.20$ slope for the SL is representative of a volcanic context.

Fitting the two Gutenberg-Richter laws for OHA and ISC catalogs would yield a relationship of $SL = 6.25 \text{ mb} + 186.00$, or conversely $mb = 0.16 \text{ SL} - 29.76$, similar to that proposed, for instance, along the North Mid-Atlantic Ridge, where $SL = 7.98 \text{ mb} + 193.58$ (Pan and Dziewonski, (2005). However, such relations generally fail to explain the scatter of mb vs. SL distribution of the events commonly identified in both hydroacoustic and teleseismic catalogs.

Results

Based on the ISC catalog, the seismic activity started with an event of 4.2 *mb* on June 9, 2016 at 21:50 UTC (SL = 211.7 dB) followed by 257 events until March 25, 2017 with magnitudes ranging between 3.2 *mb* (December 14, 2016 at 11:22) and 5.7 *mb* (January 29, 2017 at 16:42). Such events have SLs between 201.5 and 222.5 dB after the RL corrections. During this period, 17 GCMT catalog events were also reported with magnitudes ranging between $M_w = 4.8$ (August 5, 2016 at 10:43 and August 6, 2016 at 01:11) and $M_w = 5.5$ (September 16, 2016 at 18:38) within the same SL range (Figure 3a). We examined the available hydroacoustic records from June 1, 2016 to March 25, 2017 (298 days), yielding a total of 27624 events showing a 107-fold increase in event count and with SLs ranging from 185.8 dB to 227.9 dB. The events between November 28, 2016 and January 20, 2017 were picked on all hydrophones except at the SW-AMS site; hence their SL is not corrected. In these detections, 627 events showed anomalously high SL between January 9 and January 20, 2017. Their median SL was 216.2 ± 6.0 dB, which was higher by 9.6 dB than the median SL of all hydroacoustic events. Here, events were localized using S-SWIR, WKER2, S-SEIR and MAD-W stations of the OHASISBIO network. Such high SL is mainly due to relatively high RL of 118.8 ± 7.3 dB at the S-SWIR site, compared with RL of 106.0 ± 2.3 dB at WKER2, 101.1 ± 3.4 dB at S-SEIR and 100.9 ± 3.4 dB at MAD-W (Figure S5). The large dispersion in RL recorded by station S-SWIR is probably caused by a high noise-level in the ocean (storm induced) or to strumming noise since the mooring is located near the front of the deep circumpolar Antarctic current (see Orsi et al., 1995; Rintoul et al., 2001). Data from the WKER2 mooring does not display such a noise level in the 0-20 Hz bandwidth (Figure S6) and is less prone to strumming as it is located south of the main circumpolar current track.

Several peculiar events, clustered on the slopes of bathymetric highs, east of the Melville TF at $61^{\circ}25'E$ (Figure 4), are energetic up to 50-60 Hz and of short duration (~ 10 -15s) compared with ~ 200 s T-wave duration for large earthquakes (such as those reported in the ISC catalog). We have detected 118 such events with SLs ranging between 199.4 and 225.1 dB. These signals were only detected at the nearest (MAD at 621 km) as well at the farthest sites (WKER at 1858 km) of the OHASISBIO network, however not by the CTBTO network, probably due to its remoteness from the Melville TF. Hereinafter, we call them impulsive events and will discuss them in the section "Short and energetic impulsive events".

The seismic activity rate was very mild between June 1 and June 8, 2016 with only 73 events and an average of 9 events per day (solid curve in Figure 3b). On June 9, 2016, the seismic activity intensified with 143 events per day (E/D). We detected 2637 events between June 9 and June 30, 2016, ranging between 1 event and 263 E/D. The activity rate increased on June 18 and then on June 30, coinciding with the occurrence of a strong normal faulting GCMT event (June 30 at 12:20, $M_w = 5.1$, SL = 213.7 dB). In July, there were 4248 events with a frequency of 47 to 244 E/D. The time clustering of strong ISC and impulsive events coincided with bursts of seismic activity during this period. At the end of July, there were no strong events and lesser hydroacoustic activity. In August, 3638 events were detected with a frequency ranging from 43 to 254 E/D. A normal faulting GCMT event occurred in early August (August 05 at 10:43, $M_w = 4.8$, SL = 209.4 dB), coincidentally with another burst of activity. Two similar events occurred a day later (August 06 at 01:11, $M_w = 4.8$, SL = 210.6 dB; August 06 at 12:23, $M_w = 4.9$, SL = 212.4 dB). A temporal cluster of impulsive events also coincided with this burst of activity. Near the end of August, we observed two normal faulting GCMT events (August 25 at 01:02, $M_w = 5.0$, SL = 216.9 dB and August 27 at 08:59, $M_w = 5.0$, SL = 218.3 dB) and another burst in seismic activity. Then 4330 events were detected in September, with a minimum of

65 events and a maximum of 272 E/D. In this period, greater seismicity rates coincided with the September 16 at 18:38, $M_w = 5.5$ event. October 2016 displays the maximum monthly count of events in the entire duration, with a total of 4787 events and rates ranging from 68 to 297 E/D. The maximum number of E/D (297) between June 2016 and March 2017 was reached on October 11, 2016. In November, the cumulative number of events flattened as the seismicity rate decreased with 3076 events and 57 to 220 E/D. A seismic burst on November 10 coincided with a cluster of few impulsive and ISC events. Then 2040 events were detected in December with 13 to 193 E/D.

A new activity burst was observed on December 14, 2016 and another temporal clustering of ISC events coincided with small burst of seismic activity on December 26, 2016. In January 2017, 1240 events ranged between 7 to 101 E/D. A few impulsive and ISC catalog events coincided with another activity burst on January 07, 2017. After this, the seismicity gradually became milder; however, it slightly increased at the end of January 2017 coinciding with the GCMT event (January 29 at 16:42, $M_w = 5.4$, $SL = 222.5$ dB) and a dense temporal cluster of impulsive events. In February, 1127 events were detected with a minimum of 11 events and a maximum of 77 E/D. One impulsive event on February 16, 2017 coincided with another seismic activity burst. There was a normal faulting event on February 21 at 11:08 ($M_w = 5.0$, $SL = 214.0$ dB), but the activity rate did not increase after its occurrence. In March, there were only 428 events with daily occurrences between 1 and 33 events; the seismic activity gradually ended until March 25, 2017. Overall, despite the observed variations in the seismic rate, the cumulative number of events (dashed curve in Figure 3b) gradually increased until November 10 and became flat after December 14, 2016. Such a long and sawtoothed distribution of events does not resemble a single mainshock-aftershock sequence.

We computed the distance of the median location of all events per day from a reference point (RP) at $29^{\circ}19'S$, $61^{\circ}04'E$ (cross in Figure 1b) to observe the average spatial distribution of the events. The coordinate of the RP is the median location of all the events from the OHA catalog and is situated on the downslope of bathymetric highs at $61^{\circ}25'E$, and south of the ridge axis (Figure 1b inset). When it initiated, the seismicity was positioned at ~ 10 km from the RP with little fluctuations (Figure 3c and Figure 5). After a temporal cluster of ISC and impulsive events between June 09 and 16, the seismicity migrated back-and-forth between the transform valley and bathymetric highs, showing a wider spatial distribution from June 19 to August 03, 2016. At the time of higher activity on August 05 (Figure 3b), the events were focused within a ± 3 km area located ~ 10 km from the RP. Then the events shifted by ~ 30 km away from the RP and migrated back-and-forth between the valley and bathymetric highs within a ± 10 km wide area until September 21, 2016. At this time, the events were ~ 60 km away from the RP and coincided with a short episode of lower seismic activity rate between September and October 2016. Following it, the seismicity rate was higher and the events focused within an area of ± 10 km, narrowing between the transform valley and bathymetric highs until November 10, 2016. Furthermore, the events densely focused in a narrow ± 2 km area around the RP, until January 20, 2017. Then, events suddenly moved ~ 30 km away from the RP and formed a narrow band of seismicity (± 10 km) aligned along the ridge axis until February 02, 2017. Afterwards, the events were randomly distributed away from the RP until the seismicity ended.

Discussion

Seismicity and lithospheric strength near Melville TF

With an average temporal distribution of events of ~ 93 E/D over 298 days, this seismic swarm is the strongest ever reported along the SWIR in terms of duration and total number of events (Schlindwein, 2012; Schmid et al., 2017; Yu et al., 2018). Two other swarms along the SWIR, which

occurred in 2018 near Novara TF and near the RTJ, lasted for a shorter duration compared with this one, the former comprising 1109 hydroacoustic events over 13 days (85 E/D) and the latter 4880 events over 33 days (148 E/D; Ingale et al., 2021). The strong seismicity near the Melville TF could result from distinct accretion processes along this section of the SWIR axis, relative to the two other swarms. The Melville TF was established at ~ 40 Ma, time of the last major change in spreading direction of the SWIR (Patriat et al., 1997). The sub-axial crust and mantle beneath the Melville TF are cooler (Mendel et al., 1997), which is inferred from greater positive anomalies of shear wave velocity in the upper mantle (Forsyth et al., 1987; Debayle and L  v  que, 1997). This cooler mantle beneath the Melville TF results in a stronger lithosphere with a thicker brittle layer, accommodating numerous earthquakes (Schlindwein and Schmid, 2016; Grevemeyer et al., 2019) and an axial valley oblique to spreading. In this Melville TF swarm, large-magnitude events (ISC and GCMT catalogs) are clustered near the axial area, but the low-magnitude events are spread over a wider area and parallel to the ridge axis. The off-axis lithosphere near the Melville TF might therefore be more accommodative to magmato-tectonic seismicity (Rundquist and Sobolev, 2002).

Short and energetic impulsive events

The short duration, high-energy and frequency content suggest that impulsive events (Figure 4) are H-waves (i.e., water borne), meaning that the energy is directly released into the water column and does not travel into the solid crust as do regular T-waves (Bazin et al., 2022). T-waves originating from shallow earthquakes would have a much broader (i.e., dispersed) waveform due to the size of the seismoacoustic conversion area; furthermore, its magnitude should be significant to be detectable as far as 2000 km away (e.g., at WKER2), which is incompatible with a shallow earthquake depth. Additionally, records of earthquakes detected at the MAD site often display P-wave preceding T-wave arrivals by 240 – 280s (Figure S1) which are not observed before impulsive signals. This confirms that the latter events are not due to shallow earthquakes.

Hydroacoustic impulsive events have been observed at other spreading ridges (e.g., Schlindwein and Riedel, 2010; Tan et al., 2016; Caplan-Auerbach et al., 2017; Le Saout et al., 2020) and underwater volcanoes (e.g., Chadwick et al., 2008; Green et al., 2013; Dziak et al., 2015; Crone and Bohnenstiehl, 2019; Tepp et al., 2020; Bazin et al., 2022; Saurel et al., 2022). Tepp and Dziak (2021) presents a review of the different source mechanisms for such events. Among them, the signature of impulsive signals in our study resembles closely those generated by lava-water interaction when hot lava reaches seafloor, as reported on the East Pacific Rise (Tan et al., 2016) and Juan de Fuca Ridge (Caplan-Auerbach et al., 2017). The cabled array of the Ocean Observatories Initiative recorded thousands of impulsive acoustic signals with SLs in the range of 130 - 190 dB during the Axial seamount eruption on the Juan de Fuca Ridge in 2015, which were interpreted as lava-water interactions and also confirmed by a post-eruption bathymetric survey (Le Saout et al., 2020). During another volcanic eruption off Mayotte Island in 2020-2021, several impulsive events featured SLs, duration and frequency range comparable to ours (Figure S7), and were interpreted as hot lava and seawater interaction based on direct observation of active lava flows (Bazin et al., 2022; Saurel et al., 2022). This result strengthens our interpretation of impulsive events near the Melville TF being associated with hot lava-seawater interactions. However, in the latter studies, the hydrophones were less than 20 km from the Axial seamount (Le Saout et al., 2020) and about 50 km from the volcanic source off Mayotte Island (Bazin et al., 2022). The discrepancy in SL as well as in the number of impulsive events reported in these two studies vs. ours suggest that only the strongest impulsive events (SL > 199 dB; Figure 3a) were captured by the OHASISBIO hydrophones, the closest being 620 km away from their source.

Temporal distribution of events and modified Omori's law

A potential cause for the observed oscillatory pattern (Figure 3b) in the seismicity could be the occurrence of several large tectonic events. Indeed, the decay in seismic activity after a main shock can be characterized by a modified Omori's law (Utsu et al., 1995):

$$n(t) = K(c + t)^{-p}, \quad (2)$$

where $n(t)$ is the frequency of aftershocks per unit time t . The constants K , c and p are empirically derived. K reflects the productivity of a mainshock and c represents the activity within the earliest part of the sequence. The exponent p shows the aftershock sequence's decay rate and reflects the properties of the fault system (Mogi, 1967) and thermal state of the surrounding lithosphere (Kisslinger and Jones, 1991; Bohnenstiehl et al., 2002; Klein et al., 2006). It ranges from 0.6 to 2.5 with a median of 1.1 based on a compilation of more than 200 aftershock sequences (Utsu et al., 1995). For tectonic seismicity, p -values are generally found in the 0.8-1.2 range (Utsu, 1999; Schmid and Grasso, 2012; Hainzl et al., 2016) and in the range of 0.9 – 1.2 range for various aftershock sequences observed along the oceanic TF (Davis and Frohlich, 1991; Bohnenstiehl et al., 2002).

After a visual inspection of the main changes in the slope of the cumulative distribution of events as well as slope changes following the occurrence of strong ISC or GCMT events in a zoomed temporal window (month-wise), we identified 12 sequences. Each sequence starts with a sudden increase in seismicity rate, noted by a date and asterisk in Figure 3b, followed by a gradual decrease. The duration of all sequences was determined till the number of events per hour reached zero, i.e., the cumulative distribution of events became flat. Three out of these 12 sequences (1, 2 and 9) were not triggered by a large earthquake recorded by ISC or GCMT (Table 2). Out of the remaining 9 sequences, 7 were triggered by normal faulting GCMT events, for which we computed modified Omori's law parameters (equation 2). The sequences 1, 5, 6, 8 and 10 shown in Figures S8, S12, S13, S15 and S16 have p -value < 0.8 ; hence could not be classified as pure tectonic mainshock-aftershock sequences (Utsu et al., 1995; Schmid and Grasso, 2012). Sequence 2 (Figure S9) has a p -value > 0.8 , but it was not triggered by any energetic (high magnitude) earthquake; hence not classified as a typical tectonic mainshock-aftershock sequence. Although the remaining sequences 3, 4 and 7 shown in Figure S10, S11 and S14 were triggered by $M_w > 4.8$ events, they were not considered as purely tectonic in nature as they lasted only for a few hours, a duration too short for an aftershock sequence based on the statistical studies of Hainzl et al., (2016). For instance, these authors showed that aftershocks for a $M_w > 4.8$ tectonic event will last for over 7 days. Sequence 11 was triggered by a $m_b = 3.8$ ISC event (Figure S17), after which the number of events kept increasing instead of decreasing as expected for a tectonic sequence. In short, none of the sequences in this seismic swarm appeared purely tectonic in nature. The normal faulting events which triggered changes in the seismic activity rate are thus interpreted as magmato-tectonic earthquakes (McNutt, 1996; Rubin and Gillard, 1998; Müller and Jokat 2000). In short, the sequences triggered by strong normal faulting events, were interpreted as magmato-tectonic in nature, otherwise as magmatic swarms. We discuss the two remaining sequences (9 and 12) in in the section "Geographical distribution of events".

Temporal distribution of events and tidal effects

In this seismic swarm, the temporal occurrence of events displays an oscillatory pattern (Figure 3b) which could be related to either ocean or solid-Earth tide cycles (Sahoo et al., 2021). Several studies have pointed out a tidal triggering of MOR seismicity (Wilcock, 2001; Scholz et al., 2019), with increased seismicity at low tide (Tolstoy et al., 2002; Wilcock, 2009). To test the tidal

influence on the seismicity near the Melville TF, we have computed the tidal coefficients for both the ocean and solid-Earth tides using the Global Oceanic Tidal Corrections code (GOTIC2; Matsumoto et al., 2001). It uses Farrell's convolution integral based on an ocean tide model, a land-sea database and a mass loading Green's Function (Farrell, 1972). Near the Melville TF, the ocean tide varies within ± 2 m and the solid-Earth tide within ± 40 cm. To test their influence on the seismicity, we computed the number of hydroacoustic events with respect to the 2nd derivative of both ocean and solid-Earth tide individually. This 2nd derivative measures the rate of change of slope in the tide height; thus, a negative value corresponds to high tide and a positive value to low tide. In our study, 13524 events occurred during high ocean tide and 14100 events during low ocean tide, showing no obvious effect of the ocean tide (Figure S18). Similarly, 13907 and 13717 events occurred during high and low solid-Earth tides, respectively. These results indicate that neither the ocean nor the solid-Earth tidal oscillations clearly govern the seismicity, unlike, for instance, at Axial volcano on Juan de Fuca ridge where the seismicity was predominant during the periods of low tide (Tolstoy et al., 2002; Wilcock et al., 2016).

We also computed the ocean and solid-Earth tidal heights for all 12 sequences and verified whether there was any correlation between the tides and the seismic activity. Only for sequence 9, we could observe that a high seismicity rate coincides with a high ocean tide at the start of the sequence (Table 2). In order to illustrate the range of our observations, we describe two sequences (9 and 12) in the "Geographical distribution of events" section that display very distinct characteristics.

Geographical distribution of events

At the onset of seismic activity, the hydroacoustic events had a scattered spatio-temporal distribution (Figure 5), with significant fluctuations in the distance to the RP (Figure 3c). In June and July 2016, events were spread over the transform valley and bathymetric highs on the southern flank of the axial valley, east of the TF. One explanation could be that their seismic sources took place in a wide area but it is also possible that their sources originated deep within the crust and that the rough seafloor caused hydroacoustic waves to undergo propagation scattering, or a wider seismic to acoustic conversion area (Park et al., 2001; Williams et al., 2006). During the following months, the locations of the hydroacoustic events gradually narrowed down to a stripe along the ridge axis or near bathymetric highs on the flank of axial valley (Figure 3c). Although, individual bursts of seismic activity clearly stand out, no clear lateral migration of the hydroacoustic events could be observed during the entire period. Instead, the observed pattern over time could be explained by a combination of radial focusing as well as upward migration of the seismic sources. One potential geometry that would explain such observations could be diking episodes feeding from magma pooling at the base of the lithosphere. The occurrence of several impulsive events during this initial period (June to October, 2016) could suggest that few of the dikes reach on the seafloor, causing lava-seawater interactions.

On December 14, 2016, the events clustered within a 20 x 20 km area (sequence 9 in Table 2 and Figure 6a) and their rate abruptly increased to ~ 17 events per hour (from 08:00 to 12:00), followed by a gradual decrease of activity (Figure 6b). We attempted to fit a modified Omori's law (Figure 6c), and obtained a p -value of 0.84. Although such p -value falls in the range of 0.8-1.2 associated with the tectonic mainshock-aftershock sequences (e.g., Utsu et al., 1995; Utsu, 1999; Schmid and Grasso, 2012), we did not consider this sequence as purely tectonic in origin since it did not feature a triggering energetic earthquake (Figure 6b). Figure 6d shows that the sudden rise in the number of events occurs at oceanic high tide; however, we could not find any causality. The spatial clustering of events

combined with a lack of impulsive events argue for a dike emplacement that did not reach the seafloor. This scenario is illustrated by a cartoon (Figure 6e), where all the hydroacoustic events from 14 to 16 December, 2016 are projected along a SW-NE direction, at the apex of potential dikes.

After January 29, 2017, the seismicity spread in another narrow and longer band along the SWIR axis (sequence 12 in Table 2 and Figure 7a). The onset of this series of events coincides with a $M_w = 5.4$, 12 km deep, normal faulting event on January 29 at 16:42 (SL = 222.5 dB), after which the number of events gradually decreases as well as their SLs (inside dashed rectangle in Figure 7b). Despite these characteristics, this sequence is not considered as purely tectonic mainshock-aftershocks; the Omori's law p -value is only 0.54 (Figure 7c), which is much less than 0.8. Furthermore, the sequence only lasted for ~17 hours when it should have lasted at least for ~10 days for a $M_w = 5.4$ tectonic event (Hainzl et al., 2016). Hence, this sequence is likely to have a magmato-tectonic origin (Rubin, 1992; Giusti et al., 2018). Unlike the sequence in December 2016, tidal loading appears uncorrelated with seismicity rates (Figure 7d). We computed the stress change as a result of slip along a normal fault in an elastic half-space (Meade, 2007). From the two focal planes, we selected the fault plane that dips at 46° towards the axial valley (Figure 7e). Assuming the hydroacoustic relocation (SE of the ridge axis) and the depth from the GCMT catalog (12 km), the $M_w = 5.4$ event imparted horizontal extension onto the shallow crust below the axial valley, which could have triggered or facilitated the propagation of a vertical dike. The narrow band of events that we interpret as a vertical and elongated dike below the axial valley, has the same SW-NE azimuth as the normal fault bounding the axial valley to the south. The presence of impulsive events argues for the development of a volcanic fissure along the ridge axis. Such an oblique orientation with respect to the spreading direction is expected near the transform valley due to a rotation of extensional stresses. Afterwards, events scattered over a wider area in February-March 2017 as a result of stress-readjustment in the vicinity (Sohn et al., 1998; Dziak et al., 2004; Rivalta et al., 2015). In this last stage, a double-couple event occurred in February 2017 with a focal mechanism parallel to the Melville TF.

Succession of dike emplacements and normal faulting events

Migration of seismic activity and earthquake locations has been observed at both subaerial and submarine MORs and has been attributed to the vertical and/or lateral propagation of a magma-filled dike at the ridge axis (e.g., Dziak *et al.* 1995; Dziak and Fox 1999; Dziak et al., 2004; Bohnenstiehl *et al.* 2004). Several laterally migrating dike intrusions have already been documented on the SWIR: at segment 18 near the Novara TF and at segment 4 near the RTJ (Ingale et al., 2021), and at segments 7 and 8, east of the Melville TF (Schmid et al., 2017). In this study, we do not observe any lateral migration in the seismic activity. We interpret the bursts of seismic activity as diking episodes, as evidenced by the clustering of events near bathymetric highs at $61^\circ 25' E$ in December 2016 and along a narrow band in the axial valley in January 2017. Moreover, the occurrence of impulsive events suggests that magma has erupted on the seafloor, although there is so far no *in situ* evidence for it (in the absence of recent multibeam bathymetry or side-scan sonar surveys). The normal faulting GCMT and other strong earthquakes (ISC catalog) before December 2016 could have changed the stress regime in the sub-axial crust, changing the overpressure on a sub-seafloor magma body and triggering the emplacement of several dikes (Cannat et al., 2003; Baer et al., 2008; Standish and Sims, 2010; Liu and Buck, 2018; Olive and Dublanchet, 2020) and the events after December 2016 likely represented the reactivation of faults in response to stress perturbation caused by the magma eruption (Toda et al., 2002; Shuler and Nettles, 2012). As summarized in Table 2, we propose that these strong tectonic events occur in magmatic swarms, instead of distinct mainshock-aftershock sequences, as described

by McNutt (1996) in a volcanic context, and have a magmato-tectonic origin as described by Rubin and Gillard (1998). Similar observations of a magmatic swarm comprising several normal faulting events were made on the ultraslow-spreading Gakkel ridge (Müller and Jokat 2000) and later confirmed by *in situ* sonar imaging (Edwards et al., 2001). The combined evidence of seismic activity bursts, absence of clear mainshock-aftershock sequences and occurrence of impulsive events point to a magmatic origin for this long-lasting and intense swarm near the Melville TF.

Conclusions

Due to the remoteness of the Southwest Indian Ridge, most of its seismicity is known from teleseismic records over several decades but limited to magnitudes larger than $m_b = 4.1$. Furthermore, *in situ* seismicity recordings by ocean bottom seismometers are rare and limited in time. Long-term seismic monitoring with autonomous hydrophone networks bridges this gap by capturing lower magnitude (down to $m_b = 3.3$, this study) and transient events.

Here, we analyzed hydroacoustic T-waves associated with a swarm that occurred in 2016-2017, near the Melville TF, along the SWIR, using data from the OHASISBIO and IMS-CTBTO hydrophone networks. The main findings of this study are:

1. This swarm lasted for 298 days from June 01, 2016 to March 25, 2017 and counted 27624 hydroacoustic events, the strongest swarm reported on the SWIR so far.
2. The localization of events over two iterations reduced the uncertainties in location (latitude and longitude) and origin time by \sim eight-fold; these were improved to < 400 m in latitude and longitude and 0.1 s in origin time. Despite short periods of noisy data, the general high detection level allowed to identify twelve bursts of activity within this seismic swarm.
3. Although T-wave catalogs lack information about the source depth, we interpret the gradual clustering of earthquakes and the different bursts of seismic activity as the results of several dike emplacements. In addition, bands of events parallel to the SWIR axis imply the transport of magma along narrow and elongated vertical dikes. Normal faulting events were observed as magmato-tectonic in origin and associated with fault activation as well as a response to stress perturbation.
4. We detected a series of energetic and short duration (10 -15s) impulsive events, up to ~ 2000 km away from their source. We interpret them as water-borne H-waves associated with hot lava-seawater interactions caused by magma emplacement on the seafloor. However, there is yet no *in situ* evidence to confirm any recent eruption near the Melville TF, which calls for future near-bottom surveys.
5. The occurrence of impulsive events, the spatio-temporal distribution of the events and the absence of clear tectonic mainshock-aftershock sequences point to the magmatic nature of this swarm.

To understand the spatio-temporal distribution of seismicity and nature of this seismic swarm, T-wave signals were visually examined and manually picked in spectrograms where they are more discernible than in waveforms, particularly for low-magnitude events. Such analytical procedure is cumbersome and its efficiency may differ from one operator to another. As a prospective, designing a processing algorithm based on machine-learning would be a tremendous improvement (Raumer et al., 2023).

Data and Resources: The hydroacoustic catalog presented in this study is available upon request to the senior authors (SB & JYR). The supplementary material provides plots of RLs of representative events, of the improvements in the location and time errors, of the ISC catalog events along the SWIR from 2010 to 2020, of impulsive signal waveforms from this study and off Mayotte Island, of the spatio-temporal distribution with best-fitting modified Omori's law, and of number of hydroacoustic events vs. tidal heights. All figures were drafted with the Generic Mapping Tool (GMT; Wessel and Smith, 1998).

Acknowledgments: The French Polar Institute (IPEV) and the French Oceanographic Fleet funded the ship time for the deployment and recovery of the OHASISBIO network. The National Institute for Earth Sciences and Astronomy (INSU) of Centre National de la Recherche Scientifique (CNRS) provided additional support, and the Regional Council of Brittany (CPER) funded the hydrophone moorings. V.V.I. was supported by a fellowship from the University of Brest and from the Regional Council of Brittany, through the ISblue project, Interdisciplinary graduate school for the blue planet (ANR-17-EURE-0015 under the French government's program "Investissements d'Avenir" for France 2030). The authors wish to thank the captains and crew of R/V Marion Dufresne for the successful deployments and recoveries of the hydrophones of the OHASISBIO experiment. The authors acknowledge anonymous reviewers for their insightful comments and suggestions to improve the manuscript and discussion about the impulsive events.

Declaration of Competing Interests: The authors declare no competing interests.

Author Contribution: Experiment conception and data acquisition, J.-Y.R.; Analysis and original manuscript, V.V.I.; Manuscript edition, V.V.I., S.B. and J.-Y.R.; Resources, J.-Y.R. and S.B. All the authors have contributed to the data interpretation, manuscript revision, and approved the submitted version.

References

- Baer, G., Y. Hamiel, G. Shamir, and R. Nof (2008). Evolution of a magma-driven earthquake swarm and triggering of the nearby Oldoinyo Lengai eruption, as resolved by InSAR, ground observations and elastic modeling, East African Rift, 2007, *Earth Planet. Sci. Lett.* **272**(1-2), 0–352, doi: [10.1016/j.epsl.2008.04.052](https://doi.org/10.1016/j.epsl.2008.04.052).
- Baines, A. G., M. J. Cheadle, H. J. B. Dick, A. H. Scheirer, B. E. John, N. J. Kusznir, and T. Matsumoto (2007). Evolution of the Southwest Indian Ridge from 55°45'E to 62°E: Changes in plate-boundary geometry since 26 Ma, *Geochem. Geophys. Geosyst.* **8**, Q06022, doi: [10.1029/2006GC001559](https://doi.org/10.1029/2006GC001559).
- Bazin S., J.-Y., Royer, F. Dubost, F. Paquet, B. Loubrieu, A. Lavayssière, C. Deplus, N. Feuillet, É. Jacques, E. Rinnert, I. Thinon, E. Lebas, D. Pierre, L. Retailleau, J.-M. Saurel, A. Sukhovich, R. Bonnet and the REVOSIMA group (2022). Initial results from a hydroacoustic network to monitor submarine lava flows near Mayotte Island, *C. R. Geosci.* **1**, 0, doi: [10.5802/crgeos.119](https://doi.org/10.5802/crgeos.119).
- Bergman, E. A., and S. C. Solomon (1990). Earthquake swarms on the Mid-Atlantic Ridge: Products of magmatism or extensional tectonics? *J. Geophys. Res.* **95**, 4943–4965, doi: [10.1029/JB095iB04p04943](https://doi.org/10.1029/JB095iB04p04943).
- Bohnenstiehl, D. R., M. Tolstoy, R. P. Dziak, C. G. Fox, and G. Smith (2002). Aftershock sequences in the mid-ocean ridge environment: An analysis using hydroacoustic data, *Tectonophysics* **354**, 49–70, doi: [10.1016/S0040-1951\(02\)00289-5](https://doi.org/10.1016/S0040-1951(02)00289-5).
- Bohnenstiehl, D. R., and M. Tolstoy (2003). Comparison of teleseismically and hydroacoustically derived earthquake locations along the north-central Mid-Atlantic Ridge and Equatorial East Pacific Rise, *Seism. Res. Lett.* **74**, 791–802, doi: [10.1785/gssrl.74.6.791](https://doi.org/10.1785/gssrl.74.6.791).
- Bohnenstiehl, D. R., M. Tolstoy, M., D. K. Smith, C. G. Fox, and R. P. Dziak (2003). Time-clustering behavior of spreading-center seismicity between 15 and 35 N on the Mid-Atlantic Ridge: Observations from hydroacoustic monitoring, *Phys. Earth Planet. Int.* **138**, 147–161, doi: [10.1016/S0031-9201\(03\)00113-4](https://doi.org/10.1016/S0031-9201(03)00113-4).
- Bohnenstiehl, D. R., R. P. Dziak, M. Tolstoy, C. G. Fox, and M. Fowler, (2004). Temporal and spatial history of the 1999–2000 Endeavour Segment seismic series, Juan de Fuca Ridge, *Geochem. Geophys. Geosyst.* **5**(9), Q09003, doi: [10.1029/2004GC000735](https://doi.org/10.1029/2004GC000735).
- Bohnenstiehl, D. R., F. Waldhauser, and M. Tolstoy (2008). Frequency-magnitude distribution of microearthquakes beneath the 9°50'N region of the East Pacific Rise, October 2003 through April 2004, *Geochem. Geophys. Geosyst.* **9**, Q10T03, doi: [10.1029/2008GC002128](https://doi.org/10.1029/2008GC002128).
- Cannat, M., C. Rommevaux-Jestin, D. Sauter, C. Deplus, and V. Mendel (1999). Formation of the axial relief at the very slow spreading Southwest Indian Ridge (49° to 69°E), *J. Geophys. Res.* **104**, 22825–22843, doi: [10.1029/1999JB900195](https://doi.org/10.1029/1999JB900195).
- Cannat, M., C. Rommevaux-Jestin, and H. Fujimoto (2003). Melt supply variations to a magma poor ultra slow spreading ridge

- (Southwest Indian Ridge 61° to 69° E), *Geochem. Geophys. Geosyst.* **4**, 9104, doi: [10.1029/2002GC000480](https://doi.org/10.1029/2002GC000480).
- Caplan-Auerbach, J., R. P. Dziak, J. Haxel, D. R. Bohnenstiehl, and C. Garcia (2017). Explosive processes during the 2015 eruption of axial seamount, as recorded by seafloor hydrophones, *Geochem. Geophys. Geosyst.* **18**, 1761–1774, doi: [10.1002/2016GC006734](https://doi.org/10.1002/2016GC006734).
- Chadwick, W. W. Jr., K. V. Cashman, R. W. Embley, H. Matsumoto, R. P. Dziak, C. E. J. de Ronde, T. K. Lau, N. D. Deardorff, S. G. Merle (2008). Direct video and hydrophone observations of submarine explosive eruptions at NW Rota-1 Volcano, Mariana Arc, *J. Geophys. Res.* **113**, B08S10, doi: [10.1029/2007JB005215](https://doi.org/10.1029/2007JB005215).
- Chu, D., and G. R. Gordon (1999). Evidence for motion between Nubia and Somalia along the Southwest Indian Ridge, *Nature* **398**, 64–67, doi: [10.1038/18014](https://doi.org/10.1038/18014).
- Crone, T. J., and D. R. Bohnenstiehl (2019). Acoustic evidence of a long-lived gas-driven submarine volcanic eruption in the Bismarck Sea, *Geophys. J. Int.* **217**(1), 169–178, doi: [10.1093/gji/ggy542](https://doi.org/10.1093/gji/ggy542).
- Davis, D. S., C. Frohlich (1991). Single-link cluster analysis, synthetic earthquake catalogues, and aftershock identification, *Geophys. J. Int.* **104**, 2, 289–306, doi: [10.1111/j.1365-246X.1991.tb02512.x](https://doi.org/10.1111/j.1365-246X.1991.tb02512.x).
- Debayle, E., and J.-J. L  v  que (1997). Upper mantle heterogeneities in the Indian Ocean from waveform inversion, *Geophys. Res. Lett.* **24**, 245–248, doi: [10.1029/96GL03954](https://doi.org/10.1029/96GL03954).
- Dick, H. J., J. Lin, and H. Schouten (2003). An ultraslow-spreading class of ocean ridge, *Nature* **426**, 405–412, doi: [10.1038/nature02128](https://doi.org/10.1038/nature02128).
- Dziak, R. P., C. G. Fox, and A. E. Schreiner (1995). The June–July 1993 seismo-acoustic event at CoAxial segment, Juan de Fuca Ridge: evidence for a lateral dike injection, *Geophys. Res. Lett.* **22**, 135–138, doi: [10.1029/94GL01857](https://doi.org/10.1029/94GL01857).
- Dziak R. P., C. G. Fox, H. Matsumoto, and A. E. Schreiner (1997). The 1992 Cape Mendocino earthquake sequence: Seismo-Acoustic analysis using fixed hydrophone arrays, *Mar. Geophys. Res.* **19**, 137–162, doi: [10.1023/A:1004256910362](https://doi.org/10.1023/A:1004256910362).
- Dziak R. P., and C. G. Fox (1999). The January 1998 earthquake swarm at axial volcano, Juan de Fuca Ridge: hydroacoustic evidence of a seafloor volcanic activity, *Geophys. Res. Lett.* **26**, 3429–3432, doi: [10.1029/1999GL002332](https://doi.org/10.1029/1999GL002332).
- Dziak, R. P., D. K. Smith, D. R. Bohnenstiehl, C. G. Fox, D. Desbruyeres, H. Matsumoto, M. Tolstoy, and D. J. Fornari (2004). Evidence of a recent magma dike intrusion at the slow spreading Lucky Strike segment, Mid-Atlantic Ridge, *J. Geophys. Res.* **109**, B12102, doi: [10.1029/2004JB003141](https://doi.org/10.1029/2004JB003141).
- Dziak, R. P., D. R. Bohnenstiehl, and D. K. Smith (2012). Hydroacoustic monitoring of oceanic spreading centers: Past, present, and future, *Oceanography* **25**, 116–127, doi: [10.5670/oceanog.2012.10](https://doi.org/10.5670/oceanog.2012.10).
- Dziak, R. P., D. R. Bohnenstiehl, E. T. Baker, H. Matsumoto, J. Caplan-Auerbach, R. W. Embley, S. G. Merle, S. L. Walker, T.-K. Lau, and W. W. Chadwick Jr. (2015). Long-term explosive degassing and debris flow activity at West Mata submarine volcano, *Geophys. Res. Lett.* **42**, 1480–1487, doi: [10.1002/2014GL062603](https://doi.org/10.1002/2014GL062603).
- Edwards, M. H., G. J. Kurras, M. Tolstoy, D. R. Bohnenstiehl, B. J. Coackley, and J. R. Cochran (2001). Evidence of recent volcanic activity on the ultraslow-spreading Gakkel Ridge, *Nature* **409**, 808–812, doi: [10.1038/35057258](https://doi.org/10.1038/35057258).
- Eksr  m, G., M. Nettles, and A. M. Dziewonski (2012). The global CMT project 2004–2010: Centroid-moment tensors for 13,017 earthquakes, *Phys. Earth Planet. Inter.* **200–201**, 1–9, doi: [10.1016/j.pepi.2012.04.002](https://doi.org/10.1016/j.pepi.2012.04.002).
- Farrell, W. E. (1972). Deformation of the Earth by Surface Loads, *Rev. Geophys. Space Phys.* **10**, 761–797, doi: [10.1029/RG010i003p00761](https://doi.org/10.1029/RG010i003p00761).
- Forsyth, D. W., R. L. Ehrenbard, and S. Chapin (1987). Anomalous upper mantle beneath the Australian-Antarctic discordance, *Earth Planet. Sci. Lett.* **84**, 471–478, doi: [10.1016/0012-821X\(87\)90011-2](https://doi.org/10.1016/0012-821X(87)90011-2).
- Fox, C. G., R. P. Dziak, H. Matsumoto, and A. E. Schreiner (1994). Potential for monitoring low-level seismicity on the Juan-de-Fuca ridge using military hydrophone arrays, *Mar. Technol. Soc. J.* **27**, 22–30.
- Fox, C., and V. A. Squire (1994). On the oblique reflexion and transmission of ocean waves at shore fast sea ice, *Phil. Trans. R. Soc. Lond. A* **347**, 185–218, doi: [10.1098/rsta.1994.0044](https://doi.org/10.1098/rsta.1994.0044).
- Fox, C. G., W. E. Radford, R. P. Dziak, T. K. Lau, H. Matsumoto, and A. E. Schreiner (1995). Acoustic detection of a seafloor spreading episode on the Juan de Fuca Ridge using military hydrophone arrays, *Geophys. Res. Lett.* **22**, 131–134, doi: [10.1029/94GL02059](https://doi.org/10.1029/94GL02059).
- Fox, C. G., H. Matsumoto, and T. K. A. Lau (2001). Monitoring Pacific Ocean seismicity from an autonomous hydrophone array, *J. Geophys. Res.* **106**, 4183–4206, doi: [10.1029/2000JB900404](https://doi.org/10.1029/2000JB900404).
- Gibbons, S. J. (2022). The Hydroacoustic Network of the CTBT International Monitoring System: Access and Exploitation, *Journal for Peace and Nuclear Disarmament*, 1–17, doi: [10.1080/25751654.2022.2129948](https://doi.org/10.1080/25751654.2022.2129948).
- Giusti, M., J. Perrot, R. P. Dziak, A. Sukhovich, and M. Maia (2018). The August 2010 earthquake swarm at North FAMOUS–FAMOUS segments, Mid-Atlantic Ridge: Geophysical evidence of dike intrusion, *Geophys. J. Int.* **215**, 181–195, doi: [10.1093/gji/ggy239](https://doi.org/10.1093/gji/ggy239).
- Green, D. N., L. G. Evers, D. Fee, R. S. Matoza, M. Snellen, P. Smets, and D. Simons (2013). Hydroacoustic, infrasonic and seismic monitoring of the submarine eruptive activity and sub-aerial plume generation at South Sarigan, May 2010, *J. Volcanol. Geotherm. Res.* **257**, 31–43, doi: [10.1016/j.jvolgeores.2013.03.006](https://doi.org/10.1016/j.jvolgeores.2013.03.006).
- Grevenmeyer, I., N. W. Hayman, D. Lange, C. Peirce, C. Papenberg, H. J. A. Van Avendonk, F. Schmid, L. G. de La Pe  a, and A. Dannowski (2019). Constraining the maximum depth of brittle deformation at slow- and ultraslow-spreading ridges using microseismicity, *Geology* **47** (11), 1069–1073, doi: [10.1130/G46577.1](https://doi.org/10.1130/G46577.1).
- Gutenberg, B., and C. F. Richter (1954). *Seismicity of the Earth and Associated Phenomena*, Princeton University Press: Princeton, NJ, USA.
- Hainzl, S., A. Christophersen, D. Rhoades, and D. Harte (2016). Statistical estimation of the duration of aftershock sequences, *Geophys. J. Int.* **205**(2), 1180–1189, doi: [10.1093/gji/ggw075](https://doi.org/10.1093/gji/ggw075).
- Ingale V. V., S. Bazin, and J.-Y. Royer (2021). Hydroacoustic observations of two contrasted seismic swarms along the Southwest Indian Ridge in 2018, *Geosciences* **11**(6), 225, doi: [10.3390/geosciences11060225](https://doi.org/10.3390/geosciences11060225).
- ISC International Seismological Center, On-Line Bulletin (2022). Available online: (last accessed on 10 January 2022) <http://www.isc.ac.uk/iscbulletin/search/catalogue/>.
- Jamet, G., C. Guennou, L. Guillon, and J.-Y. Royer (2013). T-wave generation and propagation: a comparison between data and spectral element modeling, *J. Acoust. Soc. Am.* **134**, 3376–3385, doi: [10.1121/1.4818902](https://doi.org/10.1121/1.4818902).
- Jensen, F. B., W. A. Kuperman, M. B. Porter, and H. Schmidt (1994). *Computational Ocean Acoustic*, American Institute of Physics, New York, 14–15.
- Kisslinger, C., and L. M. Jones (1991). Properties of aftershock sequences in Southern California, *J. Geophys. Res.* **96**, 11947–11958, doi: [10.1029/91JB01200](https://doi.org/10.1029/91JB01200).
- Klein, F. W., T. Wright, and J. Nakata (2006). Aftershock decay, productivity, and stress rates in Hawaii: indicators of temperature and stress from magma sources, *J. geophys. Res.* **111**(B7), B07307, doi: [10.1029/2005JB003949](https://doi.org/10.1029/2005JB003949).
- Korger, E. I. M., and V. Schlindwein (2012). Performance of localization algorithms for teleseismic mid-ocean ridge earthquakes: The 1999 Gakkel Ridge earthquake swarm and its

- geological interpretation, *Geophys. J. Int.* **188**, 613–625, doi: [10.1111/j.1365-246X.2011.05282.x](https://doi.org/10.1111/j.1365-246X.2011.05282.x).
- Läderach, C., E. I. M. Korger, V. Schlindwein, C. Müller, and A. Eskstaller (2012). Characteristics of tectonomagmatic earthquake swarms at the Southwest Indian Ridge between 16°E and 25°E, *Geophys. J. Int.* **190**, 429–441, doi: [10.1111/j.1365-246X.2012.05480.x](https://doi.org/10.1111/j.1365-246X.2012.05480.x).
- Le Saout, M., D. R. Bohnenstiehl, J. B. Paduan, and D. A. Clague (2020). Quantification of eruption dynamics on the north rift at Axial Seamount, Juan de Fuca Ridge, *Geochem. Geophys. Geosyst.* **21**(9), e2020GC009136, doi: [10.1029/2020GC009136](https://doi.org/10.1029/2020GC009136).
- Leroy, E. C., F. Samaran, J. Bonnel, and J.-Y. Royer (2017). Identification of two potential whale calls in the southern Indian Ocean, and their geographic and seasonal occurrence, *J. Acoust. Soc. Am.* **142**, 1413, doi: [10.1121/1.5001056](https://doi.org/10.1121/1.5001056).
- Liu, Z., and W. R. Buck (2018). Magmatic controls on axial relief and faulting at mid-ocean ridges, *Earth Planet. Sci. Lett.* **491**, 226–237, doi: [10.1016/j.epsl.2018.03.045](https://doi.org/10.1016/j.epsl.2018.03.045).
- Matsumoto, K., T. Sato, T. Takanezawa, and M. Ooe (2001). GOTIC2: A Program for Computation of Oceanic Tidal Loading Effect, *J. Geod. Soc. Jpn.* **47** (1), 243–248, doi: [10.11366/sokuchi1954.47.243](https://doi.org/10.11366/sokuchi1954.47.243).
- McNutt, S.R. (1996). Seismic Monitoring and Eruption Forecasting of Volcanoes: A Review of the State-of-the-Art and Case Histories, *Monitoring and Mitigation of Volcano Hazards*. Springer, Berlin, Heidelberg and eds., R. Scarpa, and R. I. Tilling, doi: [10.1007/978-3-642-80087-0_3](https://doi.org/10.1007/978-3-642-80087-0_3).
- McGuire J. J., M. S. Boettcher, and T. H. Jordan (2005). Foreshock sequences and short-term earthquake predictability on East Pacific Rise transform faults, *Nature* **434**, 457–461, doi: [10.1038/nature03377](https://doi.org/10.1038/nature03377).
- Meade, B. (2007). Algorithms for the calculation of exact displacements, strains, and stresses for triangular dislocation elements in a uniform elastic half space, *Comp. Geosci.* **33**(8), 1064–1075, doi: [10.1016/j.cageo.2006.12.003](https://doi.org/10.1016/j.cageo.2006.12.003).
- Meier, M., and V. Schlindwein (2018). First in situ seismic record of spreading events at the ultraslow spreading Southwest Indian Ridge, *Geophys. Res. Lett.* **45**, 10360–10368, doi: [10.1029/2018GL079928](https://doi.org/10.1029/2018GL079928).
- Mendel, V., D. Sauter, L. Parson, and J. R. Vanney (1997). Segmentation and morphotectonic variations along a super slow-spreading center: The Southwest Indian Ridge (57°–70°E), *Mar. Geophys. Res.* **19**, 505–533, doi: [10.1023/A:1004232506333](https://doi.org/10.1023/A:1004232506333).
- Mendel, V., D. Sauter, C. Rommevaux-Jestin, P. Patriat, F. Lefebvre, and L. M. Parson (2003). Magmato-tectonic cyclicity at the ultra-slow spreading Southwest Indian Ridge: Evidence from variations of axial volcanic ridge morphology and abyssal hills pattern, *Geochem. Geophys. Geosyst.* **4**, 9102, doi: [10.1029/2002GC000417](https://doi.org/10.1029/2002GC000417).
- Mogi, K. (1967). Earthquakes and fractures, *Tectonophysics* **5**, 35–55, doi: [10.1016/0040-1951\(67\)90043-1](https://doi.org/10.1016/0040-1951(67)90043-1).
- Müller, C., and W. Jokat (2000). Seismic evidence for volcanic activity discovered in Central Arctic, *Eos Trans. AGU* **81**, 265–269, doi: [10.1029/00E000186](https://doi.org/10.1029/00E000186).
- Okal, E.A. (2001). T-phase Stations for the International Monitoring System of the Comprehensive Nuclear-Test Ban Treaty: A Global Perspective, *Seismol. Res. Lett.* **72**(2), 186–196, doi: [10.1785/gssrl.72.2.186](https://doi.org/10.1785/gssrl.72.2.186).
- Olive, J.-A., M. D. Behn, E. Mittelstaedt, G. Ito, and B. Z. Klein (2016). The role of elasticity in simulating long-term tectonic extension, *Geophys. J. Int.* **205**, 2, 728–743, doi: [10.1093/gji/ggw044](https://doi.org/10.1093/gji/ggw044).
- Olive, J.-A., and J. Escartín (2016). Dependence of seismic coupling on normal fault style along the Northern Mid-Atlantic Ridge, *Geochem. Geophys. Geosyst.* **17**, 4128–4152, doi: [10.1002/2016GC006460](https://doi.org/10.1002/2016GC006460).
- Olive, J.-A., and P. Dublanquet (2020). Controls on the magmatic fraction of extension at mid-ocean ridges, *Earth Planet. Sci. Lett.* **549**, 116541, doi: [10.1016/j.epsl.2020.116541](https://doi.org/10.1016/j.epsl.2020.116541).
- Orsi, A. H., Whitworth III, T., & Nowlin Jr, W. D. (1995). On the meridional extent and fronts of the Antarctic Circumpolar Current, *Deep Sea Research Part I: Oceanographic Research Papers* **42** (5), 641–673, doi: [10.1016/0967-0637\(95\)00021-W](https://doi.org/10.1016/0967-0637(95)00021-W).
- Pan, J., and A. M. Dziewonski (2005). Comparison of mid-oceanic earthquake epicentral differences of travel time, centroid locations, and those determined by autonomous underwater hydrophone arrays, *J. Geophys. Res.* **110**, B07302, doi: [10.1029/2003JB002785](https://doi.org/10.1029/2003JB002785).
- Park, M., R. I. Odom, D. J. Soukup (2001). Modal scattering: a key to understanding oceanic T-waves, *Geophys. Res. Lett.* **28** (17), 3401–3404, doi: [10.1029/2001GL013472](https://doi.org/10.1029/2001GL013472).
- Parnell-Turner, R., D. K. Smith, and R. P. Dziak (2022). Hydroacoustic monitoring of seafloor spreading and transform faulting in the equatorial Atlantic Ocean, *J. Geophys. Res. Solid Earth* **127**, e2022JB024008, doi: [10.1029/2022JB024008](https://doi.org/10.1029/2022JB024008).
- Parson, L., D. Sauter, V. Mendel, P. Patriat, and R. Searle (1997). Evolution of the Axial Geometry of the Southwest Indian Ocean Ridge between the Melville Fracture Zone and the Indian Ocean Triple Junction – Implications for Segmentation on Very Slow-Spreading Ridges, *Marine Geophysical Researches* **19**, 535–552, doi: [10.1023/A:1004335919592](https://doi.org/10.1023/A:1004335919592).
- Patriat, P., and J. Ségoufin (1988). Reconstruction of the central Indian Ocean, *Tectonophysics* **155**, 211–234, doi: [10.1016/0040-1951\(88\)90267-3](https://doi.org/10.1016/0040-1951(88)90267-3).
- Patriat, P., D. Sauter, M. Munsch, and L. M. Parson (1997). A survey of the Southwest Indian Ridge axis between Atlantis II Fracture Zone and the Indian Triple Junction: Regional setting and large scale segmentation, *Mar. Geophys. Res.* **19**, 457–480, doi: [10.1023/A:1004312623534](https://doi.org/10.1023/A:1004312623534).
- Raumer P.-Y., S. Bazin, D. Cazau, J.-Y. Royer, V. V. Ingale, and A. Lavayssiere (2023). Application of machine learning to hydro-acoustic seismic and magmatic events detections, EGU General Assembly 2023, Vienna, Austria, doi: [10.5194/egusphere-egu23-7028](https://doi.org/10.5194/egusphere-egu23-7028).
- Rintoul, S. R., C. Hughes, and D. Olbers (2001). The Antractic Circumpolar Current System, *Ocean Circulation and Climate*. New York: Academic Press, eds. G. Siedler, J. Church, and J. Gould, hdl: [10013/epic.13233](https://hdl.handle.net/10013/epic.13233), ISBN: 0-12-641351-7.
- Rivalta, E., B. Taisne, A. P. Bungler, and R. F. Katz (2015). A review of mechanical models of dike propagation: Schools of thought, results and future directions, *Tectonophysics* **638**, 1–42, doi: [10.1016/j.tecto.2014.10.003](https://doi.org/10.1016/j.tecto.2014.10.003).
- Rommevaux-Jestin, C., C. Deplus, and P. Patriat (1997). Mantle Bouguer Anomaly Along an Ultra Slow-Spreading Ridge: Implications for Accretionary Processes and Comparison with Results from Central Mid-Atlantic Ridge, *Mar. Geophys. Res.* **19**, 481–503, doi: [10.1023/A:1004269003009](https://doi.org/10.1023/A:1004269003009).
- Royer, J.-Y., P. Patriat, H. W. Bergh, and C. R. Scotese (1988). Evolution of the Southwest Indian Ridge from the Late Cretaceous (anomaly 34) to the Middle Eocene (anomaly 20), *Tectonophysics* **155**, 235–260, doi: [10.1016/0040-1951\(88\)90268-5](https://doi.org/10.1016/0040-1951(88)90268-5).
- Royer, J.-Y., J. G. Sclater, and D. T. Sandwell (1989). A preliminary tectonic fabric chart of the Indian Ocean, *Proc. Indian Acad. Sci. Earth Planet. Sci.* **98**, 7–24, doi: [10.1007/BF02880373](https://doi.org/10.1007/BF02880373).
- Royer, J.-Y. (2009). OHA-SIS-BIO: Hydroacoustic Observatory of the Seismicity and Biodiversity in the Indian Ocean, Available online: <https://campagnes.flotteoceanographique.fr/> (accessed on 10 January 2022).
- Royer, J.-Y., R. Chateau, R. P. Dziak, and D. R. Bohnenstiehl (2015). Seafloor seismicity, Antarctic ice-sounds, cetacean vocalizations and long-term ambient sound in the Indian Ocean basin, *Geophys. J. Int.* **202**, 748–762, doi: [10.1093/gji/ggv178](https://doi.org/10.1093/gji/ggv178).
- Rubin, A. M. (1992). Dike-induced faulting and graben subsidence in volcanic rift zones, *J. geophys. Res.* **97**, 1839–1858, doi: [10.1029/91JB02170](https://doi.org/10.1029/91JB02170).
- Rubin, A. M., and D. Gillard (1998). Dike-induced earthquakes: Theoretical considerations, *J. Geophys. Res.* **103**(B5), 10,017–10,030, doi: [10.1029/97JB03514](https://doi.org/10.1029/97JB03514).

- Rundquist, D. V., and P. O. Sobolev (2002). Seismicity of mid-oceanic ridges and its geodynamic implications: A review, *Earth Sci. Rev.* **58**, 143–161, doi: [10.1016/S0012-8252\(01\)00086-1](https://doi.org/10.1016/S0012-8252(01)00086-1).
- Sahoo, S., B. Senapati, D. Panda, D. K. Tiwari, M. Santosh, B. Kundu (2021). Tidal triggering of micro-seismicity associated with caldera dynamics in the Juan de Fuca ridge, *J. Volcanol. Geotherm. Res.* **417**, 107319, doi: [10.1016/j.jvolgeores.2021.107319](https://doi.org/10.1016/j.jvolgeores.2021.107319).
- Samaran, F., K. M. Stafford, T. A. Branch, J. Gedamke, J.-Y. Royer, R. P. Dziak, and C. Guinet (2013). Seasonal and geographic variation of southern blue whale subspecies in the Indian Ocean, *PLoS ONE* **8**, e71561, doi: [10.1371/journal.pone.0071561](https://doi.org/10.1371/journal.pone.0071561).
- Saurel, J.-M., L. Retailleau, C. Deplus, B. Loubrieu, D. Pierre, M. Frangieh, N. Khelifi, R. Bonnet, V. Ferrazzini, S. Bazin, P. Guyavarch, M. Moulin, REVOSIMA Seismology group, REVOSIMA Bathymetry group (2022). Combining hydro-acoustic sources and bathymetric differences to track the vent evolution of the Mayotte eruption, Mozambique Channel, *Front. Earth Sci.* **10**:983051, doi:[10.3389/feart.2022.983051](https://doi.org/10.3389/feart.2022.983051).
- Sauter, D., V. Mendel, C. Rommevaux-Jestin, L. M. Parson, H. Fujimoto, C. Mével, M. Cannat, and K. Tamaki (2004). Focused magmatism versus amagmatic spreading along the ultra-slow spreading Southwest Indian Ridge: Evidence from TOBI side scan sonar imagery, *Geochem. Geophys. Geosyst.* **5** (Q10K09), doi: [10.1029/2004GC000738](https://doi.org/10.1029/2004GC000738).
- Sauter, D., and M. Cannat (2010). The ultraslow spreading Southwest Indian ridge, In *Diversity of Hydrothermal Systems on Slow Spreading Ocean Ridges*; Geophysical Monograph Series; The American Geophysical Union: Washington, DC, USA **188**, 153–173, doi: [10.1029/2008GM000843](https://doi.org/10.1029/2008GM000843).
- Schlindwein, V. (2012). Teleseismic earthquake swarms at ultraslow spreading ridges: indicator for dyke intrusions?, *Geophys. J. Int.* **190**(1), 442–456, doi: [10.1111/j.1365-246X.2012.05502.x](https://doi.org/10.1111/j.1365-246X.2012.05502.x).
- Schlindwein, V. and C. Riedel (2010). Location and source mechanism of sound signals at Gakkel ridge, Arctic Ocean: Submarine Strombolian activity in the 1999–2001 volcanic episode, *Geochem. Geophys. Geosyst.* **11**(1), doi: [10.1029/2009GC002706](https://doi.org/10.1029/2009GC002706).
- Schlindwein, V., A. Demuth, E. Korger, C. Läderach, and F. Schmid (2015). Seismicity of the Arctic mid-ocean ridge system, *Polar Sci.* **9**, 146–157, doi: [10.1016/j.polar.2014.10.001](https://doi.org/10.1016/j.polar.2014.10.001).
- Schlindwein, V., and F. Schmid (2016). Mid-ocean-ridge seismicity reveals extreme types of ocean lithosphere, *Nature* **535**, 276–279, doi: [10.1038/nature18277](https://doi.org/10.1038/nature18277).
- Schmid, A., and J. R. Grasso (2012). Omori law for eruption foreshocks and aftershocks, *J. Geophys. Res. Solid Earth* **117**(B7), doi: [10.1029/2011JB008975](https://doi.org/10.1029/2011JB008975).
- Schmid, F., V. Schlindwein, I. Koulakov, A. Plötz, and J. R. Scholz (2017). Magma plumbing system and seismicity of an active mid-ocean ridge volcano, *Sci. Rep.* **7**, 42949, doi: [10.1038/srep42949](https://doi.org/10.1038/srep42949).
- Schreiner, A.E., C. G. Fox, and R. P. Dziak (1995). Spectra and magnitudes of T-waves from the 1993 earthquake swarm on the Juan de Fuca Ridge, *Geophys. Res. Lett.* **22**, 139–142, doi: [10.1029/94GL01912](https://doi.org/10.1029/94GL01912).
- Scholz, C. H., Y. J. Tan, and F. Albino (2019). The mechanism of tidal triggering of earthquakes at mid-ocean ridges, *Nat Commun.* **10**, 2526, doi: [10.1038/s41467-019-10605-2](https://doi.org/10.1038/s41467-019-10605-2).
- Shuler, A., and M. Nettles (2012). Earthquake source parameters for the 2010 western Gulf of Aden rifting episode, *Geophys. J. Int.* **190**, 111–1122, doi: [10.1111/j.1365-246X.2012.05529.x](https://doi.org/10.1111/j.1365-246X.2012.05529.x).
- Slack, P. D., C. G. Fox, and R. P. Dziak (1999). P wave detection thresholds, Pn velocity estimates, and T wave location uncertainty from oceanic hydrophones, *J. Geophys. Res.* **104**, 13061–13072, doi: [10.1029/1999JB900112](https://doi.org/10.1029/1999JB900112).
- Smith D. K., M. Tolstoy, C. G., Fox, D. R. Bohnenstiehl, H. Matsumoto, M. J. Fowler (2002). Hydroacoustic monitoring of seismicity at the slow-spreading Mid-Atlantic Ridge, *Geophys. Res. Lett.* **29** (11), doi: [10.1029/2001GL013912](https://doi.org/10.1029/2001GL013912).
- Smith, D. K., J. Escartin, M. Cannat, M. Tolstoy, C. G. Fox, D. R. Bohnenstiehl and S. Bazin (2003). Spatial and temporal distribution of seismicity along the northern Mid-Atlantic Ridge (15°–35°N), *J. Geophys. Res.* **108**, 2167, doi: [10.1029/2002JB001964](https://doi.org/10.1029/2002JB001964).
- Sohn, R. A., J. A. Hildebrand, and S. C. Webb (1998). Postrifting seismicity and a model for the 1993 diking event on the CoAxial segment, Juan de Fuca Ridge, *J. Geophys. Res.* **103**, 9867–9877, doi: [10.1029/98JB00391](https://doi.org/10.1029/98JB00391).
- Standish, J. J., K. W. Sims (2010). Young off-axis volcanism along the ultraslow-spreading Southwest Indian Ridge, *Nat. Geosci.* **3**, 286–292, doi: [10.1038/ngeo824](https://doi.org/10.1038/ngeo824).
- Sykes, L. R. (1970). Earthquake swarms and sea-floor spreading, *J. Geophys. Res.* **75** (32), 6598–6611, doi: [10.1029/JB075i032p06598](https://doi.org/10.1029/JB075i032p06598).
- Tan, Y. J., M. Tolstoy, F. Waldhauser, and W. Wilcock (2016). Dynamics of a seafloor-spreading episode at the east pacific rise, *Nature* **540**, 261–265, doi: [10.1038/nature20116](https://doi.org/10.1038/nature20116).
- Teague, W. J., M. J. Carron, and J. P. Hogan (1990). A comparison between the Generalized Digital Environment Model and Levitus climatologies, *J. Geophys. Res.* **95**, 7167–7183, doi: [10.1029/JC095iC05p07167](https://doi.org/10.1029/JC095iC05p07167).
- Tepp, G., and R. P. Dziak (2021). The seismo-acoustics of submarine volcanic eruptions, *J. Geophys. Res. Solid Earth* **126**, e2020JB020912, doi: [10.1029/2020JB020912](https://doi.org/10.1029/2020JB020912).
- Tepp, G., R. P. Dziak, M. M. Haney, J. J. Lyons, C. Searcy, H. Matsumoto, and J. Haxel (2020). Seismic and hydroacoustic observations of the 2016–17 Bogoslof eruption, *Bull. Volcanol.* **82**, 4, doi: [10.1007/s00445-019-1344-3](https://doi.org/10.1007/s00445-019-1344-3).
- Toda, S., R. S. Stein, and T. Sagiya (2002). Evidence from the AD 2000 Izu islands earthquake swarm that stressing rate governs seismicity, *Nature* **419**, 58–61, doi: [10.1038/nature00997](https://doi.org/10.1038/nature00997).
- Tolstoy, I., and M. Ewing (1950). The T phase of shallow-focus earthquakes, *Bull. Seism. Soc. Am.* **40**, 25–51, doi: [10.1785/BSSA0400010025](https://doi.org/10.1785/BSSA0400010025).
- Tolstoy, M., D. R. Bohnenstiehl, M. H. Edwards, and G. J. Kurras (2001). Seismic character of volcanic activity at the ultraslow-spreading Gakkel Ridge, *Geology* **29**, 1139–1142, doi: [10.1130/0091-7613\(2001\)029<1139:SCOVAA>2.0.CO;2](https://doi.org/10.1130/0091-7613(2001)029<1139:SCOVAA>2.0.CO;2).
- Tolstoy, M., F. L. Vernon, O. A. John, and W. K. (2002). Breathing of the seafloor: Tidal correlations of seismicity at Axial volcano, *Geology* **30** (6), 503–506. doi: [10.1130/0091-7613\(2002\)030<0503:BOTSTC>2.0.CO;2](https://doi.org/10.1130/0091-7613(2002)030<0503:BOTSTC>2.0.CO;2).
- Tolstoy, M., and D. R. Bohnenstiehl (2006). Hydroacoustic contributions to understanding the December 26th 2004 great Sumatra-Andaman Earthquake, *Surv. Geophys.* **27**, 633–646, doi: [10.1007/s10712-006-9003-6](https://doi.org/10.1007/s10712-006-9003-6).
- Tolstoy, M., F. Waldhauser, D. R. Bohnenstiehl, R. T. Weekly, and W.-Y. Kim (2008). Seismic identification of along-axis hydrothermal flow on the East Pacific Rise, *Nature* **451**, 181–184, doi: [10.1038/nature06424](https://doi.org/10.1038/nature06424).
- Toomey, D. R., S. C. Solomon, G. M. Purdy, and M. H. Murray (1985). Microearthquakes beneath the median valley of the Mid-Atlantic Ridge near 23°N: Hypocenters and focal mechanisms, *J. Geophys. Res.* **90**, 5443–5458, doi: [10.1029/JB090iB07p05443](https://doi.org/10.1029/JB090iB07p05443).
- Torterotot, M., F. Samaran, K. M. Stafford, and J.-Y. Royer (2020). Distribution of blue whale populations in the Southern Indian Ocean based on a decade of acoustic monitoring, *Deep Sea Res. Part II: Top. Stud. Oceanogr.* **179**, 104874, doi: [10.1016/j.dsr2.2020.104874](https://doi.org/10.1016/j.dsr2.2020.104874).
- Tsang-Hin-Sun, E., J.-Y. Royer, and J. Perrot (2016). Seismicity and active accretion processes at the ultraslow-spreading Southwest and intermediate-spreading Southeast Indian ridges from hydroacoustic data, *Geophys. J. Int.* **206**, 1232–1245, doi: [10.1093/gji/ggw201](https://doi.org/10.1093/gji/ggw201).

- Utsu, T., Y. Ogata, and R. S. Matsuura (1995). The centenary of the Omori formula for a decay law of aftershock activity, *J. Phys. Earth* **1995**, 43, 1–33, doi: [10.4294/jpe1952.43.1](https://doi.org/10.4294/jpe1952.43.1).
- Utsu, T. (1999). Representation and analysis of the earthquake size distribution: A historical review and some new approaches, *Pure Appl. Geophys.* **155**(2–4), 509–535, doi: [10.1007/s000240050276](https://doi.org/10.1007/s000240050276).
- Wessel, P., and W. H. Smith (1998). New, improved version of Generic Mapping Tools released, *Eos Trans. Am. Geophys. Union* **79**, 579, doi: [10.1029/98E000426](https://doi.org/10.1029/98E000426).
- Weston, D. E., and P. B. Rowlands (1979). Guided acoustic waves in the ocean, *Rep. Prog. Phys.* **42**, 347, doi: [10.1088/0034-4885/42/2/003/meta](https://doi.org/10.1088/0034-4885/42/2/003/meta).
- Wiens, D. A., and D. E. Petrov (1990). The largest recorded earthquake swarm: Intraplate faulting near the Southwest Indian Ridge, *J. Geophys. Res.* **95**, 4735–4750, doi: [10.1029/JB095iB04p04735](https://doi.org/10.1029/JB095iB04p04735).
- Wilcock, W. S. (2001). Tidal triggering of microearthquakes on the Juan de Fuca Ridge, *Geophys. Res. Lett.* **28**(20), 3999–4002, doi: [10.1029/2001GL013370](https://doi.org/10.1029/2001GL013370).
- Wilcock, W. S. (2009). Tidal triggering of earthquakes in the Northeast Pacific Ocean, *Geophys. J. Int.* **179**(2), 1, doi: [10.1111/j.1365-246X.2009.04319.x](https://doi.org/10.1111/j.1365-246X.2009.04319.x).
- Williams, C. M., R. A. Stephen, and D. K. Smith (2006). Hydroacoustic events located at the intersection of the Atlantis (30°N) and Kane (23°40'N) Transform Faults with the Mid-Atlantic Ridge, *Geochem. Geophys. Geosyst.* **7**, Q06015, doi: [10.1029/2005GC001127](https://doi.org/10.1029/2005GC001127).
- Wolfe, C. J., G. M. Purdy, D. R. Toomey, and S. C. Solomon (1995). Microearthquake characteristics and crustal velocity structure at 29°N on the Mid-Atlantic Ridge: The architecture of a slow spreading segment, *J. Geophys. Res.* **100**, 24449–24472, doi: [10.1029/95JB02399](https://doi.org/10.1029/95JB02399).
- Yang, Y., and D. W. Forsyth (2003). Improving epicentral and magnitude estimation of earthquakes from T phases by considering the excitation function, *Bull. Seismo. Soc. Am.* **93**(5), 2106–2122, doi: [10.1785/0120020215](https://doi.org/10.1785/0120020215).
- Yu, Z., J. Li, X. Niu, N. Rawlinson, A. Ruan, W. Wang, H. Hu, X. Wei, J. Zhang, and Y. Liang (2018). Lithospheric structure and tectonic processes constrained by microearthquake activity at the central ultraslow-spreading Southwest Indian Ridge (49.2° to 50.8°E), *J. Geophys. Res. Solid Earth* **123**, 6247–6262, doi: [10.1029/2017JB015367](https://doi.org/10.1029/2017JB015367).

Figures:

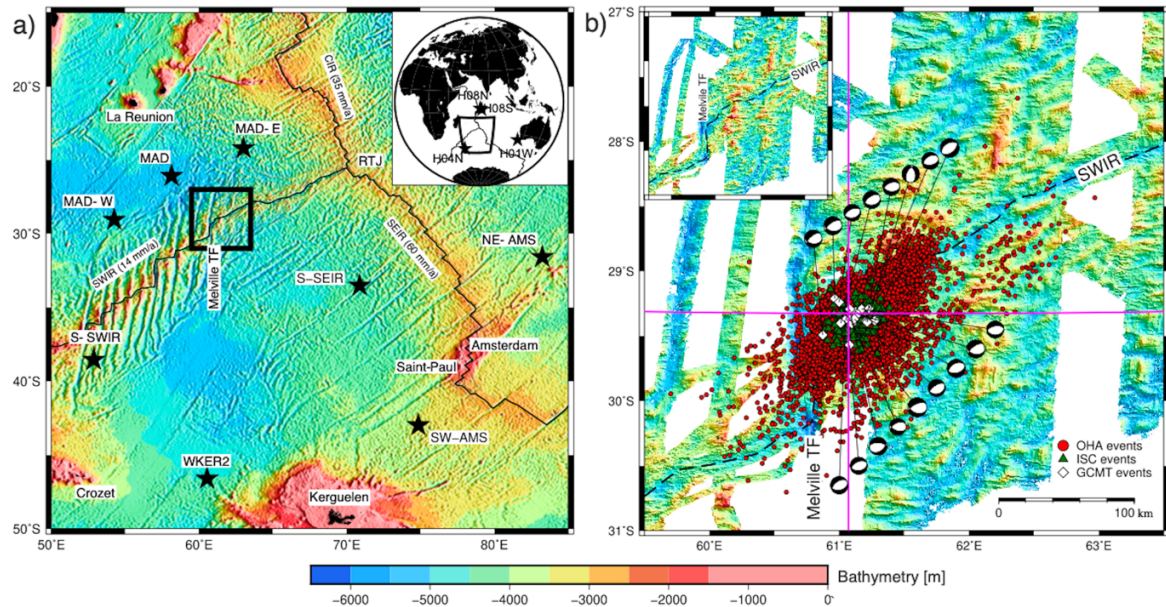


Figure 1: (a) Hydroacoustic Observatory of Seismicity and Biodiversity in the Indian Ocean (OHASISBIO) and International Monitoring System (IMS)– Comprehensive Nuclear-Test-Ban Treaty Organization (CTBTO; inset) net-works of underwater hydrophones (stars). The black lines outline the Southwest Indian ridge (SWIR), Central Indian Ridge (CIR), and Southeast Indian Ridge (SEIR) with their respective spreading rates. (b) The black rectangle shows the study area with the hydroacoustic events detected by the hydrophones (circles) and by the International Seismological Centre (ISC; triangles) and Global Centroid Moment Tensor (Global CMT; diamonds with focal mechanisms) land-based networks. The cross is the median location of all detected events (referred to RP for reference point in the “Results” section). The inset shows the same bathymetric map without events.

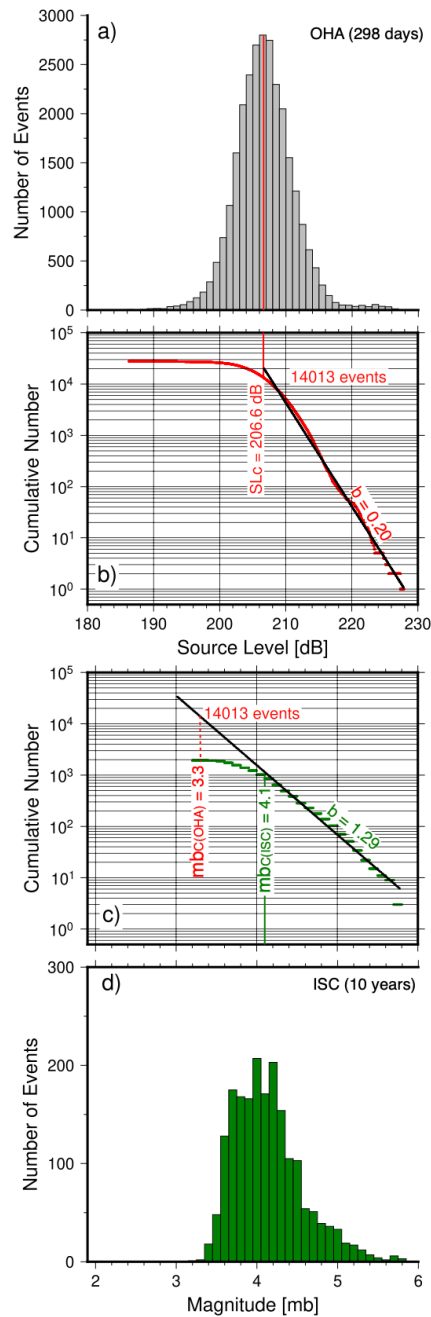


Figure 2: Completeness of source level (SL) and m_b based on best-fitting Gutenberg–Richter’s laws. (a) Histogram of the hydroacoustic (OHA) catalog from June 2016 to March 2017 (298 days). (b) Cumulative number of events in the OHA catalog. The vertical line points to the completeness, SL_C 206:6 dB with a b -value of 0.20 in the SL framework. (c) Cumulative number of events in the International Seismological Centre (ISC) catalog along the Southwest Indian Ridge (SWIR) axis reported from 2010 to 2020. The vertical line points to the magnitude of completeness $mb_{C(ISC)} = 4.1$. Extrapolating the Gutenberg–Richter’s law of this ISC catalog up to the number of events for which the OHA catalog is complete (14,013 events) yields to $mb_{C(OHA)} = 3.3$. (d) Magnitude histogram of the ISC events from 2010 to 2020 along the SWIR axis.

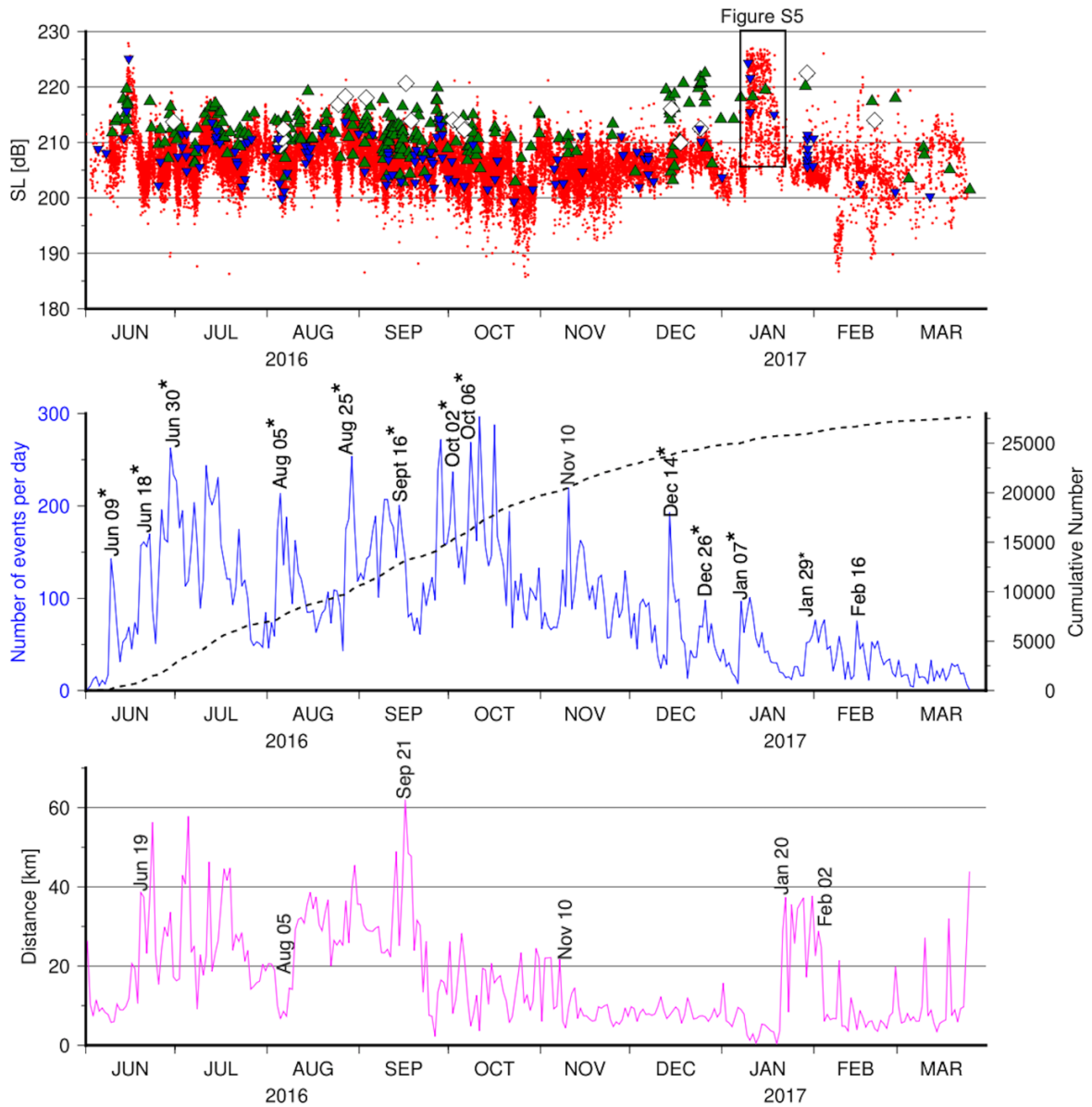


Figure 3: (a) Source level (SL) distribution of the OHA (dots), ISC (triangles), Global CMT (diamonds), and impulsive (inverted triangles) events between June 2016 and March 2017. Higher SLs between 9 and 20 January 2017 (black rectangle) are explained in Figure S5. (b) Number of events per day (solid line) and cumulative number of events versus time (dashed line). Dates mark the onset of higher seismicity between June 2016 and March 2017. Dates with asterisks point to the start of potential sequences tested against modified Omori's laws. (c) Median distance of events per day relative to a reference point (RP; marked by a cross in Fig. 1b). Dates mark significant changes in the distance of events from the RP.

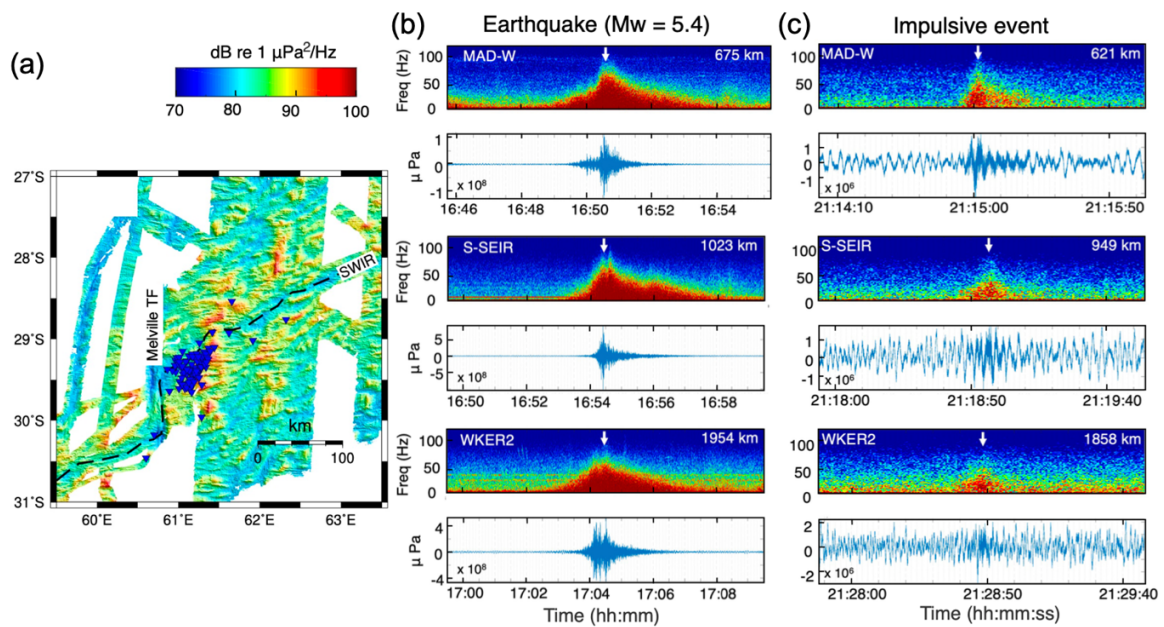


Figure 4: (a) Location of impulsive events (inverted triangles) on the slopes of bathymetric highs on the southern flank of the SWIR (dashed line) east of Melville TF. (b,c) Comparison of acoustic waveforms and spectrograms for a typical earthquake event (M_w 5.4) and for an impulsive event recorded at three sites of the OHASISBIO network (MAD-W, S-SEIR, WKER2, from top to bottom); distances in kilometers are from the earthquake location and from the cluster of impulsive events, respectively. Acoustic signals can last for ~ 200 s for an earthquake (T-wave) versus 10–15 s for an impulsive event (H-wave). The former stand out both in waveforms and spectrograms, whereas the latter mainly stand out in spectrograms. The white arrows point to the highest T-wave or H-wave energy arrivals.

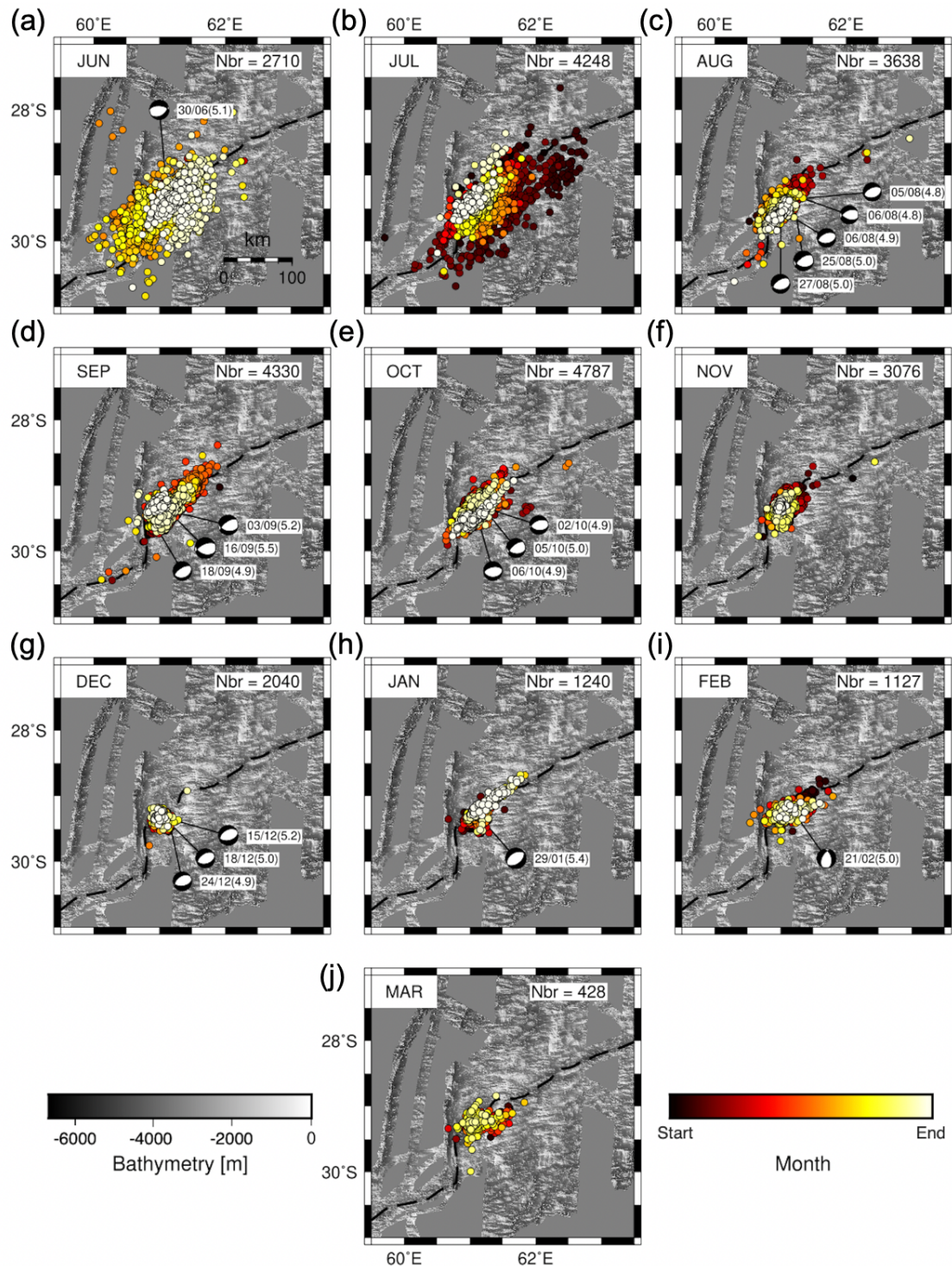


Figure 5: (a–j) Monthwise temporal distribution of events from June 2016 to March 2017, with the total number of events per month (Nbr). The dashed line shows the SWIR axis. The dark colors in the time scale denote the start of each month. Labels next to Global CMT focal mechanisms provide the date and magnitude (M_w). Note that all normal-fault planes in focal mechanisms are parallel to the SWIR axis except for the last one in February 2017 where they are parallel to the Melville transform fault (TF).

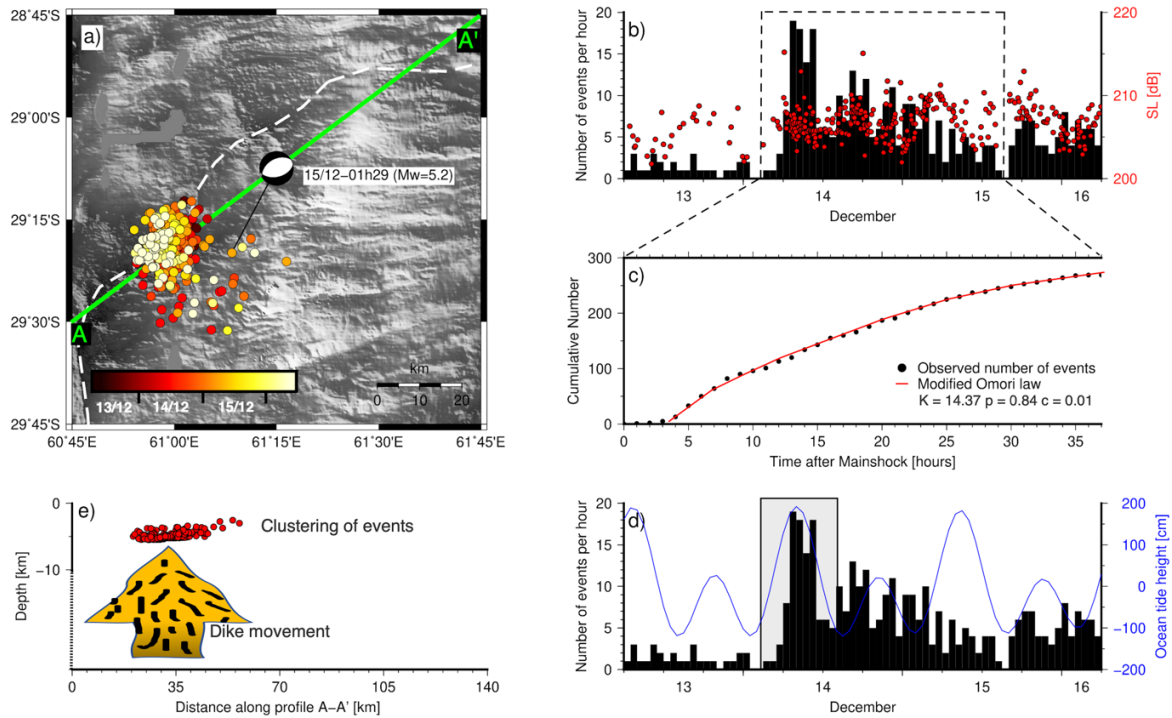


Figure 6: (a) Spatiotemporal distribution of the events between 13 December at 06:00 and 16 December at 06:00 (sequence 9), with the only Global CMT focal mechanism (15 December at 01:29, M_W 5.2) in this sequence, near its end. The dashed line shows the SWIR axis. (b) Temporal distribution of number of events per hour (histogram) with their SLs (circles). The dashed rectangle outlines the selection of events used to compute the modified Omori's law, shown in panel (c). (c) The black dots show the hourly cumulative number of events, and the solid curve shows the best-fitting modified Omori's law. (d) Temporal distribution of number of events per hour (histogram) versus ocean tide height (solid curve). This is the only sequence where high seismicity coincides with high tide (grayed area). (e) Projection of the cluster of T-wave radiating points (circles) at seafloor depth along A–A' profile (solid line in panel a). The broad vertical arrow schematizes upwelling dikes beneath the clustered events. The depth of the dikes is not constrained.

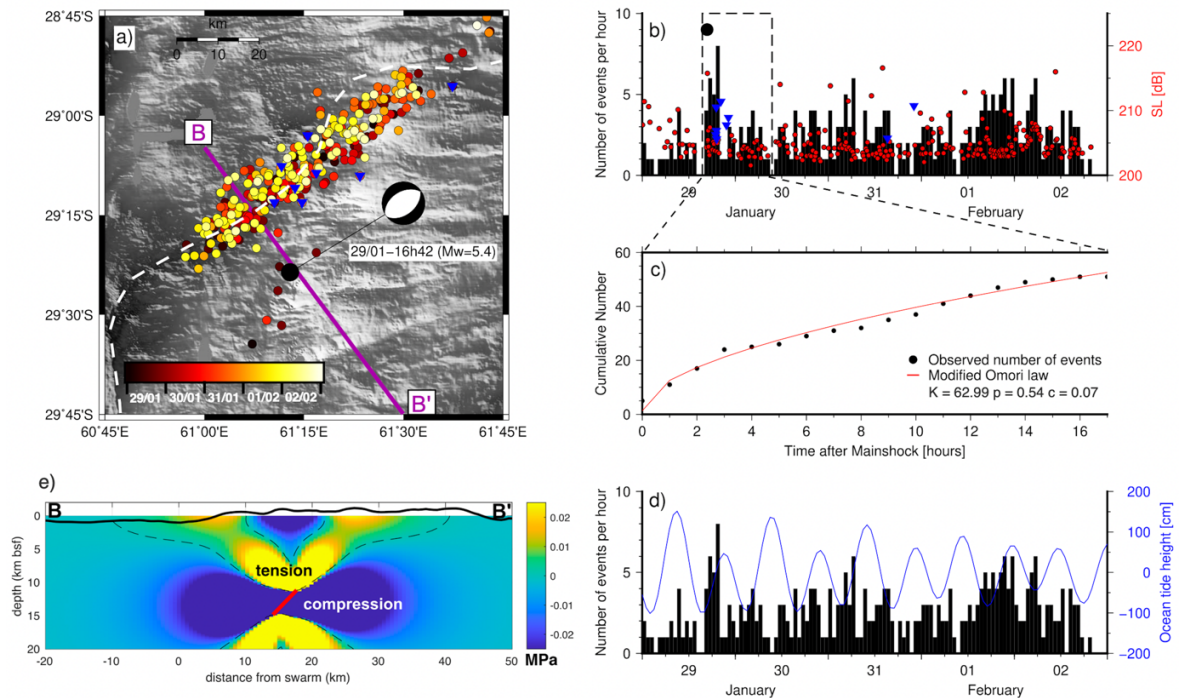


Figure 7: (a) Spatio-temporal distribution of the events between 29 January and 2 February 2017 (sequence 12) with the Global CMT focal mechanism of the strongest event that triggered the sequence on 29 January at 16:42 (M_W 5.4). The dashed line shows the SWIR axis. (b) Temporal distribution of number of events per hour (histogram) with their SLs (circles) and that of impulsive events (inverted triangles). The dashed rectangle outlines the selection of events used to compute the modified Omori's law, shown in panel (c). (c) The black dots show the hourly cumulative number of events and the solid curve shows the best-fitting modified Omori's law. (d) Temporal distribution of number of events per hour (histogram) versus ocean tide height (solid curve). (e) Schematic cross section (along B–B') showing a plausible geometry for the Global CMT fault plane (thick line), SE of the ridge axis. Contours show the predicted horizontal stress changes in MPa for an M_W 5.4 normal-slip event with a dip-slip of 18 cm over a 5.1×5.1 km square patch embedded in an elastic half-space with Young's modulus and Poisson's ratio 100 GPa and 0.25, respectively (Olive et al., 2016). The light colors indicate areas under tension, allowing for dike emplacements in the axial valley and/or local stress readjustments, at the origin of the observed alignment of events.

Table 1: Locations and acquisition parameters of the hydrophones of the OHASISBIO and CTBTO networks

Sites	MAD-W	MAD	MAD-E	S-SEIR	NE-AMS	SW-AMS3	WKER2	S-SWIR	H08S1	H01W1
Latitude [°S]	29.051	26.084	24.197	33.514	31.575	42.989	46.602	38.550	7.645	34.893
Longitude [°E]	54.260	58.140	63.010	70.867	83.241	74.850	60.547	52.879	72.474	114.154
Water depth [m]	1280	1260	1180	1210	2760	1160	980	1150	800	800
Sampling rate [Hz]	240	240	240	240	240	240	240	240	250	250
Sensitivity [dB]	-163.4	-163.7	-163.5	-163.5	-163.5	-168.6	-163.6	-163.3	-165.2	-165.2
Start Time	06/01/17	29/01/16	08/02/17	25/01/16	07/02/17	21/01/16	12/01/16	08/01/17	01/01/16	01/01/16
End Time	06/01/18	08/02/17	13/02/18	11/02/18	13/02/18	09/12/18	04/02/18	22/12/17	31/12/17	31/12/17
Clock drift [ppm]	-0.1004	-0.0393	-0.0466	-0.0021	-0.0466	-0.0162	-0.0080	-0.0205	N/A	N/A

Table 2: Summary of the number of events, tidal correlation, modified Omori's law parameters and interpretation of the 12 seismic sequences defined in Figure 3

Sr No	Dates	Duration (hours)	Nbr of OHA events	Impulsive events	ISC event *	GCMT event *	Tidal correlation	K #	c #	p-value #	Interpretation
1	09/06/16 - 10/06/16	26	136	0	N/A	N/A	NO	23.99	0.01	0.55	Magmatic swarm
2	18/06/16 - 24/06/16	144	786	0	N/A	N/A	NO	179.13	0.09	0.87	Magmatic swarm
3	30/06/16 - 02/07/16	60	515	1	<i>mb</i> = 5.2	<i>Mw</i> = 5.1	NO	14.47	0.09	0.88	Magmato-tectonic
4	05/08/16 - 06/08/16	30	230	2	<i>mb</i> = 4.7	<i>Mw</i> = 4.8	NO	198.95	0.01	0.86	Magmato-tectonic
5	25/08/16 - 26/08/16	46	130	0	<i>mb</i> = 4.5	<i>Mw</i> = 5.2	NO	90.95	0.07	0.58	Magmato-tectonic
6	16/09/16 - 19/09/16	55	201	0	<i>mb</i> = 5.5	<i>Mw</i> = 5.5	NO	9.91	0.01	0.74	Magmato-tectonic
7	02/10/16 - 04/10/16	55	357	1	<i>mb</i> = 4.8	<i>Mw</i> = 4.9	NO	8.16	0.07	0.95	Magmato-tectonic
8	06/10/16 - 07/10/16	24	86	0	<i>mb</i> = 4.7	<i>Mw</i> = 4.9	NO	10.99	0.05	0.66	Magmato-tectonic
9 [§]	14/12/16 - 16/12/16	37	269	0	N/A	N/A	YES	14.37	0.01	0.84	Magma upwelling
10	26/12/16 - 27/12/16	29	124	0	<i>mb</i> = 3.8	N/A	NO	18.34	0.09	0.57	Magmatic swarm
11	07/01/17 - 14/01/17	182	555	3	<i>mb</i> = 3.8	N/A	NO	91.06	0.09	0.91	Magmatic swarm
12 [§]	29/01/17 - 30/01/17	17	51	9	<i>mb</i> = 5.7	<i>Mw</i> = 5.4	NO	62.99	0.07	0.54	Extrusion after vertical dike

* N/A means there was no triggering event at the start of the sequence, otherwise its magnitude is given

Modified Omori's law parameters (equation 2)

§ Detailed description in Figures 6 and 7

Erratum to the BSSA article

I would like to report a small correction to the b -value calculated for the Gutenberg-Richter relation laws (p. 120 of the thesis).

The original text says that:

1. The equivalent magnitude of completeness for the OHA catalog $mb_{C(OHA)} = 3.3$ mb was estimated by extrapolating the frequency-size distribution with a b -value = **2.98** from the ISC events up to the number of events defining SL_C (Figure 2c).
2. The b -value = **2.98** for the ISC catalog means that there is likely a deficit of large events ($mb_{C(ISC)} > 4.1$) relative to small ones. This deficit suggests that a $b = 0.47$ slope for the SL is representative of a volcanic context.

The revised text is as follows:

1. The equivalent magnitude of completeness for the OHA catalog $mb_{C(OHA)} = 3.3$ mb was estimated by extrapolating the frequency-size distribution with a b -value = **1.29** from the ISC events up to the number of events defining SL_C (Figure 2c).
2. The b -value = **1.29** for the ISC catalog means that there is likely a deficit of large events ($mb_{C(ISC)} > 4.1$) relative to small ones. This deficit suggests that a $b = 0.20$ slope for the SL is representative of a volcanic context. Consequently, I have also modified the caption and label associated with the b -value in Figure 2. Previously, the b -value in the SL framework was 0.47, now modified to 0.20.

Reason: In the original text, b -values were calculated in the natural \log scale instead of \log_{10} scale, which is now corrected.

3.3 Summary of the observations of the SWIR swarms

Along the ultraslow-spreading (14 mm/yr) Southwest Indian Ridge, we analyzed hydroacoustic data for three distinct seismic swarms, near the Novara transform fault (TF), Melville TF, and segment 4 at 67°45'E. Out of them, the swarm near the Melville TF (in 2016-17) was the strongest seismic swarm detected in this study. The key observations from this chapter are:

1. The magnitude of completeness for hydroacoustic catalogs associated with three swarms (Novara TF, Melville TF, and segment 4) were 3.4, 3.3, and 3.1 mb compared to 3.9, 4.1, and 3.9, based on the ISC catalogs, respectively. This showed that the hydroacoustic catalogs are complete compared to land-based catalogs.

2. In all three swarms, detection of events over the two iterations, reduced the uncertainties in location (latitude and longitude) to ≤ 400 m and ≤ 0.2 s in origin time.
3. All three swarms were magmatic in origin based on a large number of detections per unit time (events/day), the spatial distribution of events showing a clustering near the bathymetric highs, the temporal distribution of events lacking a strong mainshock-aftershock sequence, and the presence of impulsive events.
4. Magmatic origin was associated with dike emplacement, based on the spatial distribution of events and followed by stress readjustments in the surrounding crust. We speculated lateral dike propagation near the Novata TF and segment 4 swarms and vertical dike near the Melville TF.

3.4 Résumé des observations sur les essaims SWIR (En français)

Le long de la dorsale du sud-ouest Indienne à expansion ultra-lente (14 mm/an), nous avons analysé des données hydroacoustiques relatives à trois essaims sismiques distincts, près de la faille transformante de Novara (TF), de la faille transformante de Melville (TF) et du segment 4 à 67°45'E. Parmi eux, l'essaim près de la faille transformante de Melville (en 2016-17) est l'essaim sismique le plus intense de cette étude. Les observations clés de ce chapitre sont les suivantes:

1. La magnitude de complétude des catalogues hydroacoustiques associés aux trois essaims (Novara TF, Melville TF et segment 4) est de 3,4, 3,3 et 3,1 mb, comparée à 3,9, 4,1 et 3,9, pour les catalogues de l'ISC, respectivement. Cela montre que les catalogues hydroacoustiques sont plus complets que les catalogues terrestres.
2. Pour les trois essaims, la localisation des événements après deux itérations réduit les incertitudes de localisation (latitude et longitude) à mieux que 400 m et 0,2 s en temps origine.
3. Les trois essaims sont d'origine magmatique d'après le grand nombre de détections par unité de temps (événements/jour), la distribution spatiale des événements regroupés près de hauts bathymétriques, l'absence de séquence marquée choc-répliques dans la distribution temporelle des événements, et surtout la présence d'événements impulsionnels.
4. L'origine magmatique est associée à la mise en place de dykes, sur la base de la distribution spatiale des événements, suivie d'ajustements de contraintes dans la croûte environnante. Nous avons spéculé une propagation latérale de dykes près des essaims de Novata TF et du segment 4 et une propagation verticale de dykes près de Melville TF.

Chapter 4

Central Indian Ridge Swarms

Abstract

This chapter extensively examined five seismic clusters, between 2013 and 2020, situated on the Central Indian Ridge near the Rodrigues Triple Junction, using seismoacoustic monitoring of 6 to 8 hydrophones of the OHASISBIO network. Two of five clusters occurred near the Kairei hydrothermal field (HF), in February-May 2013 and in November-December 2013. In February 2013, a simultaneous cluster occurred near the Pelagia HF, situated along the Southeast Indian Ridge, ~160 km away from Kairei HF. Although this chapter is dedicated to the CIR, the co-occurrence of these two nearby clusters at Kairei-CIR and Pelagia-SEIR may help us look for similarities or differences. The next two clusters, one in April 2019 and another in April 2020 occurred on the CIR segments 8-9 between the Egeria Fracture Zone (FZ) and the Gemino FZ. The last cluster occurred near the Edmond HF in April-September 2020.

The February-May 2013 clusters near the Pelagia and Kairei HFs showed intermittent periods of activity, interpreted as magmatic swarms. The cluster in Nov-Dec 2013, near the Kairei HF, displayed a tectonic mainshock-aftershock sequence, depicting a tectonic origin. The recurrent clusters along the CIR segments north of Edmond HF were of a magmatic origin in April 2019 and of a tectonic origin in April 2020. The cluster near the Edmond HF in April-Sept 2020, the strongest among all the CIR clusters, showed a mixed magmato-tectonic origin, comprising tectonic sequences and dike emplacement accompanied by several impulsive events pointing to lava eruptions. Two of the tectonic sequences from different regions showed a rapid decay (i.e. high MOL p -value), pointing to high hypocentral temperatures below Edmond HF and CIR segments 8-9.

Résumé

Ce chapitre examine en détail cinq essais sismiques, entre 2013 et 2020, situés sur la dorsale Centrale Indienne près de la jonction triple de Rodrigues, à partir de données de surveillance sismoacoustique de 6 à 8 hydrophones du réseau OHASISBIO. Deux des cinq essais se sont produits près du champ hydrothermal (HF) de Kairei, en février-mai 2013 et en novembre-décembre 2013. En février 2013, un essai simultané s'est produit près du champ hydrothermal Pelagia, situé le long de la dorsale sud-est Indienne, à ~160 km du champ hydrothermal Kairei. Bien que ce chapitre soit consacré à la CIR, la co-occurrence de ces deux essais proches à Kairei-CIR et Pelagia-SEIR peut nous aider à rechercher des similitudes ou des différences. Les deux essais suivants, l'un en avril 2019 et l'autre en avril 2020, se sont produits sur les segments 8-9 du CIR, entre les zones de fracture Egeria et Gemino. Le dernier essai se situe près de la HF d'Edmond en avril-septembre 2020.

Les essais de février-mai 2013 près des sites HF Pelagia et Kairei ont des périodes d'activité intermittentes, interprétées comme des essais magmatiques. L'essai de Nov-Dec 2013, près de l'HF Kairei, présente une séquence tectonique choc-répliques, donc d'origine tectonique. Les essais récurrents le long des segments CIR au nord du site HF Edmond sont d'origine magmatique en avril 2019 et d'origine tectonique en avril 2020. L'essai près d'Edmond HF en avril-sept 2020, le plus intense parmi tous les essais CIR, a une origine magmato-tectonique mixte, comprenant des séquences tectoniques et la mise en place de dykes accompagnée de plusieurs événements impulsionnels témoins d'éruptions de lave. Deux des séquences tectoniques observées présentent une décroissance rapide (c'est-à-dire un paramètre p MOL élevé), signe de températures hypocentrales élevées sous Edmond HF et les segments CIR 8-9.

4.1 Introduction

The CIR, separating the Nubian and Indo-Australian plates in the Indian Ocean, has a slow-spreading rate between 23 and 47 mm/yr (DeMets et al., 2010). The broad-scale geometry of the CIR has been revealed by regional marine geophysical studies (Schlich, 1982) and plate reconstruction models (Royer and Sandwell, 1989). The CIR has a 5 to 8-km-wide rift valley trending in the S-SE direction (N152°). The detailed axial segmentation and bathymetry of the southern CIR (between 20°S and RTJ) are documented in Briais (1995) and Okino et al. (2015). The ridge segments between 25 and 85 km in length (Fisher et al., 1971; Parson et al., 1993), are segmented by four transform faults (Egeria, Flinders, Gemino, and an unnamed one) and non-transform discontinuities. In the central axial valley, water depths range between 3200 and 4000 m (Briais, 1995).

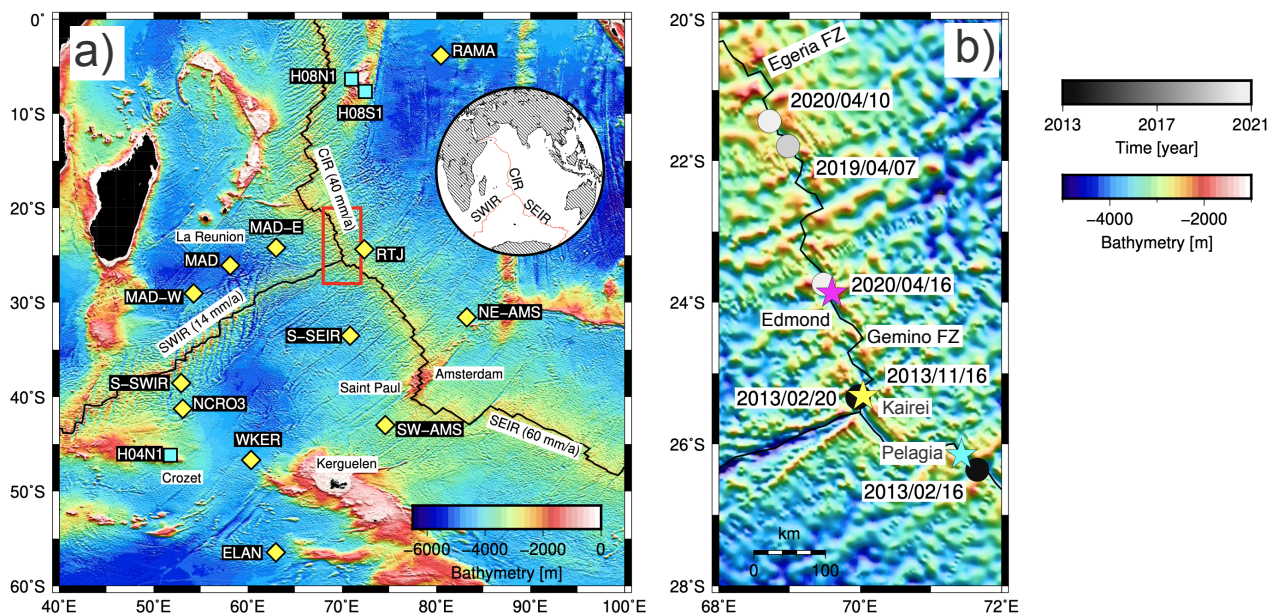


Figure 4.1: **a)** Bathymetric map showing three mid-ocean ridges: Southwest, Central, and Southeast Indian Ridges (black lines) with their respective spreading rates. Yellow diamonds and blue squares mark the site locations of the OHASISBIO and IMS-CTBTO hydrophones in the Indian Ocean. The red rectangle shows the study area along the CIR and SEIR and extended in **b)**. **b)** Locations of seismic clusters along the CIR, between the south of Egeria FZ and RTJ, and SEIR between 2013 and 2020 (in grayscale). The dates mark the onset time of each seismic cluster. Pink, yellow, and cyan stars mark the Edmond, Kairei, and Pelagia hydrothermal fields, respectively.

Along the CIR, several plume anomalies in the water column and four hydrothermal fields (HF) rich in hydrogen have been discovered (Okino et al., 2015). They include the sites Kairei at 25°19'S, Edmond at 23°52'S, Solitaire at 19°33'S and Dodo at 18°20'S. This study investigated three swarms in the vicinity of the first two HFs. The southernmost Kairei HF (yellow star in Figure 4.1b) is a black-smoker-type with a high-temperature (369 °C) vent and an unusually high concentration of H₂ (Van Dover et al., 2001). Situated ~7 km east of the neo-volcanic zone of the northern end of

asymmetric segment 1 of the CIR (segment number after [Briais, 1995](#)), Kairei HF lays at the foot of an inward normal fault scarp, at a water depth of 2140 m. High mantle Bouguer gravity anomaly suggests an ultramafic crust below a thin basaltic layer. The Edmond HF is located 160 km north of the Kairei HF (pink star in Figure 4.1b), on a small protrusion from the eastern rift valley wall which is ~6 km away from the ridge axis, on the northern end of another asymmetric segment 3, at a depth of 3255 m ([Gallant and Von Damm, 2006](#)). Edmond HF is also a high-temperature (382 °C) hydrothermal field, but its H₂ concentration is typical of basalt-hosted hydrothermal fluids ([Kumagai et al., 2008](#)). Near the Edmond HF, magmatic activity is frequent, resulting in the exposure of abundant fresh pillow lavas ([Georgen et al., 2001](#); [Cao et al., 2018](#)). ~160 km southeast of the Kairei field, there is another HF, Pelagia at 26°09'S along the SEIR, located at a depth of 3685 m. It is a high-temperature (368 °C) single chimney complex HF, situated on a ridge segment bounded by two transforms ([van der Most et al., 2023](#)).

Earthquakes in the vicinity of HFs can be attributed to two primary mechanisms. Firstly, the heat flux in these areas can induce thermal contraction, resulting in the formation of cracks and subsequently triggering earthquakes. Secondly, hydro-fracture can occur when trapped pockets of fluid undergo heating ([Sohn et al., 1999](#)). These seismic events are typically of small magnitude, with rupture diameters ranging from 1 to tens of meters. They were mostly detected by ocean bottom seismometer (OBS) arrays. For example, near the Trans-Atlantic Geotraverse (TAG) site along the Mid-Atlantic Ridge, one of the largest deep-sea HF on Earth, microseismicity showed magmatic intrusions ([Kong et al., 1992](#)). These authors suggested that the rapid cooling of magma and fracturing in the surrounding crust triggered the seismicity. In another survey near TAG in 2014, microseismicity comprising 32,708 events occurred over a period of 9 months, without any mainshock-aftershock sequence, and was interpreted as resulting from reaction-driven fracturing due to anhydrite deposition ([Pontbriand and Sohn, 2014](#)).

On the Endeavour segment of Juan de Fuca ridge, a seismic swarm of tectonic origin ([Johnson et al., 2000a](#)) and also a microearthquake swarm ([Crone et al., 2010](#)) have been reported near the Milli-Q vent. Off Taiwan, several HFs on the flanks of the Kueishan Taostrato volcano showed strong seismic activity triggered by M_w 5.4 tectonic event ([Lebrato et al., 2019](#)) which also altered the biochemistry in the vicinity of HFs. Beneath the Lucky-strike segment along the Mid-Atlantic Ridge, [Crawford et al. \(2013\)](#) recorded two-year-long seismicity using the OBSs and observed the along-axis hydrothermal cells feeding the summit vent field and the seismicity resulting from the thermal contraction of rocks at the bottom of the vent field at the Lucky-Strike segment. Near the Longqi HF on the SWIR, a single OBS recorded 2000 seismic events including volcano-tectonic microearthquakes within a 102-day period ([Liu et al., 2019](#)). A microearthquake swarm having an NNW-SSE strike and comprising of several normal faulting events has been reported by OBSs survey near the Kairei HF between 27 January and 19 March 2013 ([Sato et al., 2023](#)), although the

exact duration of the swarm activity is not given in their study.

Between 2010 and 2020, the ISC catalog reported five distinct clusters in the vicinity of the CIR HFs (Figure 4.1b): 1) near the Kairei and Pelagia HFs in February-May 2013; 2) near the Kairei HF in November-December 2013; on segments 8-9 in 3) in April 2019; 4) April 2020 (segments 8-9); and 5) in the vicinity of Edmond HF during April-September 2020. This chapter presents a comprehensive analysis of the nature of these five seismic clusters, based on the hydroacoustic data recorded by the OHASISBIO network.

4.2 Data and Methods

Network Geometry

Since the geometry of the OHASISBIO network was modified in 2017, we analyzed slightly different sets of hydrophone records for the 2013, 2019, and 2020 clusters. The hydroacoustic data include eight hydrophones in February-May 2013, six in November-December 2013, eight hydrophones in April 2019, and seven hydrophones from April to September 2020 (Table 4.1). Although the IMS-CTBTO were available in the periods of interest, we found no event originating from the clusters, perhaps due to a topographic blockage of the T-waves by the CIR fracture zones.

Year	Feb-May 2013	Nov-Dec 2013	Apr 2019	Apr-Sept 2020
MAD-W	-	-	√	√
MAD	√	√	-	-
MAD-E	-	-	√	-
RTJ	-	-	-	√
RAMA	√	-	-	-
NE-AMS	√	√	√	√
S-SEIR	-	-	√	√
SW-AMS	√	√	√	√
ELAN	-	-	√	√
WKER	√	√	√	√
NCRO3	√	√	-	-
S-SWIR	-	-	√	-
Total	8	6	8	7

Table 4.1: Hydrophones from the OHASISBIO network used in 2013, 2019, and 2020. Note here that the WKER station had three hydrophones during February-April 2013, out of which only two were recording data during November-December 2013.

Localization uncertainties

As in the SWIR swarms analyses, the iterative picking process significantly improved uncertainties in the location and origin time of OHA events. For all the events detected along the CIR between 2013 and 2020, the median errors were 12.82 km in latitude, 5.96 km in longitude, and 6.29 s in origin time; in the second iteration, the uncertainties shrunk to 0.73 km, 0.33 km, and 0.36 s, respectively (Figure 4.2). The median errors in latitude are about twice bigger than those in longitude (in both iterations). This discrepancy can likely be attributed to the geometry of hydrophones used for event localization, primarily located south of the study region since the H08 stations of the IMS did not detect any event.

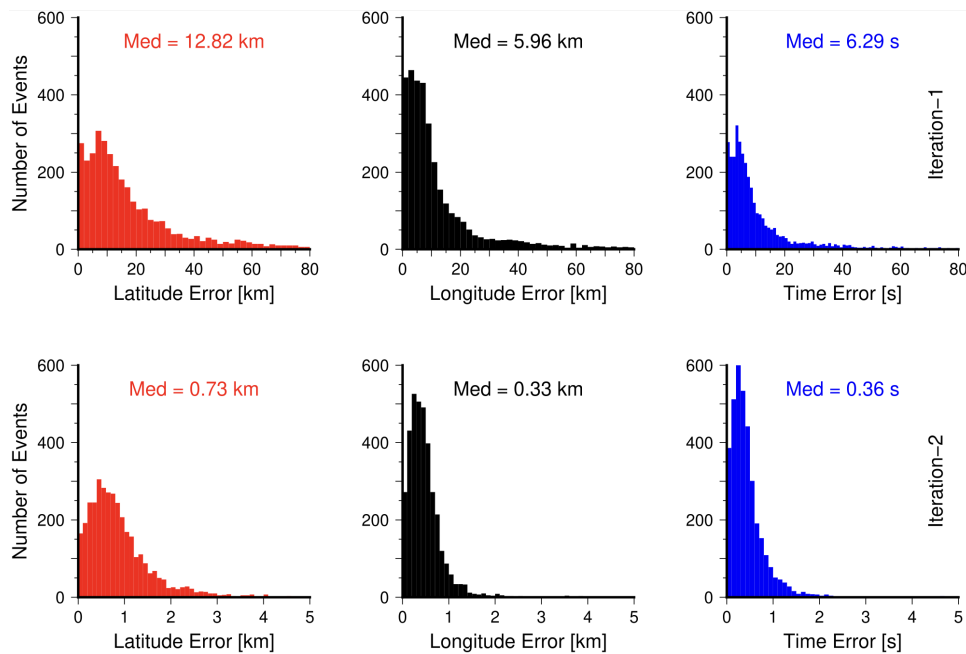


Figure 4.2: Errors obtained after acoustic triangulation in location (latitude and longitude) and origin time for all hydroacoustic events located along the CIR (red rectangle in Figure 4.1) after the first (top) and second (bottom) picking iterations. Here, events were localized by using a minimum of 4 and a maximum of 8 hydrophones. Note that the x-axis scales are different in both panels.

Magnitude of completeness

Within the OHA catalog, encompassing 3574 events derived from 5 seismic clusters, the SL_C of completeness was determined to be 211.7 dB, aligning with the peak of their normal distribution (Figure 4.3). Additionally, the roll-off point of the Gutenberg-Richter fitting for this catalog occurred at 1787. To compare SL_C with the magnitude of completeness (M_C) of seismic events, we have extracted all ISC events located in the red rectangle shown in Figure 4.1a, which share a similar tectonic context of seafloor spreading, spanning the years 2010 to 2020. This subset comprises

491 ISC events in 11 years compared to the 3574 OHA events detected in 9 months between 2013 and 2020.

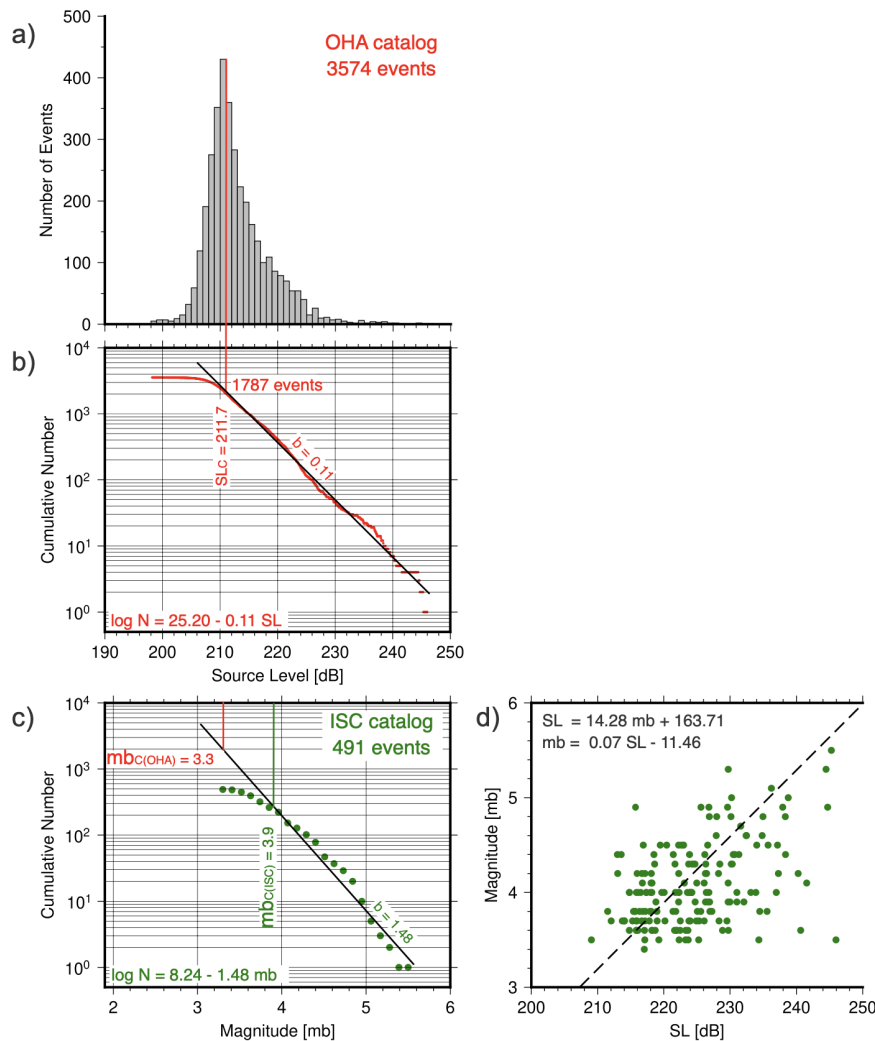


Figure 4.3: Completeness of source level (SL) and mb based on best-fitting Gutenberg–Richter's laws. **a)** Histogram of the OHA events associated with five clusters between February 2013 and September 2020. **b)** Cumulative number of events in the OHA catalog. The vertical line points to the completeness, SL_C 211.7 dB with a b -value of 0.24 in the SL framework. **c)** Cumulative number of events in the ISC catalog along the CIR axis reported from 2010 to 2020 (along the CIR area marked by a red rectangle in Figure 4.1). The vertical line points to the magnitude of completeness $mb_{C(ISC)} = 3.9$. Extrapolating the Gutenberg–Richter's law of this ISC catalog up to the number of events for which the OHA catalog is complete (1787 events) yields to $mb_{C(OHA)} = 3.3$. **d)** Regression between SL and mb of events common in both terrestrial and hydroacoustic catalogs, similar to as defined in [Pan and Dziewonski \(2005\)](#).

The magnitude of completeness for the 491 ISC events ($3.3 < mb < 5.5$) was $mb_{C(ISC)} = 3.9 mb$, and the event distribution remains skewed towards higher magnitudes. To establish a comparable measure, the equivalent magnitude of completeness for the OHA catalog is estimated as $mb_{C(OHA)} = 3.3 mb$ by extrapolating the frequency-size distribution with a b -value of 1.48 from the ISC events up to the event count defining the SL_C . This magnitude of completeness surpasses $mb_{C(ISC)}$ by 0.6 mb, demonstrating the higher sensitivity of hydrophone arrays compared to land-based networks.

The total count of events detected in five clusters by the OHASISBIO network over approximately nine months along the CIR axis is almost seven times larger than the count detected by land-based networks over an 11-year span along the CIR (2010-2020).

By fitting two Gutenberg-Richter laws to common events in the OHA and ISC catalogs, a relationship of $SL = 14.28 mb + 163.71$, or conversely $mb = 0.07 SL - 11.46$, was obtained (Figure 4.3d), similar to the proposed relationship of $SL = 7.98 mb + 193.58$, observed along the North Mid-Atlantic Ridge (Pan and Dziewonski, 2005). It is essential to acknowledge that such relationships often fail to adequately explain the scattered distribution of mb versus SL for events that are commonly identified in both hydroacoustic and teleseismic catalogs.

As pointed out by Bohnenstiehl et al. (2002), the moment magnitude (M_w) scale is deemed most suitable for earthquakes occurring at mid-oceanic ridges. It stands out as the only magnitude scale estimated based on a physical model of rupture, rather than relying on wave amplitude measurements (Kanamori, 1977). To shed more light on it, we have compared SL_C to that of completeness of different types of seismic magnitudes, such as surface-wave magnitude M_s and also M_w . Out of the 491 events in the ISC catalog, only 392 MS are reported, ranging from 2.7 to 5.7, exhibiting completeness of $M_{sC(ISC)} = 3.5$ and a b -value of 1.21 (Figure 4.4b). Since, M_w are only calculated for the events with magnitudes $mb > 4.9$, which are rarely encountered along ridges. To address this limitation, we converted all mb to M_w with the empirical relation proposed by Das et al. (2011) based on correlations across global seismic catalogs, like ISC:

$$M_w = 1.5385mb - 2.5385 \quad (4.1)$$

Equation 4.1 remains valid for mb in the range of 2.9-6.5, encompassing all the events in our catalog. Following the conversion, M_w for 491 events along the CIR ranged from 2.5 to 5.9 with the completeness of $M_{wC(ISC)} = 3.4$ and a b -value of 0.98 (Figure 4.4c) for M_w up to the event count defining the SL_C (1787), we achieved comparable completeness values of $M_{sC(OHA)} = 2.8$ and $M_{wC(OHA)} = 2.5$ for the surface (Figure 4.4b) and moment magnitudes (Figure 4.4c), respectively. These results underscore that the magnitude of completeness of the OHA catalog along the CIR exceeds $mb_{C(ISC)}$ by 0.6, $M_{sC(ISC)}$ by 0.7, and $M_{wC(ISC)}$ by 0.9, demonstrating the superior detection capability of hydrophones.

4.3 Results

4.3.1 Seismicity in February-May 2013

Based on the land-based catalogs, we observed simultaneous activity near the Kairei and Pelagia HF. On 16 February 2013 at 01:20 UTC, seismicity started with a normal-faulting event with M_w

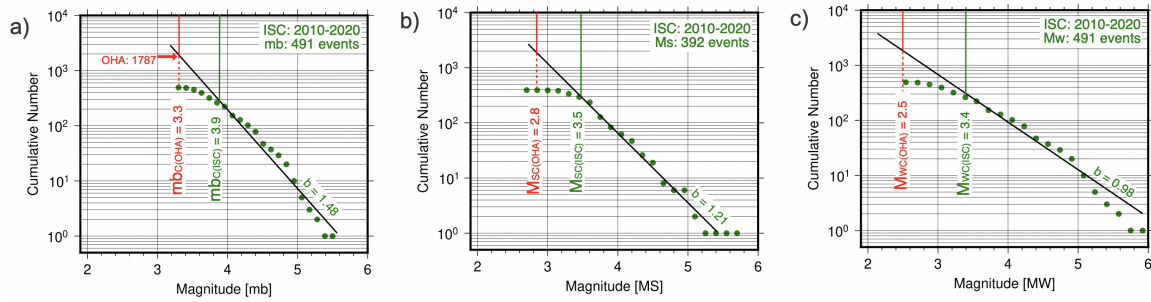


Figure 4.4: *Completeness of source level (SL) and magnitudes based on best-fitting Gutenberg–Richter’s laws. a) for body-wave magnitude scale (mb), b) surface wave magnitude (M_s) and c) moment magnitude M_w . SLs were obtained for all the events from five seismic clusters along the CIR and mb, M_s and M_w were obtained for the events from 2010 and 2020, residing along the CIR (within the area bounded by the red rectangle in Figure 4.1a).*

5.0 in the vicinity of the Pelagia HF on the SEIR (Figure 4.5a), which was followed by 28 ISC events till April, including a small cluster of 5 events on 3 April. On 20 February at 22:53 UTC, another normal-faulting event with M_w 5.0 occurred near the Kairei HF, followed by 6 ISC events, including 2 events showing GCMT solutions.

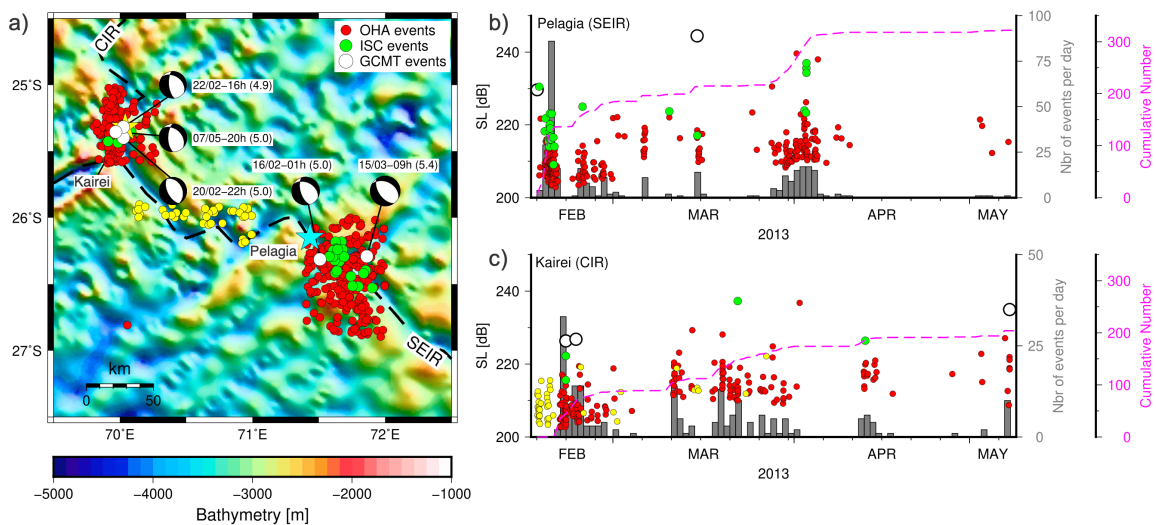


Figure 4.5: *a) Hydroacoustic locations of the GCMT (white), ISC (green), and OHA (brown) events between February and May 2013 near the Pelagia (cyan star) and Kairei (yellow star) HF. All the GCMT events show normal faulting mechanisms, 2 near Pelagia and 3 near Kairei. The events detected between RTJ and FZ west of Pelagia HF are shown by yellow circles. Bathymetry is from ETOPO1 grid (NOAA, 2009). Right panels show the temporal distribution of events per day (histogram), their SLs (circles), and the cumulative number of events (pink line) for the events near b) Pelagia, c) Kairei HF and between both of them (yellow).*

Near the Pelagia HF, the hydroacoustic data recorded 135 events, with SLs between 202.9 and 230.5 dB, within the initial four days (till 20 February), out of which 20 events are reported in the ISC catalog (Figure 4.5b). Their cumulative distribution showed a sharp rise. In the axial region between two HF, 43 events (201.2 SL 222.1 dB) were observed along the SEIR between the FZ, west of the Pelagia HF, and the RTJ, primarily concentrated in the initial phase of the activity.

Near Kairei HF, the 20 February event was preceded by 27 small magnitude events (202.7-222.2 dB) and followed by 60 events until 28 February, showing a gradual decrease in their numbers over time (Figure 4.5c). During the same period, a short episode occurred near the Pelagia HF after an $mb = 4.1$ event. There were several distinct periods of heightened seismic activity near the Pelagia HF, which coincided with reduced activity near the Kairei HF, and vice versa between 02 March and 14 March. Few more events were detected in a region between Kairei and Pelagia in March. On 15 March at 09:46 UTC, another strong M_w 5.4 event occurred near the Pelagia HF, east of the FZ, and was not preceded or followed by a large number of events.

Near the Pelagia HF, from 28 March onward, 63 events with increasing SLs were detected, preceding a cluster of five ISC events on 3 April. The cumulative distribution of events also increased sharply over this period. Subsequently, the activity declined until 10 April along with their SLs also. There were no further detections (except on 2 May). Overall, 322 OHA events with SLs ranging between 202.9 and 244.5 ($SL_C = 211.5$ dB) were observed near the Pelagia HF, compared to 28 ISC events including 2 GCMT solutions.

Near Kairei HF, on 13 April, an ISC event with $mb = 4.0$ was preceded by a few OHA events. It was then followed by a quiet period, except for a few events that occurred before a strong M_w 5.0 event on 7 May, after which activity ceased. Cumulatively, 203 OHA events with SLs from 202.6 to 237.3 ($SL_C = 212.6$ dB) were identified, in contrast to 7 ISC events, including 3 GCMT solutions near this HF.

4.3.2 Seismicity in November-December 2013

Six months later, between 24 November and 12 December 2013, a new cluster consisting of 36 ISC events was observed near the Kairei HF, which also included 11 GCMT events showing normal faulting mechanisms. The hydroacoustic analyses revealed that the seismic activity was very mild between 16 and 24 November (Figure 4.6a), comprising only 13 events with their SLs between 205.1 and 227.2 dB. Following a M_w 5.2 (SL = 238.8 dB) event on 24 November at 22:04 UTC, a gradual increase in seismic activity was observed, with 78 OHA events until 21:00 UTC on 25 November (Figure 4.6b). The SLs for these events were observed in the range of 212.3 and 235.7 dB. Later on, a heightened activity rate was observed after a M_w 5.1 (SL = 238.4 dB) event at 21:26 UTC.

Six months later, between 24 November and 12 December 2013, a new cluster consisting of 36 ISC events was observed near the Kairei HF, which also included 11 GCMT solutions showing normal faulting mechanisms, trending in the NNW direction which is parallel to the main axis azimuth. The hydroacoustic analyses revealed that the seismic activity was very mild between 16 and 24 November (Figure 4.6a), comprising only 13 events with their SLs between 205.1 and 227.2 dB. Following a M_w 5.2 (SL = 238.8 dB) event on 24 November at 22:04 UTC, a gradual increase in

seismic activity was observed, with 78 OHA events until 21:00 UTC on 25 November (Figure 4.6b). The SLs for these events were observed in the range of 212.3 and 235.7 dB. Later on, a heightened activity rate was observed after a M_w 5.1 (SL = 238.4 dB) event at 21:26 UTC.

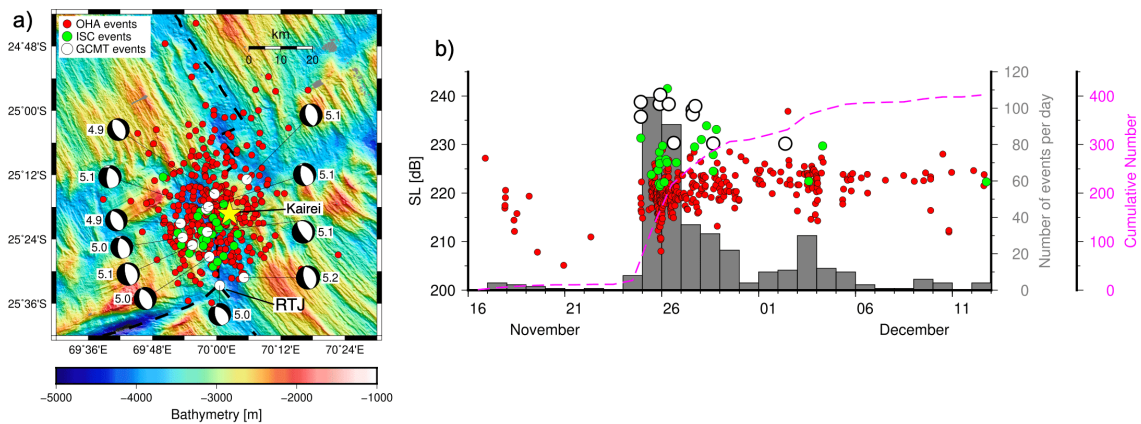


Figure 4.6: **a)** Hydroacoustic locations of the GCMT, ISC, and OHA events between November and December 2013 near the Kairei HF. All the GCMT events show normal faulting mechanisms with focal-plane azimuths parallel to the CIR axis. Bathymetry is from Okino *et al.* (2015). **b)** Temporal distribution of events, same legend as Figure 4.5b.

Following this event, a dense cluster of 212 OHA events ($213.2 < SL < 237.8$ dB), including 7 GCMT and 16 ISC events occurred until the end of 29 November. During this time, the activity rate showed a gradual decrease, whereas SLs of events on average showed an increasing trend. Another M_w 4.9 earthquake on 02 December coincided with a short episode of seismic activity (change in slope of cumulative number) which then subsided by 12 December. This period comprised 79 OHA events with their SLs between 212.0 and 236.8 dB. Overall, we detected 402 OHA events in this cluster, representing an eleven-fold increase in detection compared to the ISC catalog (36 events). The SLC during this cluster was measured at 221.3 dB.

4.3.3 Seismicity in April 2019

In April 2019, a cluster of 13 ISC events and 2 GCMT events occurred along segments 8-9 at $21^{\circ}30'S$, approximately 200 km north of the Edmond HF (Figure 4.7a). The segments are offset by ~ 4 km at $21^{\circ}25'S$. In this cluster, we have detected 165 OHA events (a 12-fold increase in detection). The resulting catalog showed that the seismicity initiated after two ISC events near $20^{\circ}S$ on 8 April. Subsequently, events were scattered over a distance of ~ 600 km along the CIR axis with mild seismic activity until 15 April, comprising 40 OHA events (Figure 4.7b). On 18 April, three ISC events occurred near $21^{\circ}30'S$, followed by two GCMT (M_w 4.9, normal faulting). These two events were separated by ~ 50 minutes (13:09 and 13:58 UTC).

As highlighted by the increase in cumulative number, 40 OHA events ($200.7 < SL < 228.9$ dB) occurred after these two GCMT events and their SLs decreased over time until 20 April. The ac-

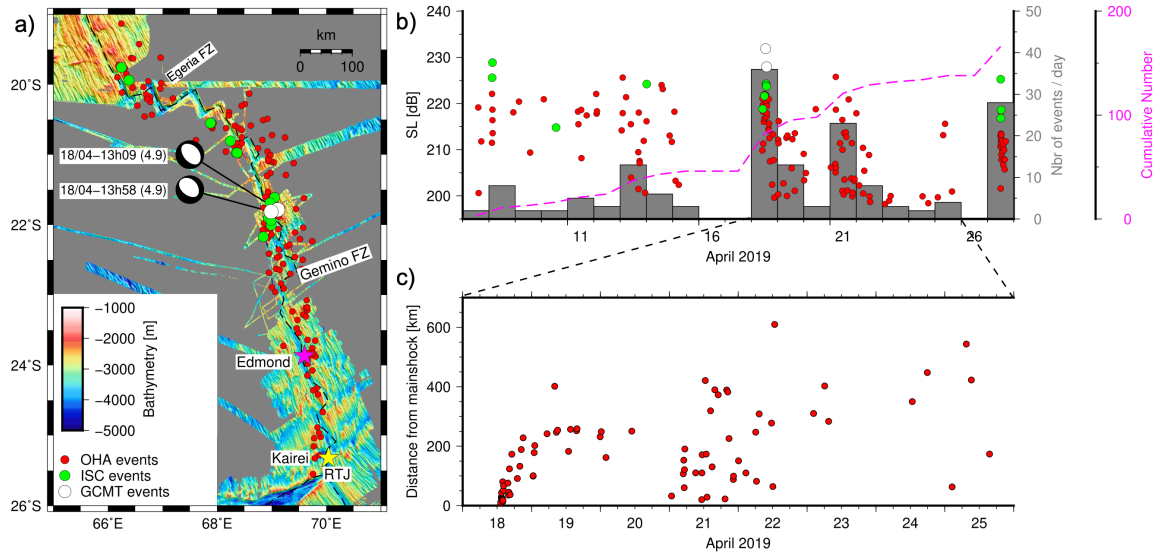


Figure 4.7: **a)** Hydroacoustic locations of GCMT, ISC, and OHA events during April 2019 along the CIR axis, south of the Egeria FZ. Two GCMT events show normal faulting mechanisms parallel to the CIR axis. Combined bathymetry from [Dyment et al. \(1999\)](#) and [Okino et al. \(2015\)](#). **b)** Temporal distribution of events, the same legend as Figure 4.5b **c)** Distance of OHA events between 18 and 25 April, from the location of the M_w 4.9 GCMT event (18 April at 13:09 UTC).

tivity rate again increased on 21 April, after which the number of events and their SLs showed a decreasing trend until 25 April. Towards the end, three ISC events occurred north of GCMT events (21°S) on 27 April, followed by 22 events with decreasing SLs. The SLs for all events from this catalog ranged between 198.2 and 231.9 dB, with $SL_C = 212.5$ dB. In this seismic cluster, events were spread over the CIR ridge axis. The events that followed the M_w 4.9 earthquake on 18 April at 13:09 UTC exhibited a steep slope in their distance from the mainshock for the first 14 hours, after which it became flat for the next 34 hours. After 21 April, this distance of events showed a scattered distribution.

4.3.4 Seismicity in April 2020

In 2020, a small cluster consisting of 19 ISC events, with no GCMT solutions, occurred between 10 and 15 April, along the same segments 8-9 at 21°30'S (Figure 4.8a) as the April 2019 cluster (Figure 4.7a). The hydroacoustic analysis of the 6 available hydrophones between 10 and 17 April detected a total of 467 events, representing a 24-fold increase in event detection. Here, SLs ranged from 203.9 to 227.0 dB with a $SL_C = 210.3$ dB. All the detected events spread in a N-S direction, slightly oblique relative to the CIR axis orientation (Figure 4.8a). Upon examining their temporal distribution, we observed that 71 events with increasing SLs occurred before the first ISC event on 10 April (Figure 4.8b). Subsequently, the number and SLs of events sharply decreased until 02:00 UTC on 11 April. Another episode of activity showing a sharp rise in cumulative distribution as well

as events with increasing SLs took place after the ISC event on 11 April. This episode consisted of 322 OHA events until the end of 13 April, the most intense phase of the activity. After 13 April the seismicity rate sharply decreased and the cumulative distribution flattened. There were two small episodes of increased seismic activity, one on 14 April and another on 15 April (both consisted of 18 OHA events), following two respective ISC events. In both episodes, the OHA events exhibited decreasing SLs over time.

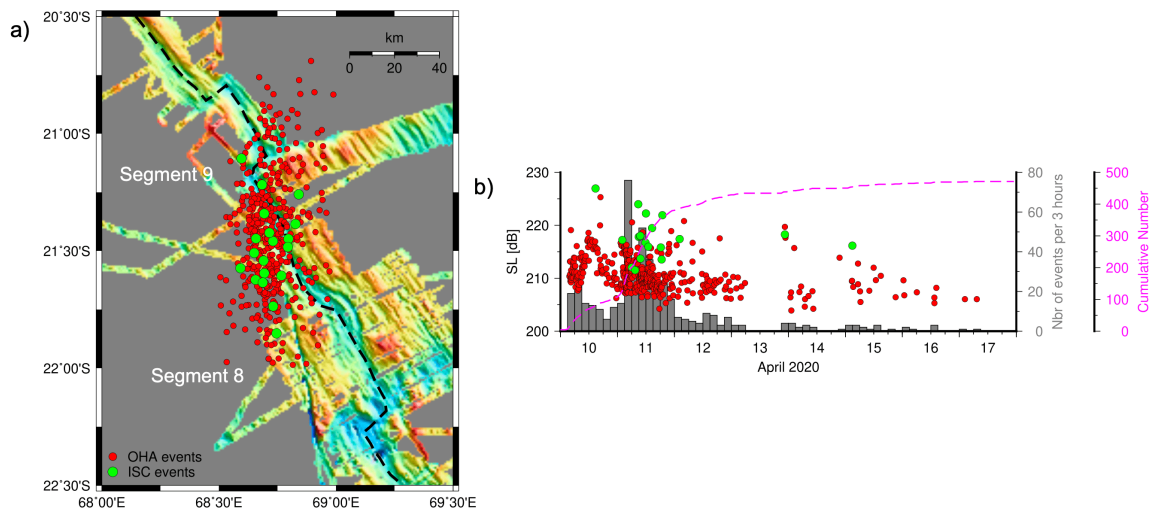


Figure 4.8: **a)** Hydroacoustic locations of ISC and OHA catalog events in April 2020 along the CIR axis. The large latitudinal spread of events is likely due to the geometry of the OHASISBIO network. Bathymetry is from [Dyment et al. \(1999\)](#). **b)** Temporal distribution of events with captions similar to Figure 4.5b.

4.3.5 Seismicity in April-September 2020

Following the activity along segments 8-9 from 10 to 15 April 2020, a strong cluster of seismic activity took place near the Edmond HF from 16 April to 4 September 2020 (Figure 4.9a). It comprises 68 ISC events and 7 GCMT events. The GCMT events exhibited three types of focal mechanisms: five with normal faulting mechanisms, one event with a reverse faulting mechanism, and one with a strike-slip mechanism, which is the last GCMT event of this cluster. Here, the hydroacoustic analyses located 2015 OHA events with an improved detection rate of 30-fold compared to the ISC catalog. Here, all the OHA events showed SLs between 198.7 and 246.0 dB, with $SL_C = 211.3$ dB (Figure 4.9a). The GCMT and ISC events focused in the vicinity of the HF, while smaller magnitude OHA events were dispersed alongside the 600-km-long axial region.

Out of 2015 events, 711 impulsive events (IMP) were clustered on the slopes of bathymetric highs, surrounding the HF. Four of them occurred near the Kairei HF, and 11 near the Gemino FZ, north of the Edmond HF. The rest of them predominantly clustered near the high-magnitude GCMT/ISC events (Figure 4.9b), slightly north of the Edmond HF. A maximum of them (710) IMP

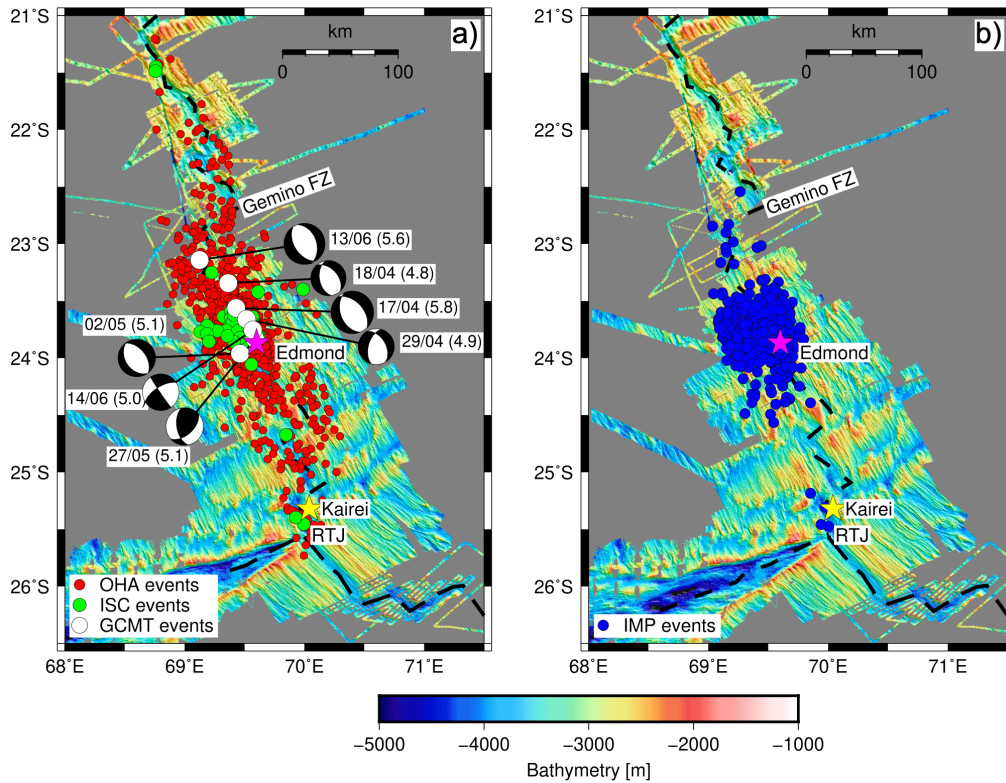


Figure 4.9: **a)** Hydroacoustic locations of GCMT, ISC, and OHA catalog events between April and September 2020 near the Edmond HF (pink star). GCMT catalog includes five events with normal faulting, one with reverse faulting, and one with strike-slip focal mechanisms. Combined bathymetry from [Dyment et al. \(1999\)](#) and [Okino et al. \(2015\)](#). **b)** Locations of impulsive events near the Edmond HF during the same time period.

were detected at the nearest RTJ station whereas the least (43), highly energetic, were detected as far as ~ 3700 km at the ELAN station.

The temporal distribution of events revealed that seismic activity was very mild, comprising only 23 events from 15 to 17 April (Figure 4.10a). Such activity rate then significantly increased after a M_w 5.8 normal faulting event on 17 April, with 48 events until the end of 17 April, and reaching a peak of 164 events on 18 April. This activity rate decreased over the following 5 days, with the detection of only 2 events on 23 April. The activity of IMP events also started mildly after the same normal faulting event (Figure 4.10b). Later on, the OHA activity increased after the ISC event $mb=3.7$ on 24 April.

The occurrence of a normal faulting M_w 4.9 (SL = 232.1 dB) event on 29 April further coincided with a higher number of OHA as well as IMP events. Then the seismicity rate decreased gradually till 20 May. Following a reverse faulting event with an M_w 5.1 on 27 May, the activity of IMP events escalated, reaching 24 events on the same day. This IMP activity was then gradually subsided by 01 June. On 07 June, they reached a new peak count (45 events). We observed another peak of 29 events in the IMP activity on 09 June, followed by a fairly strong activity (20 events/day) until 20 June. During this period, two GCMT events were observed, normal faulting (M_w 5.6) on 13 June

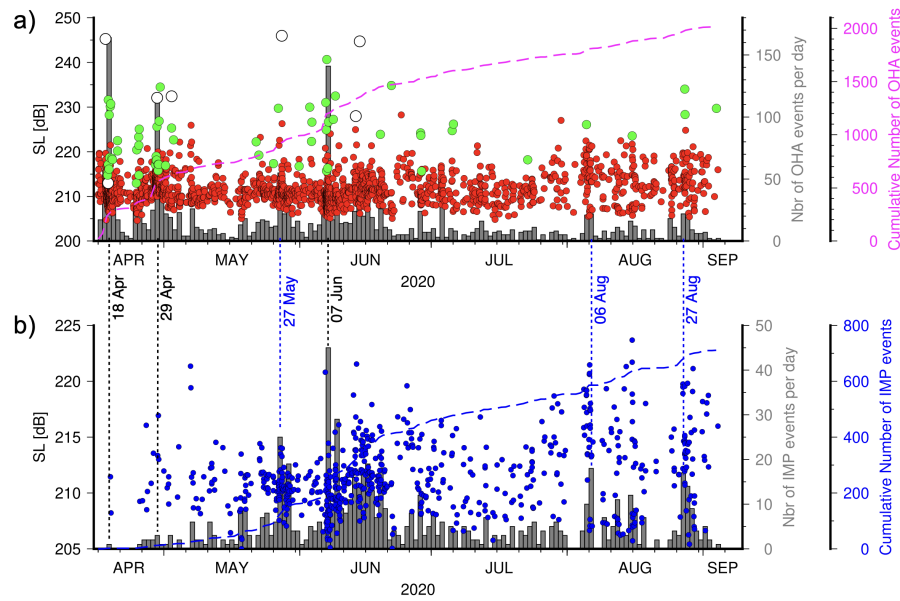


Figure 4.10: **a)** SLs of the GCMT, ISC, OHA, and IMP catalog events. Histogram of a daily number of **b)** OHA events and **c)** IMP events. Dashed pink and blue lines mark the respective cumulative number of events. The black dotted vertical lines mark the onsets of potential mainshock-aftershock sequences, while the blue dotted vertical lines mark heightened activity of impulsive events.

and strike-slip (M_w 5.0) on 14 June. In July, the IMP event activity was low with no more than 10 events/day. It continued to be recorded with two notable peaks occurring on 06 August (18 events), and 27 August (17). Following 27 August, the activity of IMP events gradually diminished, eventually leading to the cessation of seismicity near the Edmond HF by 4 September.

4.4 Discussion

4.4.1 Geographical extent of the swarms

4.4.1.1 Events in February-May 2013

The events demonstrated a greater clustering near the Kairei HF (area of $60 \times 45 \text{ km}^2$) compared to the Pelagia HF ($95 \times 60 \text{ km}^2$). To understand such a clustered distribution of seismicity in this period, we computed the stress changes associated with a M_w 5.0 event caused by the dip-slip of 11 cm along a normal fault in an elastic half-space near the Pelagia HF (Meade, 2007). From the two focal planes, we selected the fault plane that dips at 39° towards the axial valley. Assuming the hydroacoustic relocation with the depth taken from the GCMT catalog (14.9 km), this event imparted an extension onto the shallow crust below the SEIR axial valley (Figure 4.11a,b).

We projected the following events, mostly situated east of the M_w 5.0 event along a transect (A-A') perpendicular to the nodal plane. Since their depth is unknown, they are plotted at an elevation increasing above the seafloor depth according to their occurrence time (earliest on the

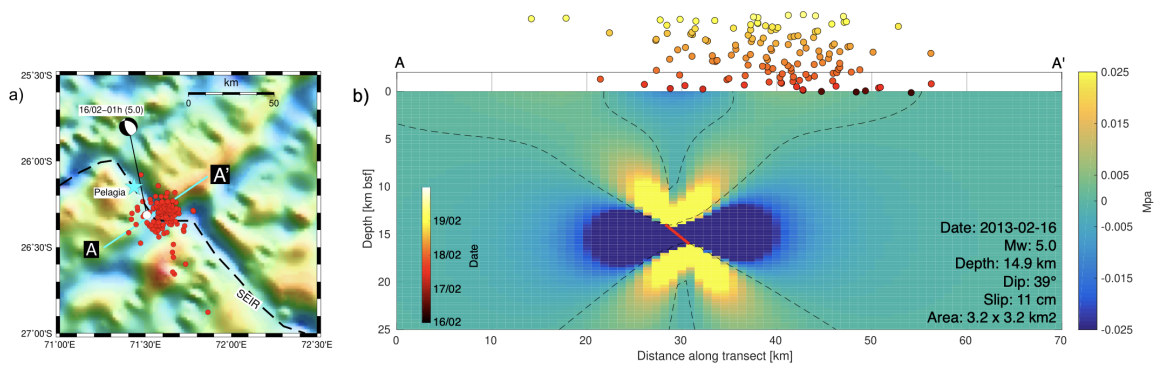


Figure 4.11: **a)** Zoomed map of the region around Pelagia HF (cyan star) showing the locations of events that occurred after the M_w 5.0 event (white) along the SEIR. **b)** Plausible geometry of the GCMT event on 16 February with its fault plane dipping at 39° towards the axial valley (red line). Contours show the predicted horizontal stress changes in MPa for an M_w 5.0 normal faulting event. The parameters are mentioned in the figures. The yellow color indicates areas under a tensional regime, potentially allowing for local dike emplacement and/or stress readjustment. The OHA events (with their temporal evolution) are projected along the A-A' transect, perpendicular to the nodal plane (shown in **a**), and placed at increasing altitudes according to their occurrence time (color-scale).

seafloor depth as shown in Figure 4.11b). Most events occurred in the area under extensional stresses that may have favored dike intrusions. We could not fit a modified Omori's law to this sequence of events, suggestive of magmatic origin. The absence of impulsive events indicated that this magmatic dike may not have reached the seafloor (Ingale et al., 2023).

Near the Kairei HF, the ~ 8 -day-long episode of seismicity was intensified after the GCMT (M_w 5.0) normal faulting event, situated ~ 8 km south of the Kairei HF. Again here, this sequence of events cannot be fitted by a modified Omori's law, suggestive of a magmatic nature. We computed the stress change as a result of a slip along a normal fault that was dipping at 58° , towards the axial valley along the CIR, similar to that observed near the Pelagia HF. Most events occurred in the area under extensional stresses that may have favored dike intrusions (Figure 4.12b).

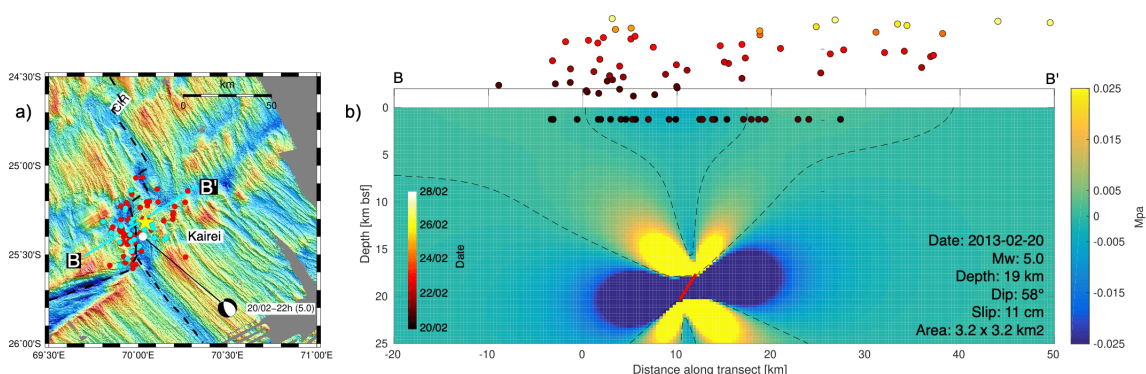


Figure 4.12: **a)** Zoomed map of the Kairei HF (yellow star) showing the locations of precursors (cyan circles) and events following (red circles) the normal faulting event (white circle). **b)** Stress modeling for the normal fault plane dipping at 58° . To outline the temporal evolution of events projected along the B-B' transect, precursors are plotted 1 km below the seafloor and the following events at increasing altitudes according to their occurrence time.

We observed both precursors and events following the normal faulting (between 20 and 28 February) on either side of the dipping fault plane. We projected them along the SW-NE orientated transect (B-B'), perpendicular to the nodal plane (Figure 4.12b). The presence of precursors could suggest that a magmatic dike intrusion may have triggered the fault rupture and the following events could have occurred as local stress readjustments. The absence of impulsive events may indicate that this magmatic activity did not reach the seafloor.

The episodic activity near both the Kairei and Pelagia HF, and the absence of mainshock-aftershock sequences point to a magmatic swarm origin. Although we detected a few events in the region between the two HFs (yellow circles in Figure 4.5a), they could not interconnect because of their distance from the normal faulting events (outside the stress-imparted region).

4.4.1.2 Events in November-December 2013

In this case, we localized the events within a 70 x 40 km area around the Kairei HF (Figure 4.6) similar to that observed in Feb-May 2013 (Figure 4.5a). A normal faulting event (M_w 5.1) that intensified the seismicity on 25 November, occurred S-W of the HF in the axial valley. The remaining events occurred as follows (Figure 4.13): four events on an extended fault scarp west of the axial valley, two events occurred at opposite corners of a fault plane north dipping away from the HF; two events were located within the axial valley (north of the HF), one near the RTJ, and one near the Non-Transform Offset (NTO) south of the Kairei (NTO is defined in Okino et al., 2015).

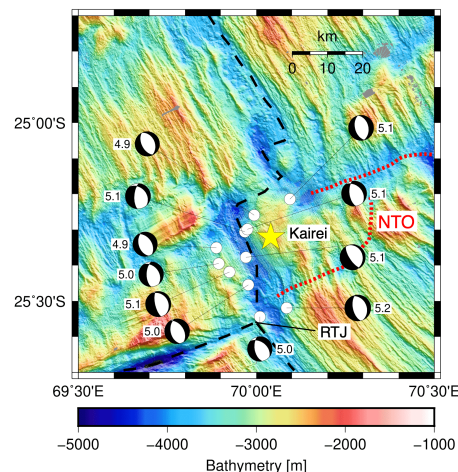


Figure 4.13: Zoomed map of the Kairei HF showing the locations of normal faulting GCMT events. The Red dashed line marked the Non-Transform Offset

Fitting a modified Omori's law (MOL) for a series of events after a M_w 5.1 event yielded a p-value of 0.81 (Figure 4.14). Here, the rapid increase followed by a gradual flattening in the cumulative distribution of events and the MOL good fit indicated a tectonic mainshock-aftershock sequence (Utsu et al., 1995; Bohnenstiehl et al., 2002). After the mainshock on 25 November, sev-

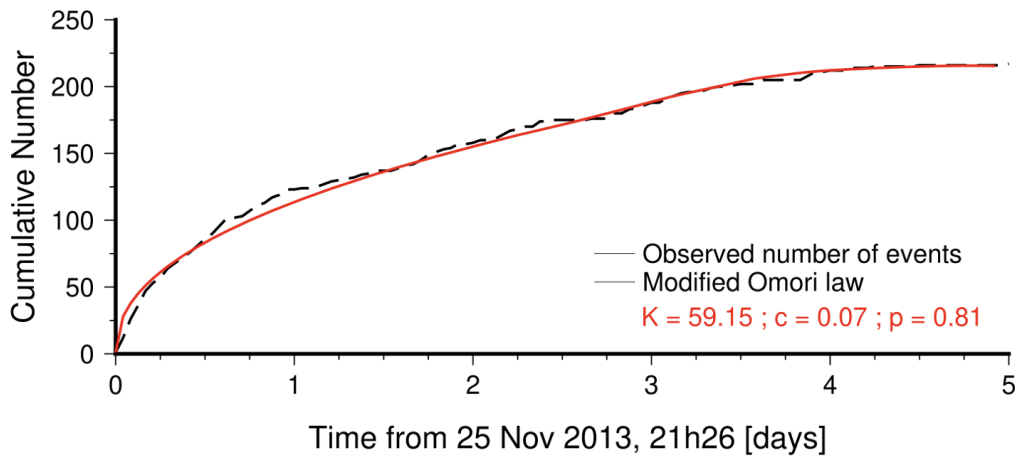


Figure 4.14: Hourly cumulative number of events (dashed line) vs. a best-fitting modified Omori's law (red line).

eral normal faulting events occurred and we propose that they could have occurred due to an induced stress change in the sub-axial crust that reactivated the pre-existing faults (Toda et al., 2002; Shuler and Nettles, 2012). The stress modeling for the mainshock shows that there was no clear relationship between the predicted stresses and the distribution of the events, suggesting widespread stress readjustments (Figure 4.15).

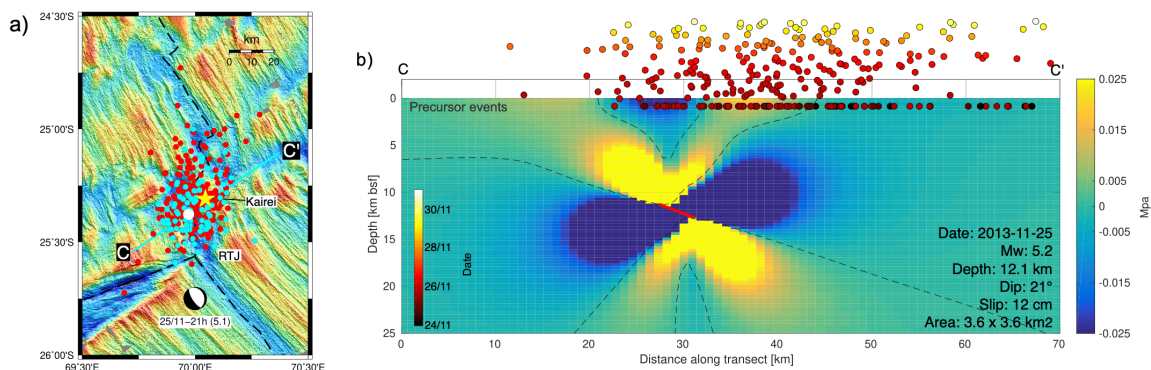


Figure 4.15: **a)** Zoomed map of the region around Kairei HF (yellow star) showing the locations of foreshocks (cyan circles) and aftershocks (red circles) relative to the normal faulting event (white). **b)** Stress modeling for the normal faulting event (red line, dipping at 21° towards the axial valley). Same legend as in Figure 4.12.

4.4.1.3 Events in April 2019 and April 2020

Along the ridge segments 8-9 at $21^\circ 30' S$, seismic clusters repeated at the same location in April 2019 and April 2020. The former one lasted for 20 days and the latter one for 7 days (Figures 4.7 and 4.8). In April 2019, events following GCMT ones could have resulted from the stress release due to normal fault rupture. In April 2020, a sharp increase in activity rate occurred after an $mb = 3.8$ event on 11 April 2020, followed by a gradual decrease. The events within the first 22 hours were located on the west side of the ridge axis (dark circles in Figure 4.16a) and after that, they were

randomly distributed east of the axis (light circles). The fitted MOL for this sequence of events yielded a p -value of 2.27 (Figure 4.16a), pointing to a tectonic mainshock-aftershock sequence.

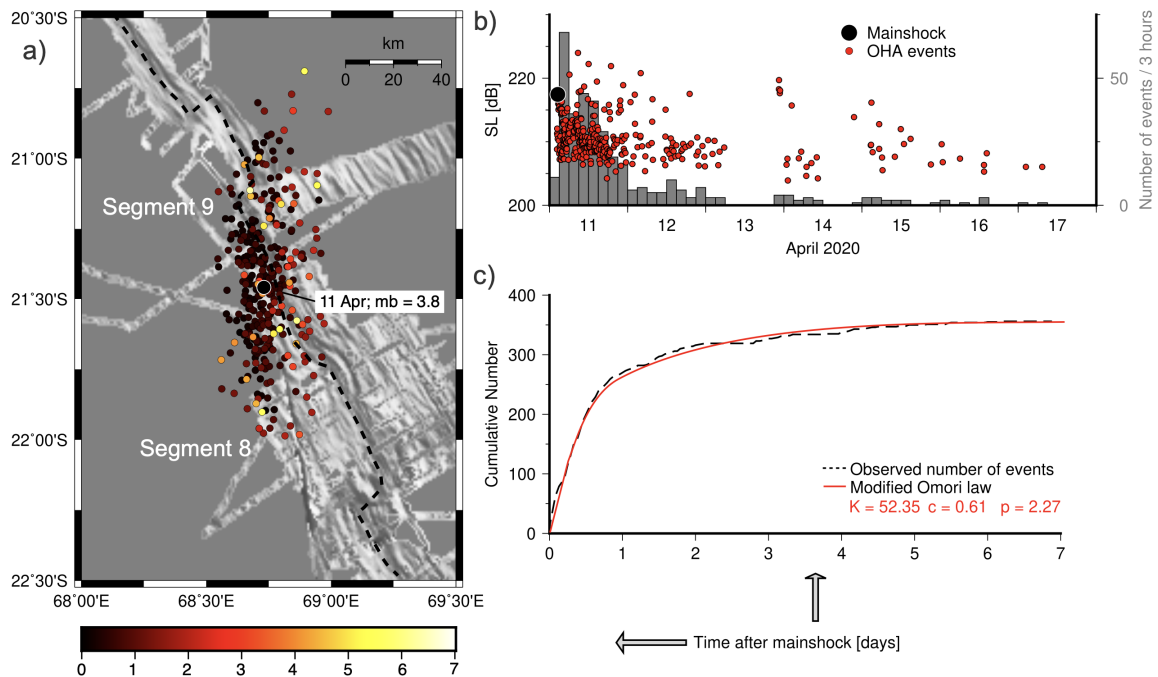


Figure 4.16: **a)** Spatiotemporal distribution of events between 11 and 17 April 2020 which were followed by $mb = 3.8$ event on 11 April 2020. **b)** Histogram of events per 3 hours along with SLs of the mainshock and aftershock events. **c)** Hourly cumulative number of events (dashed line) vs. a best-fitting modified Omori's law (red line).

This p -value falls at the higher end of the range (0.6-2.5), documented by Utsu et al. (1995) which could reflect rapid strain release where a rapid aftershock decay results from high-hypocentral temperatures (Kisslinger, 1996; Bohnenstiehl et al., 2002) due to magmatic fluid injections. Although no active hydrothermal field was reported on these segments, a deep-towed survey with an Ocean Floor Observation System (OFOS) evidenced basaltic alterations along segment 9, suggestive of a hydrothermal activity (Briais, 1995). Our high p -value is similar to p -values (2.3-2.7) observed along the Mid-Atlantic Ridge (Simão et al., 2010; Giusti et al., 2018), which were interpreted as evidence of high crustal temperatures.

4.4.1.4 Events in April-September 2020

The highest seismicity rate in the initial period of April 2020 near the Edmond HF coincided with a normal faulting M_w 5.8 event, located 40 km north of the HF on 17 April (Figure 4.17). The remaining normal faulting events were parallel to the CIR axis. Reverse faulting and strike-slip events, as here, adjacent to the HF, often occur at tips of long-lived corrugated fault scarps (Okino et al., 2015; Escartín et al., 2008); so they could point to the existence of a detachment fault. We discuss an alternative explanation further because it was preceded and followed by many impulsive events.

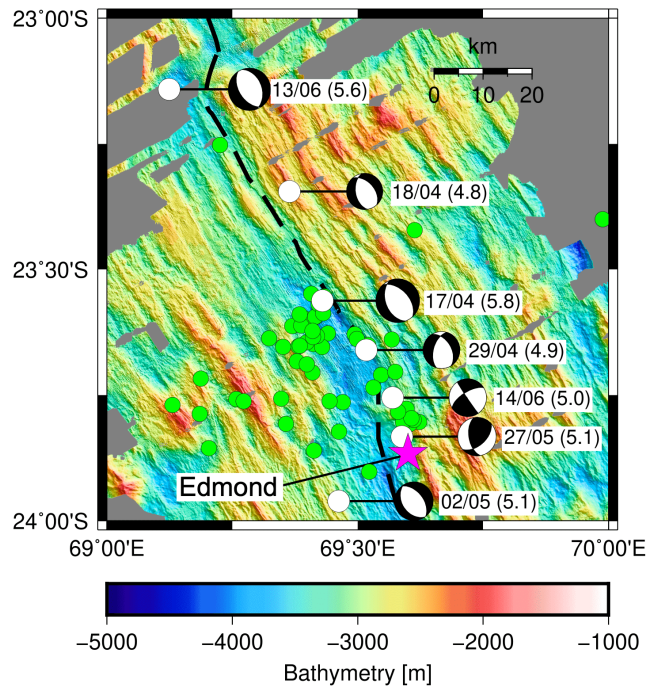


Figure 4.17: Zoomed map showing the locations of ISC (green) and GCMT (white) events during the April-September 2020 sequence north of Edmond HF.

In this cluster, the seismicity intensified after an M_w 5.8 event on 17 April and gradually decreased until 22 April. The activity showed a slight increase on 25 April coinciding with an ISC event and then declined again until 28 April (Figure 4.18a,b). Throughout this period, 378 events were widely scattered along the axis without a clear spatio-temporal pattern. Additionally, 9 IMP events were observed. We fit MOL for two successive sequences of events: one initiated by a M_w 5.8 event and lasting ~ 7 days, and the second initiated by a mb 4.5 event and lasting ~ 4 days. We excluded the IMP events from the MOL analysis. The p -values for the two sequences exhibited significant differences: $p_1 = 2.00$ and $p_2 = 0.49$ (Figure 4.18c). The first MOL clearly characterizes a tectonic mainshock-aftershock sequence (Hainzl et al., 2016) but departs from the observed cumulative distribution of events when the second sequence started, ~ 7 days later. This observation indicates the complex nature of tectonic seismicity near the HF. The large discrepancy in the MOL p -values over such a short time interval probably reflects different mechanisms. For example, the high p -value would infer high crustal temperature, similar to that observed along the segments 8-9, whereas the small p -value (0.49, outside the expected range of 0.6-2.5 for a tectonic sequence) would point to a magmatic origin for this sequence, which also includes more IMP events.

A few foreshocks before the M_w 5.8 mainshock (Figure 4.19a) could have caused alterations in the stress regime within the crust, resulting in changes in the over-pressure exerted on the magma body and would have triggered the mainshock (Baer et al., 2008). To assess the effects of the M_w 5.8 event on the observed seismicity, we predicted horizontal stress changes in MPa for a normal-slip event with a dip-slip of 28 cm along fault plane dipping at 49° , towards the axial valley (Fig-

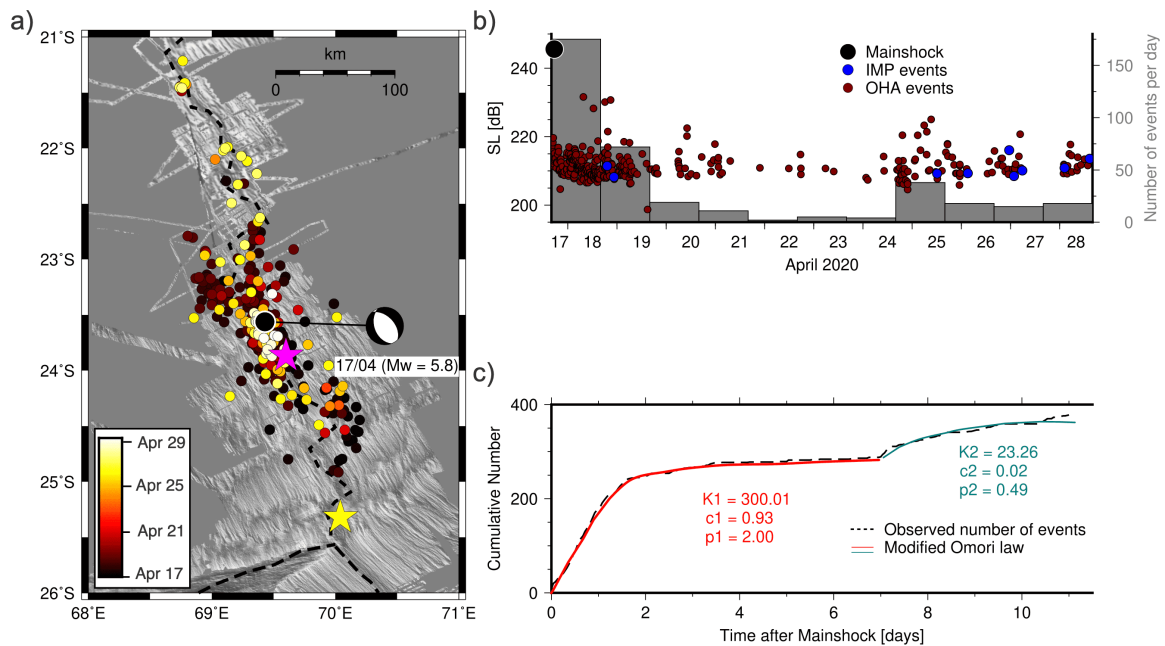


Figure 4.18: **a)** Spatiotemporal distribution of events between 17 and 28 April near the Edmond HF triggered by M_w 5.8 event. **b)** Histogram of daily events along with SLs of the mainshock, aftershocks, and impulsive events. **c)** Hourly cumulative number of events (dashed line) vs. a best-fitting modified Omori's laws (red line) after two mainshocks (M_w 5.8 and $m_b=3.8$) with two different parameters.

ure 4.19b). The aftershocks were mostly focused on the regions of predicted extensional stresses, leaving a seismic gap in the area under compression below the axial valley, suggestive of stress readjustment in the vicinity of a normal fault rupture.

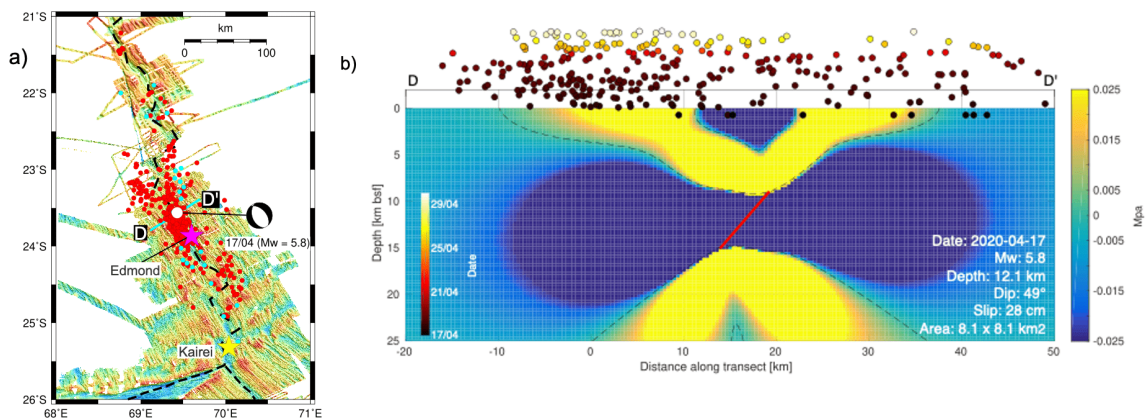


Figure 4.19: **a)** Locations of foreshocks (cyan circles) and aftershocks (red circles) to the normal faulting event (white) in the vicinity of Edmond HF (pink star). **b)** Stress modeling for the normal faulting event (red line, dipping at 49°). To outline the temporal evolution of events projected along the D-D' transect, foreshocks are plotted 1 km below the seafloor and the aftershocks at increasing altitudes.

Just after this sequence, the seismicity rate again increased after the normal faulting M_w 4.9 event on 29 April and gradually decreased until 17 May. MOL fitting this sequence yielded a p -value of 0.98, showing a tectonic origin of this mainshock-aftershock sequence. During this period, IMP events exhibited a higher rate of activity (Figure 4.20b), which could suggest dike em-

placement up to the seafloor through the rupture of faults and/or formation of volcanic fissures.

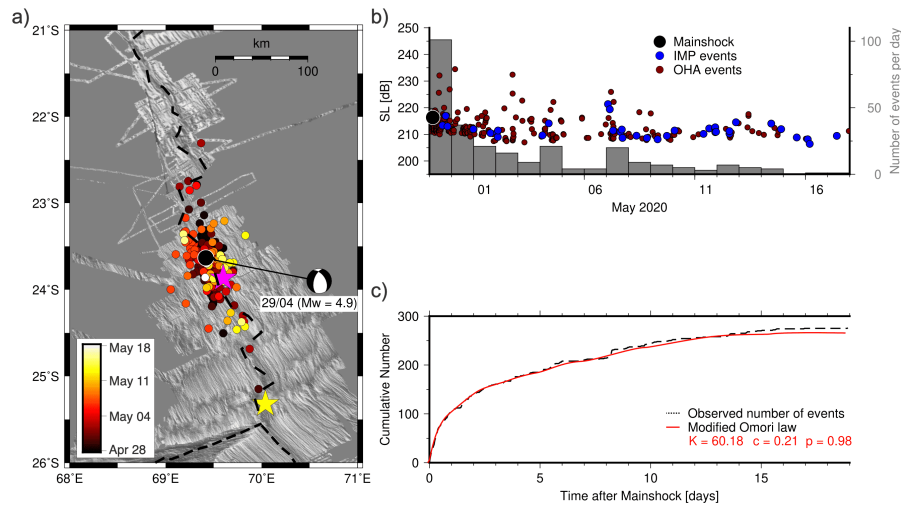


Figure 4.20: Aftershock sequence triggered by M_w 4.9 event on 29 April. Same legend as in Figure 4.16.

Stress modeling for this normal-slip event with a fault plane parallel to the axial valley and dipping at 54° towards it, showed that the induced stresses were lesser and the distribution of aftershocks looks unrelated to them, suggesting widespread stress-readjustments (Figure 4.21). The presence of a large number of IMP events could also argue for a volcanic eruption. Dike emplacements triggered by a normal fault rupture have been observed in other contexts of mid-ocean ridge such as the Lucky strike (Dziak et al., 2004) and FAMOUS segments along the Mid-Atlantic Ridge (Giusti et al., 2018). Based on the stress modeling, an embedded aftershock sequence according to the MOL parameters points to an important role of stress readjustments after a diking episode (Hainzl and Fischer, 2002). The presence of impulsive events within this part of the sequence could point to the dike extrusion on the seafloor.

On 27 May, we observed a cluster of 18 IMP events prior to a strong reverse faulting event (M_w 5.1), followed by 44 additional IMP events in the next 45 hours, close to the HF (Figure 4.22). Such activity could reflect the inflation of a magma chamber near the HF, which could have triggered this reverse faulting event (Kong et al., 1992).

The final sequence of events was initiated by a mb 4.9 earthquake on 7 June and exhibited relatively higher spatial density compared to the previous two sequences (Figure 4.23a). The activity reached its peak on the first day after the main event, followed by a diminished rate until 27 June (Figure 4.23b). During this period, associated with the IMP events, the seismicity intensified. The time distribution of the events between 7 and 27 June, excluding the IMP events, clearly departs from a MOL law, indicating that they were majorly governed by magmatic activity. All this evidence points to the occurrence of a volcanic eruption on the seafloor close to the Edmond HF.

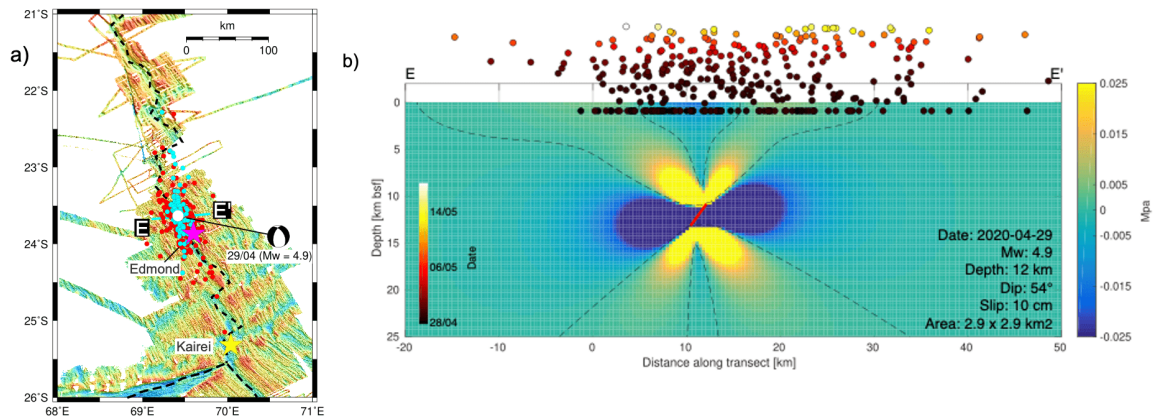


Figure 4.21: **a)** Locations of foreshocks (cyan circles) and aftershocks (red circles) to the normal faulting event (white) in the vicinity of Edmond HF (pink star). **b)** Stress modeling for the normal faulting event (red line, dipping at 47°, 12 km deep, 10 cm slip over an 8.36 km² patch). To outline the temporal evolution of events projected along the E-E' transect, foreshocks are plotted 1 km above the seafloor and aftershocks at the seafloor elevation.

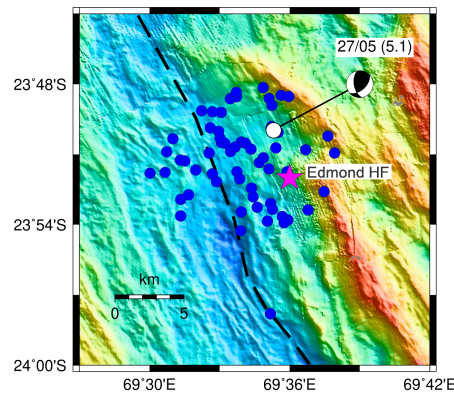


Figure 4.22: Locations of impulsive events (blue) between 27 and 30 May 2020 near the Edmond HF (pink star) along with that of the only reverse faulting event of the sequence (white).

Thus, the seismicity near the Edmond HF is clearly magmato-tectonic in nature, with tectonic mainshock-aftershock sequences, several magmatic episodes of heightened activity rate, and a large number of impulsive events (lava extrusion). The summary of different origins of seismicity near the hydrothermal fields and CIR segments between 2013 and 2020 is given in Table 4.2.

4.4.2 Tidal effect on the seismicity

There were few instances in the swarms studied here where either the SLs or the number of events showed an oscillatory trend. The events near the Pelagia HF showed episodic trends in their numbers as well as in the SLs (Figure 4.5b). As shown in Figure 4.24, events between 00:00 and 12:00 UTC on 18 February, showed a short-amplitude oscillation in their SLs, like a sinusoidal curve. Compared against the predicted ocean and solid-Earth tides, an offset of 6 hours was observed between the ocean tide and the SL oscillations between 00:00 and 12:00 UTC (Figure 4.24a), whereas

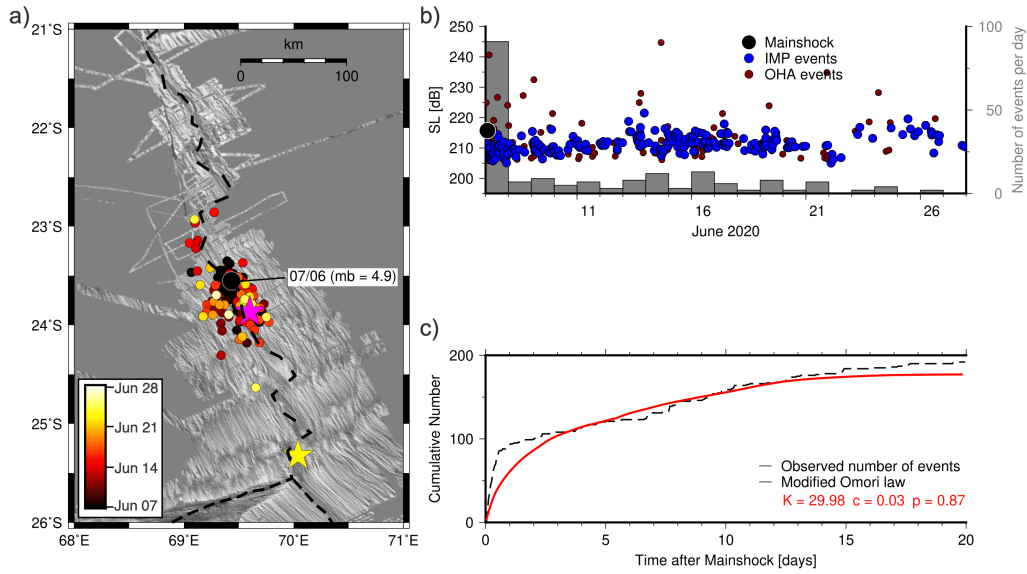


Figure 4.23: Aftershock sequence triggered by $mb = 4.9$ event on 7 June. Same legend as in Figure 4.16.

Year	2013	2013	2019	2020	2020
Date (dd/mm)	16/02-07/05	16/11-12/12	07/04-27/04	10/04-17/04	14/04-04/09
Median location	25.35°S, 69.96°E 26.36°S, 71.66°E	25.32°S, 69.98°E	21.79°S, 68.98°E	21.44°S, 68.72°E	23.74°S, 69.48°E
Region	Kairei HF Pelagia HF	Kairei HF	From Egeria FZ to RTJ	Segments 8-9	Edmond HF
Nbr of days	83	27	20	7	142
Nbr of hydrophones	6	6	7	6	6
Nbr of ISC events	35	36	13	19	68
Nbr of GCMT events	5	9	2	0	7
Nbr of OHA events	525	402	165	467	2015
Nbr of IMP events	0	0	0	0	711
OHA:ISC ratio	15	11	13	24	30
IMP:OHA fraction [%]	-	-	-	-	35
SL range [dB]	202.6 - 244.5	205.1 - 241.5	198.2 - 231.9	203.9 - 227.0	198.7 - 246.0
SL of completeness [dB]	212.1	221.3	212.5	212.5	211.3
Max events/day	86	106	164	273	30
Interpretation	Magmatic without eruption	Tectonic with low crustal temp	Magmatic without eruption	Tectonic with high crustal temp	Magmato-tectonic with eruption

Table 4.2: Summary of seismicity results along the CIR

the solid-Earth tide fits them (Figure 4.24b) only for that interval. It is still unclear why we only observe such a correlation on some occasions.

There were few instances in the swarms studied here where either the SLs or the number of events showed an oscillatory trend. The events near the Pelagia HF showed episodic trends in their numbers as well as in the SLs (Figure 4.5b). As shown in Figure 4.24, events between 00:00 and 12:00 UTC on 18 February, showed a short-amplitude oscillation in their SLs, like a sinusoidal

curve. Compared against the predicted ocean and solid-Earth tides, an offset of 6 hours was observed between the ocean tide and the SL oscillations between 00:00 and 12:00 UTC (Figure 4.24a), whereas the solid-Earth tide fits them (Figure 4.24b) only for that interval. It is still unclear why we only observe such a correlation on some occasions.

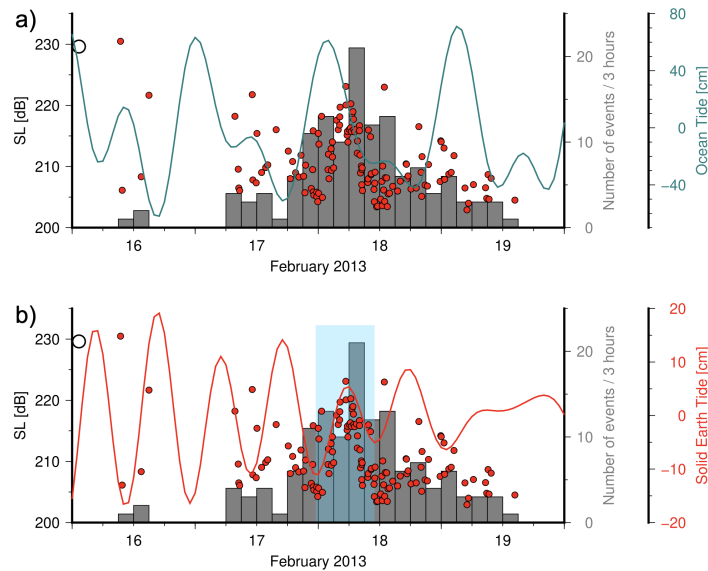


Figure 4.24: Temporal distribution of the number of events per 3 hours (histogram) with their SLs (dark circles) from 16 to 19 February near the Pelagia HF. The blue and red curves show the ocean and Earth tide heights in **a)** and **b)**, respectively. In the shaded time window, a peak in seismicity distribution coincides with that of the solid-Earth tide, and SLs also show a high resemblance.

On the other hand, the high solid-Earth tide coincided with a seismic activity rate at 06:00 UTC. This observation is consistent with that made globally by [Métivier et al. \(2009\)](#), who suggested that earthquakes occur slightly more often at the time of ground uplift by the solid-Earth tide, i.e. when normal stresses are reduced within the lithosphere. A similar tidal correlation observed along the Juan de Fuca Ridge was interpreted as a non-linear trade-off between strain and magmatic fluid fluctuations ([Wilcock, 2001](#)).

In another instance, the events that occurred along segments 8-9 (21°30'S) in 2020 also showed an oscillatory pattern in their SL, e.g. the events at the start of the seismicity (10 April; Figure 4.8). We compared SL with the ocean as well as solid-Earth tide heights in the region of the seismicity (Figure 4.25a,b). We observed that an increase in the ocean tide height coincided with increasing SLs of events between 06:00 and 12:00 UTC on 10 April (blue arrow); whereas, a simultaneous decreasing trend in regards to the solid-Earth tide between 12:00 and 18:00 UTC on the same day (red arrow). We are still not able to explain why we observe a correlation between the SL of events and the solid-Earth tide on some occasions.

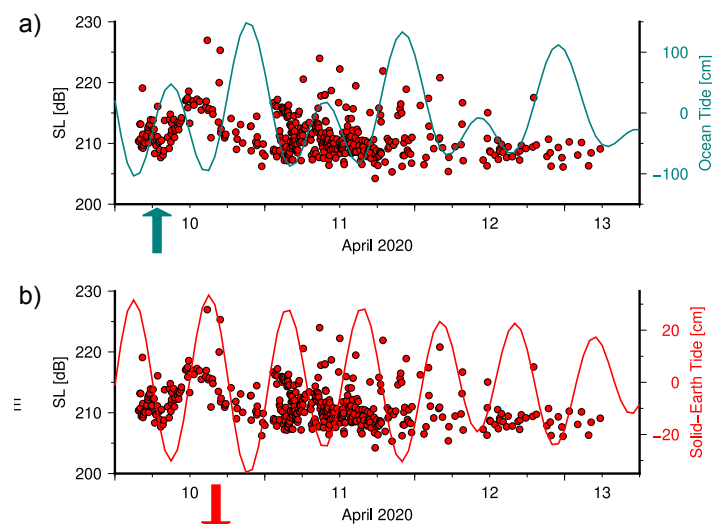


Figure 4.25: Temporal distribution of the number of events per 3 hours (histogram) with their SLs (dark circles) from 16 to 19 February near the Pelagia HF. The blue and red curves show the ocean tide height in **a**) and **b**), respectively. Blue and red arrows point to the coincidence of the SL pattern with the ocean and solid-Earth tides, respectively.

4.4.3 Magmatic and tectonic processes in the vicinity of Hydrothermal Fields

All three Kairei, Pelagia, and Edmond hydrothermal fields showed distinct characteristics of seismic activity. The Pelagia field along the SEIR did not show any recent seismicity. The absence of a tectonic sequence points to a magmatic swarm near the Pelagia HF. The Kairei HF, on the other hand, showed a recurrent seismicity, first of magmatic origin and later on of magmato-tectonic nature including dike propagation and reactivation of pre-existing faults induced by stress changes (Rubin et al., 1998; Toda et al., 2002; Shuler and Nettles, 2012). The magmato-tectonic nature of the seismicity would agree with the hypothesis of Okino et al. (2015), that the Kairei HF is magma-assisted, tectonically controlled, and ultramafic hosted HF. Finally, the seismicity near the Edmond HF showed a typical magmato-tectonic sequence with a strong normal fault event triggering dike emplacements. Being off-axis, it is not directly linked with the neo-volcanic zone (where magmatism is focused) and the magmatic fluid movement may be controlled by normal faults located along the rift valley (Okino et al., 2015). The increase in activity after the normal-faulting main-shock on 17 April could support this argument.

The seismicity rate in Feb-May 2013 was higher near the Pelagia HF (4 events per day) than at the Kairei HF (3 events/day). Later on, near the Kairei HF, it increased to 14 events/day during Nov-Dec 2013. In the vicinity of the Edmond HF, a similar seismicity rate of 14 events/day was observed in 2020. Microearthquake studies with temporary OBS arrays near other HFs showed higher seismicity rates, e.g. ~ 335 events/day near the Milli-Q HF on the Endeavour segment (Johnson et al., 2000a), ~ 33 events/day near the $9^{\circ}50'N$ hydrothermal field along the East Pacific Rise (Tolstoy

et al., 2008), ~119 events/day near the TAG in 2014 (Pontbriand and Sohn, 2014), ~20 events/day near the Longqi HF (Liu et al., 2019). Hydroacoustic surveys between 2011 and 2015 along the Mid-Atlantic Ridge recorded an average of ~4 events/day on asymmetric segments where a high number of hydrothermal vents was speculated (Parnell-Turner et al., 2022). Similar surveys along the Endeavour segment observed 4 distinct seismic sequences in March 1999 and January 2000 (Bohnenstiehl et al., 2004). The first sequence showed ~5 events/day (March 1999), the second, ~23 events/day (June 1999), the third, ~4 events/day (July 1999), and the last one, ~19 events/day (January 2000). In general, small-scale OBS arrays have a better detection threshold than large-scale hydroacoustic arrays. The similarity in the seismicity rate near the HF at the Endeavour segment and the Kairei HF, both measured by large-scale hydroacoustic arrays, suggests a similar origin combining magmatic and tectonic processes, despite the different spreading contexts (intermediate vs. slow, respectively).

4.5 Summary of the observations

In this chapter, we have studied the seismic activity from five distinct seismic clusters along the CIR axis primarily situated near hydrothermal fields and ridge segments 8-9 at 21°30'S. Our results rely only on hydroacoustic data from the OHASISBIO network since no T-wave signals were observed in the IMS-CTBTO data. The key findings are:

1. The detection of 3574 hydroacoustic events from five seismic clusters, 1) Feb-May 2013 in the vicinity of Kairei and Pelagia HF; 2) Nov-Dec 2013 near the Kairei HF; 3) April 2019 along the CIR axis (segments 8-9, south of Egeria HF), 4) April 2020 along the segments 8-9, and 5) April-September 2020 near the Edmond HF showed large variability in the spatio-temporal distribution.
2. The localization of events over two iterations reduced the uncertainties in location (latitude and longitude) and origin time. However, the localization uncertainties in latitude were twice as high (0.73 km) than that of longitude (0.33 km), likely due to the network geometry (stations mostly south of the study area).
3. The whole hydroacoustic event catalog has a magnitude of completeness of 3.3 over 13 months, compared to 3.9 for the ISC catalog events over an 11-year period (2010-2020) showing an improvement in the detection threshold.
4. Overall, we observed three types of seismicity in the southern CIR: magmatic swarms, tectonic mainshock-aftershock sequences, and magmato-tectonic sequences with dike emplacements and seafloor eruption.

5. The seismicity near the Pelagia HF was magmatic in origin (based on the episodic seismic activity); magmatic then followed by tectonic in the vicinity of the Kairei HF and magmato-tectonic with lava eruption on the seafloor near the Edmond HF.
6. The recurrent seismicity along segments 8-9 first showed amagmatic origin and/or widespread stress re-adjustments (April 2020). The high p -value in the modified Omori law associated with the tectonic mainshock-aftershock sequence in the second peak of activity (April 2020) 8-9 points to high underlying crustal temperatures.

4.6 Résumé des observations (En français)

Dans ce chapitre, nous avons étudié l'activité sismique de cinq essaims sismiques distincts le long de l'axe de la CIR, principalement situés près de champs hydrothermaux et des segments 8-9 à 21°30'S. Nos résultats reposent uniquement sur des données hydroacoustiques du réseau OHA-SISBIO, car aucun signal T n'a été observé dans les données IMS-CTBTO. Les principales conclusions sont les suivantes:

1. La détection de 3574 événements hydroacoustiques provenant de cinq essaims sismiques, 1) février-mai 2013 à proximité des champs hydrothermaux Kairei et Pelagia ; 2) novembre-décembre 2013 près du champ hydrothermal Kairei ; 3) avril 2019 le long de l'axe du CIR (segments 8-9, au sud du champ hydrothermal Egeria), 4) avril 2020 le long des segments 8-9, et 5) avril-septembre 2020 près du champ hydrothermal Edmond montrent une grande variabilité dans la distribution spatio-temporelle.
2. La localisation des événements sur deux itérations a réduit les incertitudes de localisation (latitude et longitude) et le temps origine. Cependant, les incertitudes en latitude sont deux fois plus élevées (0,73 km) qu'en longitude (0,33 km), probablement en raison de la géométrie du réseau (stations principalement au sud de la zone d'étude).
3. Le catalogue complet des événements hydroacoustiques a une magnitude de complétude de 3,3 sur 13 mois, comparée à 3,9 pour les événements du catalogue de l'ISC sur une période de 11 ans (2010-2020), montrant une amélioration du seuil de détection.
4. Dans l'ensemble, nous avons observé trois types de sismicité dans le CIR sud : essaims magmatiques, séquences choc-répliques d'origine tectonique, et séquences magmato-tectoniques avec mise en place de dykes et éruption sur le plancher océanique.

5. La sismicité près du champ hydrothermal Pelagia est d'origine magmatique d'après l'activité sismique épisodique ; magmatique puis tectonique à proximité du champ hydrothermal Kairei et magmato-tectonique avec éruption de lave près du champ hydrothermal Edmond.
6. La sismicité récurrente le long des segments 8-9 a d'abord montré une origine amagmatique et/ou des réajustements étendus de contraintes (avril 2020). La valeur élevée de p dans la loi modifiée d'Omori associée à la séquence choc-répliques dans le second pic d'activité (avril 2020) des segments 8-9 indique des températures crustales élevées sous-jacentes.

Chapter 5

Southeast Indian Ridge Swarms

Abstract

Seismic activity along mid-ocean ridges offers valuable insights into ridge segmentation and crustal accretion processes. Despite its importance of hosting few hydrothermal fields and its interaction with Saint-Paul Amsterdam plateau, the intermediate-spreading Southeast Indian Ridge (SEIR) in the Indian Ocean remains relatively underexplored due to its remote location from terrestrial seismic networks. In this chapter, we analyze hydroacoustic events recorded by a network of dedicated and autonomous hydrophones, along with data from three permanent international stations, encompassing six seismic swarms spanning from July 2012 to December 2020. Among these swarms, two are centered on the 28°S segment, three on the 29°S segment, and one along the J3 segment at 40°S, situated south of the Saint-Paul-Amsterdam plateau. The swarms in the first two segments (28°S and 29°S) exhibit repetitive patterns suggestive of a magmatic origin, characterized by their spatio-temporal distribution and the absence of strong triggering events. In contrast, the seismic swarm along the J3 segment reveals a distinctive nature, marked by energetic, short-duration impulsive events, which are interpreted as manifestations of lava-water interactions on the seafloor. The presence of a mainshock-aftershock sequence and dike emplacements imply a magmato-tectonic origin.

Résumé

L'activité sismique le long des dorsales médio-océaniques offre des informations précieuses sur la segmentation des dorsales et les processus d'accrétion crustale. Malgré la présence de champs hydrothermaux et une interaction avec le plateau de Saint-Paul Amsterdam, la dorsale sud-est In-

dienne (SEIR), à taux intermédiaires, reste relativement peu explorée en raison de son éloignement des réseaux sismiques terrestres. Dans ce chapitre, nous analysons les événements hydroacoustiques enregistrés par un réseau d'hydrophones dédiés et autonomes, ainsi que les données de trois stations internationales permanentes, englobant six essaims sismiques s'étendant de juillet 2012 à décembre 2020. Parmi ces essaims, deux sont centrés sur le segment 28°S, trois sur le segment 29°S, et un le long du segment J3 à 40°S, situé au sud du plateau de Saint-Paul-Amsterdam. Les essaims des deux premiers segments (28°S et 29°S) présentent des schémas répétitifs suggérant une origine magmatique, caractérisée par leur distribution spatio-temporelle et l'absence d'événements déclencheurs forts. En revanche, l'essaim sismique le long du segment J3 révèle une nature distincte, marquée par des événements impulsionnels énergétiques et de courte durée, interprétés comme des manifestations d'interactions entre la lave et l'eau sur le plancher océanique. La présence d'une séquence de choc-répliques et d'emplacements de dykes implique une origine magmato-tectonique.

5.1 Introduction

The Southeast Indian Ridge (SEIR) is a spreading ridge that separates the Indo-Australian and Antarctic plates. It extends from the Rodrigues Triple Junction (RTJ), passes through the Saint-Paul-Amsterdam (SPA) plateau, and connects with the Pacific-Antarctic ridge at the Macquarie Triple Junction, southeast of Australia (Figure 5.1). Its spreading rates range from intermediate to fast, averaging between 59 and 75 mm/yr. The ridge segments along the SEIR are labeled based on their correspondence to the SEIR corridors studied by [Royer and Schlich \(1988\)](#). Between the RTJ and SPA plateau, the SEIR shows a relatively smooth and blocky relief, on either side of a N135° trending axial valley. This particular section consists of multiple ridge segments that extend in an NNW-SSE orientation. The boundaries of these segments are marked by deep and linear fracture zones, which offset the SEIR axis by 20 to 100 km ([Sauter et al., 1991](#)). One notable characteristic of the SEIR is that a continuous melt lens might exist along the ridge axis ([Phipps Morgan and Chen, 1993](#)). This condition gives rise to varying thermal structures and can have significant implications for the nature of seismic activity along the ridge. The formation of the seafloor in this region is the result of a complex interplay between volcanic and tectonic processes, as evidenced by geophysical surveys ([Sauter et al., 1991](#)).

Fast-spreading ridge segments like the East Pacific Rise generally exhibit a low rate of seismic activity ([Fox et al., 2001](#)). On the other hand, slow-spreading ridge segments such as the Mid-Atlantic Ridge tend to generate a higher level of seismicity, likely due to a colder thermal regime ([Simão et al., 2010](#); [Goslin et al., 2012](#)). Intermediate-spreading ridges, lying between these two extremes, display a combination of both seismic patterns depending on their specific morphology

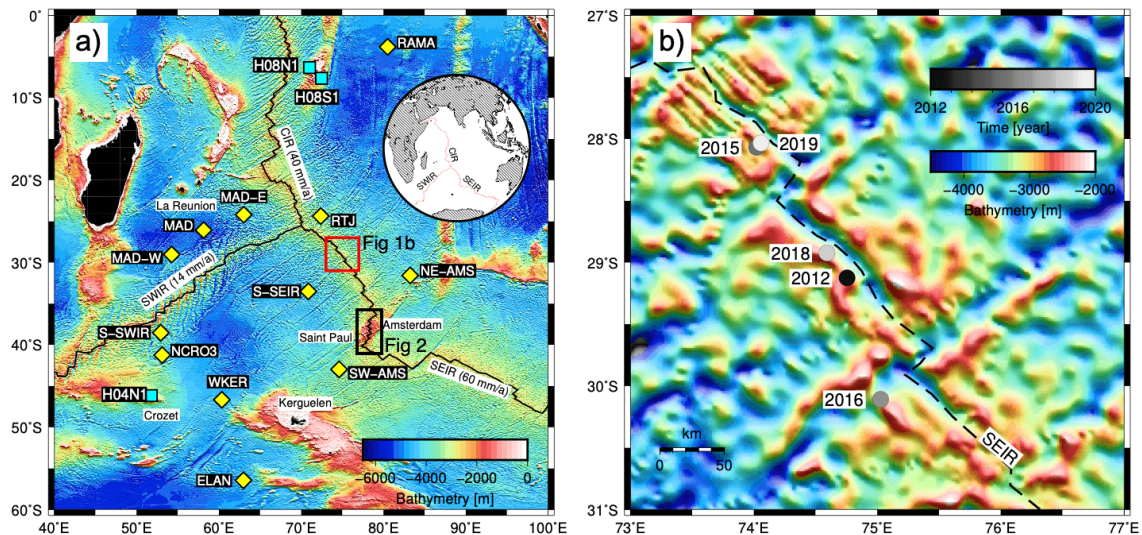


Figure 5.1: **a)** Hydrophone of the OHASISBIO (yellow diamonds) and IMS-CTBTO (blue squares) networks in the Indian Ocean. The black lines outline the Southwest, Central, and Southeast Indian ridges with their spreading rates. The red and black rectangles show the study area, extended in **b)** and in Figure 5.2, respectively. **b)** Median locations of five seismic clusters extracted from the ISC catalog between 2012 and 2020 (gray-scale) along the 28°S and 29°S segments. The dashed line shows the SEIR axis. Bathymetry is from the ETOPO1 grid (NOAA, 2009).

(Bohnenstiehl and Dziak, 2009). For instance, in the Northeast Pacific region, the Gorda Ridge consistently experiences seismic activity along its axis, while the Juan de Fuca Ridge has segments with minimal seismic activity (Dziak et al., 2012), despite both ridges sharing a similar spreading rate of 60 mm/yr.

Through terrestrial and hydroacoustic investigations (Royer et al., 2015; Tsang-Hin-Sun et al., 2016), it has been observed that seismic activity along the SEIR tends to concentrate in close proximity to the ridge axis, typically extending up to 10-20 km. The majority of seismic events occur at the ends of ridge segments and near the transform faults (Figure 1.20). The highest seismic activity is observed along the transform faults bordering the SPA plateau. Interestingly, the central regions of the ridge segments generally lack any seismic activity, except for one specific segment located 650 km away from the RTJ at 29°S. This particular segment has been consistently active since 1995. Notably, in July and December 2012, two clusters of hydroacoustic events were observed in this segment. These clusters were characterized by the absence of triggering mainshocks, brief periods of heightened seismic activity, and slight fluctuations in the source levels of events. They were interpreted as episodes of dike or magma emplacement occurring at shallow depths (Tsang-Hin-Sun et al., 2016). Also, a small number of normal faulting events were observed towards the end of the first cluster, possibly indicating the release of strain along pre-existing faults. Such clusters were then suggested as associated with an active volcanic structure and/or hydrothermal activity (Tsang-Hin-Sun et al., 2016).

Motivated by these findings, we expanded our investigation by examining the ISC catalog for additional seismic clusters in the vicinity of the 29°S segment. As a result, we identified three more clusters (Figure 5.1): one in October 2015, another in August-September 2018, and a third in August-September 2019. Among them, the 2018 cluster recurred at the center of the ridge segment at 29°S. On the other hand, the 2015 and 2019 clusters occurred at the center of a ridge segment located at 28°S, 90 km north of the previous one. In both the 2015 and 2018 clusters, a few events with either normal or reverse faulting mechanisms, as reported in the GCMT catalog, were observed. However, the 2019 cluster did not include any GCMT solutions.

South of the above-mentioned ridge segments, the SEIR interacts with a volcanic hotspot, the SPA plateau (Figure 5.2). This plateau has formed a volcanic massif that straddles the SEIR axis (Scheirer et al., 2000) and is elevated up to ~1.5 km above the ridge axis (Maia et al., 2011). To the north, segment H is offset from the plateau by the Amsterdam transform boundary. In the vicinity of this transform, we have extracted two recurrent seismic clusters, one that occurred in April 2012 and another in October-November 2012, comprising 11 and 6 ISC catalog events, respectively. The hydroacoustic results associated with these two clusters are presented in Appendix F. The SEIR segments I and J interact with the plateau and, after detailed bathymetric surveys, appeared to be divided into smaller segments (Scheirer et al., 2000; Baker et al., 2014). Four relatively short segments, I1, I2, J1, and some part of J2 run through the plateau. Their cross-axis morphology ranges from axial valleys to rifted axial highs. To the south, segment J3 featuring an axial valley a few kilometers wide forms an overlapping spreading center (OSC) with segment J4. J4 begins as an axial valley but changes to axial high including near-rectangular graben. OSCs represent a boundary along which en echelon segments overlap and are not joined by a transform fault (Sempere et al., 1984). At OSCs, accretionary processes occur along two curvilinear overlapping ridges axes, offset by 2–30 km over a distance of 10–50 km (Macdonald et al., 1992). The Miniature Autonomous Plume Recorder surveys reported active vent plumes on J3 and J4 segments using light-backscattering in the water column (e.g. Scheirer et al., 1998; Baker et al., 2014)). Based on the ISC catalog, we have found a seismic cluster, comprising 14 events, including 9 GCMT events, along the J3 segment in December 2020. It was the strongest seismic cluster observed in this section of SEIR over the last 10 years.

To investigate the seismic clusters from the low-level seismicity lacking in land-based catalogs due to their detection threshold, we analyzed hydroacoustic T-waves recorded by autonomous hydrophones of the OHASISBIO network as well as the permanent stations of the IMS-CTBTO network. By conducting a thorough analysis of this extensive and improved catalog of hydroacoustic events, we aim to gain a deeper understanding of the nature of seismicity occurring along the SEIR segments located at 28°S, 29°S, and 40°S. This comprehensive investigation will contribute to enhancing our knowledge about the seismic behavior along an intermediate spreading ridge.

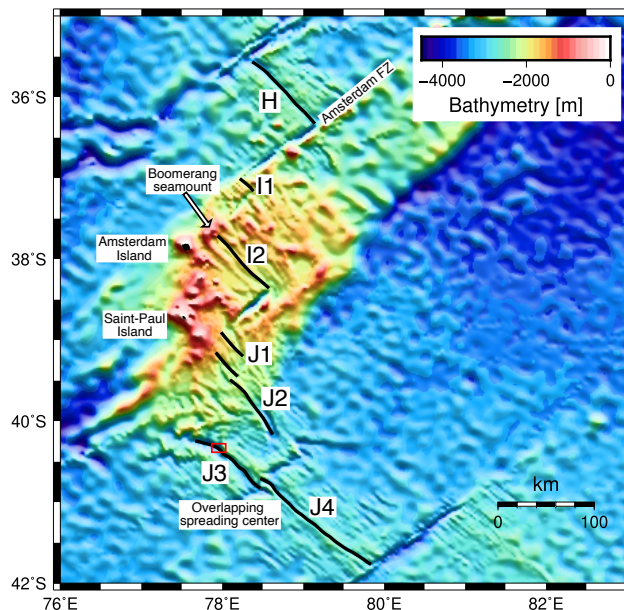


Figure 5.2: Regional map of SPA plateau intersecting with SEIR axis. The thick black lines mark the SEIR ridge segments (H, I, and J, from [Scheirer et al., 2000](#)). The red rectangle along the J3 segment marks the study region. Bathymetry is from the ETOPO1 grid ([NOAA, 2009](#)).

5.2 Data and Methods

Localization uncertainties

In this investigation, in addition to OHASISBIO hydrophones, we used one hydrophone from the H08S (H08S1), H04N (H04N3), and H01W (H01W1) triads of the IMS-CTBTO network (Figure 5.1, Table 5.2). As in the SWIR and CIR studies, we created the OHA catalog in two iterations, allowing for more exact manual re-picking of arrival times and hydroacoustic event relocation with increased precision. For all the events detected along the SEIR segments 29°S and 28°S between 2012 and 2019, the median errors were 6.08 km in latitude, 4.58 km in longitude, and 2.99 s in origin time; in the second iteration, the uncertainties reduced to 0.46 km, 0.33 km, and 0.23 s, respectively (Figure 5.3).

Magnitude of completeness

For the OHA catalog including all the events from the five clusters along the 28°S and 29°S segments, the SL of completeness (SL_C) was 220.5 dB for 978 events with a roll-off point of the Gutenberg-Richter fitting line at 493 (Figure 5.4). For a comparison with earthquake magnitudes, we considered all ISC events located along the section of SEIR, enclosed in the red rectangle in Figure 5.1a (i.e., in a similar tectonic context of ridge segments) for the years 2010 to 2020. This collection amounted to 241 ISC events vs. 978 OHA events detected in 68 days between 2012 and 2019. The

Year	2012	2015	2018	2019	2020
MAD-W	-	-	✓	✓	✓
MAD	✓	✓	-	-	-
MAD-E	-	-	-	✓	-
RTJ	-	-	✓	-	✓
RAMA	✓	-	-	-	-
NE-AMS	✓	-	✓	✓	✓
S-SEIR	-	✓	✓	✓	✓
SW-AMS	✓	✓	✓	✓	✓
ELAN	-	-	✓	✓	✓
WKER	✓	✓	-	✓	-
NCRO3	✓	-	-	-	-
S-SWIR	-	-	✓	✓	-
H08S	✓	✓	✓	✓	-
H08N	✓	-	-	-	-
H01W	✓	✓	✓	✓	-
H04N	-	-	✓	✓	-
Total	11	8	10	11	6

Table 5.1: Hydrophones from the OHASISBIO network used in 2012, 2015, 2018, 2019, and 2020. Note here that the WKER and SW-AMS stations had three hydrophones in 2012 and 2015, respectively.

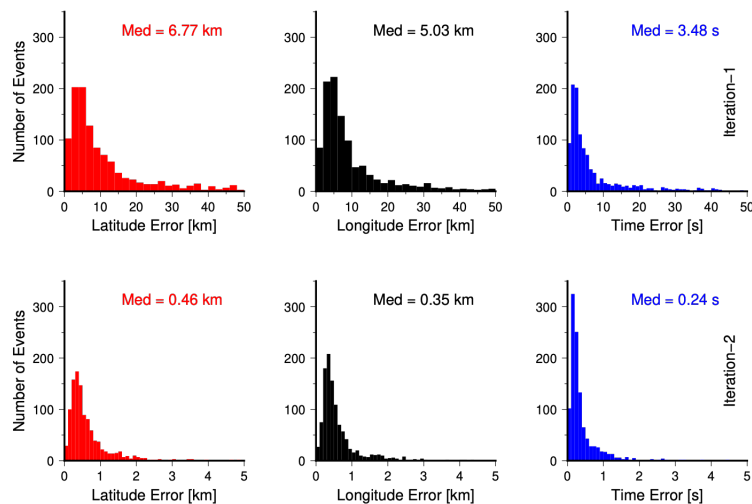


Figure 5.3: Errors obtained after acoustic triangulation in location (latitude and longitude) and origin time for all hydroacoustic events located along the SEIR (red rectangle in Figure 5.1a) after the first (top) and second (bottom) picking iterations. Note that the x-axis scales are different in both panels.

magnitude (mb) of completeness of the 241 ISC catalog events was $mb_{C(ISC)} = 3.9 mb$ and with an event distribution biased towards high magnitudes. We then estimated the equivalent magnitude of completeness for the OHA catalog $mb_{C(OHA)} = 3.5 mb$ by extrapolating the frequency-size distribution with a b -value = 1.32 from the ISC events up to the number of events defining SL_C . The total number of events from all five clusters detected by the OHASISBIO and IMS-CTBTO networks

over 68 days at two ridge segments is ~ 5 times larger than that detected by land-based networks over 11 years (2010-2020).

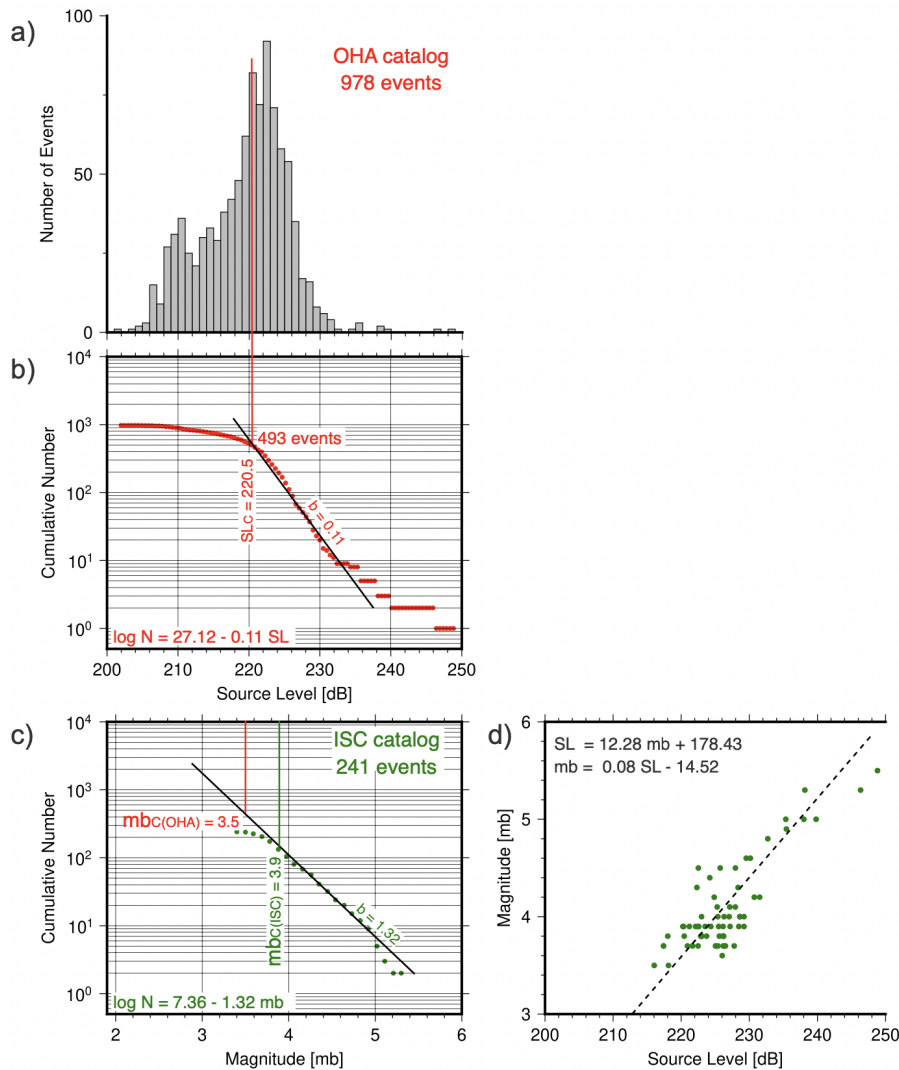


Figure 5.4: Completeness of source level (SL) and mb based on best-fitting Gutenberg–Richter's laws. **a)** SL distribution of the OHA events associated with five clusters between July 2012 and September 2019. **b)** Cumulative number of events in the OHA catalog. The vertical line points to the completeness, SL_C 220.5 dB with a b -value of 0.23 in the SL framework. **c)** Cumulative number of events in the ISC catalog reported from 2010 to 2020 (in the SEIR section within the red rectangle in Figure 5.1). The vertical line points to the magnitude of completeness $mb_{C(ISC)} = 3.9$. Extrapolating the Gutenberg–Richter's law of this ISC catalog up to the number of events for which the OHA catalog is complete (493 events) yields $mb_{C(OHA)}$ of 3.45. **d)** Regression between SL and mb , based on fitting the two Gutenberg-Richter lines, applied to events common in both terrestrial and hydroacoustic catalogs.

We also compared SL_C to that of completeness of different seismic magnitudes like M_s and M_w . Among the 241 events in the ISC catalog, only 116 events had a reported M_s , in the range of 2.8-5.3, with the completeness of $M_{sC(ISC)} = 3.4$ and a b -value of 1.11 (Figure 5.5b). Given the paucity of GCMT solutions, we had to convert all mb to M_w using the empirical relation shown in equation 4.1. After conversion for 241 events along the SEIR, M_w ranged between 2.7 and 5.6

with the completeness of $M_{wC(ISC)} = 3.4$ and a b -value of 0.92 (Figure 5.5c). After extrapolating the slopes of $b = 1.11$ for M_s and 0.92 for M_w up to the event count defining the SL_C (493), we obtained comparable completeness of 2.8 for both $M_{sC(ISC)}$ and $M_{wC(ISC)}$. The magnitude of completeness of the OHA catalog along the 28°S and 29°S segments surpass $mb_{C(ISC)}$ by 0.4, $M_{sC(ISC)}$ by 0.6, and $M_{wC(ISC)}$ by 0.6 demonstrating that hydrophone arrays are equally complete with respect to M_s and M_w .

As the J3 segment possesses a different tectonic setting as compared to that of 28°S and 29°S segments, we have compared the SL_C with that of $mb_{C(ISC)}$, $M_{sC(ISC)}$ and $M_{wC(ISC)}$ for the ISC catalog events residing in the close vicinity of the J3 segment between 2010 and 2020 (red rectangle in Figure 5.2). There were 93 events possessing mb , out of which only 70 showed M_s . Here again, we converted mb to M_w similar to the previous case. We obtained $mb_{C(ISC)} = 4.2$, $M_{sC(ISC)} = 3.8$ and $M_{wC(ISC)} = 3.8$ (Figure 5.6). In the OHA catalog, we obtained SL_C of 212.0 dB. After extrapolating the slopes of $b = 1.68$ for mb , 1.09 for M_s and 0.81 for M_w up to the event numbers defining SL_C (367), we obtained equivalent completeness of 3.7 mb , 3.2 M_s and 2.9 M_w , respectively. For this case, the OHA catalog is more complete with respect to M_w .

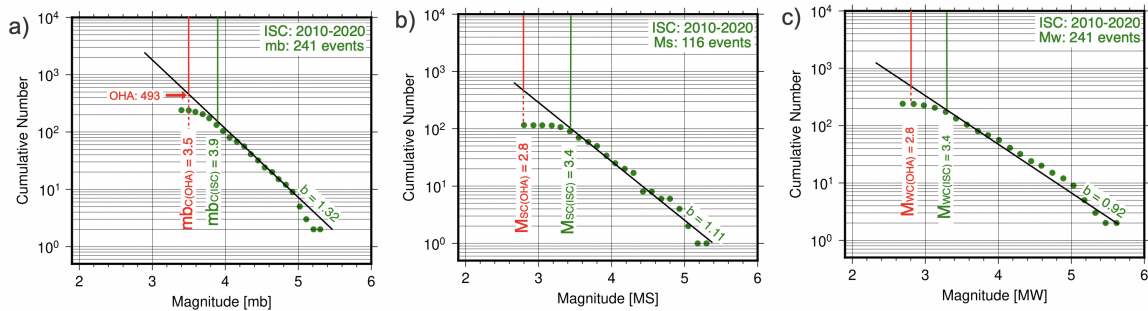


Figure 5.5: Completeness of source level (SL) and magnitudes based on best-fitting Gutenberg–Richter’s laws for the events along the 28°S–29°S segments of the SEIR. **a)** for body-wave magnitude scale (mb), **b)** surface wave magnitude (M_s) and **c)** moment magnitude M_w . SL_C were obtained for all the events from five seismic clusters along the SEIR and mb , M_s and M_w were obtained for the events between 2010 and 2020, residing along the SEIR (within the area bounded by the red rectangle in Figure 5.1a).

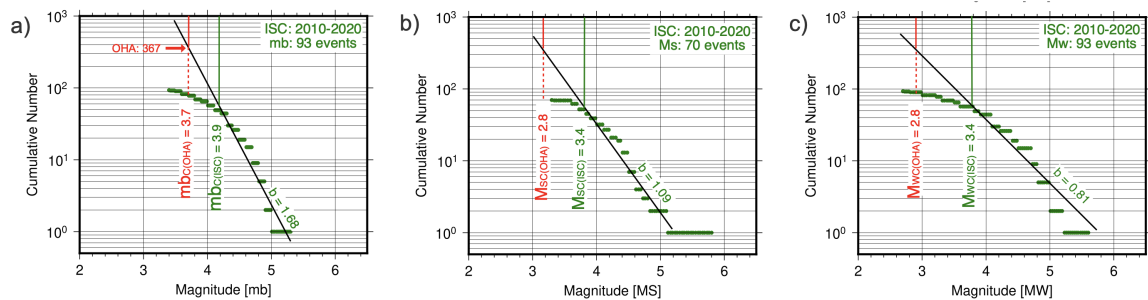


Figure 5.6: Completeness of source level (SL) and magnitudes based on best-fitting Gutenberg–Richter’s laws for the events along the J3 segment. Same legends as in Figure 5.5

5.3 Results

5.3.1 On SEIR Segment at 29°S

July 2012

Among the three clusters identified in the ISC catalog on the 29°S segment (Figure 5.1), the first occurred in July 2012, comprising 19 ISC and 2 GCMT events. The results presented here are an extension of the analysis done by [Tsang-Hin-Sun et al. \(2016\)](#). We have detected 452 events (Figure 5.7a) with SLs ranging between 208.0 and 230.4 dB. This catalog was complete at SL_C of 221.0 dB. The maximum events were detected by the nearest hydrophones at the NE-AMS and SW-AMS stations (S-SEIR was not installed yet), and the least was recorded by H01W1. These events were predominantly concentrated in the center of the ridge segment at 29°S and aligned in a northwest orientation, parallel to the ridge axis and to the azimuth of two normal faulting events. The activity started with 10 OHA events on 01 July and increased to 52 events on 04 July after an $mb = 3.9$ (SL = 222.6 dB) event (Figure 5.7c). Until the end of 04 July, both the number and SLs of events showed an increasing trend. Following this, 182 OHA events between 05 and 10 July showed an arbitrary pattern in their number as well as SLs. After a $mb = 3.8$ event on 10 July, the activity rate started increasing and reached its maximum on 11 July (90 events). Between 10 July and 11 July, 51 OHA events showed a slightly decreasing trend in their SLs. The seismicity was then followed by the two GCMT events on 12 July (M_w 5.0 and 4.9), only 7 minutes apart (16:18 and 16:25 UTC). The 55 events before the normal faulting events exhibited increasing SLs. After these GCMT events, the seismicity became weak and eventually ended by 13 July.

December 2012

In December 2012, another seismic cluster was observed along the same ridge segment and comprised 13 ISC events on 12 December, not strong enough to provide GCMT solutions. We then detected 76 OHA events within a span of 21 hours. Their SLs ranged from 210.4 to 230.0 dB with the completeness of $SL_C = 225.5$ dB. This cluster had slightly shifted further north, with event locations becoming denser, compared to that observed in July (Figure 5.7b). The activity was stronger in the first 6 hours (69 events), reaching a maximum of 18 events between 02:00 and 03:00 UTC. After 07:00 UTC, seismicity started decreasing and ended by 21:00 UTC (Figure 5.7d). The ISC events were observed continuously in this period.

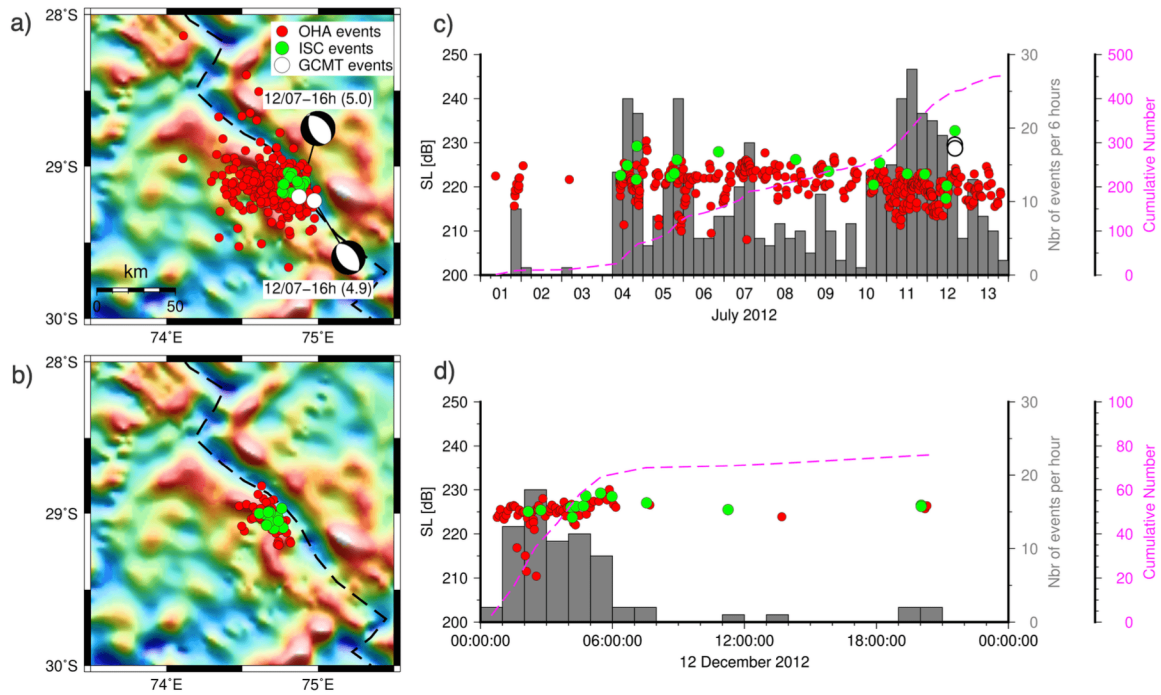


Figure 5.7: Locations of all GCMT (white), ISC (green), and OHA (red) catalog events detected in **a)** July 2012 and **b)** on December 12, 2012. GCMT events were only observed in July 2012. Temporal distribution of Source Levels of all the OHA, ISC, and GCMT events; histogram (gray) and cumulative number (pink line) of all detected events **c)** in July 2012 and **d)** on December 12, 2012.

August-September 2018

In 2018, another cluster of 21 ISC events including 3 GCMT events occurred between 26 August and 16 September 2018 along the same ridge segment. GCMT solutions showed one normal and two reverse faulting mechanisms. The two reverse faulting events (M_w 5.4) were located on a bathymetric high next to the ridge segment and a normal faulting event on the transform boundary, north of the segment. Hydroacoustic events based on 10 hydrophones amounted to 266 events between 21 August and 16 September (Figure 5.8a). The SLs were 202.0-248.8 with $SL_C = 214.3$ dB. The seismicity showed a spatial clustering of events between two ends: denser than those from July 2012 and wider than those from December 2012. Unlike in 2012 events, the 2018 ones showed an episodic trend in their temporal distribution (Figure 5.8b). The activity primarily started on 26 August, with 18 events before a cluster of 4 ISC events between 00:00 and 01:00 UTC on 27 August. It was then followed by 101 events until the end of 27 August, showing a decreasing trend in their SLs.

Between 28 and 30 August, the activity rate was very low, only comprising 12 events. Starting from 31 August, the number and SLs of OHA events have increased over time before the occurrence of M_w 5.4 reverse faulting event on 1 September. Although the activity rate decreased between 1 and 3 September, the SLs of events showed an increasing trend. Another small episode of height-

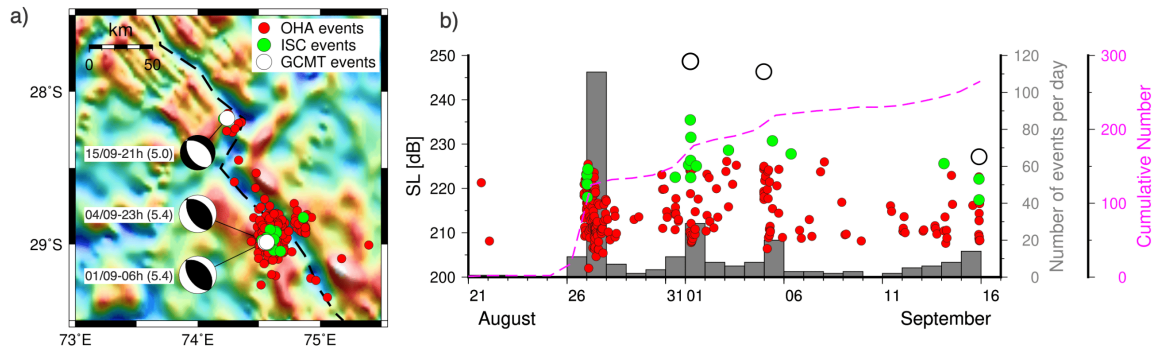


Figure 5.8: **a)** and **b)** Similar captions as that of Figure 5.9 for the events between August-September 2018. **c)** Stress modelling for M_w 5.4 reverse-faulting event on the SEIR ridge segment. White and pink circles show the events before and after M_w 5.4 event, respectively.

ened seismicity occurred after the M_w 5.4 reverse faulting event on 4 September. Following this, a gradual decrease in the frequency of events as well as their SLs was observed until 10 September. From 11 September, a steady increase in activity rate was observed until the normal faulting event (M_w 5.0) of the sequence on 15 September, after which the activity ceased.

5.3.2 On SEIR Segment at 28°S

October 2015

A seismic cluster comprising 10 ISC and 2 GCMT events occurred on 21-22 October 2015, at 28°S ridge segment, ~90 km north of 2012 seismic clusters. The GCMT events (with M_w 5.4 and 5.2) display normal faulting mechanisms parallel to the ridge axis (Figure 5.9a). The hydroacoustic analyses between 16 and 22 October yielded 110 events showing an 11-fold increase in the detection. The SLs range between 213.7 and 238.1 dB with $SL_C = 224.2$ dB. These events spread over a broader geographical area in the SW-NE direction, oblique to the ridge axis and centered on the ridge segment, bounded by two adjacent FZs. The strongest events formed a narrow patch along a trace on the SW side of the ridge axis, in the rift valley. A few of the small-magnitude events were localized parallel to the FZ, south of the ridge segment. The temporal distribution of events showed that activity started on 16 October with 9 events, and reduced between 17 and 20 October (Figure 5.9b). It then increased at the start of 21 October with 42 events and reached its maximum with 48 events after an M_w 5.4 event on 22 October at 00:32 UTC. Until the subsequent M_w 5.2 event at 07:50 UTC, the activity rate was high and suddenly dropped down afterward, until the activity ended on 22 October. In this case, both the GCMT and ISC events occurred primarily towards the end of the sequence, similar to the July 2012 cluster.

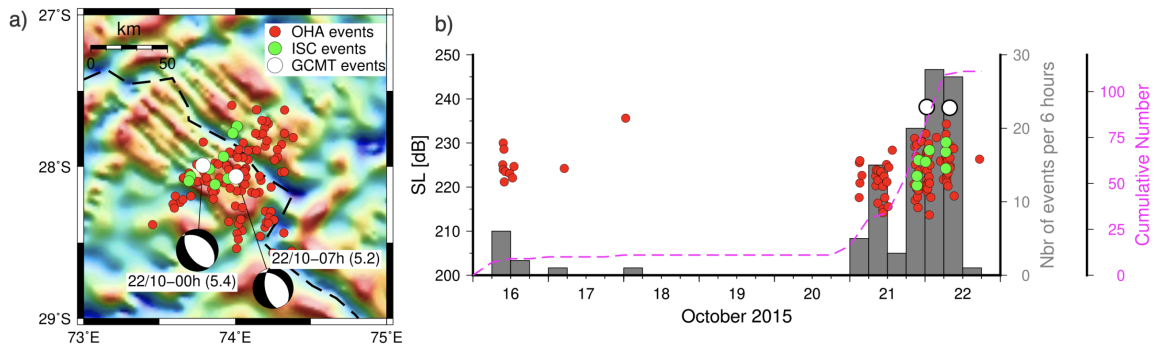


Figure 5.9: **a)** Locations of all GCMT, ISC, and OHA events detected in October 2015. **b)** Temporal distribution of source levels of all the OHA, ISC, and GCMT events; histogram (gray) and cumulative number (pink) of all the detected events.

August-September 2019

In 2019, a new cluster of 5 ISC events occurred on 12 September on the ridge segment at 28°S. We have detected 74 OHA events starting from 30 August to 12 September. Their SLs ranged between 203.5 and 239.8 with a completeness of 211.8 dB. These events showed a relatively dense geographical distribution compared with those observed in 2015 (Figure 5.10a). Here, the activity started mildly on 30 August with 11 OHA events. These events showed increasing SLs over time (Figure 5.10b). After that, a steady activity was observed till 11 September comprising only 24 events. It then intensified on 12 September with 16 OHA events prior to a cluster of 5 ISC events and followed by 18 OHA events. Here also, the strong ISC events occurred primarily towards the end of the sequence.

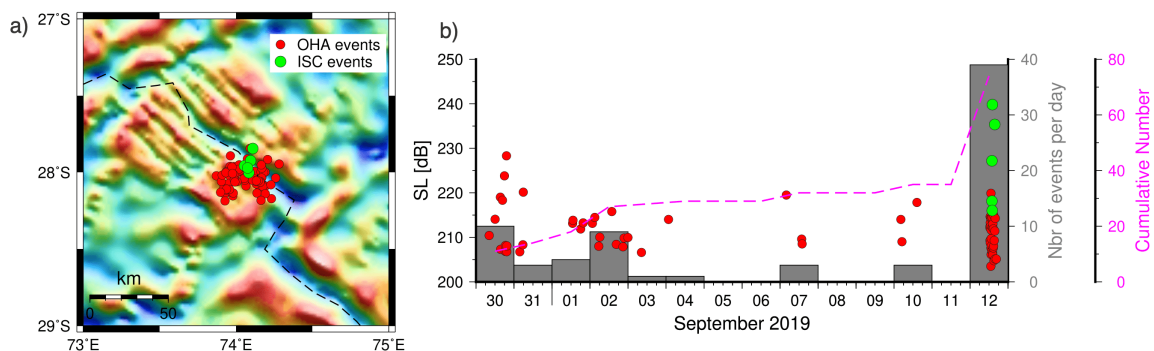


Figure 5.10: Similar captions as that of Figure 5.9a,b for the events between August-September 2019

5.3.3 On SEIR Segment at 40°S

December 2020

The ISC catalog has reported a cluster of 14 events between 3 and 14 December 2020 along the J3 segment at 40°S. Out of them, nine had GCMT solutions, with M_w 4.9 and 5.0, exhibiting normal

faulting mechanisms.

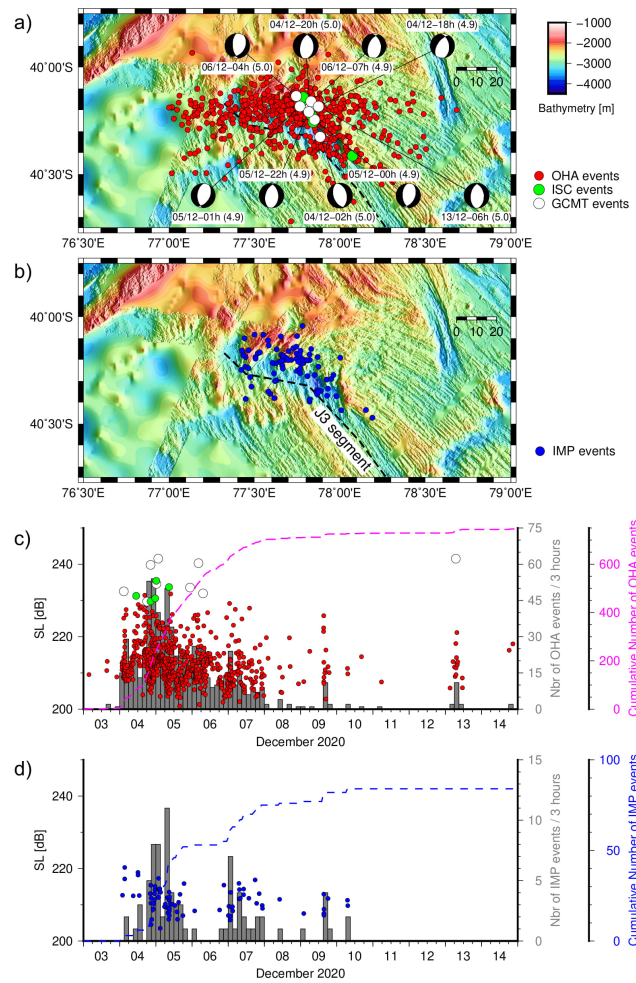


Figure 5.11: Locations of **a)** all the GCMT, ISC, and OHA as well as **b)** IMP events, were detected south of the SPA plateau along the J3 segment in December 2020. **c)** and **d)** SLs of the GCMT, ISC, OHA, and IMP catalog events. Three-hour histogram of **c)** OHA events and **d)** IMP events. Pink and blue lines mark the respective cumulative number of events. Combined bathymetric grids from [Scheirer et al. \(2000\)](#) and [Maia et al. \(2011\)](#), with additional tracks compiled with 150 m resolution by [Loubrieu Benoît, Royer Jean-Yves and Maia Marcia \(2020\)](#).

Using hydroacoustic data, we detected 745 OHA events (Figure 5.11a). Their SLs ranged from 199.8 to 241.5 with $SL_C = 212.0$ dB. None of the events were recorded on the ELAN station due to the topographic blockage by the Kerguelen plateau and a few events on the NE-AMS station due to the SPA plateau. The stronger events, in ISC/GCMT and OHA catalogs, were primarily situated along segment J3 where the SEIR axis abuts the SPA plateau. The spatial distribution of OHA events was wider in the longitudinal extent, spanning approximately ~ 130 km, and narrower in the latitudinal extent, covering around ~ 65 km (Figure 5.11a). This broader spatial distribution compared to the clusters at 28°S and 29°S may be due to a less favorable hydrophone array geometry as they were mostly situated east of the study region. This is also reflected by the distribution of localization errors (Figure 5.12). The errors in longitude are largely spread with a median value of 23.66 km,

which was ~ 5 times that of the median of latitude errors (5.01 km) in the first iteration. Also, this median longitude error is ~ 5 times higher than that observed along the 28°S-29°S segments, where it was (5.03 km; Figure 5.3). In the second iteration, although the errors in longitude improved to less than a km (0.68 km), they were still 2 times higher than those observed along the other two segments (0.35 km). These precise uncertainties are formal errors in both location and origin time estimation and do not represent the true uncertainties.

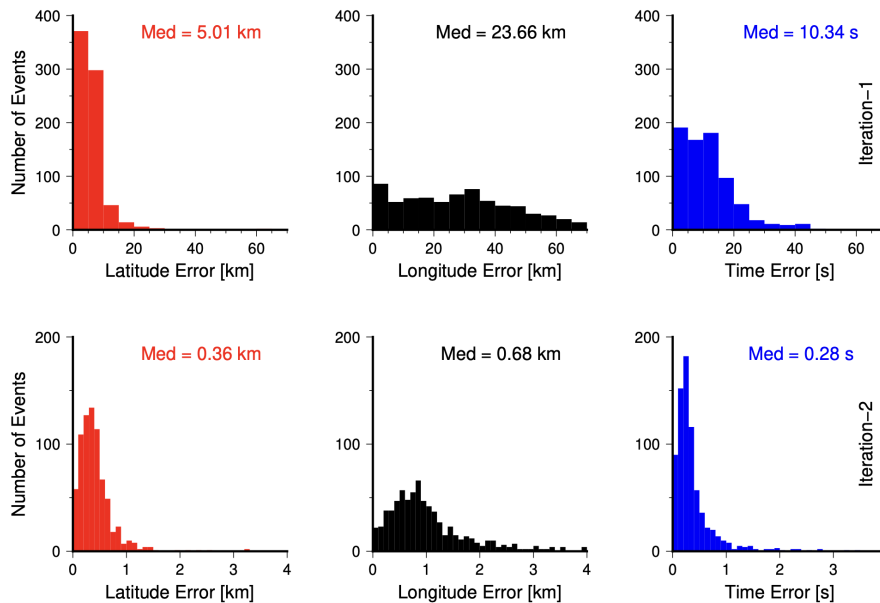


Figure 5.12: *Uncertainties obtained after acoustic triangulation in location (latitude and longitude) and origin time for all hydroacoustic events located along the J3 segment after the first (top) and second (bottom) picking iterations. The spread in longitude errors could explain the E-W wider distribution in seismicity, due to the geometry of the hydrophones, mostly west of the cluster. Note that the x-axis scales are different in both panels.*

In this cluster, we also detected 84 impulsive events (IMP), which were clustered in the same vicinity of ISC/GCMT events and are located on the slopes of bathymetric highs. The onset of this seismic activity including IMP events coincided with a normal faulting event with M_w 5.0 on 4 December at 02:44 UTC (Figure 5.11c,d). It was followed by intense seismic activity over the next four days. The activity of IMP events intensified following an M_w 4.9 event at 18:10 UTC and their SLs exhibited an increasing trend until 03:30 UTC on 5 December (for ~ 9 hours). The peak of IMP events coincided with a higher rate of seismicity for all OHA events on 5 December, before a $mb = 4.3$ event, then placid down until 6 December. There was another small episode of IMP events on 7 December. After 8 December, OHA events activity was mild, except for a small burst on 13 December coinciding with an M_w 5.0 event.

5.4 Discussion

5.4.1 Tidal effect on seismicity distribution

The events in 2018 at 28°S showed episodic occurrences in their temporal distribution (Figure 5.8b). Such episodic trends could be related to ocean and/or solid-Earth tide variations (Sahoo et al., 2021). For example, several studies have pointed out that increased seismicity occurred during low tides (e.g. Wilcock, 2001; Tolstoy and Bohnenstiehl, 2002; Wilcock, 2009). This has motivated us to compare the temporal distribution of events with tidal variations.

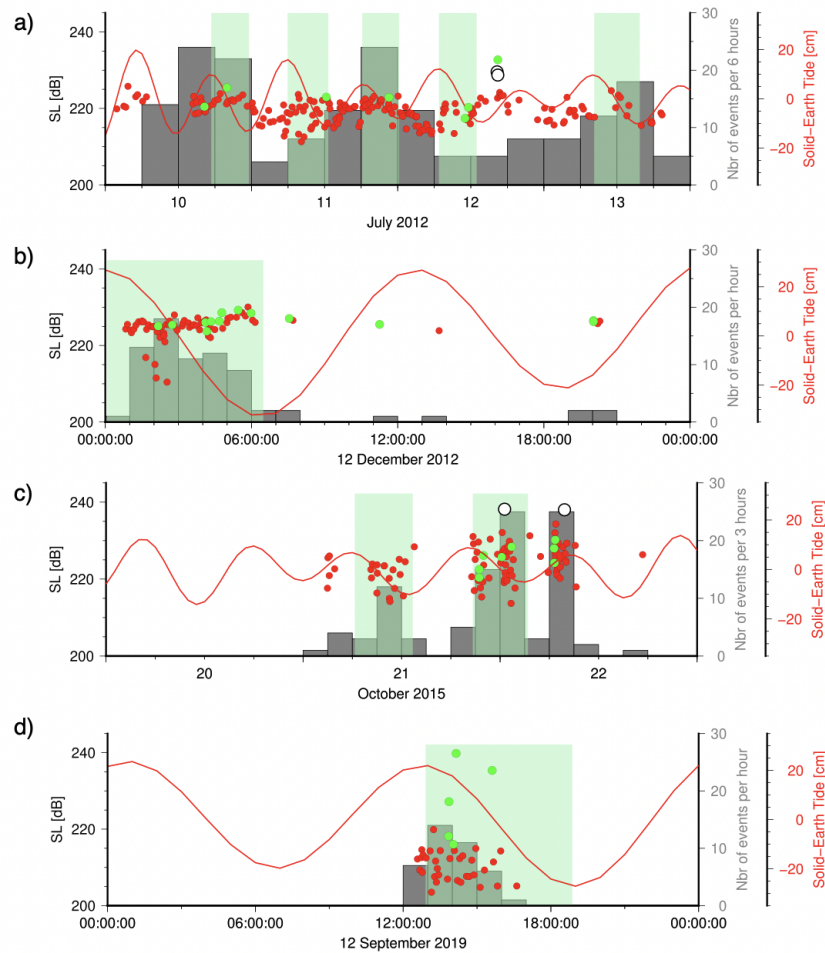


Figure 5.13: Comparison of solid-Earth tidal variations and the observed seismicity in the four seismic swarms along the 28°S and 29°S segments: **a)** July 2012; **b)** December 2012; **c)** October 2015; **d)** September 2019. In all four panels, SLs of OHA, ISC, and GCMT events are marked by red, green, and white circles, respectively. The number of events is shown by gray histograms. The solid-Earth tide (red curve) in **a),b)** was computed at the center of the 29°S segment and in **c),d)** at the center 28°S segment. The green shaded area marks the coincidence of higher seismicity during the total unloading (positive to negative amplitude).

We computed both the ocean and solid-Earth tidal variations at the center of 28°S and 29°S segments using the GOTIC2 program (Matsumoto et al., 2001). For the events in July 2012, activity was intense between 10 and 14 July. In this interval, the number of events was high during the

solid-Earth tidal unloading (tide varying from positive peak to negative), as shown in Figure 5.14a. There were two instances, one on 11 July and the other on 13 July, where SLs of events followed the same pattern as that of the tidal height. Moreover, on 12 December, the cluster of events occurred within the period of tidal unloading (Figure 5.14b). We observed similar observations of higher seismic activity at the periods of tidal unloading in 2015 and 2019 at 28°S which we assumed to have resulted from the same mechanisms (Figure 5.14c,d). During the solid-Earth tidal unloading, the earth's surface moves down and at the same time, the magma supply at the center of the ridge segment could have intensified from the underlying chamber, leading to a higher seismic activity (Métivier et al., 2009; Sahoo et al., 2021). A schematic showing the relation between tidal height and magma inflation along with increased seismicity is shown in Figure 5.14, (Sahoo et al., 2021).

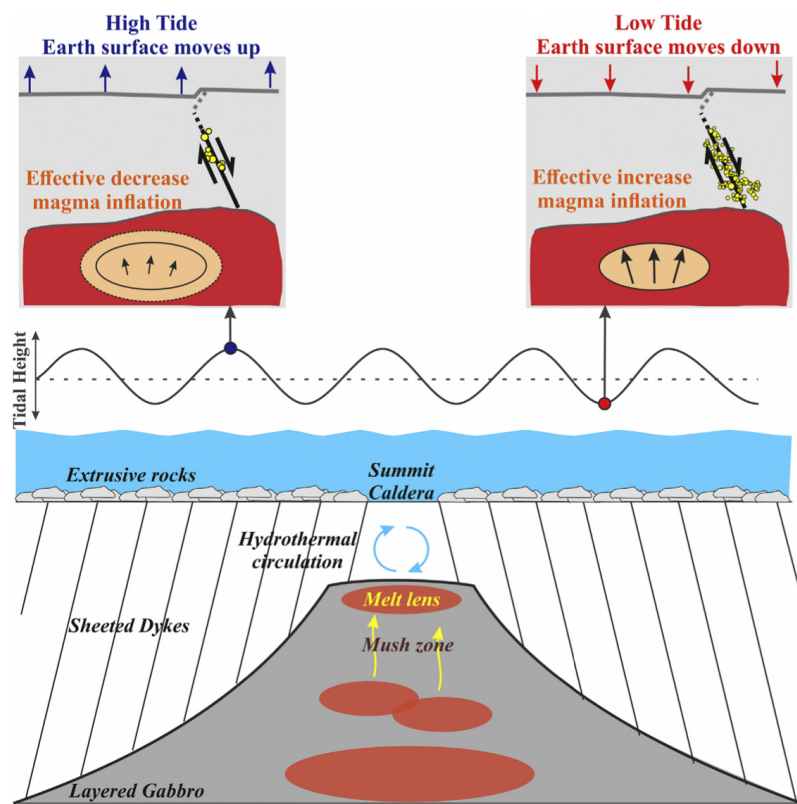


Figure 5.14: A conceptual model illustrating the dynamics of a magma chamber and the tidal influence: a decrease in magma chamber inflation at high tide and an increase at low tide (After Sahoo et al., 2021).

In 2018, the seismicity was both spatially and temporally clustered in the initial phase (26-28 August) along the 29°S segment. During this phase, 107 out of a total of 266 events on 27 August clustered in a small area at the center of the segment (Figure 5.15a). Such spatio-temporal clustering of events points to a magmatic dike intrusion, similar to that observed along the Juan de Fuca Ridge (Dziak et al., 1995; Bohnenstiehl et al., 2004). This magmatic episode might have corresponded with a magma chamber emptying. This small cluster of events concurred during tidal unloading (Figure 5.15d). Later on, the reverse faulting event on 01 September occurred during

the low tide. The events following it (till 22:00 UTC on 04 September) occurred in the wider region. Another reverse faulting event on 04 September (23:00 UTC) occurred during tidal loading (tidal height increase). Here also, successive events occurred in the wider spatial region. The wider distribution of events following the reverse faulting events could have resulted from the stress readjustment in the underlying crust after the magmatic episode (Rundquist and Sobolev, 2002).

Along the J3 segment, we did not observe any such tidal correlation.

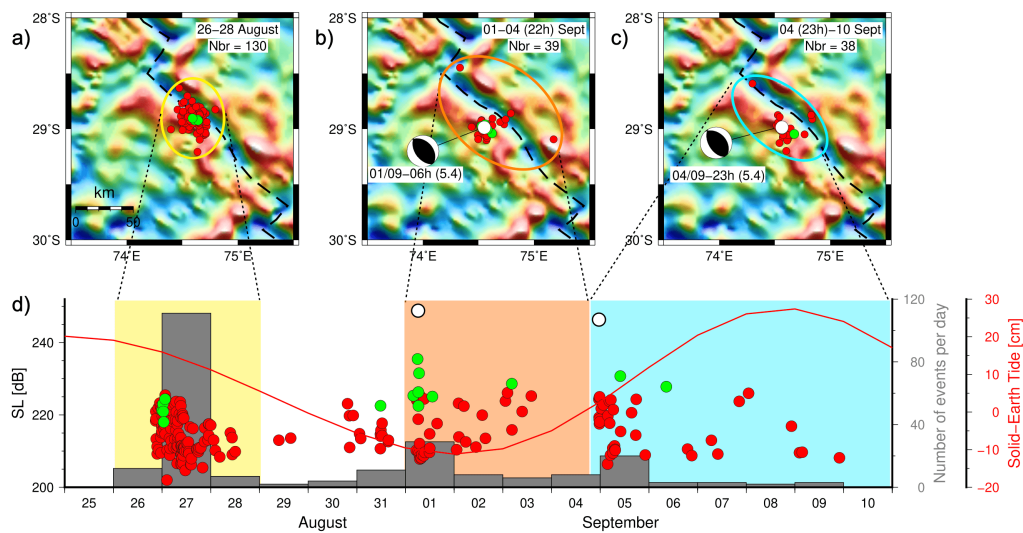


Figure 5.15: Spatial distribution of the events between 26 August and 10 September 2018 at the center of 28°S segment: **a)** 26 - 28 Aug; **b)** 01 Sept - 04 (22h) Sept; **c)** 04 (23h) Sept - 10 Sept. The spatial distribution in the respective cases is marked by yellow, orange, and blue ellipses. **d)** Comparison of the solid-Earth tide with respect to SLs and the number of events per day. The red, green, and white circles mark the SLs of OHA, ISC, and GCMT (reverse faulting) events respectively. The yellow, orange, and blue shaded areas mark the temporal outline for the events shown in **a)**, **b)**, **c)**, respectively.

5.4.2 Nature of seismicity and accretion process

Along the 28°S and 29°S segments

Swarms along ridge segments at 28°S and 29°S showed distinct characteristics, such as occurrence of low-magnitude (SL) events preceding stronger events (found in the ISC/GCMT catalogs), and high activity rate during tidal unloading. To the first order, we interpreted them as magmatic swarms, based on the spatio-temporal distribution of events, the lack of a tectonic mainshock-aftershock sequence (Sykes, 1970; Utsu et al., 1995; Schlindwein, 2012), weak variability in SL of the events (Tsang-Hin-Sun et al., 2016). Similar characteristics were observed during the Axial volcano eruption along the Juan de Fuca Ridge (e.g. Dziak et al., 1995; Dziak and Fox, 1999) and during the Krafla volcanic eruption in 1978 in Iceland (Einarsson et al., 1980). All five swarms occur at the center of ridge segments, where magmatic events are thought to focus (e.g. Cannat, 1996; Dziak and Fox, 1999; Goslin et al., 2012). We did not observe any impulsive event in these

swarms, which suggests that magmatic activity did not trigger any eruption on the seafloor. There was no significant difference in seismicity distribution along both segments. Additionally, the July 2012 swarm showed wider geographical distribution compared with the December 2012 swarm, and only the former one comprised GCMT events. Similarly, the 2015 swarm consisting of GCMT events showed wider distribution compared to the 2019 swarm. In both the December 2012 and 2019 swarms, we observed strong events (ISC) for a short period of time (less than a day). On the Lucky Strike segment along the MAR, such spatially dense swarms were interpreted as magma replenishment events (Dziak et al., 2004). The reverse faulting events that occurred in 2018 along the 29°S segment, were likely triggered by the inflation of the magma chamber, similar to that observed on the ridge segment at 26°N along the Mid-Atlantic Ridge (Kong et al., 1992).

Along the 40°S segment

We observed that the rate of seismicity increased after an M_w 5.0 normal faulting event on 4 December at 02:44 UTC, which was located in the axial valley along the J3 segment (Figure 5.16a). It was then followed by 619 events plus 75 IMP events until 8 December, when the cumulative distribution of events flattened down which became the potential candidate for the mainshock-aftershocks sequence (Figure 5.16b,c). These events were randomly scattered away from the M_w 5.0 event (although their longitude is imprecise). We computed modified Omori's law parameters for this sequence of events with the exclusion of IMP events and obtained a p -value of 1.77 (Figure 5.16c), suggesting that this event distribution represents a tectonic mainshock-aftershock sequence (Utsu et al., 1995; Schmid and Grasso, 2012). The high p -value could suggest increased hypocentral temperatures, similar to that observed along the CIR (Figure 4.16). The 15 foreshocks with lower SLs, which occurred a day before the mainshock, could have altered the stress regime within the crust, resulting in changes in the overpressure exerted on the magma body. As a consequence, this stress-induced scenario could have triggered the mainshock (Baer et al., 2008).

To comprehend the distribution of foreshocks and aftershocks to the stress changes (Figure 5.17) induced by the M_w 5.0 event, we predicted horizontal stress changes for M_w 5.0 normal-slip event with a dip-slip of 11 cm. From the two focal planes, we selected the fault plane that dips at 43° towards the axial valley. Assuming the hydroacoustic relocation with the depth taken from the GCMT catalog (19 km), this event imparted an extension onto the shallow crust below the J3 segment (Figure 5.17). We projected both foreshocks and aftershocks along a transect (A-A') perpendicular to the nodal plane, the former ones are placed 1 km below the seafloor and the latter ones at increasing altitudes according to their occurrence time. The predicted stresses in the shallow crust, 10 km north of the mainshock are weak and aftershocks are widely distributed (also potentially due to large formal longitudinal uncertainties), suggestive of widespread stress readjustments.

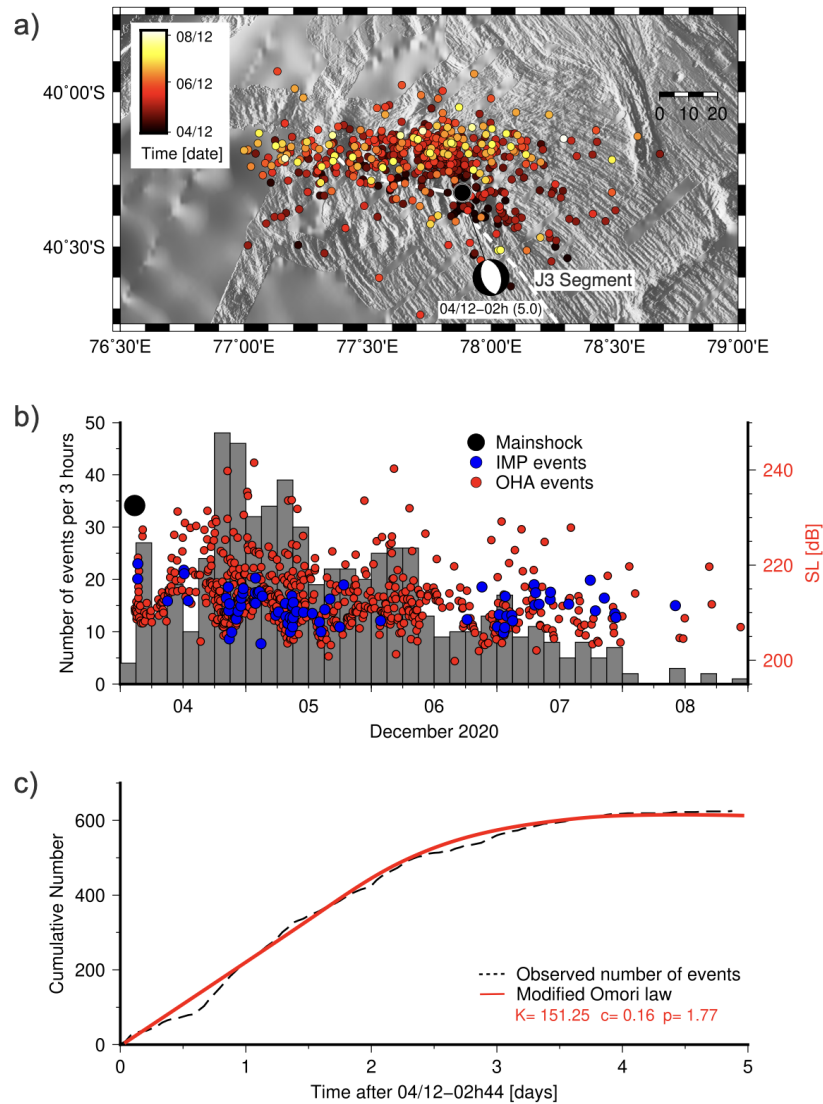


Figure 5.16: **a)** Spatiotemporal distribution of events between 4 and 8 December triggered after M_w 5.0 event. **b)** Histogram of the number of events per 3 hours along with SLs of the mainshock, aftershocks, and impulsive events. **c)** Hourly cumulative number of events (dashed line) vs. the best-fitting modified Omori's law (red line).

The remaining normal faulting events after the mainshock primarily occurred during an intense phase of seismic activity, and we propose that they have a magmato-tectonic origin as described by Rubin et al. (1998). The occurrence of tectonic sequence and impulsive events on the J3 segment (OSC along the SEIR) could be explained in the following manner. OSCs commonly manifest above regions characterized by diminished magma supply (Macdonald et al., 1992; Schouten et al., 1985). White et al. (2009) proposed that lower magma supply at OSCs results from diffuse volcanism and crustal deformation. However, observation of increased volcanic extrusion at the tip of the propagating limb at the 9°03'N OSC along the EPR (Kent et al., 2000; Bazin et al., 2003) suggests that the plate divergence along OSCs is mostly accommodated by substantial tectonic and magmatic activity, similar to that observed in our study.

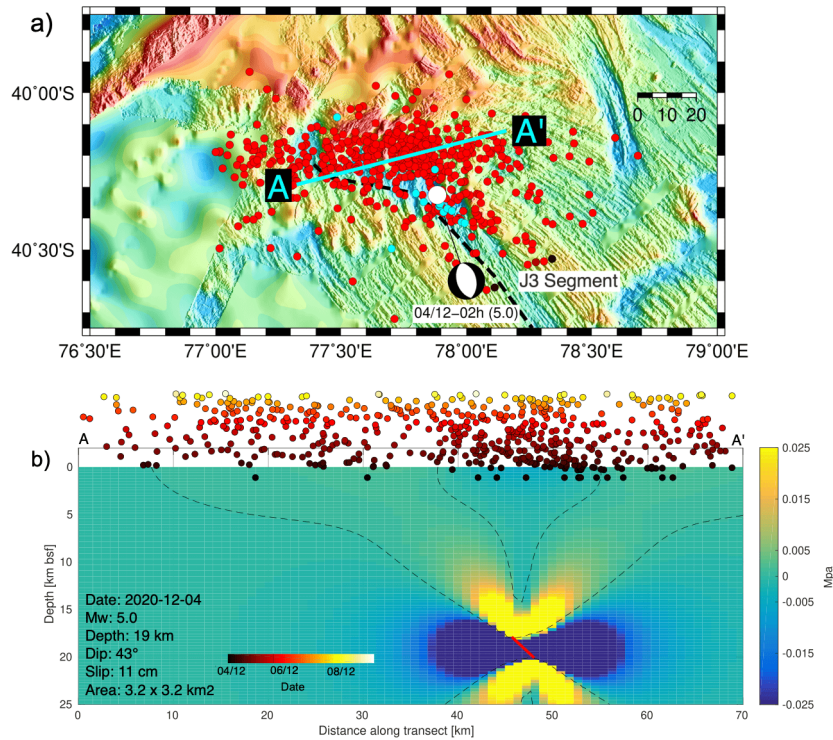


Figure 5.17: **a)** Locations of foreshocks (cyan), mainshock (white), and aftershocks (red) OHA along the J3 segment. **b)** A plausible geometry of the mainshock event on 04 December 2020 with fault plane dipping at 43° (thick red line). Contours show the predicted horizontal stress changes in MPa for an M_w 5.0 normal event at 14.9 km with a dip-slip of 11 cm over a 3.2×3.2 km² square patch embedded in an elastic half-space with Young's modulus and Poisson's ratio 100 GPa and 0.25, respectively (Olive and Escartín, 2016). The yellow color indicates areas under tension, allowing for local dike emplacements. The temporal distribution of foreshocks (plotted 1 km below the seafloor) and aftershocks (at increasing altitudes from the seafloor) after their projection along the A-A' transect (cyan colored line in a)).

We, therefore, interpret the seismic cluster along the J3 segment (OSC) as magmato-tectonic in origin. The presence of the mainshock-aftershock sequence points to tectonism (extensional faulting) and the impulsive events point to the formation of volcanic fissures and/or lava extrusion on the seafloor. Based on the stress modeling, an embedded aftershock sequence according to the MOL parameters points to an important role in stress re-adjustment (Hainzl and Fischer, 2002). Table 5.2 summarizes the results and possible interpretation of the swarms along the SEIR ridge segments studied in this chapter.

5.4.3 Repetitive nature of swarms

Magma ascent, in one case, could lead to strong volcanic eruption (Schmid et al., 2017), whereas, in cases, when it does not reach the surface, it could generate several magma intrusions (e.g. Schlindwein, 2012). Most of the seismic swarms are associated with such magmatic intrusions before the magma eventually erupts on the surface. During these intrusive phases, magma stalls at depth episodically, for several years or decades, as evidenced by occurrences of repeated seis-

Year	2012	2012	2015	2018	2019	2020
Date (dd/mm)	01/07-13/07	12/12	16/10-22/10	21/08-16/09	30/08-12/09	04/12-15/12
Median location	29.14°S, 74.78°E	29.02°S, 74.69°E	28.07°S, 74.02°E	28.92°S, 74.59°E	28.03°S, 74.06°E	40.21°S, 77.78°E
Nbr of days	13	1	7	27	14	13
Nbr of hydrophones	11	11	8	10	11	6
Nbr of ISC events	18	13	10	21	5	14
Nbr of GCMT events	2	0	2	3	0	9
Nbr of OHA events	452	76	110	266	74	745
Nbr of IMP events	-	-	-	-	-	84
OHA:ISC ratio	25	6	11	13	15	53
IMP:OHA fraction [%]	-	-	-	-	-	11
SL range [dB]	208.0 - 230.4	210.4 - 230.0	213.7 - 238.1	202.0 - 248.8	203.5 - 239.8	199.8 - 241.5
SL of completeness [dB]	221.0	225.5	224.2	214.3	211.8	212.0
Max events/day	90	-	57	107	39	250
Area (NS-EW) [km ²]	114 x 87	44 x 33	100 x 98	133 x 117	37 x 38	66 x 135
Interpretation	Magmatic intrusion without eruption					Magmato-tectonic with eruption

Table 5.2: Summary of seismicity results along the SEIR

mic swarms. Several teleseismically repetitive swarms observed on the Mid-Atlantic and Reykjanes ridges were considered as associated with magmatic intrusions (Bergman and Solomon, 1990). Along the SWIR (18°S-19°S), repeated swarms detected both teleseismically (Schlindwein, 2012) and by Neumayer seismic array (Läderach et al., 2011) were also interpreted as associated with magmatic intrusions. On land, significant repetitive magmatic swarms preceding large volcanic eruptions were observed. For example, swarms in La Palma on the Canary Islands (Torres-González et al., 2020), the Izu Peninsula in Japan (Nakada et al., 1999), Chaiten in Chile (Lange et al., 2008), Chichon in Mexico (Yokoyama et al., 1992), Paricutin in Mexico (Legrand et al., 2023), Krafla in Iceland (Einarsson et al., 1980) showed repetitive swarms before eruptions. Hence, the repeated swarms observed along 28°S and 29°S segments of SEIR could be associated with magmatic intrusions which may probably lead to volcanic eruptions in the axial valley.

Magma ascent, in one case, could lead to strong volcanic eruption (Schmid et al., 2017), whereas, in cases, when it does not reach the surface, it could generate several magma intrusions (e.g. Schlindwein, 2012). Most of the seismic swarms are associated with such magmatic intrusions before the magma eventually erupts on the surface. During these intrusive phases, magma stalls at depth episodically, for several years or decades, as speculated by occurrences of repeated seismic swarms (Dziak et al., 2012). Several teleseismically repetitive swarms observed on the Mid-Atlantic and Reykjanes ridges were considered as associated with magmatic intrusions (Bergman and Solomon, 1990). Along the SWIR (18°S-19°S), repeated swarms detected both teleseismically (Schlindwein, 2012) and by Neumayer seismic array (Läderach et al., 2011) were also interpreted

as associated with magmatic intrusions. Near the Axial Seamount along the Juan de Fuca Ridge, several magmatic swarms were observed between 2007 and 2011, prior to intense intrusive activity on 6 April 2011 (Dziak et al., 2012). On land, significant repetitive magmatic swarms preceding large volcanic eruptions were observed. For example, swarms in La Palma on the Canary Islands (Torres-González et al., 2020), the Izu Peninsula in Japan (Nakada et al., 1999), Chaiten in Chile (Lange et al., 2008), Chichon in Mexico (Yokoyama et al., 1992), Paricutin in Mexico (Legrand et al., 2023), Krafla in Iceland (Einarsson et al., 1980) showed repetitive swarms before eruptions. Hence, the repeated swarms observed along 28°S and 29°S segments of SEIR could be associated with magmatic intrusions which may probably lead to volcanic eruptions in the axial valley.

5.5 Summary of observations of the SEIR swarms

Based on the OHASISBIO and IMS-CTBTO hydroacoustic data, our analysis of seismic swarms along the intermediate spreading Southeast Indian Ridge segments of the SEIR, at 28°S, 29°S, and 40°S (J3 segment) brought down the following conclusions:

1. Repetitive swarms along the 28°S and 29°S segments that were interpreted as magmatic in nature based on the spatio-temporal distribution of events, the lack of a tectonic mainshock-aftershock sequence, and weak variability in the SL of the events.
2. Some of the events in these swarms occurred during tidal unloading favoring a magma supply beneath the center of the ridge segments.
3. Along the J3 segment, an overlapping spreading center, we detected a series of energetic and short-duration (10-15s) impulsive events. We interpret them as water-borne H-waves associated with hot lava-seawater interactions caused by dike intrusion reaching the seafloor. However, there is yet no *in situ* evidence to confirm any recent eruption along the J3 segment, which calls for future near-bottom surveys.
4. The presence of a tectonic mainshock-aftershock sequence along with the impulsive events on the J3 segment led us to interpret this seismicity as magmato-tectonic in nature, including dike emplacement on the seafloor or the formation of volcanic fissures.

5.6 Résumé des observations sur les essais SEIR (En français)

Sur la base des données hydroacoustiques de OHASISBIO et IMS-CTBTO, notre analyse des essais sismiques le long des segments de la dorsale intermédiaire du Sud-Est Indienne, à 28°S, 29°S et 40°S (segment J3), conduit aux conclusions suivantes :

1. Les essaims répétés le long des segments 28°S et 29°S sont interprétés comme étant d'origine magmatique d'après la distribution spatio-temporelle des événements, l'absence de séquences choc-répliques, et la faible variabilité du niveau source des événements.
2. Certains événements dans ces essaims ont lieu pendant le déchargement tidal, favorisant la (ré-)alimentation des chambres magmatiques sous le centre des segments de la dorsale.
3. Sur le segment J3, on observe une série d'événements impulsionnels énergétiques et de courte durée (10-15 s). Nous les interprétons comme des ondes H associées à des interactions entre la lave chaude et l'eau de mer causées par l'intrusion de dykes atteignant le plancher océanique. Cependant, il n'y a encore aucune preuve in situ confirmant une éruption récente le long du segment J3, qui demanderait des observations directes fond de mer.
4. La présence d'une séquence choc-répliques aux côtés des événements impulsionnels sur le segment J3 nous conduit à interpréter cette sismicité comme étant de nature magmato-tectonique, y compris l'emplacement de dykes sur le plancher océanique ou la formation de fissures volcaniques.

Chapter 6

Discussion

6.1 Contribution of hydroacoustics

Magmatism and extensional faulting are the two fundamental processes governing the dynamics of MORs. The identification of magmatic intrusions and occurrences of rifting along MORs holds significant importance for our comprehension of the global rate of geodynamical activities along the MORs. Equally important is the transient yet impactful influence these processes exert on the physical and chemical aspects of oceanic and seafloor ecosystems. Since many magmatic and rifting processes occur completely submerged, they can easily pass unnoticed. Even when eruptive products reach the sea surface (volcanic eruptions) and are recorded by satellites or noted by observers, the remote locations of the eruptions may make the source hard to pinpoint. The seismicity generated during such processes into brittle oceanic crust goes largely undetected by terrestrial seismic networks, generally too remote to capture events with $mb \leq 4$. As observed in the last three chapters, hydrophones moored in the SOFAR channel provide an effective means for detecting lower-magnitude earthquakes, down to $mb \sim 3$.

In this study, we have focused on the characterization of seismic swarms along the three Indian MORs. The key parameters for comparing each of the swarms are the magnitude of completeness, the temporal distribution of events that fit a modified Omori's law, and the presence or absence of impulsive events. Based on these criteria, we were able to distinguish the swarms into three main categories, magmatic, tectonic, and magmato-tectonic swarms. The following sections elaborate on each of these parameters.

6.1.1 Magnitude of completeness

As observed in the previous chapters, the magnitude of completeness varies from one swarm to another. Table 6.1 compares the completeness of OHA catalogs with that of extended 11-year-long ISC catalogs (2010-2020). In this period, 1933 events were reported along the SWIR axis, with a uniform distribution of events. Along the CIR, 491 events primarily clustered near hydrothermal fields. Along the SEIR axis, 241 events clustered on the 28°S-29°S segments and 93 events near the J3 segment (both regions are tectonically different). In the extended ISC catalogs, only a few events were reported with a surface magnitude M_s (1022 on the SWIR, 392 on the CIR, 116 on 28°S- 29°S segments and 70 on the J3 segment), and even less with a moment magnitude M_w , for which, when it was lacking, we converted mb to M_w . The resulting $mb_{C(ISC)}$ varied between 3.9 and 4.2. The $M_{sC(ISC)}$ as well as $M_{wC(ISC)}$ ranged from 3.4 to 3.8. Along the SWIR, we computed the completeness values of individual OHA catalogs with that of an 11-year-long ISC catalog, except for near the Novara TF, since there were fewer events (1109) than in the ISC catalog (1933). The plots comparing the magnitude of completeness of OHA catalogs along the SWIR with that of the ISC catalogs are shown in Appendix E. Along the CIR, since the number of events in individual OHA catalogs was less than in the extended ISC catalog, we merged the OHA catalogs to derive their completeness (Figure 4.4). We applied a similar approach for the events along the 28°S-29°S segments of the SEIR (Figure 5.5). We have compared the OHA catalog from 2020 along the J3 segment with that of the extended ISC catalog in its vicinity (Figure 5.6).

For the different OHA catalogs, the equivalent magnitude of completeness ($mb_{C(OHA)}$) ranged between 3.4 and 3.7 mb , the least near the Melville TF and the highest along the J3 segment. Based on these observations, the magnitude of completeness does not depend on the ratio of the number of events in the OHA and the extended ISC catalog. For example, near the Melville TF and along the CIR, this ratio was 14 (27624 vs. 1933) and 7 (3574 vs. 491), respectively; however, in both cases, the $mb_{C(OHA)}$ was 3.3 mb . The $M_{sC(OHA)}$ followed the same pattern, least near the Melville TF (M_s 2.1) and highest along the J3 segment (M_s 3.2). On the other hand, $M_{wC(OHA)}$, based on the conversion from mb to M_w , was the least near the Melville TF (M_w 2.4) and the highest along segment4 at 67°45'E (M_w 3.0). The lower value of completeness near the Melville TF could result either from a large number of events or the lower SL_C .

This shows that the OHA catalogs are more complete with respect to M_{sC} , followed by M_{wC} , and the least complete for mb_C . Broadly speaking, M_C of the OHA catalogs was the least along the SWIR, higher along the CIR, and the highest along the SEIR, probably due to the number of OHA events (which were highest along the SWIR, followed by CIR and then SEIR). Such different values of MC do not convey the distribution of the events in the different spreading (or tectonic) contexts. The seismic magnitude of an earthquake estimates the energy release (elastic wave propagation)

Region	N_{OHA}	N_{mb}	SL_C	$mb_{C(ISC)}$	$mb_{C(OHA)}$	$M_{sC(ISC)}$	$M_{sC(OHA)}$	$M_{wC(ISC)}$	$M_{wC(OHA)}$
Novara TF	1109	231	212.8	3.9	3.4	3.6	2.5	3.5	2.8
Melville TF	27624	258	206.6	4.1	3.3	3.4	2.1	3.8	2.4
Seg 4 at 67°45'E	4880	92	209.5	4.1	3.6	3.4	2.6	3.8	3.0
Along the CIR	3574	171	211.7	3.9	3.3	3.5	2.8	3.4	2.5
28°S and 29°S seg	978	68	220.5	3.9	3.5	3.4	2.8	3.4	2.8
J3 segment	745	14	212.0	4.2	3.7	3.8	3.2	3.8	2.9

Table 6.1: Summary of the detection thresholds of each seismic swarm along the three Indian Ocean ridges in terms of the SL equivalent magnitude of completeness. N_{OHA} and N_{mb} denote the number of events in hydroacoustic (OHA) and land-based ISC catalog for the respective swarms along the three ridges. The SL magnitudes of completeness are derived from the comparison of SLs with the different magnitudes of events in the ISC catalog.

as a function of the size and displacement on a fault plane. In addition, the Source Level reflects the efficiency of the seismic to acoustic wave conversion at the seafloor and the multiple interactions of the latter with the propagating medium. This means that SL does not provide an actual estimate of the energy released by an earthquake. As mentioned in Table 6.1, variations in SL_C do not directly imply the detection of any small or large magnitude earthquakes.

To have a better estimate of the magnitude of completeness of the hydroacoustic catalogs built up in this study, we combined the events from all 15 swarms along the three ridges. Merging these events should yield completeness unbiased by different instrumental sensitivities in different periods of detection. The combined OHA catalog consisted of 38,910 events and Gutenberg-Richter fitting has yielded a SL of completeness (SL_C) of 206.2 dB and an averaged b -value = 0.09 since the slope is variable. This b -value is much smaller than the ones found on individual swarms or groups of swarms (0.20). The roll-off point of the Gutenberg-Richter relation for the observed event distribution would then be 27,978 (Figure 6.1). To compare it with the ISC catalog completeness, we considered all ISC events along the three Indian Ocean ridges between 2010 and 2020, comprising 2798 events. We used such an extended ISC catalog because the number of ISC events (834) in the 15 swarms only would be too small for a meaningful comparison, furthermore biased towards high magnitudes. The magnitude of completeness of the ISC catalog was $mb_{C(ISC)} = 3.9 mb$. By extrapolating the frequency-size distribution with a b -value = 1.27 of the ISC events up to the roll-off point of the hydroacoustic catalog, we obtained an equivalent magnitude of completeness for the OHA catalog of $mb_{C(OHA)} = 3.1 mb$. This showed an improvement of 0.8 mb to the magnitude of completeness for the hydroacoustic catalog. A similar analysis of extrapolating the b -value of ISC events' distribution up to the roll-off point was performed for the events near the Melville TF (Ingale et al., 2023).

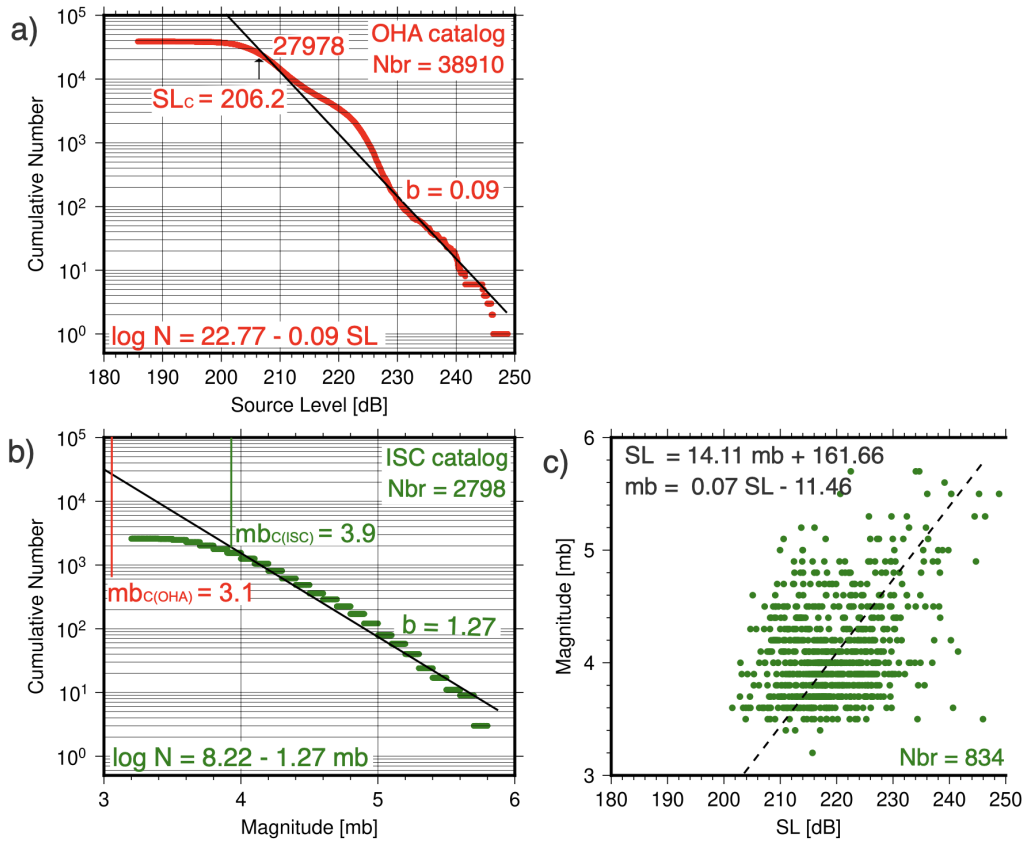


Figure 6.1: *Completeness of source level (SL) and mb based on best-fitting Gutenberg–Richter's laws for all the events from total 15 swarms of this study. a)* Cumulative number of events in the OHA catalog. The vertical line points to the completeness, SL_C 206.2 dB with a b -value of 0.09. *b)* Cumulative number of events in the ISC catalog reported from 2010 to 2020 along the three Indian Ocean ridges. The vertical line points to the magnitude of completeness $mb_{C(ISC)} = 3.9$. Extrapolating the Gutenberg–Richter's law of this ISC catalog up to the number of events for which the OHA catalog is complete (27978 events) yields $mb_{C(OHA)}$ of 3.1. *c)* Regression between SL and mb, based on fitting the two Gutenberg–Richter lines, applied to events common in both terrestrial and hydroacoustic catalogs.

6.1.2 Spatial variation in b -values

The Gutenberg-Richter relationship tells about the size-frequency distribution of earthquakes. The intercept a and slope b (positive value by convention although it is a downward line) of the fitting line between magnitudes M and the cumulative number of earthquakes N with magnitudes $\geq M$ are empirical constants. The a -value is contingent upon the total number of events, acting as an indicator of the seismicity rate. The b -value regulates the frequency of smaller earthquakes relative to larger ones. Similar to continental earthquakes, seismic events occurring along MORs also adhere to the Gutenberg-Richter law (Francis, 1968). Several OBS surveys along different MORs have reported b -values in different tectonic settings (summarized by Bohnenstiehl et al., 2008). It shows that the b -value varies from 0.75, along the transform fault (Cessaro and Hussong, 1986) to 1.65 at the center of the ridge segment (Kong et al., 1992). Nearly two decades ago, Bohnenstiehl et al. (2002) established an empirical size-frequency relationship based on the Source Level of hy-

droacoustic events (equation 2.12), which we extended to our datasets. To elaborate more on the b -value, we have attempted to compute its spatial variation in each of the swarms. For this we have designed the following criteria:

1. Divide the events from individual swarms along all three Indian MORs in grid-cells of 0.25 degrees in latitude and longitude.
2. Near the Kairei HF along CIR, we merged two swarms that occurred in different time periods (Feb-May and Nov-Dec 2013) to calculate b -values, as a larger number of events per grid will enhance its representativeness and this will help to characterize the nature of oceanic crust in the HF's vicinity.
3. Likewise, in order to elucidate the characteristics of ridge segments along the SEIR, we combined the events from both the 2015 and 2019 swarms that occurred on the 28°S segment. Furthermore, we merged the events from July 2012, December 2012, and 2018 swarms occurring on the 29°S segment.
4. If the number of events per grid-cell is less than 5, we did not calculate a b -value.

We calculated the b -value by fitting a straight line to the Gutenberg-Richter-like cumulative distribution of SLs for the three ridges (Table 6.2), where it is quite similar. In order to discern a pattern in different tectonic contexts, we compared three distinct settings: first along the transform faults (TF) such as Novara and Melville TFs on the SWIR (Figure 6.2); second on the ridge segments like segment 4 (67°45'S) along the SWIR, segments 28°S-29°S on the SEIR and segments 8-9 (21°30'S) along CIR at (Figure 6.3); the last near the hydrothermal fields such as Kairei and Edmond on the CIR, and Pelagia on the SEIR (Figure 6.4).

Ridge	SWIR	CIR	SEIR
Min number of events/grid-cell	6	5	5
Max number of events/grid-cell	7238	381	319
Min b -value/grid-cell	0.04	0.04	0.05
Max b -value/grid-cell	0.28	0.28	0.34

Table 6.2: Summary of b -value computed along SWIR, CIR, and SEIR

Before interpreting b -values in terms of tectonic contexts, it is necessary to examine the distribution of events and SLs in a grid-cell from which b -values were derived. For the same number of events, b -values were very different in each of the swarms. As an illustration, within a swarm along the Novara Transform Fault, two distinct grid-cells exhibited 6 events and their respective b -values were 0.16 and 0.06 (Figure 6.2a). In another example, on segments 8-9 along the CIR, 41 events in

two different grid-cells showed b -values of 0.06 and 0.12 (Figure 6.3d). Conversely, different numbers of events per grid-cell may yield similar b -value, e.g. $b = 0.10$ was observed for both 6 and 138 events per grid-cell (Figure 6.2a). As mentioned earlier, b -values depend on the proportion of lower to higher SLs of events. The range of SL within a grid also varies a lot irrespective of the number of events per grid-cell (Table 6.3). For example, in the Novara TF swarm, 138 events in a grid-cell having a difference of ~ 6 dB in their SLs with the completeness of SL_C 212.2 dB showed a b -value of 0.10. In the same swarm, 26 events in another grid-cell having ~ 29 dB difference in their SL with the same SL_C yielded a similar b -value of 0.10. This shows that b -values derived from a small number of events with a wide range of SL, or from a large number of events with a small range of SL may not be representative. Hence, instead of interpreting the b -values for each swarm, we have obtained a general overview of their spatial distribution in three different tectonic settings: near transform faults, along ridge segments, and near hydrothermal fields.

Tectonic context	Transform fault		Ridge segments				Hydrothermal fields		
	Novara TF	Melville TF	67°45'E seg	28°S seg	29°S seg	21°30'S seg	Pelagia	Kairei	Edmond
min(δ SL) [dB]	5.9	4.9	9.9	6.5	3.5	8.6	12.6	7.34	3.88
Nbr for min(δ SL)	138	240	6	19	32	31	14	5	10
SL_C for min(δ SL)	212.2	204.0	219.2	216.4	218.4	210.5	206.6	220.1	211.4
b for min(δ SL)	0.10	0.09	0.08	0.08	0.17	0.10	0.12	0.15	0.08
max(δ SL) [dB]	28.9	41.2	44.0	32.14	54.17	22.72	37.7	38.9	40.9
Nbr for max(δ SL)	26	3978	121	41	319	126	33	258	381
SL_C for max(δ SL)	212.2	207.4	217.3	219.4	221.3	211.0	212.6	219.5	211.8
b for max(δ SL)	0.10	0.23	0.09	0.16	0.28	0.11	0.04	0.08	0.04

Table 6.3: Summary of b -value computed in different tectonic contexts for minimum and maximum range of SLs

Near transform faults

For the events near the Novara and Melville transform faults along the SWIR, we observed large variations in the b -values (Figure 6.2). Within a single swarm, we observed a large heterogeneity in the spatial distribution. The b -values ranged between 0.10 and 0.45 near the Novara TF and from 0.06 to 0.29 near the Melville TF. The results of the Melville case may be more representative than the Novara case thanks to greater SL characteristics. Along the Melville TF itself, b -values were relatively low (0.08 to 0.15) with respect to the surrounding crust (0.06 to 0.29). Similar observations of lower b -values along the TF were made along other mid-ocean ridges. For example, from the land-based catalogs Francis (1968), and microearthquakes detected using OBSs, Cessaro and Hussong (1986) observed lower b -values along the TF.

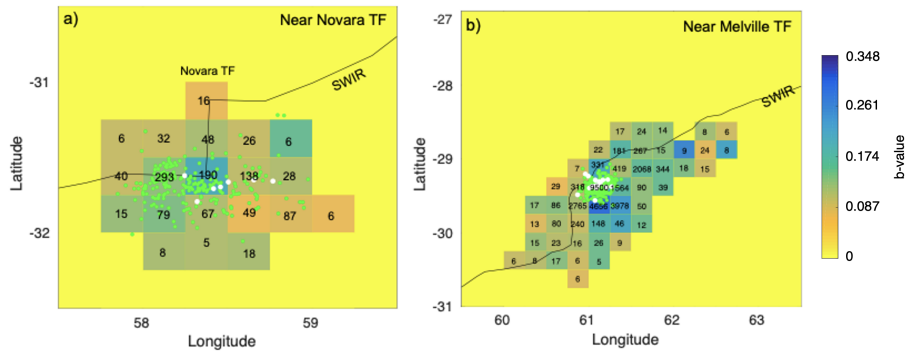


Figure 6.2: Spatial variation in the b -values computed for the events per quarter of a degree in latitude and longitude **a)** along the segment 18 near Novara TF and near **b)** near the Melville TF. The number of events per grid-cell is specified for representation. Hydroacoustic locations of ISC/GCMT events are shown by green/white circles.

Along ridge segments

We have compared the b -values along the 4 different ridge segments, one each along the SWIR and CIR, and two along the SEIR (Figure 6.3). All of them showed higher b -values in the proximity of segment centers, with a maximum ($b = 0.34$) along the 29°S segment center of SEIR. Three out of them (excluding the CIR segment), also showed higher b -values in the vicinity of the ISC/GCMT events clusters. Several observations of high b -values were made along the Mid-Atlantic Ridge segments (e.g. Francis, 1974; Kong et al., 1992). Also, a high b -value is generally associated with the magmatic processes as they generate several low-magnitude events (Tolstoy et al., 2001).

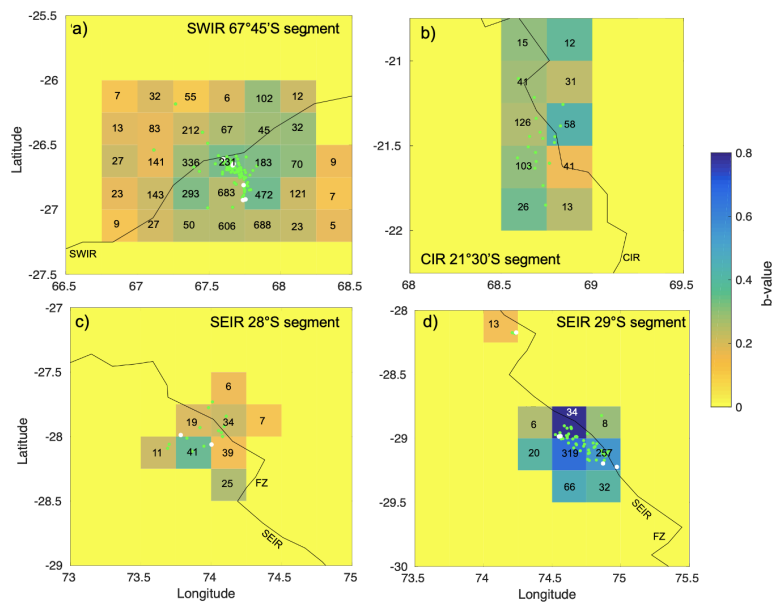


Figure 6.3: Spatial variation in the b -values computed for the events per quarter of a degree in latitude and longitude on the ridge segments on **a)** along the SWIR, **b)** along the CIR and **c), d)** along the SEIR. Same legends as in Figure 6.2

Near hydrothermal fields

In the vicinity of Kairei and Pelagia hydrothermal fields (HF), b -values were the same (0.12) and it was the least near the Edmond HF (0.04). The low values in the vicinity of HF point to the relative absence of small SL events, which is counterintuitive as we suspect a volcanic eruption in 2020 near Edmond HF.

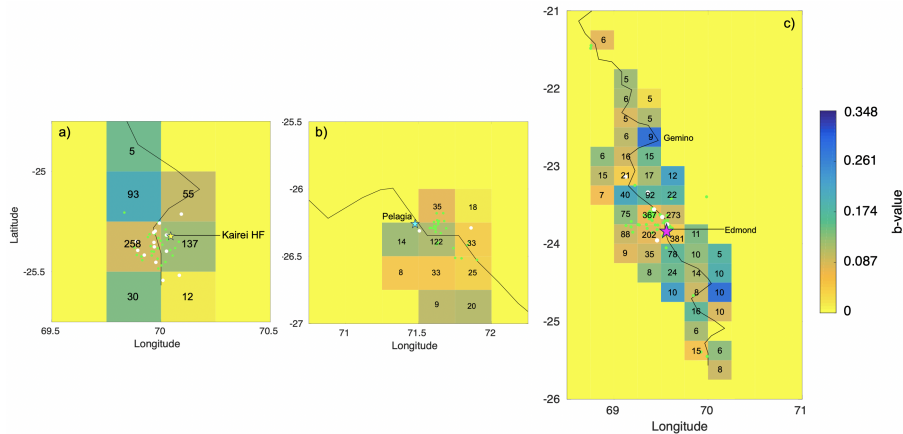


Figure 6.4: Spatial variation in the b -values computed for the events per quarter of a degree in latitude and longitude near the **a)** Kairei, **b)** Pelagia and **c), d)** Edmond hydrothermal fields. Same legends as in Figure 6.2.

Overall, the b -values show a strong heterogeneity in the swarms but are on average higher along SEIR, followed by SWIR and then CIR. They were highest along the 29°S segment of the SEIR, and lowest in the vicinity of Edmond HF along the CIR.

6.1.3 Mainshock-aftershock sequences (modified Omori's laws)

Measuring the characteristics of aftershock sequences along MORs has posed challenges, primarily due to the limited number of sizable events within these sequences that can be detected by terrestrial seismic catalogs. Using the hydroacoustic data, we observed that the event sequences from only 5 swarms out of 15 were well-fitted by a modified Omori's law (MOL) model. These sequences include near 1) the Melville TF, 2) the Kairei HF, 3) segments 8-9, 4) the Edmond HF, and 5) the J3 segment. The decay parameter, p -value of the MOL model varied from 0.49 to 2.27. The lower p -values fall outside the observed range of 0.6-2.5 (Utsu et al., 1995). As mentioned in section 2.7.5, the p -values could reflect the thermal properties of the underlying lithosphere.

Near the Melville TF along the SWIR, we observed lower p -values (0.54 to 0.95) for 12 sub-sequences (Chapter 3). We compared our results with p -values observed elsewhere near the TFs, e.g. the Discovery and Siqueiros TFs along the East-Pacific-Rise (0.96 and 1.09), Blanco TF along the Juan de Fuca Ridge (1.07), as summarized by Bohnenstiehl et al. (2002). Such lower p -values observed for the Melville TF sequences could possibly signify diminished hypocentral temper-

atures. This phenomenon might arise from a potential reduction in asthenospheric upwelling, consequently leading to a decline in the heat advection process and a subsequent inhibition of melt generation (Morgan and Forsyth, 1988). The observations of the greater positive anomaly of shear wave velocity (Debayle and L  v  que, 1997) have inferred the diminished sub-axial crustal and mantle cooling beneath the Melville TF (Mendel et al., 1997).

In contrast, we observed high p -values at segments 8-9 on the CIR (2.27) and J3 on the SEIR (1.77), much higher than those near the TF. They suggest high hypocentral temperatures beneath the segment centers (Kisslinger, 1996). Due to this, the strain releases rapidly which results in a rapid aftershock decay. The presence of an active plume near the J3 segment (Baker et al., 2014) may help to explain the observed p -values. Higher p -values observed along the ridge segments, in comparison to the transform fault, could align with the suggested connection between hypocentral temperature and p -value.

Near the Kairei and Edmond hydrothermal fields, p -values were also low, in the range of 0.49 to 0.98, except for 2.00 in the sequence triggered by a M_w 5.8 event near the Edmond HF. The lower p -values in the vicinity of the Kairei HF (0.81), compared to the Edmond HF (2.00), could also reflect the measured temperature differences between the two fields, 369  C vs. 382  C, respectively (Van Dover et al., 2001; Kumagai et al., 2008). Other low p -values (0.49, 0.87, and 0.98) near the Edmond HF, fail to explain their association with higher temperature in the vicinity of the field. Tentatively, the p -values were nearly the same (low) for aftershock sequences in the vicinity of transform faults as well as hydrothermal fields, and were highest for the sequences in the segment centers, suggesting different temperatures of the underlying lithosphere.

6.1.4 Presence of impulsive events

The occurrence of impulsive (IMP) events along the fast-spreading East-Pacific Rise at 9 50'N (Tan et al., 2016) and the ultra-slow Gakkel Ridge (Schlindwein et al., 2005; Schlindwein and Riedel, 2010) suggest that they are common during MOR eruptions independently of the spreading rate. Our observation of a multitude of IMP events across all three Indian MORs concurs with this statement. We assumed that all these events are associated with lava-water interactions.

Off Mayotte Island in 2020-2021, during the Tiktak a large number of events with short duration (10-15 s) and high energy (frequency up to 60 Hz) were observed by Bazin et al. (2023), shown in Figure 6.5a. This submarine volcanic activity had been monitored by repeated ship-borne multi-beam bathymetric surveys and Autonomous Underwater Vehicles. Bathymetric differences (Δz) between successive surveys documented the spatial evolution of the volcanic activity and pinpointed the superposition of new lava flows. Also, a deep-tow camera survey observed incandescent lava flows near the center of the Tiktak area (Figure 6.5a). The superposition of new lava

flows confirmed by bathymetric and camera surveys, and the occurrence of IMP signals during the eruptive phase strongly suggest that such events result from lava-seawater interactions (Bazin et al., 2023; Saurel et al., 2022). The resemblance in spectrogram characteristics between the IMP signals detected in the vicinity of the Tiktak volcano (Figure 6.5b) and those examined in our current investigation (e.g. near the Melville TF, Figure 6.5c,d) has led us to construe their origin as linked to interactions between lava and water.

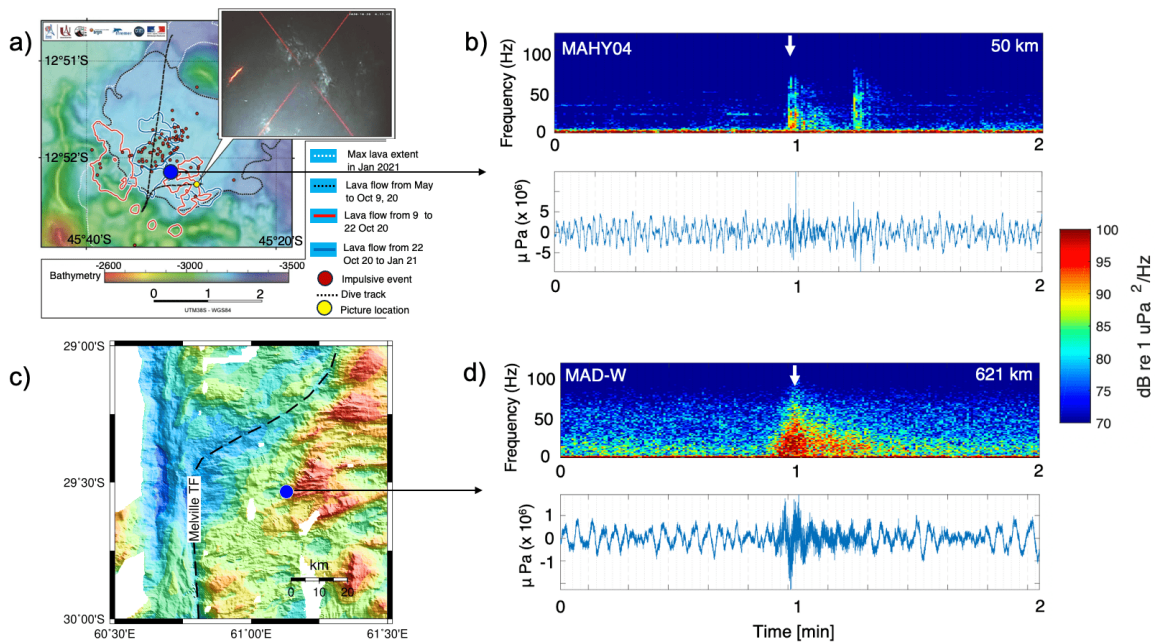


Figure 6.5: **a)** Location of impulsive events (red circles) in the Tiktak area. The blue and red solid lines outline the recent lava flows. The left inset shows the photograph of incandescent lava at the position marked by a yellow circle. This figure is modified from (Bazin et al., 2023). **b)** Two-minute spectrogram and waveform window of the impulsive event, marked by the blue circle in **a)**. **c)** Location of the impulsive event recorded east of Melville TF and its corresponding spectrogram and waveform in **d)**. The event in **b)** is recorded 50 km away from the source and that in **d)** is recorded 621 km away from the source (MAD-W). The similarity in waveform and frequency contents of these two events suggest a common origin, that is interactions between hot lavas and seawater.

Motivated by the success of the Tiktak volcano monitoring, we searched for evidence of new lava flows near Edmond HF, based on the bathymetric data available in the area. Okino et al. (2015) compiled multibeam bathymetry data at a resolution of 50 m along the CIR, including the region of Edmond HF (Figure 6.6a), collected during two cruises (KH-06-4 in 2006 and YK13-9 in 2013). Recent bathymetric data collected during MD238 and MD240 cruises onboard R/V *Marion Dufresne* were compiled in 2022 at a resolution of 58 m (Figure 6.6b). To compare the Δz , we re-sampled this grid at a resolution of 50 m, similar to the former one. The difference shows a series of $\pm 150\text{m}$ bathymetry changes in a large corridor east of the ridge axis (Figure 6.6c).

Such a high range of positive and negative Δz in a hilly region is likely an artifact due to a navigational offset between the two bathymetric surveys (offset perpendicular to the abyssal hills).

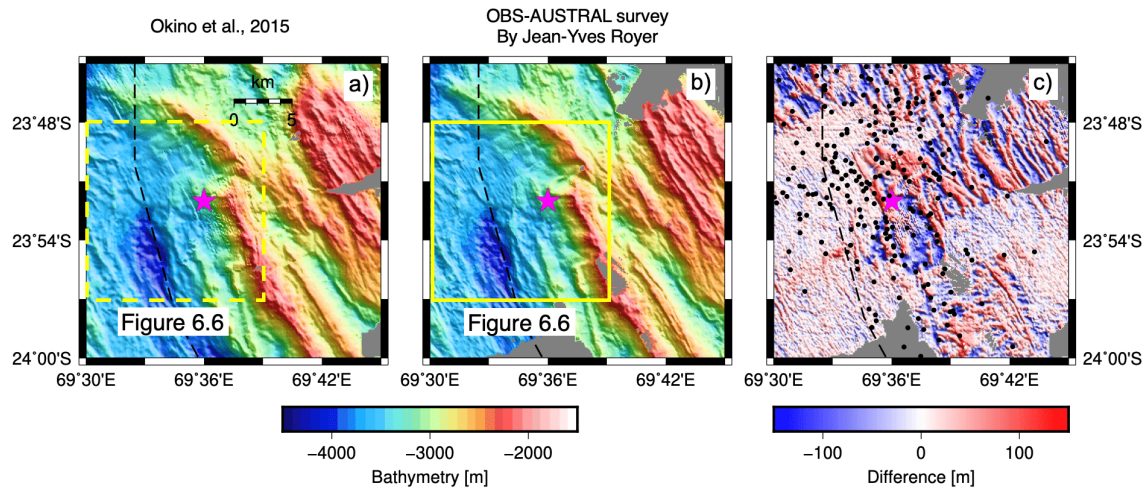


Figure 6.6: **a)** Combined bathymetry collected by *Okino et al. (2015)* pre-seismic activity near the Edmond HF (pink star) in 2006 and 2013 (Japanese surveys), **b)** Post-seismic bathymetry collected on R/V Marion Dufresne (MD238 in June 2021 and MD240 in February 2022), **c)** Difference between post- and pre-seismic bathymetry. The black dashed line marked the CIR axis and black dots in **c)** show the impulsive events. The area within the yellow rectangle is extended in Figure 6.7.

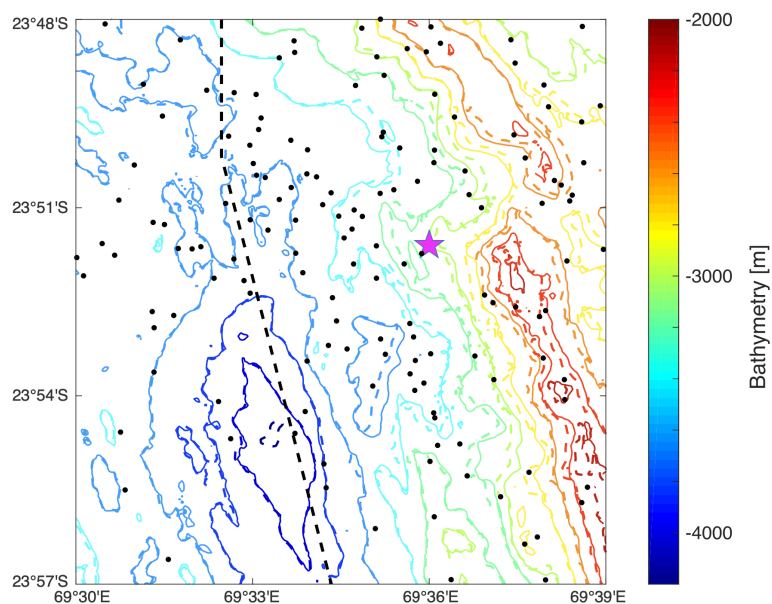


Figure 6.7: Contour maps of pre- (dashed lines; 2006 & 2013 Japanese surveys) and post-seismic (solid lines; 2022 French surveys). The black line marks the CIR axis and the black dots show the impulsive events. Both sets of contours match in the axial valley (blue contours) but are slightly offset east of the axial valley but in steeper abyssal hills (warm-color contours).

The computed difference presents NNW-SSE stripes that resemble the cucumber pattern of young seafloor. The only signal that might be interpretable, is the blue patch SE of Edmond HF that could be caused by the deflation when emptying a magma chamber. It is always challenging to compute differences between diachronous surveys when collected in rough terrain. Few hints point to an artifact: these changes occur in off-axis areas, east and north of the ridge axis, supposedly inactive; positive and negative changes would mean eruption and subsidence alternating in parallel and

next areas; all bathymetric changes are within an echosounder swath width. In the axial valley, in the vicinity of the Edmond HF, the comparison of bathymetric contours does not show significant differences, except in steep slopes where contours are slightly offset from each other (Figure 6.7). Hence due to the poor resolution of the bathymetric grids (50 m) and potential offsets in the navigation, it would be not wise to interpret positive vertical offsets Δz as post-seismic lava flows (or negative Δz as subsidence).

Backscatter data shows that the axial valley west of the Edmond HF is highly reflective (black areas in Figure 6.8), which is indicative of unsedimented bare rocks. It also coincides with the location of impulsive events. However, it is not possible to outline potential new lava flows as in the Mayotte area.

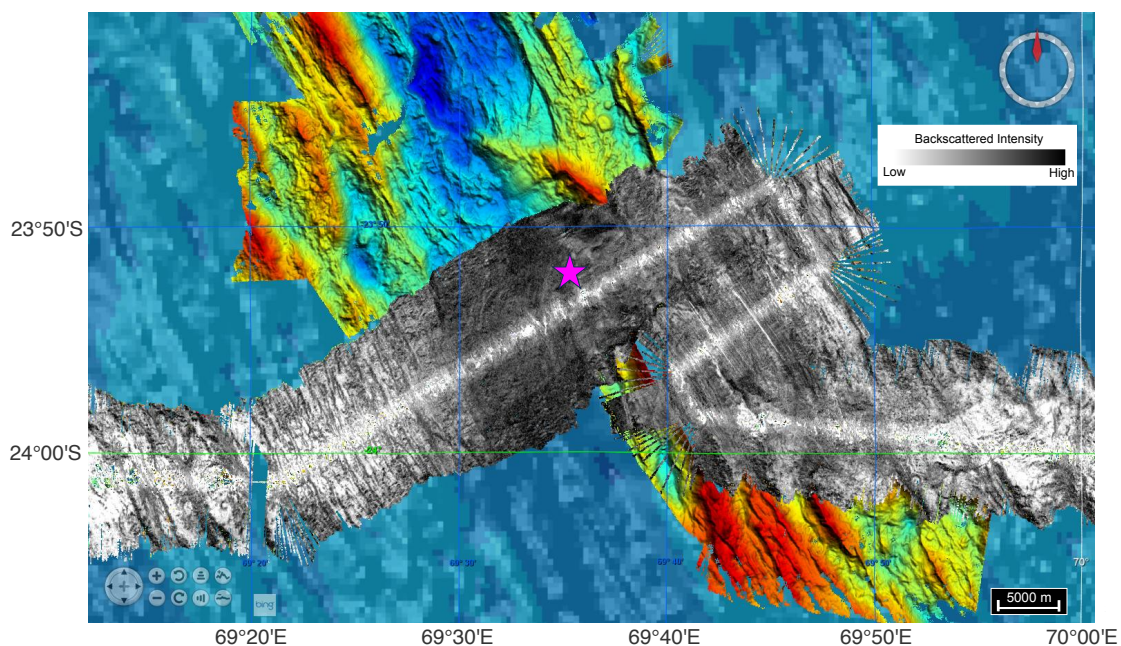


Figure 6.8: Backscattered energy near the Edmond HF (pink star), dark-gray for the high intensity and light-gray for low intensity. Data from MD238 (June 2021) and MD240 (Feb. 2022) cruises of R/V Marion Dufresne (Figure from A. Briais, personal communication 2023).

In the context of the SWIR, we detected impulsive events within each of the three identified swarms. Along the CIR, they occurred in the vicinity of the Edmond HF and on the J3 segment along the SEIR. A detailed summary of IMP events is given in Table 6.4.

Comparatively, there are few differences in the distribution and number of IMP events observed along the three ridges:

- **The SWIR:** The number of IMP events compared to total detections was very low ($< 7\%$) in the three swarms on the SWIR (Table 6.4). As mentioned earlier in the Introduction chapter (Figure 1.8), along ultraslow spreading ridges, the magma supply is very poor and the frequency of seafloor eruption is low. The region between segment 18 and segment 4 of SWIR,

was established from ~55 Ma to ~10 Ma, the time of the last major change in the spreading direction of the SWIR (Patriat et al., 1997). The sub-axial crust and mantle beneath this section are cooler (Mendel et al., 1997), which is inferred from greater positive anomalies of shear wave velocity in the upper mantle (Debayle and L ev eque, 1997). This cooler mantle results in lower partial melting and less magma supply to ridge segments (Cannat et al., 1999) and hence a lower number of IMP events.

- **The CIR and SEIR:** The rate of IMP activity near the Edmond HF (on CIR) and along the J3 segment (SEIR) exhibited sporadic patterns, differing from the activity noted along the SWIR. The high activity along the J3 segment, likely attributed to a ridge-hotspot interaction in this region, surpasses that observed along the SWIR. In contrast, it is relatively lower than the IMP activity proximate to the Edmond HF. It is important to refrain from generalizing this observation, as this heightened activity might potentially be influenced by higher hydrothermal circulations in this area.

Ridge	SWIR			CIR	SEIR
Region	Novara TF	Melville TF	67°45'E Segment	Edmond HF	J3 segment
Median location	29.14°S, 74.78°E	29.02°S, 74.69°E	28.07°S, 74.02°E	28.92°S, 74.59°E	28.03°S, 74.06°E
Nbr of days	13	298	33	142	14
Nbr of OHA events	1109	27624	4880	2015	745
Nbr of ISC events	231	258	92	68	14
Nbr of GCMT events	7	17	6	7	9
Nbr of IMP events	69	118	58	711	84
IMP vs OHA ratio [%]	6.2	1.2	0.4	35.3	11.3
IMP vs GCMT ratio	10	11	10	102	9
IMP vs ISC ratio	0.3	0.5	0.6	10.5	6
SL range of IMP [dB]	205.6 - 232.6	199.8 - 225.1	208.8 - 230.2	205.0 - 223.7	203.5 - 220.3
SL_C of IMP [dB]	215.5	207.6	221.2	211.1	211.3

Table 6.4: Summary of impulsive events detected along the SWIR, CIR, and SEIR

The signals generated by underwater controlled sources could have a similar signature (high energy and short duration) as that generated by lava-water interactions. Indeed, air-gun shots used in seismic surveys for exploration, produce impulsive signals very similar to those observed along the MORs; however, their regular repetition (every 10 s to 1 minute) makes them easy to discriminate. The following paper, presented at the Underwater Seismoacoustic Conference and Exhibition (UACE 2023 in Kalamata Greece), shows the similarity of the signals generated by an artificial underwater explosion and by lava-water interactions and summarizes how they can be distinguished from each other.



Cited as: Ingale, V. V., Bazin, S., and Royer, J.-Y. (2023). Energetic and short water-born signals from mid-oceanic ridges, Underwater Acoustics Conference and Exhibition Series (UACE), June 2023, Kalamata, Greece

ENERGETIC AND SHORT WATER-BORN SIGNALS FROM MID-OCEANIC RIDGES

Vaibhav Vijay Ingale^a, Sara Bazin^a, Jean-Yves Royer^a

^aLab Geo-Ocean, University of Brest, CNRS, Ifremer, UMR6538, F-29280, Plouzané, France

Contact Author: Vaibhav Vijay Ingale (vaibhavvijay.ingale@univ-brest.fr)

Abstract: *The OHASISBIO network of autonomous hydrophones moored in the SOFAR channel of the southern Indian Ocean detected many short-duration and energetic acoustic events originating at mid-oceanic spreading ridge axes. Their average duration of 10 to 15s makes them “impulsive” relative to the 80 to 200s-long T-waves generated by submarine earthquakes. Their frequency goes up to 50-60 Hz and their source level ranges from 200 to 233 dB. Most of them are detected as far as 3700 km away from their source where received levels can reach up to 108 dB. They are associated with seismic swarms located on ridge axes where new seafloor is produced. Along the Southwest Indian Ridge (ultra-slow spreading rate at 14 mm/yr), such impulsive events (IMP) were found near Novara transform fault (58°20'E), with 69 IMP among 1109 seismic events, near Melville transform fault (61°00'E), with 118 IMP among 27624 events, and at 67°45'E, with 58 IMP among 4880 events. Along the Central Indian Ridge (slow spreading rate at 40 mm/yr), 711 IMP among 2015 seismic events were found near an active hydrothermal field at 23°52'S, 69°30'E. The short duration, high energy and frequency content of IMP suggest that their source is punctual and generates water-borne waves, thus not resulting from the conversion of seismic waves on the seafloor. IMP sources are often located at the foot or slopes of bathymetric highs and occur in clusters after large-magnitude earthquakes nearby. All these clues point to a volcanic origin, perhaps to hot lava and seawater interactions during magmatic eruptions, after dike intrusion triggered earthquakes. This hypothesis calls for in-situ inspections with a submarine vehicle to be confirmed. Except for their locations, these events could be mistaken for man-made underwater explosions. These narrow and energetic events could also provide useful sources to investigate the effects of long-distance propagation of acoustic waves in the ocean or to monitor sound-speed or temperature anomalies at long range.*

Keywords: *Impulsive events, Hydroacoustics, Mid-ocean Ridges, Indian Ocean, Volcanic activity*

1. INTRODUCTION

The majority of volcanic activity on Earth is concentrated along mid-oceanic spreading ridges (MOR), where new seafloor is created. Despite this prevalence, however, understanding the mechanisms that drive submarine volcanic eruptions remains limited due to their often-unnoticed nature. Their detection and characterization pose significant challenges due to remoteness from terrestrial seismic networks. To address this issue, passive acoustic monitoring has emerged as a valuable approach for identifying and analyzing such eruptions [e.g. 1] and provided critical insights into the dynamics of these volcanic phenomena, thereby contributing to a better understanding of geological processes that shape the Earth.

MORs are divergent plate boundaries in the plate tectonic realm. The southern Indian Ocean is home to three MORs where its seafloor is created. The Southwest Indian Ridge (SWIR) separates the African and Antarctic plates, while the Central Indian Ridge (CIR) separates the African and Indo-Australian plates, and the Southeast Indian Ridge (SEIR) separates the Indo-Australian and Antarctic plates (Fig. 1). These three ridges meet at a point called Rodrigues Triple Junction (RTJ). Their spreading rates span from ultraslow at about 14 mm/yr along the SWIR, to slow at about 40 mm/yr along the CIR, and intermediate at about 60 mm/yr along the SEIR. The spreading rates determine the MOR morphology and the preponderance between tectonic and volcanic processes.

As divergent plate boundaries, these MORs are characterized by a complex interplay of volcanic and tectonic processes where molten rock rises to the seafloor or where the young crust undergoes extension as a result of the separation of plates, both processes generating numerous earthquakes. However, detecting the low-level seismicity associated with these processes is challenging with conventional land-based seismic networks due to the remote locations of these ridges and the rapid attenuation of seismic waves over distance. Nonetheless, earthquakes generate low-frequency Twaves in the water column. Such T-waves (or tertiary waves) result from the seismoacoustic conversion of seismic waves at the seafloor, and travel at the water sound-speed, thus much slower than seismic primary (P) and secondary (S) waves. They also travel over much longer distances due to a minimal attenuation through the oceanic acoustic waveguide [2]. To detect the low-level seismicity associated with the three Indian MORs, a network of autonomous underwater hydrophones of the Hydroacoustic Observatory of Seismicity and Biodiversity in the Indian Ocean (OHASISBIO), has been deployed between 2010 and 2023. It was also set up to monitor the cryogenic and biological activity in the southern Indian Ocean [3]. In this study, we present peculiar acoustic events occurring in clusters at several swarms of events detected between 2016 and 2020 along the SWIR and CIR axes.

2. DATA AND METHODS

The occurrence of a sound fixing and ranging (SOFAR) channel in most of the world ocean allows sound waves to travel with little dissipation compared to seismic waves in the Earth, making hydroacoustic data particularly useful for detecting underwater events over long distances. In this

study, the hydroacoustic data was recorded continuously at a sampling rate of 240 Hz by 3 to 9 hydrophones moored at depths between 1000 m and 1300 m, in the SOFAR channel. The arrival times of hydroacoustic events in the data were picked on the highest energy arrival in T-wave spectrograms; their location and time of origin were then estimated using a non-linear least square minimization of these arrival times [2]. The travel times were converted into distances using oceanic sound velocities based on the three-dimensional (3D) Global Digital Environment Model [4]. The Source Level (SL) of hydroacoustic events was inferred from the Received Levels (RL) at each hydrophone, after accounting for cylindrical and spherical transmission losses between an event and a hydrophone. The RL is a decibel measurement with respect to 1 micro-Pascal at 1 m (hereinafter simply noted as dB) of an average power spectral density in a 10s-time window centered on the energy peak of the acoustic signal, in the 5-60 Hz frequency range.

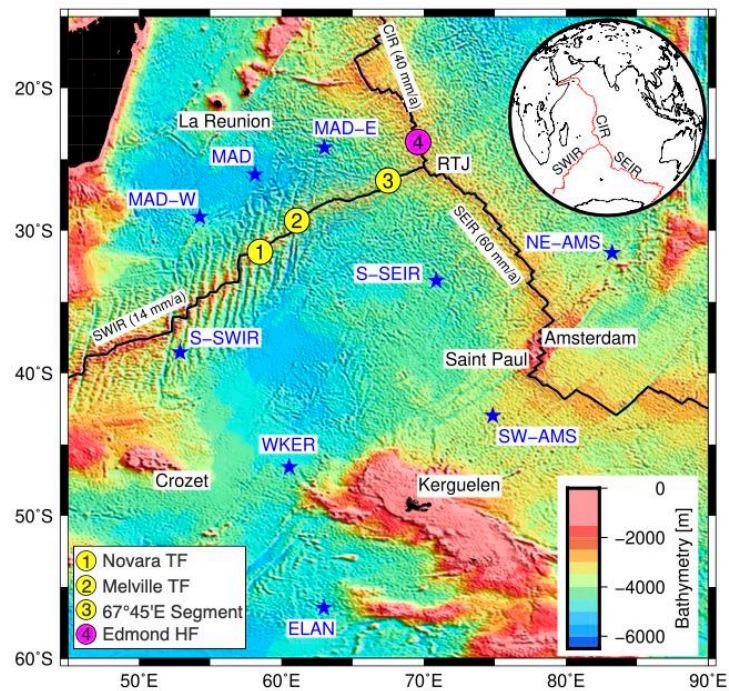


Fig. 1 - Bathymetric map of the southern Indian Ocean with mid-ocean ridges (black lines) and locations of the OHASISBIO stations (blue stars). Yellow and purple circles mark the study regions along the SWIR and CIR, respectively.

3. RESULTS

In this study, we investigated hydroacoustic T-waves from four distinct swarms, located along the SWIR (yellow circles in Fig. 1), and CIR (purple circle). To locate these swarms, we first looked for seismic clusters in the catalog from the International Seismological Centre (ISC; Table 1; [5]). In the first swarm, situated near Novara transform fault (TF; 58°20'E), the ISC catalog reported a total of 231 seismic events over a 13-day period in July 2018, whereas we were able to detect 1109 hydroacoustic events [6]. The TF is a seismically active boundary that offsets two

MOR segments and where tectonic plates slide past each other horizontally in opposite directions. In the second swarm near Melville TF (61°00'E), 258 ISC seismic events were reported over a period of 298 days from June 2016 to March 2017; we found that it was the most intense seismic swarm along the SWIR, with 27624 hydroacoustic events [7]. In the third swarm, located near a segment at 67°45'E along the SWIR (~200 km from RTJ), we detected 4880 hydroacoustic events compared to the 92 ISC events reported over a 33-day period in September to October 2018. Lastly, near the Edmond hydrothermal field (HF) along the CIR (at 69°30'E), we detected a swarm of 2015 hydroacoustic events over a period of 142 days from April to September 2020, while the ISC catalog reported only 68 events in the same time period. The Edmond HF is an active vent field, discovered in the late eighties [8], where geothermally heated water discharges near the ridge axis. In the four areas, all events were localized with small uncertainties less than 0.3 s in their origin time and 400 m in location, compared to that of 10-20 km reported in the ISC catalog. The SL of completeness, which is the minimum SL above which all hydroacoustic events are reliably recorded, was 212, 206, 209 and 210 dB based on all the events from each of the four respective regions, respectively. The findings confirm that hydroacoustic monitoring is an accurate and sensitive method for detecting seismic activity in remote regions of the ocean.

	Swarm 1	Swarm 2	Swarm 3	Swarm 4
Spreading ridge	SWIR	SWIR	SWIR	CIR
Region	Novara TF	Melville TF	Segment at 67°45'E	Edmond HF
Longitude	58°20'E	61°00'E	67°45'E	69°30'E
Dates span (dd/mm/yy)	06/07/18 - 18/07/18	01/06/16 - 25/03/17	27/09/18 - 27/10/18	16/04/20 - 04/09/20
Duration (days)	13	298	33	142
Number of ISC events	231	258	92	68
Number of OHA events	1109	27624	4880	2015
Number of IMP events	69	118	58	711
SL of OHA events (dB)	201 - 236	186 - 228	196 - 240	199 - 246
SL of IMP events (dB)	206 - 233	200 - 225	209 - 230	205 - 224
SL of completeness (dB)	212	206	209	210

Table 1 - Detection summary of four seismic swarms in the southern Indian Ocean. OHA are the hydroacoustic events recorded by the OHASISBIO network and IMP are impulsive events.

Among all the hydroacoustic events, a number of peculiar events, short and energetic up to 60 Hz were observed: 69 near the Novara TF, 118 near the Melville TF, 58 near the segment at 67°45'E and 711 on the CIR (Fig. 2). Their SL values ranged between 200 and 233 dB with a most frequent value at 211 dB (Fig. 2e). Out of these 952 events, 576 (60 %) have SLs above this value. So, compared to T-waves from high magnitude earthquakes reported in the ISC catalog, these events combine a high SL, a high frequency content (up to 50-60 Hz) and a much shorter duration (1015s) versus 80 to 200s for regular T-waves. Unlike typical T-wave events, their rise time is also very

sharp. From all these characteristics, they can be qualified as impulsive events (IMP). As an example, the spectrogram in Fig. 2f shows an IMP event, originating near the Edmond HF and detected at the ELAN site, 3757 km away with a RL of 109 dB. Their short duration and high frequency content suggest that these signals are water-borne H-waves, meaning that the energy is directly released into the water and does not originate from waves having traveled into the solid crust, like regular T-waves. Finally, aside from being associated with seismic swarms on spreading ridge axes, IMP sources are mostly located at the foot or slopes of bathymetric highs and generally occur in clusters after large-magnitude earthquakes nearby, as if triggered by them [6,7].

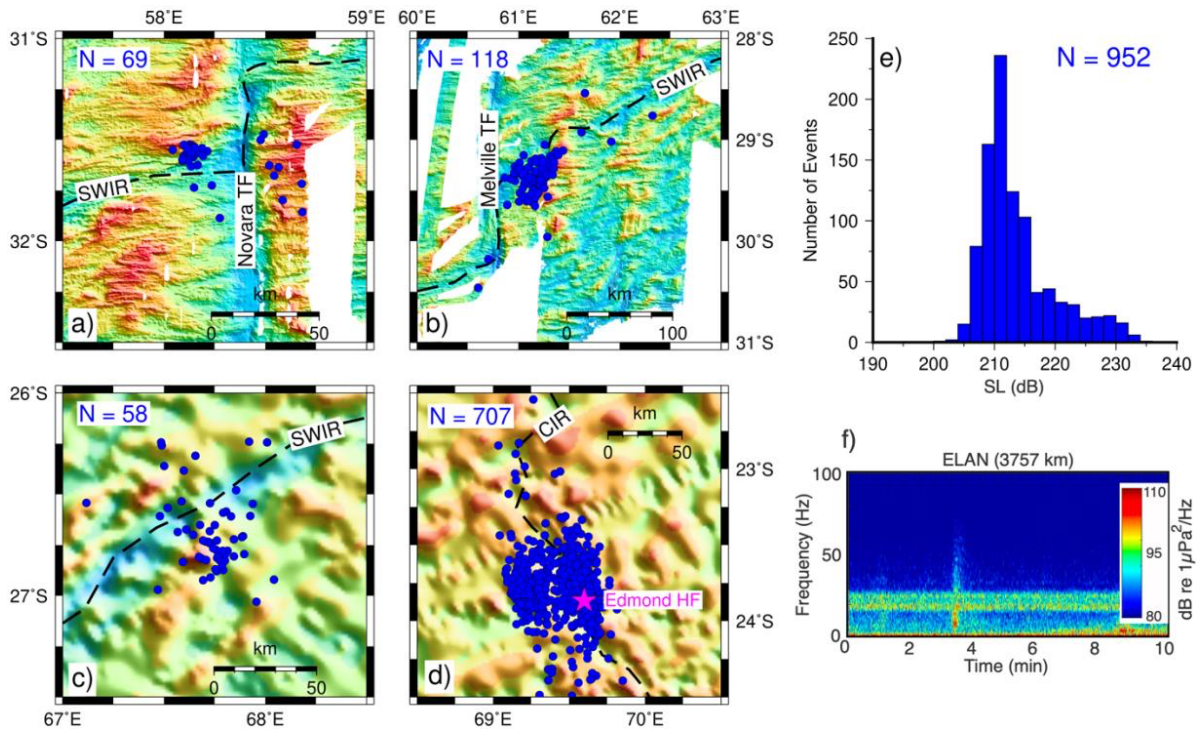


Fig. 2 - Locations of IMP events (blue dots) along the SWIR: a) near Novara TF; b) near Melville TF; c) near segment at 67°45'E, and the CIR; d) near Edmond HF, bathymetry is from [9]. e) SL histogram of the 952 impulsive events shown in a)-d). f) Spectrogram of an IMP event originating near the Edmond HF and recorded 3757 km away (ELAN site, Fig. 1).

4. DISCUSSION

Hydroacoustic IMP events have been observed on several spreading ridges as well as during underwater volcanic eruptions [e.g. 1,10]. In this study, the absence of precursory P and S seismic arrivals, as well as the short duration and frequency range of IMP events, suggest that they are not produced by shallow earthquakes, which would generate broader waveforms. Instead, as demonstrated in other studies, IMP events showing similar signatures as ours likely result from hot lava and seawater interactions at the seafloor. For example, during a recent volcanic eruption off Mayotte Island [11,12], similar events originated from a location with direct evidence of active lava flows, within a 50 km range of the hydrophones. During the Axial seamount eruption on the

Juan de Fuca Ridge in 2015 [13], similar events with SLs ranging from 130 to 190 dB, recorded at a closer range (< 20 km), were interpreted as hot lava and seawater interactions.

Natural IMP events along MORs may have different source mechanisms. One possibility is that they are associated with the steaming of cold (~2-4 °C) seawater in contact with hot lava at the seafloor. Another mechanism could be the implosions of rising magmatic gas (sudden inward bubble collapse). Additionally, “bomb-like” lava fragmentations could produce high frequency compressional acoustic waves [14]. Moreover, they could also arise from the cracking of rapidly cooling lava or lava quenching on the seafloor.

Natural IMP events have similar signatures as that of signals generated by underwater controlled source experiments. Fig. 3 compares the spectrogram of an IMP event generated near the Edmond HF on CIR, recorded at WKER site (2737 km away) with that of an explosion of a 102 kg of TNT offshore Argentina (45°40’S, 59°25’W) on 1st December 2017 [15]. This manmade signal has been recorded at a distance of 8195 km at the WKER site near Kerguelen Island. This experiment was carried out by the International Monitoring System of Comprehensive Nuclear Test-Ban-Treaty Organization in an attempt to characterize an unknown signal originating from a submarine of the Argentina Navy that went missing on 15 November 2017. This comparison shows that IMP events, here interpreted as hot lava and seawater interactions, can be mistaken for manmade underwater explosions. However, natural IMP events occur in long-lasting clusters (weeks or months) centered on spreading-ridges or underwater volcanoes, and generally nearby highmagnitude earthquakes.

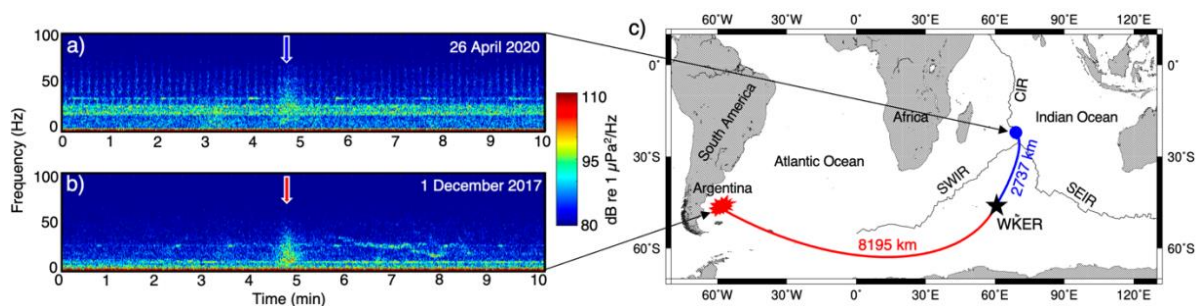


Fig. 3 - Spectrograms of impulsive signals recorded at WKER site (black star) and resulting from a) lava-water interaction on the CIR (blue) vs. b) controlled source explosion offshore Argentina (red).

5. CONCLUSIONS AND PROSPECTIVES

This seismoacoustic study of swarms along the SWIR and CIR in the Indian Ocean evidence many energetic and short duration impulsive events which can be recorded as far as ~3800 km away from their source. Their relative abundance on the CIR with respect to the SWIR may reflect different interplay of volcanic and tectonic processes. Impulsive events are interpreted as waterborne H-waves resulting from hot lava and seawater interactions on the seafloor. They cluster

near or on the ridge axis, at the foot or slopes of bathymetric highs, and occur after large-magnitude earthquakes nearby, possibly caused by dike intrusions. Despite their very similar signatures, such events of volcanic origin should not be misinterpreted as acoustic impulse responses generated by man-made explosions. Machine learning algorithms may be able to discriminate them from more specific characteristics [16].

This study also calls for *in-situ* oceanic campaigns to better understand the origin of these impulsive events. Although it is a challenge to monitor such events in real-time, there would be several ways to study them apart from collecting hydroacoustic data. For example, by repeating high-resolution multibeam bathymetric surveys to detect changes in seafloor morphology, sidescan sonar surveys to highlight freshly formed lava from the backscattered energy, and/or deepsea camera surveys from autonomous underwater vehicles.

As shown in Fig. 2a-2d, impulsive events mostly originate from the same location over extended periods of several weeks to months. They generate water-borne signals with a high acoustic-energy (> 200 dB) directly released into the water column, which, through the SOFAR channel, can travel long distances (e.g. > 1000 s km as in Fig. 2e and 3). On distant receivers, their narrow signature makes their arrivals more easily discernible on spectrograms than the long cigarshaped T-wave signals, resulting from the complex conversion of seismic to acoustic energy at the seafloor. With their impulsive nature, these events may, thus, provide useful natural sources for analyzing the effects of long-range propagation of acoustic waves [e.g. 17], as well as for monitoring the sound-speed and thermography of the ocean at long range [e.g. 18].

ACKNOWLEDGEMENTS

The French Polar Institute (IPEV) and the French Oceanographic Fleet funded the ship's time for the deployment and recovery of the OHASISBIO network through yearly voyages of RV *Marion Dufresne*. INSU-CNRS provided additional support and the Regional Council of Brittany funded the hydrophone moorings. V.V.I. was supported by a fellowship from the University of Brest and from the Regional Council of Brittany, through the ISblue project, Interdisciplinary graduate school for the blue planet (ANR-17-EURE-0015) and co-funded by a grant from the French government under the program "Investissements d'Avenir".

REFERENCES

- [1] **Tepp, G., and R. P. Dziak**, The seismo-acoustics of submarine volcanic eruptions, *J. Geophys. Res. Solid Earth*, 126, e2020JB020912, 2021.
- [2] **Fox, C. G., H. Matsumoto, and T. K. Lau**, Monitoring Pacific Ocean seismicity from an autonomous hydrophone array, *J. Geophys. Res.*, 106, 4183–4206, 2001.
- [3] **Royer, J.-Y.**, OHA-SIS-BIO: Hydroacoustic observatory of the seismicity and biodiversity in the Indian Ocean, available online at <https://campagnes.flotteoceanographique.fr/>, 2009. [4]

Teague, W. J., M. J. Carron, and J. P. Hogan, A comparison between the Generalized Digital Environment Model and Levitus climatologies, *J. Geophys. Res.*, 95, 7167–7183, 1990.

[5] **International Seismological Center (ISC)**, Online Bulletin, available online at <http://www.isc.ac.uk/iscbulletin/search/catalogue/> (last accessed January 2022).

[6] **Ingale, V. V., S. Bazin, and J.-Y. Royer**, Hydroacoustic observations of two contrasted seismic swarms along the Southwest Indian Ridge in 2018, *Geosciences*, 11(6), 225, 2021. [7] **Ingale, V. V., S. Bazin, J.-A. Olive, A. Briais, and J.-Y. Royer**, Hydroacoustic study of a seismic swarm in 2016–2017 near the Melville transform fault on the Southwest Indian Ridge, *Bull. Seis. Soc. Am.*, 1-19, 2023.

[8] **Herzig, P. M., and W. L. Plueger**, Exploration for hydrothermal activity near the Rodriguez triple junction, Indian Ocean, *Can. Mineral.*, 26(3), 721-736, 1988.

[9] **Okino, K., K. Nakamura, and H. Sato**, Tectonic background of four hydrothermal fields along the Central Indian Ridge, In *Subseafloor Biosphere Linked to Hydrothermal Systems*, Springer, Tokyo, 2015.

[10] **Wu, J.-N., R. Parnell-Turner, D. J. Fornari, G. Kurras, N. Berrios-Rivera, et al.**, Extent and volume of lava flows erupted at 9°50'N, East Pacific Rise in 2005–2006 from autonomous underwater vehicle surveys, *Geochem. Geophys. Geosyst.*, 23, e2021GC010213, 2022.

[11] **Bazin, S., J.-Y. Royer, F. Dubost, F. Paquet, B. Loubrieu, et al.**, Initial results from a hydroacoustic network to monitor submarine lava flows near Mayotte Island, *C. R. Geoscience*, 10.5802/crgeos.119, 2022.

[12] **Saurel, J.-M., L. Retailleau, C. Deplus, B. Loubrieu, D. Pierre, et al.**, Combining hydroacoustic sources and bathymetric differences to track the vent evolution of the Mayotte eruption, Mozambique Channel. *Front. Earth Sci.*, 10:983051, 2022.

[13] **Le Saout, M., D. R. Bohnenstiehl, J. B. Paduan, and D. A. Clague**, Quantification of eruption dynamics on the north rift at Axial Seamount, Juan de Fuca Ridge, *Geochem. Geophys. Geosyst.*, 21, 9, e2020GC009136, 2020.

[14] **Banerjee, P. and Y. Shen**, Hydrovolcanic explosions at the lava ocean entry of the 2018 Kilauea eruption recorded by ocean-bottom seismometers, *Seism. Res. Let.*, 94(3), 1488-1494, 2023.

[15] **Nielsen, P. L., M. Zampolli, R. L. Bras, P. Mialle, P. Bittner, et al.**, CTBTO's data and analysis pertaining to the search for the missing Argentine submarine ARA San Juan, *Pure Appl. Geophys.*, 178, 2557-2577, 2021.

[16] **Raumer, P.-Y., S. Bazin, D. Cazau, V. V. Ingale, A. Lavayssière and J.-Y. Royer**, Application of machine learning to hydro-acoustic volcanic event detections, *HPC Workshop for Nuclear Explosion Monitoring proceedings (CTBTO)*, 15-17 May 2023, Vienna, 2023.

[17] **Castor, K., P. Gerstoft, P. Roux, W. A. Kuperman, B. E. McDonald**, Long-range propagation of finite-amplitude acoustic waves in an ocean waveguide, *J. Acoust. Soc. Am.*, 116 (4), 2004–2010, 2004

[18] **Wu, W., Z. Zhan, S. Peng, S. Ni, and J. Callies**, Seismic ocean thermometry, *Science*, 369, 1510-1515, 2020.

6.2 Effects of the network geometry on localization errors

Calculating uncertainties (errors) in the localization and time origin of events requires detecting T-waves from the same event on at least 4 hydrophones. We localized all events in the swarms with a minimum of 4 hydrophones, except in the Melville TF swarm, when only 3 hydrophones were available for a short period (28 November 2016 - 06 January 2017). This analysis thus did not consider the 2095 events detected in this period. After comparing all the swarms, it is observed that the distribution of the uncertainties in the hydroacoustic events may be biased by the network geometry. For example, we detected all events located along the SWIR or on the SEIR segments at 28°S and 29°S with hydrophones surrounding the swarms. Hence, the median uncertainties in latitude and longitude were nearly equal and, on average, were less than 6 km in the first iteration of picking and less than < 600 m in the second one (Figure 6.9, Table 6.5).

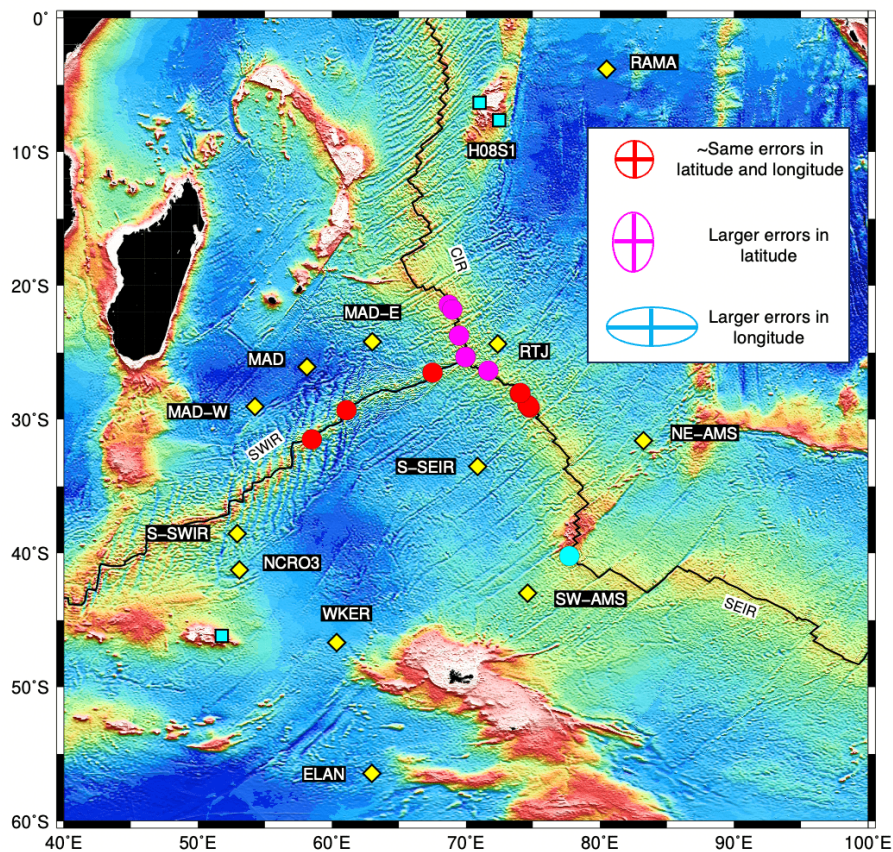


Figure 6.9: Median locations of individual swarms along the three Indian MORs. The red circles mark the swarms with minimum errors in latitude and longitude. The pink circles mark the swarms with higher errors in latitude and a cyan circle marks the swarm on the J3 segment as having higher longitude errors.

With respect to the CIR axis, the hydrophones are mostly located south of the swarms, providing better constraints in the East-West direction; as a result, the uncertainties in latitude are nearly twice that in longitude (consistently in both iterations). Although the IMS-CTBTO stations

are situated north of the swarms, we could not detect a single event, probably due to a bathymetric blockage. Relative to the J3 segment on the SEIR, hydrophones were primarily on the eastern side, which resulted in errors in longitude almost 5 times that in latitude.

Hence the network geometry plays an important role in localizing hydroacoustic events. In an experiment conducted in the Atlantic Ocean, errors in location for events within the Equatorial Atlantic ranged from ~ 8 km up to ~ 30 km for events outside the networks; such range was attributed to a varying spatial distribution of the available hydrophones over time (Parnell-Turner et al., 2022). Previously, Royer et al. (2015) and Tsang-Hin-Sun et al. (2016) also observed larger uncertainties in location for the events detected outside either the DEFLO or OHASISBIO array in the Indian Ocean. They were less than ~ 5 km for the events within the array and were greater than ~ 15 km for the outliers (Tsang-Hin-Sun et al., 2016).

Ridge	Sr No	Year	Region	Duration (days)	Nbr of AUHs	Nbr of events	Iteration 1 uncertainties (1σ)			Iteration 2 uncertainties (1σ)		
							Lat (km)	Lon (km)	Time (s)	Lat (km)	Lon (s)	Time (s)
SEIR	4	2012	29°S segment	13	11	452	6.43	5.12	2.89	0.53	0.31	0.35
SEIR	5	2012	29°S segment	1	11	76	4.72	3.36	2.29	0.37	0.25	0.28
SEIR	6	2015	28°S segment	7	8	110	6.58	4.43	3.64	0.31	0.49	0.44
SWIR	1	2016	Melville TF	298	9	27624	2.88	2.90	0.90	0.38	0.38	0.11
SWIR	2	2018	Novara TF	13	9	1109	4.33	3.60	1.99	0.44	0.35	0.19
SWIR	3	2018	Segment 18	33	7	4880	4.00	2.89	1.92	0.33	0.26	0.18
SEIR	7	2018	29°S segment	27	10	266	3.83	4.02	2.08	0.30	0.33	0.16
SEIR	8	2019	28°S segment	14	11	74	6.18	5.98	3.32	0.58	0.33	0.31
CIR	9	2013	Kairei HF	83	6	203	13.70	8.97	6.20	0.61	0.41	0.22
SEIR	10	2013	Pelagia HF	83	6	322	12.22	8.06	5.01	0.44	0.29	0.33
CIR	11	2013	Kairei HF	27	6	402	8.36	4.23	4.09	0.68	0.31	0.33
CIR	12	2019	Segments 8-9	20	7	165	14.32	8.56	6.56	1.59	0.82	0.94
CIR	13	2020	Segments 8-9	7	6	467	11.26	4.67	5.87	1.05	0.29	0.56
CIR	14	2020	Edmond HF	142	6	2015	13.31	6.63	6.64	0.70	0.33	0.34
SEIR	15	2020	J3 segment	13	6	745	5.01	23.66	10.34	0.36	0.68	0.28

Table 6.5: Summary of error distribution of the events from each seismic swarms along the three Indian MORs

For a given geometry, the localization errors also depend on the number of hydrophones used to detect the events. For the events detected along the CIR, median uncertainties in the first iteration of picking in latitude and longitude were nearly the same, ~ 13 km and 6 km for the events detected either by 4 or 5 hydrophones. They reduced down to ~ 8 and 4 km with 6 hydrophones. In the second iteration, the uncertainties were ~ 0.8 km and 0.4 km in latitude and longitude with either 4 or 5 hydrophones and reduced down to ~ 0.7 km and 0.3 km in the detections using 6 hydrophones (Figure 6.10).

For a given geometry, the localization errors also depend on the number of hydrophones used to detect the events. For the events detected along the CIR, median uncertainties in the first iteration of picking in latitude and longitude were nearly the same, ~ 13 km and 6 km for the events detected either by 4 or 5 hydrophones. They reduced down to 8 and 4 km with 6 hydrophones. In the second iteration, the uncertainties were ~ 0.8 km and 0.4 km in latitude and longitude with either 4 or 5 hydrophones and reduced down to ~ 0.7 km and 0.3 km in the localization using 6 hydrophones (Figure 6.10).

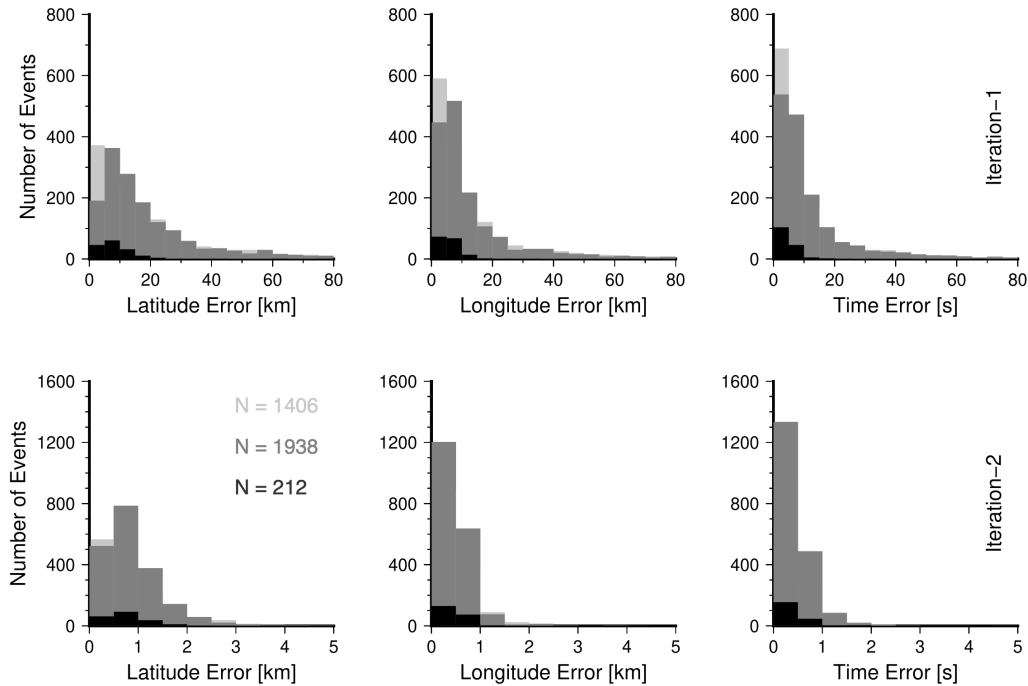


Figure 6.10: *Uncertainties distribution in the latitude and longitudes for the events located within the area marked by red rectangle along the CIR in Figure 4.1. N denotes the number of detections by four hydrophones (light gray), five hydrophones (dark gray), and six hydrophones (black).*

Also, to understand the effect of network geometry on localization of events, it is interesting to examine the uncertainty distribution for individual events. For example, the network geometry slightly changed three times during the swarm near the Melville TF between June 2016 and 2017 (Figure 6.11). In the initial period from June to November 2016, events were detected by 4 to 6 hydrophones and the median uncertainties were 0.38 km in latitude, 0.40 km in longitude and 0.17 s in origin time estimation (Figure 6.11). Between November 2016 and January 2017, one hydrophone at SW-AMS station stopped working and most of the events were detected by only 3 hydrophones, thus lacking the information about uncertainty estimation. Later on, between January and March 2017, we detected events with 7 to 9 hydrophones resulting in better uncertainties of 0.35 km (latitude), 0.27 km (longitude) and 0.10 s (origin time) compared to the initial period. This individual event analysis demonstrates the importance of the network geometry on the uncertainties in location and origin time.

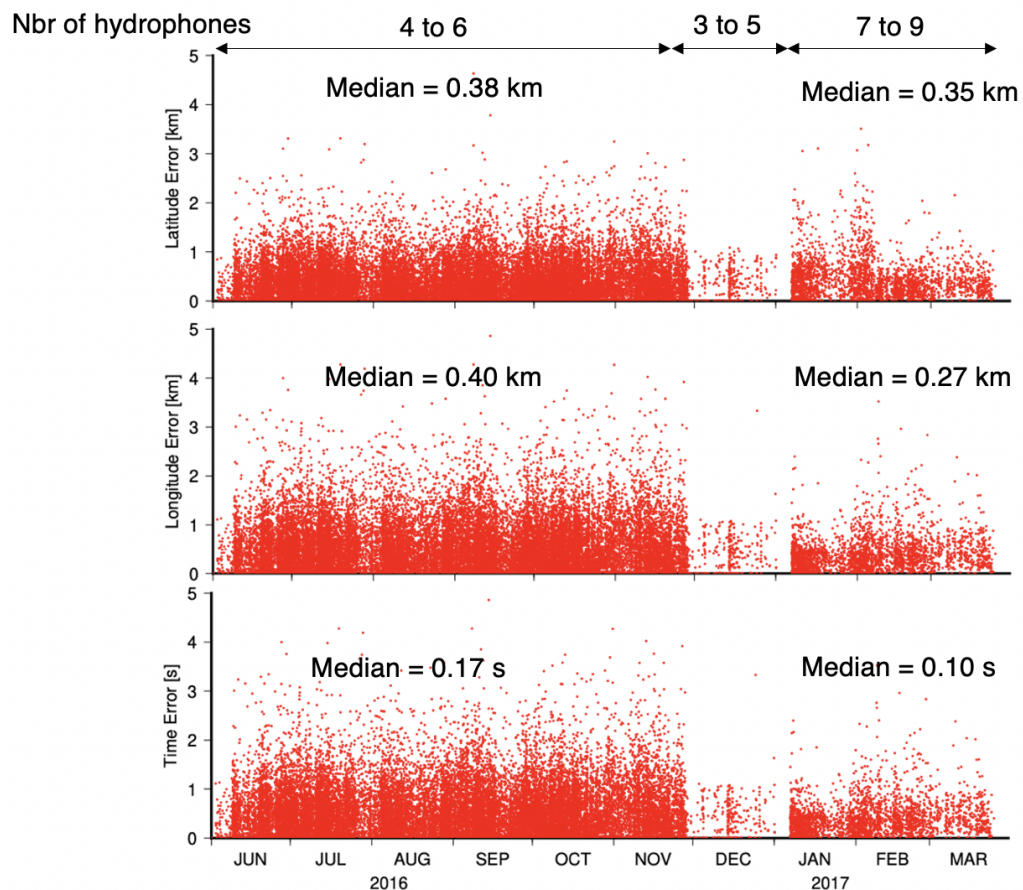


Figure 6.11: Temporal distribution of uncertainties in the latitude, longitudes and origin time for the events located between June 2016 and March 2017 near the Melville TF along the SWIR. Between June and November, events were detected by 4 to 6 hydrophones, by 3 to 5 in December and 7 to 9 in January-March 2017.

6.3 Origin of the seismic swarms along the three Indian ridges

Thanks to the long-term hydroacoustic monitoring of the three Indian Ocean ridges, we were able to detect 39000 events compared with 830 events from the land-based ISC catalog between 2012 and 2020, along the different ridges. A closer examination of this comprehensive hydroacoustic catalog has enabled us to characterize one swarm from another, which would not have been clearly evident on the basis of the terrestrial catalogs. For example, we observed several pulses of intense and focused seismicity within a swarm, interpreted as magmatic episodes (e.g. near the Melville TF). In other instances, we interpreted the migration of events as dike propagations (e.g. near the Novara TF). The detection of IMP events (short duration, high energy) interpreted as seafloor eruption was one of the key observations in this study. Table 6.6 gives a summary of each seismic swarm analyzed in this study and Table 6.7 outlines the key observations and their possible interpretation.

Ridge	Sr No	Year	Region	Dates (dd/mm)	Nbr of days	Nbr of AUHs	Nbr of ISC	Nbr of GCMT	Nbr of OHA	SLC (dB)	OHA per day	Nbr of IMP	OHA/ISC ratio
SWIR	1	2016	Melville TF	01/06/16-25/03/17	298	9	258	17	27624	206.6	93	118	107
SWIR	2	2018	Novara TF	06/07-18/07	13	9	231	7	1109	212.8	85	69	5
SWIR	3	2018	Segment 4	25/09-27/10	33	7	92	6	4880	209.5	148	58	53
CIR	4	2013	Kairei HF	16/02-07/05	83	6	7	3	203	212.6	2	0	29
CIR	5	2013	Kairei HF	16/11-12/12	27	6	36	9	402	220.9	15	0	11
CIR	6	2019	Segments 8-9	07/04-27/04	20	7	13	2	165	212.5	8	0	13
CIR	7	2020	Segments 8-9	10/04-17/04	7	6	19	0	467	210.3	67	0	24
CIR	8	2020	Edmond HF	16/04-04/09	142	6	68	7	2015	211.3	14	711	30
SEIR	9	2012	29°S segment	01/07-13/07	13	11	19	2	452	220.9	35	0	24
SEIR	10	2012	29°S segment	12/12	1	11	13	0	76	225.5	76	0	6
SEIR	11	2013	Pelagia HF	16/02-07/05	83	6	28	2	322	211.5	4	0	12
SEIR	12	2015	28°S segment	16/10-22/10	7	8	10	0	110	224.2	16	0	11
SEIR	13	2018	29°S segment	21/08-16/09	27	10	21	3	266	214.4	10	0	13
SEIR	14	2019	28°S segment	30/08-12/09	14	11	5	0	74	211.8	5	0	15
SEIR	15	2020	J3 segment	03/12-15/12	13	6	14	9	745	212.0	57	84	53

Table 6.6: Summary of event detections along the three Indian Ocean Ridges using the hydrophones of OHASISBIO and IMS-CTBTO networks containing numerical information.

Ridge	Sr No	Year	Region	Impulsive events	MOL	Interpretation	Origin
SWIR	1	2016	Melville TF	Observed	-	Lava extrusion	Magmatic
SWIR	2	2018	Novara TF	Observed	-	Lava extrusion	Magmatic
SWIR	3	2018	Segment 4	Observed	-	Lava extrusion	Magmatic
CIR	4	2013	Kairei HF	-	-	Magma intrusion	Magmatic
CIR	5	2013	Kairei HF	-	Tectonic MA	Low crustal temperature	Tectonic
CIR	6	2019	Segments 8-9	-	-	Magma intrusion	Magmatic
CIR	7	2020	Segments 8-9	-	Tectonic MA	High crustal temperature	Tectonic
CIR	8	2020	Edmond HF	Observed	Tectonic MA	Lava extrusion	Magmato-tectonic
SEIR	9	2012	29°S segment	-	-	Magma intrusion	Magmatic
SEIR	10	2012	29°S segment	-	-	Magma intrusion	Magmatic
SEIR	11	2013	Pelagia HF	-	-	Magma intrusion	Magmatic
SEIR	12	2015	28°S segment	-	-	Magma intrusion	Magmatic
SEIR	13	2018	29°S segment	-	-	Magma intrusion	Magmatic
SEIR	14	2019	28°S segment	-	-	Magma intrusion	Magmatic
SEIR	15	2020	J3 segment	Observed	Tectonic MA	Lava extrusion	Magmato-tectonic

Table 6.7: Interpretation of seismic swarms studied in this thesis. MOL stands for Modified Omori's Law, MA for Mainshock-Aftershocks sequence (tectonic). Lava extrusion occurs when we observe impulsive events; otherwise magma intrusion.

In the introduction of this thesis, we posed fundamental questions for guiding our research focus. Through our comprehensive analysis of seismic swarms or sequences along the three Indian Ocean ridges, we have been able to establish preliminary insights addressing these questions:

1. What are the different types of seismic activity ?

Based on the detections of 15 different seismic clusters along the three Indian Ocean ridges, we classify them into three different types:

Tectonic sequences: The seismicity of a tectonic nature along mid-ocean ridges arises from the intricate interplay of stresses and movements linked to the divergent motion of tectonic plates. Temporal patterns within tectonic sequences manifest as a mainshock followed by aftershocks, a behavior observed when an exponential decay in the number of aftershocks could be found (modified Omori's law). While several instances of mainshock-aftershock sequences have been noted, it is significant to highlight that within the majority of sequences, tectonic seismicity does not solely dominate. An instance of note is the cluster observed in April 2020 along segments 8-9 of the CIR (Table 6.6 and 6.7), wherein a mainshock-aftershock sequence was evident, supplemented by a high p -value indicative of tectonic origin.

Magmatic swarms: Magmatic swarms along mid-ocean ridges, associated with magma intrusions are primarily characterized by a lack of strong tectonic mainshock, a long spatio-

temporal distribution, and a constant level in SLs. We also observed several episodes of increase in activity rate, distributed unevenly within the swarms. Their duration could either last less than a day (e.g. on 29°S segment in December 2012; Table 6.6), up to a week (e.g. on 28°S segment in 2015) or up to several months (e.g. near Melville TF). Eleven out of 15 seismic clusters were magmatic swarm in nature: 3 along the SWIR, 2 along the CIR, and 6 along the SEIR. These swarms are likely caused by magmatic intrusions. Based on either the migration of events or several episodes of intense and clustered seismic activity, we were able to suggest dike propagation within the crust or emplacement, respectively. In some swarms, we observed impulsive events indicating lava extrusions.

Magmato-tectonic sequences: This type of seismicity shows a complex interplay between magmatic and tectonic processes. It arises from the intricate interaction between the movement of magma and regional tectonic stresses. Three swarms, one near the Kairei HF, another near the Edmond HF, and the last along the J3 segment showed a magmato-tectonic nature. All of them comprised mainshock-aftershocks sequences. The magmatic intrusions can induce stress changes in the surrounding rocks, potentially triggering strong tectonic earthquakes (e.g. near the Edmond HF). Conversely, tectonic stress perturbations can influence magma migration (e.g. along the J3 segment).

2. What did we learn from stress modeling?

In the context of MORs, extension is primarily accommodated through displacements along normal faults. These faults entail the separation of material due to tension, which subsequently results in stress relaxation through seismic ruptures during both tectonic events and magmatic accretion. This process can trigger seismic events, including earthquakes, along with volcanic eruptions, favoring hydrothermal circulation. In this study, we performed stress modeling for some strong events, with normal faulting mechanisms and selecting the fault plane dipping towards the axial valley.

Along the SWIR (near the Melville TF), the events after M_w 5.4 event aligned with the obliquity of the ridge axis and parallel to the azimuth of the fault plane (Figure 7 in [Ingale et al., 2023](#)). The absence of MOL fitting this sequence of events pointed to a magmatic origin. The narrow band of events occurred in the area where the M_w 5.4 event imparted horizontal extension onto the shallow crust below the axial valley, which could have triggered or facilitated the propagation of a vertical dike.

Along the CIR (near the Kairei and Pelagia HFs in Feb 2013), the absence of a mainshock-aftershocks sequence clearly suggests a magmatic origin. Most events occurred in the area under extensional stresses that may have favored dike intrusions (Figure 4.11 and 4.12). In

November 2013, we observed a tectonic mainshock-aftershocks sequence near the Kairei HF. There is no clear relationship between the predicted stresses and the distribution of the events, suggesting widespread stress readjustments (Figure 4.15).

In the vicinity of the Edmond HF, we speculated dikes would have reached the seafloor (presence of impulsive events) and also observed two clear tectonic mainshock-aftershocks sequences. The aftershocks triggered by the M_w 5.8 event mostly focused on the regions of predicted extensional stresses, leaving a seismic gap in the area under compression below the axial valley (Figure 4.19). For the other event of lesser magnitude (M_w 4.9), the induced stresses are lesser and the distribution of aftershocks looks unrelated to them (Figure 4.21).

Along the J3 segment of the SEIR, we observed dike extrusions as well as a tectonic mainshock-aftershocks sequence. The predicted stresses in the shallow crust, 10 km north of the mainshock (M_w 5.0), are weak and aftershocks are widely distributed, also potentially due to large longitudinal uncertainties (Figure 5.17).

3. What did the swarms tell about the underlying lithosphere?

The seismicity observed across different spreading environments is notably indicative of underlying lithospheric characteristics. Through the analysis of hydroacoustic data, we have detected a total of 33,613, 3,252, and 2,045 events along the SWIR, CIR, and SEIR, respectively, in contrast to 581, 143, and 110 events catalogued by the ISC. This comparison extends to the ratio of hydroacoustic to teleseismic events, which follows a consistent trend: 58 along the SWIR, 23 along the CIR, and 19 along the SEIR. Notably, the overall averaged seismicity rate, quantified by the number of detections per day within individual swarms, diverges from this pattern. The rate is highest along the SWIR (98 events/day), whereas similar along the SEIR (13), and CIR (12). This difference in seismicity rate suggests an absence of a discernible systematic relationship between seismicity rate and spreading rates.

The first-order inverse relation of either a total number of event detections or the ratio of OHA to ISC events along the SWIR, CIR, and SEIR reflects the varying strength of the lithosphere beneath these three ridges. As previously mentioned, the SWIR shows a relatively cool underlying mantle, coupled with a robust lithosphere and a thicker brittle layer. These geological attributes make the SWIR more prone to a substantial number of large earthquakes. In order to account for the size and frequency of these seismic events, it becomes necessary to consider rapid magma intrusion mechanisms within a colder and more substantial crustal environment. At slow-spreading rates, characteristic of the CIR, a moderation in the strength of the underlying lithosphere coupled with a relatively thinner brittle layer contributes to a reduction in earthquake occurrence. On the other hand, the intermediate spreading SEIR is distinguished by a thin lithosphere and a continuous magma supply

that results in diminished lithospheric strength. This intrinsic geological setup translates into a lower capacity to accommodate seismic events, as evident from our comprehensive analysis.

4. Are the swarms different in different spreading environments?

Recurrence of swarms

We observed notable instances of recurrent seismic activity in specific locations, such as near the Kairei HF, segments 8-9 of the CIR, and along the 28°S and 29°S segments of the SEIR (Table 6.6). Close to the Kairei HF, two distinct types of seismicity occurred at a 6-month interval (Feb-May and Nov-Dec 2013). The initial one showed a magmatic swarm origin, while the latter one displayed a magmato-tectonic nature. In segments 8-9 of the CIR, a similar pattern emerged with two distinct clusters separated by a year, occurring in April 2019 and April 2020. The former had a magmatic swarm origin, whereas the latter displayed a tectonic mainshock-aftershock sequence. These intricate patterns underscore the magmatic and tectonic complexity of recurrent seismicity within the context of the slow-spreading CIR.

Moving to the SEIR, a distinct temporal gap of four years was observed between the two swarms along the 28°S segment, manifesting in 2015 and 2019. In contrast, the 29°S segment displayed three distinct swarms, with two occurring within a five-month interval (July and December 2012), and the third emerging after approximately six years later in 2018. We interpreted all these swarms as magmatic in origin, a feature possibly attributable to a consistent but episodic magma supply beneath the SEIR.

So, the slow-spreading CIR has a higher recurrence of swarms compared with the intermediate-spreading SEIR.

Strong events in swarms

All seismic swarms exhibited large-magnitude events with focal mechanisms (GCMT solutions), except the December 2012 and September 2019 swarms along the SEIR, and the April 2020 sequence along the CIR.

Distinct observations arose along the SWIR, where exclusively normal faulting events were identified, predominantly occurring within magmatic swarms, as inferred by a lack of mainshock-aftershocks sequences (i.e. no MOL decay). Such events could either be associated with dike emplacements (Rubin and Pollard, 1988) or the reactivation of pre-existing faults in response to stress perturbations.

On the CIR, the seismicity proximal to hydrothermal fields is triggered by normal faulting events. The latter occurred primarily along the asymmetric segment associated with the

detachment fault off the Kairei HF (Okino et al., 2015). Near the Edmond HF, we speculated an intense dike emplacement which could have resulted from a rupture along normal faults. Along the 28°S-29°S segments of SEIR, the strong events showing normal faulting mechanisms mainly occurred at the end of the individual swarm activity. They likely represent the reactivation of faults or stress readjustments in response to the magmatic intrusion.

A noteworthy observation was the occurrence of reverse-faulting mechanisms close to the Edmond HF and in the 29°S segment. They were followed by increased seismic activity. We interpreted these events as a result of crustal inflation (i.e. underlying magma chamber inflation), reactivating in reverse preexisting normal faults, followed by subsidence when the magma chamber emptied. Near the Edmond HF, the increase in impulsive events (lava extrusion) after the reverse faulting event supports this hypothesis.

Hence, the occurrence of strong events in swarms looks unrelated to the spreading rates but rather reflects the local crustal dynamics.

5. **Do events at transform faults have precursors?** Along the Blanco transform fault, offsetting the Gorda and Juan de Fuca Ridge, Dziak et al. (2003) observed precursors prior to a M_w 6.2 event (72 events within 12 hours before the mainshock) using hydroacoustic data. The fast-spreading East Pacific Rise showed intense precursor activity with ~ 20000 events during the seven days prior to a strong event (M_w 6.0), located on the Gofar transform fault, based on an OBS survey (McGuire et al., 2005). Although we reported seismicity near transform faults, especially along the SWIR, we did not observe any precursor prior to strong events ($M_w \geq 5$). Along the SEIR, we observed only one normal faulting event (M_w 5.0 on 15 Sept 2018) on the transform offsetting the 28°S-29°S segments, but it was preceded by only 10 events (Figure 5.8), which is moderate compared to the Juan de Fuca or the East Pacific Rise. So, in the absence of clusters in our collection with strong strike-slip events, our study adds little information about the presence of precursors on transform faults.

6. How did the swarms found along the Indian ridges compare with other ridges?

The SWIR and the Gakkel Ridge in the Arctic Ocean, both characterized by ultraslow spreading rates, exhibit notable similarities in terms of seismic activity. A particularly major seismic swarm was detected along the Gakkel Ridge, with a substantial and prolonged sequence involving approximately 200 teleseismic events, including 23 with GCMT solutions indicating normal faulting mechanisms (Müller et al., 2000). This swarm was attributed to a magmatic origin, with the normal faulting events interpreted as magmato-tectonic in nature. Seismic tomography (Koulakov et al., 2022a) further unveiled indications of low-degree mantle melts beneath this section of the Gakkel Ridge, suggesting a lithosphere characterized by semi-

brittle and high-strength material, thus prone to the observed seismicity. Similarly, along the SWIR, analogous instances of robust and enduring magmatic swarms were identified, thereby reinforcing the supposition of a shared underlying mechanism.

The CIR and the Mid-Atlantic Ridge (MAR) are characterized by slow-spreading rates. Notably, the regions of active hydrothermal vent sites along the MAR are associated with heightened seismicity rates (e.g. [Simão et al., 2010](#)). The seismic activity patterns (activity rate) near the Kairei and Edmond hydrothermal fields align with those documented along the MAR's corresponding regions. Although no active hydrothermal field has been reported beneath segments 8-9, findings from deep-towed Ocean Floor Observation System (OFOS) surveys revealed basalt alterations beneath segment 9, suggestive of potential hydrothermal activity ([Briais, 1995](#)). According to [Escartín et al. \(2008\)](#), variations in tectonic stresses of slow-spreading ridges could significantly influence the observed high seismicity rates, also characterized by stress modeling in our study. Apart from this, the seismicity near the HF along the Endeavour segment ([Bohnenstiehl et al., 2004](#)) and Kairei HF (this study) showed similar characteristics, associated with magmatic and tectonic processes.

The SEIR, as well as the Explorer and Gorda ridges in the Pacific Ocean, share intermediate spreading rates. An intriguing observation emerges from the center of ridge segments along the Explorer and Gorda Ridges, where transient periods of magmatic swarm activity are interspersed with prolonged quiescent phases, a phenomenon characterized by hydroacoustic data ([Dziak et al., 2011](#)). [Fox and Dziak \(1998\)](#) previously interpreted the seismic episodes along the Gorda Ridge as being linked to magmatic intrusions, as we proposed for those along the segments.

7. What does the distribution of seismic swarms tell us about accretionary processes?

Looking at the distribution of the swarms, we observe that they come in distinct patches along the SWIR and SEIR, but form a continuous patch at the southern end of the CIR.

The ridge morphology of the **SWIR** is well documented by [Patriat et al. \(1997\)](#), [Cannat et al. \(1999\)](#) and [Sauter and Cannat \(2010\)](#). Their study shows that magmatism is present along the SWIR despite a low melt supply; however, it is focused on discrete magmatic pockets, resulting in magmatic and amagmatic segments of the SWIR. The axial segmentation also shows high and low values of the Mantle Bouguer Anomaly (MBA), where the MBA low corresponds to a lower crustal density consistent with a high magmatic supply ([Cannat et al., 1999](#)). In our study, the discrete and strongest seismic swarms studied along the SWIR were primarily observed on segments with low MBA. Geographically, the hydroacoustic events were spread over a large area (within the uncertainty limit) near the Melville TF and Novara

TF and were very focused along segment 4, which suggests a focused magma supply beneath segment 4.

Along the MAR, most of the swarms exhibiting several mainshock-aftershock sequences with high p -values are associated with detachment faults and/or hydrothermal fields (e.g. [Simão et al., 2010](#); [Giusti et al., 2018](#)). The **CIR** also exhibited swarms with several mainshock-aftershock sequences, in the vicinity of HFs and in segments 8-9, also with high p -values. Since high temperature and migration of hydrothermal fluids reduce the strength of faults, this analogy suggests high hypocentral temperatures in this section of the CIR.

The **SEIR**, fastest among the three ridges, showed seismic swarms at segment centers. Previous studies observed that the seismic activity mostly focuses on segment ends or transform faults, except in the 29°S segment ([Royer et al., 2015](#); [Tsang-Hin-Sun et al., 2016](#)). The absence of clusters at segment ends between 2010 and 2020 means that episodic magmatic intrusion (magma emptying and refilling) is not widespread and only occurs at specific spreading centers, only in the center of ridge segments and even repeatedly as shown in this study.

8. Do the tidal heights trigger some seismicity?

We compared the episodic nature of seismicity within a few of the swarms with either the ocean or solid-Earth tides. Along the SWIR and CIR, we did not observe any convincing correlations of tide heights with the seismicity rate. Only the SEIR segment magmatic swarms showed a correlation with solid-Earth tidal unloading and we suggested that it could be linked with the inflation of magma chamber. There were also a few instances of coincident variations of SLs with tide height, a detailed analysis would help to identify a cause-and-effect relationship.

6.4 Origine des essaims sismiques le long des trois dorsales indiennes

Grâce à la surveillance hydroacoustique à long terme des trois dorsales de l'océan Indien, nous avons pu détecter environ 39 000 événements par rapport à environ 830 événements du catalogue terrestre ISC entre 2012 et 2020, le long des différentes dorsales. Un examen approfondi de ce catalogue hydroacoustique nous a permis de caractériser différents essaims, ce qui n'aurait pas été possible sur la base des catalogues terrestres. Par exemple, nous avons observé de nombreux événements impulsionnels dans certains essaims, interprétés comme des épisodes éruptifs (par exemple, près de la faille de Melville). Dans d'autres cas, nous avons interprété la migration d'événements comme une propagation de dyke (par exemple, près de la faille de Novara). La dé-

tection d'événements IMP (courte durée, haute énergie) interprétés comme résultant d'éruptions en fond de mer a été l'une des observations clés de cette étude. Le Tableau 6.6 donne un résumé de chaque essaim sismique analysé dans cette étude, et le Tableau 6.7 présente les observations clés et leur interprétation possible.

Dans l'introduction de cette thèse, nous avons posé des questions fondamentales dans le but de guider notre recherche. Grâce à notre analyse approfondie des essais sismiques ou des séquences le long des trois dorsales de l'océan Indien, nous avons pu établir des premières perspectives pour répondre à ces questions :

1. Quels sont les différents types d'activité sismique ?

En se basant sur les détections de 15 essais sismiques distincts le long des trois dorsales de l'océan Indien, nous les classifions en trois types différents :

- **Séquences tectoniques:** La sismicité d'origine tectonique le long des dorsales médio-océaniques résulte de l'interaction complexe entre champs de contraintes et déplacements liés au mouvement divergent des plaques tectoniques. Les séquences tectoniques se manifestent par un séisme principal suivi de répliques, un comportement observé lorsque le nombre de répliques décroît exponentiellement (loi modifiée d'Omori). Bien que plusieurs exemples de séquences choc-répliques aient été notés, il est important de souligner que, dans la majorité des séquences, la sismicité d'origine tectonique ne domine pas exclusivement. Un exemple notable est l'essai d'avril 2020 le long des segments 8-9 du CIR (Tableau 6.6 et 6.7), où une séquence choc-répliques était évidente, complétée par une valeur élevée de p indicative d'une origine tectonique.
- **Essais magmatiques:** Les essais magmatiques le long des dorsales médio-océaniques, associés à des intrusions magmatiques, se caractérisent principalement par l'absence d'un séisme tectonique principal fort, une distribution spatio-temporelle prolongée et des niveaux constants dans les SL. Nous avons également observé plusieurs épisodes d'augmentation d'activité, répartis de manière inégale au sein des essais. Leur durée peut être inférieure à une journée (par exemple, sur le segment 29°S en décembre 2012 ; Tableau 6.6), ou durer une semaine (par exemple, sur le segment 28°S en 2015) ou même plusieurs mois (par exemple, près du Melville TF). Onze des 15 essais sismiques se sont révélés d'origine magmatique : 3 le long du SWIR, 2 le long du CIR et 6 le long du SEIR. Ces essais sont probablement causés par des intrusions magmatiques. La migration d'événements, ou plusieurs épisodes d'activité sismique intense et groupée, suggèrent la propagation de dykes dans la croûte ou leur mise en place en

profondeur, respectivement. Dans certains essaims, ils sont associés à des événements impulsionsnels indiquant l'extrusion de lave.

- **Séquences magmato-tectoniques:** Ce type de sismicité résulte d'une interaction complexe entre processus magmatiques et tectoniques, c'est-à-dire entre des mouvements de magma et les contraintes tectoniques régionales. Trois essaims, près du Kairei HF et du Edmond HF, le dernier le long du segment J3, montre clairement une origine magmato-tectonique. Tous comprenaient des séquences choc-répliques. Les intrusions magmatiques peuvent induire des changements de contrainte dans les roches environnantes, déclenchant potentiellement de forts séismes d'origine tectonique (par exemple, près du Edmond HF). Inversement, les perturbations de contrainte tectonique peuvent faciliter la migration du magma (par exemple, le long du segment J3).

2. Qu'avons-nous appris de la modélisation du stress ?

Dans le contexte des dorsales médio-océaniques (MOR), l'extension est principalement accommodée par des déplacements le long de failles normales. Ces failles impliquent la séparation de matériaux en raison de la tension, ce qui entraîne ensuite une relaxation du stress par des ruptures sismiques lors d'événements tectoniques et d'accrétion magmatique. Ce processus peut déclencher des événements sismiques, tremblements de terre ou éruptions volcaniques, favorisant la circulation hydrothermale. Dans cette étude, nous avons effectué une modélisation du stress pour certains événements forts, avec des mécanismes en faille normale et en sélectionnant le plan de faille incliné vers la vallée axiale.

Le long du SWIR (près de la faille transformante de Melville), les événements après l'événement M_w 5.4 sont alignés sur l'axe de la dorsale et parallèlement à l'azimut du plan de faille (Figure 7 dans [Ingale et al., 2023](#)). L'absence de loi modifiée d'Omori (MOL) s'adaptant à cette séquence d'événements indiquait une origine magmatique. La bande étroite d'événements se concentre dans la région où l'événement M_w 5.4 induisait un contexte en extension horizontale dans la croûte peu profonde sous la vallée axiale, qui aurait pu déclencher ou faciliter la propagation d'un dyke vertical.

Le long du CIR (près des champs hydrothermaux Kairei et Pelagia en février 2013), l'absence d'une séquence de choc-répliques suggère clairement une origine magmatique. La plupart des événements dans un contexte en extension traduisent ou ont pu favoriser des intrusions de dykes (Figure 4.11 and 4.12). En novembre 2013, la séquence tectonique avec choc principal et répliques près du site Kairei HF ne montre pas de relation claire entre les contraintes prédites et la distribution des événements, suggérant des réajustements généralisés des contraintes (Figure 4.15).

Dans le voisinage du site Edmond HF, nous avons spéculé que les dykes auraient atteint le fond marin (présence d'événements impulsionsnels) et avons également observé deux séquences tectoniques claires choc-répliques. Les répliques déclenchées par l'événement M_w 5.8 sont principalement concentrées sur les régions de contraintes d'extension prédites, laissant un vide sismique dans la zone sous compression sous la vallée axiale (Figure 4.19). Pour l'autre événement de moindre magnitude (M_w 4.9), les contraintes induites sont moindres et la distribution des répliques semble sans rapport avec elles (Figure 4.21).

Le long du segment J3 du SEIR, nous avons observé des extrusions de dykes ainsi qu'une séquence tectonique choc-répliques. Les contraintes prédites dans la croûte peu profonde, à 10 km au nord du séisme principal (M_w 5.0), sont faibles et les répliques sont largement réparties, potentiellement en raison de grandes incertitudes longitudinales (Figure 5.17).

3. Que révèlent les essais sur la lithosphère sous-jacente?

La sismicité observée dans ces différents contextes d'accrétion est particulièrement indicative des caractéristiques de la lithosphère sous-jacente. À travers l'analyse des données hydroacoustiques, nous avons détecté un total de 33 613, 3 252 et 2 045 événements le long du SWIR, du CIR et du SEIR, respectivement, par rapport à 581, 143 et 110 événements répertoriés par l'ISC. Cette comparaison s'étend au ratio d'événements hydroacoustiques par rapport aux événements téléismiques, qui suit une tendance constante : 58 le long du SWIR, 23 le long du CIR et 19 le long du SEIR. Notamment, le taux moyen global de sismicité, quantifié par le nombre de détections par jour au sein des essais individuels, ne suit pas cette tendance. Le taux est le plus élevé le long du SWIR (98), tandis qu'il est le même le long des dorsales SEIR (13) et CIR (12). Cette disparité de taux de sismicité suggère une absence de relation systématique discernable entre taux de sismicité et taux d'ouverture.

La relation inverse, au premier ordre, entre nombre total de détections d'événements ou du ratio d'événements OHA par rapport aux événements ISC le long du SWIR, du CIR et du SEIR reflète une résistance mécanique variable de la lithosphère sous ces trois dorsales. Comme mentionné précédemment, la dorsale SWIR a un manteau sous-jacent relativement froid, associé à une lithosphère résistante et une croûte fragile plus épaisse. Ces attributs géologiques rendent la SWIR capable d'accommoder un nombre substantiel de tremblements de terre de forte magnitude. Pour rendre compte de la taille et de la fréquence de ces événements sismiques, il devient nécessaire de prendre en compte des mécanismes rapides d'intrusion magmatique au sein d'un environnement crustal plus froid et plus fragile. À des vitesses d'ouverture lentes, caractéristiques de la CIR, une résistance modérée de la lithosphère sous-jacente associée à une croûte cassante relativement plus mince contribue à une réduction de l'occurrence des tremblements de terre. D'autre part, la dorsale SEIR, à

tauc d'ouverture intermédiaire, est caractérisée par une lithosphère mince et une alimentation continue en magma qui se traduit par une résistance lithosphérique diminuée. Cette configuration géologique intrinsèque se traduit par une capacité réduite à accommoder des événements sismiques, comme le montre notre analyse.

4. 4. Les essaims sont-ils différents dans différents environnements de propagation?

Répétition des essaims

Nous avons observé des instances notables d'activité sismique récurrente à certains sites, tels qu'à proximité du site Kairei HF, des segments 8-9 de la CIR ou le long des segments 28°S et 29°S de la SEIR (Tableau 6.6). Près du Kairei HF, deux épisodes distincts de sismicité se sont produits à un intervalle de 6 mois (février-mai et novembre-décembre 2013). Le premier est d'origine magmatique, tandis que le second de nature magmato-tectonique. Dans les segments 8-9 du CIR, un schéma similaire est apparu avec deux essaims distincts à un an d'intervalle, en avril 2019 et en avril 2020. Le premier est d'origine magmatique, tandis que le second était une séquence tectonique avec choc principal et répliques. Ces exemples soulignent l'interaction des processus magmatique et tectonique dans la sismicité récurrente dans le contexte d'ouverture lente de la CIR.

Concernant la dorsale SEIR, un intervalle de quatre ans sépare deux essaims le long du segment 28°S, se manifestant en 2015 et 2019. En revanche, au segment 29°S, sur trois essaims distincts, deux se sont produits dans un intervalle de cinq mois (juillet et décembre 2012), et le troisième s'est produit six ans plus tard en 2018. Nous avons interprété tous ces essaims comme d'origine magmatique, une caractéristique attribuable à une alimentation continue en magma sous la SEIR.

Ainsi, l'expansion lente de la CIR présente une récurrence plus élevée d'essaims par rapport à l'ouverture à taux intermédiaire de la SEIR.

Événements de forte magnitude dans les essaims

Tous les essaims sismiques présentent des événements de forte magnitude dont on connaît les mécanismes au foyer (solutions GCMT), à l'exception des essaims de décembre 2012 et septembre 2019 le long de la SEIR, et de la séquence d'avril 2020 sur la CIR.

Des événements en faille normale sur la SWIR ont été identifiés au sein d'essaims magmatiques, sans être associés à une séquence choc-répliques (i.e. sans décroissance de type MOL). De tels événements seraient alors associés à des emplacements de dykes (Rubin and Pollard, 1988) ou à la réactivation de failles préexistantes en réponse à des perturbations du champ de contrainte.

Sur la CIR, la sismicité à proximité des champs hydrothermaux est déclenchée par des événements en faille normale. Ces derniers sont localisés principalement le long du segment asymétrique associé à la faille de détachement au large du Kairei HF (Okino et al., 2015). Près du site Edmond HF, nous avons spéculé sur la mise en place de dykes qui aurait pu résulter de la rupture le long de failles normales.

Le long des segments 28°S-29°S de la SEIR, les événements avec des mécanismes de faille normale se sont produits à la fin de l'activité de chaque essaim. Ils représentent probablement la réactivation de failles ou un réajustement de contrainte en réponse aux intrusions magmatiques. Une observation remarquable est l'occurrence de mécanismes en faille inverse à proximité du site Edmond HF et dans le segment 29°S. Ils sont suivis par une augmentation de l'activité sismique interprétée comme le résultat d'une inflation crustale (associée à l'inflation d'une chambre magmatique sous-jacente) suivie d'une subsidence lorsque la chambre magmatique s'est vidée. Près du site Edmond HF, l'apparition d'événements impulsionsnels (extrusion de lave) après l'événement en faille inverse soutient cette hypothèse. Ainsi, l'occurrence d'événements de forte magnitude dans les essaims semble sans rapport avec les taux d'ouverture, mais reflète plutôt la dynamique crustale locale.

5. Les événements aux failles transformantes ont-ils des précurseurs?

Le long de la faille transformante Blanco, entre les dorsales Gorda et Juan de Fuca, Dziak et al. (2003) ont observé des précurseurs avant l'événement M_w 6.2 (72 événements dans les 12 heures précédant le séisme principal) à partir de données hydroacoustiques. La dorsale rapide Est-Pacifique a montré une activité de précurseur intense avec environ 20 000 événements au cours des sept jours précédant un événement fort (M_w 6.0), situé sur la faille transformante Gofar, à partir de données d'OBS (McGuire et al., 2005). Bien que nous ayons observé une sismicité près des failles transformantes, en particulier le long de la SWIR, nous n'avons pas observé de précurseur avant des événements $M_w \geq 5$. Le long de la SEIR, nous n'avons observé qu'un événement en faille normale (M_w 5.0 le 15 septembre 2018) sur la faille séparant les segments 28°S-29°S, mais il est précédé de seulement 10 événements (Figure 5.8), ce qui est modéré par rapport aux observations sur les dorsales Juan de Fuca ou Est-Pacifique. Ainsi, notre étude ajoute peu d'évidence de présence de précurseurs sismiques sur les failles transformantes.

6. Comment les essaims trouvés le long des crêtes indiennes se comparent-ils à d'autres crêtes?

Les dorsales SWIR et de Gakkel dans l'océan Arctique, caractérisées toutes deux par des taux d'ouverture ultra-lents, présentent des similitudes notables en termes d'activité sismique.

Un essaim sismique particulièrement important a été détecté le long de la dorsale de Gakkel, avec une séquence substantielle et prolongée impliquant environ 200 événements télésismiques, dont 23 avec des mécanismes en faille normale (Müller et al., 2000). Cet essaim est interprété comme d'origine magmatique, et les événements en faille normale comme de nature magmato-tectonique. La tomographie sismique (Koulakov et al., 2022b) donne des indices de fusion partielle mantellique de faible degré sous cette section de la dorsale de Gakkel, suggérant une lithosphère semi-fragile et à haute résistance, donc propice à la sismicité observée. De manière similaire, le long de la SWIR, la présence analogue d'essaims magmatiques robustes et durables renforce l'hypothèse d'une lithosphère sous-jacente analogue.

Les dorsales CIR et médio-atlantique (MAR) sont caractérisées par des taux d'expansion lents. Notamment, les sites actifs avec des sources hydrothermales le long de la MAR présentent des taux de sismicité élevés (e.g. Simão et al., 2010), semblables à ceux observés près des champs hydrothermaux Kairei et Edmond. Bien qu'aucun site hydrothermal actif n'ait été signalé sous les segments 8-9, les observations du plancher océanique (OFOS) ont révélé des altérations de basalte sous le segment 9, suggérant une activité hydrothermale potentielle (Briais, 1995). Selon (Escartín et al., 2008), les variations des contraintes tectoniques des dorsales lentes influenceraient de manière significative les taux de sismicité élevés observés, comme le souligne la modélisation des contraintes dans notre étude. Par ailleurs, la sismicité près d'un site hydrothermal du segment Endeavour (Bohnenstiehl et al., 2004) (Bohnenstiehl et al., 2004) présente des caractéristiques similaires, associées à des processus magmatiques et tectoniques.

Les dorsales SEIR, Explorer et Gorda dans l'océan Pacifique, ont des taux d'expansion intermédiaires. Comme sur la dorsale SEIR, certains segments des dorsales Explorer et Gorda présentent des essaims d'origine magmatique transitoires entrecoupés de phases de quiescence prolongées (Dziak et al., 2011). Fox and Dziak (1998) ont aussi interprété les épisodes sismiques le long de la dorsale de Gorda comme étant liés à des intrusions magmatiques, comme nous l'avons proposé pour la dorsale SEIR.

7. Que nous dit la distribution des essaims sismiques sur les processus d'accrétion?

En examinant la distribution des essaims, nous observons qu'ils se distribuent sur des sites distincts le long des dorsales SWIR et SEIR, mais s'étendent sur une zone continue à l'extrémité sud de la CIR.

La morphologie de la dorsale SWIR, bien documentée par Patriat et al. (1997), Cannat et al. (1999) et Sauter and Cannat (2010), montre que le magmatisme est présent le long de la SWIR

mais limité. Le magmatisme extrusif est concentré sur certains segments, en une succession de segments magmatiques et amagmatiques. Cette segmentation axiale se traduit aussi par une succession d'anomalies de Bouguer du manteau (MBA), où une faible MBA correspond à une densité crustale inférieure, en cohérence avec un apport magmatique élevé (Cannat et al., 1999). Dans notre étude, les essais sismiques discrets et les plus intenses sont principalement observés sur des segments à faible MBA. Géographiquement, les événements hydroacoustiques s'étendent sur une grande superficie (aux incertitudes près) près des transformantes Melville et Novara et sont plus focalisés le long du segment 4, ce qui suggère un apport de magma concentré sous le segment 4.

Le long de la MAR, la plupart des essais présentant plusieurs séquences choc-répliques avec des paramètres p élevés sont associés à des failles de détachement et/ou des champs hydrothermaux (e.g. Simão et al., 2010; Giusti et al., 2018). La dorsale CIR présente également des essais avec plusieurs séquences choc-répliques, à proximité des sites HF et dans les segments 8-9, également avec des p élevés. Comme la température élevée et la migration des fluides hydrothermaux réduisent la résistance des failles, cette analogie suggère des températures hypocentrales élevées dans cette section de la CIR.

La dorsale SEIR, le plus rapide des trois, présente des essais sismiques au centre des segments. Des études antérieures ont observé que l'activité sismique se concentre principalement aux extrémités des segments ou aux failles transformantes, sauf dans le segment 29°S (Royer et al., 2015; Tsang-Hin-Sun et al., 2016). L'absence d'essais majeurs aux extrémités des segments entre 2010 et 2020 signifie que l'intrusion magmatique épisodique (vidange et remplissage du magma) n'est pas généralisée et se produit uniquement à des centres d'expansion spécifiques, uniquement au centre des segments et même de manière répétée comme le montre cette étude.

8. Les hauteurs de marée déclenchent-elles une sismicité?

Nous avons comparé la nature épisodique de la sismicité au sein de quelques essais avec les marées océaniques ou terrestres solides. Le long des SWIR et CIR, nous n'avons observé aucune corrélation convaincante entre les hauteurs de marée et le taux de sismicité. Seuls les essais magmatiques du segment SEIR ont montré une corrélation avec le déchargement terrestre solide des marées, qui pourrait être à l'origine de l'inflation de la chambre magmatique, elle-même génératrice de sismicité. Il y a également quelques cas de variations coïncidentes entre SL et hauteur des marées, mais qui demanderaient une analyse détaillée pour identifier une relation de cause à effet.

Conclusions

The creation of new oceanic crust unfolds through magma-driven processes embedded within the mid-ocean ridge (MOR) system, a realm characterized by dynamic activities encompassing fluid circulation, cooling, and faulting. These contributory processes transpire beneath the overarching sub-axial crust, shaping the evolving landscape of oceanic spreading ridge axes. A hydroacoustic approach provides a complementary vantage point into the intricate interplay between tectonic and magmatic processes along mid-ocean ridges. Hydroacoustic signals allow the precise determination of diverse parameters, encompassing event localization, Source Levels (acoustic magnitude), and frequency content. By delving into temporal dynamics, which adhere to modified Omori's laws, and spatial distributions that encompass the migration of hydroacoustic epicenters and the emergence of clustering patterns, a discerning framework emerges. This framework enables the classification of seismic clusters along the three distinct ridges, serving as a powerful tool to discriminate among their origins, whether tectonic sequences, magmatic swarms, or a complex fusion of both, known as magmato-tectonic clusters.

Within the scope of this investigation, a total of 38,910 hydroacoustic events were detected along the three Indian Ocean Ridges in data recorded between 2012 and 2020 by hydrophones of the OHASISBIO and IMS-CTBTO networks. Notably, the ultraslow-spreading Southwest Indian Ridge (SWIR) exhibited an abundance of events, followed by the slow-spreading Central Indian Ridge (CIR), and finally, the intermediate-spreading Southeast Indian Ridge (SEIR; Table 6.6). However, there is no systematic correlation between the seismicity rate (number of detections per day) and the ridge spreading rate.

Within the scope of this investigation, in this study, we detected a total of 38,910 hydroacoustic events along the three Indian Ocean Ridges in data recorded between 2012 and 2020 using data from the OHASISBIO and IMS-CTBTO hydrophone networks. Notably, the ultraslow-spreading Southwest Indian Ridge exhibited an abundance of events, followed by the slow-spreading Central Indian Ridge, and finally, the intermediate-spreading Southeast Indian Ridge (Table 6.6). But, we did not observe any systematic correlation between the seismicity rate (number of detections per day) and the ridge spreading rate.

To enhance the precision in localizing "T-phase" sources, we manually scrutinized continuous T-wave spectrograms through two successive iterations. This methodology yielded notable improvements in both the uncertainties associated with event location and origin time. Unsurprisingly, events confined within the network boundary exhibited higher accuracy, and events identified on a greater number of hydrophones exhibited diminished uncertainties.

The Source Level (SL), the acoustic magnitude of "T-phase" sources, is more difficult to interpret than seismic magnitudes since they not only reflect the actual energy of an event but also the efficiency of the seismo-acoustic conversion at the seafloor and the interactions of these acoustic waves with the propagating medium. Despite that, SL demonstrates a frequency-size distribution akin to that described by the Gutenberg-Richter law for seismic magnitudes. The terrestrial seismic catalogs in this study exhibited a completeness threshold of $M_C \geq 3.9 mb$, which is improved by ~ 0.6 (i.e. $\sim 3.3 mb$) from the detailed hydroacoustic catalogs. This observation stands for other seismic magnitudes; hydroacoustic completeness is ~ 2.1 with respect to surface-wave magnitude M_s , ~ 2.4 with respect to moment magnitude M_w .

The Source Level (SL), the acoustic magnitude of "T-phase" sources, is more difficult to interpret than seismic magnitudes since they not only reflect the actual energy of an event but also the efficiency of the seismo-acoustic conversion at the seafloor and the interactions of these acoustic waves with the propagating medium. Despite that, SL demonstrates a frequency-size distribution akin to that described by the Gutenberg-Richter law for seismic magnitudes. The terrestrial seismic catalogs in this study exhibited a completeness threshold of $M_C \geq 3.9 mb$, which is improved by ~ 0.6 (i.e. $\sim 3.3 mb$) from the detailed hydroacoustic catalogs. This observation stands for other seismic magnitudes: hydroacoustic completeness is ~ 2.1 with respect to surface-wave magnitude M_s , ~ 2.4 with respect to moment magnitude M_w .

This study also accounts for spatial variation in the computed b-value, the slope of the Gutenberg-Richter law, which represents the proportion of small magnitude (SL) vs. large magnitude events. Tentatively, b -value showed high values at segment centers (e.g. 29°S segment on the SEIR), lesser near transform faults (e.g. Melville TF), and the lowest near hydrothermal fields (e.g. Edmond HF). The b -value for all 15 swarms is 0.09.

Along with the regular "T-phases", we also detected several energetic and short-duration, "H-waves", called impulsive events. Based on their duration, high energy, and frequency content, we attribute them to lava-water interactions. Underwater-controlled source explosions generate similar signals. Thus, a single impulsive event can be mistaken for a man-made underwater explosion. Since natural impulsive events occur periodically or sporadically (weeks to months) in clusters centered on spreading ridges or at underwater volcanoes, and generally nearby high-magnitude earthquakes (recorded on land, e.g. ISC or GCMT catalogs), such confusion would be unlikely. Also, these events do not exhibit a fixed cadency which is a common feature of air-gun shots used

for seismic exploration.

The swarms detected along the SWIR, two near transform faults (Novara and Melville) and one swarm on segment 4 at 67°45'E, underscore a magmatic origin, resulting in focused magmatism beneath distinctive parts of the ridge. The CIR, marked by five seismic clusters, three near hydrothermal fields, and two along ridge segments, reveals diverse behaviors ranging from either magmatic swarm or tectonic sequence or magmato-tectonic cluster, reflecting varying magma supplies and tectonically active processes. Along the SEIR, seismic swarms at the center of segments or near the Pelagia hydrothermal field present a magmatic origin; however, the swarm in the vicinity of the St Paul-Amsterdam Plateau shows a magmato-tectonic behavior in the context of an overlapping spreading center (OSC).

The decay parameter of Modified Omori law, or p value, is relatively low along the SWIR, which could reflect a colder and/or thicker sub-axial crust, and is high along the CIR and at 40°S (OSC) on the SEIR, reflecting higher hypocentral temperatures.

Overall, this hydroacoustic study along the Indian MOR system helped us to characterize nuances among swarms based on the spatio-temporal distribution of ~39,000 events that have escaped to terrestrial networks. The tectonic or magmatic origin of each swarm seemed independent from the spreading regime; however, considered all together, they do reflect characteristics of the different spreading contexts.

Conclusions (En français)

La création d'une nouvelle croûte océanique est le résultat de processus magmatiques le long des dorsales médio-océaniques (MOR), domaines caractérisés par des processus dynamiques englobant circulations de fluides, refroidissement et formation de failles. Ces processus contributifs à l'axe des dorsales façonnent la morphologie des dorsales. L'approche hydroacoustique offre un point de vue complémentaire sur l'interaction complexe entre processus tectoniques et magmatiques le long des dorsales médio-océaniques. Les signaux hydroacoustiques permettent de déterminer avec précision divers paramètres, notamment la localisation des événements, leur niveau source (amplitude acoustique) et leur contenu fréquentielle. En examinant la dynamique temporelle des essaims, qui adhère aux lois d'Omori modifiées, et les distributions spatiales qui englobent la migration des épicentres hydroacoustiques ou leur focalisation, un cadre en émerge et permet de classer les essaims sismiques le long des trois dorsales distinctes. Cette approche constitue un outil puissant pour distinguer l'origine de ces essaims, qu'il s'agisse de séquences tectoniques, d'essaims magmatiques ou d'une interaction complexe des deux processus, connue sous le nom d'essaims magmato-tectoniques.

Dans le cadre de cette étude, un total de 38 910 événements hydroacoustiques a été détecté le long des trois dorsales de l'océan Indien dans les données enregistrées entre 2012 et 2020 par les hydrophones des réseaux OHASISBIO et IMS-CTBTO. Notamment, la dorsale sud-ouest Indienne (SWIR) à ouverture ultra-lente présente une abondance sismicité, suivie par la dorsale centrale Indienne (CIR) à ouverture lente, et enfin, la dorsale sud-est Indienne (SEIR ; [Tableau 6.6](#)) à ouverture intermédiaire. Il n'y a cependant pas de corrélation systématique entre le taux de sismicité (nombre de détections par jour) et la vitesse d'ouverture de la dorsale.

Pour améliorer la précision de la localisation des sources des ondes T, les spectrogrammes continus ont été examinés manuellement en deux itérations successives. Cette méthodologie a permis d'améliorer sensiblement les incertitudes associées à la localisation des événements et à l'heure d'origine. Sans surprise, les événements confinés à l'intérieur du réseau sont localisés avec une plus grande précision, ainsi que les événements identifiés sur un plus grand nombre

d'hydrophones.

Le niveau source (SL), ou magnitude acoustique des sources des ondes T, est plus difficile à interpréter que les magnitudes sismiques, car il ne reflète pas seulement l'énergie réelle d'un événement, mais aussi l'efficacité de la conversion sismo-acoustique au fond de la mer et les interactions de ces ondes acoustiques avec le milieu lors de leur propagation. Malgré cela, les SL suivent une distribution fréquence-taille semblable à celle décrite par la loi de Gutenberg-Richter pour les magnitudes sismiques. Les catalogues sismologiques terrestres dans la zone d'étude présentent un seuil de complétude $MC \geq 3,9$ mb, qui est amélioré $\sim 3,3$ mb ($-0,6$ mb) par nos catalogues hydroacoustiques. Cette observation est valable en comparaison d'autres magnitudes sismiques : la complétude hydroacoustique est de $\sim 2,1$ en magnitude d'onde de surface MS, et de $\sim 2,4$ en magnitude de moment M_w .

Cette étude tient également compte de la variation spatiale du paramètre b, ou pente de la distribution de Gutenberg-Richter, qui représente la proportion d'événements de faible magnitude (SL) par rapport aux événements de forte magnitude. Ce paramètre montre des valeurs plus élevées au centre des segments (ex. : au segment 29°S sur la SEIR), des valeurs moindres à proximité des failles transformantes (ex. : Melville TF), et des valeurs faibles à proximité des champs hydrothermaux (ex. : Edmond HF). Le paramètre b pour l'ensemble des 15 essais étudiés est de 0,09.

Outre les ondes T « classiques », plusieurs "ondes H" énergétiques et de courte durée, appelées événements impulsionnels, sont détectées. Sur la base de leur durée, de leur haute énergie et de leur contenu fréquentiel, nous les attribuons à des interactions entre la lave et l'eau de mer. L'explosion de sources contrôlées sous l'eau génère des signaux similaires. Ainsi, un seul événement impulsionnel peut être confondu avec une explosion sous-marine d'origine humaine. Cependant, étant donné que les événements impulsionnels naturels se produisent périodiquement ou sporadiquement (quelques semaines à quelques mois) en groupes centrés sur des dorsales ou sur des volcans sous-marins, et généralement à proximité de tremblements de terre de forte magnitude (enregistrés à terre, e.g. catalogues ISC ou GCMT), une telle confusion est peu probable. En outre, ces événements ne présentent pas une cadence fixe, caractéristique commune des tirs de canon à air utilisés pour l'exploration sismique.

Les essais détectés sur la dorsale SWIR, deux à proximité des failles transformantes (Novara et Melville) et un sur le segment 4 à 67°45'E, sont d'origine magmatique, c'est-à-dire résultant d'un magmatisme focalisé sous des parties distinctes de la dorsale. La dorsale CIR, marquée par cinq essais sismiques, trois près de champs hydrothermaux et deux le long de segments de la dorsale, est le siège d'essais purement magmatiques ou purement tectoniques ou d'essais magmato-tectoniques, témoins d'un magmatisme variable ou de processus tectoniques actifs. Le long de la dorsale SEIR, les essais sismiques au centre des segments ou près du champ hydrothermal

de Pelagia ont une origine magmatique ; cependant, l'essai à proximité du plateau de St Paul et Amsterdam présente un comportement magmato-tectonique dans un contexte de segments de dorsale chevauchants (OSC).

Le paramètre de décroissance de la loi d'Omori modifiée, ou paramètre p , est relativement faible le long de la SWIR, ce qui pourrait refléter une croûte sub-axiale plus froide et/ou épaisse, et est élevé le long de la CIR et à 40°S (OSC) sur la SEIR, reflétant des températures hypocentrales plus élevées.

Dans l'ensemble, cette étude hydroacoustique le long du système des dorsales Indiennes nous a aidés à caractériser 15 essais sur la base de la distribution spatio-temporelle d'environ 39 000 événements qui ont échappé aux réseaux terrestres. L'origine magmatique ou tectonique de chaque essai semble indépendante du régime d'accrétion ; toutefois, pris dans leur ensemble, ces essais reflètent bien les caractéristiques des différents contextes d'accrétion.

Prospects

This study focused on a limited number of outstanding seismic swarms extracted from teleseismic catalogs between 2012 and 2020. In order to evaluate how representative these swarms are with respect to the long-term seismicity of the three Indian MORs, it would be necessary to have access to a comprehensive hydroacoustic catalog for all three ridges over the same time period. Towards such a formidable task, developing an automatic picking algorithm would be welcomed. The next sections develop this perspective and other potential avenues raised in this study like the mechanism underlying impulsive events.

Automatic picking of events

In this thesis, my approach involved a thorough visual examination and manual identification of T-wave signals in spectrograms over two iterations. This choice was based on the fact that these signals are often more distinct in spectrograms than in waveforms, especially for events with low magnitudes; furthermore, arrival times are generally undiscernible in waveforms. It is important to acknowledge that this analytical process is labor-intensive and its effectiveness might vary among different operators. For example, picking 27624 events over two iterations (2×27624) near the Melville TF (the strongest swarm of this study) took me nearly 6 months, ~ 4 months for the first iteration, and ~ 2 months for the second iteration. To overcome this labor-intensive work, an automatic algorithm for picking and classifying events would be a major enhancement.

From a forward-looking perspective, the implementation of a semi-supervised machine learning algorithm holds great promise as an advancement. A recent study by [Raumer et al. \(2023\)](#) highlights the potential benefits of such an approach based on Convolutional Neural Networks (CNN), which could significantly enhance the efficiency of event detection (Figure 1). This method is based on designing and training an automatic detector in a spectrogram window. As impulsive event waveforms are easily discernible, the proposed model was initially tested on these events.

The first step of this method requires an annotated dataset (catalog built by manual picking in this study), in order to build a train set for the machine learning algorithm. A CNN is then trained

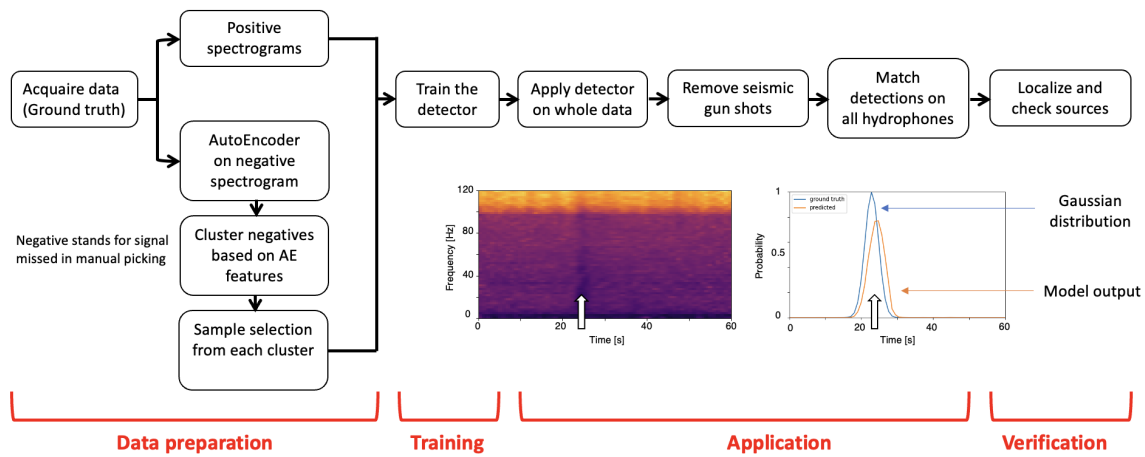


Figure I: Work-flow for an algorithm based on Convolutional Neural Network for the selection, detection, and localization of events. The spectrogram in the center shows a manually-picked impulsive signal alongside its probabilistic distribution, here said "positive" (after Raumer et al., 2023).

to take spectrograms from the train set as input and to output a value comprised in the interval $[0,1]$ for each time-bin of the spectrogram. Applying this CNN to the non-annotated dataset, Raumer et al. (2023) yields a catalog of signals for each station, from which a simple filter removes the most obvious irrelevant signals, e.g. seismic airgun-shots. Signals from different stations are then automatically associated to localize the corresponding sources. Using custom software, the user is then able to check manually these detections.

A preliminary evaluation showed highly efficient performances compared to manual picking. For example, using this method, the detection and verification of ~ 200 impulsive events required around 1 hour, compared to a manual picking at 30 events per hour. As of now, this model works smoothly for impulsive events, which have a distinct and easily identifiable signature. The next challenge, based on comprehensive manually picked catalogs, will be to automatically detect T-waves with less characterized signatures.

Modeling of hydroacoustic waves

This study focused on the manual detection of both T and H waves, but not on their modeling. Using the SPECFEM2D/3D numerical code based on spectral finite element methods, several studies attempted to characterize the generation and propagation of T-waves generated at the interface of a solid-fluid medium (e.g. Jamet et al., 2013; Lecoulant et al., 2019). Abyssal T-waves are generally explained by the scattering of acoustic waves on a rough seafloor, but the initial idea of scattering by a rough sea surface (Johnson and Norris, 1968b) is now revived (Bottero et al., 2023). This would open up a whole new field of investigation, as T-wave signatures would then depend on the sea state. The mechanisms generating H-waves associated with lava-water interactions (produc-

ing impulsive events) have also yet to be explained.

Characterizing the context of impulsive events

The Tiktak volcano, off Mayotte Island, is one example where impulsive events could be associated with an active submarine eruption (hydrophones were ~50 km from the site). A similar association was proposed at the axial seamount, on the Juan de Fuca ridge, but from hydrophones at a closer range (few km; e.g. [Le Saout et al., 2020](#)). Our study showed that these impulsive events are common along spreading ridges and detectable at very long ranges (up to 3700 km in this study). Hydroacoustic networks could therefore become a unique tool to detect active eruptions associated with seafloor spreading. Studying these impulsive events would also call for *in-situ* oceanic campaigns to better understand their context: for example, by repeating near-bottom and high-resolution multibeam bathymetric surveys to detect changes in seafloor morphology, side-scan sonar surveys to highlight freshly formed lava from the back-scattered energy, and/or deep-sea camera surveys from autonomous underwater vehicles.

Perspectives (En français)

Cette étude s'est concentrée sur un nombre limité d'essais sismiques exceptionnels extraits des catalogues téléismiques entre 2012 et 2020. Afin d'évaluer dans quelle mesure ces essais sont représentatifs de la sismicité à long terme des trois dorsales Indiennes, il serait nécessaire d'avoir accès à un catalogue hydroacoustique complet pour les trois dorsales sur la même période. Pour entreprendre une tâche aussi formidable, le développement d'un algorithme de détection automatique serait bienvenu. Les prochains paragraphes développent cette perspective et d'autres pistes potentielles soulevées dans cette étude, telles que le mécanisme à l'origine des événements impulsionnels.

Sélection automatique des événements

Dans cette thèse, mon approche a nécessité un examen visuel approfondi et l'identification manuelle des signaux d'ondes T dans les spectrogrammes sur deux itérations. Ce choix était basé sur le fait que ces signaux sont souvent plus distincts dans les spectrogrammes que dans les formes d'ondes, surtout pour les événements de faible magnitude ; de plus, les temps d'arrivée sont généralement indiscernables dans les formes d'ondes. Il est important de souligner que ce processus analytique est exigeant en main-d'œuvre et que son efficacité et son exhaustivité peuvent varier selon les opérateurs. Par exemple, la sélection de 27624 événements sur deux itérations (2 x 27624) près de la faille de Melville (le plus fort essaim de cette étude) m'a pris près de 6 mois, environ ~4 mois pour la première itération et ~2 mois pour la seconde.

Pour surmonter ce travail intensif, un algorithme automatique de sélection et de classification des événements constituerait une amélioration majeure. D'un point de vue prospectif, la mise en œuvre d'un algorithme d'apprentissage automatique semi-supervisé paraît prometteuse. Une étude récente de [Raumer et al. \(2023\)](#) souligne les avantages potentiels d'une telle approche basée sur des réseaux neuronaux convolutionnels (CNN), qui pourrait améliorer considérablement l'efficacité de la détection d'événements (Figure I). Cette méthode consiste à concevoir et à former un détecteur automatique dans une fenêtre de spectrogramme. Comme les formes d'ondes

des événements impulsionnels sont facilement discernables, le modèle proposé a été initialement testé sur ces événements.

La première étape de cette méthode nécessite un ensemble de données annotées (catalogue construit par sélection manuelle, comme dans cette étude), afin de construire un jeu d'entraînement pour l'algorithme d'apprentissage automatique. Un CNN est ensuite formé pour prendre les spectrogrammes du jeu d'entraînement en entrée et produire une valeur comprise dans l'intervalle $[0,1]$ pour chaque fenêtre temporelle du spectrogramme. En appliquant ce CNN à l'ensemble de données non annotées, [Raumer et al. \(2023\)](#) obtiennent un catalogue de signaux pour chaque station, à partir duquel un filtre simple élimine les signaux évidemment non pertinents, par exemple les tirs sismiques de canons à air. Les signaux provenant de différentes stations sont ensuite automatiquement associés pour localiser les sources correspondantes. À l'aide d'un logiciel personnalisé, l'utilisateur peut ensuite vérifier manuellement ces détections.

Une évaluation préliminaire a montré des performances très efficaces par rapport à la sélection manuelle. Par exemple, avec cette approche, la détection et la vérification d'environ 200 événements impulsionnels ont nécessité environ 1 heure, contre une sélection manuelle de 30 événements par heure. À l'heure actuelle, ce modèle fonctionne bien pour les événements impulsionnels, qui ont une signature distincte et facilement identifiable. Le prochain défi, basé sur des catalogues manuellement sélectionnés de manière exhaustive, sera de détecter automatiquement les ondes T avec des signatures moins caractéristiques.

Modélisation des ondes hydroacoustiques

Cette étude s'est concentrée sur la détection manuelle des ondes T et H, mais pas sur leur modélisation. En utilisant le code numérique SPEC-FEM2D/3D basé sur des méthodes d'éléments finis spectraux, plusieurs études ont tenté de caractériser la génération et la propagation des ondes T générées à l'interface d'un milieu solide-fluide (e.g. [Jamet et al., 2013](#); [Lecoulant et al., 2019](#)). Les ondes T abyssales sont généralement expliquées par la diffusion des ondes acoustiques sur un fond marin accidenté, mais l'idée initiale de la diffusion par une surface de mer rugueuse ([Johnson and Norris, 1968b](#)) est maintenant ravivée ([Bottero et al., 2023](#)). Cela ouvrirait un nouveau champ d'investigation, car les signatures des ondes T dépendraient alors de l'état de la mer. Les mécanismes générant les ondes H associées aux interactions lave-eau (produisant des événements impulsionnels) restent aussi à expliquer.

Caractérisation du contexte des événements impulsionsnels

Le volcan Tiktak, au large de l'île de Mayotte, est un exemple où des événements impulsionsnels sont associés à une éruption sous-marine active (les hydrophones étaient à environ 50 km du site). Une association similaire a été proposée au volcan sous-marin axial, sur la dorsale Juan de Fuca, mais à partir d'hydrophones à une distance plus proche (quelques kilomètres ; e.g. [Le Saout et al., 2020](#)). Notre étude a montré que ces événements impulsionsnels sont courants le long des dorsales médio-océaniques et détectables à des distances très grandes (jusqu'à 3700 km dans notre étude). Les réseaux hydroacoustiques pourraient alors devenir un outil unique pour détecter les éruptions actives associées à l'accrétion du plancher océanique.

L'étude de ces événements impulsionsnels nécessiterait toutefois des campagnes océaniques d'observation in situ pour mieux comprendre leur contexte : par exemple, en répétant des levés bathymétriques multifaisceaux près du fond avec une résolution élevée pour détecter les changements dans la morphologie du fond marin, des levés sonar latéral pour mettre en évidence la lave fraîchement formée à partir de l'énergie rétrodiffusée, et/ou des levés de caméras en haute mer à partir de véhicules sous-marins autonomes.

Appendix

Content of the appendices:

- (A) User manual for picking hydroacoustic signals using *Seas* software
- (B) Table describing hydrophone sensitivities provided by the manufacturer
- (C) Supplementary material for the MDPI-Geoscience Paper
- (D) Supplementary material for the BSSA Paper
- (E) Magnitude of completeness of the three swarms along the SWIR
- (F) Results of swarms detected in 2012 near the Saint-Paul-Amsterdam plateau along the SEIR

Appendix A

Seas Manual

Seas software used in this study to pick hydroacoustic waves was developed at NOAA-PMEL. I have used the 6th version of this software, last modified by Jean-Yves Royer in January 2022. Here I provide a detailed manual for picking T-waves and the information of input and output files.

A.1 *Seas*: Picking and Analysis

1. Make sure that the workstation is connected with LGO's local network to access the IDL license server (*Seas* is developed in IDL language)
2. If a workstation is outside the LGO's network then contact the lab administration
3. On user's workstation, put sub-directories like *local* and *moored* into a single parent-folder
4. In the parent folder, keep other files like:
 - station description file (ending with **.loc*)
 - *seasick* and *seasick6v1_Eve* executables
 - Input file specifying the path and properties of data (ending with **.input*)
5. Open the terminal through the parent folder and type `idl`, then IDL will open. After this, type *seasick_Eve* in IDL window
6. The Sound Speed Data window will pop up where select the Indian Ocean Sound Speed Model (or depend on the study region)
7. Another window will open, where enter the name of the input file (**.input*) and click OK
8. Then a total of 4 windows will open:

- Window 1: T-phase Data Display which shows the signal of all channels that are arranged in the order mentioned in *.input*
- Window 2: Events Marking Status Window and it is a black window
- Window 3: Main Manual for T-Phase Data Processing (TPD6v1) which includes all the possible operations for picking
- Window 4: Individual T-Phase channel and scrolling control which displays the station names, scrolling, and stop buttons

9. Detailed description of Window 3 (TPD6v1) options:

- Select either Signal Only or Spectrum Only or Signal + Spectrum. Prefer to choose Signal + Spectrum
- Option 1: Change the window size (width and height in pixels). Adjust it according to the user's screen configuration. Then click on the retain off button to get the same size window all the time
- Option 2: Select the color table according to the user's choice (preferably Gamma II scheme)
- Option 3: Erase the data displayed on the screen to get a blank screen
- Option 4: Retain the display screen
- Option 5: Take the screen capture of the current window in .ps format. Output file name as per user's wish; need to improve this option as it is not giving desired output; need to interchange the landscape and portrait labels
- Option 6: Show time at every line. Be careful with this option as Seasick generally crashes down after clicking on it
- Option 7: Define the time label intervals and can also change the format
- Option 8: Plot the time labels: 1) label with mask (label above the signal); 2) label without a mask (label below the signal); 3) label off (no time axis label)
- Option 9: Adjust the scrolling speed: 1) 1 = default speed; 2) > 1 = reduce down the speed; 3) < 1 = increase the speed
- Option 10: Change the frequency range of the displayed spectrum; insert the value having an upper limit divided by 10
- Option 11: Change the signal and spectrum plotting ranges; need to improve this option

- Option 12: Change the default parameters using input parameters files
- Option 13: Display the names of input T-phase data files (*.w) in a terminal window
- Option 14: Scroll all the stations' data at the synchronized time given in the YYYY-JJJ-hh-mm-ss format
- Option 15: Scroll at the different times for different channels/stations
- Option 16: To locate the T-phase event and save the desired output
 - Click on locate T-phase origin: then select Pick event 1st
 - Click on the spectrum window (Window 1: T-phase data display) on at least 4 channels/stations showing the event signature
 - Click the middle button of the mouse: 1) If the arrival-time delay between two stations is too high, then a warning window will pop up. In that case (if possible) reconsider the detected picks on each channel
 - After this, the user can give a tentative location (latitude, longitude) as input. Generally, keep it blank and click Enter (do not click on Quit).
 - Then SHOW-LOCATED-RESULT window will pop up summarizing the information about the picked event:
 - * It shows the initial and final location of the detected event
 - * Computed origin time and respective arrival time on corresponding stations (origin time < arrival time)
 - * Weighted and non-weighted residuals between initial and final solution (least-square minimization)
 - * Sound velocity profile value
 - Then Click on OK
 - In the next window, it shows a one-line summary of the detected event along with other options:
 - * Name of the unpicked/unselected stations
 - * If the user wants to pick the event on those stations without changing the time scale then click on YES
 - * If there is a need to change the time scale then click on YES WITH DETAIL and then input the time values (in seconds) by which the user wants to increase/reduce the time resolution
 - * If there is no need to pick the event on unpicked stations then click on NO

- Another window will pop up asking to scroll the rest of the channels (picked channels), generally click on YES if the user has clicked YES in the previous window
- If the user wants to save the result then click on YES in the next window
- Enter the short word to indicate the nature of the picked event
- Enter the output file name which will save the result/output
- Output is saved in two files: one with a detailed description and another with a summary of the detection
- Option 17: Locate T-phase (Quick version): It does the same analysis as described in Option 16; but does not plot the necessary graphs. Its output is the same as the output of Option 16.
- Option 18: Locate T-phase (Haru phones): it is similar to options 16 and 17. Pick up the T-phase on more than 3 channels; select the event; check the residuals; the screen will automatically adjust to synchronized time; then save the result
- Option 19: Apply the filters to the displayed T-phase signal
- Option 20: signal analysis
 - Only blue whale options are implemented in the pre-defined settings
 - Display the amplitude vs. time graph of the signal selected on a single station
 - Plot the spectrum resolution using 6 parameters which are mentioned in the pop-up window
 - Dump the current spectrum image of the selected signal in .ps format
- Option 21: Convert the T-phase signal to an audio signal
- Option 22: Seismic analysis
- Option 23: Plot spectrum and time series together and save in *.idl or *.png
- Option 24: Select and examine the T-phase data by plotting the FFT
- Option 25: Perform the spectrum equalization
- Option 26: Draw X-axis ticks on the displayed window
- Option 27: Save the selected column into either IDL or wave file
- Option 28-31: Depends on the input file with an extension of *.posit. Perform the re-picking analysis
 - The format of the *.posit file the taken from the final one-line summary output of Option 16.
- Option 32: Synchronised the time based on the input file
- Option 33: Two types of clocks can be switched: On-set or Q-tech

A.2 Format of Input files

Station description files (*.loc)

An example of a loc file for the hydrophone at the ELAN site is shown in Figure A.1 and a detailed explanation is given below.

```

1 ELAN ; Hydrophone ID (Only 1st 6 characters will be used)
2 -56.466167 62.970000 1065 ; Lat, Lng (Degrees), & Depth (M) of the Hydrophone
3 3355443.200000 ; Counts/Volt, Hydrophone A/D Sensitivity.
4 -163.8 ; db from the Hydrophone Response Curve

```

Figure A.1: Example of loc file describing the station information.

- line 1: Name of station ID (only first 6 characters will be used)
- line 2: latitude, longitude (in °), and depth (in m) of given hydrophone
- line 3: Counts/volt: A/D sensitivity of hydrophone (Analog signal is sampled at Nyquist frequency, then determine the resolution of a signal based on sampling and then set the binary values to signal to get digital output).
- line 4: Hydrophone Response Curve at the level of interest (Sensitivity in dB re: 1V/ μ Pa)

Files describing the path of input data (*.input)

An example of an input file used for picking events along the SEIR segment in 2018 is shown in Figure A.2 and the detailed explanation of the file is as follows:

- Add the description or instructions about the data at the start of the file where the line should begin;
- Give the number tells that how many T-phase files are to be read
- Give a path of *.wf disc file which restores the summary of data recorded on that particular hydrophone
- The number at the start defines the binary number format used (5 = i4)
- Given a path of *.loc file


```

1  4 ; <- This number tells how many lines must be skipped before read.
2  ;
3  ; Files relative the 10 July 2018 crisis along the SWIR
4  ; Begin input
5  ;
6  10 ; number of T-phase files to be read.
7  5 /data/OHASISBIO_Data/2018_OHA/2018_RTJ_utc.wfdisc
8  /home/ingale/SeaSick_Analysis/03_SEIR/02_Complete/2018_SEIR_08Aug_29S_74E/02_Processing/2018_RTJ.loc
9  04, 300000.0, 6.0, 2.0, 2.0, 0.1, 5, 5, 60, 0.0
10 RTJ
11 5 /data/OHASISBIO_Data/2018_OHA/2018_NEAMS_utc.wfdisc
12 /home/ingale/SeaSick_Analysis/03_SEIR/02_Complete/2018_SEIR_08Aug_29S_74E/02_Processing/2018_NEAMS.loc
13 08, 300000.0, 6.0, 2.0, 2.0, 0.1, 5, 5, 60, 0.0
14 NEAMS
15 5 /data/OHASISBIO_Data/2018_OHA/2018_SSEIR_utc.wfdisc
16 /home/ingale/SeaSick_Analysis/03_SEIR/02_Complete/2018_SEIR_08Aug_29S_74E/02_Processing/2018_SSEIR.loc
17 07, 300000.0, 6.0, 2.0, 2.0, 0.1, 5, 5, 60, 0.0
18 SSEIR
19 5 /data/OHASISBIO_Data/2018_OHA/2018_SWAMS_Bot_utc.wfdisc
20 /home/ingale/SeaSick_Analysis/03_SEIR/02_Complete/2018_SEIR_08Aug_29S_74E/02_Processing/2018_SWAMS_Bot.loc
21 11, 300000.0, 6.0, 2.0, 2.0, 0.1, 5, 5, 60, 0.0
22 SWAMS
23 5 /data/OHASISBIO_Data/2018_OHA/2018_ELAN_utc.wfdisc
24 /home/ingale/SeaSick_Analysis/03_SEIR/02_Complete/2018_SEIR_08Aug_29S_74E/02_Processing/2018_ELAN.loc
25 08, 300000.0, 6.0, 2.0, 2.0, 0.1, 5, 5, 60, 0.0
26 ELAN
27 5 /data/OHASISBIO_Data/2018_OHA/2018_SSWIR_utc.wfdisc
28 /home/ingale/SeaSick_Analysis/03_SEIR/02_Complete/2018_SEIR_08Aug_29S_74E/02_Processing/2018_SSWIR.loc
29 03, 300000.0, 6.0, 2.0, 2.0, 0.1, 5, 5, 60, 0.0
30 SSWIR
31 5 /data/OHASISBIO_Data/2018_OHA/2018_MADW_utc.wfdisc
32 /home/ingale/SeaSick_Analysis/03_SEIR/02_Complete/2018_SEIR_08Aug_29S_74E/02_Processing/2018_MADW.loc
33 01, 300000.0, 6.0, 2.0, 2.0, 0.1, 5, 5, 60, 0.0
34 MADW
35 5 /data/OHASISBIO_Data/2018_OHA/2018_H08S1/2018_H08S1_SEIR.wfdisc
36 /home/ingale/SeaSick_Analysis/03_SEIR/02_Complete/2018_SEIR_08Aug_29S_74E/02_Processing/2018_H08S1.loc
37 01, 300000.0, 6.0, 2.0, 2.0, 0.1, 5, 5, 30, 0.0
38 H08S1
39 5 /data/OHASISBIO_Data/2018_OHA/2018_H04N1/2018_H04N1_SEIR.wfdisc
40 /home/ingale/SeaSick_Analysis/03_SEIR/02_Complete/2018_SEIR_08Aug_29S_74E/02_Processing/2018_H04N1.loc
41 01, 300000.0, 6.0, 2.0, 2.0, 0.1, 5, 5, 30, 0.0
42 H04N1
43 5 /data/OHASISBIO_Data/2018_OHA/2018_H01W1/2018_H01W1_SEIR.wfdisc
44 /home/ingale/SeaSick_Analysis/03_SEIR/02_Complete/2018_SEIR_08Aug_29S_74E/02_Processing/2018_H01W1.loc
45 01, 300000.0, 6.0, 2.0, 2.0, 0.1, 5, 5, 30, 0.0
46 H01W1
47 10 MID
48 -24.379167 -31.575833 -33.517500 -42.951333 -56.460167 -38.546500 -29.047333 -7.64535 -46.1772 -34.89299
49 72.372000 83.242333 70.865667 74.597500 62.976000 52.928667 54.258000 72.47444 51.7830 114.153980
50 A, B, C, D, E, F, G, H, J, I
51 0.01, 0.01
52 ;
53 ; End Input

```

Figure A.2: Example of input file describing network and hydrophone parameters.

- Arrange the parameters in the following order and in a single line: 1) channel number; 2) signal (amplitude) range; 3) maximum frequency ($n.0 = n \cdot 10$, i.e. 4.0 = 0-40 Hz); 4) sample rate in seconds; 5) data to be read next (in seconds; $5 \leq$); 6) sample rate for cosine taper filter; 7) design the time window by the number of seconds before and after of T-wave pick; 8)-9) frequency range for maximum spectrum value selection; 10) if 0 then no spectrum equalization
- Parameters 8)-9) are used to calculate RL based on T-wave picking
- In the next line, give the name of the station ID
- lines below label MID contains latitude of all stations used (line 1); longitude of all stations (line 2); assigned single letter alphabet to each station.
- Note that this latitude, longitude, and single alphabet should occur in the order of stations described in the lines above

File describing the configuration of input data (*.wfdisc)

An example of a wfdisc file is shown in Figure A.3. A detailed explanation for the columns in an individual line is given below.

```

1 ELAN      9446  1516123851.86100      1      1  2018016  1516147153.54382  5592405  240.0000053      0.000000      0.000000      CF2 x i4
  /data/OHASISBIO_Data/2018_OHA/2018_ELAN
2 ELAN      9446  1516147153.54800      1      1  2018016  1516170455.23082  5592405  240.0000053      0.000000      0.000000      CF2 x i4 x
  /data/OHASISBIO_Data/2018_OHA/2018_ELAN
3 ELAN      9446  1516170455.23500      1      1  2018017  1516193756.91782  5592405  240.0000053      0.000000      0.000000      CF2 x i4 x
  /data/OHASISBIO_Data/2018_OHA/2018_ELAN
4 ELAN      9446  1516193756.92200      1      1  2018017  1516217058.60482  5592405  240.0000053      0.000000      0.000000      CF2 x i4 x
  /data/OHASISBIO_Data/2018_OHA/2018_ELAN
5 ELAN      9446  1516217058.60900      1      1  2018017  1516240360.29182  5592405  240.0000053      0.000000      0.000000      CF2 x i4 x
  /data/OHASISBIO_Data/2018_OHA/2018_ELAN
6 ELAN      9446  1516240360.29600      1      1  2018018  1516263661.97882  5592405  240.0000053      0.000000      0.000000      CF2 x i4 x
  /data/OHASISBIO_Data/2018_OHA/2018_ELAN
7 ELAN      9446  1516263661.98300      1      1  2018018  1516286963.66582  5592405  240.0000053      0.000000      0.000000      CF2 x i4 x
  /data/OHASISBIO_Data/2018_OHA/2018_ELAN
8 ELAN      9446  1516286963.67000      1      1  2018018  1516310265.35282  5592405  240.0000053      0.000000      0.000000      CF2 x i4 x
  /data/OHASISBIO_Data/2018_OHA/2018_ELAN
9 ELAN      9446  1516310265.35700      1      1  2018018  1516333567.03981  5592405  240.0000053      0.000000      0.000000      CF2 x i4 x
  /data/OHASISBIO_Data/2018_OHA/2018_ELAN
10 ELAN     9446  1516333567.04400      1      1  2018019  1516356868.72682  5592405  240.0000053      0.000000      0.000000      CF2 x i4 x
  /data/OHASISBIO_Data/2018_OHA/2018_ELAN
11 ELAN     9446  1516356868.73100      1      1  2018019  1516380170.41382  5592405  240.0000053      0.000000      0.000000      CF2 x i4 x
  /data/OHASISBIO_Data/2018_OHA/2018_ELAN
12 ELAN     9446  1516380170.41800      1      1  2018019  1516403472.10082  5592405  240.0000053      0.000000      0.000000      CF2 x i4 x
  /data/OHASISBIO_Data/2018_OHA/2018_ELAN
13 ELAN     9446  1516403472.10500      1      1  2018019  1516426773.78782  5592405  240.0000053      0.000000      0.000000      CF2 x i4 x
  /data/OHASISBIO_Data/2018_OHA/2018_ELAN
14 ELAN     9446  1516426773.79200      1      1  2018020  1516450075.47482  5592405  240.0000053      0.000000      0.000000      CF2 x i4 x
  /data/OHASISBIO_Data/2018_OHA/2018_ELAN
15 ELAN     9446  1516450075.47900      1      1  2018020  1516473377.16182  5592405  240.0000053      0.000000      0.000000      CF2 x i4 x
  /data/OHASISBIO_Data/2018_OHA/2018_ELAN
16 ELAN     9446  1516473377.16600      1      1  2018020  1516496678.84882  5592405  240.0000053      0.000000      0.000000      CF2 x i4 x
  /data/OHASISBIO_Data/2018_OHA/2018_ELAN
17 ELAN     9446  1516496678.85300      1      1  2018021  1516519980.53582  5592405  240.0000053      0.000000      0.000000      CF2 x i4 x
  /data/OHASISBIO_Data/2018_OHA/2018_ELAN
18 ELAN     9446  1516519980.54000      1      1  2018021  1516543282.22282  5592405  240.0000053      0.000000      0.000000      CF2 x i4 x
  /data/OHASISBIO_Data/2018_OHA/2018_ELAN
19 ELAN     9446  1516543282.22700      1      1  2018021  1516566583.90982  5592405  240.0000053      0.000000      0.000000      CF2 x i4 x
  /data/OHASISBIO_Data/2018_OHA/2018_ELAN
20 ELAN     9446  1516566583.91400      1      1  2018021  1516589885.59682  5592405  240.0000053      0.000000      0.000000      CF2 x i4 x
  /data/OHASISBIO_Data/2018_OHA/2018_ELAN

```

Figure A.3: Example of wfdisc file describing parameters of the individual file input file. Refer to the text for a detailed column-wise explanation.

- Column 1: channel name (hydrophone name)
- Column 2: 1 = single channel of given hydrophone
- Column 3: start time w.r.t. Unix time;
- Column 6: date (YYYYJJJ; Y = year, J = Julian day)
- Column 7: end time w.r.t. Unix time;
- Column 8: total number of samples (in seconds)
- Column 9: Sampling rate corrected over clock drift (in Hz)
- Column 15: i4 = 4-byte integer format
- Column 17: directory where the data files are stored
- Column 18: Name of a data file
- Column 21: date of extraction of data
- Most important: Keep the spacing between all the characters/columns consistent to avoid errors while reading this file

Appendix B

Hydrophone sensitivities

Sensor	Serial Number	Hydrophone Sensitivity (dB re 1V/ μ Pa)	Current (mA)
HTI-90-U/3V	580004	-163.5	0.72
"	580005	-163.7	0.73
"	580006	-163.5	0.83
"	580007	-163.4	0.72
"	580008	-164.0	0.69
"	580009	-163.9	0.79
"	580010	-163.9	0.80
"	580011	-163.8	0.79
"	580012	-163.7	0.80
"	580013	-164.2	0.63
"	580014	-163.8	0.72
"	580015	-163.7	0.70
"	580016	-163.7	0.71
"	580017	-163.5	0.69
"	580018	-163.3	0.70
"	580019	-163.5	0.76
"	580020	-163.5	0.64
"	580021	-163.4	0.68
"	580022	-163.3	0.65
"	580023	-163.6	0.65
"	580024	-163.2	0.73
"	580025	-163.5	0.64
HTI-04-PCA/ULF	580026	-167.9	0.65
"	580027	-168.6	0.63

Appendix C

Supplementary material for MDPI-Geoscience Paper

Contents of this File

- Table S1: Strongest acoustic events in swarm-1 (SL > 230 dB)
- Table S2: Strongest acoustic events in swarm-2 (SL > 230 dB)
- Figure S1: Error distribution improvements in the two picking iterations of swarm-1 events
- Figure S2: Error distribution improvements in the two picking iterations of swarm-2 events
- Figure S3: Analysis of swarm-2 events after 28 September- 07h06, 2018 event
- Figure S4: Analysis of swarm-2 events after 14 October- 12h32, 2018 event
- Figure S5: Detailed bathymetric maps of the swarm-1 and swarm-2 areas

Supplementary Material: Hydroacoustic observations of two contrasted seismic swarms along the Southwest Indian Ridge in 2018. *Geosciences*, 11, 225, doi:

<https://www.mdpi.com/article/10.3390/geosciences11060225/s1>.

Table S1. List of the strongest acoustic events in swarm-1 (SL > 230 dB)

Origin Time	Latitude (°S)	Longitude (°E)	Source Level (dB)	Magnitude (mb) ^a
10 July-08h44	31.667	58.506	231.82	5.1
10 July-10h26	31.711	58.419	236.08	5.5
10 July-16h05	31.700	58.460	234.65	5.7
10 July-18h41	31.780	58.674	232.81	4.0
10 July-23h28	31.661	58.770	232.84	5.2
11 July-00h33	31.653	58.657	235.84	5.2
11 July-02h22	31.744	58.570	231.14	4.8
11 July-05h00	31.652	58.429	234.87	4.0
12 July-11h14	31.559	58.123	231.95	--
13 July-01h20	31.561	58.126	232.47	--

Table S2. List of the strongest acoustic events in swarm-2 (SL > 230 dB)

Origin Time	Latitude (°S)	Longitude (°E)	Source Level (dB)	Magnitude (mb) ^a
28 September-05h56	26.736	67.789	230.41	4.9
28 September-06h21	26.924	67.758	240.33	5.5
28 September-07h06	26.929	67.741	239.14	5.6
28 September-11h01	26.764	67.773	232.28	4.6
01 October-04h07	26.806	67.284	240.08	--
01 October-04h17	26.978	67.723	234.24	--
01 October-04h21	26.905	67.869	232.76	--
01 October-07h21	26.649	67.675	232.46	5.3
01 October-16h31	26.673	67.470	230.95	--
01 October-18h16	26.613	67.603	234.03	5.7
02 October-01h22	26.392	66.887	232.10	--
04 October-13h00	26.355	67.803	230.76	--
04 October-13h06	26.397	67.912	231.07	--
05 October-17h58	26.903	67.476	238.11	--
06 October-10h36	27.012	68.024	230.84	--
11 October-00h12	26.254	68.186	230.27	--
14 October-15h44	26.651	67.512	232.38	--
14 October-04h57	26.805	67.922	240.21	--
14 October-12h32	26.603	67.457	240.79	--
14 October-12h53	26.729	68.034	239.98	--
14 October-16h18	26.711	67.931	235.57	--
15 October-08h09	26.712	67.318	230.12	--
15 October-23h34	26.567	67.518	230.20	--
18 October-22h53	26.851	67.785	237.07	4.9

^a Only for events reported in the ISC catalogue.

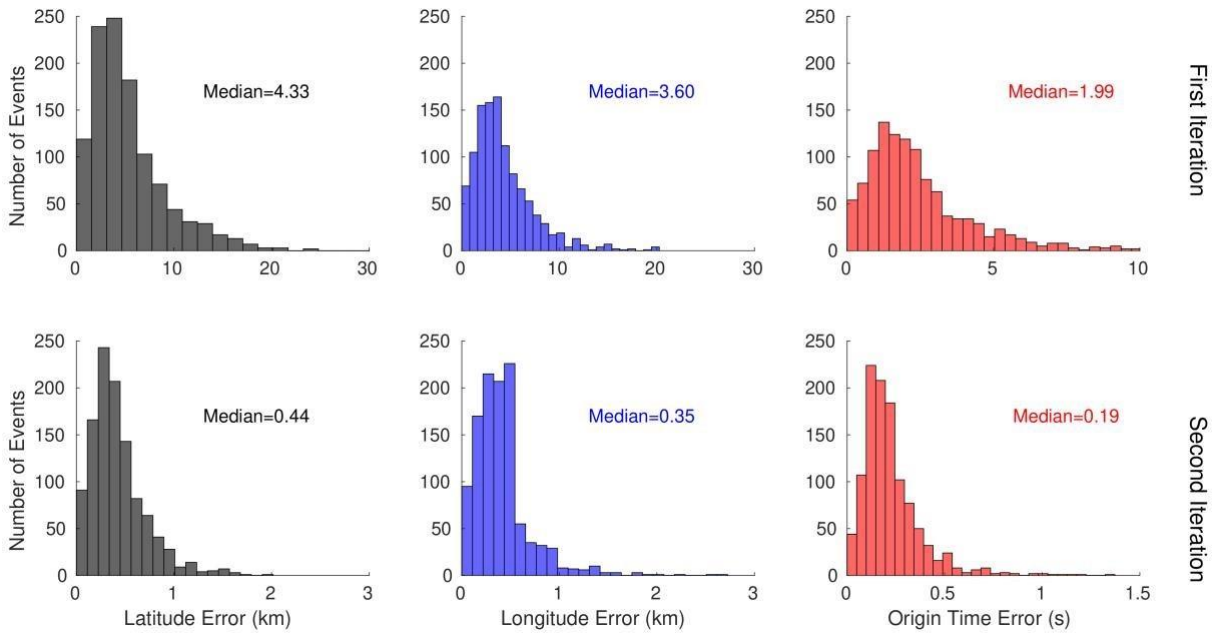


Figure S1: Improvements in the error distributions in location (latitude and longitude) and origin time for all hydroacoustic events from swarm-1 between the first iteration (initial picking, upper panel) and the second iteration (repicking, lower panel).

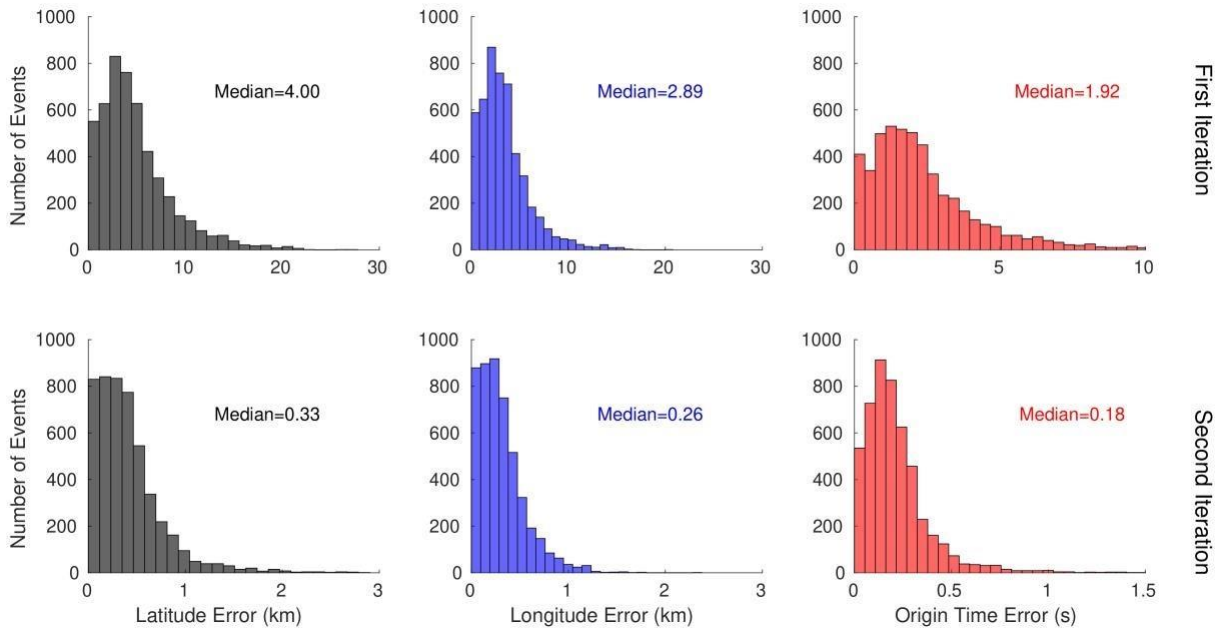


Figure S2: Improvements in the error distributions in location (latitude and longitude) and origin time for all hydroacoustic events from swarm-2 between the first iteration (initial picking, upper panel) and the second iteration (repicking, lower panel).

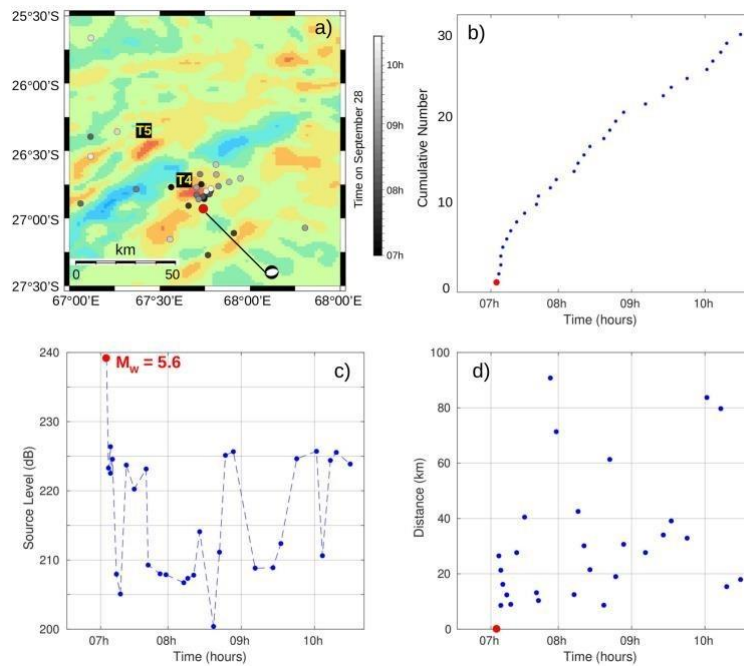


Figure S3. a) Location of the events that occurred after a $M_w=5.6$ normal faulting event on 28 September, 2018 (red dot). T4 and T5 denotes the seamounts. Events are plotted according to their origin time (in gray colorscale). b) Cumulative Number of events after mainshock (red dot). c) Source Level of events shown in a). d) Distance of events from the mainshock vs time. These distributions do not resemble to a classical tectonic mainshock-aftershocks sequence.

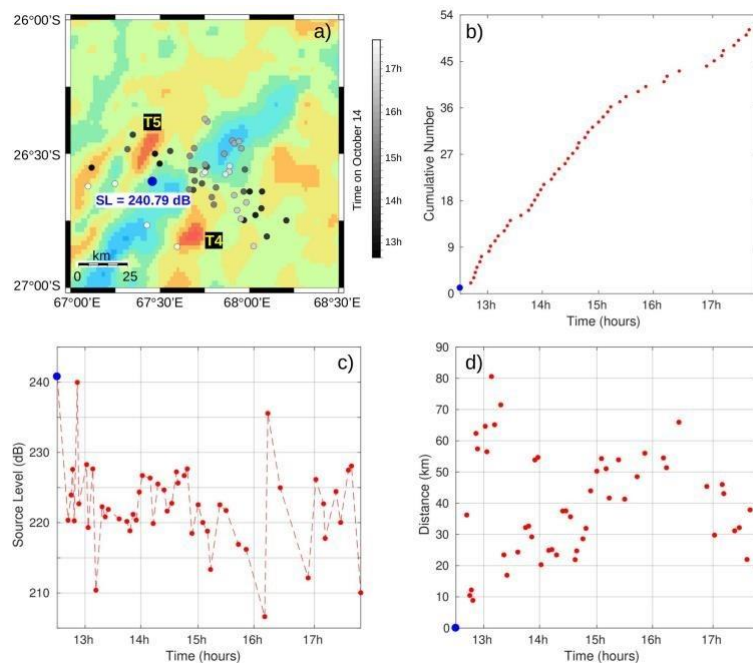


Figure S4. a) Location of the events that occurred after a strong event on 14 October, 2018 (SL = 240.79 dB; blue dot). T4 and T5 denotes the seamounts. Events are plotted according to their origin time (in gray colorscale). b) Cumulative Number of events after the 240.79 dB event. c) Source Level of events shown in a). d) Distance of events from the 240.79 dB event vs time. These distributions do not resemble to a classical tectonic mainshock-aftershocks sequence.

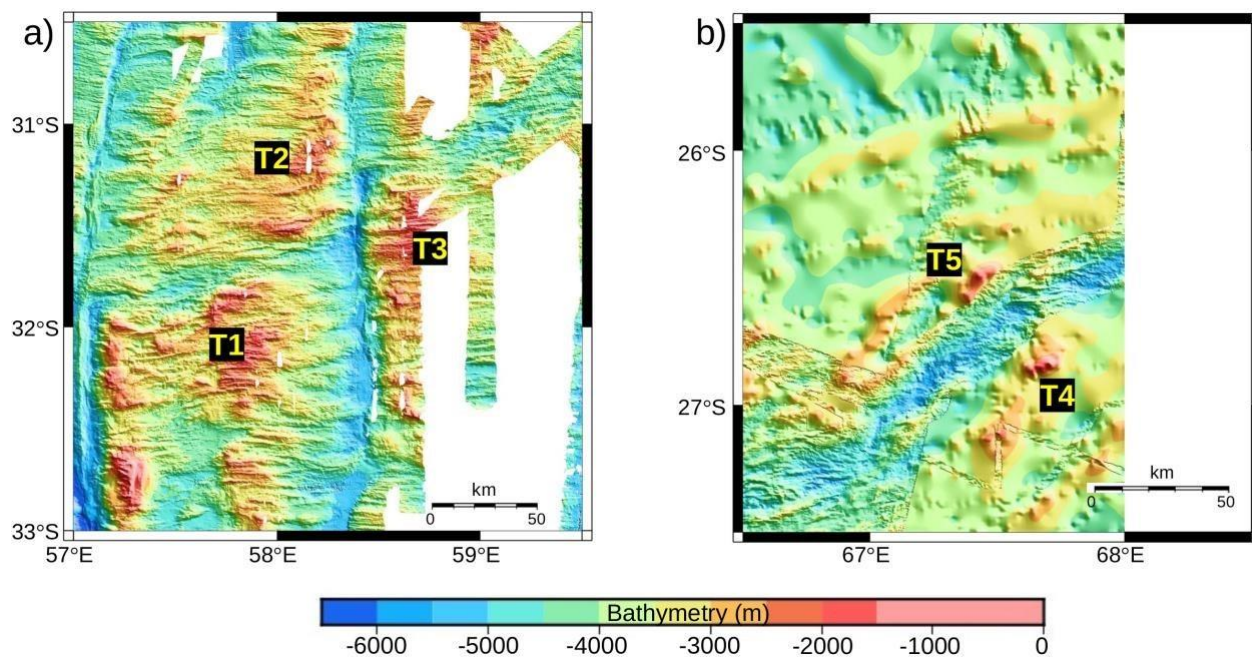


Figure S5. Detailed bathymetric maps of the swarm areas: **a)** For swarm-1; T1, T2 and T3 are three main local seamounts. **b)** For swarm-2; T4 and T5 shows two local seamounts on either side of the rift valley. Bathymetric grids are from [32].

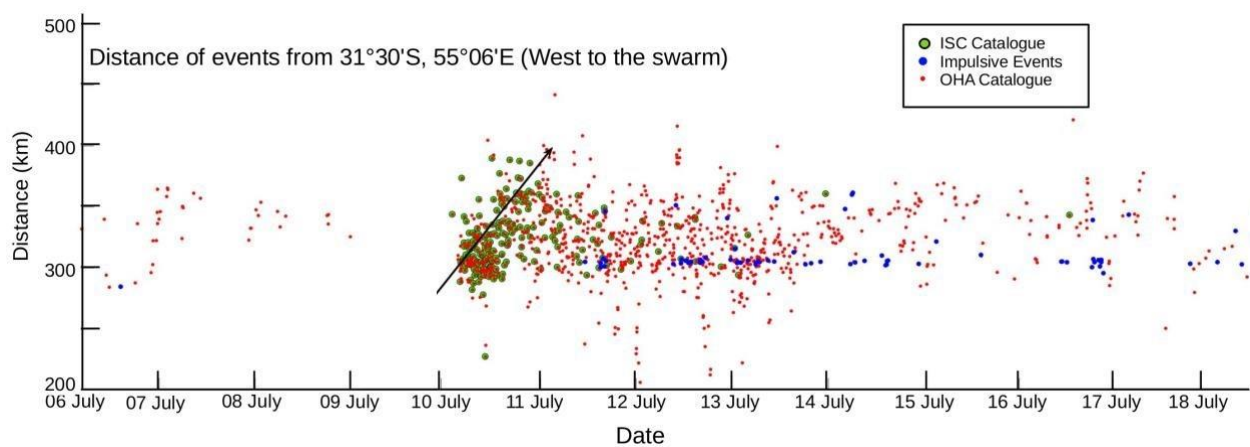


Figure S6. Distance of all hydroacoustic events of swarm-1 relative to an arbitrary reference point set at West (31°30'S, 55°06'E) from the center of swarm. All dots are hydroacoustic events (red); among them, blue dots are impulsive events and green outlines events reported in ISC catalogue. The black arrow shows the initial eastward direction of propagation of events.

Appendix D

Supplementary material for BSSA Paper

- Figure S1: Spectrograms and waveforms of some representative T-wave signals
- Figure S2: Corrections in SL of events based on received level (RL) for each hydrophone
- Figure S3: Improvements in error distribution after two picking iterations
- Figure S4: ISC catalog events along the SWIR axis
- Figure S5: Anomalous SL of events between January 09 and 20, 2017 and variations in RL
- Figure S6: Spectrograms of S-SWIR and WKER2 hydrophones
- Figure S7: Impulsive events near the Melville TF and a volcano off Mayotte Island
- Figure S8: 09 June 2016 sequence No. 1
- Figure S9: 18 June 2016 sequence No. 2
- Figure S10: 30 June 2016 sequence No. 3
- Figure S11: 05 August 2016 sequence No. 4
- Figure S12: 25 August 2016 sequence No. 5
- Figure S13: 16 September 2016 sequence No. 6
- Figure S14: 02 October 2016 sequence No. 7
- Figure S15: 06 October 2016 sequence No. 8
- Figure S16: 26 December 2016 sequence No. 10
- Figure S17: 07 January 2017 sequence No. 11
- Figure S18: Distribution of earthquakes vs. tidal heights

Supplementary Material: Hydroacoustic study of a seismic swarm in 2016-2017 near the Melville Transform Fault on the Southwest Indian Ridge. *Bulletin of Seismological Society of America*, 113 (4), 1523-1541, doi:

<https://www.editorialmanager.com/bssa/download.aspx?id=604430&guid=ceb515a5-307a-41e7-933f-f341f3617db8&scheme=1>

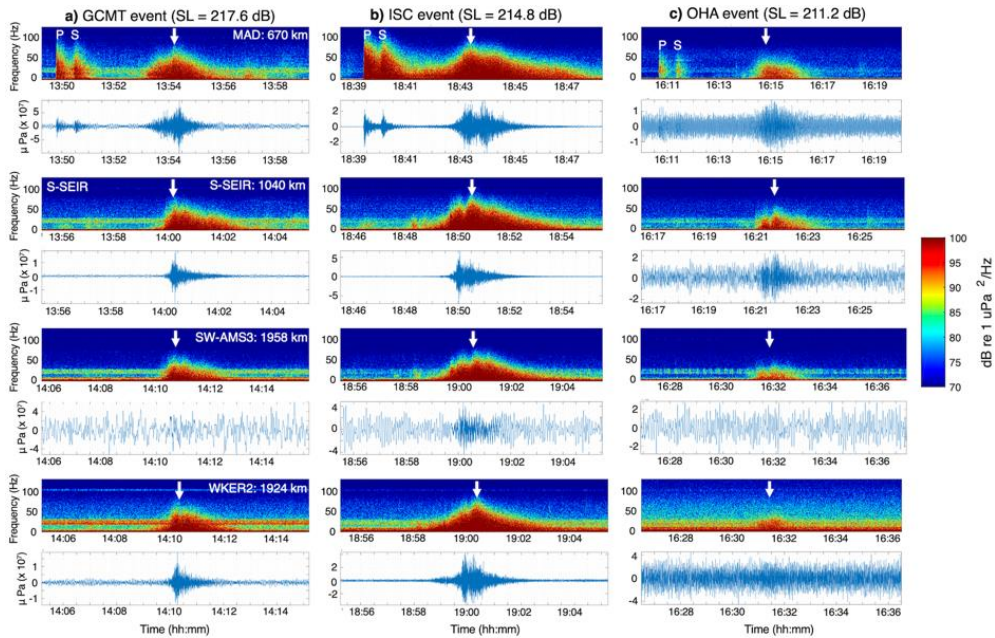


Figure S1 – Comparison of waveforms and spectrograms: Raw waveforms and spectrograms of some representative T-wave signals: **a)** ISC catalog event, **b)** GCMT catalog event; **c)** OHA catalog event, recorded at four hydrophones of the OHASISBIO network (MAD, S-SEIR, SW-AMS3, WKER2; from top to bottom); their distances in kilometers are from the reference point (cross in Figure 2). For all the three events, the peak of T-wave energy (marked by arrows) occurs in the 0-60 Hz frequency range. Note that for the first two large events ($m_b = 4.7$ and $M_w = 5.5$), the nearest hydrophone MAD (~ 670 km away) also recorded P and S wave arrivals, i.e., converted T-waves generated at the foot of the mooring.

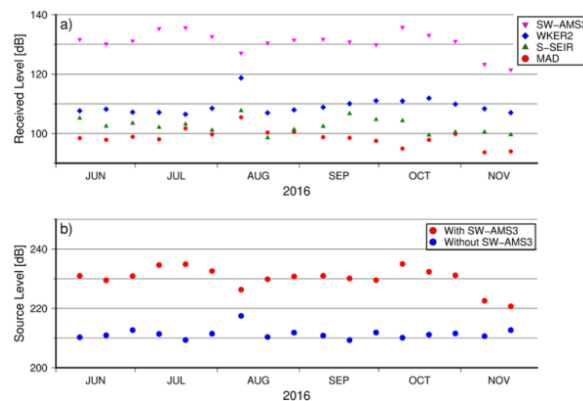


Figure S2 - Source Level corrections: **a)** Received Level (RL) in dB for a selection of events picked on SW-AMS3, WKER2, S-SEIR and MAD. Here SW-AMS3 has higher RL compared with the other three stations due to a higher sensor-sensitivity (see Table 1 in the paper). **b)** Source Level (SL) in dB for the events picked with (red) and without (blue) SW-AMS3. An averaged difference of 19.8 dB was applied to correct the SL of all events observed with SW-AMS3 in order to account for the network inhomogeneity in sensitivity.

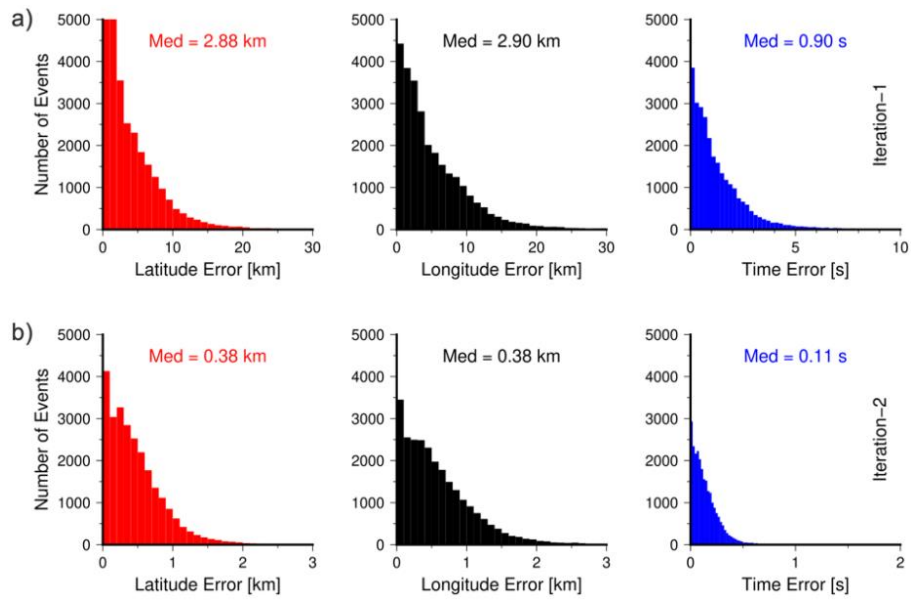


Figure S3 - Source localization errors: Errors obtained after acoustic triangulation in location (latitude and longitude) and origin time for all hydroacoustic events from the seismic cluster after the first (**top**) and second (**bottom**) picking iterations. Note here that x-axis scales are different in **a)** and **b)**.

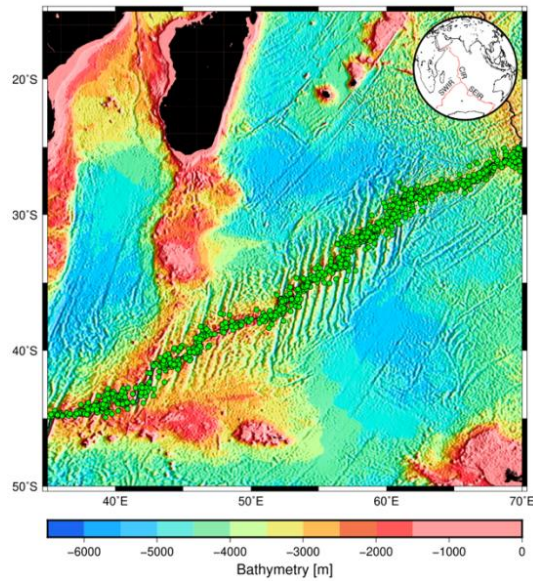


Figure S4 – ISC catalog of events along the SWIR axis: Geospatial distribution of 1933 events reported in the ISC catalog between 2010 and 2020 along the SWIR axis (ISC, 2022). Their magnitude (mb) is used for generating the trade-off between completeness of mb and SL of hydroacoustic events detected between June 2016 and March 2017 (Figure 3).

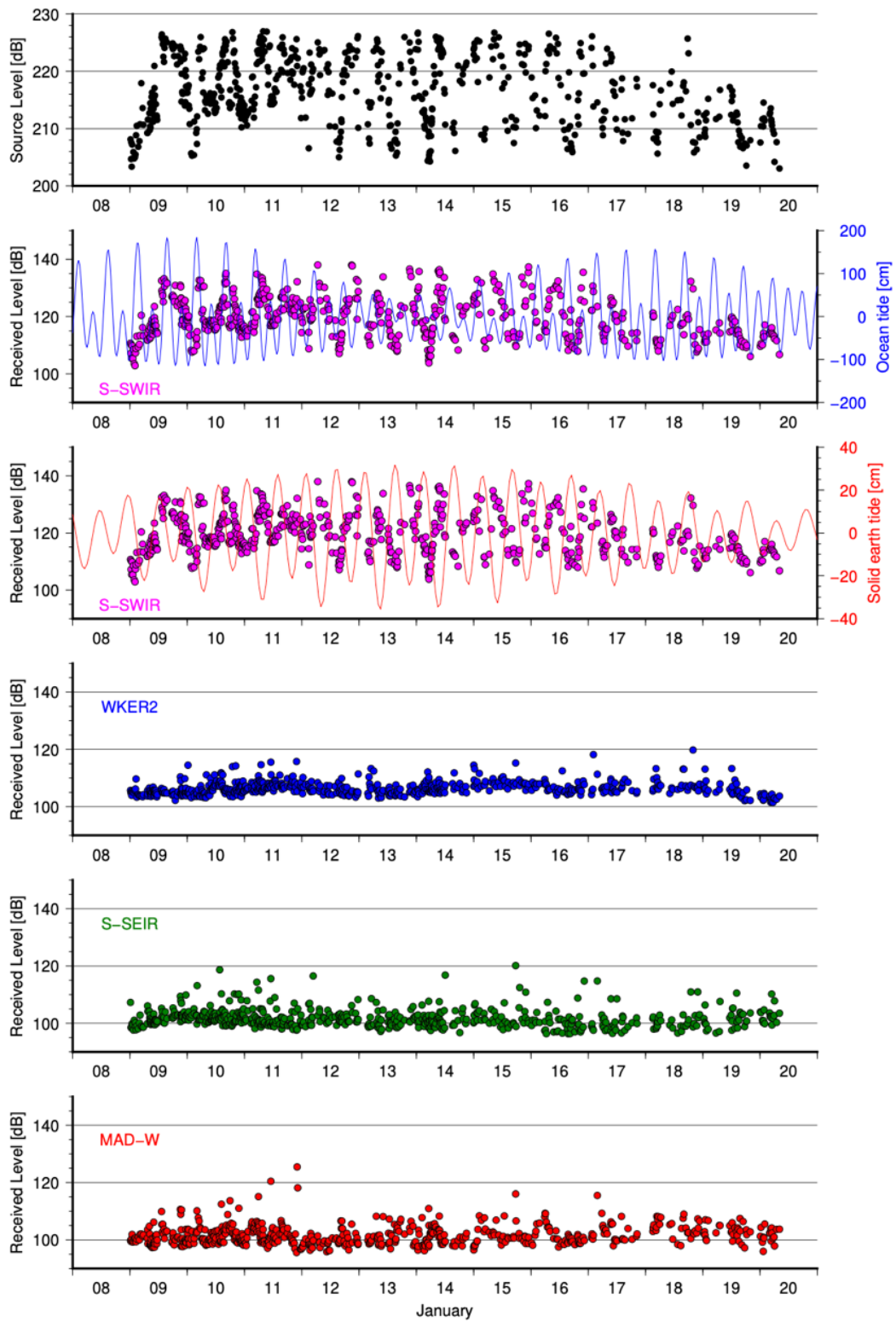


Figure S5 - Anomalous SL: Source Level of all events picked between January 8 and January 20, 2017 (black dots) compared to the received levels of these events at each hydrophone: S-SWIR (magenta dots), WKER2 (blue dots), S-SEIR (green dots), and MAD-W (red dots). Blue and red curves are ocean and solid Earth tidal heights, respectively.

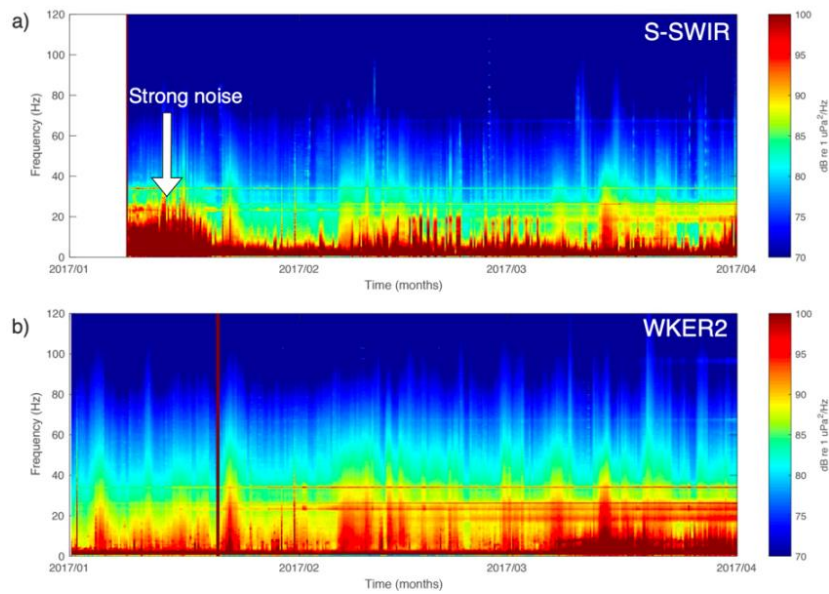


Figure S6 - Four-month long spectrograms at the S-SWIR and WKER2 sites in 2017 in the 0-120Hz frequency range (sampling rate is 240Hz). Each vertical line is a 6h-long average spectrum. The hydrophone sensitivities are -163.5 and -163.6 dB for S-SWIR and WKER2 respectively. A strong noise obscured the 0-30 Hz signal at the S-SWIR site in mid-January 2017.

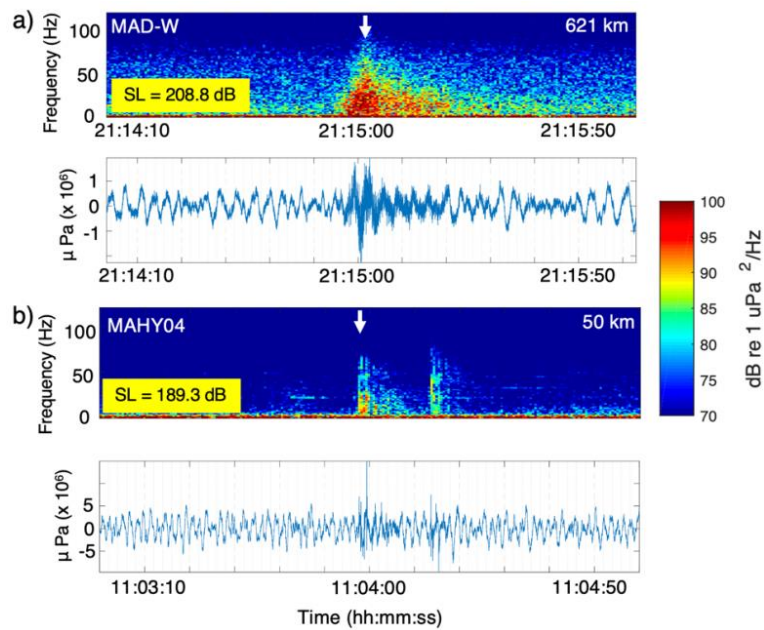


Figure S7 – Comparison of impulsive events near the Melville TF and near a volcano off Mayotte Island: Two-minute-long spectrograms and waveforms of an impulsive event recorded near the Melville TF (this study) and during a volcanic eruption off Mayotte Island (from Bazin et al., 2022). The event in **a**) is recorded 621 km away from the source (MAD-W), that in **b**) is recorded 50 km away (MAHY03) from the source. The SL is 208.8 dB for the first event vs. 189.3 dB for the second. Off Mayotte Island all impulsive events originate from recent active lava flows, mapped and observed from submersibles; the similarity in waveform and frequency contents of these two events suggest a common origin, that is interactions between hot lavas and seawater.

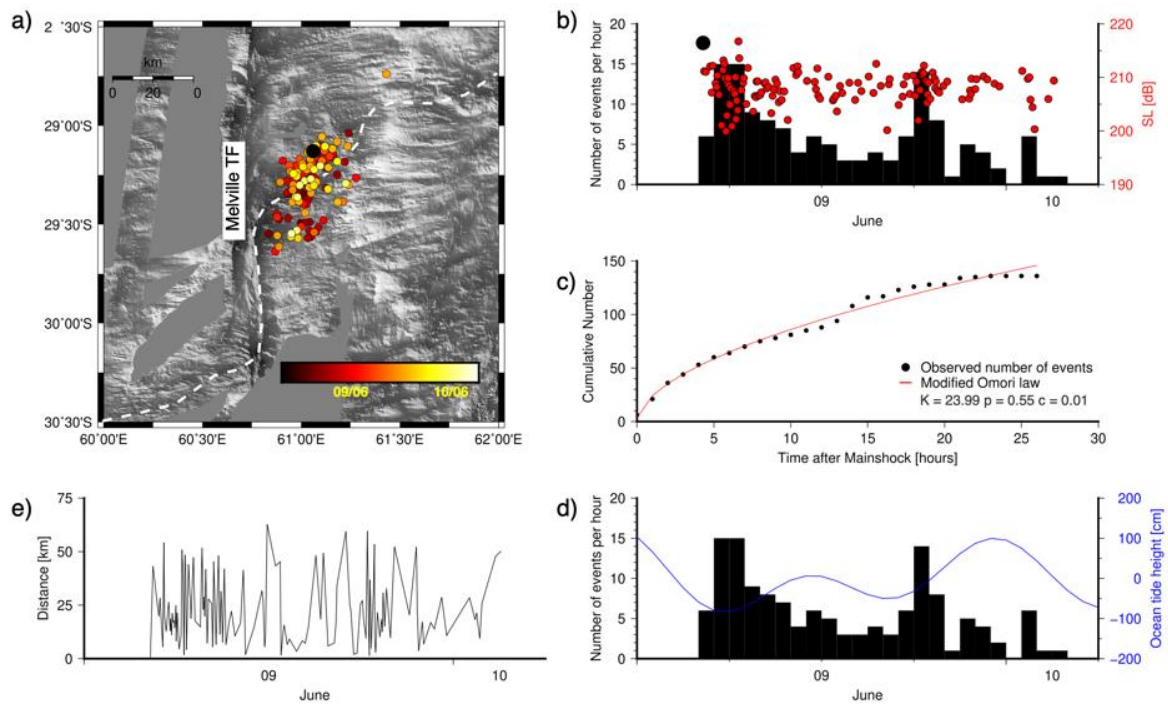


Figure S8 – 9th of June 2016 sequence 1: a) Spatio-temporal distribution of the events between June 09 and 10, 2016. The dashed line shows the SWIR axis. b) Histogram of number of events per hour in black color. Black and red circles show the SLs of T-waves for the first and following events, respectively. c) Black dots show the hourly cumulative number of events the red curve shows the modified Omori's law fit with the fitting parameters. d) Histogram of number of events per hour in black color and the ocean tide height in blue color. Tide height is computed with the Global Tidal Corrections program (Matsumoto et al., 2001). e) Distance of the events from the first event of the sequence.

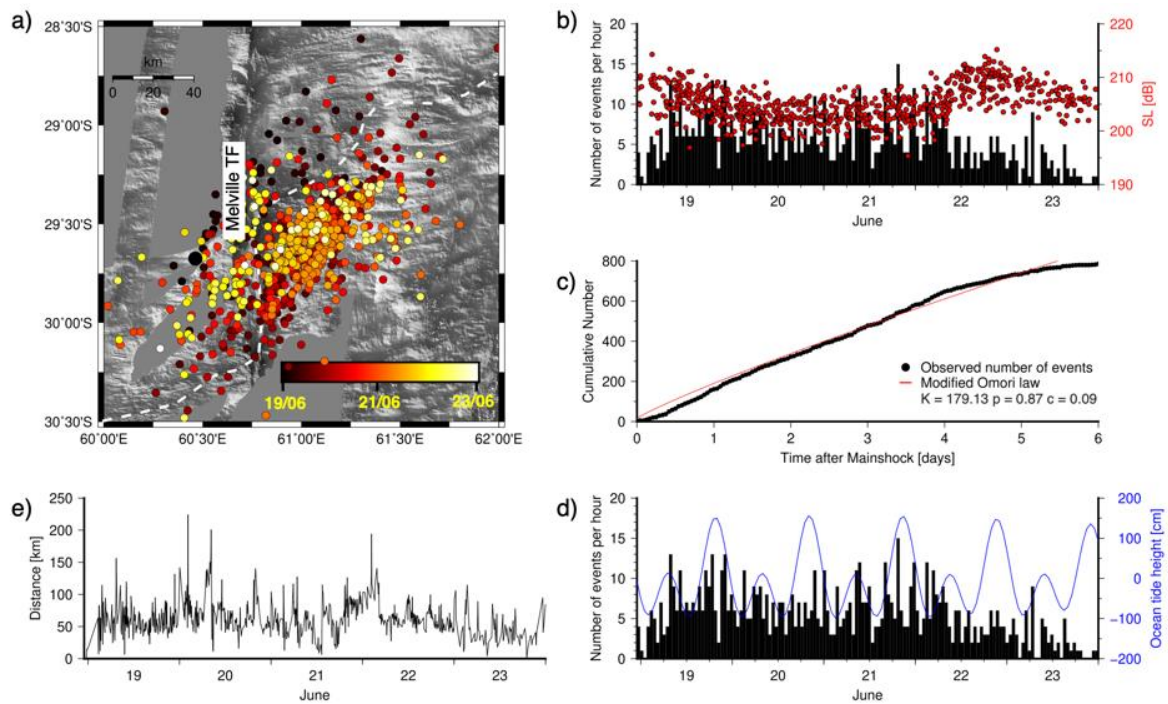


Figure S9 – 18th of June 2016 sequence 2

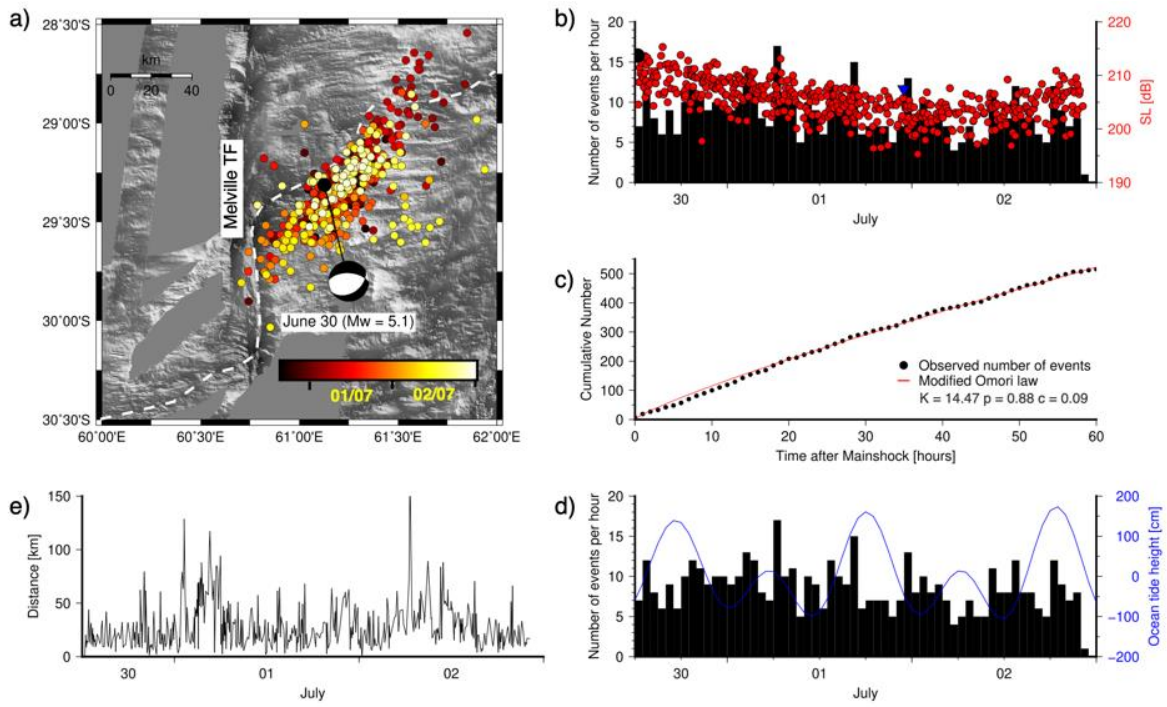


Figure S10 – 30th of June 2016 sequence 3

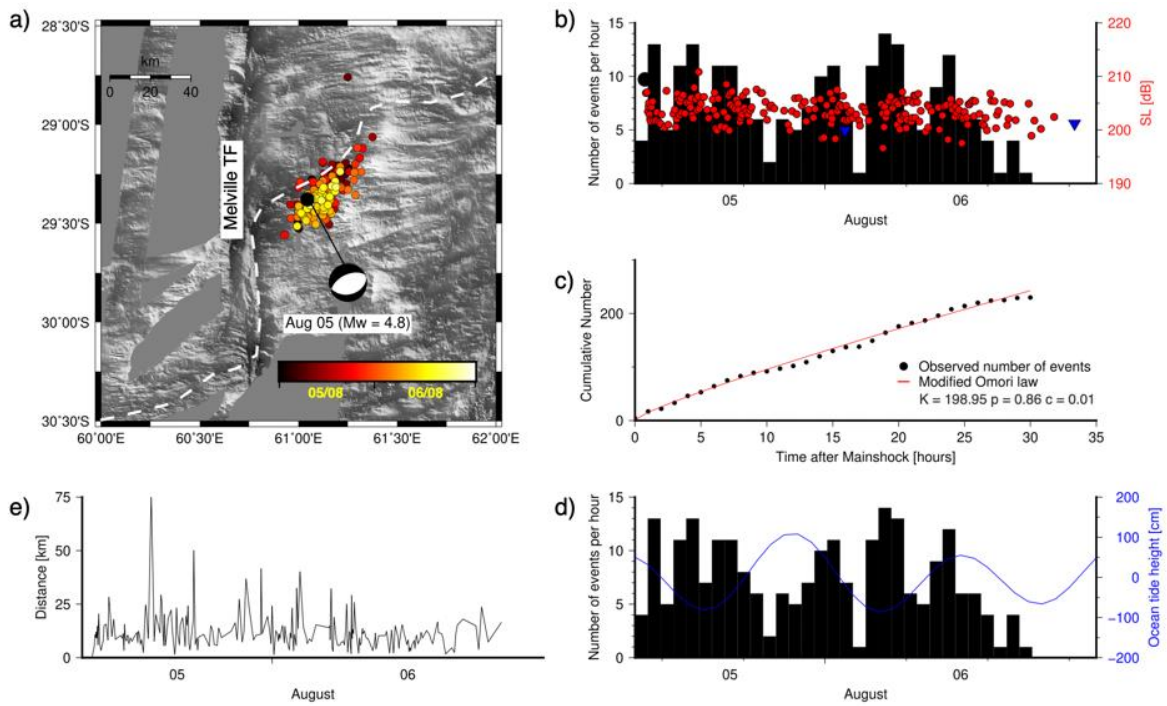


Figure S11 – 5th of August 2016 sequence 4

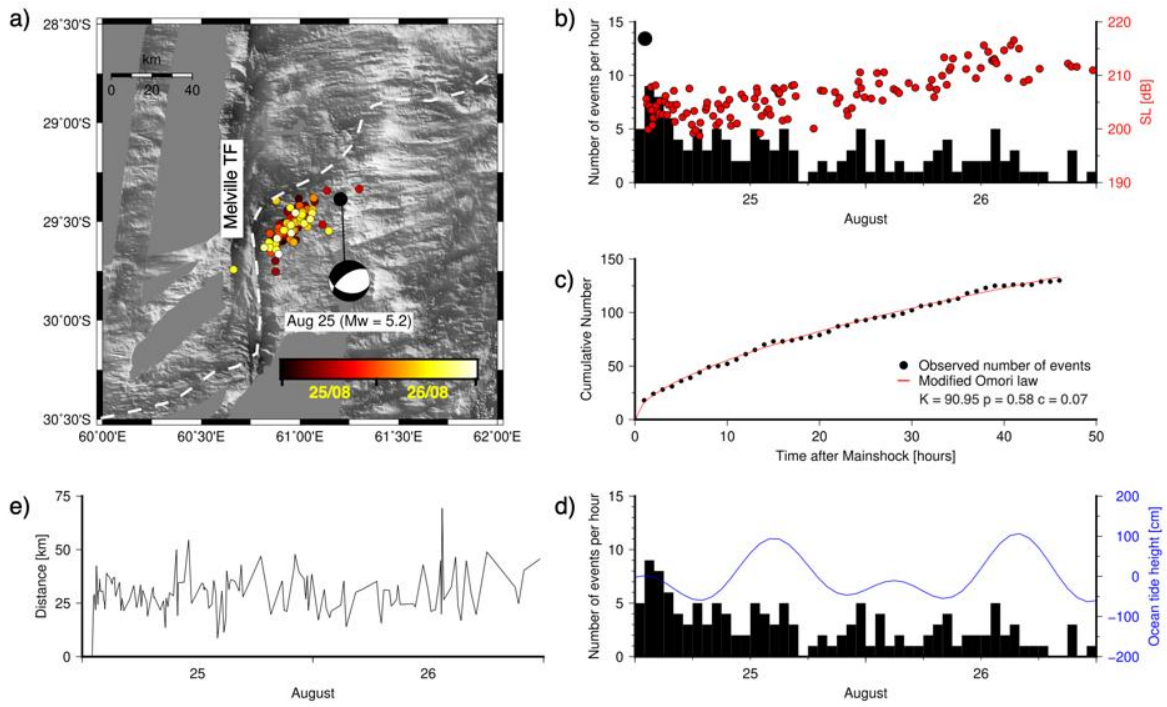


Figure S12 – 25th of August 2016 sequence 5

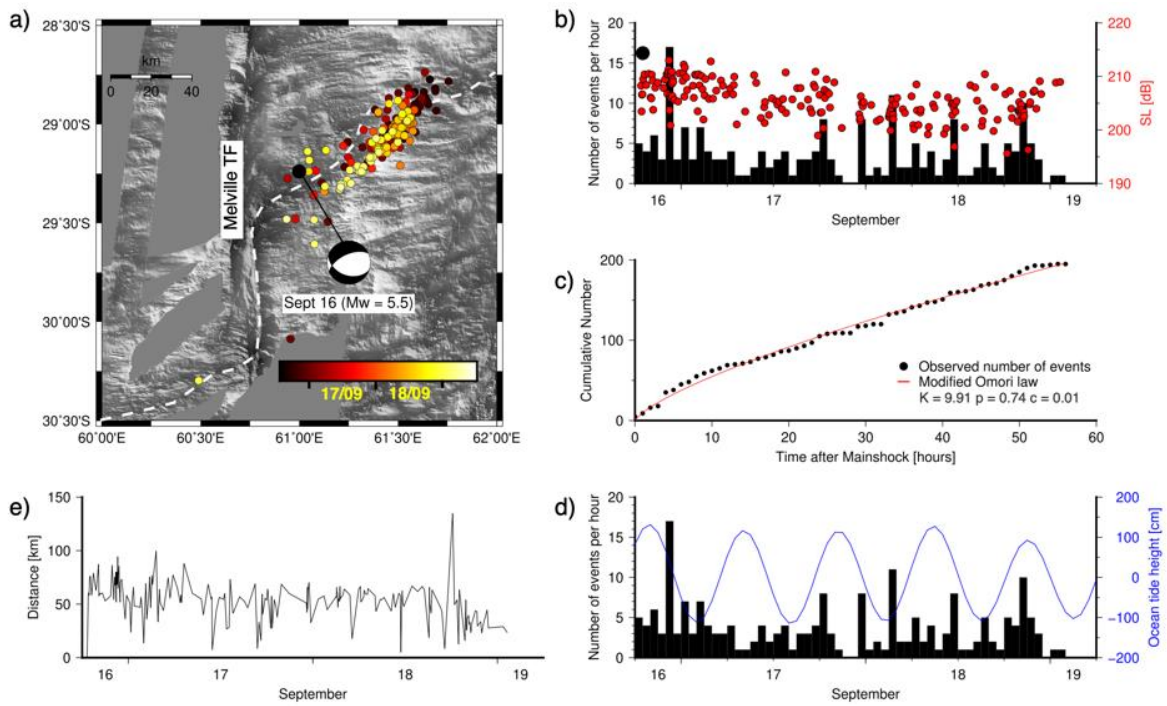


Figure S13 – 16th of September 2016 sequence 6

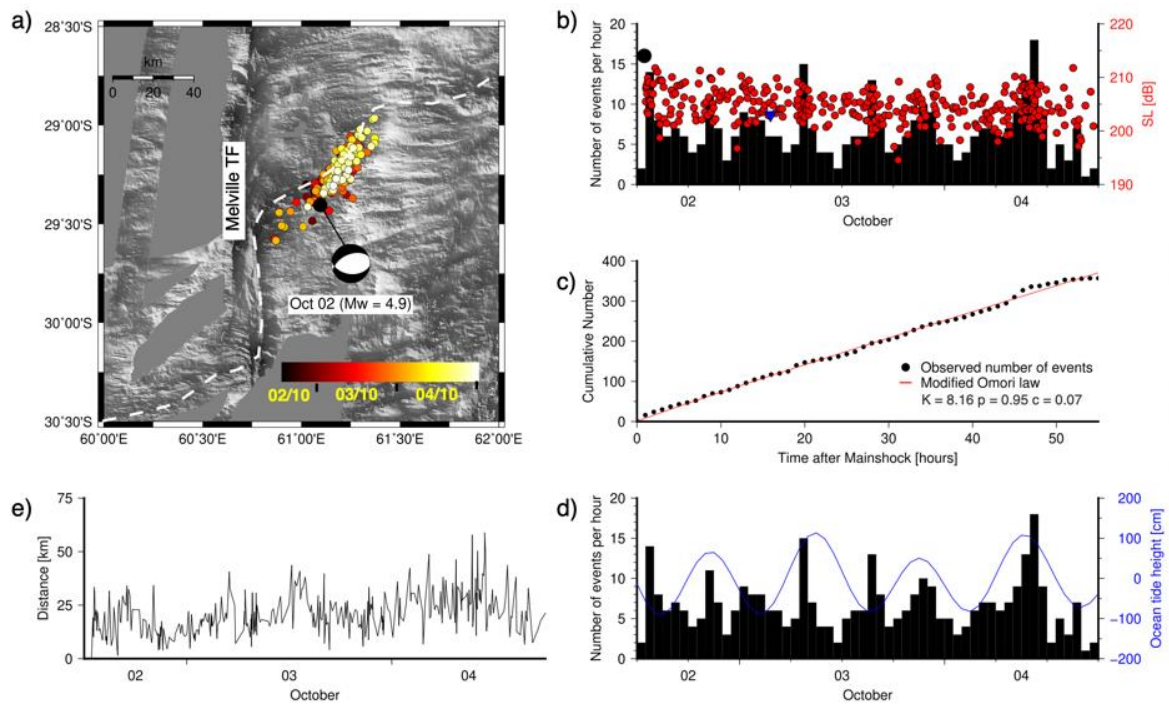


Figure S14 – 2nd of October 2016 sequence 7

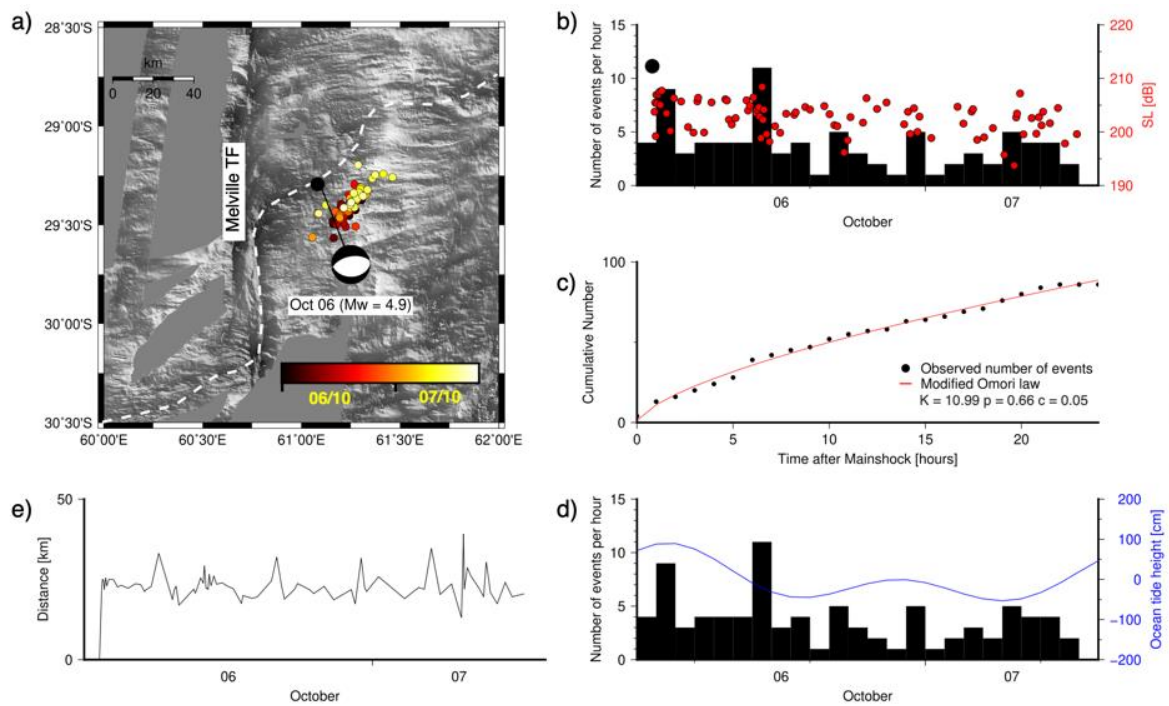


Figure S15 – 6th of October 2016 sequence 8

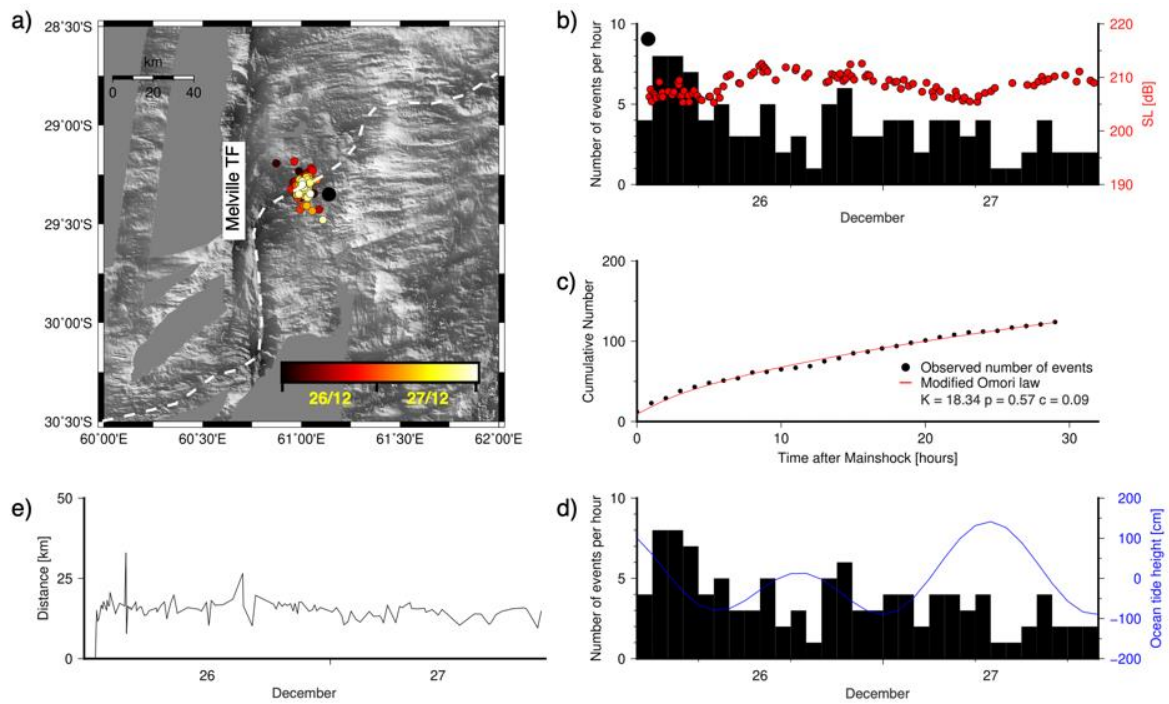


Figure S16 – 26th of December 2016 sequence 10

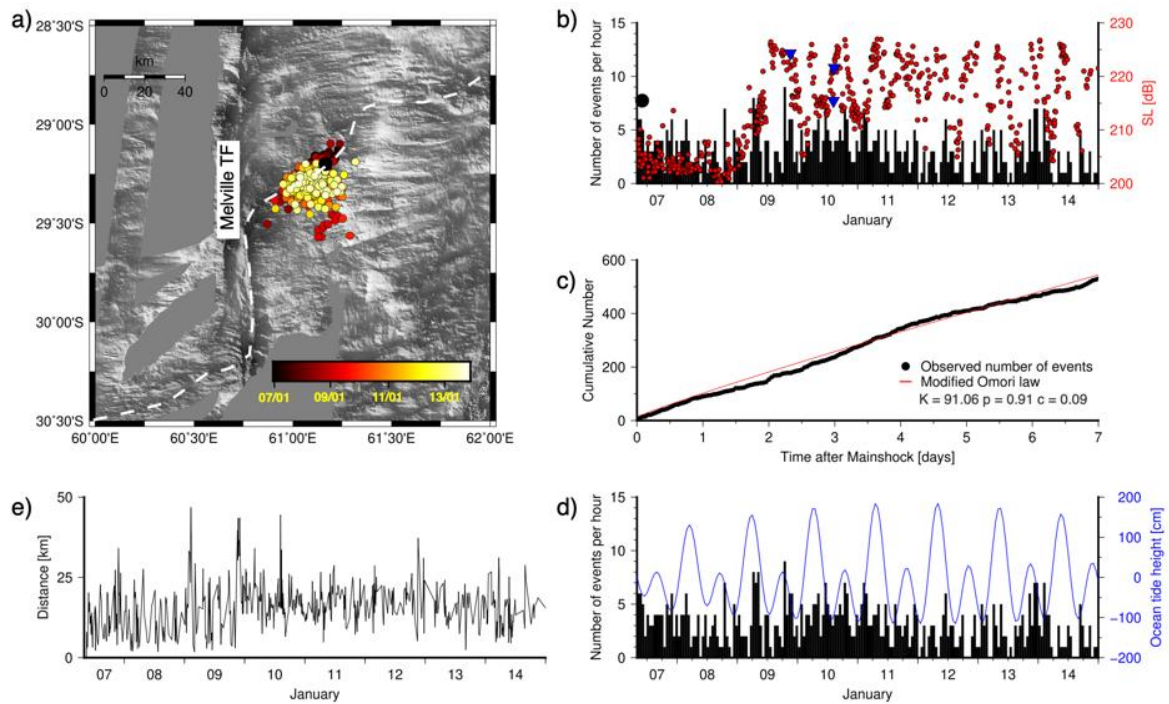


Figure S17 – 7th of January 2017 sequence 11

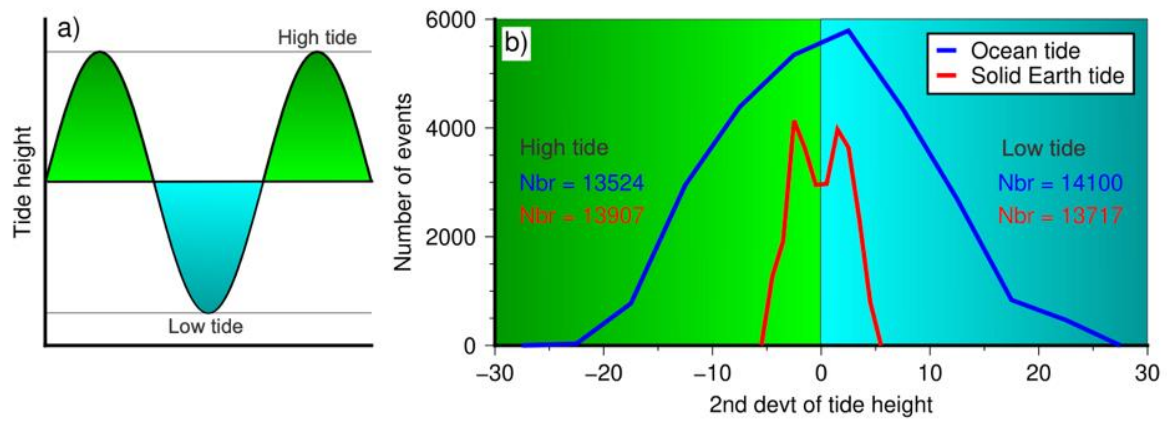


Figure S18 - Tidal effects on seismicity: a) Definitions of high tide (green) and low tide (cyan). **b)** Second derivative of ocean (blue curve) and solid-Earth tide (red curve). A positive 2nd derivative corresponds to low tide period (cyan colored region) and a negative 2nd derivative corresponds to high tide period (green colored region). Numbers represent the events counted during high tide (green side) and during low tide (cyan side); blue and red, fonts and curves, refer to the ocean or solid-Earth tide

Appendix E

Magnitude of Completeness

Source Level of completeness (SL_C) and equivalent comparison with different magnitude scales like mb , M_s and M_w for the three seismic swarms detected along the Southwest Indian Ridge

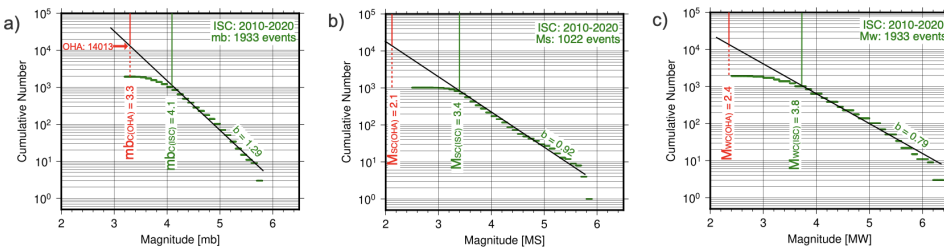


Figure E.1: Completeness of SL and magnitudes based on best-fitting Gutenberg–Richter’s laws for the events near the Melville TF **a)** for body-wave magnitude scale (mb), **b)** surface wave magnitude (M_s) and **c)** moment magnitude (M_w).

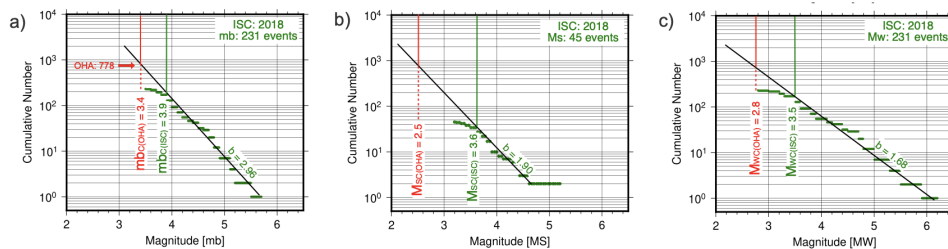


Figure E.2: For the events near the Novara TF. Same legends as of Figure E.1

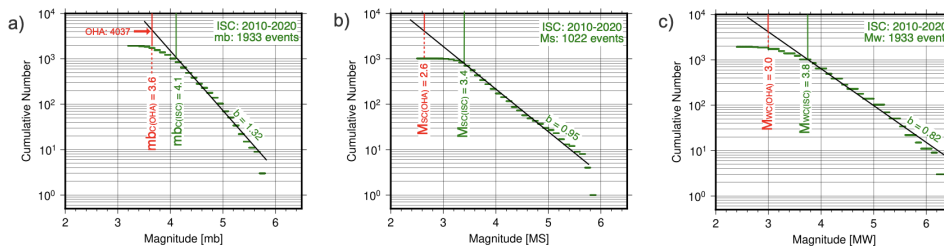


Figure E.3: For the events along the segment 4. Same legends as of Figure E.1

Appendix F

Swarms near Saint-Paul-Amsterdam Plateau

The SEIR crossing the Saint-Paul-Amsterdam plateau (Figure 5.2), exhibited two discrete instances of seismic swarms near the Amsterdam transform boundary. During April 2012, there were 11 events listed in the ISC catalog. Among them, one demonstrated reverse faulting, while three were characterized by a strike-slip mechanism (GCMT catalog). Subsequently, in October-November 2012, the ISC catalog recorded 6 events, with 3 of them displaying a strike-slip faulting mechanism. We analyzed hydroacoustic data recorded by both the OHASISBIO and IMS-CTBTO hydrophones in these two periods; from 11 March to 18 April, where we detected 998 OHA events, and from between 10 October to 14 November 2012, where 628 OHA events were detected (Figure F1). The source Level for the events detected in March-April was in the range of 204.9-252.2 with SL_C 222.3 dB and 202.8-248.8 with SL_C of 215.0 dB for the events in October-November. It was observed that the seismicity is not well constrained, scattered randomly over the SPA plateau, probably due to network geometry.

The strong events (as reported in ISC/GCMT catalogs) from both periods (March-April and October-November), were primarily aligned parallel to the Amsterdam transform boundary. The only reverse faulting event (M_w 5.1 on 16 April) of this swarm was located on the ridge segment, north of the transform. One of the events showing a strike-slip mechanism (M_w 5.3 on 12 November) was located along the Boomerang transform (Figure F1b). The presence of strike-slip mechanisms confirmed the dominant activity of transform boundaries compared with accretion centers. However, small-magnitude events were broadly scattered over an area of 300 x 300 km in the vicinity of the SPA plateau. This could be explained by the distribution of localization errors. In this analysis, the first iteration of picking yielded median errors of 7.83 km in latitude, 11.66 km in longitude, and 3.04 s in origin time; which were improved to 0.43 km, 0.57 km, and 0.16 s in the second iteration (Figure F2).

In this case, as the hydrophone sites were a long way from the SPA plateau, location uncertainties are non-negligible. The errors in longitude were broadly spread with a median value of

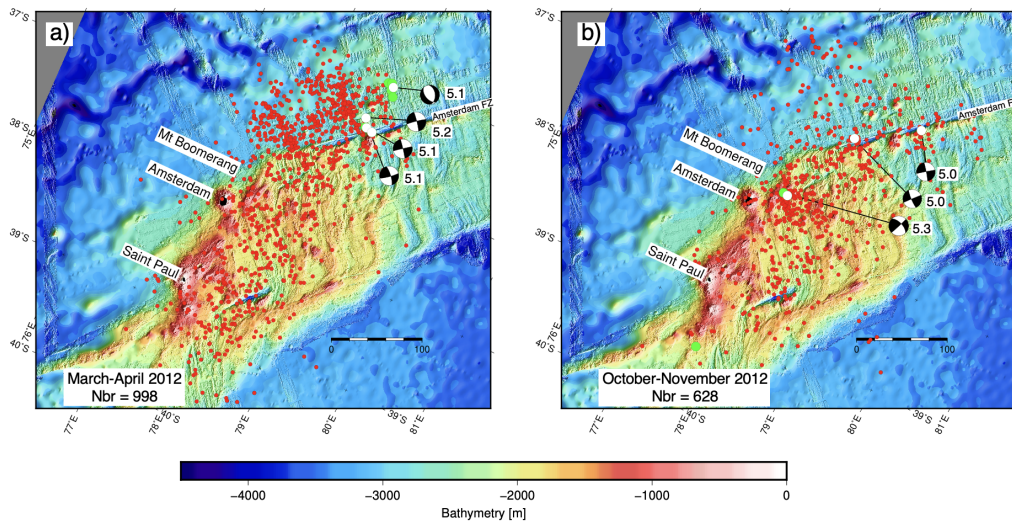


Figure F1: Locations of OHA (red), ISC (green), and GCMT (white) events along the SPA plateau detected in 2012 using hydrophones of OHASISBIO and IMS-CTBTO network: **a)** March-April and **b)** October-November. The GCMT solutions show both reverse and strike-slip mechanisms in **a)** while only strike-slip in **b)**

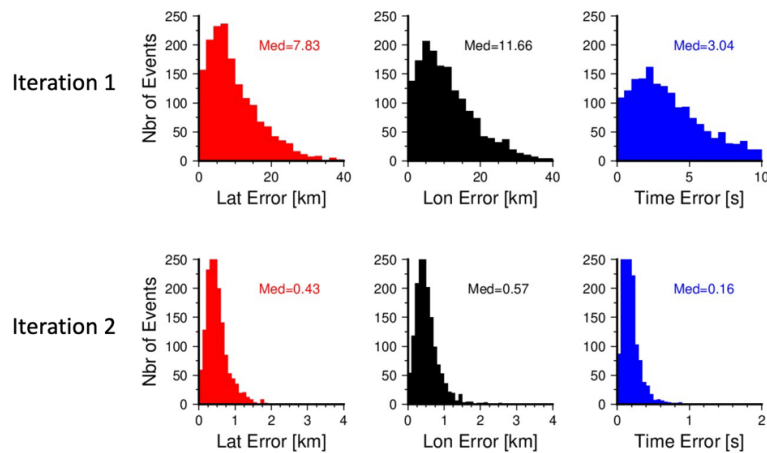


Figure F2: Improvements in the error distributions in location (latitude and longitude) and origin time for all hydroacoustic events from seismic cluster near SPA plateau between the first iteration (upper panel) and the second iteration (lower panel).

11.66 km, which was ~ 2 times that of the median of longitude errors (5.03 km) along segments at 28°S-29°S and nearly half of that for the events along the J3 segment (23.66 km). The median latitude error is smaller compared with that of the longitude error and it is of similar extent to that observed in two other regions. The comparison of localization errors observed in this region with that of the other two sections of the SEIR fails to give a concrete answer to the spatial distribution of the events.

In March-April, the seismic activity was distributed in an episodic manner (Figure F3). Between 10-12 March, it showed a mild seismic activity rate (number of events per 3 hours), here ≤ 4 . At the end of 14 March, the activity rate increased to ~ 18 and it decreased gradually by 19 March. It then increased up to ~ 15 on 20 March followed by a diminished activity rate until 23 March.

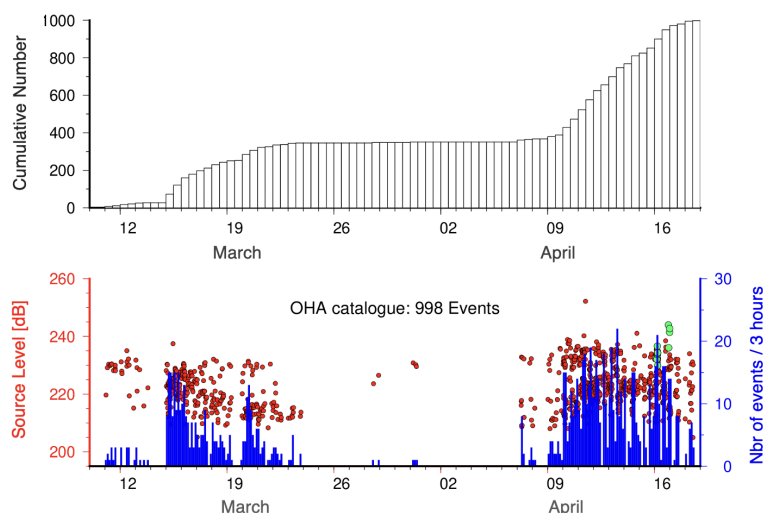


Figure F3: *Top panel: the cumulative number histogram for events in March-April 2012. Bottom panel: the histogram of event count per 3 hours (blue) with SL of OHA (red) and ISC (green) events.*

Between 24 March and 07 April, the seismicity showed quiescence. After 8 April, the activity rate was consistently high for the next 10 days with few instances showing ≥ 20 events per 3 hours. Out of 998 events, 633 events were detected in these 10 days. The strong events (ISC/GCMT) were observed near the end of the seismicity, similar to that observed along 28°S-29°S segments of the SEIR (Figures 5.7, 5.9). We did not observe any mainshock-aftershock sequence fitting the MOL in this swarm.

In October-November, activity was mildly started on 11 October after an event already reported in the ISC catalog (Figure F4). This seismicity steadily decreased until 15 October, followed by a short quiet period. The activity rate increased sharply on 16 October, after an M_w 5.0 event show-

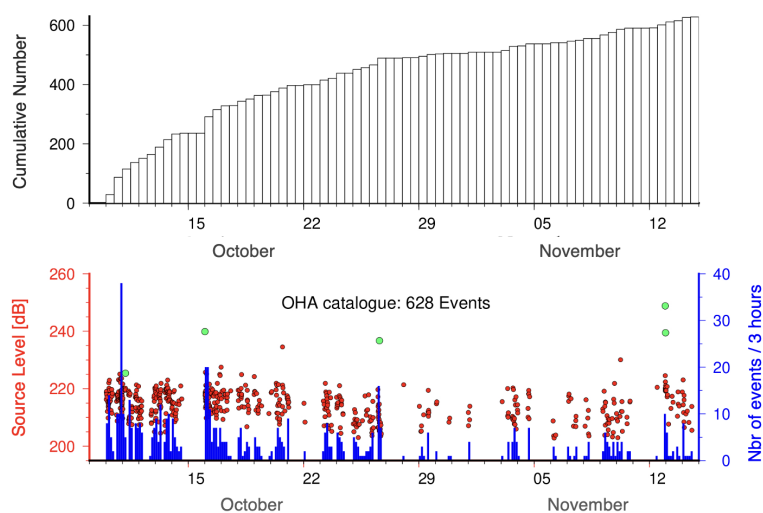


Figure F4: *Top panel: the cumulative number histogram for events in October-November 2012. Bottom panel: the histogram of event count per 3 hours (blue) with SL of OHA (red) and ISC (green) events.*

ing a strike-slip mechanism, along the transform boundary. It was followed by alternate periods of

high and low activity rates until 20 October. Again, there was a quiescence on 21-22 October. Between 22 and 26 October, the activity rate again fluctuated until the next event showed a strike-slip mechanism (M_w 5.0 on 26 October). Between 27 October and 11 November, the activity rate was very mild, with uneven periods of quiescence and seismic activity. The strongest event of both the swarms with M_w 5.3, occurred on 12 November near the Boomerang transform boundary, after which the seismic activity ceased down and eventually ended by 14 November. The episodic activity prior to or following the strong events was likewise observed along the 29°S segment in 2018 (Figure 5.8).

In this thesis, I have tried to understand the nature of individual swarms by looking at the spatio-temporal distribution of the events. For the case of events near the SPA plateau, the temporal distribution showed similarities with that observed along the 29°S segment. In contrast, the spatial distribution of events remained scattered even after two iterations of picking.

References

- Andrew, R. K., Howe, B. M., Mercer, J. A., and Dzieciuch, M. A. (2002). Ocean ambient sound: comparing the 1960s with the 1990s for a receiver off the California coast. *Acoustics research letters online*, 3(2):65–70.
- Baer, G., Hamiel, Y., Shamir, G., and Nof, R. (2008). Evolution of a magma-driven earthquake swarm and triggering of the nearby Oldoinyo Lengai eruption, as resolved by InSAR, ground observations and elastic modeling, East African Rift, 2007. *Earth and Planetary Science Letters*, 272(1-2):339–352.
- Baker, E. T., H'èmond, C., Briaies, A., Maia, M., Scheirer, D. S., Walker, S. L., Wang, T., and Chen, Y. J. (2014). Correlated patterns in hydrothermal plume distribution and apparent magmatic budget along 2500 km of the Southeast Indian Ridge. *Geochemistry, Geophysics, Geosystems*, 15(8):3198–3211.
- Balanche, A., Guennou, C., Goslin, J., and Mazoyer, C. (2009). Generation of hydroacoustic signals by oceanic sub-seafloor earthquakes: A mechanical model. *Geophysical Journal International*, 177(2):476–480.
- Bazin, S., Harding, A., Kent, G., Orcutt, J., Singh, S., Tong, C., Pye, J., Barton, P., Sinha, M., White, R., and others (2003). A three-dimensional study of a crustal low velocity region beneath the 9°03'N overlapping spreading center. *Geophysical research letters*, 30(2).
- Bazin, S., Royer, J.-Y., Dubost, E., Paquet, F., Loubrieu, B., Lavyssièrè, A., Deplus, C., Feuillet, N., Jacques, c., Rinnert, E., Thinon, I., Lebas, c., Pierre, D., Retaillèau, L., Saurel, J.-M., Sukhovich, A., Bonnet, R., and The Revosima Group (2023). Initial results from a hydroacoustic network to monitor submarine lava flows near Mayotte Island. *Comptes Rendus. Geoscience*, 354(S2):257–273.
- Bergman, E. A. and Solomon, S. C. (1990). Earthquake swarms on the Mid-Atlantic Ridge: Products of magmatism or extensional tectonics? *Journal of Geophysical Research: Solid Earth*, 95(B4):4943–4965.
- Bevington, P. R., Robinson, D. K., Blair, J. M., Mallinckrodt, A. J., and McKay, S. (1993). Data reduction and error analysis for the physical sciences. *Computers in Physics*, 7(4):415–416.
- Boettcher, M. S. and Jordan, T. H. (2004). Earthquake scaling relations for mid-ocean ridge transform faults. *Journal of Geophysical Research: Solid Earth*, 109(B12).
- Bohnenstiehl, D. and Dziak, R. (2009). *Mid-Ocean Ridge Seismicity*.
- Bohnenstiehl, D. R. (2005). A different kind of foreshock. *Nature*, 434(7032):445–447.
- Bohnenstiehl, D. R., Dziak, R. P., Tolstoy, M., Fox, C. G., and Fowler, M. (2004). Temporal and spatial history of the 1999-2000 Endeavour Segment seismic series, Juan de Fuca Ridge. *Geochemistry, Geophysics, Geosystems*, 5(9).

- Bohnenstiehl, D. R. and Tolstoy, M. (2003). Comparison of Teleseismically and Hydroacoustically Derived Earthquake Locations along the North-central Mid-Atlantic Ridge and Equatorial East Pacific Rise. *Seismological Research Letters*, 74(6):791–802.
- Bohnenstiehl, D. R., Tolstoy, M., Dziak, R. P., Fox, C. G., and Smith, D. K. (2002). Aftershock sequences in the mid-ocean ridge environment: an analysis using hydroacoustic data. *Tectonophysics*, 354(1):49–70.
- Bohnenstiehl, D. R., Waldhauser, F., and Tolstoy, M. (2008). Frequency-magnitude distribution of microearthquakes beneath the 9°42' N region of the East Pacific Rise, October 2003 through April 2004. *Geochemistry, Geophysics, Geosystems*, 9(10).
- Bottero, A., Cristini, P., Monteiller, V., and Oleg, G. (2023). 3d numerical modeling of abyssal t-wave generation by scattering on rough ocean surfaces. In *Underwater Acoustics Conference and Exhibition*. UACE, Kalamata, Greece.
- Briais, A. (1995). Structural analysis of the segmentation of the Central Indian Ridge between 20°S and 25°S (Rodriguez Triple Junction). *Mar Geophys Res*, 17(5):431–467.
- Burgmann, R., Ayhan, M. E., Fielding, E. J., Wright, T. J., McClusky, S., Aktug, B., Demir, C., Lenk, O., and Turkezer, A. (2002). Deformation during the 12 november 1999 duzce, turkey, earthquake, from gps and insar data. *Bulletin of the Seismological Society of America*, 92(1):161–171.
- Cannat, M. (1996). How thick is the magmatic crust at slow spreading oceanic ridges? *Journal of Geophysical Research: Solid Earth*, 101(B2):2847–2857.
- Cannat, M., Rommevaux-Jestin, C., Sauter, D., Deplus, C., and Mendel, V. (1999). Formation of the axial relief at the very slow spreading Southwest Indian Ridge (49° to 69°E). *Journal of Geophysical Research: Solid Earth*, 104(B10):22825–22843.
- Cao, H., Sun, Z., Zhai, S., Cao, Z., Jiang, X., Huang, W., Wang, L., Zhang, X., and He, Y. (2018). Hydrothermal processes in the Edmond deposits, slow-to intermediate-spreading Central Indian Ridge. *Journal of Marine Systems*, 180:197–210.
- Cesca, S., Metz, M., Büyükakpınar, P., and Dahm, T. (2023). The Energetic 2022 Seismic Unrest Related to Magma Intrusion at the North Mid-Atlantic Ridge. *Geophysical Research Letters*, 50(13):e2023GL102782.
- Cessaro, R. K. and Hussong, D. M. (1986). Transform seismicity at the intersection of the oceanographer fracture zone and the Mid-Atlantic Ridge. *Journal of Geophysical Research: Solid Earth*, 91(B5):4839–4853.
- Chapman, N. and Marrett, R. (2006). The directionality of acoustic T-phase signals from small magnitude submarine earthquakes. *The Journal of the Acoustical Society of America*, 119(6):3669–3675.
- Chen, J., Crawford, W. C., and Cannat, M. (2023). Microseismicity and lithosphere thickness at a nearly-amagmatic oceanic detachment fault system. *Nature Communications*, 14(1):430.
- Chu, D. and Gordon, R. G. (1999). Evidence for motion between Nubia and Somalia along the Southwest Indian ridge. *Nature*, 398(6722):64–67.
- Collins, M. P. (1936). Bulletin Number 5. In *Harvard University Seismograph Station*, page 23.

- Conder, J. A., Scheirer, D. S., and Forsyth, D. W. (2000). Seafloor spreading on the Amsterdam-St. Paul hotspot plateau. *Journal of Geophysical Research: Solid Earth*, 105(B4):8263–8277.
- Crawford, W. C., Rai, A., Singh, S. C., Cannat, M., Escartín, J., Wang, H., Daniel, R., and Combier, V. (2013). Hydrothermal seismicity beneath the summit of lucky strike volcano, mid-atlantic ridge. *Earth and Planetary Science Letters*, 373:118–128.
- Creamer, F. (1993). The relation between temperature and the Omori decay parameter for aftershock sequences near Japan. *EOS*, 74(43):417.
- Crone, T. J., Wilcock, W. S., and McDuff, R. E. (2010). Flow rate perturbations in a black smoker hydrothermal vent in response to a mid-ocean ridge earthquake swarm. *Geochemistry, Geophysics, Geosystems*, 11(3).
- Das, R., Wason, H., and Sharma, M. L. (2011). Global regression relations for conversion of surface wave and body wave magnitudes to moment magnitude. *Natural hazards*, 59:801–810.
- Davis, S. D. and Frohlich, C. (1991). Single-link cluster analysis, synthetic earthquake catalogues, and aftershock identification. *Geophysical Journal International*, 104(2):289–306.
- de Groot-Hedlin, C. D. and Orcutt, J. A. (1999). Synthesis of earthquake-generated T-waves. *Geophysical Research Letters*, 26(9):1227–1230.
- Debayle, E. and Lévêque, J. J. (1997). Upper mantle heterogeneities in the Indian Ocean from waveform inversion. *Geophysical Research Letters*, 24(3):245–248.
- DeMets, C., Gordon, R. G., Argus, D., and Stein, S. (1990). Current plate motions. *Geophysical journal international*, 101(2):425–478.
- DeMets, C., Gordon, R. G., and Argus, D. F. (2010). Geologically current plate motions. *Geophysical Journal International*, 181(1):1–80.
- Dieterich, J. (1994). A constitutive law for rate of earthquake production and its application to earthquake clustering. *Journal of Geophysical Research: Solid Earth*, 99(B2):2601–2618.
- Dyment, J., Gallet, Y., and the Magofond 2 scientific party (1999). The magofond 2 cruise: a surface and deep-tow survey on the past and present central indian ridge. *International Ridge-Crest Research*, 8(1):25–31.
- Dziak, R., Bohnenstiehl, D., Cowen, J., Baker, E., Rubin, K., Haxel, J., and Fowler, M. (2007). Rapid dike emplacement leads to eruptions and hydrothermal plume release during seafloor spreading events. *Geology*, 35(7):579–582.
- Dziak, R., Hammond, S., and Fox, C. (2011). A 20-Year Hydroacoustic Time Series of Seismic and Volcanic Events in the Northeast Pacific Ocean. *Oceanography*, 24(3):280–293.
- Dziak, R., Haxel, J., Bohnenstiehl, D., Chadwick Jr, W., Noonan, S. L., Fowler, M., Matsumoto, H., and Butterfield, D. (2012). Seismic precursors and magma ascent before the April 2011 eruption at Axial Seamount. *Nature Geoscience*, 5(7):478–482.
- Dziak, R. P. (2001). Empirical relationship of T-wave energy and fault parameters of northeast Pacific Ocean earthquakes. *Geophysical Research Letters*, 28(13):2537–2540.

- Dziak, R. P., Chadwick Jr, W. W., Fox, C. G., and Embley, R. W. (2003). Hydrothermal temperature changes at the southern Juan de Fuca ridge associated with MW 6.2 Blanco Transform earthquake. *Geology*, 31(2):119–122.
- Dziak, R. P., Fowler, M. J., Matsumoto, H., Bohnenstiehl, D. R., Park, M., Warren, K., and Lee, W. S. (2013). Life and death sounds of iceberg A53a. *Oceanography*, 26(2):10–13.
- Dziak, R. P. and Fox, C. G. (1999). The January 1998 Earthquake swarm at Axial Volcano, Juan de Fuca Ridge: Hydroacoustic evidence of seafloor volcanic activity. *Geophysical Research Letters*, 26(23):3429–3432.
- Dziak, R. P., Fox, C. G., and Schreiner, A. E. (1995). The June–July 1993 seismo-acoustic event at CoAxial segment, Juan de Fuca Ridge: Evidence for a lateral dike injection. *Geophysical Research Letters*, 22(2):135–138.
- Dziak, R. P., Smith, D. K., Bohnenstiehl, D. R., Fox, C. G., Desbruyeres, D., Matsumoto, H., Tolstoy, M., and Fornari, D. J. (2004). Evidence of a recent magma dike intrusion at the slow spreading Lucky Strike segment, Mid-Atlantic Ridge. *Journal of Geophysical Research: Solid Earth*, 109(B12).
- Einarsson, P., Brandsdóttir, B., and others (1980). Seismological evidence for lateral magma intrusion during the July 1978 deflation of the Krafla volcano in NE-Iceland. *Journal of Geophysics*, 47(1):160–165.
- Ekström, G., Nettles, M., and Dziewoński, A. (2012). The global CMT project 2004–2010: Centroid-moment tensors for 13,017 earthquakes. *Physics of the Earth and Planetary Interiors*, 200:1–9.
- Engeln, J. F., Wiens, D. A., and Stein, S. (1986). Mechanisms and depths of Atlantic transform earthquakes. *Journal of Geophysical Research: Solid Earth*, 91(B1):548–577.
- Escartín, J., Smith, D. K., Cann, J., Schouten, H., Langmuir, C. H., and Escrig, S. (2008). Central role of detachment faults in accretion of slow-spreading oceanic lithosphere. *Nature*, 455(7214):790–794.
- Escartín, J., Soule, S. A., Fornari, D. J., Tivey, M. A., Schouten, H., and Perfit, M. R. (2007). Interplay between faults and lava flows in construction of the upper oceanic crust: The East Pacific Rise crest 9°25′–9°58′N. *Geochemistry, Geophysics, Geosystems*, 8(6).
- Ewing, M., Woollard, G. P., Vine, A., and Worzel, J. (1946). Recent results in submarine geophysics. *Geological Society of America Bulletin*, 57(10):909–934.
- Farrell, W. (1972). Deformation of the earth by surface loads. *Reviews of Geophysics*, 10(3):761–797.
- Fisher, R. L., SCLATER, J. G., and MCKENZIE, D. P. (1971). Evolution of the Central Indian Ridge, Western Indian Ocean. *GSA Bulletin*, 82(3):553–562.
- Forsyth, D. and Uyeda, S. (1975). On the relative importance of the driving forces of plate motion. *Geophysical Journal International*, 43(1):163–200.
- Fox, C. G. and Dziak, R. P. (1998). Hydroacoustic detection of volcanic activity on the Gorda Ridge, February–March 1996. *Deep Sea Research Part II: Topical Studies in Oceanography*, 45(12):2513–2530.
- Fox, C. G., Matsumoto, H., and Lau, T.-K. A. (2001). Monitoring Pacific Ocean seismicity from an autonomous hydrophone array. *Journal of Geophysical Research: Solid Earth*, 106(B3):4183–4206.

- Fox, C. G., Radford, W. E., Dziak, R. P., Lau, T.-K., Matsumoto, H., and Schreiner, A. E. (1995). Acoustic detection of a seafloor spreading episode on the Juan de Fuca Ridge using military hydrophone arrays. *Geophysical Research Letters*, 22(2):131–134.
- Francis, T. (1974). A new interpretation of the 1968 Fernandina caldera collapse and its implications for the mid-oceanic ridges. *Geophysical Journal International*, 39(2):301–318.
- Francis, T., Porter, I., and Lilwall, R. (1978). Microearthquakes near the eastern end of St Paul's Fracture Zone. *Geophysical Journal International*, 53(2):201–217.
- Francis, T. J. G. (1968). Seismicity of Mid-oceanic Ridges and its relation to Properties of the Upper Mantle and Crust. *Nature*, 220(5170):899–901.
- Frohlich, C. and Davis, S. D. (1993). Teleseismic b values; or, much ado about 1.0. *Journal of Geophysical Research: Solid Earth*, 98(B1):631–644.
- Gallant, R. and Von Damm, K. (2006). Geochemical controls on hydrothermal fluids from the Kairei and Edmond vent fields, 23–25°S, Central Indian Ridge. *Geochemistry, Geophysics, Geosystems*, 7(6).
- Georgen, J. E., Lin, J., and Dick, H. J. (2001). Evidence from gravity anomalies for interactions of the Marion and Bouvet hotspots with the Southwest Indian Ridge: Effects of transform offsets. *Earth and Planetary Science Letters*, 187(3-4):283–300.
- Giusti, M., Perrot, J., Dziak, R. P., Sukhovich, A., and Maia, M. (2018). The August 2010 earthquake swarm at North FAMOUS-FAMOUS segments, Mid-Atlantic Ridge: geophysical evidence of dike intrusion. *Geophysical Journal International*, 215(1):181–195.
- Glen, W. (1982). *The road to Jaramillo: Critical years of the revolution in earth science*. Stanford University Press.
- Goslin, J., Lourenço, N., Dziak, R. P., Bohnenstiehl, D. R., Haxel, J., and Luis, J. (2005). Long-term seismicity of the Reykjanes Ridge (North Atlantic) recorded by a regional hydrophone array. *Geophysical Journal International*, 162(2):516–524.
- Goslin, J., Perrot, J., Royer, J.-Y., Martin, C., Lourenço, N., Luis, J., Dziak, R. P., Matsumoto, H., Fowler, M. J., Fox, C. G., Lau, A. T.-K., and Bazin, S. (2012). Spatiotemporal distribution of the seismicity along the Mid-Atlantic Ridge north of the Azores from hydroacoustic data: Insights into seismogenic processes in a ridge-hot spot context. *Geochemistry, Geophysics, Geosystems*, 13(2):Q02010.
- Grandin, R., Jacques, E., Nercessian, A., Ayele, A., Doubre, C., Socquet, A., Keir, D., Kassim, M., Lemarchand, A., and King, G. C. (2011). Seismicity during lateral dike propagation: Insights from new data in the recent Manda Hararo–Dabbahu rifting episode (Afar, Ethiopia). *Geochemistry, Geophysics, Geosystems*, 12(4).
- Grevemeyer, I., Hayman, N. W., Lange, D., Peirce, C., Papenberg, C., Van Avendonk, H. J., Schmid, F., De La Peña, L. G., and Dannowski, A. (2019). Constraining the maximum depth of brittle deformation at slow- and ultraslow-spreading ridges using microseismicity. *Geology*, 47(11):1069–1073.
- Gutenberg, B. and Richter, C. (1954). *Seismicity of the earth and associated phenomena*.

- Hainzl, S., Christophersen, A., Rhoades, D., and Harte, D. (2016). Statistical estimation of the duration of aftershock sequences. *Geophysical Journal International*, 205(2):1180–1189.
- Hainzl, S. and Fischer, T. (2002). Indications for a successively triggered rupture growth underlying the 2000 earthquake swarm in vogtland/nw bohemia. *Journal of Geophysical Research-Part B-Solid Earth*, 107(12).
- Hanks, T. C. and Bakun, W. H. (2002). A bilinear source-scaling model for m-log a observations of continental earthquakes. *Bulletin of the Seismological Society of America*, 92(5):1841–1846.
- Hanson, J. A. and Bowman, J. R. (2005). Indian Ocean ridge seismicity observed with a permanent hydroacoustic network. *Geophysical Research Letters*, 32(6).
- Heezen, B. C., Tharp, M., and Ewing, M. (1959). *The floors of the oceans*, volume 65. Geological Society of America New York.
- Hildebrand, J. A. (2009). Anthropogenic and natural sources of ambient noise in the ocean. *Marine Ecology Progress Series*, 395:5–20.
- Hill, D. P. (1977). A model for earthquake swarms. *Journal of Geophysical Research*, 82(8):1347–1352.
- Ingale, V. V., Bazin, S., Olive, J.-A., Briais, A., and Royer, J.-Y. (2023). Hydroacoustic Study of a Seismic Swarm in 2016–2017 near the Melville Transform Fault on the Southwest Indian Ridge. *Bulletin of the Seismological Society of America*, 113(4):1523–1541.
- Ingale, V. V., Bazin, S., and Royer, J.-Y. (2021). Hydroacoustic observations of two contrasted seismic swarms along the Southwest Indian ridge in 2018. *Geosciences*, 11(6):225.
- Jaggard, T. (1930). How the seismograph works. *The Volcano Letter*, 268:1–4.
- Jamet, G., Guennou, C., Guillon, L., Mazoyer, C., and Royer, J.-Y. (2013). T-wave generation and propagation: A comparison between data and spectral element modeling. *The Journal of the Acoustical Society of America*, 134(4):3376–3385.
- Jensen, F. B., Kuperman, W. A., Porter, M. B., Schmidt, H., and Tolstoy, A. (1994). Computational Ocean Acoustics. *Physics Today*, 47(11):91–92.
- Johnson, H. P., Hutnak, M., Dziak, R. P., Fox, C. G., Urcuyo, I., Cowen, J. P., Nabelek, J., and Fisher, C. (2000a). Earthquake-induced changes in a hydrothermal system on the Juan de Fuca mid-ocean ridge. *Nature*, 407(6801):174–177.
- Johnson, K. T. M., Graham, D. W., Rubin, K. H., Nicolaysen, K., Scheirer, D. S., Forsyth, D. W., Baker, E. T., and Douglas-Priebe, L. M. (2000b). Boomerang Seamount: the active expression of the Amsterdam'96St. Paul hotspot, Southeast Indian Ridge. *Earth and Planetary Science Letters*, 183(1):245–259.
- Johnson, R. H. and Norris, R. A. (1968a). Geographic variation of Sofar speed and axis depth in the Pacific Ocean. *Journal of Geophysical Research*, 73(14):4695–4700.
- Johnson, R. H. and Norris, R. A. (1968b). T-phase radiators in the Western Aleutians. *Bulletin of the Seismological Society of America*, 58(1):1–10.

- Johnson, R. H., Northrop, J., and Eppley, R. (1963). Sources of Pacific T phases. *Journal of Geophysical Research*, 68(14):4251–4260.
- Julian, B. R. and Sipkin, S. A. (1985). Earthquake processes in the Long Valley caldera area, California. *Journal of Geophysical Research: Solid Earth*, 90(B13):11155–11169.
- Kanamori, H. (1977). The energy release in great earthquakes. *Journal of geophysical research*, 82(20):2981–2987.
- Kearey, P., Klepeis, K. A., and Vine, F. J. (2009). *Global tectonics*. John Wiley & Sons.
- Kelemen, P. B., Koga, K., and Shimizu, N. (1997). Geochemistry of gabbro sills in the crust-mantle transition zone of the Oman ophiolite: Implications for the origin of the oceanic lower crust. *Earth and Planetary Science Letters*, 146(3-4):475–488.
- Kent, G., Singh, S., Harding, A., Sinha, M., Orcutt, J., Barton, P., White, R., Bazin, S., Hobbs, R., Tong, C., and others (2000). Evidence from three-dimensional seismic reflectivity images for enhanced melt supply beneath mid-ocean-ridge discontinuities. *Nature*, 406(6796):614–618.
- Kibblewhite, A. and Jones, D. (1976). Ambient noise under Antarctic sea ice. *The Journal of the Acoustical Society of America*, 59(4):790–798.
- Kisslinger, C. (1996). Aftershocks and fault-zone properties. *Advances in geophysics*, 38:1–36.
- Klein, F. W. (1982). Earthquakes at Loihi submarine volcano and the Hawaiian hot spot. *Journal of Geophysical Research: Solid Earth*, 87(B9):7719–7726.
- Kong, L. S. L., Solomon, S. C., and Purdy, G. M. (1992). Microearthquake Characteristics of a Mid-Ocean Ridge along-axis high. *Journal of Geophysical Research*, 97(B2):1659–1685.
- Koulakov, I., Schlindwein, V., Liu, M., Gerya, T., Jakovlev, A., and Ivanov, A. (2022a). Low-degree mantle melting controls the deep seismicity and explosive volcanism of the gakkel ridge. *Nature Communications*, 13(1):3122.
- Koulakov, I., Schlindwein, V., Liu, M., Gerya, T., Jakovlev, A., and Ivanov, A. (2022b). Low-degree mantle melting controls the deep seismicity and explosive volcanism of the Gakkel Ridge. *Nat Commun*, 13(1):3122.
- Kumagai, H., Nakamura, K., Toki, T., Morishita, T., Okino, K., Ishibashi, J.-i., Tsunogai, U., Kawagucci, S., Gamo, T., Shibuya, T., Sawaguchi, T., Neo, N., Joshima, M., Sato, T., and Takai, K. (2008). Geological background of the Kairei and Edmond hydrothermal fields along the Central Indian Ridge: Implications of their vent fluids'92 distinct chemistry. *Geofluids*, 8(4):239–251.
- Lange, D., Cembrano, J., Rietbrock, A., Haberland, C., Dahm, T., and Bataille, K. (2008). First seismic record for intra-arc strike-slip tectonics along the Liqui ne-Ofqui fault zone at the obliquely convergent plate margin of the southern Andes. *Tectonophysics*, 455(1-4):14–24.
- Le Pichon, X. (1968). Sea-floor spreading and continental drift. *Journal of geophysical research*, 73(12):3661–3697.
- Le Saout, M., Bohnenstiehl, D. R., Paduan, J. B., and Clague, D. A. (2020). Quantification of Eruption Dynamics on the North Rift at Axial Seamount, Juan de Fuca Ridge. *Geochemistry, Geophysics, Geosystems*, 21(9).

- Lebrato, M., Wang, Y. V., Tseng, L.-C., Achterberg, E. P., Chen, X.-G., Molinero, J.-C., Bremer, K., Westernströer, U., Söding, E., Dahms, H.-U., and others (2019). Earthquake and typhoon trigger unprecedented transient shifts in shallow hydrothermal vents biogeochemistry. *Scientific Reports*, 9(1):16926.
- Lecoulant, J., Guennou, C., Guillon, L., and Royer, J.-Y. (2019). Three-dimensional modeling of earthquake generated acoustic waves in the ocean in simplified configurations. *The Journal of the Acoustical Society of America*, 146(3):2113–2123.
- Legrand, D., Pertou, M., Macías, J., Siebe, C., Pacheco, J., Chacón, E., Lermo, J., Quintanar, L., and Cisneros, G. (2023). Repeated seismic swarms near Paricutin volcano: precursors to the birth of a new monogenetic volcano in the michoacán-Guanajuato volcanic field, México? *Bulletin of Volcanology*, 85(5):30.
- Leroy, E. C., Samaran, F., Bonnel, J., and Royer, J.-Y. (2016). Seasonal and Diel Vocalization Patterns of Antarctic Blue Whale (*Balaenoptera musculus intermedia*) in the Southern Indian Ocean: A Multi-Year and Multi-Site Study. *PLOS ONE*, 11(11):e0163587.
- Lilwall, R. (1982). Seismicity of the oceanic rifts. *Continental and oceanic rifts*, 8:63–80.
- Linehan, D. (1940). Earthquakes in the West Indian region. *Eos, Transactions American Geophysical Union*, 21(2):229–232.
- Liu, Y., Tao, C., Liu, C., Qiu, L., Schlindwein, V., Zhang, H., Tian, Y., and Wang, H. (2019). Seismic activity recorded by a single OBS/H near the active Longqi hydrothermal vent at the ultraslow spreading Southwest Indian Ridge (49°39'E). *Marine Georesources & Geotechnology*, 37(2):201–211.
- Loubrieu Benoît, Royer Jean-Yves and Maia Marcia (2020). Bathymétrie - St-Paul et Amsterdam, au pas de 150 mètres. doi: <http://dx.doi.org/10.12770/342b2892-b0de-4566-bd77-520fb3bf4eaa>.
- Läderach, C., Korger, E. I. M., Schlindwein, V., M'fcller, C., and Eskstaller, A. (2012). Characteristics of tectonomagmatic earthquake swarms at the Southwest Indian Ridge between 16°b0E and 25°b0E. *Geophysical Journal International*, 190(1):429–441.
- Läderach, C., Schlindwein, V., Schenke, H.-W., and Jokat, W. (2011). Seismicity and active tectonic processes in the ultra-slow spreading Lena Trough, Arctic Ocean. *Geophysical Journal International*, 184(3):1354–1370.
- Macdonald, K. C., Fox, P., Alexander, R. T., Pockalny, R., and Gente, P. (1996). Volcanic growth faults and the origin of Pacific abyssal hills. *Nature*, 380(6570):125–129.
- Macdonald, K. C., Fox, P. J., Miller, S., Carbotte, S., Edwards, M. H., Eisen, M., Fornari, D. J., Perram, L., Pockalny, R., Scheirer, D., and others (1992). The East Pacific Rise and its flanks 8–18 N: History of segmentation, propagation and spreading direction based on SeaMARC II and Sea Beam studies. *Marine Geophysical Researches*, 14:299–344.
- Maia, M., Pessanha, I., Courrèges, E., Patriat, M., Gente, P., Hémond, C., Janin, M., Johnson, K., Roest, W., Royer, J.-Y., and Vatteville, J. (2011). Building of the Amsterdam-Saint Paul plateau: A 10 Myr history of a ridge-hot spot interaction and variations in the strength of the hot spot source. *Journal of Geophysical Research: Solid Earth*, 116(B9).
- Matsumoto, K., Sato, T., Takanezawa, T., and Ooe, M. (2001). GOTIC2: A program for computation of oceanic tidal loading effect. *Journal of the Geodetic Society of Japan*, 47(1):243–248.

- McGuire, J. J., Boettcher, M. S., and Jordan, T. H. (2005). Foreshock sequences and short-term earthquake predictability on East Pacific Rise transform faults. *Nature*, 434(7032):457–461.
- McGuire, J. J., Collins, J. A., Gouédard, P., Roland, E., Lizarralde, D., Boettcher, M. S., Behn, M. D., and Van Der Hilst, R. D. (2012). Variations in earthquake rupture properties along the Gofar transform fault, East Pacific Rise. *Nature Geoscience*, 5(5):336–341.
- McKenzie, D. P. (1967). Some remarks on heat flow and gravity anomalies. *Journal of Geophysical Research*, 72(24):6261–6273.
- McKenzie, D. P. and Parker, R. L. (1967). The North Pacific: an example of tectonics on a sphere. *Nature*, 216(5122):1276–1280.
- Meade, B. J. (2007). Algorithms for the calculation of exact displacements, strains, and stresses for triangular dislocation elements in a uniform elastic half space. *Computers & geosciences*, 33(8):1064–1075.
- Medwin, H. (1975). Speed of sound in water: A simple equation for realistic parameters. *The Journal of the Acoustical Society of America*, 58(6):1318–1319.
- Mendel, V., Sauter, D., Parson, L., and Vanney, J.-R. (1997). Segmentation and Morphotectonic Variations Along a Super Slow-Spreading Center: The Southwest Indian Ridge (57°E-70°E). *Marine Geophysical Researches*, 19(6):505–533.
- Mendel, V., Sauter, D., Rommevaux-Jestin, C., Patriat, P., Lefebvre, E., and Parson, L. M. (2003). Magmato-Tectonic Cyclicity at the Ultra-Slow Spreading Southwest Indian Ridge: Evidence from Variations of Axial Volcanic Ridge Morphology and Abyssal Hills Pattern. *Geochemistry, Geophysics, Geosystems*, 4(5).
- Miksis-Olds, J. L., Bradley, D. L., and Maggie Niu, X. (2013). Decadal trends in Indian Ocean ambient sound. *The Journal of the Acoustical Society of America*, 134(5):3464–3475.
- Mogi, K. (1967). Earthquakes and fractures. *Tectonophysics*, 5(1):35–55.
- Morgan, J. P. and Forsyth, D. W. (1988). Three-dimensional flow and temperature perturbations due to a transform offset: Effects on oceanic crustal and upper mantle structure. *Journal of Geophysical Research: Solid Earth*, 93(B4):2955.
- Métivier, L., de Viron, O., Conrad, C. P., Renault, S., Diamant, M., and Patau, G. (2009). Evidence of earthquake triggering by the solid earth tides. *Earth and Planetary Science Letters*, 278(3-4):370–375.
- Müller, M. R., Minshull, T. A., and White, R. S. (2000). Crustal structure of the Southwest Indian Ridge at the Atlantis II Fracture Zone. *Journal of Geophysical Research*, 105(B11):25809–25828.
- Nakada, S., Shimizu, H., and Ohta, K. (1999). Overview of the 1990–1995 eruption at Unzen Volcano. *Journal of Volcanology and Geothermal Research*, 89(1-4):1–22.
- Nicolaysen, K. P., Frey, F. A., Mahoney, J. J., Johnson, K. T. M., and Graham, D. W. (2007). Influence of the Amsterdam/St. Paul hot spot along the Southeast Indian Ridge between 77° and 88°E: Correlations of Sr, Nd, Pb, and He isotopic variations with ridge segmentation. *Geochemistry, Geophysics, Geosystems*, 8(9).

- Nielsen, P. L., Zampolli, M., Le Bras, R., Mialle, P., Bittner, P., Poplavskiy, A., Rozhkov, M., Haralabus, G., Tomuta, E., Bell, R., and others (2021). CTBTO's data and analysis pertaining to the search for the missing Argentine submarine ARA San Juan. *Pure and Applied Geophysics*, 178(7):2557–2577.
- NOAA (2009). Etopo 2022 15 arc-second global relief model. noaa national centers for environmental information. doi: <https://doi.org/10.25921/fd45-gt74>.
- Ogata, Y. (1983). Estimation of the Parameters in the Modified Omori Formula for Aftershock Frequencies by the Maximum Likelihood Procedure. *Journal of Physics of the Earth*, 31(2):115–124.
- Okal, E. A. (2001). T-phase stations for the International Monitoring System of the Comprehensive Nuclear-Test Ban Treaty: A global perspective. *Seismological Research Letters*, 72(2):186–196.
- Okal, E. A. (2008). The generation of T waves by earthquakes. *Advances in Geophysics*, 49:1–65.
- Okino, K., Nakamura, K., and Sato, H. (2015). Tectonic Background of Four Hydrothermal Fields Along the Central Indian Ridge. In Ishibashi, J.-i., Okino, K., and Sunamura, M., editors, *Subseafloor Biosphere Linked to Hydrothermal Systems*, pages 133–146. Springer Japan, Tokyo.
- Olive, J.-A. (2023). Mid-Ocean Ridges: geodynamics written in the seafloor. In *Dynamics of plate tectonics and mantle convection*, pages 483–510. Elsevier.
- Olive, J.-A. and Escartín, J. (2016). Dependence of seismic coupling on normal fault style along the northern mid-atlantic ridge. *Geochemistry, Geophysics, Geosystems*, 17(10):4128–4152.
- Omori, F. (1894). On the after-shocks of earthquakes. *Journal of the College of Science (Imperial University of Tokyo)*, 7:111–120.
- Pan, J. and Dziewonski, A. M. (2005). Comparison of mid-oceanic earthquake epicentral differences of travel time, centroid locations, and those determined by autonomous underwater hydrophone arrays. *Journal of Geophysical Research: Solid Earth*, 110(B7).
- Park, M., Odom, R. I., and Soukup, D. J. (2001). Modal scattering: A key to understanding oceanic T-waves. *Geophysical Research Letters*, 28(17):3401–3404.
- Parnell-Turner, R., Smith, D. K., and Dziak, R. P. (2022). Hydroacoustic Monitoring of Seafloor Spreading and Transform Faulting in the Equatorial Atlantic Ocean. *Journal of Geophysical Research: Solid Earth*, 127(7).
- Parson, L. M., Patriat, P., Searle, R. C., and Briais, A. R. (1993). Segmentation of the Central Indian Ridge between 12°12'S and the Indian Ocean Triple Junction. *Marine Geophysical Researches*, 15(4):265–282.
- Patriat, P., Sauter, D., Munsch, M., and Parson, L. (1997). A Survey of the Southwest Indian Ridge Axis Between Atlantis II Fracture Zone and the Indian Ocean Triple Junction: Regional Setting and Large Scale Segmentation. *Marine Geophysical Researches*, 19(6):457–480.
- Phipps Morgan, J. and Chen, Y. J. (1993). Dependence of ridge-axis morphology on magma supply and spreading rate. *Nature*, 364(6439):706–708.
- Pontbriand, C. W. and Sohn, R. A. (2014). Microearthquake evidence for reaction-driven cracking within the Trans-Atlantic Geotraverse active hydrothermal deposit. *Journal of Geophysical Research: Solid Earth*, 119(2):822–839.

- Raumer, P.-Y., Bazin, S., Cazau, D., Ingale, V. V., Lavayssière, A., and Royer, J.-Y. (2023). Application of machine learning to hydro-acoustic seismic and magmatic events detections. EGU General Assembly, 2023, Vienna, Austria. doi: 10.5194/egusphere-egu23-7028.
- Reichle, M. and Reid, I. (1977). Detailed study of earthquake swarms from the Gulf of California. *Bulletin of the Seismological Society of America*, 67(1):159–171.
- Royer, J.-Y. (2008). VT 95/DEFLO-HYDRO-A cruise, RV Marion Dufresne. doi: <https://doi.org/10.17600/18000740>.
- Royer, J.-Y. (2009). OHA-SIS-BIO - observatoire hydroacoustique. Technical report. doi: <https://doi.org/10.18142/229>.
- Royer, J.-Y., Chateau, R., Dziak, R. P., and Bohnenstiehl, D. R. (2015). Seafloor seismicity, Antarctic ice-sounds, cetacean vocalizations and long-term ambient sound in the Indian Ocean basin. *Geophysical Journal International*, 202(2):748–762.
- Royer, J.-Y. and Sandwell, D. T. (1989). Evolution of the eastern Indian Ocean since the Late Cretaceous: Constraints from Geosat altimetry. *Journal of Geophysical Research: Solid Earth*, 94(B10):13755–13782.
- Royer, J.-Y. and Schlich, R. (1988). Southeast Indian Ridge Between the Rodriguez Triple Junction and the Amsterdam and Saint-Paul Islands: Detailed Kinematics for the Past 20 m.y. *Journal of Geophysical Research: Solid Earth*, 93(B11):13524–13550.
- Rubin, A. M., Gillard, D., and Got, J.-L. (1998). A reinterpretation of seismicity associated with the January 1983 dike intrusion at Kilauea Volcano, Hawaii. *Journal of Geophysical Research: Solid Earth*, 103(B5):10003–10015.
- Rubin, A. M. and Pollard, D. D. (1988). Dike-induced faulting in rift zones of Iceland and Afar. *Geology*, 16(5):413–417.
- Rundquist, D. V. and Sobolev, P. O. (2002). Seismicity of mid-oceanic ridges and its geodynamic implications: a review. *Earth-Science Reviews*, 58(1):143–161.
- Sahoo, S., Senapati, B., Panda, D., Tiwari, D. K., Santosh, M., and Kundu, B. (2021). Tidal triggering of micro-seismicity associated with caldera dynamics in the Juan de Fuca ridge. *Journal of Volcanology and Geothermal Research*, 417:107319.
- Sato, T., Takata, H., Morii, A., Yamada, S., Yamada, T., and Shinohara, M. (2023). Seismic velocity structure and seismicity at the kairei hydrothermal vent field near the rodriguez triple junction in the indian ocean. *Available at SSRN 4472332 (non peer reviewed)*.
- Saurel, J.-M., Retailleau, L., Deplus, C., Loubrieu, B., Pierre, D., Frangieh, M., Khelifi, N., Bonnet, R., Ferrazzini, V., Bazin, S., Guyavarch, P., Moulin, M., Revosima Seismology Group, and Revosima Bathymetry Group (2022). Combining hydro-acoustic sources and bathymetric differences to track the vent evolution of the Mayotte eruption, Mozambique Channel. *Frontiers of Earth Science*, 10:983051.
- Sauter, D. and Cannat, M. (2010). The ultraslow spreading Southwest Indian Ridge. In Rona, P. A., Devey, C. W., Dymont, J., and Murton, B. J., editors, *Geophysical Monograph Series*, volume 188, pages 153–173. American Geophysical Union, Washington, D. C.
- Sauter, D., Cannat, M., Rouméjon, S., Andreani, M., Birot, D., Bronner, A., Brunelli, D., Carlut, J., Delacour, A., Guyader, V., and others (2013). Continuous exhumation of mantle-derived rocks at the Southwest Indian Ridge for 11 million years. *Nature Geoscience*, 6(4):314–320.

- Sauter, D., Whitechurch, H., Munsch, M., and Humler, E. (1991). Periodicity in the accretion process on the Southeast Indian Ridge at 27°42'S. *Tectonophysics*, 195(1):47–64.
- Scheirer, D. S., Baker, E. T., and Johnson, K. T. M. (1998). Detection of hydrothermal plumes along the Southeast Indian Ridge near the Amsterdam-St. Paul Plateau. *Geophysical Research Letters*, 25(1):97–100.
- Scheirer, D. S., Forsyth, D. W., Conder, J. A., Eberle, M. A., Hung, S.-H., Johnson, K. T. M., and Graham, D. W. (2000). Anomalous seafloor spreading of the Southeast Indian Ridge near the Amsterdam-St. Paul Plateau. *Journal of Geophysical Research: Solid Earth*, 105(B4):8243–8262.
- Schlich, R. (1982). The Indian Ocean: aseismic ridges, spreading centers, and oceanic basins. *The Ocean Basins and Margins: The Indian Ocean*, pages 51–147.
- Schlindwein, V. (2012). Teleseismic earthquake swarms at ultraslow spreading ridges: indicator for dyke intrusions? *Geophysical Journal International*, 190(1):442–456.
- Schlindwein, V., Demuth, A., Korger, E., Läderach, C., and Schmid, F. (2015). Seismicity of the Arctic mid-ocean Ridge system. *Polar Science*, 9(1):146–157.
- Schlindwein, V., Müller, C., and Jokat, W. (2005). Seismoacoustic evidence for volcanic activity on the ultraslow-spreading Gakkel Ridge, Arctic Ocean. *Geophysical Research Letters*, 32(18).
- Schlindwein, V., Müller, C., and Jokat, W. (2007). Microseismicity of the ultraslow-spreading Gakkel ridge, Arctic Ocean: a pilot study. *Geophysical Journal International*, 169(1):100–112.
- Schlindwein, V. and Riedel, C. (2010). Location and source mechanism of sound signals at Gakkel ridge, Arctic Ocean: Submarine Strombolian activity in the 1999-2001 volcanic episode: STROMBOLIAN ERUPTIONS AT GAKKEL RIDGE. *Geochemistry, Geophysics, Geosystems*, 11(1).
- Schmid, A. and Grasso, J.-R. (2012). Omori law for eruption foreshocks and aftershocks. *Journal of Geophysical Research: Solid Earth*, 117(B7).
- Schmid, F. and Schlindwein, V. (2016). Microearthquake activity, lithospheric structure, and deformation modes at an amagmatic ultraslow spreading Southwest Indian Ridge segment. *Geochemistry, Geophysics, Geosystems*, 17(7):2905–2921.
- Schmid, F., Schlindwein, V., Koulakov, I., Plötz, A., and Scholz, J.-R. (2017). Magma plumbing system and seismicity of an active mid-ocean ridge volcano. *Nature Scientific Reports*, 7(1):42949.
- Scholz, C. H., Tan, Y. J., and Albino, F. (2019). The mechanism of tidal triggering of earthquakes at mid-ocean ridges. *Nature Communications*, 10(1):2526.
- Schouten, H., Klitgord, K. D., and Whitehead, J. A. (1985). Segmentation of mid-ocean ridges. *Nature*, 317(6034):225–229.
- Sempere, J.-C., Macdonald, K. C., and Miller, S. P. (1984). Overlapping spreading centres: 3-D inversion of the magnetic field at 9°03'N on the East Pacific Rise. *Geophysical Journal International*, 79(3):799–811.
- Shaw, H. R. and Hargraves, R. (1980). The fracture mechanisms of magma transport from the mantle to the surface. *Physics of magmatic processes*, 64:201–264.

- Shuler, A. and Nettles, M. (2012). Earthquake source parameters for the 2010 western Gulf of Aden rifting episode. *Geophysical Journal International*, 190(2):1111–1122.
- Simão, N., Escartín, J., Goslin, J., Haxel, J., Cannat, M., and Dziak, R. (2010). Regional seismicity of the Mid-Atlantic Ridge: observations from autonomous hydrophone arrays. *Geophysical Journal International*, 183(3):1559–1578.
- Slack, P. D., Fox, C. G., and Dziak, R. P. (1999). P wave detection thresholds, Pn velocity estimates, and T wave location uncertainty from oceanic hydrophones. *Journal of Geophysical Research: Solid Earth*, 104(B6):13061–13072.
- Smith, D. K. (2002). Hydroacoustic monitoring of seismicity at the slow-spreading Mid-Atlantic Ridge. *Geophysical Research Letters*, 29(11):1518.
- Smith, D. K., Escartín, J., Cannat, M., Tolstoy, M., Fox, C. G., Bohnenstiehl, D. R., and Bazin, S. (2003). Spatial and temporal distribution of seismicity along the northern Mid-Atlantic Ridge (15°–35°N). *Journal of Geophysical Research: Solid Earth*, 108(B3).
- Sohn, R. A., Hildebrand, J. A., and Webb, S. C. (1999). A microearthquake survey of the high-temperature vent fields on the volcanically active East Pacific Rise (9°42'N). *Journal of Geophysical Research*, 104(B11):25367–25377.
- Solomon, S. C. and Toomey, D. R. (1992). The structure of mid-ocean ridges. *Annual Review of Earth and Planetary Sciences*, 20(1):329–366.
- Swainson, O. (1936). Velocity and ray paths of sound waves in sea water. *US Coast and Geodetic Survey, Field Engineers Bull.*, 10:64.
- Sykes, L. R. (1967). Mechanism of earthquakes and nature of faulting on the mid-oceanic ridges. *Journal of Geophysical Research*, 72(8):2131–2153.
- Sykes, L. R. (1970). Earthquake swarms and sea-floor spreading. *Journal of Geophysical Research*, 75(32):6598–6611.
- Sykes, L. R. and Sbar, M. L. (1973). Intraplate earthquakes, lithospheric stresses and the driving mechanism of plate tectonics. *Nature*, 245(5424):298–302.
- Talandier, J., Hyvernaud, O., Reymond, D., and Okal, E. A. (2006). Hydroacoustic signals generated by parked and drifting icebergs in the Southern Indian and Pacific Oceans. *Geophysical Journal International*, 165(3):817–834.
- Talandier, J. and Okal, E. A. (1998). On the mechanism of conversion of seismic waves to and from textitT waves in the vicinity of island shores. *Bulletin of the Seismological Society of America*, 88(2):621–632.
- Tan, Y. J., Tolstoy, M., Waldhauser, F., and Wilcock, W. S. D. (2016). Dynamics of a seafloor-spreading episode at the East Pacific Rise. *Nature*, 540(7632):261–265.
- Teague, W. J., Carron, M. J., and Hogan, P. J. (1990). A Comparison Between the Generalized Digital Environmental Model and Levitus climatologies. *Journal of Geophysical Research: Oceans*, 95(C5):7167–7183.
- Tivey, M. A. and Johnson, H. P. (2002). Crustal magnetization reveals subsurface structure of Juan de Fuca Ridge hydrothermal vent fields. *Geology*, 30(11):979–982.
- Toda, S., Stein, R. S., and Sagiya, T. (2002). Evidence from the ad 2000 Izu islands earthquake swarm that stressing rate governs seismicity. *Nature*, 419(6902):58–61.

- Tolstoy, I. and Ewing, M. (1950). The T phase of shallow-focus earthquakes. *Bulletin of the Seismological Society of America*, 40(1):25–51.
- Tolstoy, M. and Bohnenstiehl, D. (2002). ANALYSIS OF HYDROACOUSTIC SIGNALS IN THE INDIAN OCEAN.
- Tolstoy, M., Bohnenstiehl, D., Edwards, M., and Kurras, G. (2001). Seismic character of volcanic activity at the ultraslow-spreading Gakkel Ridge. *Geology*, 29(12):1139–1142.
- Tolstoy, M. and Bohnenstiehl, D. R. (2006). Hydroacoustic contributions to understanding the December 26th 2004 great Sumatra-Andaman Earthquake. *Surv Geophys*, 27(6):633–646.
- Tolstoy, M., Cowen, J. P., Baker, E. T., Fornari, D. J., Rubin, K. H., Shank, T. M., Waldhauser, F., Bohnenstiehl, D. R., Forsyth, D. W., Holmes, R. C., Love, B., Perfit, M. R., Weekly, R. T., Soule, S. A., and Glazer, B. (2006). A Sea-Floor Spreading Event Captured by Seismometers. *Science*, 314(5807):1920–1922.
- Tolstoy, M., Vernon, F. L., Orcutt, J. A., and Wyatt, F. K. (2002). Breathing of the seafloor: Tidal correlations of seismicity at Axial volcano. *Geology*, 30(6):503.
- Tolstoy, M., Waldhauser, F., Bohnenstiehl, D. R., Weekly, R. T., and Kim, W.-Y. (2008). Seismic identification of along-axis hydrothermal flow on the East Pacific Rise. *Nature*, 451(7175):181–184.
- Torres-González, P. A., Luengo-Oroz, N., Lamolda, H., D'Alessandro, W., Albert, H., Iribarren, I. n., Moure-García, D., and Soler, V. (2020). Unrest signals after 46 years of quiescence at cumbre vieja, La Palma, Canary Islands. *Journal of Volcanology and Geothermal Research*, 392:106757.
- Tournadre, J. (2014). Anthropogenic pressure on the open ocean: The growth of ship traffic revealed by altimeter data analysis. *Geophysical Research Letters*, 41(22):7924–7932.
- Tsang-Hin-Sun, E., Royer, J., and Perrot, J. (2016). Seismicity and active accretion processes at the ultraslow-spreading Southwest and intermediate-spreading Southeast Indian ridges from hydroacoustic data. *Geophysical Journal International*, 206(2):1232–1245.
- Tsang-Hin-Sun, E., Royer, J.-Y., and Leroy, E. C. (2015). Low-frequency sound level in the Southern Indian Ocean. *The Journal of the Acoustical Society of America*, 138(6):3439–3446.
- Utsu, T. (1999). Representation and Analysis of the Earthquake Size Distribution: A Historical Review and Some New Approaches. *Pure Applied Geophysics*, 155(2-4):509–535.
- Utsu, T., Ogata, Y., Ritsuko, S., and Matsu-ura (1995). The Centenary of the Omori Formula for a Decay Law of After-shock Activity.
- van der Most, N., Qian, P.-Y., Gao, Y., and Gollner, S. (2023). Active hydrothermal vent ecosystems in the Indian Ocean are in need of protection. *Frontiers in Marine Science*, 9:1067912.
- Van Dover, C. L., Humphris, S. E., Fornari, D., Cavanaugh, C. M., Collier, R., Goffredi, S. K., Hashimoto, J., et al. (2001). Biogeography and Ecological Setting of Indian Ocean Hydrothermal Vents. *Science*, 294(5543):818–823.
- Waldhauser, F. and Tolstoy, M. (2011). Seismogenic structure and processes associated with magma inflation and hydrothermal circulation beneath the East Pacific Rise at 9°42'N. *Geochemistry, Geophysics, Geosystems*, 12(8).

- Wenz, G. M. (1962). Acoustic ambient noise in the ocean: Spectra and sources. *The Journal of the Acoustical Society of America*, 34(12):1936–1956.
- Wessel, P. and Smith, W. H. (1996). A global, self-consistent, hierarchical, high-resolution shoreline database. *Journal of Geophysical Research: Solid Earth*, 101(B4):8741–8743.
- White, S. M., Mason, J. L., Macdonald, K. C., Perfit, M. R., Wanless, V. D., and Klein, E. M. (2009). Significance of widespread low effusion rate eruptions over the past two million years for delivery of magma to the overlapping spreading centers at 9°N East Pacific Rise. *Earth and Planetary Science Letters*, 280(1-4):175–184.
- Wilcock, W. S., Hooft, E. E., Toomey, D. R., McGill, P. R., Barclay, A. H., Stakes, D. S., and Ramirez, T. M. (2009). The role of magma injection in localizing black-smoker activity. *Nature Geoscience*, 2(7):509–513.
- Wilcock, W. S., Stafford, K. M., Andrew, R. K., and Odom, R. I. (2014). Sounds in the ocean at 1–100 Hz. *Annual review of marine science*, 6:117–140.
- Wilcock, W. S. D. (2001). Tidal triggering of microearthquakes on the Juan de Fuca Ridge. *Geophysical Research Letters*, 28(20):3999–4002.
- Wilcock, W. S. D. (2009). Tidal triggering of earthquakes in the Northeast Pacific Ocean. *Geophysical Journal International*, 179(2):1055–1070.
- Williams, C. M., Stephen, R. A., and Smith, D. K. (2006). Hydroacoustic events located at the intersection of the Atlantis (30°N) and Kane (23°40'N) Transform Faults with the Mid-Atlantic Ridge. *Geochemistry, Geophysics, Geosystems*, 7(6).
- Yang, Y. and Forsyth, D. W. (2003). Improving Epicentral and Magnitude Estimation of Earthquakes from T Phases by Considering the Excitation Function. *Bulletin of the Seismological Society of America*, 93(5):2106–2122.
- Yokoyama, I., De la Cruz-Reyna, S., and Esp'indola, J. (1992). Energy partition in the 1982 eruption of El Chich'on volcano, Chiapas, México. *Journal of Volcanology and Geothermal Research*, 51(1-2):1–21.
- Yu, Z., Li, J., Niu, X., Rawlinson, N., Ruan, A., Wang, W., Hu, H., Wei, X., Zhang, J., and Liang, Y. (2018). Lithospheric Structure and Tectonic Processes Constrained by Microearthquake Activity at the Central Ultraslow-Spreading Southwest Indian Ridge (49.2° to 50.8°E). *Journal of Geophysical Research: Solid Earth*, 123(8):6247–6262.
- Zampolli, M., Nielsen, P., Bras, R. L., Bittner, P., Haralabous, G., and Stanley, J. (2021). Detections at IMS hydrophone stations of Primary and Tertiary phases from the sixth announced DPRK underground nuclear test. In *Science and Technology Conference*. CTBTO, Vienna.

Titre : Dynamique de l'accrétion océanique à partir de l'analyse de données hydroacoustiques sur des essaims sismiques le long des trois dorsales de l'océan Indien

Mots clés : essaims sismiques, dorsales médio-océaniques, hydroacoustique, événements impulsifs, océan Indien

Résumé : Les dorsales médio-océaniques sont des limites de plaques caractérisées par l'interaction de processus volcaniques et tectoniques, entraînant la création de nouveaux fonds océaniques. Ces interactions complexes génèrent de nombreux séismes de faible magnitude ($M \leq 4$), qui passent souvent inaperçus auprès des réseaux sismiques terrestres en raison de l'atténuation rapide des ondes sismiques dans la croûte terrestre. Mais, ces séismes génèrent des ondes T (avec des fréquences allant jusqu'à 60 Hz) dans la colonne d'eau à partir de la conversion de l'énergie sismique en ondes hydroacoustiques basse-fréquence au niveau du plancher océanique; celles-ci se propagent sur de grandes distances (plusieurs milliers de km) avec une faible atténuation à travers le guide d'onde acoustique appelé canal SOFAR (*sound fixing and ranging*). Les réseaux d'hydrophones OHASISBIO et IMS-CTBTO, conçus pour enregistrer ces ondes T dans l'océan Indien, englobent trois dorsales médio-océaniques aux vitesses d'expansion contrastées: la dorsale sud-ouest Indienne ultra-lente (SWIR; 14 mm/an), la dorsale centrale Indienne lente (CIR; 40 mm/an) et la dorsale sud-est Indienne à taux intermédiaire (SEIR; 60 mm/an)

qui convergent à la jonction triple de Rodrigues. Dans cette étude, nous avons examiné des essaims sismiques le long de ces trois dorsales à partir d'un ensemble de données hydroacoustiques continues de 2012 à 2020. Un catalogue exhaustif de 38 910 événements hydroacoustiques, couvrant 15 essaims sismiques distincts répartis le long des dorsales SWIR (3), CIR (5), et SEIR (7), a été établi. Ils sont observés à proximité de deux failles transformantes de la SWIR, le long de segments de dorsales des trois rides, et à proximité de champs hydrothermaux de la CIR et de la SEIR. Cinq essaims comprennent de nombreux événements impulsifs de courte durée (10-15 secondes) et de haute énergie, jusqu'à 60 Hz, que nous attribuons à des interactions entre laves éruptives et eau de mer. En examinant la distribution spatio-temporelle des événements de chaque essaim, nous discernons trois origines: magmatique, tectonique, ou une interaction complexe des deux processus. Ces processus semblent être indépendants des taux d'expansion, mais varier avec le contexte tectonique.

Title : Dynamics of seafloor spreading from hydroacoustic analyses of seismic swarms along the three Indian Ocean ridges

Keywords : seismic swarms, mid-oceanic ridges, hydroacoustics, impulsive events, Indian Ocean

Abstract : Mid-ocean ridges represent divergent plate boundaries characterized by the interaction of volcanic and tectonic processes, resulting in the creation of new ocean floor. These complex interactions lead to the occurrence of numerous low-magnitude earthquakes ($M \leq 4$), which often go unnoticed by terrestrial seismic networks due to the rapid attenuation of seismic waves within the Earth's crust. But these earthquakes generate T-waves (with frequencies up to 60 Hz) in the water column from the conversion of seismic waves into low-frequency hydroacoustic waves at the seafloor which propagate over large distances (several thousands of km) with little attenuation through an acoustic waveguide known as the sound fixing and ranging (SOFAR) channel. The OHASISBIO and IMS-CTBTO networks of hydrophones, designed to record these T-waves in the Indian Ocean, encompass three mid-ocean ridges with contrasted spreading rates: the ultra-slow spreading Southwest Indian Ridge (SWIR; 14 mm/yr), the slow spreading Central Indian Ridge (CIR; 40 mm/yr), and the intermediate spreading Southeast Indian Ridge (SEIR; 60 mm/yr) which converge at Rodrigues Triple Junction.

In this study, we have investigated seismic swarms along these three ridges through the analysis of continuous hydroacoustic records from 2012 to 2020. A comprehensive catalog of 38,910 hydroacoustic events, associated with 15 discrete seismic swarms distributed along the SWIR (3), CIR (5), and SEIR (7) has been constructed. They are observed near two transform faults along the SWIR, on ridge segments along the three ridges, and in the vicinity of hydrothermal fields along the CIR and SEIR. Five swarms include many short-duration (~10-15 seconds) and high-energy impulsive events up to 60 Hz, which we attribute to interactions between hot lava and seawater. Through a closer examination of the spatio-temporal distribution of events within each seismic swarm, we have discerned three distinct origins: magmatic, tectonic, or a complex interplay of both processes. These processes are independent of the spreading rates, but depend on the tectonic environments.